CENTRALITY DEPENDENCE OF TWO-PARTICLE NUMBER AND TRANSVERSE MOMENTUM CORRELATIONS IN $\sqrt{s_{NN}}$ = 200 GeV Au+Au COLLISIONS AT RHIC

by

LAURENCE TARINI

DISSERTATION

Submitted to the Graduate School

of Wayne State University,

Detroit, Michigan

in partial fulfillment of the requirements

for the degree of

DOCTOR OF PHILOSOPHY

2011

MAJOR: PHYSICS

Approved by:

_____

Adviser Date

_____

_____

_____

DEDICATION

This work is dedicated to my wife Patty

ACKNOWLEDGEMENTS

I wish to thank above all my adviser, Sergei Voloshin, not least for his patience and humor, and the members of my thesis committee, Claude Pruneau, Sean Gavin and T. C. Sun.

I am deeply grateful to the professors who supported me as a graduate student, Sergei Voloshin, Claude Pruneau, Paul Karchin and David Cinabro, for giving me the opportunity to study physics. I thank also Ratna Naik and Jo Wadehra for their guidance and counsel, and the members of the STAR Collaboration for their collegial support.

The debt of knowledge that I owe to all my professors at Wayne State, Berkeley and Columbia, I will try my best to pay forward.

And thanks especially to my companions in physics, Adam Lincoln, Nagesh Kulkarni, Monika Sharma, Muhammad Elnimr, George Moschelli, Sarah LaPointe, Anthony Timmins, Raj Pokharel, Chanaka da Silva, Joceyln Mlynarz and Vera Loggins. May they be happy and successful.

Considerate la vostra semenza:
fatti non foste a viver come bruti,
ma per seguir virtute e canoscenza
Consider your true nature:
you were not made to live as beasts,
but to follow virtue and knowledge

$\sim$ *Dante*

TABLE OF CONTENTS

LIST OF TABLES

LIST OF FIGURES

Chapter 1

Introduction

Since 2001, experiments with Au+Au heavy ion collisions at $\sqrt{s_{NN}} = 200$ GeV beam energy conducted at the Relativistic Heavy Ion Collider (RHIC) have provided a growing stream of evidence consistent with the formation of a strongly interacting phase of matter in which the fundamental degrees of freedom are quarks and gluons. The quark-gluon plasma (QGP) that is thought to be created in collisions of ultra-relativistic gold nuclei exhibits fluid-like properties, in particular elliptic flow, that is a final state momentum anisotropy due to initial state spatial anisotropy of the overlapping nuclei, and jet quenching, that is the suppression of back-to-back high-p_T correlations due to energy loss in the dense medium of the plasma.

Two-particle correlations have historically been used to great effect in the study of multiparticle production at hadron colliders. Since correlations can reveal particle associations from the initial stages of QGP formation, they have proved to be a useful research tool in the analysis of heavy ion collisions at RHIC. The discovery of jet quenching was an early result of two-particle correlations with high-p_T particle pairs. Further high-p_T correlation studies revealed an unexpected "ridge" feature, that is enhanced long-range correlations in pseudorapidity, not seen in the $p + p$ collisions which constitute a baseline reference for heavy ions.

In this work we present plots of the pattern of particle formation in $\sqrt{s_{NN}} = 200$ GeV Au+Au heavy ion collisions at the RHIC using three different two-particle cor-

relation measurements of number and transverse momentum as a function of relative azimuth, pseudorapidity and centrality. In all three observables, R_2, C, and ΔP_T, we see the onset with increasing centrality of a near-side "ridge" of enhanced correlations in pseudorapidity.

The correlation plots of real data are then compared to plots of simulations, first using data from RQMD (relativistic quantum molecular dynamics) and second, using data from a simple "cluster" model. The "cluster" dataset is a simplistic cartoon of a collision event involving an invariant mass that decays and receives a longitudinal and then transverse Lorentz boost. The effect of radial flow on clusters is shown in two ways, with the radial boost applied to individual clusters as well as collectively. We find that the transport-theoretical RQMD model does not produce a "ridge", however the effect of radial flow in simulated cluster data produces a near-side "ridge", purely kinematic in origin, that is quite similar to that seen in the data.

Chapter 2

Background

2.1 The Perfect Liquid

We live in a frozen world. The air we breathe, the food we eat, the structures that shelter us, the ground under our feet and the sun that shines upon us are all forms of baryonic ice. Stable baryonic matter, bound in atoms, was once identified with the totality of the universe but is now estimated to constitute only a small portion of it, no more than a few percent of what exists. Due to the light energy it emits, baryonic matter is the part of the universe that we are able to directly observe, as planets, stars and galaxies. The remainder of the universe is dark matter and dark energy. Dark matter is supposed to account for the deviation of the gravitational rotation of galaxies from the predictions of general relativity. Dark energy is supposed to account for the accelerating expansion of the universe. Dark matter and dark energy are currently not well understood.

Atoms are baryonic matter because they have a nucleus consisting of two kinds of baryons (Gk. *baryos* "heavy"), the positively charged proton and the neutral neutron (collectively, nucleons). The number of protons in the nucleus, the atomic number, determines the element. The number of neutrons in the nucleus determines the isotope. The baryonic nucleus of an atom is surrounded by a cloud of negatively charged leptons (Gk. *leptos* "light"), electrons, bound to the protons of the nucleus by the electromagnetic force between their opposite charges. The baryonic nucleons

are two hundred times more massive than the leptonic electrons.

The proton and neutron are not fundamental particles like the electron. The proton and nucleon are each composed of three constituent particles called quarks which are fundamental. The quarks are bound together by exchanging particles called gluons. The force exerted by the gluons to bind the three quarks together into a nucleon is so strong that its residue also binds the nucleons to one another in the nucleus. The gluonic "strong" force is over one hundred times stronger than the force of electromagnetic repulsion that would otherwise keep the protons apart. The strong force is also called the color force. While the electromagnetic force has only one kind of charge and anti-charge, the strong force has three, which are labeled with colors: red, green, blue, anti-red, anti-green, anti-blue. When reactors unbind the nucleons from each other in the process of nuclear fission, we are harvesting the energy of the color force.

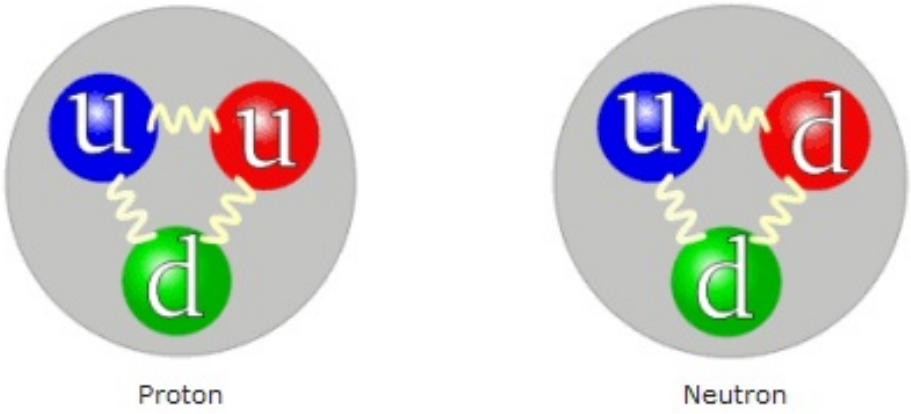

Figure 2.1: Schematic of the proton and neutron as three constituent quarks, bound by gluons. Images created by Arpad Horvath for *Wikipedia*.

With the exception of the most energetic cosmic rays, or perhaps at the core of the densest dead stars, there is no process in the universe today that can "melt" the glue that binds the quarks into a nucleon. However, what nature may no longer do, human beings have achieved. In the laboratories of high energy physics, scientists use particle

colliders ("atom smashers") to accelerate the nuclei of heavy atoms such as gold to light speed before colliding them together, head-on. The unworldly combination of pressure and temperature in the collision fireball melts the nucleons together into a dense boiling droplet of nearly perfect liquid, a quark-gluon plasma or QGP. The melting temperature of nuclear matter is a billion times hotter than the surface of the Sun. The relevant physics however is not the melting temperature, which is merely a number. What is significant is the phase change itself.

For an instant that recalls the beginning of the Universe, the collision releases the quarks and gluons from their icy nucleon bonds to flow freely, unconfined. Many more quarks and gluons (collectively, partons) are excited into creation from the vacuum as the nucleons' violent energy converts itself into equal amounts matter and anti-matter according to Einstein's formula $E = mc^2$. The droplet then explodes and refreezes into a shower of thousands of particles and light. The produced particles are frozen states of quark matter called hadrons, and the freezing process is called hadronization. Examples of hadrons are three-quark baryons, like the proton and neutron, or quark-antiquark mesons, the most common of which is the pion. There is also anti-matter produced such as the anti-proton consisting of three anti-quarks. The process of hadronization, the reconfinement of partons into quark bound states, is not fully understood.

The pattern of the produced particles preserves information about the behavior of the color force in the domain of nuclear deconfinement at extremely high temperature and pressure at the earliest stage of the collision. My analysis is a representation of the produced particle pattern using three observables which rely on the method of statistical correlations.

2.2 The Forces of Nature

Science currently admits four fundamental forces of nature: gravity, electromagnetism, the weak nuclear force and the strong nuclear force. The last three forces are thought to be fully described by a comprehensive theory called the Standard Model. The Standard Model uses quantum field theory to describe the interactions between fundamental particles as an exchange, that is emission and absorption, of force-carrying particles called vector bosons. The force-carrying vector boson of the electromagnetic force is the massless quantum of light, the photon. The quantum field theory of the electromagnetic force is called quantum electrodynamics or QED, and its accuracy has been verified to fifteen decimal places, making it the most precise theory in all of science. The theory of gravity, general relativity, currently lacks a quantum theory of interaction, and the gravitational constant G is known to only six decimal places. A summary of the four forces is shown in Figure 2.2.

Fundamental Force Particles

Force	Particles Experiencing	Force Carrier Particle	Range	Relative Strength*
Gravity acts between objects with mass	all particles with mass	graviton (not yet observed)	infinity	much weaker
Weak Force governs particle decay	quarks and leptons	W^+, W^-, Z^0 (W and Z)	short range	
Electromagnetism acts between electrically charged particles	electrically charged	γ (photon)	infinity	
Strong Force** binds quarks together	quarks and gluons	g (gluon)	short range	much stronger

Figure 2.2: The Four Fundamental Forces and the force carriers. Image courtesy of PBS.

The weak nuclear force has three massive force carriers, the neutral Z and the charged W^+ and W^-. In 1979 Glashow, Weinberg and Salam received Nobel prizes for showing that the electromagnetic force and weak nuclear force could be unified in a single electroweak interaction in which linear combinations of the photon, Z, W^+ and W^- bosons are the force carriers. The separateness of the two forces today, and the cause of non-zero mass in some particles, is believed due to a spontaneous symmetry breaking whose signature is the highly-sought Higgs boson.

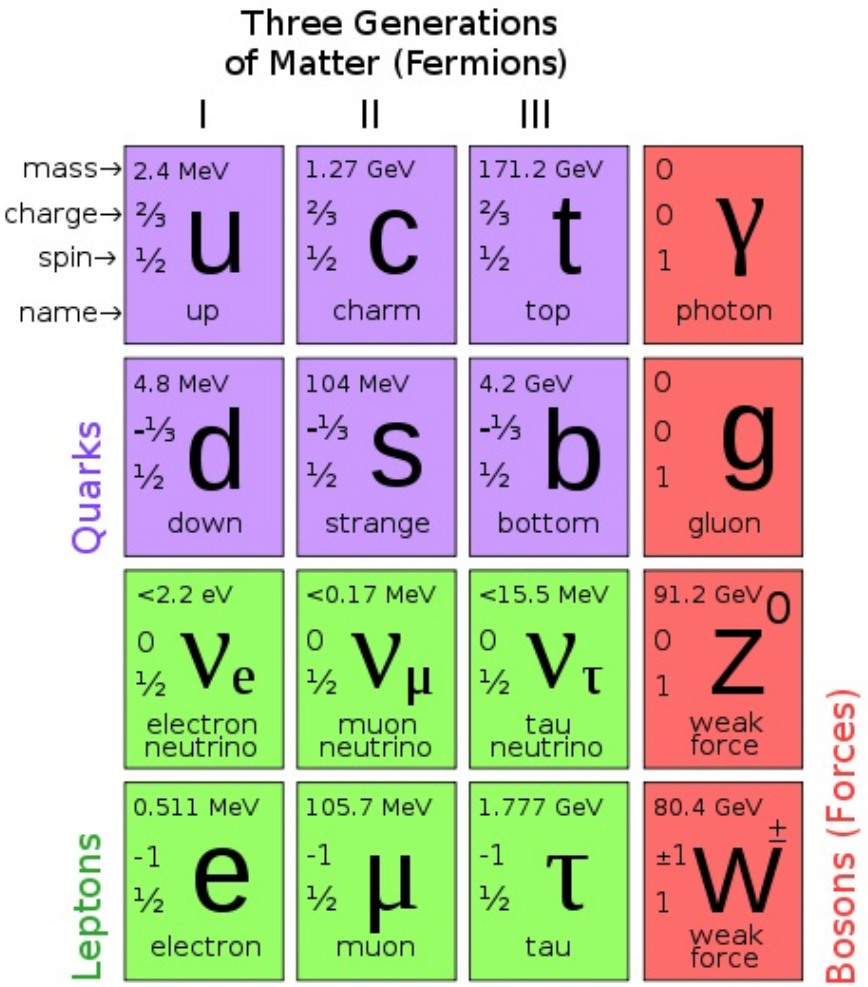

Figure 2.3: The Standard Model: three generations of matter. Image courtesy of Particle Data Group.

The fundamental particles which the forces affect, called fermions, are of two kinds,

quarks and leptons. The quarks and leptons come in three families, or generations. Within each quark or lepton family every particle belongs to a doublet, there is an "up" sibling and a dual "down" sibling particle whose electromagnetic charge differs by -1. The terms "up" or "down" derive by antonomasia from the names of the up/down doublet of quarks in the first, lightest quark family. Quark mass increases by orders of magnitude in the doublets of the second and third generation, strange/charm and top/bottom. Quark particles have fractional electromagnetic charge. Up-type quarks have charge $+2/3$ and down-type quarks have charge $-1/3$. The reality of fractional charge suggests that quarks and leptons with charge greater than $1/3$ may not be fundamental.

Lepton particles also come in three families of doublets. Leptons do not have color charge and so do not feel the strong nuclear force. "Down"-type leptons are the electron, muon and tau, all with electromagnetic charge -1. The "up" siblings in each doublet are (electron-, muon-, or tau-) neutrinos. In each family a neutrino forms a doublet with a charged lepton, just as up- and down-type quarks form a doublet in each quark family. Neutrinos have no electromagnetic charge and hence feel only the weak force.

Every particle in the families of quarks and leptons also has an anti-particle in an anti-family with electromagnetic charge of opposite sign, or zero if the particle has charge zero. The three generations of matter particles and the force carriers are shown in Figure 2.3. One seldom sees the chart for anti-particles, because the visible Universe is predominantly made of matter.

The weak nuclear force can transmute a quark from one family into its dual, or even into a quark of another family. Recent studies have shown that transmutation also occurs among lepton families. Observed neutrino transmutation from one family to another, called "mixing", implies that neutrinos possess a small but non-zero mass. They were originally supposed to be massless. Experiments are underway to

determine if transmutation between charged leptons may also, though rarely, occur. Evidence of transmutation between quark and lepton families themselves would be of fundamental theoretical importance to our understanding of the Universe. None yet exists.

2.3 The Strong Force

The quantum field theory of the strong force, or color force, is called quantum chromodynamics or QCD. The theory of QCD was created by analogy with quantum electrodynamics, or QED. The interactions of the Standard Model, electroweak and strong nuclear, have analogous mathematical structure, they are gauge theories. Each interaction gauge theory has a defining Lagrangian function that possesses a characteristic symmetry, that is the theory is invariant under the action of a continuous group of local transformations. The existence of a symmetry implies the existence of conserved physical quantities, called currents. Each interaction has a set of initially massless particles, or Weyl neutrinos, that are solutions of Dirac's equation and which possess "charge" appropriate to the interaction. Each generator of the symmetry group, or gauge group, corresponds to a gauge field. Each gauge field represents a force-carrying particle, or gauge boson, of the interaction. The gauge bosons couple to the massless particles of the interaction through a covariant derivative in the Lagrangian. The mathematical coupling models the physical interaction. The strength of the interaction is determined by a coupling constant whose value, along with the masses of the particles, must be determined empirically [1].

The group of symmetries for the electromagnetic interaction is $U(1)$, the unitary group represented by 1×1 complex matrices whose inverse is given by their conjugate transpose. $U(1)$ has a single generator, corresponding to the photon gauge field. For the weak interaction the symmetry group is $SU(2)$, the special unitary group represented by the set of 2×2 complex unitary matrices with determinant unity.

$SU(2)$ has three generators corresponding to the Z, W^+ and W^- gauge fields of the weak interaction. The unified electroweak interaction has as its symmetry the direct product $SU(2) \times U(1)$ with four generators. The symmetry group of QCD is $SU(3)$ with eight generators that correspond to eight gluon fields. For the Standard Model overall the symmetry group is the direct product $SU(3) \times SU(2) \times U(1)$ [1].

In contrast to the electromagnetic charge of QED, the color charge of QCD that quarks possess is not observable. Every quark individually has a charge of red, green or blue, anti-quarks have color anti-red, anti-green or anti-blue. To mediate the color interaction, the gluon force carriers must possess both color and anti-color. Naively, nine gluons should exist as a direct product of the three colors and anti-colors, but the $SU(3)$ color symmetry of QCD produces an octet of gluon gauge bosons with paired color and anti-color, or linear combinations of thereof, along with a singlet state which is colorless and hence noninteracting. Thus only eight colored gluons exist to mediate the strong interaction [2].

A striking characteristic of QCD is that all hadrons, the "frozen" bound states of quark matter, must be colorless overall. A baryon must contain quarks of all three colors, the quark and anti-quark in a meson must have a color and its anti-color. The phenomenon of the strong interaction that every hadron be colorless is known as quark confinement, or simply confinement. The color charge was first proposed (with different terminology) by O. W. Greenberg in 1964 as a quantum number to solve the apparent violation of the Pauli Exclusion Principle in symmetric baryon resonances such as Δ^{++} (uuu), Δ^- (ddd) and Ω^- (sss) [3]. Fundamental particles have an intrinsic angular momentum called "spin", which may be half-integer or integer in value, accordingly the particle is classified as a fermion or a boson. Quarks and leptons are fermions with spin 1/2, and the Pauli Exclusion Principle excludes identical fermions from occupying the same state, so color was proposed as a quantum number to make the quarks within the baryon distinguishable.

It was initially thought impossible to construct a color-based gauge field theory of QCD, analogous to the gauge field theory of QED, because the asymptotic strength of the strong interaction coupling was the reverse of the behavior of the running coupling constant α in QED [4]. The term "running" means that the strength of the coupling is a function of the distance at which the interaction takes place, or equivalently of the momentum transferred in the interaction, with short distances corresponding to high momentum and conversely. In QED, the bare charge of the electron becomes infinite at the shortest distances (highest momentum transfer Q^2), but is "screened" due to an effect known as vacuum polarization, yielding a finite limit $\alpha \approx 1/137$. The behavior of the QED and QCD coupling constants is contrasted in Figure 2.4.

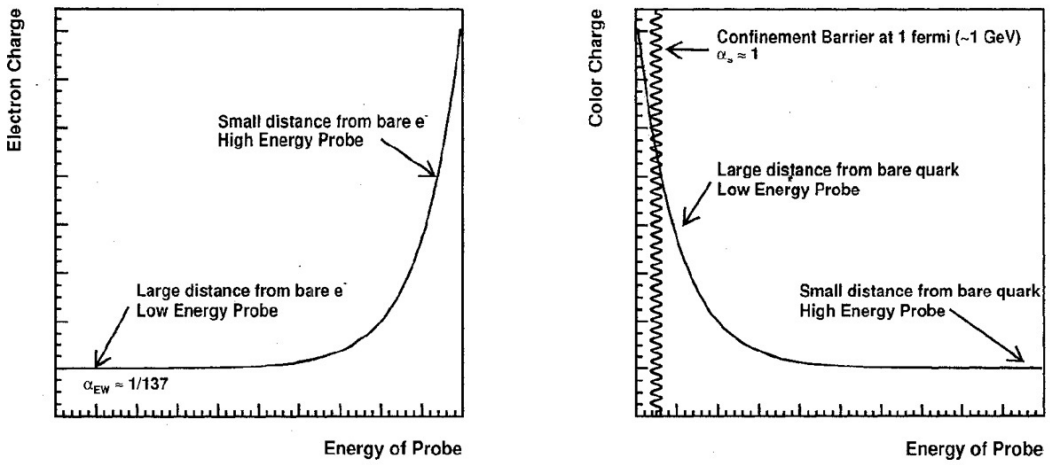

Figure 2.4: QED and QCD coupling constants. Image from H.F. Wolfe, doctoral dissertation, U. of Wisconsin (2008).

The small value of the QED coupling constant $\alpha \ll 1$ means that interactions in QED are perturbative; infinite series in α converge to give a finite result. The calculation of perturbation series in QED is simplified because the $U(1)$ gauge symmetry group of QED is commutative. Commutativity implies that photons do not interact with each other. However the color interaction gauge symmetry group of QCD, $SU(3)$, is non-commutative, as a consequence gluons couple to one another to

create an effect known as "anti-screening" [2]. The effect of non-commutativity is to cause the QCD coupling constant α_s to behave in a sense opposite to the α of QED: the QCD constant shows strong coupling at low momentum, causing confinement of quarks into colorless bound states, while at high momentum the coupling becomes weak, a phenomenon called "asymptotic freedom."

Gross, Politzer and Wilczek received Nobel prizes in 2004 for the discovery of asymptotic freedom in the strong interaction. The asymptotically free, weak coupling of the color force has as a consequence that QCD calculation is perturbative and convergent for high-momentum transfer experiments such as deep inelastic photon scattering which probed the proton and revealed its partonic inner structure, but calculations are divergent and nonperturbative for the low momentum transfer bulk particle interactions of the strongly-coupled quark-gluon plasma. However, progress in computability has allowed CPU-intensive direct calculations using a discrete approximation of the continuum, known as "lattice QCD", to estimate the parameters of the QCD phase diagram in the non-perturbative regime of thermal equilibrium [5].

Chapter 3

The Experiment

3.1 Multiparticle Production

Quark-gluon plasma studies evolved naturally from a particular subfield of strong interaction research, known as "multiparticle production," which was underway well before QCD, quarks or color were an established part of theory. The modern study of particles is less than a century old. At the beginning of the quantum era only three particles were known to scientists, these particles were considered fundamental, and in order of discovery they were the electron, the proton and the neutron. Wolfgang Pauli postulated a fourth particle, named by Enrico Fermi the *neutrino* or "little neutral one", in order to explain the measured distribution of momentum of the particles (electrons) emitted in β-decay, a process now known to be an interaction of the weak nuclear force that transforms a neutron into a proton, electron and anti-neutrino. The underlying interaction is a transmutation of a neutron constituent "down" quark into an "up" quark, thus turning the neutron into a proton.

Though evidence for the neutrino was not discovered until the 1950s, theoretical arguments for its existence were sufficiently convincing for its acceptance as a fundamental particle. The quantum of light known as the photon was distinguished as being radiation while the proton, neutron, electron and neutrino, all constituents of the atom, were considered matter. Today, quarks and leptons are considered matter while force-carriers, chiefly the photon because the force-carriers of the nuclear forces

have exceedingly short range, are radiation. Because of the wave-particle duality in quantum mechanics, however, the distinction between radiation and matter is no longer so clear.

The stable particle inventory of the first half of the century changed rather suddenly just prior to the second World War when new particles were discovered by scientists examining the traces left by cosmic rays on special photographic films. The particles are now known as the muon and the pion. Cosmic ray events, however, were too random a process for systematic study, so high-energy particle accelerators were built to mimic the collisions of cosmic ray protons with the protons in our atmosphere. In the early 1950s the Cosmotron at Brookhaven National Laboratory, a fixed target proton synchrotron, achieved a then-record 3.3 GeV projectile energy while creating "V-particles". The name "V-particle", typical of the descriptive nomenclature of the time, reflects the track shape left in a bubble chamber by the two decay products of an unknown uncharged, and hence undetectable, particle.

Other accelerators soon followed the Cosmotron, eventually adopting the "collider" format, with particles accelerating in opposite directions at equal speed, in order to increase the rest-mass energy of the collision. Scores, and then hundreds, of new particles known as "resonances" were produced. While the muon and pion brought Nobel prizes to their discoverers, soon scientists had added so many new species to the growing inventory that a wag observed that the next discoverer of a particle deserved a fine rather than a prize. The classification of these many new particles was the chief task of the post-war particle theorists. The regularity of the particle inventory led directly to Murray Gell-Man's group-theoretical explanation using $SU(3)$ flavor symmetry acting on three quark constituents, up u, down d and strange s (and the anti-particle anti-quarks $\overline{u}$, $\overline{d}$, $\overline{s}$) which is at the heart of the Standard Model.

Although the most energetic protons in the world by far (10^{10} GeV) still fall from

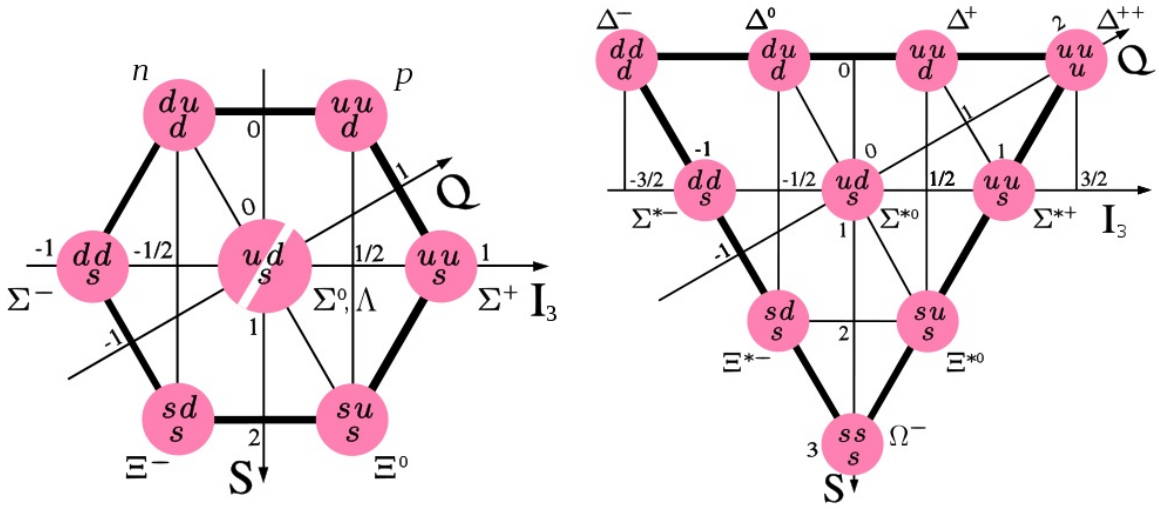

Figure 3.1: Flavor symmetry: spin 1/2 baryon octet and spin 3/2 baryon decuplet plotted on axes of isospin, strangeness and electromagnetic charge. Each baryon is composed of u, d and s constitutent quarks.

the sky, ever since the Cosmotron multiparticle production has been an endeavor pursued at government facilities, where multinational collaborations attend to hadron colliders of ever-increasing center-of-mass energy (see Table 3.1).

However, from the beginning of the accelerator era there were scientists who were interested not so much in the production of specific particles, but rather in what is called the "underlying event", the inclusive totality of particles produced, also known as "multiparticle production". Multiparticle production seeks to understand the same underlying strong force interaction that is responsible for the inventory of resonances. A simple observable of multiparticle production is the rapidity y (or pseudorapidity η) distribution of charged particles, denoted variously as $\rho(y)$ or dN_{ch}/dy. Rapidity is a measure of the longitudinal velocity and pseudorapidity is an approximation to rapidity used by experimentalists that is exact in the limit of massless particles. As seen in Figure 3.1, multiparticle pseudorapidity distributions for $p(\overline{p}) + p$ collisions show surprising similarity over a wide range of energies.

Hadron collisions eventually progressed beyond collisions of protons, that is hydrogen ions, to include heavier ions such as silicon, copper, gold and lead, always

Accelerator/Collider (Organization)	**Epoch**	**Energy (Species)**
Cosmotron (BNL)	1947-1966	3.3 GeV (p)
PS Proton Synchrotron (CERN)	1959-	28 GeV (p)
AGS Alternating Gradient Synchrotron (BNL)	1960–	33 GeV (p)
U70 Serpukhhov (IHEP)	1967–	70 GeV (p)
ISR Intersecting Storage Rings (CERN)	1971-1984	30+30 GeV ($p+p$)
SPS Super Proton Synchrotron (CERN)	1981-1984	400 GeV (p)
ISABELLE (BNL)	aborted 1983	200+200 GeV ($p+p$)
Tevatron (FNAL)	1987-2011	980-980 GeV ($p+\overline{p}$)
SSC Superconducting Super Collider (U.S.)	aborted 1993	10+10 TeV ($p+p$)
RHIC Relativistic Heavy Ion Collider (BNL)	2000–	100+100 GeV/N
LHC Large Hadron Collider (CERN)	2009	7+7 TeV (GeV/N)
VLHC Very Large Hadron Collider	(?)	(?)

Table 3.1: Partial listing of hadron accelerators and colliders. (PS and AGS accelerators were recycled as first stages of later colliders.)

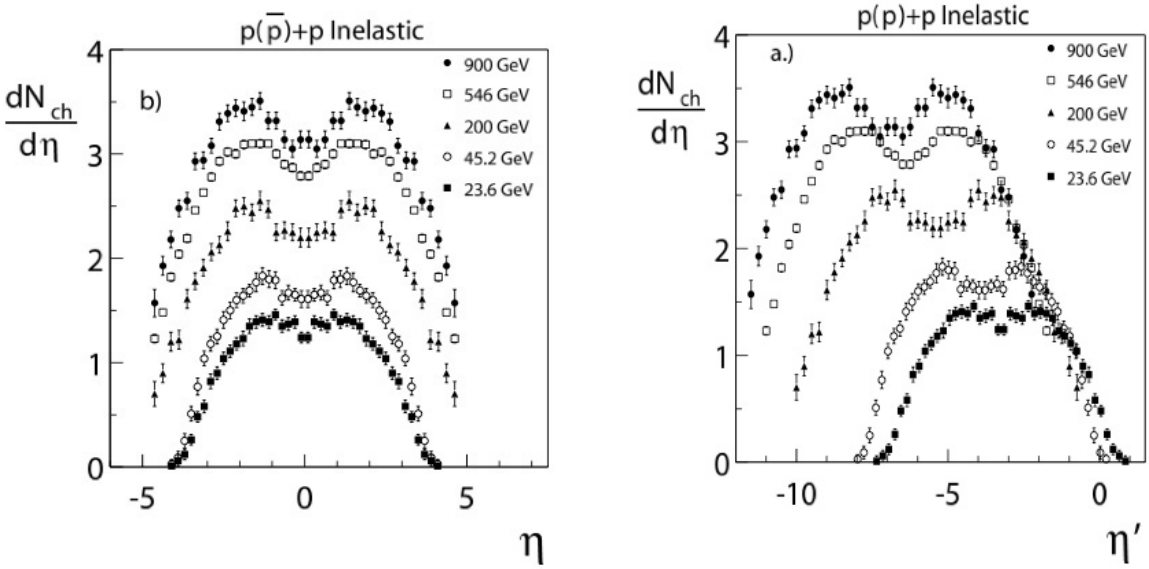

Figure 3.2: Pseudorapidity distributions for $p(\overline{p})+p$ collisions at various $\sqrt{s}$ energies.

producing a similar spectrum of particle production as that seen in proton-proton. Figure 3.1 shows rapidity distributions for Au+Au heavy ion collisions over a range of energies, which have a natural Gaussian shape. The bimodal shape of the pseudo-rapidity distribution present in the $p + p$ plots is an artifact of the Jacobian for the change of variable from rapidity y to pseudorapidity η.

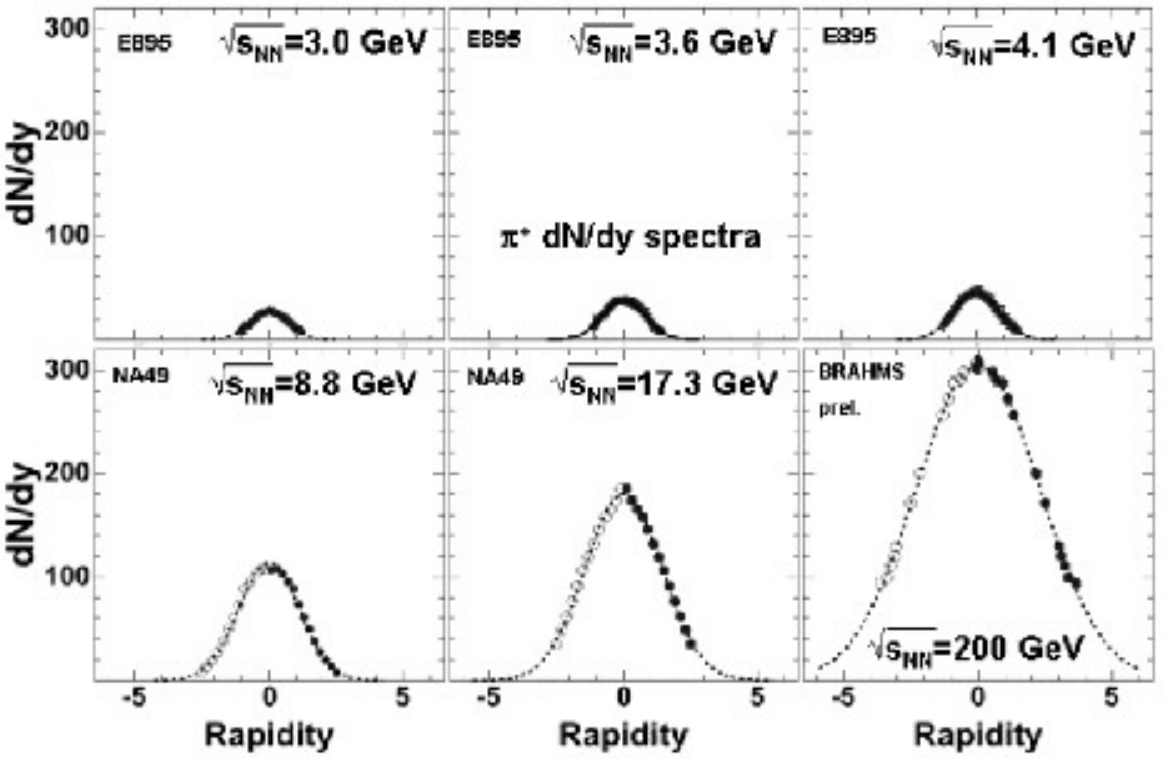

Figure 3.3: Rapidity distributions for $A + A$ heavy ion collisions at various $\sqrt{s_{NN}}$ energies.

It was realized in the 1970s that particles from hadron collisions are well-modeled assuming production in "clusters". The idea of cluster production goes beyond the idea of simple resonance decay. In cluster production, decay particles are produced in discrete bunches, but without being traceable to a single invariant mass source as in the case of a resonance. With higher energy and increased particle multiplicity, it became feasible to treat the cluster phenomenon statistically, using correlation methods.

3.2 Two-Particle Correlations with R_2

The historical observable of choice to investigate cluster production was the two-particle correlation function known as R_2. R_2 will be discussed in detail later, indeed it is the primary observable for our analysis, but briefly it is a function that measures the ratio of correlated to uncorrelated pairs created in the collision event. R_2 gives a positive value when the number of produced pairs exceeds random expectations, and a negative value otherwise. For random particle production R_2 is identically zero.

To construct R_2, begin with the one-particle rapidity (or pseudorapidity) distribution normalized to the mean number of particles per event; the two-particle distribution is normalized to the mean number of pairs:

$$\int \rho_1(y)dy = \langle n \rangle \tag{3.1}$$

$$\int \rho_2(y_1, y_2)dy_1dy_2 = \langle n(n-1) \rangle \tag{3.2}$$

The cumulant correlation function C_2 is then defined as the difference between correlated and uncorrelated, or same-event and mixed, pairs. The cumulant is designed to vanish when the elements of the pairs are independent. It therefore measures the degree and location of non-randomness in the collision.

$$\rho_2(y_1, y_2) = \rho_1(y_1)\rho_1(y_2) + C_2(y_1, y_2) \Longrightarrow C_2(y_1, y_2) = \rho_2(y_1, y_2) - \rho_1(y_1)\rho_1(y_2) \tag{3.3}$$

The correlation function R_2 is created from C_2 by normalizing by uncorrelated pairs. Many detector artifacts and other sources of systematic error cancel in the ratio.

$$R_2 = \frac{C_2(y_1, y_2)}{\rho_1(y_1)\rho_1(y_2)} = \frac{\rho_2(y_1, y_2)}{\rho_1(y_1)\rho_1(y_2)} - 1 \tag{3.4}$$

To extract the maximum information from the data, the R_2 correlation function

is applied to particle pairs in various sign combinations. R_2^{ci} correlation ("charge-independent") includes all charged particle pairs; unlike- and like-sign correlations R_2^{+-}, R_2^{++}, R_2^{--} are used to study charge conservation effects; $R_2^{h_1 h_2}$ analyzes the correlation between specific hadron types h_1 and h_2. When measuring correlations with the R_2 correlation function, a distinction is made between long-range and short-range correlations. Intuitively, having selected a particle for consideration, a long-range correlation affects all other produced particles, while a short-range correlation involves only those particles which are nearby in momentum space.

Although the dividing line between long- and short-range is somewhat arbitrary, the intention is to create a distinction between different mechanisms affecting the distribution. Common "cluster" origin of produced particles creates short-range correlations, while conservation laws (charge, momentum, isospin) enforce both short- and long-range correlations [6].

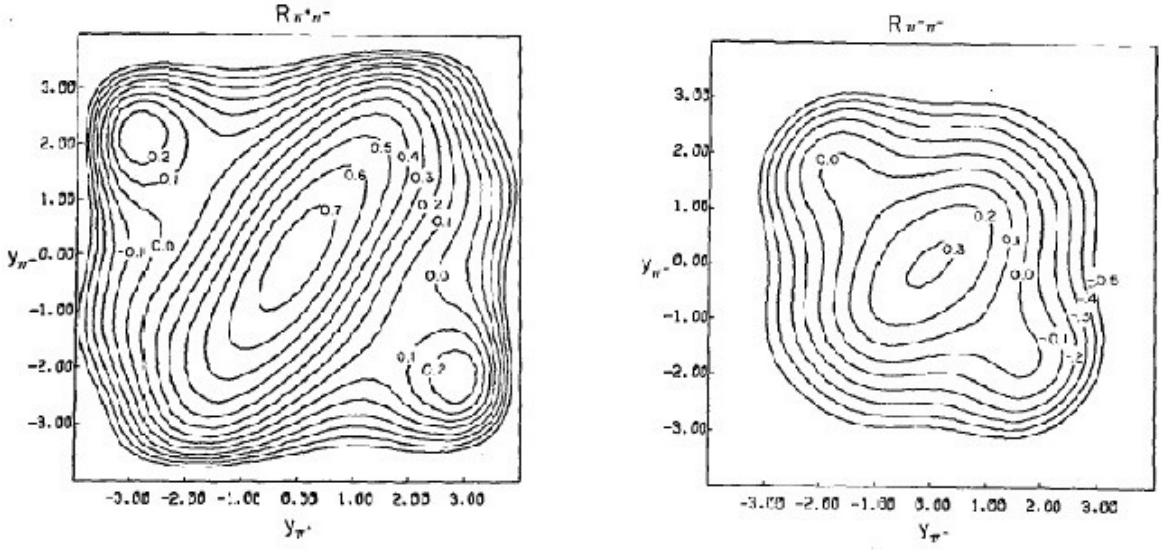

Figure 3.4: $R_2^{\pi^+\pi^-}$ and $R_2^{\pi^-\pi^-}$ for $\sqrt{s} = 27$ GeV $p + p$ collisions at FNAL.

Plots of p+p collisions from the 1970s at FNAL and CERN ISR showed a persistent pattern of short-range correlations, attributable to clusters, at various beam energies. An example from $p + p$ collisions at FNAL shows the R_2 correlation function for

like-sign and unlike-sign pion pairs (see Figure 3.4). The regions of enhanced R_2 correlation levels for $\pi^+\pi^-$ as opposed to $\pi^-\pi^-$ indicate both short-range correlations (at the central maximum) and long-range correlations (at the two secondary maxima). Evidence of the mechanism is much diminished, but not absent, in the like-sign plot [7].

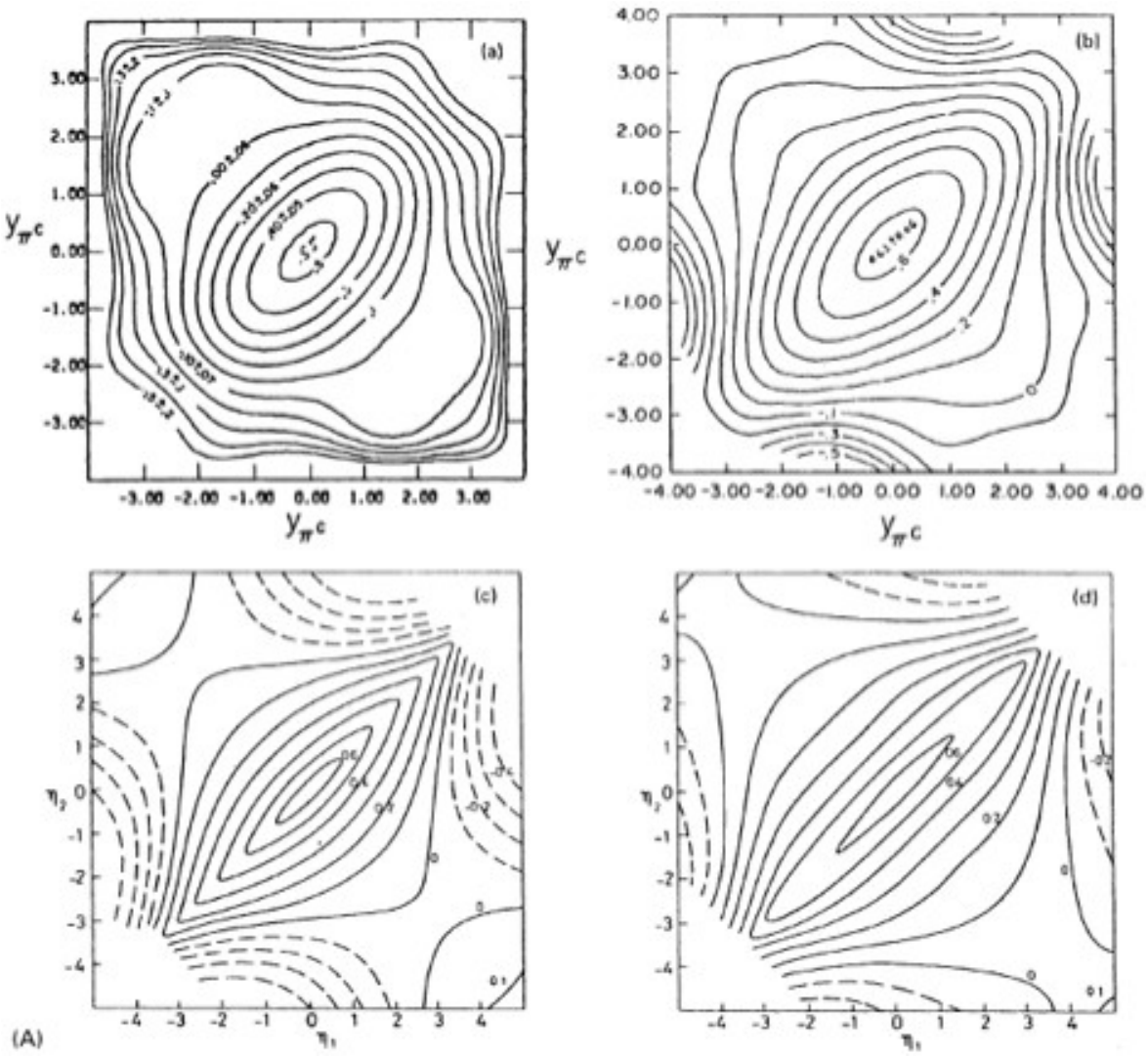

Figure 3.5: R_2^{cc} for $p+p$ collisions at FNAL (a-b)and CERN ISR (c-d): $\sqrt{s}$ = 13.7, 27, 23, 63 GeV.

Figure 3.5 shows R_2^{cc} (R_2^{ci}) for beam energy $\sqrt{s}$ = 13.7, 27, 23 and 63 GeV. The plots show a "mountain" with maximum R_2^{cc} value ∼0.6 at $(\eta_1, \eta_2) = (0, 0)$ holding nearly constant along the $y_1 = y_2$ diagonal but falling off rapidly in the orthogonal

Δy direction. As energy increases, the short-range positive correlations maintain the same maximum value while extending further along the line $y_1 = y_2$. In the Δy direction correlations are smaller but still positive for $y_1 = -y_2$, indicating a "burst" of particles of opposite rapidity.

As may be seen from the plots, as $\sqrt{s}$ energy increases, the value of R_2 becomes nearly constant along diagonals of fixed Δy, especially for values of $|y_{1,2}| < 2$. For this reason a transformation in rapidity (or rather pseudorapidity) space is usually made to change the independent variables from (η_1, η_2) to $(\bar{\eta}, \Delta\eta)$.

The correlation plots above may be considered the *Ur*-plots for the "cluster" model of multiparticle production. The defining features of the cluster model were collected by in a review article that remains influential [6]:

- post-collision creation of "clusters" which subsequently decay into final-state particles;
- absence of correlations among clusters;
- isotropic decay of clusters in their rest frames;
- Lorentz invariant translation of cluster distributions in pseudorapidity.

Though the cluster model has been superseded by the QCD language of color field / flux tube / string fragmentation, the underlying phenomenology is still a prime motivation for two-particle correlation analyses.

My research captures the pattern of particle formation in heavy ion collisions using three different two-particle correlation observables in number and momentum, as a function of relative azimuth, pseudorapidity and centrality. The patterns of real data are then compared to simulations using RQMD data and data from a simple "cluster" model. The intent of the analysis is not so much to discriminate among phenomenological models as to offer canonical representations of the three observables.

3.3 The RHIC Collider

The idea of heavy ion collisions, beyond their multiparticle production capability, was proposed as early as 1975 by T.D. Lee to explore whether "at high densities there may exist a new type of nuclear state" [8]. Later, theoretical work to create a phase diagram for QCD indicated the possible existence of a phase transition at high temperature and baryon density to a state of matter consisting not of nucleons but of their deconfined constituent quarks and gluons, the quark-gluon plasma. Many studies with heavy-ion collisions were performed at CERN in the eighties and nineties but the most spectacular results awaited the construction and implementation of the Relativistic Heavy Ion Collider at Brookhaven National Laboratory in eastern Long Island, former home of the Cosmotron.

The Relativistic Heavy Ion Collider at Brookhaven National Laboratory (RHIC at BNL) is a high energy particle accelerator commissioned in 2000 for the purpose of reproducing in miniature a state of matter thought not to have existed since the initial microseconds following "the Big Bang." According to the standard cosmological model, the "Big Bang" was the original singularity from which our expanding Universe began its evolution over 13 billion years ago [9]. In the RHIC collider, gold nuclei are accelerated to nearly light speed, attaining energies of 200 GeV per nucleon pair.

The most central Au+Au collisions create a "mini-Bang" droplet of primordial matter that is characterized by extremely high temperature within a volume of a few cubic fermi, the size of a single gold nucleus. Most of the energy deposited in the volume is due to the kinetic energy of the nucleons. The resulting energy density, up to 30 times that of the 1 GeV nucleon rest mass, causes the struck nucleons of the colliding nuclei to dissolve. Following the collision, within a formation time of order 1 fm/c, the deconfined quarks and gluons interact strongly, rapidly forming a kinetically and chemically thermalized system, the quark-gluon plasma. The QGP phase lasts of order 10^{-23} sec after which the intense pressure within the system causes

a longitudinal and radial expansion accompanied by adiabatic cooling. Expansion and cooling of the system continues until "freeze-out" temperature is reached, at which time the quarks and gluons undergo a phase transition and the system of deconfined partons recombines into a gas of hadrons.

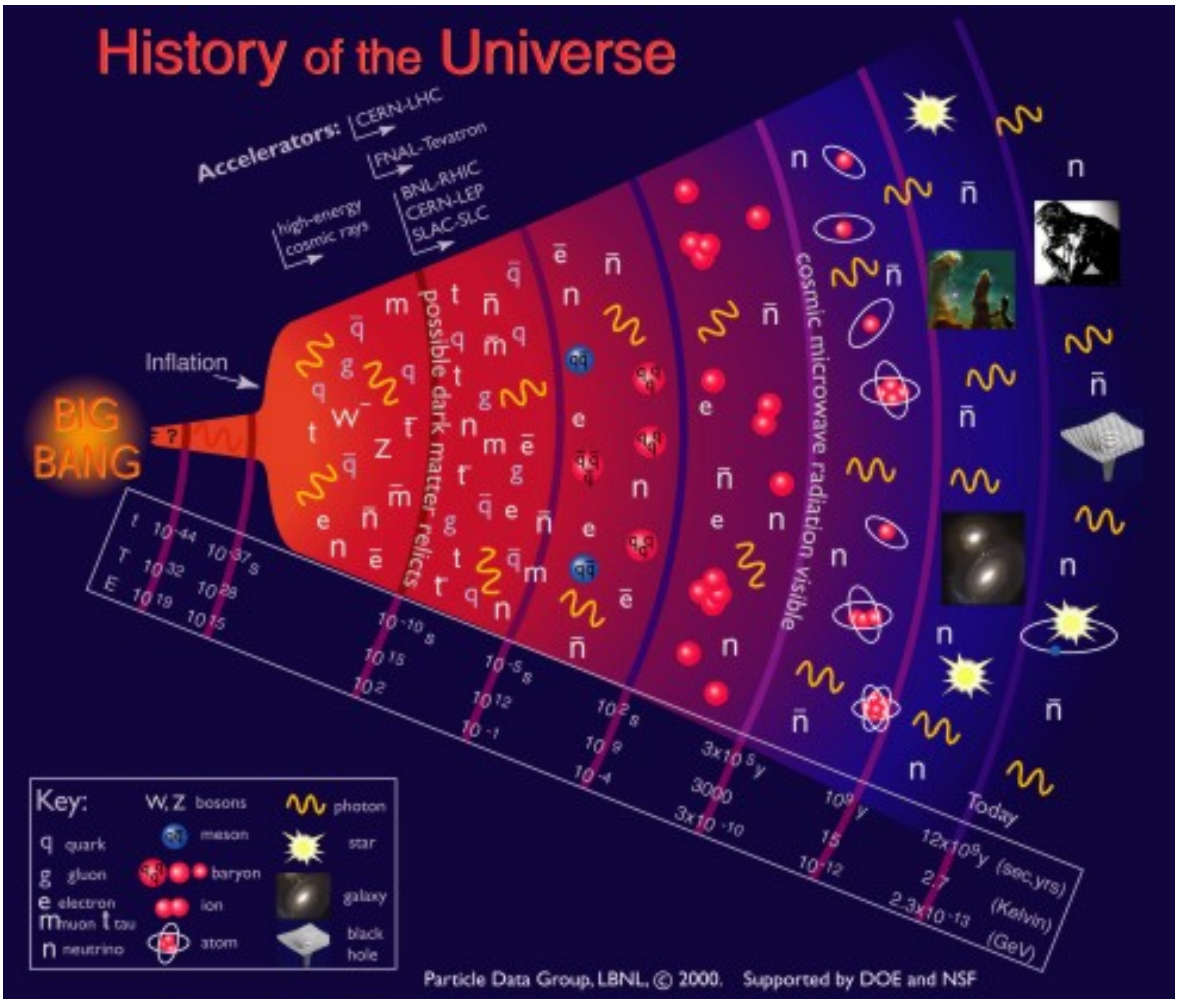

Figure 3.6: Time evolution of the "Big Bang" singularity.

A thermalized system is by definition characterizable by a thermodynamic equation of state (EoS). The equation of state determines the quark matter phase diagram, shown in Figure 3.8. Using the finite calculational methods of quantum chromodynamics, called lattice QCD, the temperature of the phase boundary between partons and hadrons has been estimated to be in the range 160-190 MeV [10][11]. (For com-

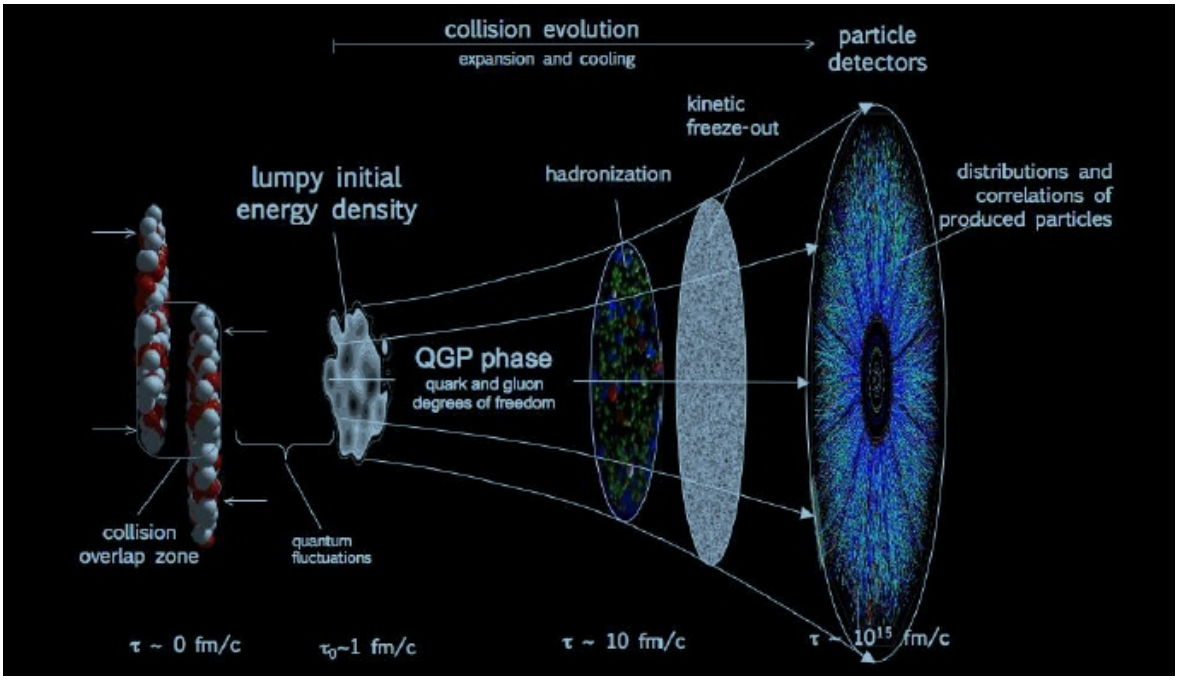

Figure 3.7: Time evolution of a relativistic heavy ion collision.

parison, 100 MeV = 1.16 x 10^{12} K, with the temperature at the surface of the Sun approximately 6000 K.) The lifetime of the thermalized system from QGP formation to freeze-out has been estimated using the Hanbury-Brown/Twiss method of identical particle pion interferometry, and is estimated to be of order of 10 fm/c [12][13].

After freeze-out interaction ceases and the newly-formed particles stream toward the detectors. The majority of particles detected are light hadrons plus a small percentage of direct photons and electron-positron pairs formed in the initial fireball along with numerous leptons from hadronic resonance decays. Information regarding the transient QGP phase is encoded in the detected particles which typically number in the thousands. Due to the large number of particles created, complete event reconstruction is problematic. Statistical methods are therefore the key tool for the experimenter seeking to analyze the event phenomenology.

The term QGP is historic. Many scientists who anticipated heavy ion collisions to produce deconfinement, expected it to be a weakly-interacting parton plasma. In-

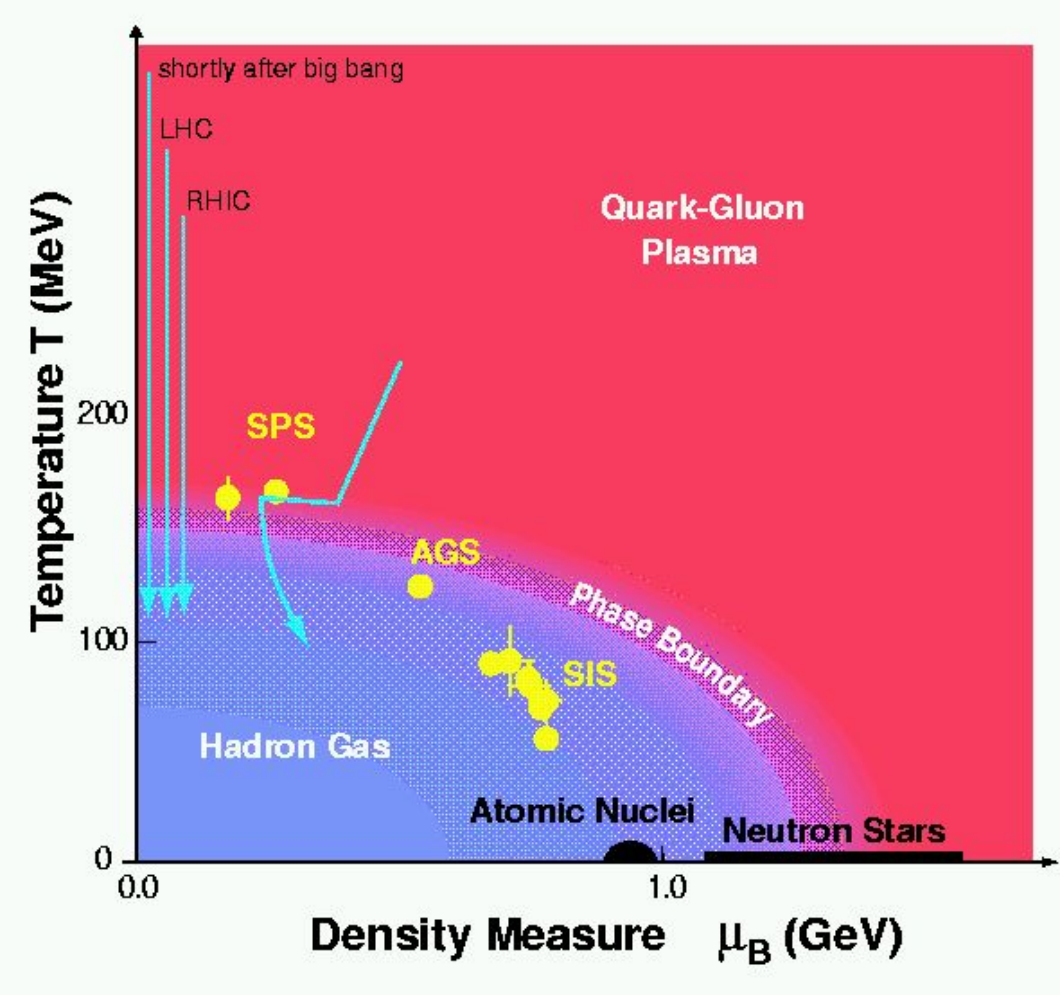

Figure 3.8: Phase diagram of nuclear matter.

stead, the QGP was found to be a strongly-interacting, low-viscosity fluid, often called the sQGP in recognition of this fact. The evidence for fluid behavior is of several kinds. Foremost, the evolving system of the QGP up to freeze-out is well-approximated by relativistic transport models of ideal hydrodynamic flow [14][15][16][17]. Two early results from RHIC, elliptic flow and jet quenching, also provide strong evidence for the fluidlike properties of the QGP.

Elliptic flow is a consequence of the spatial anisotropy of the overlap region of a nucleus-nucleus collision. Given a uniform pressure gradient on the boundary of the roughly elliptical overlap region involved in the collision, the spatial anisotropy of the overlap converts to a momentum anisotropy due to greater pressure along the minor axis of the ellipse. A schematic of the collision is shown in Figure 3.9.

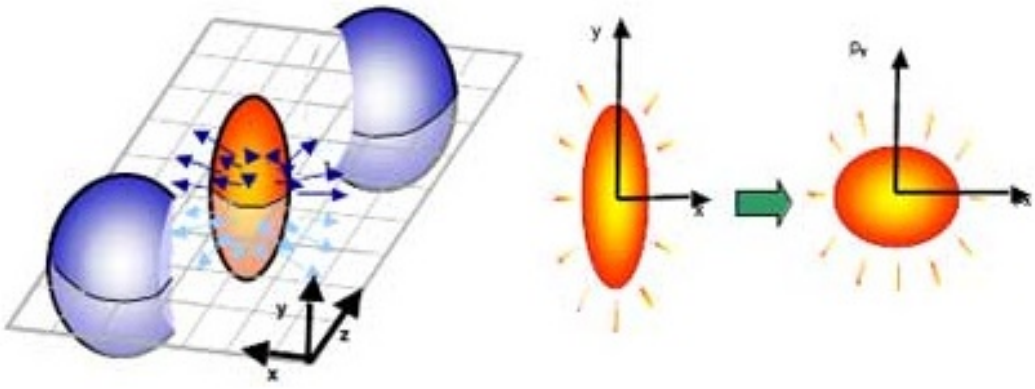

Figure 3.9: Elliptic flow: integrated v_2 as a function of collision centrality for various energies.

The azimuthal momentum anisotropy due to the pressure gradient may be measured by the coefficients of a Fourier decomposition of the normalized particle distribution in azimuth:

$$\frac{dN}{d\phi} = 1 + 2v_1 \cos(\phi - \Psi_{RP}) + 2v_2 \cos[2(\psi - \Psi_{RP})] + \cdots \tag{3.5}$$

where

$$v_n = \langle cos(n(\phi - \Psi_{RP})) \rangle \tag{3.6}$$

Here, ϕ is the azimuthal angle in the detector and Ψ_{RP} is the reaction plane of the collision, identified with the major axis of the elliptical overlap region. Elliptic flow is represented by the second coefficient, v_2. Though not present in $p + p$, and weakest in the most central heavy ion collisions, v_2 has a non-zero value for a range of centralities and energies, as shown in Figure 3.10.

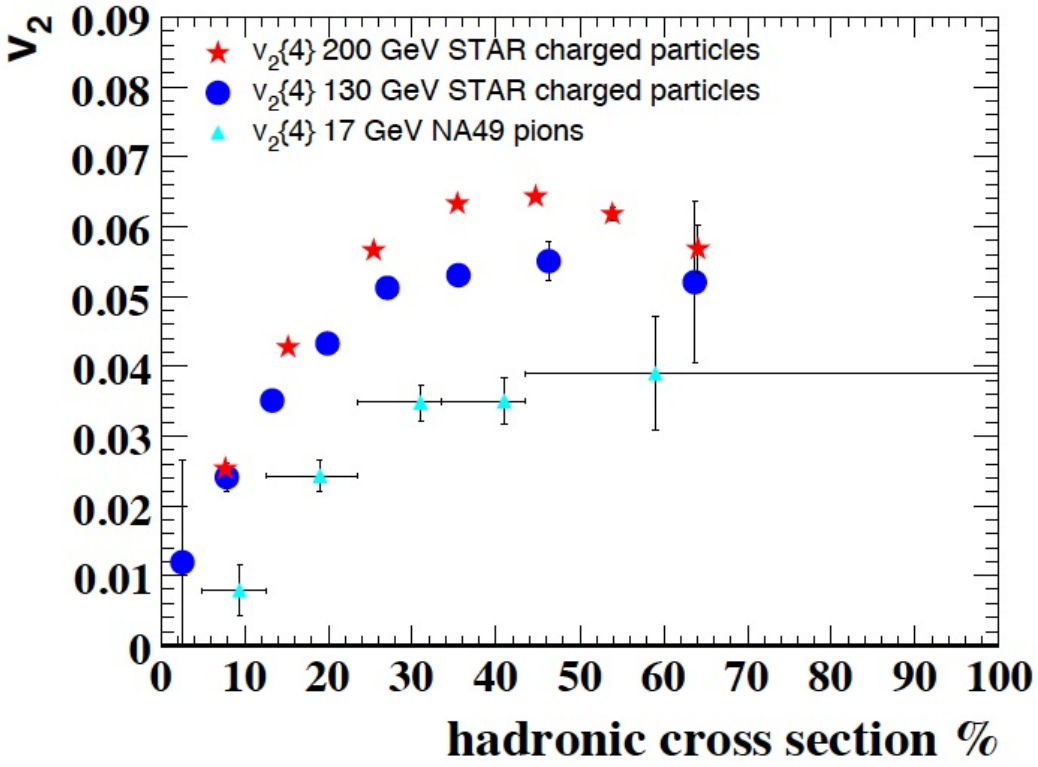

Figure 3.10: Elliptic flow: integrated v_2 as a function of collision centrality for various energies.

Extensive measurements of elliptic flow for identified particles have been conducted at RHIC. Quite good agreement is obtained when the particle species are divided by the number of quarks, a result known as quark-number scaling. Quark-number scaling, that is to say quark flow, is consistent with QGP formation, with

quark degrees of freedom replacing hadrons in the initial stages of the collision.

Jet quenching is measured by two-particle azimuthal correlations between a high-p_T "trigger" first particle and a second "associated" particle of similar or lower p_T. The plot in Figure 3.11 compares the distribution of trigger-and-associated pairs for three collision combinations, $p+p$, d+Au and Au+Au central [18]. In the latter the correlations at $\Delta\phi \sim \pi$, the so-called "away side", are consistent with zero. The away-side suppression is not seen in the d+Au collisions of "cold" nuclear matter, indicating that "the suppression phenomena seen in central Au+Au collisions are due to final-state interactions with the dense system generated in the collision" [18].

While the away-side suppression seen in azimuthal correlation plots reveals jet quenching, an even more striking phenomenon of heavy ion collisions is revealed on the near side of correlation plots that show both relative azimuth and relative pseudorapidity, that is the so-called "ridge."

3.4 The Ridge

A feature of primary interest to this analysis is the phenomenon, first observed in heavy ion collisions at RHIC, known as "the ridge". As in the study of jet quenching, two-particle correlation plots for heavy ion collisions were constructed using "hard" triggers and associated partners. The experimenters obtained a plot with enhanced near-side yield at large $|\Delta\eta|$, in excess of the elliptic flow background and occurring well beyond the region about zero where jet production usually locates. No similar feature was seen in d+Au plots where correlations remained located in the region about the origin. The normalized distribution functions for trigger-and-associated pairs in Au+Au and d+Au collisions are shown in Figure 3.12.

The "ridge" plot has generated considerable interest not only for high-p_T jet studies, where it is called the "hard" ridge, but also among experimenters studying low-momentum "bulk" correlations, where it is seen as a "soft" ridge. The ridge was found

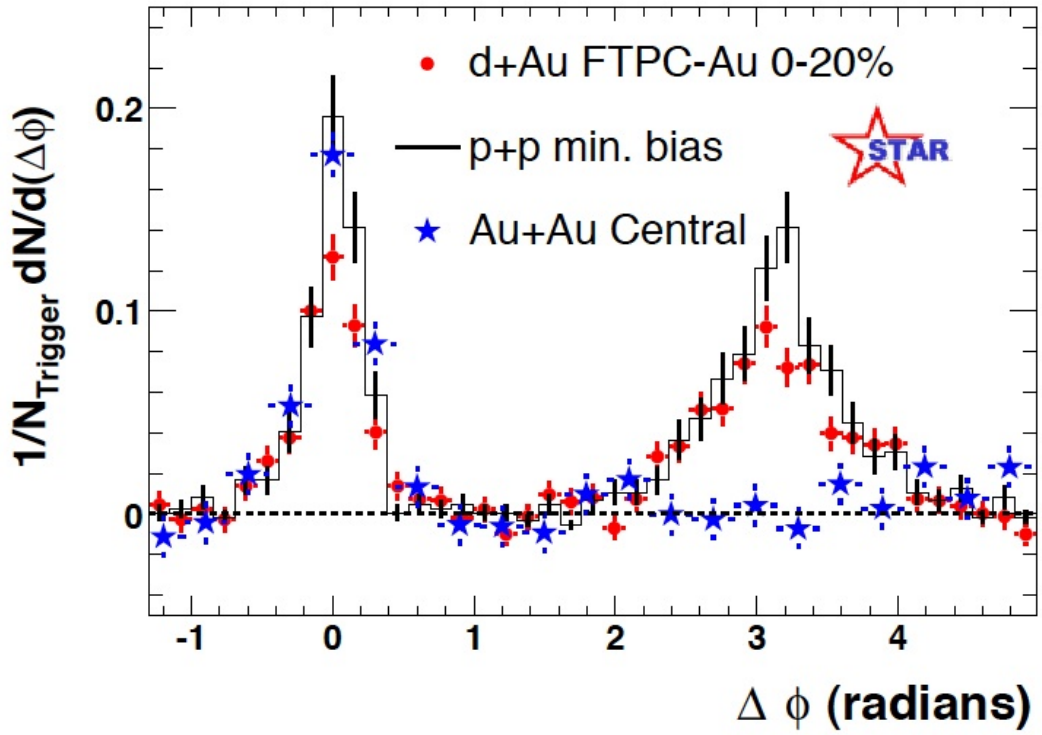

Figure 3.11: Jet quenching: suppression of away-side correlations in heavy ion collisions.

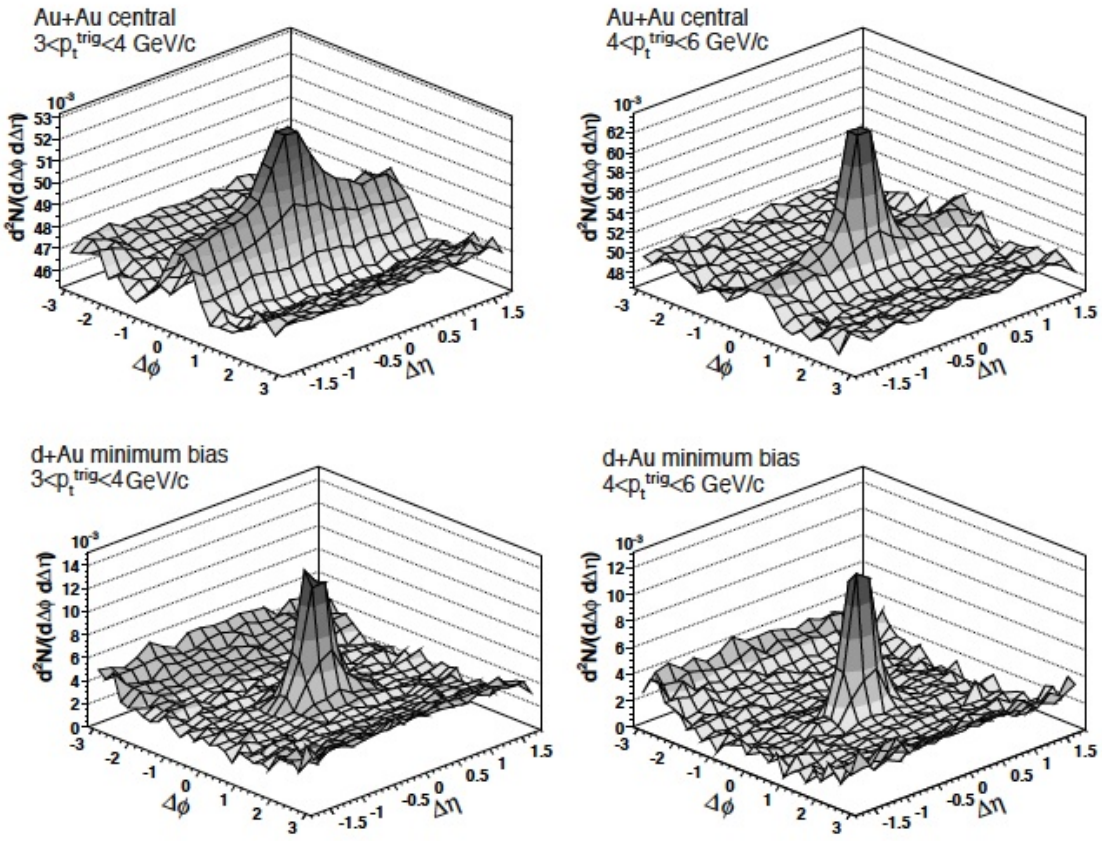

Figure 3.12: Normalized distribution function for trigger-and-associated pairs at $\sqrt{s_{NN}} = 200$ GeV: (*top row*) central Au+Au $3 < p_T < 4$ GeV trigger, $4 < p_T < 6$ GeV trigger, (*bottom row*) d+Au $3 < p_T < 4$ GeV trigger, $4 < p_T < 6$ GeV trigger

to be a feature not just of high-p_T trigger-and-associated correlations but also of low-p_T correlations using particles restricted to $p_T < 2.0$ GeV. Numerous hypotheses were put forth to explain its appearance in heavy ion collisions:

- coupling to longitudinal flow of induced radiation of energetic partons propagating through the medium [19];
- color field turbulence [20];
- anisotropic plasma [21];
- jet-quenching combined with strong radial flow [22];
- recombination of thermally enhanced partons [23].

Readers interested in a detailed account of ridge phenomenology are urged to consult the doctoral dissertation of George Moschelli [24]. In a seminal paper using a "blast wave" model Gavin and Moschelli provided support to Voloshin's proposal that radial flow created the ridge correlations through a kind of kinematic focusing [25]. The authors were able to reproduce closely the ridge yield observed in STAR data, as shown in Figure 3.13.

Moschelli argues for a single methodology of ridge creation, rather than separate "hard" and "soft" ridge phenomena, and indeed we will find that the appearance of the ridge does not depend strongly on the p_T of the trigger.

Representative reference plots of the two-particle correlation function R_2, weighted by particle multiplicity, for p+p, Cu+Cu and Au+Au collisions are shown in in Figure 3.14. The correlation functions are constructed using inclusive charged particles, with no momentum restrictions.

The ridge is seen to be less a phenomenon of trigger particle momentum, and more a function of collision energy density. As the energy density increases, the $p+p$ correlations shift from a broad ridge in $\Delta\phi$, narrow in $\Delta\eta$, becoming for Au+Au a

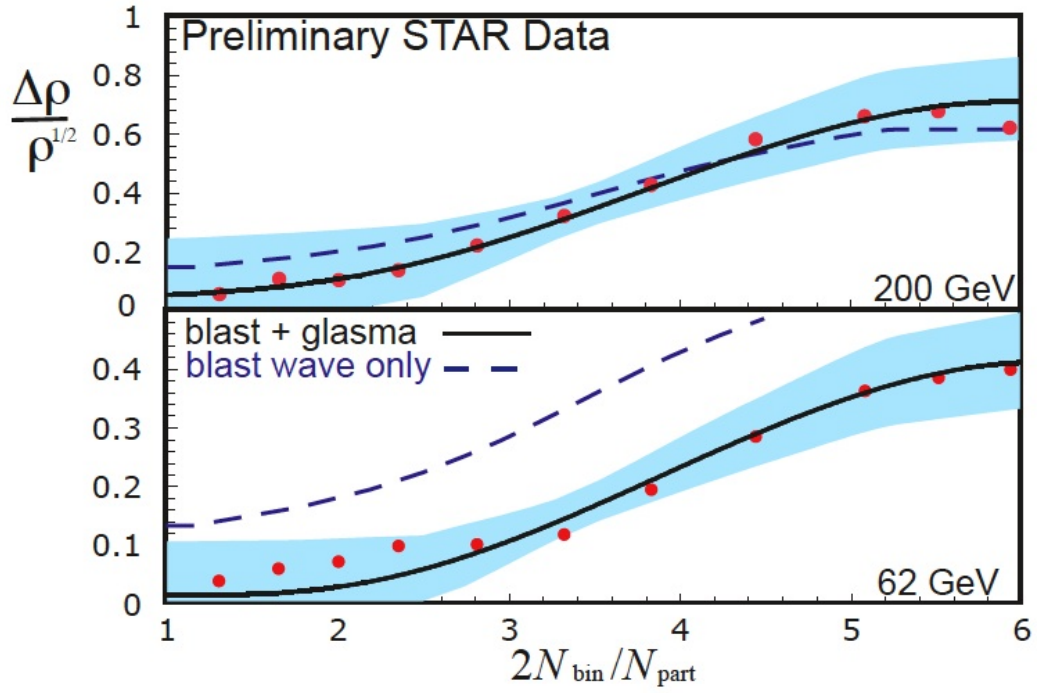

Figure 3.13: Height of the near side peak in Gavin and Moschelli's blast wave model *vs.* centrality for 200 GeV (*top*) and 62 GeV (*bottom*). STAR data points in red.

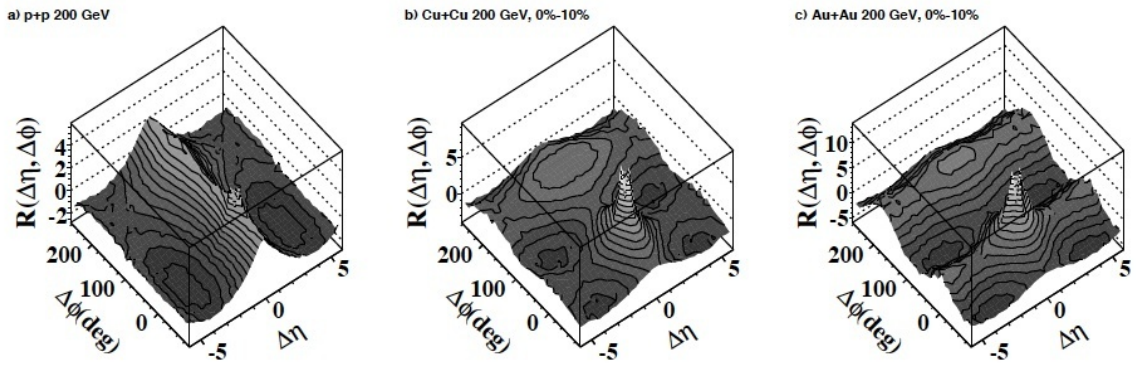

Figure 3.14: R_2 correlation function weighted by event multiplicity for p+p, Cu+Cu, and Au+Au 200 $\sqrt{s_{NN}} = 200$ GeV collisions.

broad near-side ridge in $\Delta\eta$, narrow in $\Delta\phi$. The Cu+Cu plot is intermediate between the two. The Au+Au correlations show strong enhancement on the near and away side, with maxima at $\Delta\phi = 0$ and $\Delta\phi = \pi$, due to elliptic flow. Taken together, the three plots suggest a strong association between the presence of radial flow, as proposed by Voloshin, and the appearance of the ridge in heavy ion collisions. We shall see the pattern of R_2 correlations seen here for collisions of different species at the same energy is entirely recapitulated with Au+Au correlations as collision centrality is increased.

Chapter 4

Data and Observables

4.1 The STAR Detector

Until the Large Hadron Collider at CERN began Pb+Pb collisions in 2010, RHIC at BNL held the record as the highest-energy accelerator of heavy ions. With two concentric 3.7-km long acceleration and storage rings, RHIC achieves a center of mass beam energy of $\sqrt{s} = 200$ GeV per nucleon pair in Au+Au collisions. The rings are independent and may be used for collisions using other hadron species such as Cu+Cu, $p + p$ and d+Au for the purpose of taking baseline measurements. Using "Siberian Snakes" technology, the RHIC collider also has presently the foremost capability in the world to accelerate spin-polarized proton beams. When running $p + p$, maximum achievable center of mass beam energy is $\sqrt{s} = 500$ GeV per collision. Typically for Au+Au heavy ion running, two beams each containing ∼60 bunches of 10^9 gold ions circulate in opposite directions with peak luminosity $\sim 10^{30}$ cm^{-2}s^{-1}.

Collision points are designed at six crossing points about the ring, four of which have hosted experiments: STAR, PHENIX, PHOBOS and BRAHMS. BRAHMS is a small acceptance high precision hadron spectrometer designed to measure particle multiplicity as a function of the scattering angle with respect to the beam axis. PHOBOS is a large acceptance hadron spectrometer sensitive to unusual signatures that may indicate QGP formation. (BRAHMS and PHOBOS have concluded taking data and are now in data analysis mode exclusively.) PHENIX is a multi-purpose

detector sensitive to event evolution observables, especially lepton pairs and direct photons from the early thermalization phase.

My research was conducted as a member of the STAR collaboration. STAR (Solenoidal Tracker at RHIC) is a massive cylindrical gas-filled object two stories tall housing a magnetic field strong enough to levitate a workman's wrench. As a monument to collective human enterprise it is the modern analogue of a Gothic cathedral. STAR has the largest acceptance overall of the four experiments. It can detect a broad range of hadronic and leptonic observables using tracking, particle identification and electromagnetic calorimetry with excellent capability to measure high-p_T jets [26].

The STAR detector is actually an ensemble of specialized subdetectors, nearly all having full azimuthal acceptance. A complete categorical description of each subdetector is beyond the scope of this work, but a review of their key features is essential to understanding how the events of our data ensemble were recorded and reconstructed.

At the heart of the STAR detector, situated in a room-temperature 0.5 Tesla magnetic field, is the primary tracking device, the Time Projection Chamber or TPC. The cylindrical TPC has radius 2.0 meters and length 4.2 meters, at the time of its completion the largest such detector in the world [27]. The TPC is an axial drift chamber that measures the momentum and energy loss of charged particles. Combined with the SVT, momentum resolution within 2 percent is achievable for a majority of tracks in the TPC [28]. While the pseudorapidity acceptance is reported as +/- 1.8 units of pseudorapidity, in practice, due to variation in the collision z-vertex, the effective acceptance is not more than $|\eta| < 1.2$, and quality cuts of $|\eta| < 1.0$ are standard at STAR.

The Silicon Vertex Detector (SVT) and Forward Time Projection Chamber (FTPC) provide additional tracking data at mid- and forward rapidity, respectively. The

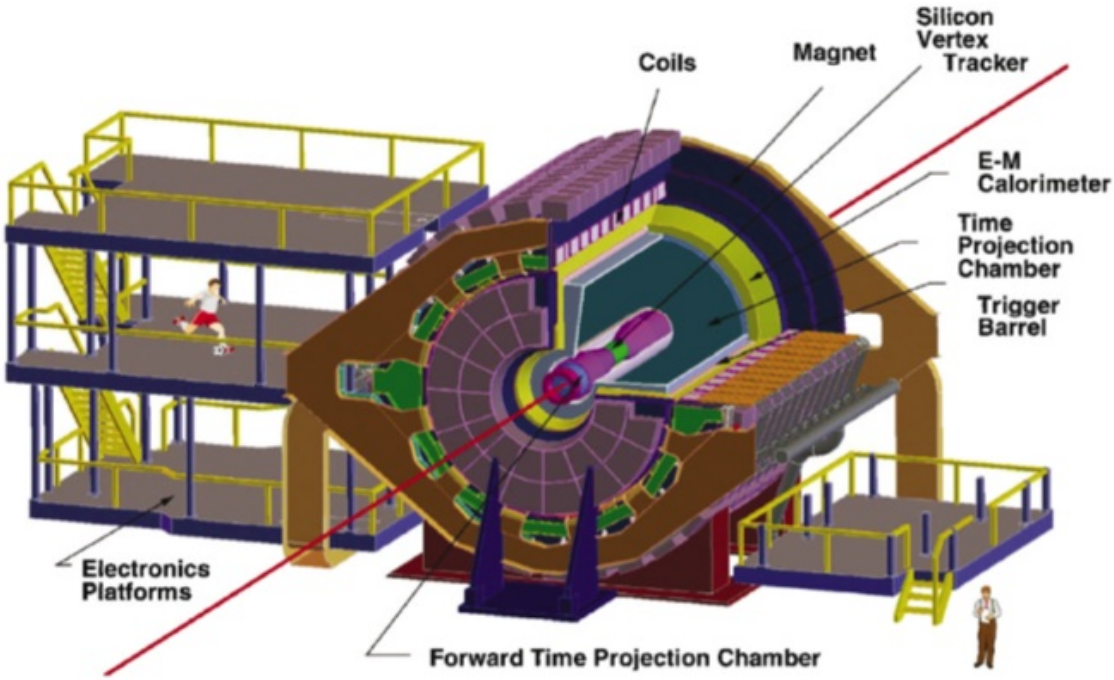

Figure 4.1: A schematic view of the STAR detector.

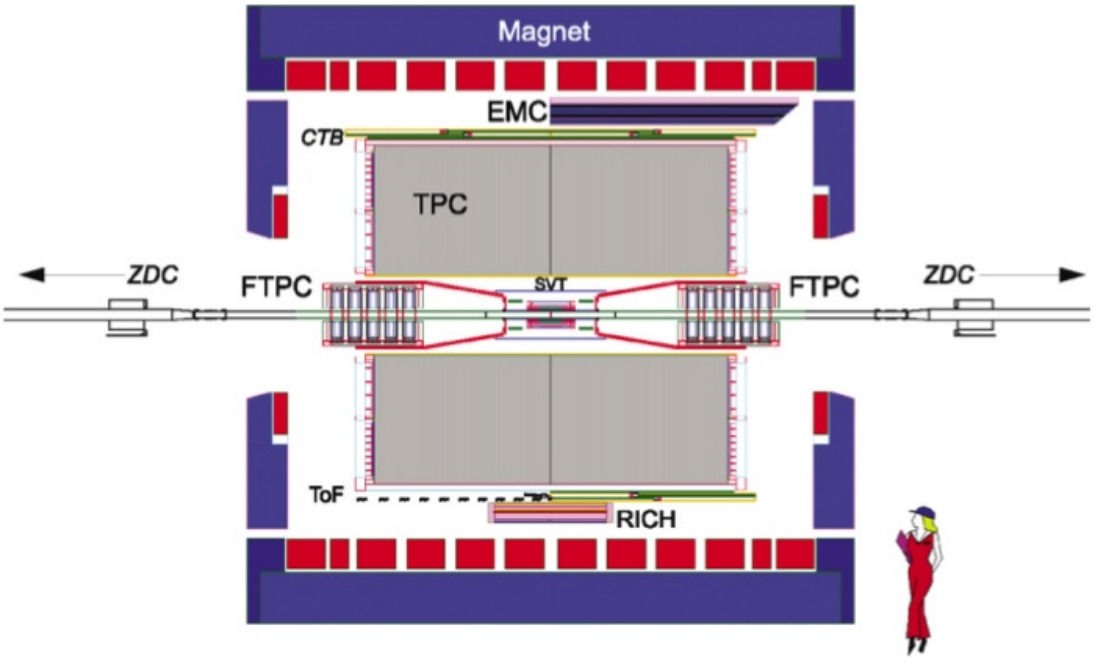

Figure 4.2: Cutaway view of the STAR detector

FTPC is a radial drift time projection chamber consisting of two units with combined acceptance in the range $2.5 < |\eta| < 4.0$. Photons, electrons and positrons from the electromagnetic decay of neutral hadrons are detected by the Barrel Electromagnetic Calorimeter (BEMC) and a single Endcap Electromagnetic Calorimeter (EEMC). The BEMC and EEMC together have a combined acceptance of $-1.0 < \eta < 2.0$ [28].

Essential to triggering and event characterization at STAR are the "fast" detectors, the Central Trigger Barrel (CTB) and the Zero Degree Calorimeters (ZDC). The CTB, with acceptance $|\eta| < 1.0$, surrounds the TPC to record the flux of charged particles in an event. The ZDCs are calorimeters located at +/- 18 meters of the collision to record the energy of undeflected remnant "spectator" neutrons. "Minimum bias" events, such as used in this analysis, are triggered by a coincident signal larger than one neutron in each of the two ZDCs. In the case of smaller impact parameter an algorithm combining signals in the ZDC and CTB is employed for min-bias triggering [28]. The ZDCs are also used to measure beam luminosity; each of the four RHIC experiments has an identical pair of ZDCs[29].

For the purposes of this analysis the key particle observables are pseudorapidity η, azimuthal angle ϕ, transverse momentum p_T and electric charge, all of which rely heavily on the capabilities of the TPC.

4.2 STAR Run IV Au+Au Data

The current analysis uses Au+Au collision data at $\sqrt{s_{NN}} = 200$ GeV recorded by the STAR experiment during year 2004 (Run IV). To minimize truncation of the pseudorapidity distributions, events with collision z-vertex more distant than 25 cm from the center of the TPC are excluded. (For some diagnostic studies, the exclusion boundary was relaxed to 30 cm.) To insure track quality, particles are restricted to the momentum range $p_T > 0.2$ GeV/c. The particle detection efficiency of the TPC falls off rapidly outside $|\eta| = 1$, so only particles recorded within the pseudorapidity

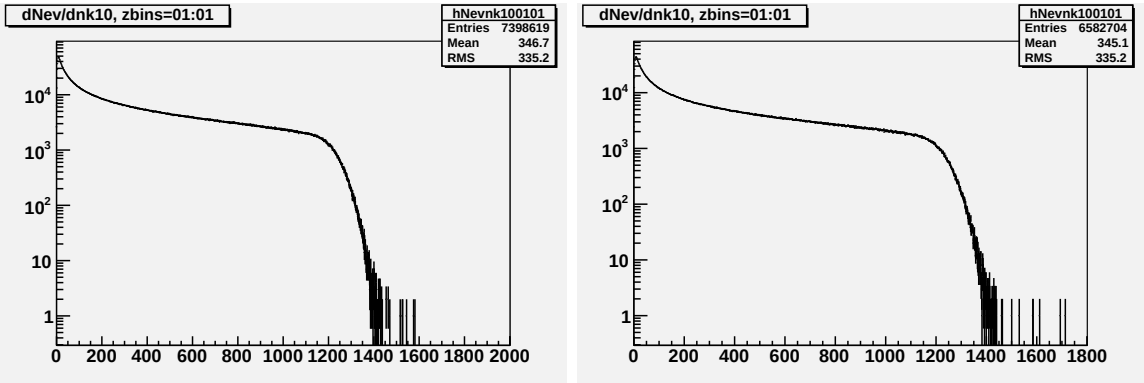

Figure 4.3: Event distribution dN_{ev}/dN for $|\eta| < 1.0$ centrality definitions. Full Field (*left*), Reverse Full Field (*right*).

range $|\eta| < 1.0$ are used. To minimize the effects of track splitting, each particle track must have a minimum of 15 "fit" points in the TPC detector, and the ratio of actual fit points to possible fit points must equal .52 or greater. The total number of usable events in the analysis is nearly 14 million, 7,398,619 with the magnet at Full Field of 0.5 Tesla, and 6,582,704 with the field reversed.

4.3 Statistical Distributions

Because the number of particles produced in a heavy-ion collision is so large, it is feasible to study the event as a statistical ensemble. Historically, the functions most used for such study were the C_2 cumulant and the R_2 correlation function, which is a normalized version of the C_2 cumulant. Cumulants have applications in many areas of statistical physics. We begin with the definition and notation we will use for a statistical distribution.

Let X be a random variable that expresses a global quantity associated with an event in our data ensemble. The statistical distribution of X with respect to a point x in momentum space is a function which gives a value proportional to the fraction of the global quantity that occurs locally at x. Two global quantities of interest in this analysis are the total number of charged particles in an event N and the total transverse momentum of the charged particles in an event p_T. The statistical distributions used in this analysis are of two kinds, closely related: 1) an experimental, sampling distribution determined event-by-event from the data ensemble on a discretized set of points ("bins"), and 2) a theoretical, continuous analytical distribution that is supposed to result in passing to the limit of infinitesimal binsize, infinite trial events and 100 percent detector efficiency.

We begin with the experimental, sampling distribution. Let N_{ev} be the number of events in our data ensemble and $n_k^{(\alpha)}$ be the number of particles in the k^{th} event. The superscript α represents the set of quality and kinematic criteria applied to the particle. Choosing, for concreteness, the variable x in momentum space to be the rapidity y, we define the sampling distributions of $N^{(\alpha)}$ and $P_T^{(\alpha)}$ for a fixed finite bin, denoted δy:

$$\frac{dN^{(\alpha)}}{dy}(\delta y) = \frac{1}{N_{ev}} \sum_{k=1}^{N_{ev}} \sum_{i=1}^{n_k^{(\alpha)}} n_{ki}^{(\alpha)}(\delta y) \frac{1}{|\delta y|} \tag{4.1}$$

$$\frac{dP_T^{(\alpha)}}{dy}(\delta y) = \frac{1}{N_{ev}} \sum_{k=1}^{N_{ev}} \sum_{i=1}^{n_k^{(\alpha)}} n_{ki}^{(\alpha)}(\delta y) p_{Tki} \frac{1}{|\delta y|} \tag{4.2}$$

Here, $n_{ki}^{(\alpha)}$ is a Bernoulli random variable, with $n_{ki}^{(\alpha)} = 1$ if the rapidity of the i^{th} (α-qualified) particle in the k^{th} event is located in the interval δy, else $n_{ki}^{(\alpha)} = 0$. p_{Tki} is the magnitude of the transverse momentum of the i^{th} particle in the k^{th} event.

Notation : Henceforth we omit the superscript α, except where needed as a reminder. The symbol N alone, as a default, will refer to all charged primary particles satisfying a specified set of kinematic criteria. When a particular subset of charged particles or charged pairs is intended the notation will so indicate, *e.g.* N^{+-} or N_2^{++}. We also substitute the point y for the finite bin δy with the understanding that for sampling distributions the equations hold binwise rather than pointwise. Accordingly *we will omit the explicit division by the binsize* $|\delta y|$ that is required to convert the histogram of recorded data to a sampling distribution; the context will generally make clear when the binsize factor is necessary. Last, since the Leibniz notation displays the independent variables in the denominator, the explicit functional dependence shown in parentheses is redundant, and so will be omitted for the *sampling* distribution but retained for the *analytical* distribution. The definitions then simplify:

$$\frac{dN}{dy} = \frac{1}{N_{ev}} \sum_{k=1}^{N_{ev}} \sum_{i=1}^{n_k^{(\alpha)}} n_{ki}(y) \tag{4.3}$$

$$\frac{dp_T}{dy} = \frac{1}{N_{ev}} \sum_{k=1}^{N_{ev}} \sum_{i=1}^{n_k^{(\alpha)}} n_{ki}(y) p_{Tki} \tag{4.4}$$

These formulas are by definition equivalent to, respectively, the ensemble sample means of the number of particles per event and the transverse momentum per event, recorded in bin δy, which is now represented by the point y:

$$\frac{dN}{dy} = \langle n_k(y) \rangle \tag{4.5}$$

$$\frac{dp_T}{dy} = \langle p_{T\,k}(y) \rangle \tag{4.6}$$

Passing to the limit of infinitesimal binsize, infinite events and ideal detector efficiency gives us the continuous analytical distributions:

$$\rho_1(y) = \lim_{\substack{|\delta y| \to 0 \\ N_{ev} \to \infty}} \frac{dN}{dy} \tag{4.7}$$

$$\rho_1^{p_T}(y) = \lim_{\substack{|\delta y| \to 0 \\ N_{ev} \to \infty}} \frac{dp_T}{dy} \tag{4.8}$$

We must keep in mind however that for a finite number of events N_{ev} the sampling distributions are only a statistical estimate of the analytical distributions. Also, in our analysis we must take account of the detector inefficiencies. We define $\epsilon_1(y)$ to be the efficiency of the detector at (the bin containing) y, with respect to the *given distribution*. The efficiency function ϵ for counting numbers of particles need not be identical to the efficiency function for recording transverse momentum of particles. With this understanding, to relate the sampling and analytical distributions for finite N_{ev} we use the expression:

$$\rho_1(y) * \epsilon_1(y) = \frac{dN}{dy} \tag{4.9}$$

$$\rho_1^{p_T}(y) * \epsilon_1(y) = \frac{dp_T}{dy} \tag{4.10}$$

We proceed to the pair distributions. First we show the two-particle distributions for number pairs and transverse momentum pairs:

$$\rho_2(y_1, y_2) \approx \frac{d^2 N_2}{dy_1 dy_2} = \frac{1}{N_{ev}} \sum_{k=1}^{N_{ev}} \sum_{i=1}^{n_k^{(\alpha_1)}} \sum_{j \neq i}^{n_k^{(\alpha_2)}} n_{ki}(y_1) n_{kj}(y_2) \tag{4.11}$$

$$\rho_2^{p_{T1} p_{T2}}(y_1, y_2) \approx \frac{d^2 p_{T1} p_{T2}}{dy_1 dy_2} = \frac{1}{N_{ev}} \sum_{k=1}^{N_{ev}} \sum_{i=1}^{n_k^{(\alpha_1)}} \sum_{j \neq i}^{n_k^{(\alpha_2)}} n_{ki}(y_1) n_{kj}(y_2) p_{T\,ki} p_{T\,kj} \tag{4.12}$$

To define our third pair distribution we need the ensemble average particle momentum, defined by:

$$\overline{p}_{T_1}(y_1) = \frac{\rho_1^{p_T}(y_1)}{\rho_1(y_1)} \approx \frac{dp_T/dy}{dN/dy} = \frac{\sum_{k=1}^{N_{ev}} \sum_{i=1}^{n_k^{(\alpha)}} n_{ki}(y_1) * p_{Tki}}{\sum_{k=1}^{N_{ev}} \sum_{i=1}^{n_k^{(\alpha)}} n_{ki}(y_1)} \tag{4.13}$$

We adopt the overline notation to indicate ensemble average per particle, since we already use $\langle\ \rangle$ to denote the ensemble average per event. Letting $\Delta p_{Tki} = p_{Tki} - \overline{p}_{T_1}(y_1)$ denote the deviation of the transverse momentum of the i^{th} first particle in the k^{th} event from the ensemble particle average at y_1, and $\Delta p_{Tkj} = p_{Tkj} - \overline{p}_{T_1}(y_2)$ denote the deviation of the transverse momentum of the j^{th} second particle in the k^{th} event from the ensemble particle average at y_2, we define the two-particle distribution for transverse momentum variance, or $\rho_2^{\Delta p_{T1}\Delta p_{T2}}$:

$$\rho_2^{\Delta p_{T1}\Delta p_{T2}}(y_1, y_2) \approx \frac{d^2\Delta p_{T1}\Delta p_{T2}}{dy_1 dy_2} = \frac{1}{N_{ev}} \sum_{k=1}^{N_{ev}} \sum_{i=1}^{n_k^{(\alpha_1)}} \sum_{j\neq i}^{n_k^{(\alpha_2)}} n_{ki}(y_1) n_{kj}(y_2) \Delta p_{Tki} \Delta p_{Tkj} \tag{4.14}$$

Each of the three two-particle distributions above, ρ_2, $\rho_2^{p_{T1}p_{T2}}$, and $\rho_2^{\Delta p_{T1}\Delta p_{T2}}$ contains information about correlated, same-event particle pairs that will be incorporated in our three correlation observables described in the next section.

Note that in the two-particle distributions we may have $\alpha_1 \neq \alpha_2$, that is the sets of kinematic criteria for the first and second particle may differ. In such analyses of non-identical sets of particles the pair $i = j$ is to be included in the sum.

As was the case for the single-particle distributions, the two particle distributions may be written in the form of an ensemble sample mean:

$$\frac{d^2N_2}{dy_1 dy_2} = \langle n_k^{(\alpha)}(y_1)(n_k^{(\alpha)}(y_2) - 1)\rangle \tag{4.15}$$

$$\frac{d^2N_2}{dy_1dy_2} = \langle n_k^{(\alpha_1)}(y_1)n_k^{(\alpha_2)}(y_2)\rangle \tag{4.16}$$

The first equation holds when the criteria α are identical for the first and second sets of particles, the second equation holds for $\alpha_1 \neq \alpha_2$.

We write the relation between the two-particle sampling and analytical distributions as:

$$\rho_2(y_1, y_2) * \epsilon_2(y_1, y_2) \ = \frac{d^2N_2}{dy_1dy_2} \tag{4.17}$$

It will be seen that, to first order, the two-particle detector efficiency factors into a product of single-particle efficiencies:

$$\epsilon_2(y_1, y_2) = \epsilon_1(y_1) * \epsilon_1(y_2) \tag{4.18}$$

This fact will motivate the normalization of the C_2 cumulant to form the R_2 correlation function in the next section.

Over all momentum space, the normalization for the one- and two-particle number distributions is:

$$\int \frac{dN}{dy}dy = \langle n_k\rangle \tag{4.19}$$

$$\int \frac{d^2N_2}{dy_1dy_2}dy_1dy_2 = \langle n_k(n_k-1)\rangle \tag{4.20}$$

where n_k is the number of particles in the k^{th} event and $\langle\ \rangle$ denotes the sample mean taken over all the events in the data ensemble.

4.4 Correlation Cumulants

Correlation cumulants are a measure of the deviation from randomness of a multiparticle distribution. They are defined so as to vanish when no correlations exist

between the particles.

Given a two-particle distribution ρ_2, it is equal to a decomposition into a term which is a product of the two single-particle distributions plus a balancing term known as the C_2 cumulant. For concreteness we again use rapidity y as the momentum space variable.

$$\rho_2(y_1, y_2) = \rho_1(y_1)\rho_2(y_2) + C_2(y_1, y_2) \tag{4.21}$$

We refer to the product of single particle distributions $\rho_1(y_1)\rho_1(y_2)$ as the *uncorrelated* pair distribution and $\rho_2(y_1, y_2)$ as the *correlated* pair distribution. Using this terminology, the C_2 cumulant is equal to the correlated pair distribution minus the uncorrelated pair distribution:

$$C_2(y_1, y_2) = \rho_2(y_1, y_2) - \rho_1(y_1)\rho_1(y_2) \tag{4.22}$$

In this way, the properties of the two-particle distribution which pertain exclusively to correlated pairs are relegated to a separate function, the C_2 cumulant. Those properties which are simply the random result of taking the product of the single-particle distributions are subtracted away. In the event that the correlated pair distribution is not different from the random, uncorrelated pair distribution, the C_2 cumulant vanishes.

Higher order cumulants. Though we will not use them in this analysis, higher-order cumulants may be defined similarly. Given a multivariate distribution of n quantities, ρ_n, there is a decomposition of the distribution as a sum of products of distributions and cumulants each with less than n quantities [30]. The number of terms in the decomposition is equal to a partition of n.

For example, given a three-particle distribution ρ_3, it is equal to a decomposition where the terms on the right hand side are the three single-particle distributions multiplied together, plus the first single-particle distribution multiplied by the two-

particle cumulant of the second and third particle, plus a term which is the second single-particle distribution multiplied by the two-particle cumulant of the first and third particle, plus a term which is the the third single-particle distribution multiplied by the two-particle distribution of the first and second particle, plus a final term, the C_3 cumulant, which contains all the properties of the three-particle distribution which are not attributable to lower-order distributions or cumulants. Briefly:

$$\rho_3(y_1, y_2, y_3) = \rho_1(y_1)\rho_1(y_2)\rho_1(y_3) + \sum_{\binom{3}{1}\text{terms}} \rho_1(y_1)C_2(y_2, y_3) + C_3(y_1, y_2, y_3) \quad (4.23)$$

The higher-order cumulants are obtained by inversion after substituting for all lower-order cumulants:

$$C_3(y_1, y_2, y_3) = \rho_3(y_1, y_2, y_3) - \sum_{\binom{3}{1}\text{terms}} \rho_1(y_1)\rho_2(y_2, y_3) + 2\rho_1(y_1)\rho_1(y_2)\rho_1(y_3) \quad (4.24)$$

Semi-inclusive vs. inclusive cumulants. Up to this point we have been dealing with the inclusive C_2 cumulant which is created from all collisions regardless of the topological multiplicity n of the decay particles. We define the semi-inclusive $C_2^{(n)}$ cumulant to be the C_2 cumulant created when a fixed number n of particles are produced in an event.

$$C_2^{(n)}(y_1, y_2) = \rho_2^{(n)}(y_1, y_2) - \rho_1^{(n)}(y_1)\rho_1^{(n)}(y_2) \quad (4.25)$$

The inclusive C_2 cumulant has an algebraic decomposition into a weighted sum of the semi-inclusive $C_2^{(n)}$ cumulants plus a term that is the weighted sum of the convolution product of the difference between the inclusive single-particle distribution

and the single-particle distribution for fixed n.

$$C_2(y_1, y_2) = \langle C_2^{(n)} \rangle + \langle (\rho_1^{(n)} - \rho_1)(\rho_1^{(n)} - \rho_1) \rangle \tag{4.26}$$

$$= C_S + C_L \tag{4.27}$$

All instrinsic correlations must be present in the first C_S term on the right hand side, the weighted sum of semi-inclusive cumulants, since it is the only term which contains same-event pairs. The second C_L term on the right hand side contributes to the C_2 cumulant only by correlations between events with different multiplicity, *i.e.* from the mixing of events. The subscripts S and L recall historical notation describing the two terms as "short"- and "long"-range correlations respectively. More precise terminology would call the first term the "intrinsic" term and the second term the "multiplicity" term, since it depends on fluctuations in the multiplicity of particles n.

4.5 The Three Correlation Observables R_2, ΔP_T and C

The three correlation observables of our analysis are R_2, ΔP_T and C (R^{p_T}). The first and most important of the three is the R_2 number correlation function. The R_2 correlation is derived from the C_2 cumulant by dividing by the product of the first and second single-particle number distributions, that is the uncorrelated pair distribution or mixed-event distribution.

$$R_2 = \frac{C_2(y_1, y_2)}{\rho_1(y_1)\rho_1(y_2)} \tag{4.28}$$

From the definition of C_2 it is clear that R_2 is equal to the ratio of the correlated to the uncorrelated pair distribution, minus one:

$$R_2 = \frac{\rho_2(y_1, y_2)}{\rho_1(y_1)\rho_1(y_2)} - 1 \tag{4.29}$$

We define the semi-inclusive $R_2^{(n)}$ function as the semi-inclusive $C_2^{(n)}$ function

normalized by the inclusive $\rho_1\rho_1$ uncorrelated pair distribution.

$$R_2^{(n)}(y_1, y_2) = \frac{C_2^{(n)}(y_1, y_2)}{\rho_1(y_1)\rho_1(y_2)} \tag{4.30}$$

The inclusive R_2 correlation function inherits from C_2 the algebraic decomposition into a same-event, intrinsic term, R_S, and a mixed-event or multiplicity term, R_L.

$$R_2(y_1, y_2) = \frac{\langle C_2^{(n)} \rangle}{\rho_1(y_1)\rho_1(y_2)} + \frac{\langle (\rho_1^{(n)} - \rho_1)(\rho_1^{(n)} - \rho_1) \rangle}{\rho_1(y_1)\rho_1(y_2)} \tag{4.31}$$

$$= \frac{C_S}{\rho_1(y_1)\rho_1(y_2)} + \frac{C_L}{\rho_1(y_1)\rho_1(y_2)} \tag{4.32}$$

$$= R_S + R_L \tag{4.33}$$

The decomposition of R_2 into R_S and R_L will be useful when we analyze simulated data from a simple deterministic cluster model.

When the same-event pair distribution $\rho_2(y_1, y_2)$ contains no correlations, it then factors into the product of the single-particle number distributions, $\rho_1(y_1)\rho_1(y_2)$. In that case the R_2 correlation function becomes identically zero. This is the most common construction for the R_2 correlation function. However, different normalizations have historically been used for the R_2 correlation function, depending on what normalization is adopted for the particle distributions themselves. As stated previously we normalize the single-particle distribution to equal the average number of particles per event:

$$\int \rho_1(y) dy = \langle n \rangle \tag{4.34}$$

Similarly, the two-particle distribution function is normalized to equal the average number of particle pairs per event in the ensemble, which is the average of n times $n-1$, since a particle is never paired with itself.

$$\int \rho_2(y_1, y_2) dy_1 dy_2 = \langle n(n-1) \rangle \tag{4.35}$$

In some analyses correlations are made between sets of particles that are not identical. In that case, the normalization for the two-particle number distribution function ρ_2 would equal the average of the product of the number of particles in the first set times the number of particles in the second set, with the average being taken over the entire ensemble.

$$\int \rho_2(y_1, y_2) dy_1 dy_2 = \langle n_1 n_2 \rangle \tag{4.36}$$

Our second correlation observable is ΔP_T, which measures transverse momentum correlations, specifically the transverse momentum covariance per correlated pair. We define

$$\Delta P_T(y_1, y_2) = \frac{\rho_2^{\Delta p_{T1} \Delta p_{T2}}(y_1, y_2)}{\rho_2(y_1, y_2)} \tag{4.37}$$

ΔP_T is positive when both particles of a pair are more likely to be both higher or both lower than the average transverse momentum $\overline{p}_T$, and negative when a high p_T particle is more likely to be accompanied by a particle with p_T lower than average.

Our third correlation observable C ($R_2^{p_T}$) is a hybrid that combines number and transverse momentum correlations. The construction procedure follows that of the two-particle number correlation observable R_2, but with number distributions replaced by momentum distributions. We begin by constructing a cumulant, a transverse momentum version of C_2, call it $C_2^{p_T}$, that is the correlated momentum pair distribution minus the uncorrelated momentum pair distribution:

$$C_2^{p_T}(y_1, y_2) = \rho_2^{p_{T1} p_{T2}}(y_1, y_2) - \rho_1^{p_{T1}}(y_1) \rho_1^{p_{T2}}(y_2) \tag{4.38}$$

As we did to construct R_2, we normalize the cumulant by dividing by the uncor-

related (number) pair distribution,

$$R_2^{p_T}(y_1, y_2) = \frac{C_2^{p_T}}{\rho_1(y_1)\rho_1(y_2)} = \frac{\rho_2^{p_{T1}p_{T2}}(y_1, y_2) - \rho_1^{p_{T1}}(y_1)\rho_1^{p_{T2}}(y_2)}{\rho_1(y_1)\rho_1(y_2)} \tag{4.39}$$

Since $\rho_1^{p_T}(y_1)/\rho_1(y_1) = \overline{p}_{T_1}(y_1)$, this may be rewritten as

$$R_2^{p_T}(y_1, y_2) = \frac{\rho_2^{p_{T1}p_{T2}}(y_1, y_2)}{\rho_1(y_1)\rho_1(y_2)} - \overline{p}_{T_1}(y_1)\overline{p}_{T_2}(y_2) \tag{4.40}$$

The relation between $R_2^{p_T}$ and R_2 may be made explicit if we manipulate the equation to show the transverse momentum correlations normalized with correlated number pairs (as in the definition of ΔP_T):

$$R_2^{p_T}(y_1, y_2) = \frac{\rho_2^{p_{T1}p_{T2}}(y_1, y_2)}{\rho_2(y_1, y_2)} \frac{\rho_2(y_1, y_2)}{\rho_1(y_1)\rho_1(y_2)} - \overline{p}_{T_1}(y_1)\overline{p}_{T_2}(y_2) \tag{4.41}$$

$$= \frac{\rho_2^{p_{T1}p_{T2}}(y_1, y_2)}{\rho_2(y_1, y_2)}(R_2(y_1, y_2) + 1) - \overline{p}_{T_1}(y_1)\overline{p}_{T_2}(y_2) \tag{4.42}$$

The above relation is the justification for interpreting $R_2^{p_T}$ as a "transverse momentum current correlation." From this point forward we will denote $R_2^{p_T}$, the "transverse momentum current correlation" observable, by the letter C in agreement with the notation of Gavin *et al.* who used C to study viscosity of the strongly coupled quark-gluon plasma [31].

Change of Independent Variable. In the derivations above, the independent variable was taken for concreteness to be the rapidity y. In the analysis to follow, however, all three correlation observables have relative pseudorapidity $\Delta\eta$ and relative azimuth $\Delta\phi$ as independent variables. For brevity, the variables relative pseudorapidity and relative azimuth are often referred to collectively as relative *angle*, since ϕ is a proper angle and the pseudorapidity y is a hyperbolic function of the angle with respect to

the z-axis. The observables in the relative angle variables are:

$$R_2 = \frac{\rho_2(\Delta\eta, \Delta\phi)}{\rho_1 * \rho_1(\Delta\eta, \Delta\phi)} - 1 \tag{4.43}$$

$$C = \frac{\rho_2^{p_{T1}p_{T2}}(\Delta\eta, \Delta\phi)}{\rho_1 * \rho_1(\Delta\eta, \Delta\phi)} - \overline{p}_{T_1} * \overline{p}_{T_2}(\Delta\eta, \Delta\phi) \tag{4.44}$$

$$\Delta P_T = \frac{\rho_2^{\Delta p_{T1}\Delta p_{T2}}(\Delta\eta, \Delta\phi)}{\rho_2(\Delta\eta, \Delta\phi)} \tag{4.45}$$

The adjustments necessary to construct R_2, ΔP_T and C ($R_2^{p_T}$) for the variables $\Delta\eta$ and $\Delta\phi$ are discussed in the next section.

Normalization by N_{part}. Both R_2 and C ($R_2^{p_T}$) have the form of a same-event pair distribution normalized by a mixed-event pair distribution. Such correlation observables show a dilution of signal with increasing centrality, since the total number of same-event pairs has a linear dependence on the average charged particle multiplicity, $\rho_2 \sim \langle N \rangle$, while the mixed-event pairs show a quadratic dependence on average charged particle multiplicity, $\rho_1 * \rho_1 \sim \langle N^2 \rangle$. As different centrality percentile bins have, by construction, different values of $\langle N \rangle$, correlation signal strength as a function of centrality varies accordingly. To offset the dilution caused by multiplicity, for each centrality one can multiply the correlation observable by the average number of participants $\langle N_{part} \rangle$ calculated for that bin to create new observables, $R_2(NP)$ and $C(NP)$. In the Results section we will show the $R_2(NP)$ and $C(NP)$ for comparison with R_2 and C.

4.6 Computer Algorithm

We now describe the computer algorithm for the construction of the three correlation observables R_2, ΔP_T and C as a function of the independent variables $\Delta\eta$ and $\Delta\phi$, that is the relative pseudorapidity and relative azimuth. We concentrate on the R_2 correlation function and only at the end will we note the slight modifications to

the procedure that are needed to construct ΔP_T and C. For simplicity, we first construct our observable as if we had a 100 percent efficient, ideal detector. We assume the ideal detector may detect all particles that are produced in the collisions. Later when we perform our data analysis we apply corrections to the data that must be made to compensate for the reality of our detector.

The quantities of interest for our three correlation observables are particle number and transverse momentum. Each charged particle produced in the collision has a momentum that is displayed by the radius of the path the particle traces by ionizing the gas in the uniform axial magnetic field inside the detector. By fitting a curve to the particle path and tracing backward along the trail of ions, the original angle in η and ϕ of the track emerging from the collision may be calculated.

The dataset of our analysis comprises an ensemble of events. Each event is a Au+Au heavy ion collision. We represent the total number of such events by N_{ev}. The total number of individual particles produced in event k is represented by n_k. Since we are interested in correlated pairs, we distinguish between "first" and "second" particles when forming pairs from the n_k particles in event k. In general, the first and second particles considered belong to (possibly distinct) subsets of the total number of particles n_k produced in the event. The cardinality of the two subsets may differ, $n_k^{(\alpha_1)} \neq n_k^{(\alpha_2)}$, as well as the composition. The subsets result from the application of selection criteria such as track quality, kinematic and dynamic properties, charge, particle species, *etc*. When studying the properties of "bulk" particles, the two subsets have identical distributions. However, one could also choose for the first distribution to represent a "trigger" particle chosen from a high-p_T range and the second distribution to represent an "associated" particle of lesser or equal transverse momentum. In such case the first and second particle are from subsets of the event with different kinematic properties. An even simpler example of non-identical subsets is unlike-sign particle pairs.

The basic structure of the analysis program to scan the data ensemble consists of three nested loops. The three loops correspond to the three summations that appear in the definition of the number and transverse momentum pair distributions. The first, outer loop is taken over the number of events N_{ev} in our ensemble. To create the sampling distribution corresponding to ρ_1, we construct the sample mean of the number of particles per event as a function of the independent variables (η, ϕ), represented by finite bins in a 2-dimensional histogram.

With each iteration over the index k of the outer loop of events, the next innermost loop with index i completes a loop over the number of first particles $n_k^{(\alpha_1)}$ in the event that meet the requirements of the set of selection criteria α. At the completion of each iteration of the i loop the number and transverse momentum p_T for each particle are recorded in "temporary" histograms labeled by charge and binned in pseudorapidity η and azimuthal angle ϕ. After reaching the last particle index $n_k^{(\alpha_1)}$ in the event, the total number of particles and total momentum of the particles recorded for each bin is added to a two-dimensional event-by-event histogram with the same partition of the (η, ϕ) coordinate grid as the temporary histograms. The square of the total number and total momentum in the event is also recorded in the histogram as "error" to later calculate the sample variance needed to calculate the error on the sample mean. The error on the sample mean for each bin, known as the standard deviation of the mean or σ_m, is calculated at the conclusion of the outer event loop by dividing the sample variance s^2 by the number of events (N_{ev}) and then taking the square root:

$$s^2 = \frac{1}{N_{ev}-1}\sum_{k=1}^{N_{ev}}(x_k - \overline{x})^2 \tag{4.46}$$

$$= \frac{N_{ev}}{N_{ev}-1}[\sum_{k=1}^{N_{ev}}(x_k)^2 - (\sum_{k=1}^{N_{ev}} x_k)^2] \tag{4.47}$$

$$\sigma_m = \sqrt{\frac{s^2}{N_{ev}}} \tag{4.48}$$

with $x_k = \sum_{i=1}^{n_k^{(\alpha)}} n_{ki}(y)$ in our notation.

To calculate the pair distribution ρ_2, a second particle loop with index j (third loop overall) is nested inside the first particle loop. The second particle loop with index j is completed within every iteration of the particle index i. The second loop runs over a second subset α_2 of particles which, for bulk correlations, will be the same subset α_1 as the first particles. In the bulk particle case, when the two sets of particles are the same, we omit the particle pair with j equal to i as this pair constitutes a particle paired with itself rather than a pair of distinct particles.

Note that a pair distribution of identical particles has symmetry with respect to the origin of the coordinate grid, since every pair appears twice, the second time with the particle order reversed. Reversing the order of the particles causes a reflection through the origin as the values of $\Delta\eta$ and $\Delta\phi$ are multiplied by minus one. When the first and second subsets of particles are different, however, this symmetry is not present. Like-sign and unlike-sign correlations are the most common example of identical and non-identical particle subsets.

In the limit as the number of events goes to infinity, for an ideal detector, there should be absolute physical symmetry with respect to the origin, with respect to the $\Delta\eta$-axis, and with respect to the $\Delta\phi$-axis. For a finite number of events N_{ev} and for non-identical particles, this symmetry is only approximate. For identical particles, however, the symmetry with respect to the origin by construction is exact.

The particle pairs for a representative event may be visualized as an event matrix, with each of the n_k particles in the event appearing as both a row and column index. In a bulk particle analysis, when the first and second set of particles forming the pairs are the same, we do not include the self-pairs of particles along the diagonal (i, i) of the event matrix. When the subsets of first and second particles are disjoint, no pairs appear on the diagonal of the event matrix since the indices will always be distinct. We may describe the set of same-event pairs as the direct product of the subset of

first particles and the subset of second particles, minus the event diagonal in the case of identical subsets.

Once the end of the nested loops of first and second particles is reached for the event k, the number of pairs and their product momentum for each bin of the grid in relative pseudorapidity $\Delta\eta$ and relative azimuth $\Delta\phi$ are recorded in histograms along with the squared value which, as stated above, is used to calculate the standard deviation of the mean for the value of the average number of pairs.

When the outermost event loop reaches the end of the dataset and the full ensemble of events has been scanned, the ρ_1 single-particle distribution with its error σ_m, and the ρ_2 pair distribution with its error are calculated. The next step is to construct the $\rho_1 * \rho_1$ product distribution, also called the uncorrelated pair distribution or mixed-event pair distribution, which is used to create the R_2 correlation function from the C_2 cumulant. In a four-dimensional space of η_1, η_2, ϕ_1, ϕ_2, the product distribution would simply be the two single-particle distributions $\rho_1(\eta_1, \phi_1)$, $\rho_1(\eta_2, \phi_2)$ multiplied together binwise. However, our independent variables are relative pseudorapidity $\Delta\eta$ and relative azimuthal angle $\Delta\phi$, therefore the quantity we seek needs to be the *convolution* of the first single-particle distribution $\rho_1(\eta_1, \phi_1)$ with the second single-particle distribution $\rho_1(\eta_2, \phi_2)$. The convolution is achieved by means of a quadruple loop undertaken after the scan of the event ensemble is completed: two loops for the variables η and ϕ, two loops for the first and second particle distributions. The effect of the convolution is to gather into a single bin in $(\Delta\eta, \Delta\phi)$ pairs of particles which have the same relative η and relative ϕ though they differ in absolute η and absolute ϕ.

The formula for a convolution gives the distribution for the sum of two random variables in terms of the individual distributions. A similar formula applies to the difference of two random variables, in which case the convolution is more correctly called a *cross-correlation*. The cross-correlation (denoted by $\star$) is simply a convolution

(denoted by $*$) with a negative argument. Analytically, some care must be taken with the variable ϕ, as the domain of integration is not an interval but a circle. However, for a real variable η on a finite interval, the cross-correlation of $\rho_1(\eta_1)$ and $\rho_1(\eta_2)$ to construct $\rho_1 \star \rho_1(\Delta\eta)$, where $\Delta\eta = \eta_2 - \eta_1$, is defined as:

$$\rho_1^{(1)} \star \rho_1^{(2)}(\Delta\eta) = \rho_1^{(1)}(-\eta) * \rho_1^{(2)}(\eta) \tag{4.49}$$

$$= \int_{\eta_{min}}^{\eta_{max}} \rho^{(1)}(-\eta')\rho^{(2)}(\Delta\eta - \eta')d\eta' \tag{4.50}$$

$$= \int_{-\eta_{max}}^{-\eta_{min}} \rho^{(1)}(\eta')\rho^{(2)}(\Delta\eta + \eta')d\eta' \tag{4.51}$$

$$= \int_{\eta_{min}}^{\eta_{max}} \rho^{(1)}(\eta')\rho^{(2)}(\Delta\eta + \eta')d\eta' \tag{4.52}$$

The last equality holds because our histogram is defined for an interval in η that is symmetric about zero. Going forward we will drop the pedantry and refer to the product of single-particle distributions simply as the convolution $\rho_1 * \rho_1$.

Many analyses would be content to stop at this step in the construction of $\rho_1 * \rho_1$. However, to be absolutely correct, a small adjustment must be made since we are dealing with a finite, sampling distribution rather than a theoretical, analytical distribution: we wish to exclude those pairs of particles in the convolution which come from the same event, since these are by definition correlated. Our $\rho_1 * \rho_1$ convolution should contain only mixed-event pairs of particles that are formed with the first and second particle taken from different events. If our ensemble of events is visualized as a matrix, the same-event matrices appear as N_{ev} block matrices along with diagonal, with the k^{th} block having dimension $n_k \times n_k$.

We omit from the $\rho_1 * \rho_1$ convolution those pairs of particles from the same-event block matrices along the diagonal of the event ensemble matrix, since these block matrices on the diagonal contain only pairs formed from the same event. Those pairs of same-event particles that we wish to omit from the $\rho_1 * \rho_1$ convolution include

the pairs that comprise the ρ_2 pair distribution, since by construction it contains all distinct pairs formed in the same event. However, we recall that ρ_2 does not contain same-event particle self-pairs, which should also be excluded from the $\rho_1 * \rho_1$ convolution. Therefore the same-event particle pairs in the block matrices along the ensemble diagonal must be excluded in their entirety in the creation of the $\rho_1 * \rho_1$ convolution.

This correction to the $\rho_1 * \rho_1$ convolution requires a corresponding slight change in normalization, because the total number of event-event pairs is no longer $(N_{ev})^2$, since we have omitted N_{ev} events that lay on the diagonal of the event ensemble matrix. Rather, the normalization factor will be $N_{ev}(N_{ev} - 1)$. The resulting $\rho_1 * \rho_1$ convolution represents the number of particle pairs we would find in an event if the particles were completely uncorrelated. In some analyses, this normalized $\rho_1 * \rho_1$ function, the uncorrelated or mixed-event pair distribution, is obtained by a mixing procedure which takes particles from different events that have similar event parameters. The process of re-grouping according to similarity of parameters is known as disaggregation, which will be discussed when we turn from an ideal detector to a real one in the next section.

To construct the distributions for the C and ΔP_T observables, two modifications to the above algorithm are needed. First, a separate, preliminary event loop must be run prior to the main event loop to produce the transverse momentum ensemble averages per particle. For bulk correlations with $\alpha_1 = \alpha_2$ the averages are equal.

$$\overline{p}_{T_1}(y_1) = \frac{\rho_1^{p_T}(y_1)}{\rho_1(y_1)} \tag{4.53}$$

$$\overline{p}_{T_2}(y_2) = \frac{\rho_1^{p_T}(y_2)}{\rho_1(y_2)} \tag{4.54}$$

Once the transverse momentum ensemble averages per particle are obtained, they are used in the main body of the program to construct $\rho_2^{\Delta p_{T1}\Delta p_{T2}}$, which is needed

for ΔP_T.

Second, when the event loop in the main body completes, the transverse momentum per particle convolution needed for C ($R_2^{p_T}$) is calculated:

$$\overline{p}_{T_1}(y_1) * \overline{p}_{T_2}(y_2) = \frac{\rho_1^{p_{T1}}(y_1) * \rho_1^{p_{T2}}(y_2)}{\rho_1(y_1) * \rho_1(y_2)} \tag{4.55}$$

The numerator and denominator are calculated separately and then divided bin-wise.

Chapter 5

Data Corrections

5.1 Event Disaggregation

We now describe various post-production programming routines which are necessary to account for the fact that our detector is not ideal. Although the corrections apply generally to all three correlation observables, our examples will show the R_2 correlation function where the effect is most visible. The corrections employed are mainly of two kinds: corrections with respect to events, and corrections with respect to particles (tracks). The corrections with respect to events employ the technique of disaggregation. Disaggregation is a common methodology in statistics that may be simply characterized as "comparing apples to apples". However, with apples and oranges we have the advantage that the set of equivalence classes of fruit is finite; the set of fruit does not form a continuum. However, when we disaggregate events in order to compare them, we find that our event parameters vary continuously and to disaggregate we must make an arbitrary partition to form equivalence classes of our events. We will then compare events within an equivalence class with themselves.

5.2 Centrality Binning

The key parameter for our analysis is event centrality. The centrality of a collision is a geometric parameter with a continuous range. We separate our events into percentiles of centrality based on the multiplicity of particles in the event. (Various

methods of determination of centrality will be discussed later.) The idea of centrality is to show how heavy-ion collisions of the most peripheral kind resemble $p + p$ collisions, while as the centrality of the collision increases, heavy ion collisions show characteristics indicative of the formation of a fluidlike medium, the quark-gluon plasma. The first correction to our R_2 correlation function will therefore be to disaggregate events by centrality percentile. For illustrative purposes, throughout the current section a centrality definition based on the Zero Degree Calorimeter is used which divides the dataset into five percentiles, 0-5, 5-10, 10-20, and 30-100. Later, in the analysis proper, results will be presented using a centrality definition based on recorded primary particle multiplicity in the Time Projection Chamber range of $|\eta| < 1.0$ for ten percentile bins 0-5, 5-10, 10-20, . . . , 70-80, 80-100.

5.3 z-vertex Binning

The next type of disaggregation concerns the fact that our detector has a finite central axis. The z-vertex of the collision may occur at any point along the axis. The efficiency of the detector at recording the tracks of the particles produced varies as the location moves from the center of the cylinder away toward the edge. Figure 5.1 shows the tail of the event distribution recorded for three z-vertex bins of width 2.5 cm separated by a distance of 22.5 cm.

We observe that events with a z-vertex displaced from the center have fewer particles recorded than those that occur in the center. Such events, even when the geometric impact parameter may be identical, will record different numbers of particles produced and be assigned to different centralities, causing systematic error.

Additionally, a collision taking place at large positive z produces an asymmetric distribution of particles shifted toward negative η, while a collision taking place at large negative z will produce a distribution shifted toward positive η. Figure 5.2 shows the ρ_1 distribution function for the 0-5 percent most central events for three

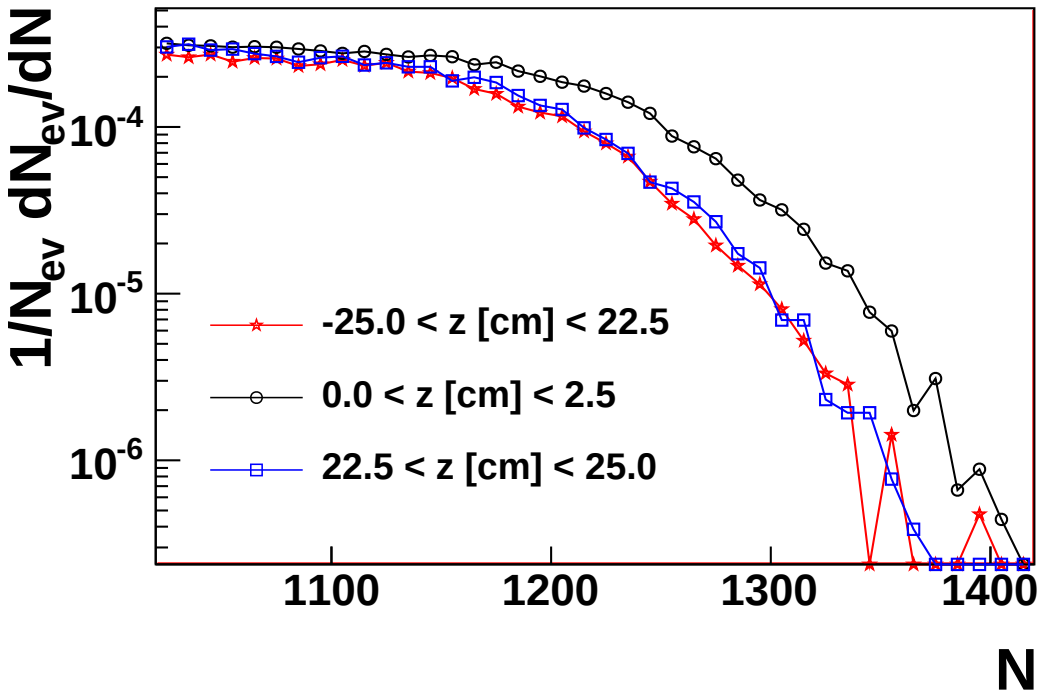

Figure 5.1: Tail distribution of dN_{ev}/dN in three distinct z-vertex bins of width 2.5 cm, separated by 22.5 cm, showing reduced efficiency in peripheral bins.

z-vertex bins of width 2.0 cm separated by a distance of 28 cm.

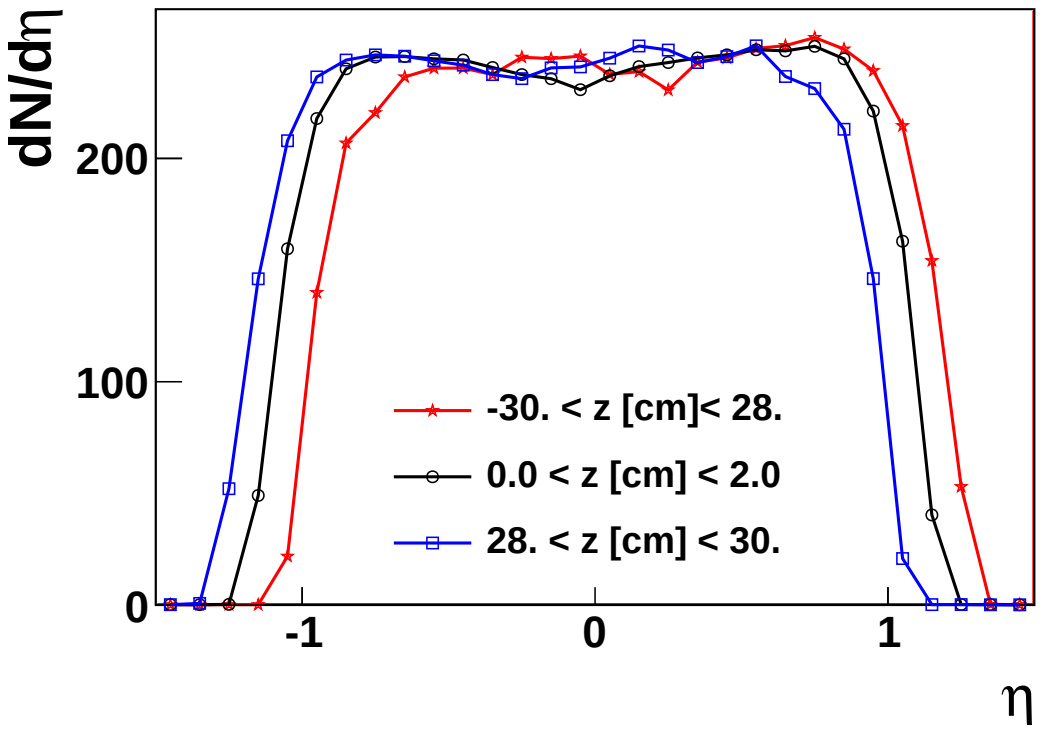

Figure 5.2: Single-particle distribution $\rho_1(\eta)$ in three distinct z-vertex bins of width 2.0 cm, separated by 28 cm, showing shifted efficiency in peripheral bins.

The ρ_1 single-particle distributions for the most peripheral of the three z-vertex bins of collisions are shifted away from the center. As a result, when we form the $\rho_1 * \rho_1$ convolution, particle pairs for large $\Delta\eta$ will be constructed that cannot physically exist in a single event because the spread in η exceeds the range of acceptance of the detector. Such pairs introduce undesirable "pseudocorrelations" into our R_2 observable. To avoid these pseudocorrelations, we partition the z-axis into bins of equal width, and calculate ρ_1, ρ_2, and $\rho_1 * \rho_1$ independently for each bin in z. Each bin in the partition of the z-axis represents an equivalence class of events and the R_2 correlation function is calculated for that bin. The final R_2 correlation function is then taken as the weighted average of the R_2 correlation functions calculated in each separate bin in z, weighted by the number of events occurring in that bin. The

effect of such z-binning may be clearly seen in Figure 5.3 thru Figure 5.6 which show plots of R_2 before and after z-binning correction. The deficit of correlations, previously concealed, that appears at $\Delta\eta = 0$ after correction, as shown in Figure 5.4 and Figure 5.6, is due to track merging, which will be discussed in the next section.

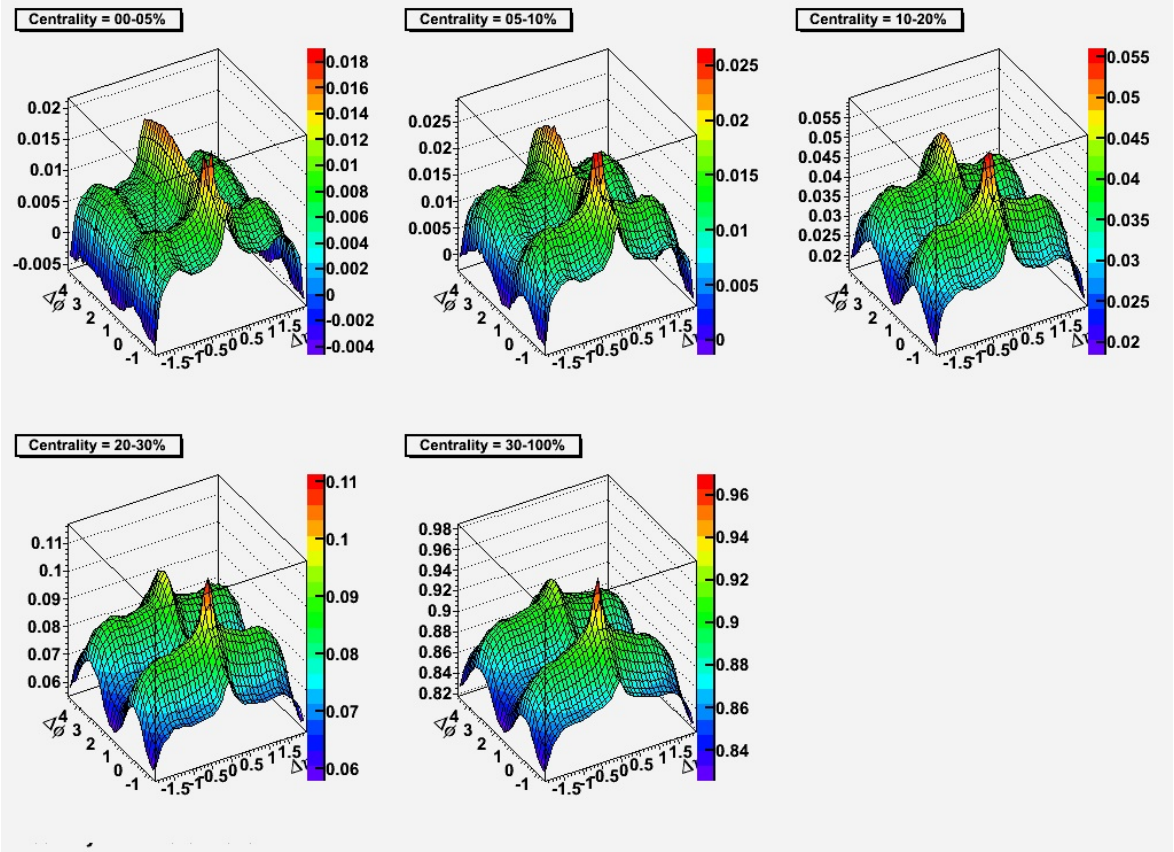

Figure 5.3: Before z-binning (3-d view): two-particle correlation function $R_2(\Delta\eta, \Delta\phi)$ calculated using a single z-vertex bin of width 60.0 cm. Pseudocorrelation artifacts due to mixing of events occurring at widely separated z-vertices appear near 0 and at large $|\Delta\eta|$.

Figure 5.3 and Figure 5.5 shows the R_2 correlation function calculated for a single equivalence class comprising the entire z-axis within 30 cm of the origin. There is only one z-bin, all events (at the given centrality shown) belong to the same equivalence class. In Figure 5.4 and Figure 5.6, the z-axis has been partitioned into thirty 2-cm bins. The R_2 correlation function is calculated separately for each bin, then the individual functions are summed weighted by the number of events occurring in each

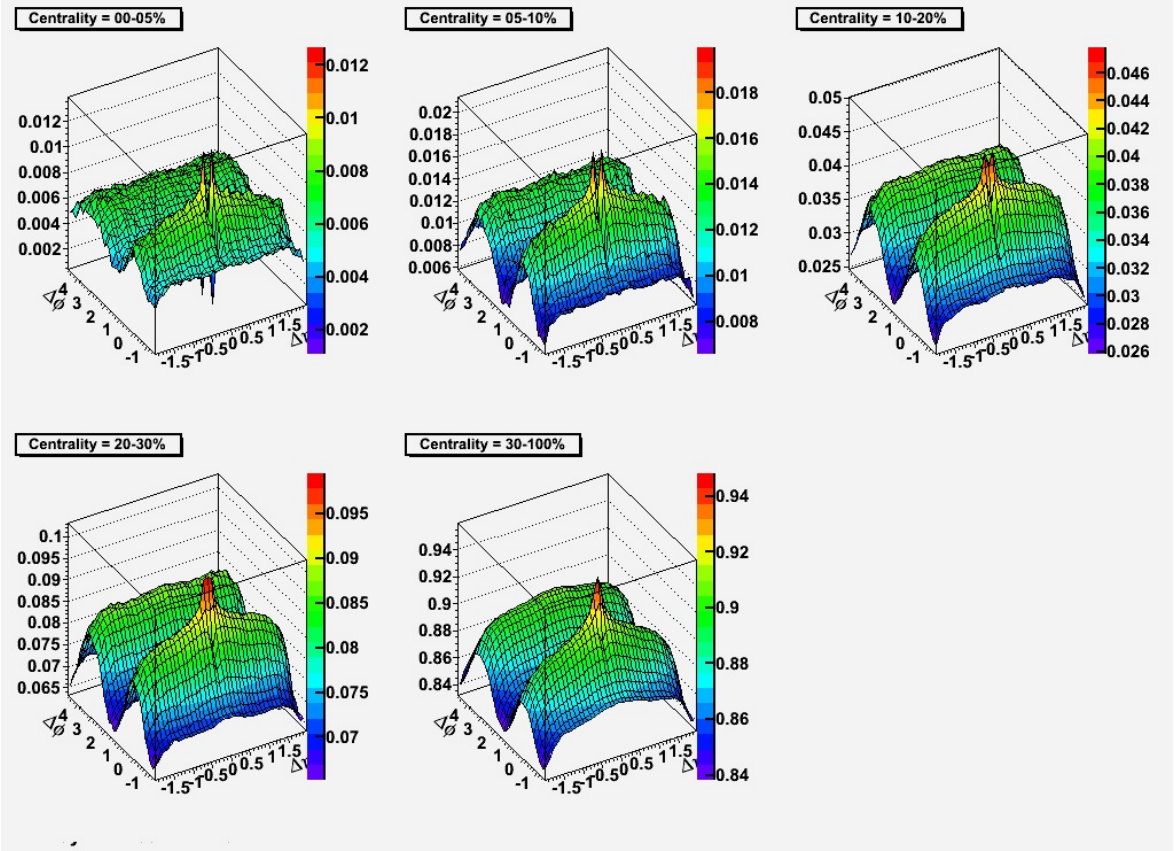

Figure 5.4: After z-binning (3-d view): two-particle correlation function $R_2(\Delta\eta, \Delta\phi)$ calculated using thirty z-vertex bins of width 2.0 cm each. Pseudocorrelation artifacts due to mixing of events occurring at widely separated z-vertices are eliminated.

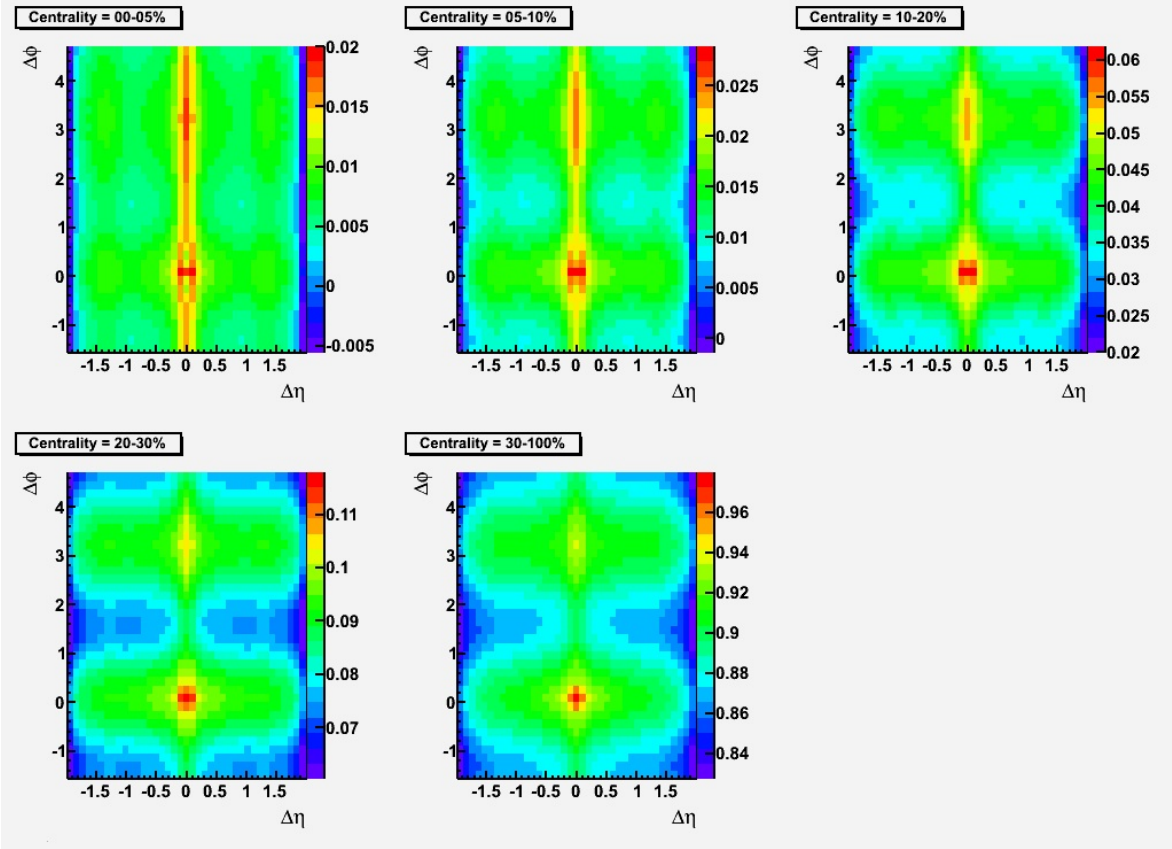

Figure 5.5: Before z-binning (2-d view): two-particle correlation function $R_2(\Delta\eta, \Delta\phi)$ calculated using a single z-vertex bin of width 60.0 cm. Pseudocorrelation artifacts due to mixing of events occurring at widely separated z-vertices appear near 0 and at large $|\Delta\eta|$.

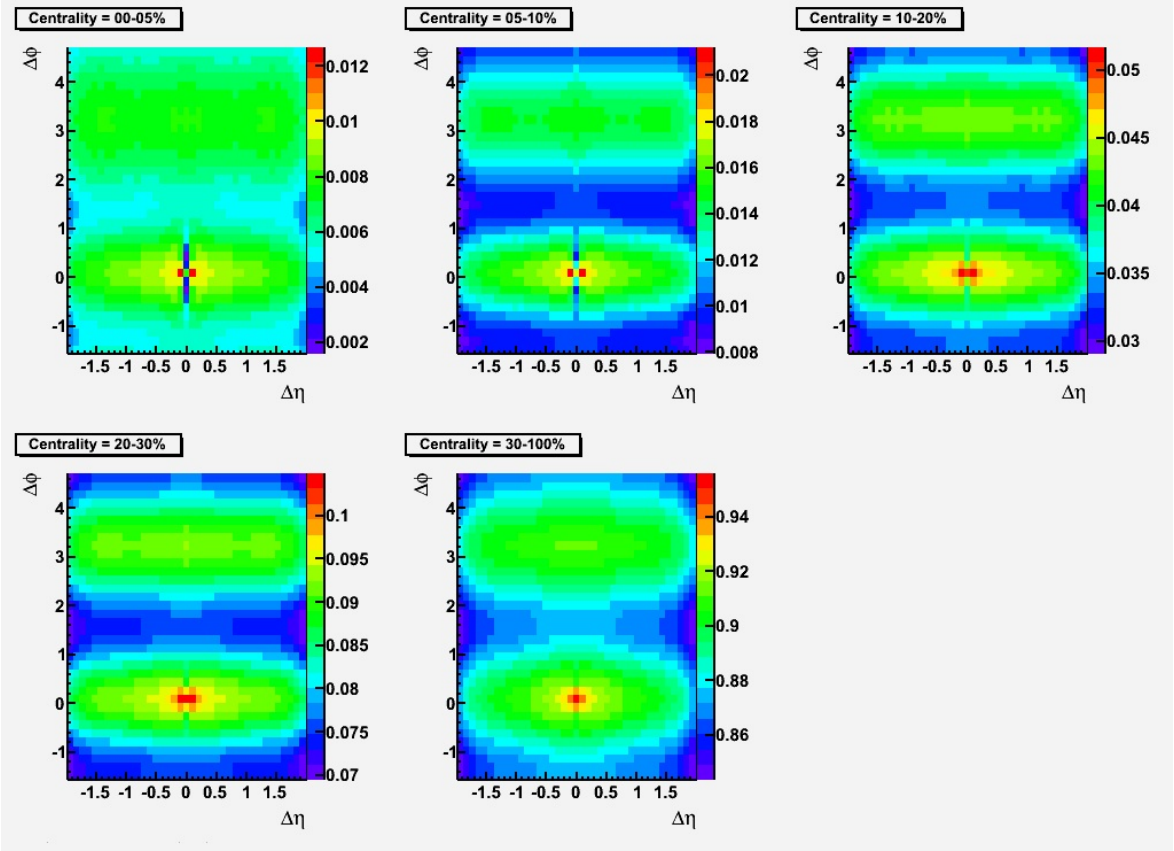

Figure 5.6: After z-binning (2-d view): two-particle correlation function $R_2(\Delta\eta, \Delta\phi)$ calculated using thirty z-vertex bins of width 2.0 cm each. Pseudocorrelation artifacts due to mixing of events occurring at widely separated z-vertices are eliminated.

z-bin. The same procedure is applied separately to the Full Field dataset and the Reverse Full Field dataset; the correlation observables for each bin are weighted by the number of events and re-summed. In this way we correct the R_2 correlation function to eliminate unwanted pseudocorrelations due to variation in the collision z-vertex.

In order to determine an optimal number of bins to use for the disaggregation of the z-vertex, we use an iteration procedure. We begin with a single bin over the full range in z and create the corresponding R_2 correlation function. We then double the number of bins and create the weighted R_2 function following the procedure described above. At each doubling of bin number we take the ratio of the more finely binned R_2 with the previous R_2. We stop the process when the number of bins is fine enough that the magnitude of the ratio becomes sufficiently small. Since the correlated pair distribution ρ_2 does not mix events with different z-vertices, there is no effect if the z-binning procedure is applied to it. However, the binning procedure may be applied to the mixed-event, uncorrelated pair distribution, $\rho_1 * \rho_1$. Figure 5.7 shows the ratio of $\rho_1 * \rho_1$ to itself for successive doublings of the number of z-bins. For a binsize of 2 cm versus 4 cm the ratio is of order 10^{-5}.

Because the efficiency of the detector varies as the z-vertex of the location of the collision is displaced from the center of the detector, each event properly sees a different detector, with a different efficiency. The efficiency is highest for collisions at the center of the detector and falls off as one moves away from zero in z. If the centrality of an event is determined by the multiplicity of particles recorded in a range in η, the multiplicities recorded for events at the periphery of the detector are not strictly comparable with those from events occurring at the center. Strictly speaking, every point on the z-axis has its own set of multiplicities corresponding to centrality percentiles, reflecting the efficiency of the detector at that point. However, if we were to continue to increase the number of z-vertex bins indefinitely the improvement in

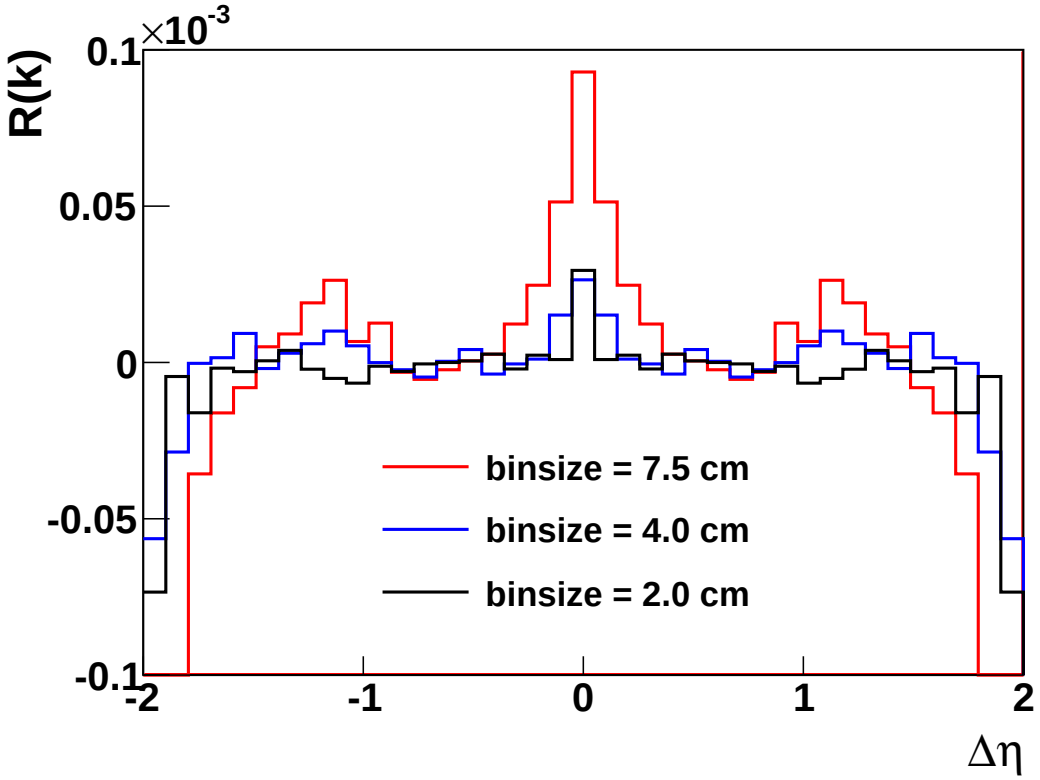

Figure 5.7: Ratio of the mixed-event distribution $\rho_1 * \rho_1(\Delta\eta)$ to itself for successive doublings of the number of z-bins.

R_2 would be offset by the decrease in statistics per bin. Higher statistics permit finer binning. For this analysis, we have selected as optimal a z-bin size of 2.0 cm for the z-vertex range of $|z| < 30$ cm used to investigate systematic error and a z-bin size of 2.5 cm for the z-vertex range $|z| < 25$ cm used for the analysis proper.

5.4 Track Merging

We now turn from the subject of disaggregation of events in our dataset ensemble to corrections that must be made to tracks within an event. The chief correction of this kind is for track merging. Track merging results from the fact that our detector, far from being an ideal detector with infinite spatial resolution, in fact has finite resolution and cannot resolve two individual tracks that occur within a certain distance of each other. As a result, the "hit" points of ions from two separate tracks may be recorded as being from a single track, leading to a deficit of tracks at certain bin combinations in $\Delta\eta$, $\Delta\phi$ which are susceptible to such merging. The areas prone to track merging differ for different charge combinations of pairs, due to the fact that the curvature of the tracks has different convexity depending on whether the charge is positive or negative.

We first discuss the case of track merging that occurs in unlike-sign pairs, as it is simplest. In unlike-sign track merging, the sign of the charges and thus the sign of the curvature differs for the two tracks. They cross one another. For merging to occur, the two tracks must have $\Delta\eta$ equal to zero and $\Delta\phi$ not equal to zero, as the tracks cannot be produced at the same angle and still cross. In order for the tracks to be confused as a single track, their p_T, transverse momentum must be similar enough that the tracks will re-cross, thus appearing to the detector as a single track. For this merging the p_T of the two particles need not be exactly the same, but the greater the difference in p_T, the more likely the detector will be able to resolve them into distinct tracks due to the difference in curvature. The bins affected by unlike-sign

track merging are thus the bin with $\Delta\eta$ equal to zero, along with the bins offset to one side of zero in $\Delta\phi$, lasting over an area of four or five bins out of a total of 36. Figure 5.8 and Figure 5.9 show uncorrected track merging in plots of $R_2^{+-}(\Delta\eta, \Delta\phi)$ and $R_2^{-+}(\Delta\eta, \Delta\phi)$ respectively. The second plot is a reflection of the first through the origin.

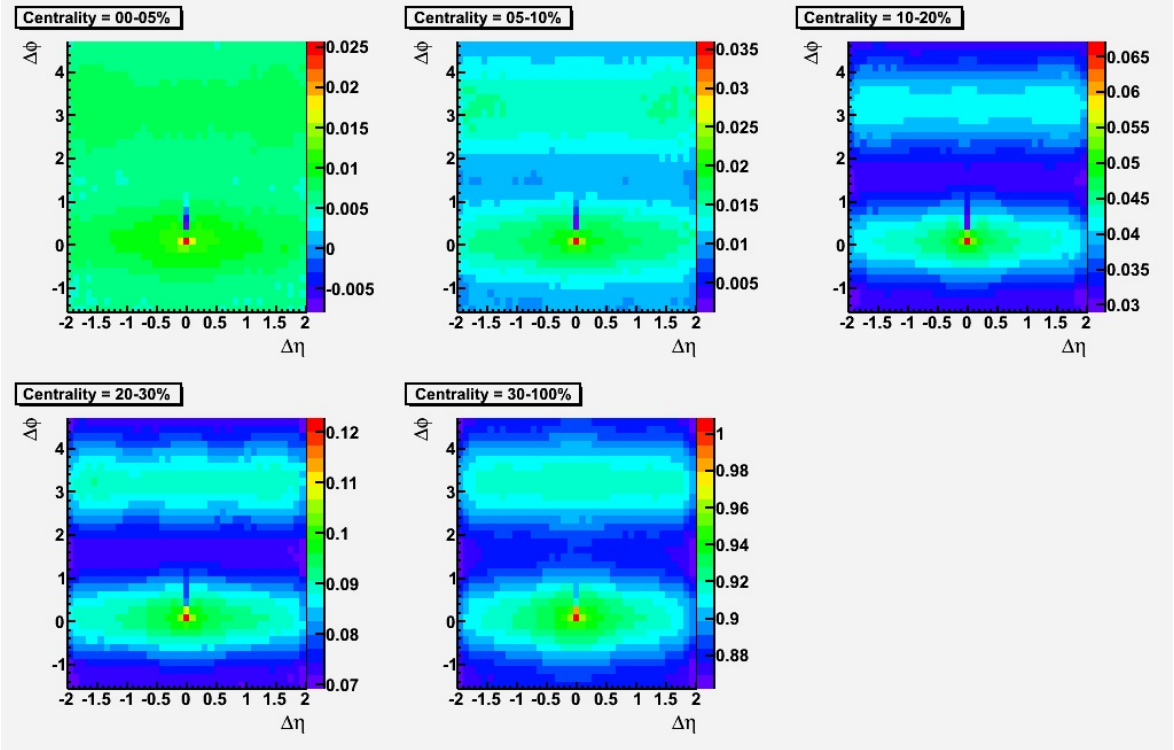

Figure 5.8: Plot of $R_2^{+-}(\Delta\eta, \Delta\phi)$ with uncorrected track merging at $\Delta\eta = 0$, in $\Delta\phi$ bins offset from zero.

The situation with particles of the same sign is easier to visualize but unfortunately more difficult to correct by symmetry methods. It begins with the *ansatz* of two particles of the same sign, and similar η, ϕ and p_T up to a small quantity ϵ that is less than the resolution of the detector. Such a pair may be recorded as a single merged track in the $(0, 0)$ bin. If we increase $\Delta\eta$, the particle pair will tend to unmerge quickly. However, if we increase $\Delta\phi$ while also decreasing the p_T of one of the particles, we find that the change in curvature compensates for the change in $\Delta\phi$, the tracks will remain close together, and the pair will again be recorded as a merged

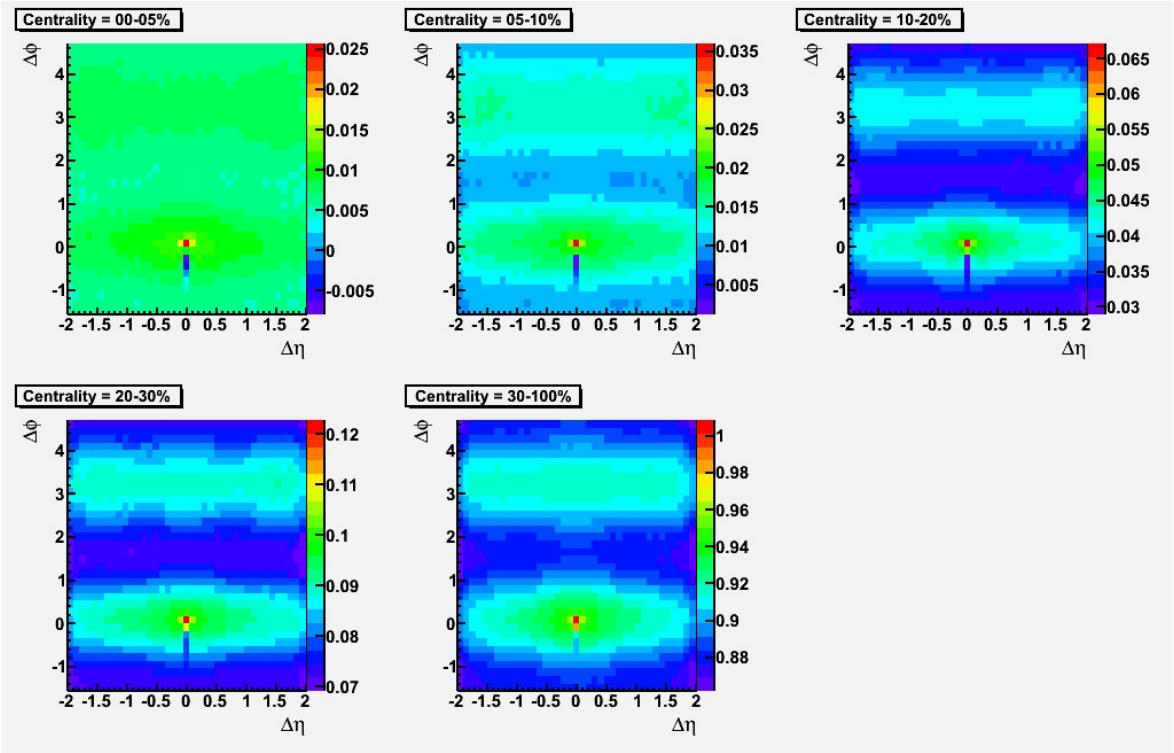

Figure 5.9: Plot of $R_2^{-+}(\Delta\eta, \Delta\phi)$ with uncorrected track merging at $\Delta\eta = 0$, in $\Delta\phi$ bins offset from zero. Plot is a reflection through the origin of $R_2^{+-}(\Delta\eta, \Delta\phi)$ in the previous figure.

track. Thus for like-sign track merging, we find that the deficit starts at $\Delta\phi$ equal to zero and includes a few bins in $\Delta\phi$ to one side of zero, depending on the shared sign of the two tracks, in contrast to unlike-sign merging where the deficit is offset from zero in $\Delta\phi$.

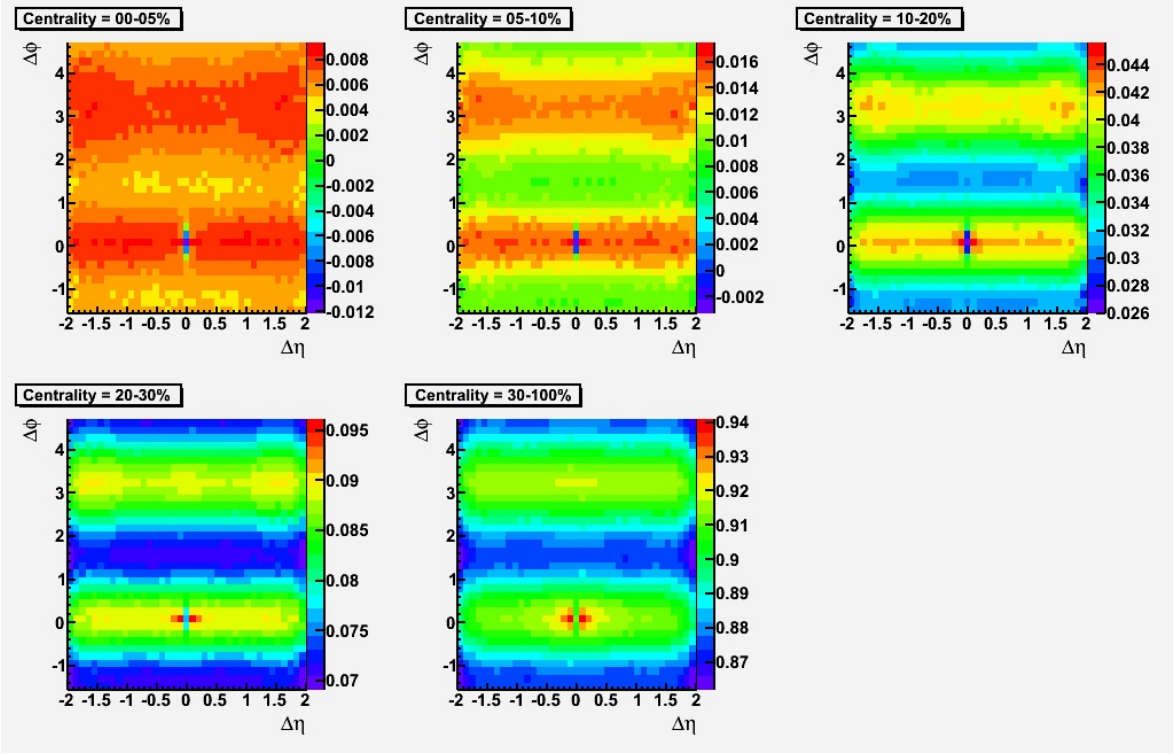

Figure 5.10: Plot of $R_2^{++}(\Delta\eta, \Delta\phi)$ with uncorrected track merging at $\Delta\eta = 0$, in $\Delta\phi$ bins both above and below zero. Natural symmetry of the like-sign plot creates reflection of values through the origin.

In both the unlike- and like-sign cases there is a visible deficit for several contiguous bins in $\Delta\phi$ with $\Delta\eta$ equal to zero. The track merging is clearly visible in our R_2 correlation function, because as a same-event phenomenon it affects the ρ_2 numerator but is not present in the $\rho_1 * \rho_1$ convolution in the denominator. No track merging can be present in the convolution since it is by construction formed from mixed events.

The correction employed for track merging uses the symmetry of the plots, although rather more effectively in the case of unlike-sign track merging than for like-sign track merging. In the case of unlike-sign we have by construction that the R_2 plot

of the +/- charge combination is the reflection through the origin of the -/+ charge combination. Therefore, where one of the two will have a track merging deficit, the other will be whole. To apply the correction, we simply replace those bins with a track merging deficit with the bins from the reflected plot. This is equivalent to replacing the merged bins with the bins in the same plot that are symmetric with respect to the origin. Figure 5.11 and Figure 5.12 show plots of $R_2^{+-}(\Delta\eta, \Delta\phi)$ and $R_2^{-+}(\Delta\eta, \Delta\phi)$ respectively, corrected using the reflection technique. The second plot is a reflection of the first through the origin.

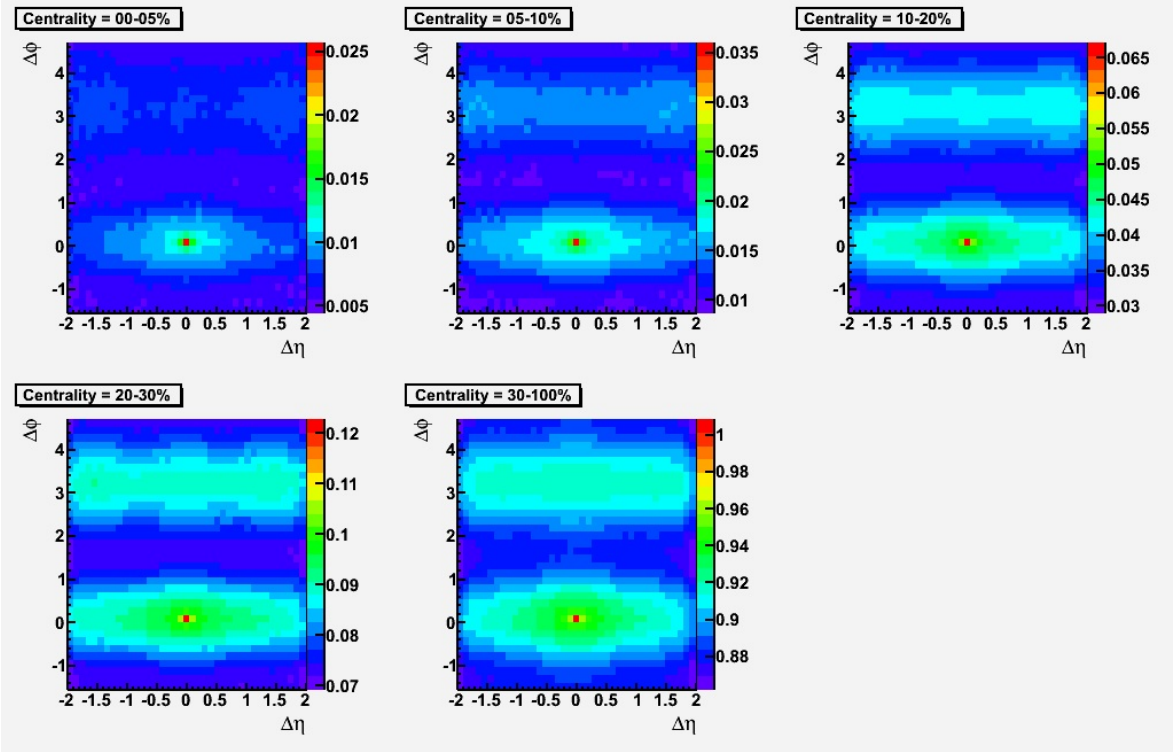

Figure 5.11: Plot of $R_2^{+-}(\Delta\eta, \Delta\phi)$ with track merging at $\Delta\eta = 0$ corrected using a reflection technique.

The validity of this procedure, which is almost 100 percent effective in restoring the affected bins, is allowable given our assumption that the overall properties of the R_2 correlation function, in the limit of infinite events, should be symmetric with respect to the $\Delta\eta$ and $\Delta\phi$ axes. We do not expect to see different physics in different quadrants of the $\Delta\eta$, $\Delta\phi$ coordinate grid, and therefore the reflection procedure may

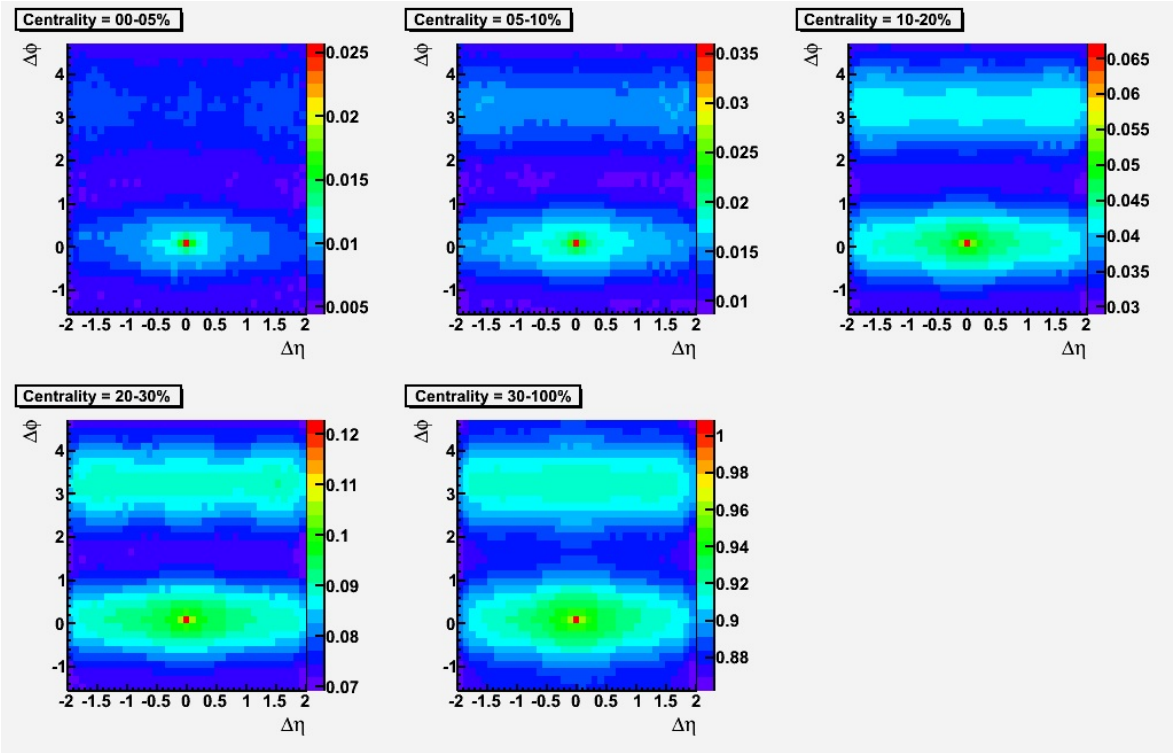

Figure 5.12: Plot of $R_2^{-+}(\Delta\eta, \Delta\phi)$ with track merging at $\Delta\eta = 0$ corrected using a reflection technique. Plot is a reflection through the origin of $R_2^{+-}(\Delta\eta, \Delta\phi)$ in the previous figure.

be considered a valid one.

The track merging situation for like-sign plots is complicated by the fact that our like-sign plots, by construction, have absolute symmetry with respect to the origin. Any track merging deficit in a given bin on one side of the origin will show the same deficit in the mirror bin where the particle order is reversed. Therefore we do not have available, as in unlike-sign merging, an intact part of the plot with which to replace our affected bins. To remedy this, we must impose an artificial asymmetry on the like-sign plot. This is done by changing our original computer algorithm to calculate an asymmetric ρ_2. Rather than form all of the like-sign pairs in the event excluding the self-pairs with i equal to j, we create a ρ_2 that takes only the upper diagonal where j is greater than i. Then we re-label the order of the particles in the like-sign pair so that the first particle always has the greater transverse momentum. In our event block matrix, this is equivalent to listing the particles in each event in order of decreasing momentum and then taking only the pairs of the upper diagonal where j is greater than i.

The result of the momentum ordering is to create a like-sign plot of R_2 that has half the number of pairs as the symmetric version, but for which the track merging now appears entirely on one side of the origin. Because of the nature of like-sign track merging, the bin at the origin always contains a pair deficit. Unfortunately, the pair deficit at the origin is not correctable by the reflection method because the mirror bin is antipodal and not useful. A plot of the symmetric like-sign R_2 plot showing the deficit due to track merging above and below zero is shown in Figure 5.13. A plot of the reduced, asymmetric like-sign R_2 plot is shown in Figure 5.14 with track merging above and including zero, but not below.

Note that in the asymmetric plot of Figure 5.14 the twelve sector boundaries of the detector are readily apparent, forming a saw-tooth pattern with a period of three bins over the 36 bins in $\Delta\phi$. Because of the strong periodicity of the sector boundaries

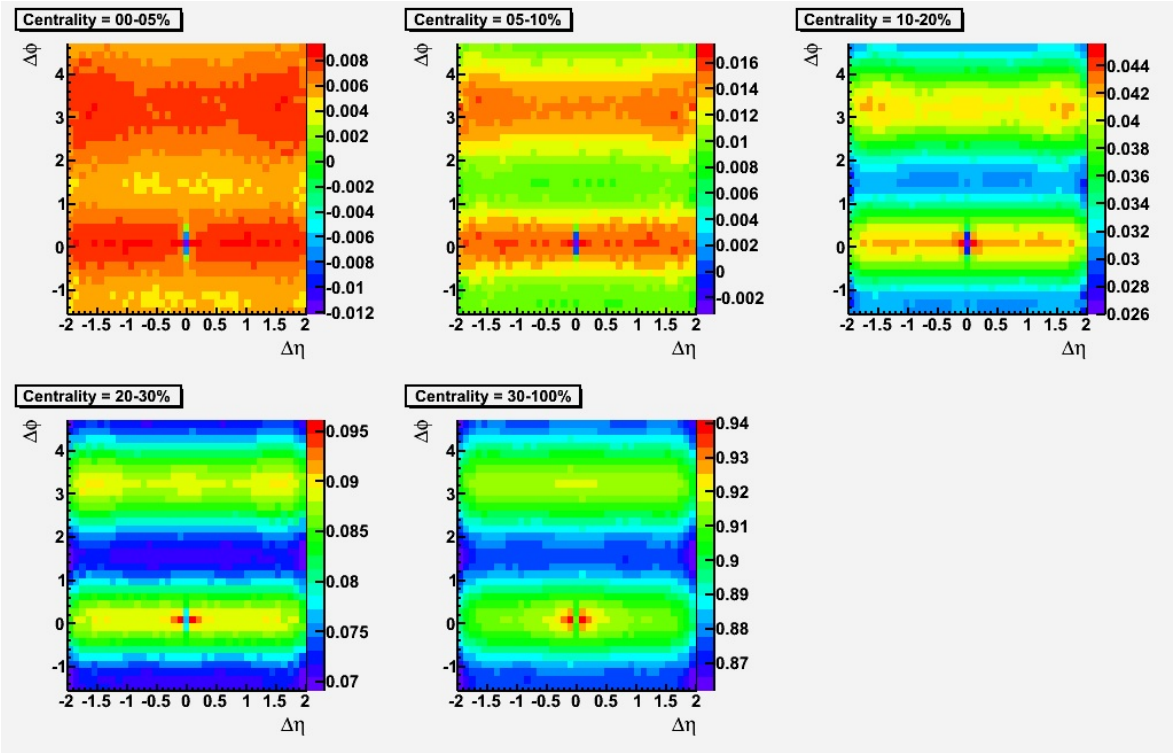

Figure 5.13: Plot of symmetric $R_2^{++}(\Delta\eta, \Delta\phi)$ with uncorrected track merging at $\Delta\eta = 0$, in $\Delta\phi$ bins above and below zero. Natural symmetry of the like-sign plot is due to each particle pair occurring twice, the second time with particle order reversed.

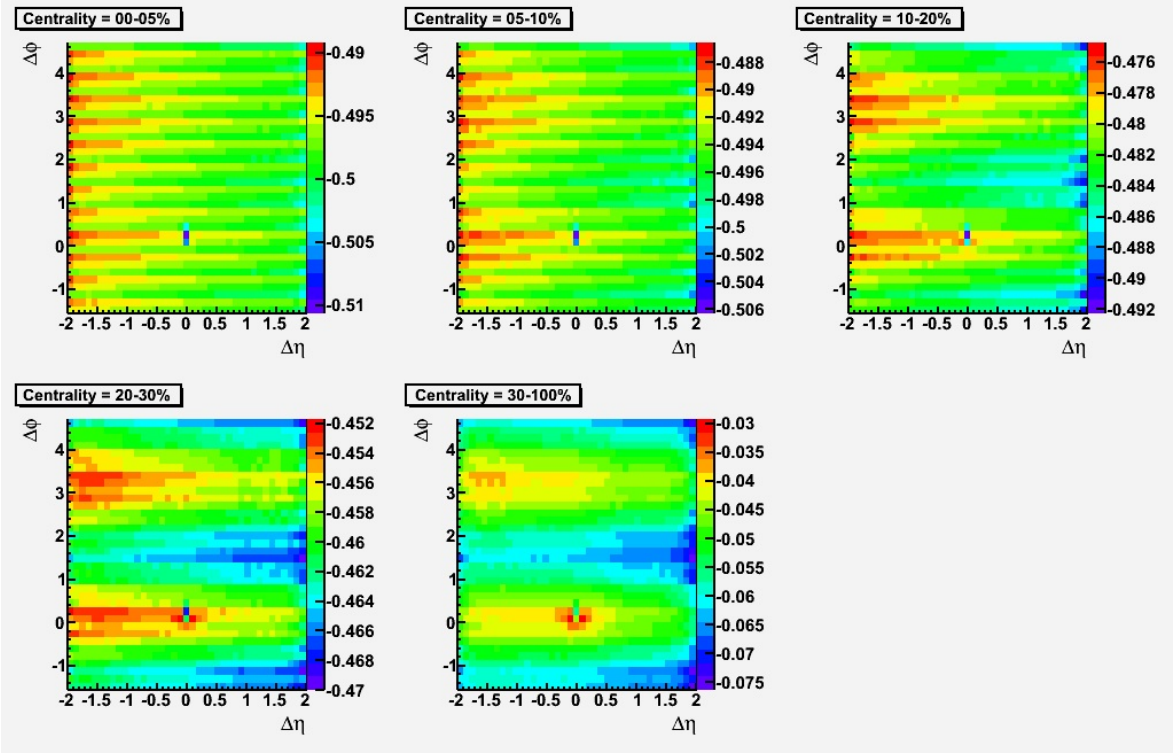

Figure 5.14: Plot of asymmetric $R_2^{++}(\Delta\eta, \Delta\phi)$ with uncorrected track merging at $\Delta\eta = 0$, in $\Delta\phi$ bins above and including zero, but not below. Natural symmetry of the like-sign plot has been removed by ordering particles within pairs by decreasing transverse momentum.

in the asymmetric like-sign plot, we cannot simply replace a bin that shows a deficit with its mirror value. A more accurate technique, used in this analysis, is to replace the deficit with the value not from the mirror bin, but from the nearest neighbor of the mirror bin that has the same value (mod 3) as the original bin. For like-sign track merging, the mirror bin neighbor is a more accurate replacement for the original bin. Using the mirror bin neighbor instead of the mirror bin itself takes advantage of symmetry but also respects the modular systematic error caused by the sector boundaries of the detector.

To complete the track-corrected like-sign R_2 correlation function, after the replacement of bins affected by track merging with their mirror bin neighbors, we add to it a copy of the corrected plot reflected through the origin, thus restoring the absolute symmetry with respect to the origin. A procedure analogous to that used for R_2^{++} is used to correct track merging in R_2^{--}.

Because the reflection method cannot remedy the track merging deficit at zero that occurs for like-sign plots, a simple expedient is employed in order to obtain a smooth graph. Namely, the zero bin is set set equal to the average of its neighbors in Δy. For consistency, this is also done for unlike-sign plots.

While the method of correction for track merging by reflection is somewhat intrusive and not completely satisfying, it is likely less intrusive than track merging methods which use arbitrary pair cuts to the mixed-event denominator. For our purposes of analyzing global properties of the correlation function, the symmetry method here adopted is sufficient.

5.5 Centrality Definition

We turn now to a discussion of the key feature of the analysis, namely the variation of the correlation observables with centrality. The most important fact is that collision centrality is not directly observable. If we consider two nuclei in collision, there will

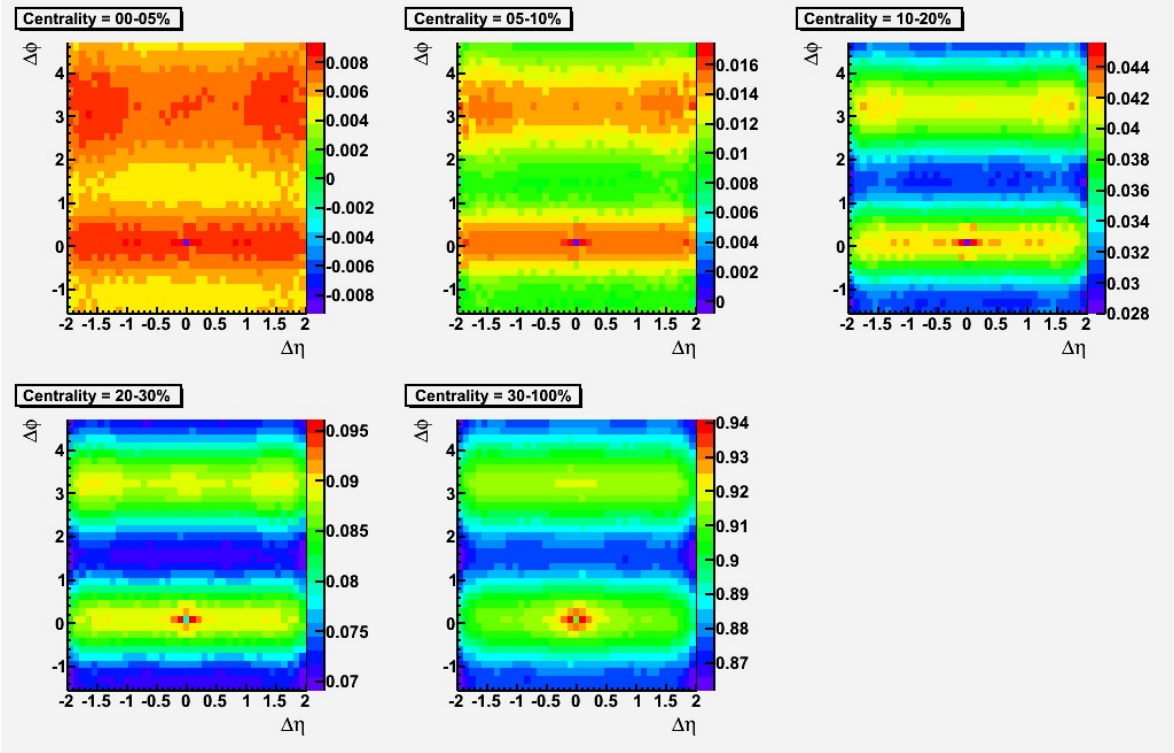

Figure 5.15: Plot of symmetric $R_2^{++}(\Delta\eta, \Delta\phi)$ with track merging at $\Delta\eta = 0$ corrected using a reflection technique, except for bin at $\Delta\phi = 0$. Natural symmetry of the like-sign plot has been restored by adding together the previous plot plus a copy of itself reflected through the origin.

be an overlapping area, and we may define the geometric parameter b as the distance between the centers of the two nuclei. For perfectly spherical nuclei, the values of b form a continuous interval ranging from zero for a collision with perfect overlap up to the diameter of the nucleus species, at which point the two nuclei make contact at a single point.

To understand the evolution of the collision properties as a function of impact parameter, we wish to construct an observable measure of centrality that has a strong correlation to the linear ordering of the impact parameter b. The difficulties in doing so are immediately seen. For one, our nuclei are not perfectly spherical, thus even for identical values b the nuclei themselves may have different shapes and the collision different properties. Second, particle production is not a deterministic process but rather a quantum mechanical one, and quantum variations will cause fluctuations in the number of particles produced even for identical initial conditions. Even if two collisions produced an identical number of particles, all of them recorded by the detector, there would be a natural variation in the underlying collision parameter due to both the quantum variation of the process and the nonspherical shape of the nuclei. Third, using the multiplicity of particles produced as a proxy for impact parameter, we must recognize that our real detector only records a sample of the particles produced, rather than recording the full topological cross-section. Thus in all methods of determining centrality based on multiplicity there will be a sampling bias due to the choice of the region of the detector in which particles are counted.

The most widely used measure of centrality in the STAR collaboration is the observable known as Reference Multiplicity (RefMult), which is a quantity derived from a Monte Carlo simulation based on the Glauber model of particle production in heavy ion collisions [32]. The number of particles produced in the simulation that fall within the psueodrapidity range $|\eta| < .5$ is declared to be the Reference Multiplicity and an array of multiplicity breakpoints representing the centrality percentiles is

obtained by integrating the distribution of simulated data.

An alternative method of determining centrality is to count, not the multiplicity of particles N which are produced from the participant nucleons of the collision, counted as N_{part}, but to measure instead the residue of energy of the spectator nucleons, or more precisely spectator neutrons, since the spectator protons of the collision cannot be detected since their charge causes them to be deflected from the beamline. Spectator neutrons are not deflected and leave energy in the zero-degree calorimeters.

The values of multiplicities used to determine centralities in RefMult are theoretical rather than experimental quantities. However, we may reproduce them experimentally to good accuracy using recorded events, as follows. We record the number of primary charged particles for each event in our Au+Au dataset that fall within the range $|\eta| < .5$ and then integrate the distribution to determine the breakpoint multiplicities for the percentile bin ranges 0-5, 5-10, *etc*.. We do not, however, obtain the same RefMult breakpoints as were determined theoretically. To reproduce the RefMult percentiles we must first account for "lost events". Lost events are events for which the post-production track reconstruction algorithm could not converge on a z-vertex for the collision within acceptable bounds, therefore the event is not labeled as a good event in the dataset. The event is recorded but no vertex is assigned. Lost events are assumed to be peripheral and the failure of reconstruction due to the lack of sufficient tracks in the event, on the order of 10 or less. For the Full Field dataset in Run IV, the proportion of lost events is 8.3 percent of the total and for the Reverse Full Field dataset the proportion is 7.3 percent of the total.

If we allow for lost events by including multiplicative factors of 1.083 and 1.073 when we integrate the Full Field and Reverse Full Field event distributions respectively, we come very near to the theoretical multiplicity percentiles determined using the Glauber model. The percentiles and the multiplicity breakpoints for RefMult and the loss-corrected Full Field and Reverse Full Field recorded multiplicities for Run 4

Au+Au 200 Gev collisions are shown in Table 5.1.

Percentile	**5**	**10**	**20**	**30**	**40**	**50**	**60**	**70**	**80**
RefMult	520	441	319	222	150	96	57	31	14
FF, $\|\eta\| < 0.5$ (loss corrected)	518	441	319	225	153	98	59	31	14
RFF, $\|\eta\| < 0.5$ (loss Corrected)	519	442	320	226	154	99	59	32	15

Table 5.1: Comparison of Reference Multiplicity (RefMult) breakpoints with loss-corrected Full Field and Reverse Full Field recorded $|\eta| < 0.5$ multiplicities for STAR Run IV Au+Au $\sqrt{s_{NN}} = 200$ GeV event centrality.

This procedure suggests a method for determining custom centralities based on different ranges in η within the acceptance of the TPC. For example, we may count tracks that fall within $|\eta| < .75$, or $|\eta| < 1.0$, or even at the limits of the TPC acceptance, $|\eta| < 1.3$. We then integrate the event distribution dN_{ev}/dN using the same Run IV factors of lost events determined above for RefMult. The resulting multiplicities found from integration are used as the percentile breakpoints, creating a custom centrality definition based on a given acceptance range in η. Table 5.2 shows multiplicity breakpoints for standard percentile bins obtained for the custom centrality defined by tracks in the range $|\eta| < 1.0$.

Percentile	**5**	**10**	**20**	**30**	**40**	**50**	**60**	**70**	**80**
FF, $\|\eta\| < 1.0$ (loss corrected)	1028	869	622	436	295	189	112	60	27
RFF, $\|\eta\| < 1.0$ (loss corrected)	1029	870	624	438	297	190	114	61	28

Table 5.2: Breakpoints for loss-corrected Full Field and Reverse Full Field recorded $|\eta| < 1.0$ multiplicities for STAR Run IV Au+Au $\sqrt{s_{NN}} = 200$ GeV event centrality.

The correlation observable calculated using the custom centrality can then be compared to the one formed using standard RefMult centrality. The comparison reveals that the appearance of two-particle correlations is highly dependent on the centrality definition. To analyze this dependence, we begin by looking at examples of the ρ_1 single-particle distribution for different definitions of centrality.

Figure 5.16 shows the ρ_1 distribution for the most central 0-5 percent events for four different definitions of centrality. So that there is no mixing of z-vertices, the distributions are all recorded in a single z-vertex bin of width 2.5 cm that surrounds the mean z-vertex for the event ensemble. Three definitions are based on the TPC with increasing range in η, and one is based on the ZDC which depends on spectators rather than participants, and thus has no bias with respect to the number of particles recorded in the TPC.

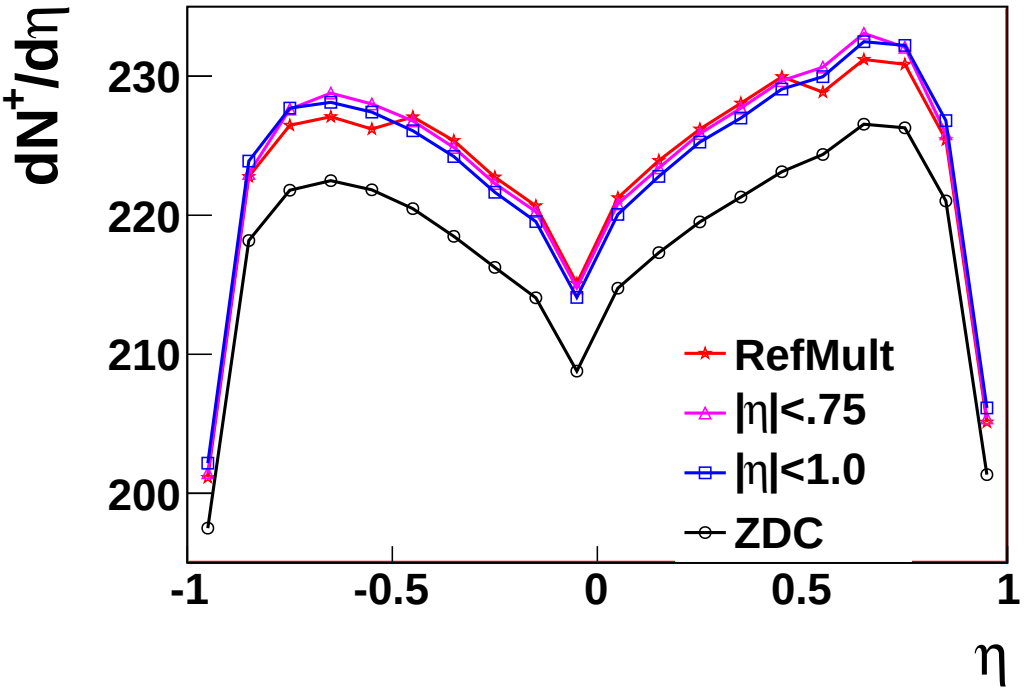

Figure 5.16: $dN^+/d\eta$, the uncorrected number distribution by pseudorapidity for positively charged bulk particles for four different centrality definitions. The distributions are calculated for a single z-vertex bin $2.5 < z < 5.0$ cm.

Because of the sampling bias, each of the TPC centrality definitions shows a surplus of particles with respect to the ZDC centrality. The bias is made more explicit if we divide the three TPC-based multiplicity distributions by the ZDC distribution, after normalizing to agree with ZDC in the bin for $\eta = 0$, as shown in Figure 5.17.

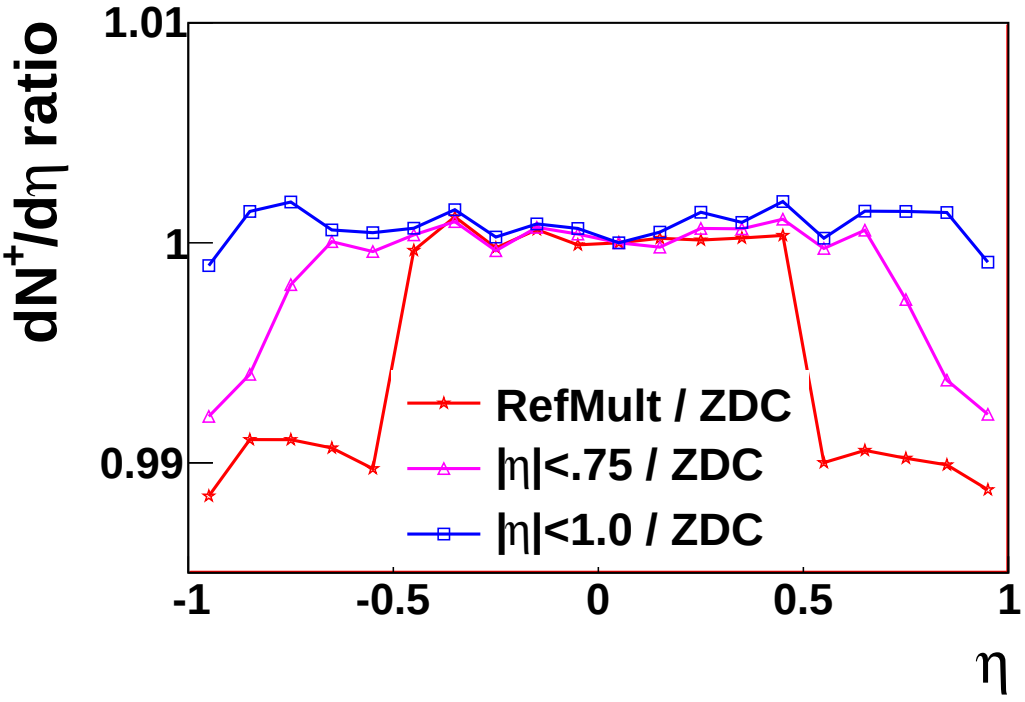

Figure 5.17: Ratios of three TPC-based $dN^+/d\eta$ distributions in the previous figure to the ZDC-based distribution, after normalizing to agree with ZDC in the bin for $\Delta\eta = 0$.

We see similar behavior at large $\Delta\eta$ for the ρ_2 function as was seen for ρ_1. Figure 5.18 shows for ρ_2 the ratios of the three TPC-based definitions to the ZDC-based distribution, after normalizing to agree with ZDC in the bin for $\Delta\eta = 0$.

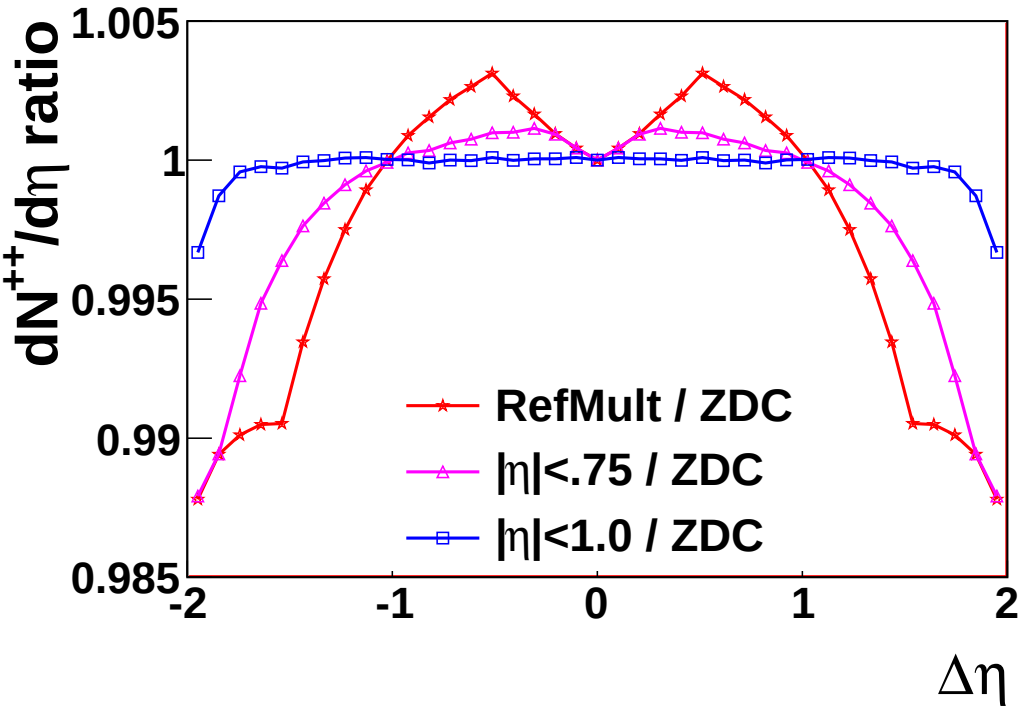

Figure 5.18: Ratios of three TPC-based $dN^{++}/d\eta$ distributions to the ZDC-based distribution, after normalizing to agree with ZDC in the bin for $\Delta\eta = 0$.

The centrality artifacts persist when one forms the ratio $\rho_2/\rho_1 * \rho_1$ and constructs R_2. In Figure 5.19 and Figure 5.20 we show near-side projections of the R_2 correlation function for the same four centrality definitions for 0-5 percent most central events and 20-30 percent, respectively. The fluctuation in the R_2 correlation function is greatest for the the centrality definition that is least constrained in η, namely the RefMult centrality based on multiplicity in the range $|\eta| < .5$.

As the η range of the centrality definition is increased to include the full acceptance of the TPC we see that the artifacts at large $\Delta\eta$ are more controlled and more resemble those of the ZDC centrality, which unlike the TPC has no sampling bias

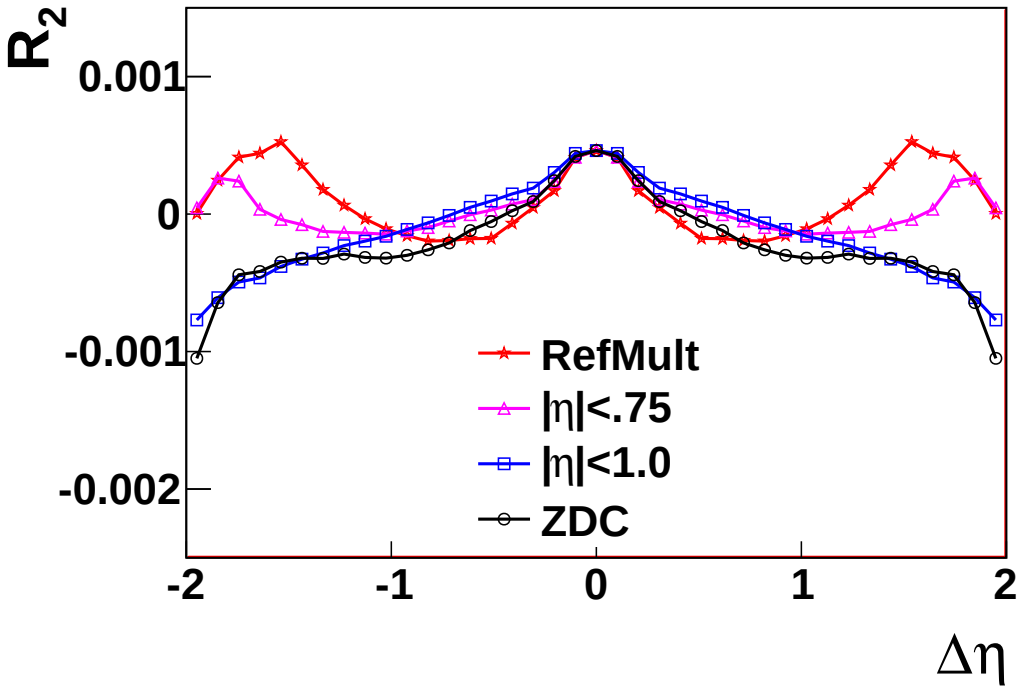

Figure 5.19: Near-side projection of the R_2 correlation function for 0-5 percent most central events, shown for three TPC-based and one ZDC-based centrality definitions, normalized to RefMult amplitude at $\Delta\eta = 0$.

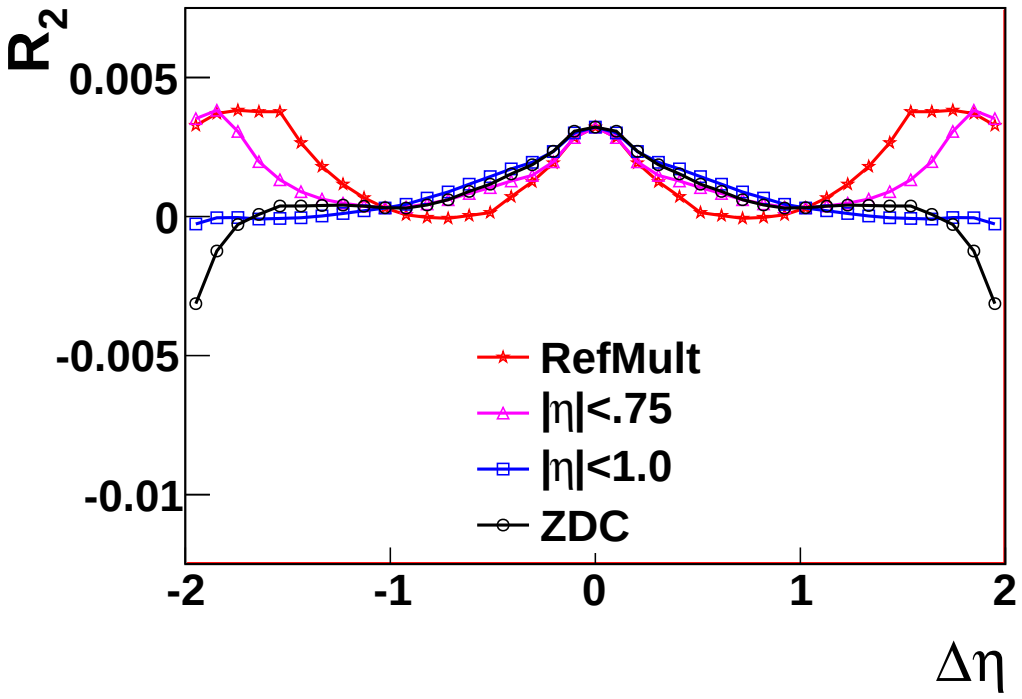

Figure 5.20: Near-side projection of the R_2 correlation function for 20-30 percent most central events, shown for three TPC-based and one ZDC-based centrality definitions, normalized to RefMult amplitude at $\Delta\eta = 0$.

in η. Furthermore, even though the differences in the centrality definitions are most apparent in the 0-5 percent most events, at the extreme boundary of our centrality bin range, nevertheless the R_2 artifacts persist at 20-30 percent and, indeed, over every percentile centrality. Since the TPC centrality definition with $|\eta| < 1.0$ most closely resembles that for the TPC-neutral ZDC centrality, we have chosen $|\eta| < 1.0$ as the centrality definition for this analysis.

Due to acceptance limitations of the TPC, $|\eta| < 1.0$ is the closest we can approach to the ideal of counting the topological multiplicity of particles produced in the collision. Unfortunately the ZDC energy does not have a monotonic correlation with TPC multiplicity so may not be used to construct a full range of centrality percentiles. However, a hybrid centrality definition using the ZDC detector and the Central Trigger Barrel is discussed in Appendix B.

Each of the different centrality definitions above, the three TPC centralities based on ranges in η and the ZDC centrality, represents a different ordering from most central to most peripheral of the events in the dataset. Even if we were to make the percentile ranges finer and finer, assuming infinite data so that we would not run short on statistics, we would find that as the percentile ranges became smaller and smaller, each of the four centrality definitions would still offer different representations of the two-particle correlations, since each centrality definition mixes events in its own way.

5.6 Finite Centrality Binning Factor

To motivate the correction for finite centrality binning, we recall that when no correlations are present in the R_2 correlation function, it should vanish. Specifically, for stochastically independent pair production, the pair distribution ρ_2 should factor into the product of single-particle distributions $\rho_1 * \rho_1$, and the ratio of the pair distribution to the product of single-particle distribtions will equal unity. Let us assume the pair distribution factors into the product of the first and second particle

distributions, $\rho_2 = \rho^{(1)}\rho^{(2)}$. If we integrate the factored pair distribution weighted by the centrality density $1/N_{ev}\ dN_{ev}/db$, then divide by the product of the weighted integral of the first particle distribution times the weighted integral of the second particle distribution, suitably normalized, we find that this ratio, the integral being taken over a finite interval in centrality, is not equal to one.

$$\frac{\langle\, \rho^{(1)}(b)\rho^{(2)}(b)\,\rangle}{\langle\, \rho^{(1)}(b)\,\rangle\,\langle\, \rho^{(2)}(b)\,\rangle} = \frac{\int n_1^{(1)} n_1^{(2)} \frac{1}{N_{ev}} \frac{dN_{ev}}{db} db}{\int n_1^{(1)} \frac{1}{N_{ev}} \frac{dN_{ev}}{db} db \int n_1^{(2)} \frac{1}{N_{ev}} \frac{dN_{ev}}{db} db} \tag{5.1}$$

where $n^{(1)} = dN^{(1)}/db$, the number distribution of primary charged particles with respect to centrality (similarly $n^{(2)}$).

The quantity may be abbreviated as $\langle n^{(1)}n^{(2)}\rangle/\langle n^{(1)}\rangle\langle n^{(2)}\rangle$, calculated over a fixed range of impact parameter b. The ensemble mean $\langle\ \rangle$ is taken with respect to dN_{ev}/db, that is the distribution of events with respect to the particular centrality definition being used (usually charged particle multiplicity). As discussed in the previous section, in this analysis the event distribution used is dN_{ev}/dN, with N representing the number of primary charged particles per event with $|\eta| < 1.0$. If we calculate the ratio $\langle n^{(1)}n^{(2)}\rangle/\langle n^{(1)}\rangle\langle n^{(2)}\rangle$ for each of the centrality percentile bins in our study, for the $|\eta| < 1.0$ centrality we obtain the values shown in Table 5.3:

Percentile	**0**	**5**	**10**	**20**	**30**
FF, $\|\eta\| < 1.0$ (loss corrected)	1.003	1.002	1.009	1.010	1.012
RFF, $\|\eta\| < 1.0$ (loss Corrected)	1.003	1.002	1.008	1.010	1.012
	40	**50**	**60**	**70**	**80**
FF, $\|\eta\| < 1.0$ (loss corrected)	1.016	1.023	1.032	1.052	1.23
RFF, $\|\eta\| < 1.0$ (loss Corrected)	1.016	1.022	1.032	1.050	1.23

Table 5.3: Finite centrality binning correction factors for loss-corrected Full Field and Reverse Full Field recorded $|\eta| < 1.0$ multiplicities for STAR Run IV Au+Au $\sqrt{s_{NN}} = 200$ GeV event centrality.

The correction factors thus cover two orders of magnitude. For a given centrality, the factor is of the same order as the correlation strength. By applying the appropriate

correction factor for a given centrality to the correlation observables which have the $\rho_1 * \rho_1$ convolution appearing in the denominator, the effect caused by binning into finite percentage ranges is mitigated. For each centrality bin, the correction removes a pedestal from the amplitude of the correlations. After the correction, the absolute level of correlations which had previously been positive definite for every centrality becomes signed. The plot is not qualitatively altered, but positive and negative values are now present, signifying the regions of surplus and deficit of same-event pairs formed in the collision, relative to the random expectation.

Historically, it was early noted that values in the semi-inclusive, fixed multiplicity two-particle correlation function, denoted $R_2^{(n)}$, are inherently signed. However, when events with different multiplicity are combined in the inclusive R_2 function a pedestal is added to the correlations so that they become positive. The results from the cluster model simulation data in Chapter 7 will provide us with further insight into the shape of the pedestal in R_2 that results from combining events with different multiplicity.

From the normalization of the R_2 correlation function the following formula should hold globally:

$$\frac{\langle\, \rho_2(\Delta\eta, \Delta\phi)\rangle}{\langle\, \rho_1 * \rho_1(\Delta\eta, \Delta\phi)\rangle} = \frac{\langle N(N-1)\rangle}{\langle N\rangle^2} \tag{5.2}$$

$$= 1 - \frac{1}{\langle N\rangle} \tag{5.3}$$

If we integrate the numerator and denominator of the R_2 function corrected for finite centrality binning, we should recover the value of the normalization, namely $-1/\langle N\rangle$. The values of $-1/\langle N\rangle$, based on the dN_{ev}/dN distribution for each of the centrality percentile bins used in the analysis, obtained by integration of the R_2^{++} correlation function after correction for finite centrality binning, are shown in Table 5.4.

Percentile	**0**	**5**	**10**	**20**	**30**
FF, $\|\eta\| < 1.0$	-.0012	-.0014	-.0018	-.0026	-.0037
RFF, $\|\eta\| < 1.0$	-.0012	-.0014	-.0018	-.0026	-.0037
	40	**50**	**60**	**70**	**80**
FF, $\|\eta\| < 1.0$	-.0057	-.0091	-.0160	-.0314	-.0800
RFF, $\|\eta\| < 1.0$	-.0056	-.0090	-.0157	-.0309	-.0776

Table 5.4: Calculated value of $-1/\langle N \rangle$ for R_2^{++} correlation function after correction for finite centrality binning.

Chapter 6

Plots of the Three Correlation Observables

We now present the plots of the three correlation observables for Run IV Au+Au $\sqrt{s_{NN}}$ = 200 GeV data. We define "bulk" two-particle correlations as correlations between pairs of primary charged particles with $p_T < 2.0$ GeV/c, passing track quality cuts. For "inclusive" correlations we remove the p_T restriction. "Triggered" correlations are here obtained by taking the difference between inclusive and bulk correlations. Comparison of bulk and triggered correlations for the three correlation observables are shown in Appendix C.

Centrality bins are defined using the multiplicity of all charged primary particles recorded in the region $|\eta| < 1.0$. For correlation purposes, particles with $|\eta| > 1.0$ or $p_T < .02$ GeV/c are rejected. Correlations are constructed as a weighted average of Full Field and Reverse Full Field events. Corrections for z-vertex variation, track merging, and finite centrality binning are made as described in the chapter on data corrections. Sign combinations are defined as follows: ls "like sign" is the average of $++$ and $--$ correlations, us "unlike sign" is the average of $+-$ and $-+$ correlations, cd "charge dependent" is the difference of us minus ls, ci "charge independent" is the average of us and ls.

We show first the plots with the best statistics, a comparison of the charge independent bulk correlations for R_2, C, ΔP_T. We then proceed to each observable separately, first studying the basic plots $++$, $+-$ and $--$, followed by the sign com-

binations ls, us and cd. All plots have been symmetrized in the independent variables. Three representative centralities, peripheral, mid-central and most central, are shown.

6.1 Charge Independent Bulk Correlations for R_2, C, ΔP_T

The key features of the three correlation observables are similar at each centrality. The amplitude of correlations is greatest for R_2, decreases by half in C, and further decreases by an order of magnitude in ΔP_T. All show expected dilution of correlations from peripheral to central. Peripheral correlations have a prominent near-side peak centered at $(0, 0)$ and a low ridge on the away side, broad in azimuth, extending to the limits of acceptance in pseudorapidity. In central correlations the near-side peak is enveloped by a high ridge, narrow in azimuth, extended in pseudorapidity.

Elliptic flow modulates the plots most prominently in mid-central events, where it is almost perfectly symmetric in $\Delta\phi$, less prominently in central events, and is scarcely noticeable in peripheral. Peripheral events for all three observables strongly resemble the 200 GeV $p + p$ plot shown in Figure 3.14. The broadness in pseudorapidity of the away-side correlations for each observable and centrality reflects momentum conservation effects. Particles emitted back-to-back enhance correlations at $\Delta\eta = 0$, $\Delta\eta = \pi$ but are not constrained in pseudorapidity due to longitudinal boosting when colliding partons carry different momentum fractions x.

Differences between the observables are also found. The away-side for peripheral R_2 and C has two local minima that persist in mid-central then merge into a saddle point in central, while the away side of ΔP_T has a small maximum that becomes constant in mid-central and a small minimum in central. The ridge formation in C as a function of centrality is more convex than in R_2 and ΔP_T, which are similar. In C, the ridge and peak begin to combine in mid-central events and actually merge together in central events. In central C it is not determinable whether the jet has broadened or the ridge has risen around it. The correlations in the ΔP_T plot, because

they are constructed from the square of the momentum deviation, that is to say a quantity that fluctuates around zero, are not as smooth and show larger error than those of the other two observables.

Overall, the most prominent effects in all plots is the modulation by elliptic flow, greatest at mid-centrality, the appearance of the near-side ridge at mid-centrality, and the dominance of the ridge relative to the away side in central events. In the chapter on simulated data, we will produce a near-side ridge by applying a transverse boost, as a proxy for radial flow, to a longitudinally boosted cluster decay.

6.2 Charge Dependent R_2

Of the four basic sign combinations, $++$, $+-$, $--$ and $-+$ the last contains no independent information since it is a reflection of the $+-$ plot through the origin. Thus it is sufficient to look for variation within the first three. As seen in Figure 6.2, the amplitude of the unlike-sign $+-$ plot is more than double that of the $++$ and $--$ plots. Thus the features of the charge independent *ci* plot, discussed above, must be inherited primarily from the $+-$ plot. The two like-sign plots, $++$ and $--$, are virtually indistinguishable, in fact a difference plot of $++$ and $--$ reveals only statistical noise. The plots of $++$ and $+-$ are very similar for peripheral events, with $+-$ showing overall greater amplitude as well as broader features, particularly in the near-side peak at $(0, 0)$ and the smaller prominence at $(0, \pi)$. Charge conservation in addition to momentum conservation is responsible for the enhancement.

Charge conservation in collimated emission is present in all centralities of $+-$, with a round near-side peak and a smaller round prominence on the away side. The dominance of the near-side peak over the smaller prominence on the away side increases with centrality and is likely due to "kinematic focusing", that is when a cluster of correlated particles is given a transverse boost by radial flow to form short-range correlations in azimuth and pseudorapidity. In contrast, the $++$ plot, which

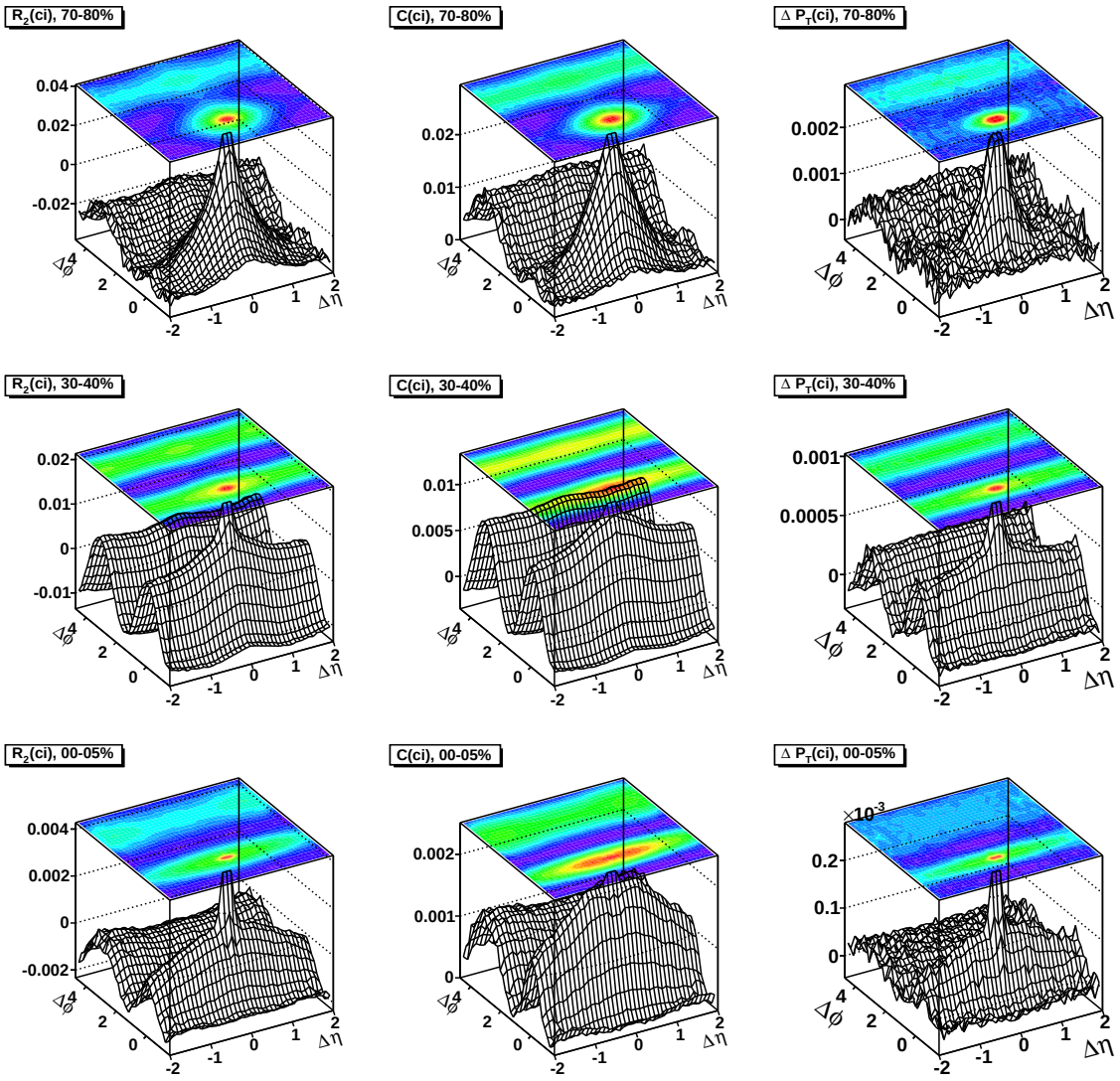

Figure 6.1: Correlation functions $R_2^{ci}(\Delta\eta, \Delta\phi)$ (*left*), $C^{ci}(\Delta\eta, \Delta\phi)$ (center), $\Delta P_T^{ci}(\Delta\eta, \Delta\phi)$ (*right*), for charged particles in the ranges $|\eta| < 1.0$, $0.2 < p_T < 2.0$ GeV/c for three representative collision centralities.

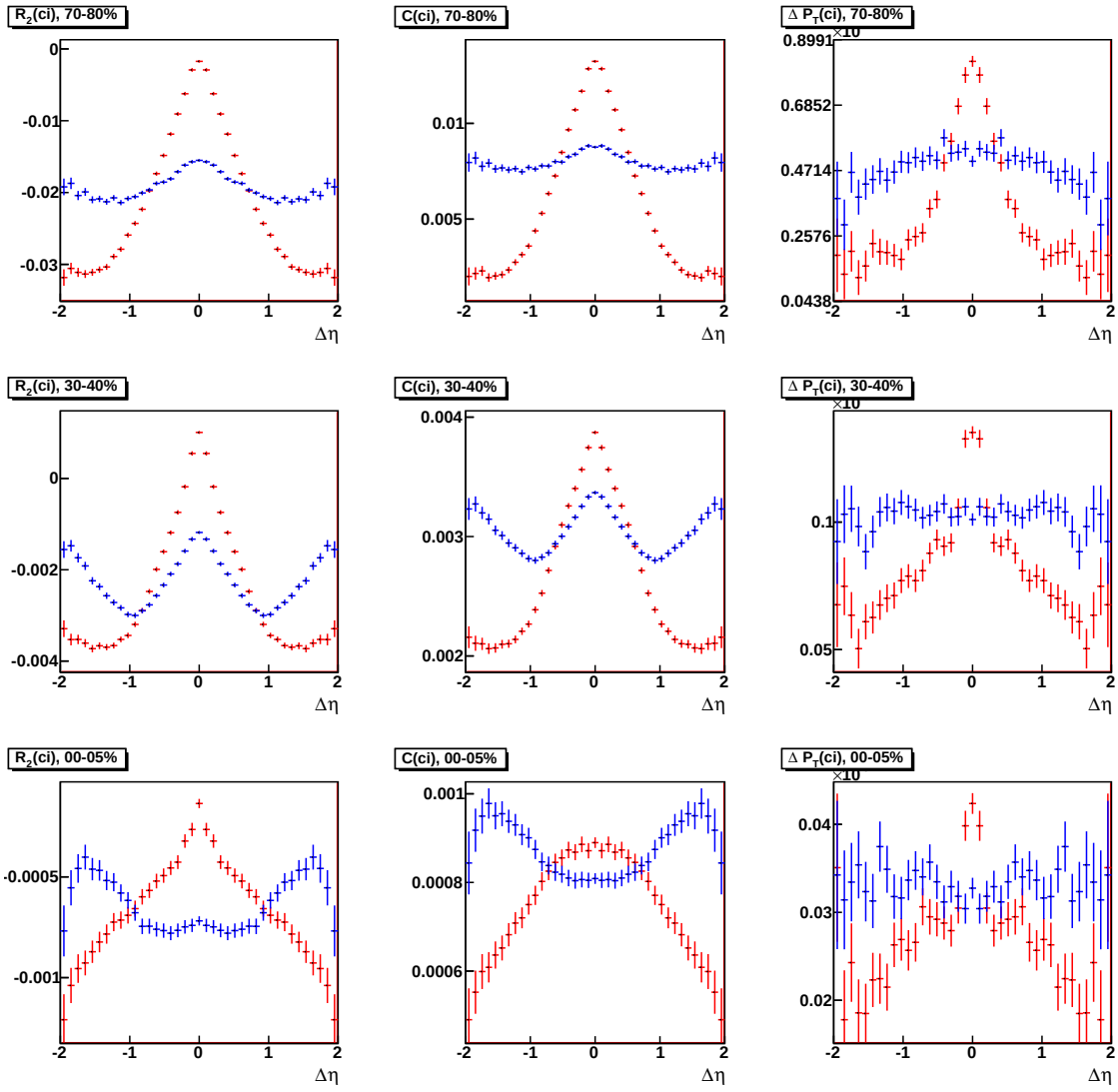

Figure 6.2: Near- (red) and away-side (blue) projections of the correlation functions $R_2^{ci}(\Delta\eta, \Delta\phi)$ (*left*), $C^{ci}(\Delta\eta, \Delta\phi)$ (center), $\Delta P^{ci}(\Delta\eta, \Delta\phi)$ (*right*), for charged particles in the ranges $|\eta| < 1.0$, $0.2 < p_T < 2.0$ GeV/c for three representative collision centralities.

for peripheral events is generally similar to $+-$ but with diminished amplitude, as centrality increases we see the local maxima of correlations about $(0, 0)$ and $(0, \pi)$ disappear completely; that is, at short range in pseudorapidity there is evidently an anti-correlation of like-sign particles on both the near- and away-side in the most central events. Overall, the presence of charge conservation in the $+-$ plot provides smoother correlations compared to $++$.

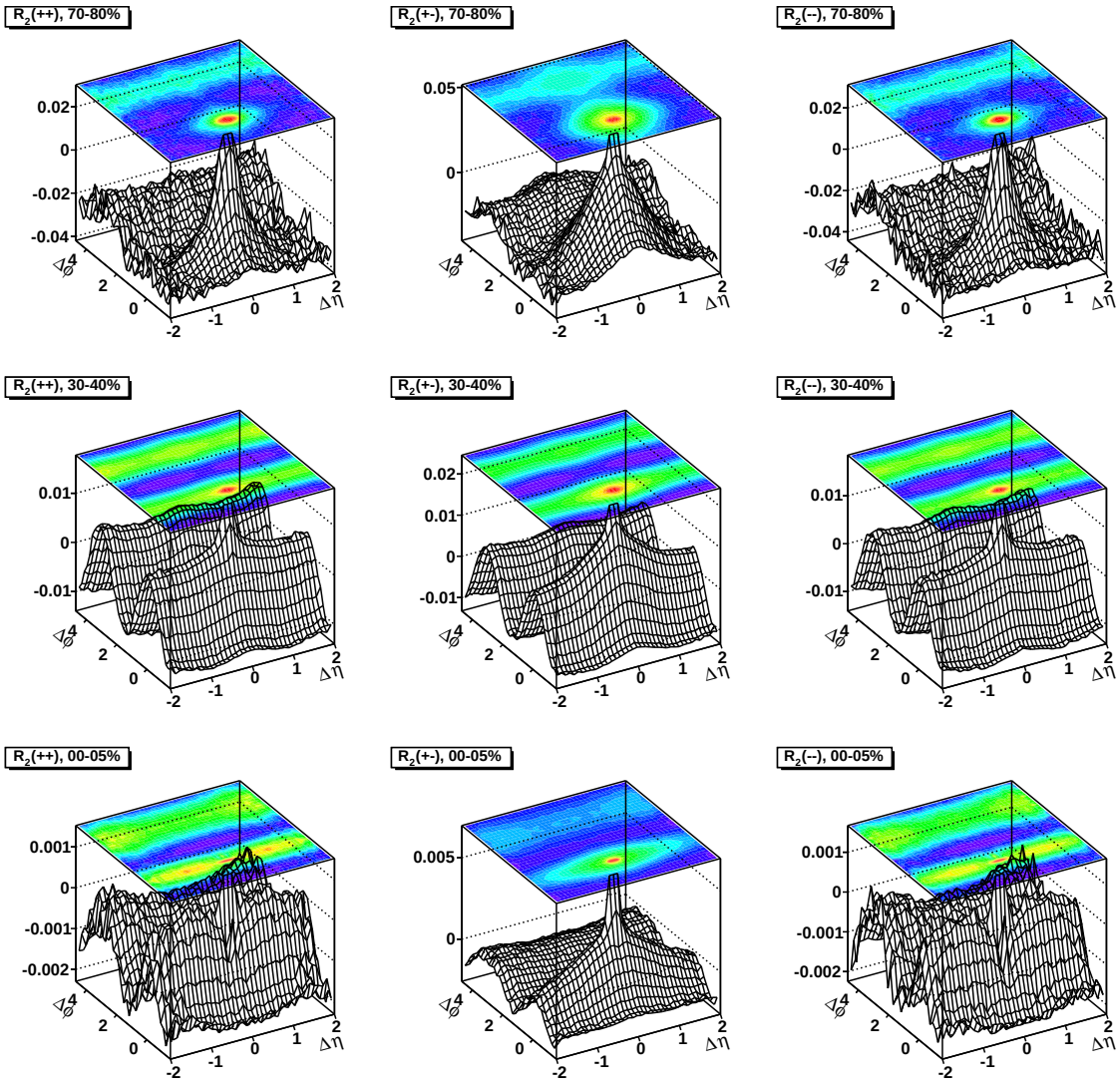

Figure 6.3: Correlation functions $R_2^{++}(\Delta\eta, \Delta\phi)$ (*left*), $R_2^{+-}(\Delta\eta, \Delta\phi)$ (center), $R_2^{--}(\Delta\eta, \Delta\phi)$ (*right*), for charged particles in the ranges $|\eta| < 1.0$, $0.2 < p_T < 2.0$ GeV/c for three representative collision centralities.

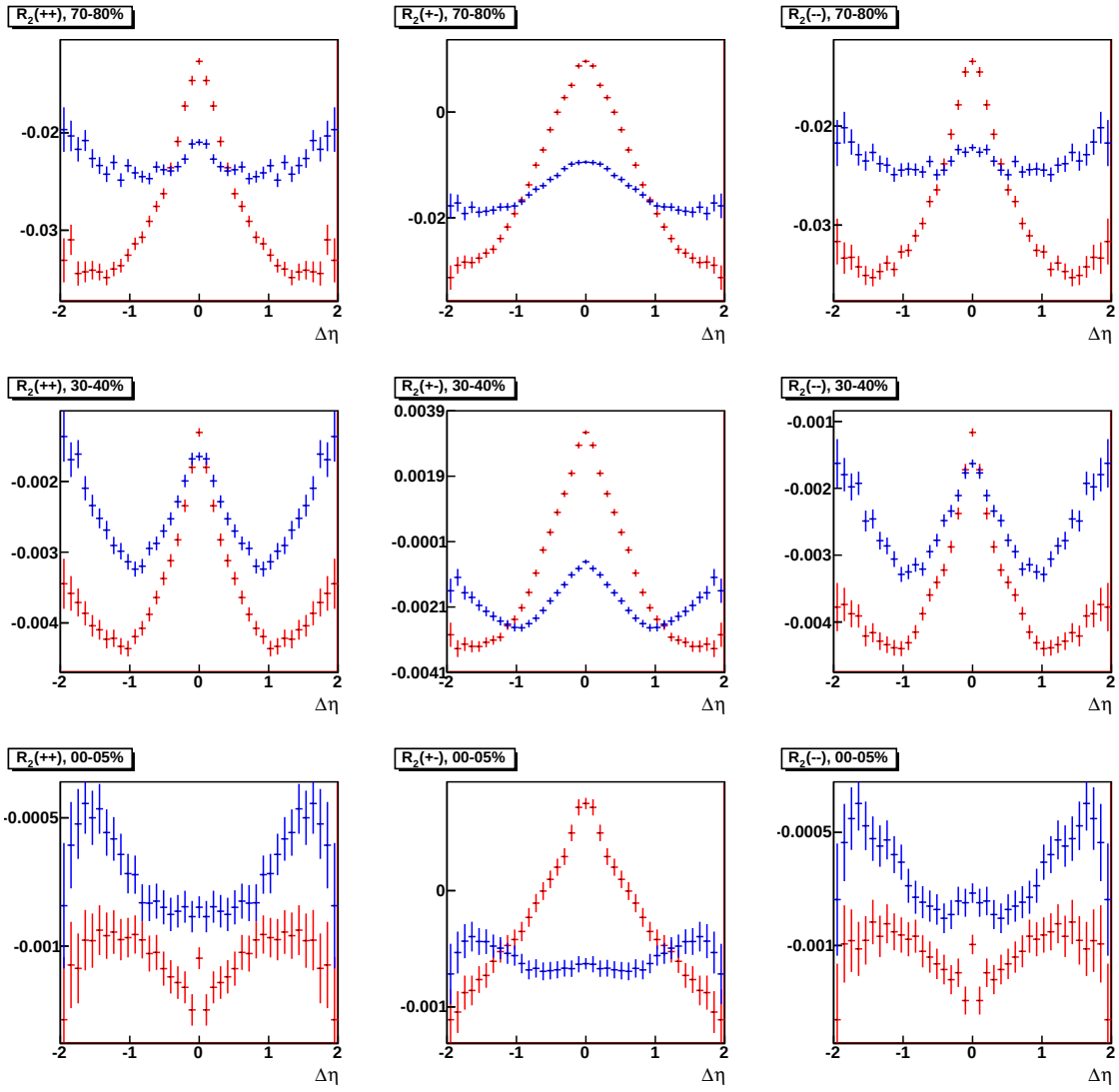

Figure 6.4: Near- (red) and away-side (blue) projections of the correlation functions $R_2^{++}(\Delta\eta, \Delta\phi)$ (*left*), $R_2^{+-}(\Delta\eta, \Delta\phi)$ (center), $R_2^{--}(\Delta\eta, \Delta\phi)$ (*right*), for charged particles in the ranges $|\eta| < 1.0$, $0.2 < p_T < 2.0$ GeV/c for three representative collision centralities.

The plots of like-sign ls and unlike-sign us show with better statistics the features of the $++$ and $+-$ plots. As remarked earlier, the presence of charge conservation in addition to momentum conservation in the unlike-sign plot provides an overall surplus of correlations relative to like-sign. The charge dependent cd plot gives the location of the surplus; it is primarily on the near side in peripheral events, and becomes exclusively so in central, to the extent that the away-side is virtually flat. Evidently charge conservation provides no added probability of penetrating the fluid medium that is created as the centrality of the collision increases. The presence of a "caldera" in peripheral cd shows where the narrower near-side like-sign peak has been subtracted, while the remnant peak in the most central cd is a consequence of the disappearance, already noted, of short-range correlations on the near side in central same-sign events, leaving the unlike-sign peak alone to remain in central cd.

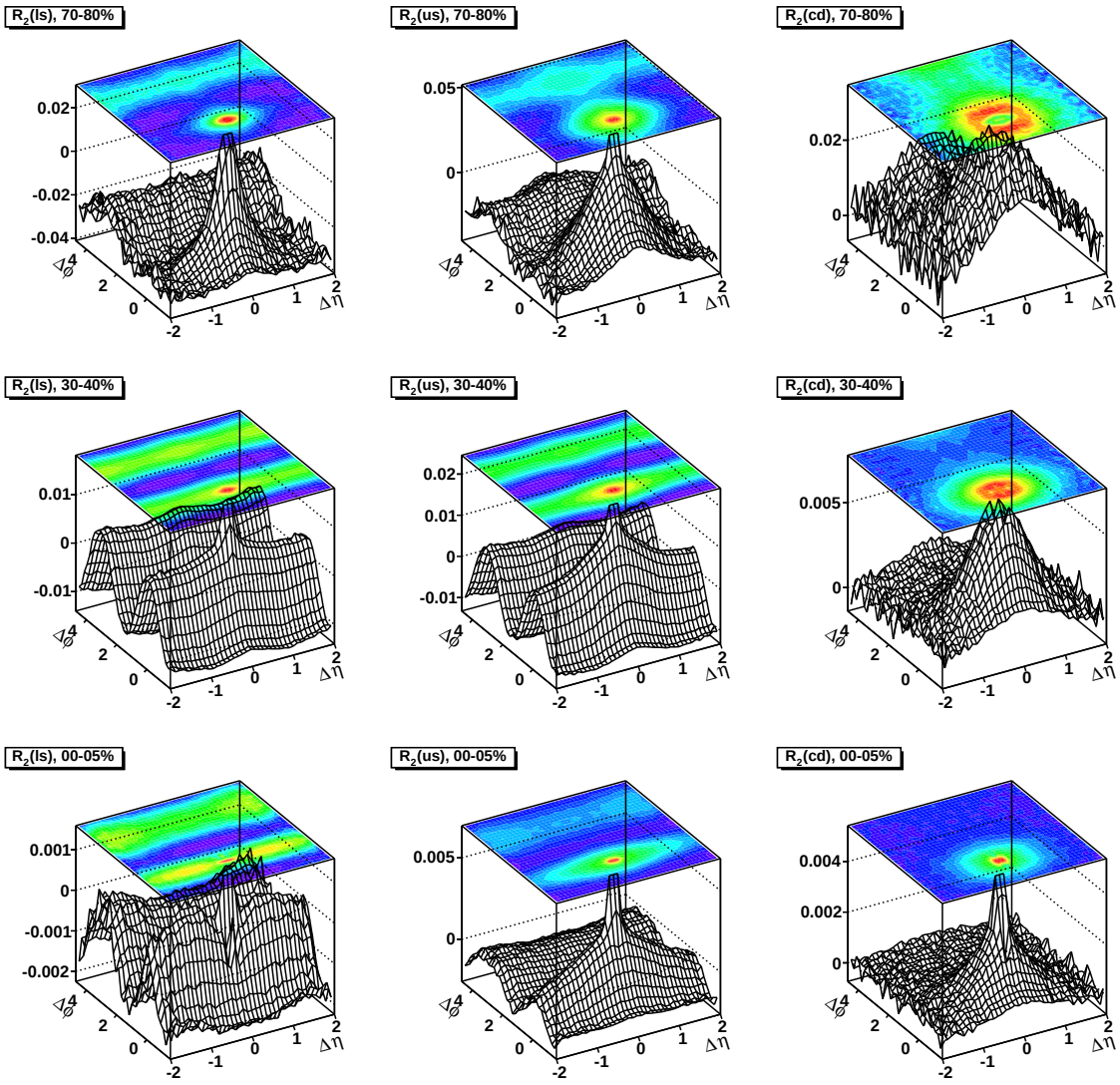

Figure 6.5: Correlation functions $R_2^{ls}(\Delta\eta, \Delta\phi)$ (*left*), $R_2^{us}(\Delta\eta, \Delta\phi)$ (center), $R_2^{cd}(\Delta\eta, \Delta\phi)$ (*right*), for charged particles in the ranges $|\eta| < 1.0$, $0.2 < p_T < 2.0$ GeV/c for three representative collision centralities.

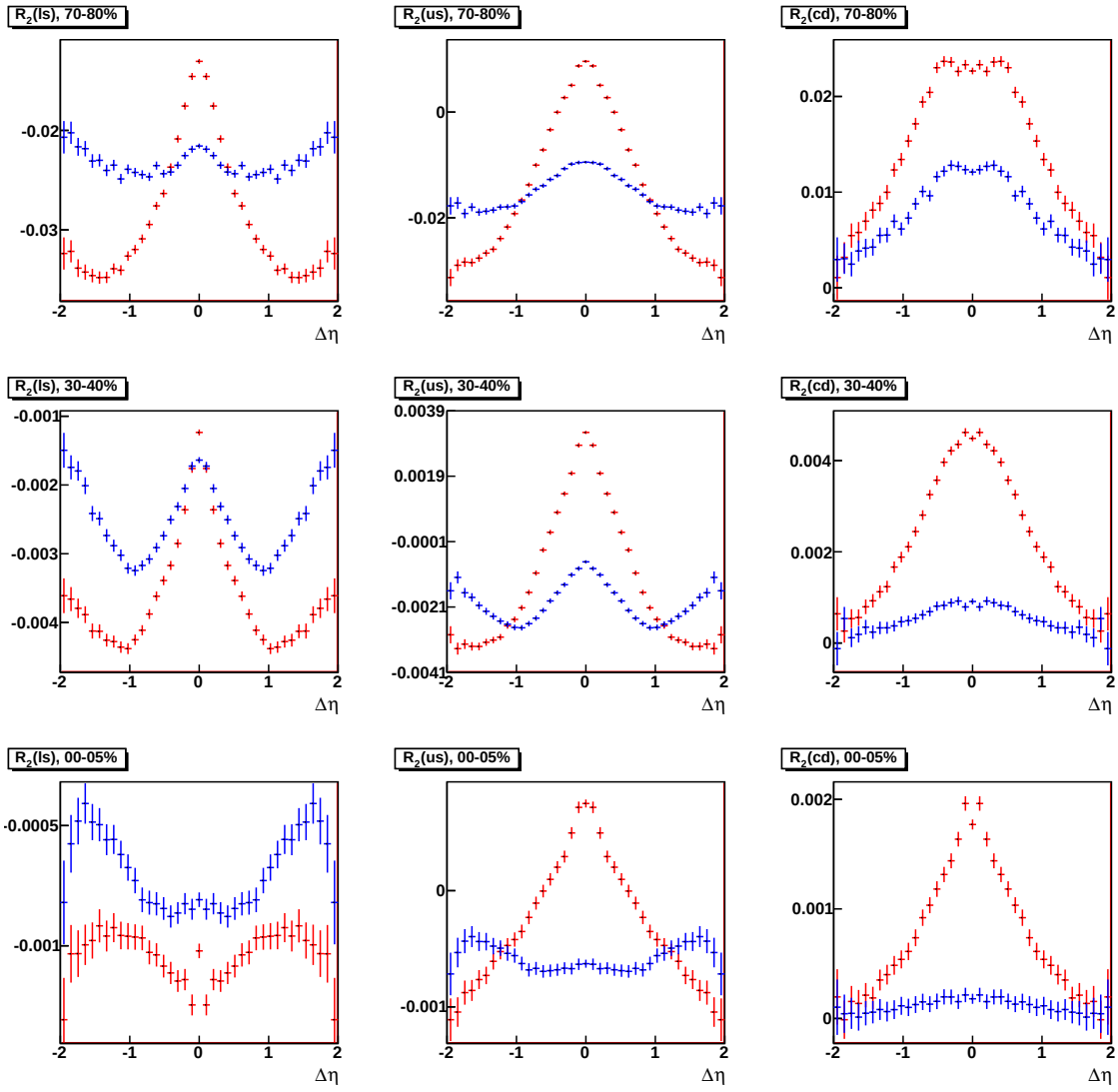

Figure 6.6: Near- (red) and away-side (blue) projections of the correlation functions $R_2^{ls}(\Delta\eta, \Delta\phi)$ (*left*), $R_2^{us}(\Delta\eta, \Delta\phi)$ (center), $R_2^{cd}(\Delta\eta, \Delta\phi)$ (*right*), for charged particles in the ranges $|\eta| < 1.0$, $0.2 < p_T < 2.0$ GeV/c for three representative collision centralities.

6.3 Charge Dependent C

In the section on the construction of the three correlation observables it was noted that C has the form of a cumulant for transverse momentum that is normalized by the uncorrelated pair distribution. As such it is a version of R_2 constructed to show transverse momentum current. The relation to R_2 may be made explicit:

$$C = R_2^{p_T}(\Delta\eta, \Delta\phi) = \frac{C_2^{p_T}}{\rho_1 * \rho_1(\Delta\eta, \Delta\phi)} \tag{6.1}$$

$$= \frac{\rho_2^{p_{T1}p_{T2}}(\Delta\eta, \Delta\phi) - \rho_1^{p_{T1}} * \rho_1^{p_{T2}}(\Delta\eta, \Delta\phi)}{\rho_1 * \rho_1(\Delta\eta, \Delta\phi)} \tag{6.2}$$

$$= \frac{\rho_2^{p_{T1}p_{T2}}(\Delta\eta, \Delta\phi)}{\rho_1 * \rho_1(\Delta\eta, \Delta\phi)} - \overline{p}_{T_1} * \overline{p}_{T_2}(\Delta\eta, \Delta\phi) \tag{6.3}$$

$$= \frac{\rho_2^{p_{T1}p_{T2}}(\Delta\eta, \Delta\phi)}{\rho_2(\Delta\eta, \Delta\phi)} \frac{\rho_2(\Delta\eta, \Delta\phi)}{\rho_1 * \rho_1(\Delta\eta, \Delta\phi)} - \overline{p}_{T_1} * \overline{p}_{T_2}(\Delta\eta, \Delta\phi) \tag{6.4}$$

$$= \frac{\rho_2^{p_{T1}p_{T2}}(\Delta\eta, \Delta\phi)}{\rho_2(\Delta\eta, \Delta\phi)}(R_2(\Delta\eta, \Delta\phi) + 1) - \overline{p}_{T_1} * \overline{p}_{T_2}(\Delta\eta, \Delta\phi) \tag{6.5}$$

Since R_2, or rather R_2 normalized to unity instead of zero, appears as a factor in C, we may expect that the plots of C will inherit from the plots of R_2 in key ways, and indeed the features are in general quite similar. There are differences, but subtle ones. Unlike R_2 which has signed correlations, C is positive due to the momentum entering quadratically. For like-sign plots, it is clear in the $\Delta\eta$ projections that the difference in the amplitude of correlations for the near and away-side at all centralities is much more pronounced for C than for R_2. For like-sign plots the local maximum at $(0, \pi)$ on the away side is slightly less convex for C than for R_2. Regarding unlike-sign plots, other than the different range of values for R_2 and C, the shapes are similar other than a slight broadening of the near-side peak of C in the most central events.

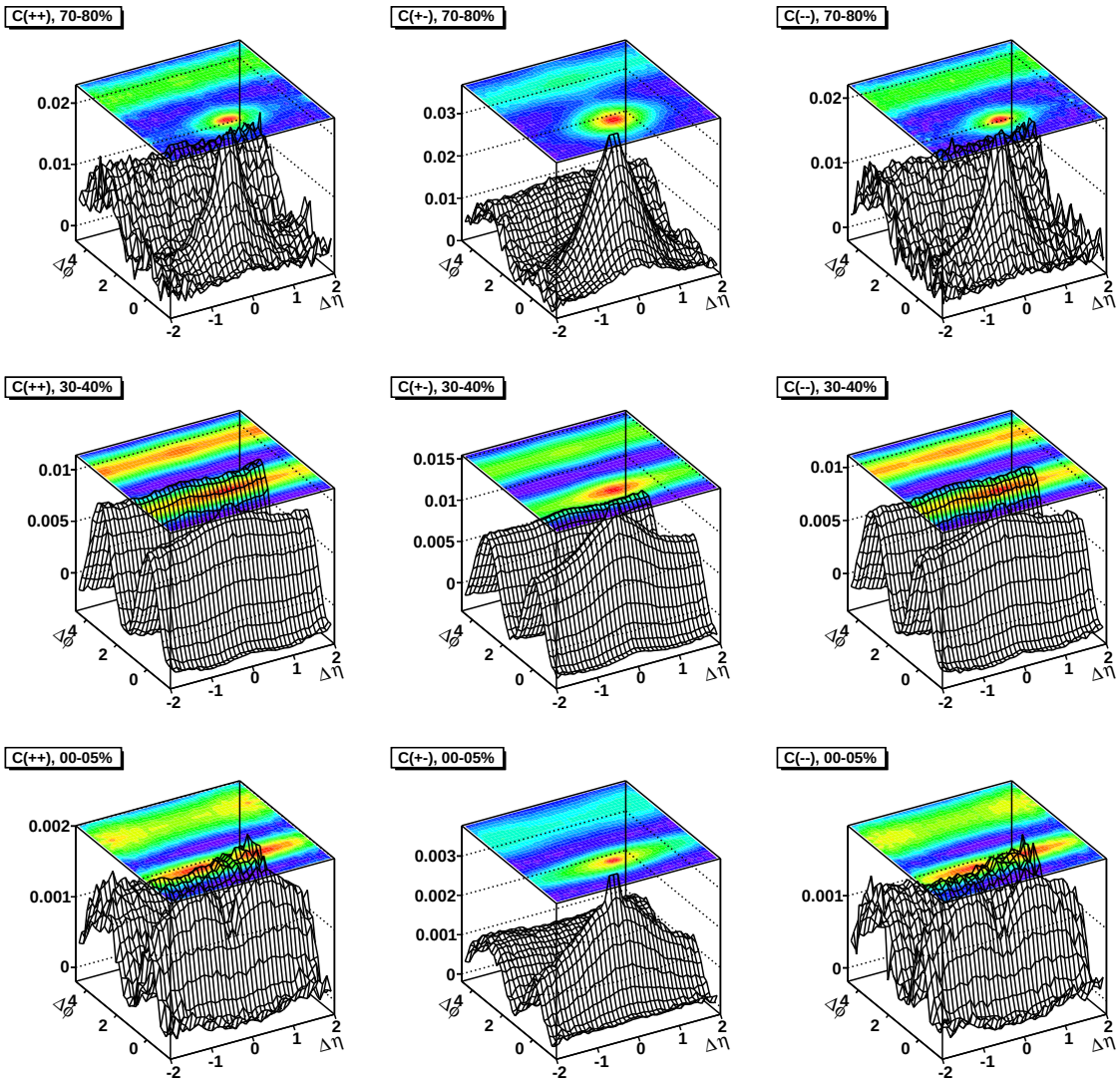

Figure 6.7: Correlation functions $C^{++}(\Delta\eta, \Delta\phi)$ (*left*), $C^{+-}(\Delta\eta, \Delta\phi)$ (center), $C^{--}(\Delta\eta, \Delta\phi)$ (*right*), for charged particles in the ranges $|\eta| < 1.0$, $0.2 < p_T < 2.0$ GeV/c for three representative collision centralities.

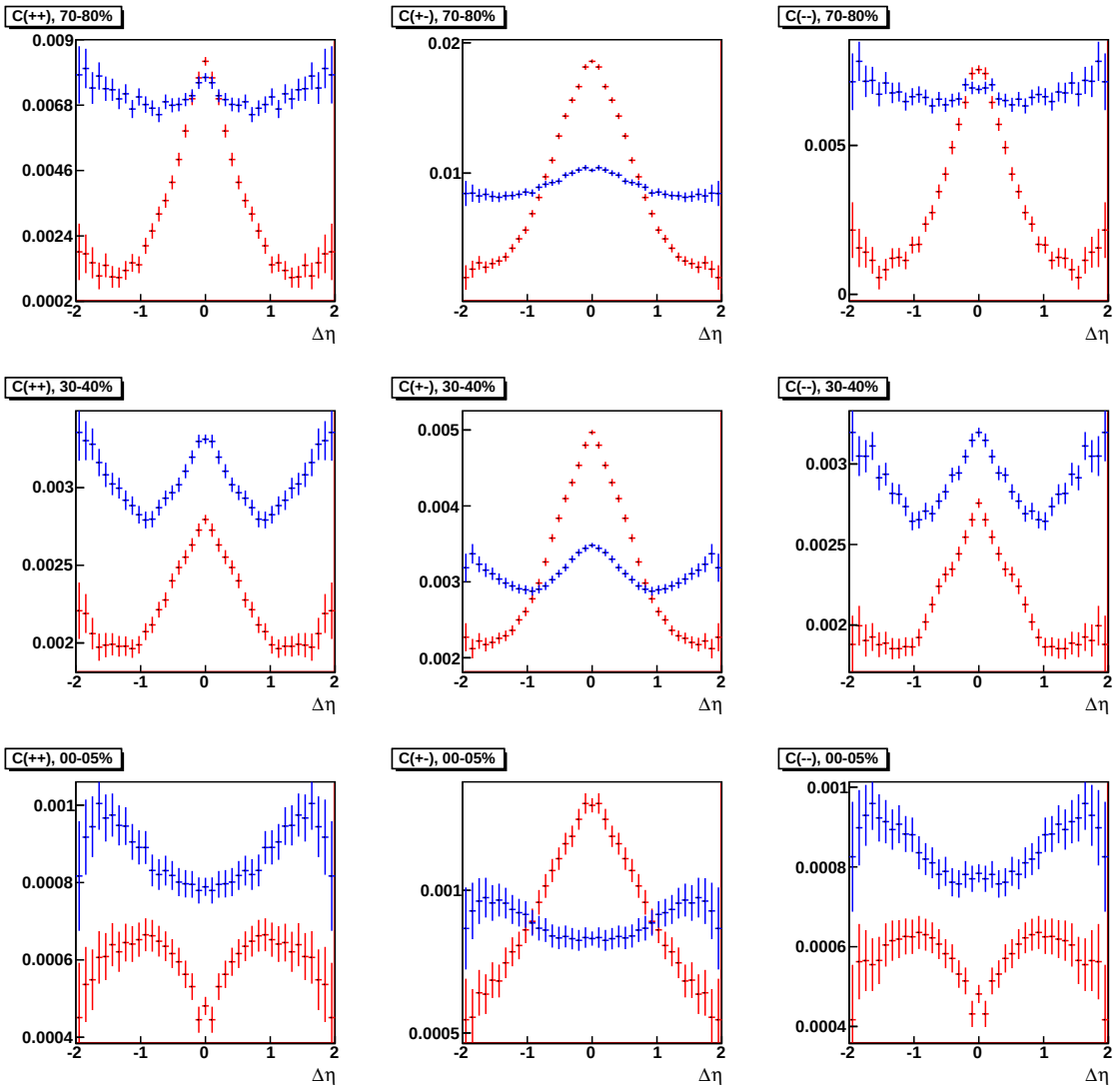

Figure 6.8: Near- (red) and away-side (blue) projections of the correlation functions $C^{++}(\Delta\eta, \Delta\phi)$ (*left*), $C^{+-}(\Delta\eta, \Delta\phi)$ (center), $C^{--}(\Delta\eta, \Delta\phi)$ (*right*), for charged particles in the ranges $|\eta| < 1.0$, $0.2 < p_T < 2.0$ GeV/c for three representative collision centralities.

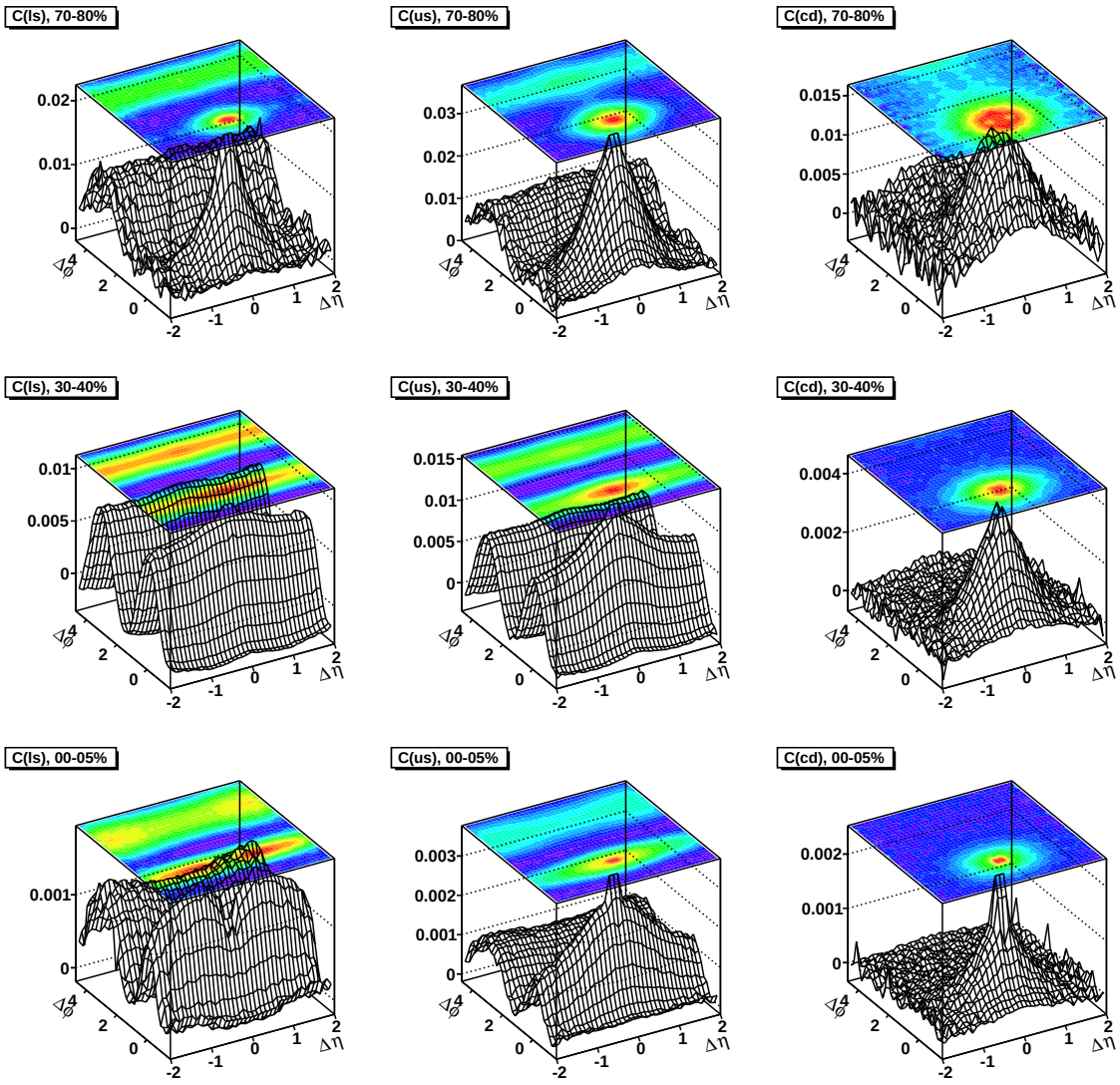

Figure 6.9: Correlation functions $C^{ls}(\Delta\eta, \Delta\phi)$ (*left*), $C^{us}(\Delta\eta, \Delta\phi)$ (center), $C^{cd}(\Delta\eta, \Delta\phi)$ (*right*), for charged particles in the ranges $|\eta| < 1.0$, $0.2 < p_T < 2.0$ GeV/c for three representative collision centralities.

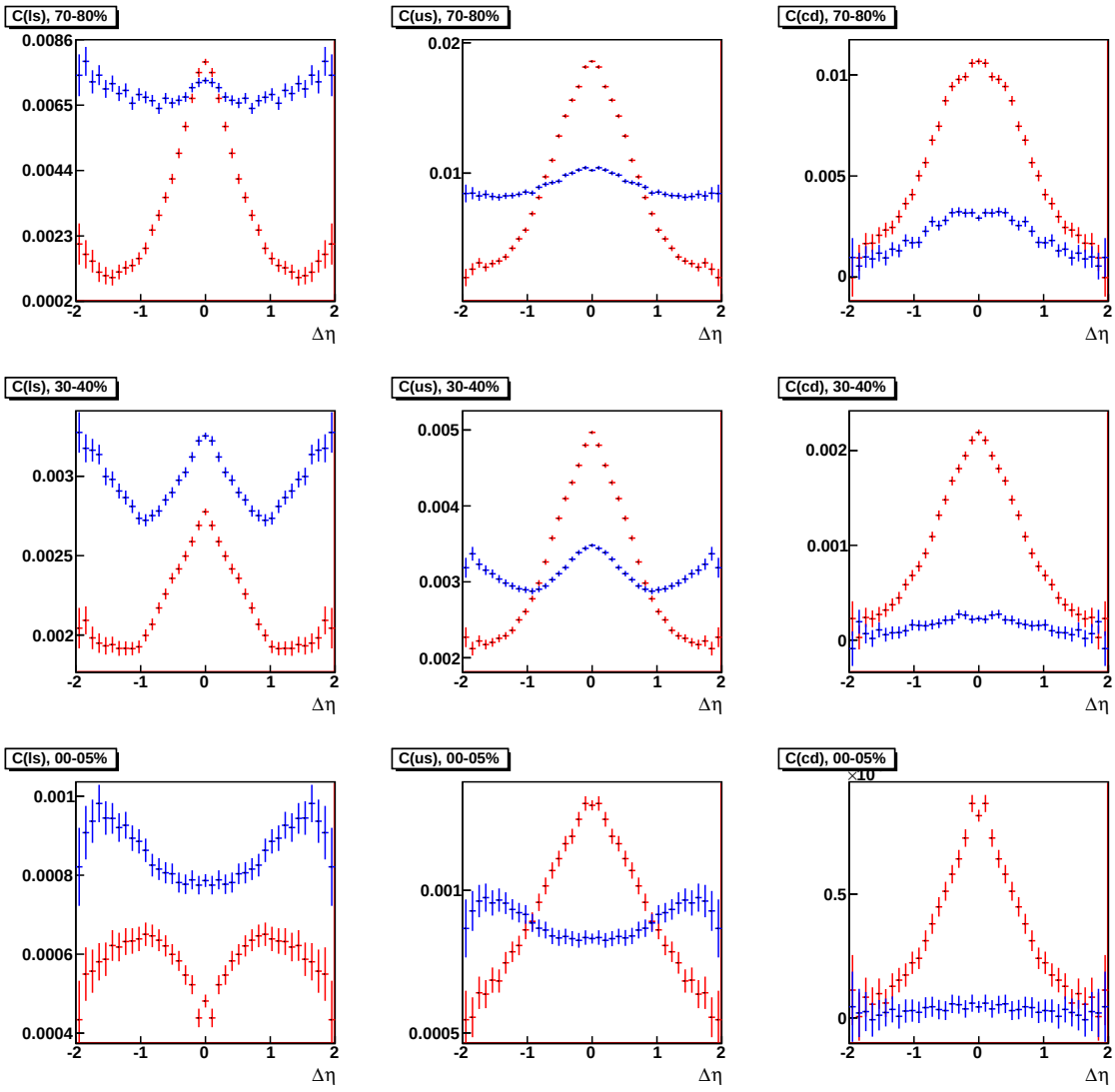

Figure 6.10: Near- (red) and away-side (blue) projections of the correlation functions $C^{ls}(\Delta\eta, \Delta\phi)$ (*left*), $C^{us}(\Delta\eta, \Delta\phi)$ (center), $C^{cd}(\Delta\eta, \Delta\phi)$ (*right*), for charged particles in the ranges $|\eta| < 1.0$, $0.2 < p_T < 2.0$ GeV/c for three representative collision centralities.

6.4 Charge Dependent ΔP_T

In contrast to R_2 and C ($R_2^{p_T}$), ΔP_T is normalized by the same-event, correlated pair distribution rather than the uncorrelated mixed-event distribution. We recall ΔP_T is defined by

$$\Delta P_T(\Delta\eta, \Delta\phi) = \frac{\rho_2^{\Delta p_{T1}\Delta p_{T2}}(\Delta\eta, \Delta\phi)}{\rho_2(\Delta\eta, \Delta\phi)} \tag{6.6}$$

where Δp_{T_i} is the deviation of the i^{th} particle from the ensemble mean transverse momentum per particle.

As stated earlier in the chapter on the three correlation observables, ΔP_T is positive when both particles of a pair are more likely be both higher or both lower than the average transverse momentum $\overline{p}_T$, and negative when a high p_T particle is more likely to be accompanied by a particle with p_T lower than average. Larger positive values are obtained when the particles of a pair have transverse momentum that is nearly equal than when the same momentum is shared unequally.

For all sign combinations, the amplitude of correlations in ΔP_T is an order of magnitude less than for the other two observables R_2 and C. The momentum correlations values are everywhere positive, indicating that pairs are more likely to have momentum above or below the ensemble mean per particle. The unlike-sign plots of ΔP_T for all centralities have a near-side prominence centered at $(0, 0)$ that is nearly conical in peripheral events, but becomes wider in η as centrality increases, with the appearance of the ridge underneath. The same effect was seen for unlike-sign plots in the transverse moment current correlations of C.

The like-sign plots ΔP_T at all centralities have an unexpected peak centered at $\Delta\eta = \Delta\phi = 0$. No charge conservation effect is available in the like-sign plot to enforce such strong correlations on the near side, as is the case in the unlike-sign plots of all three observables. The peak may be due to nearly equal momentum in particles of a cluster that is subject to kinematic focusing. Another hypothesis would be a

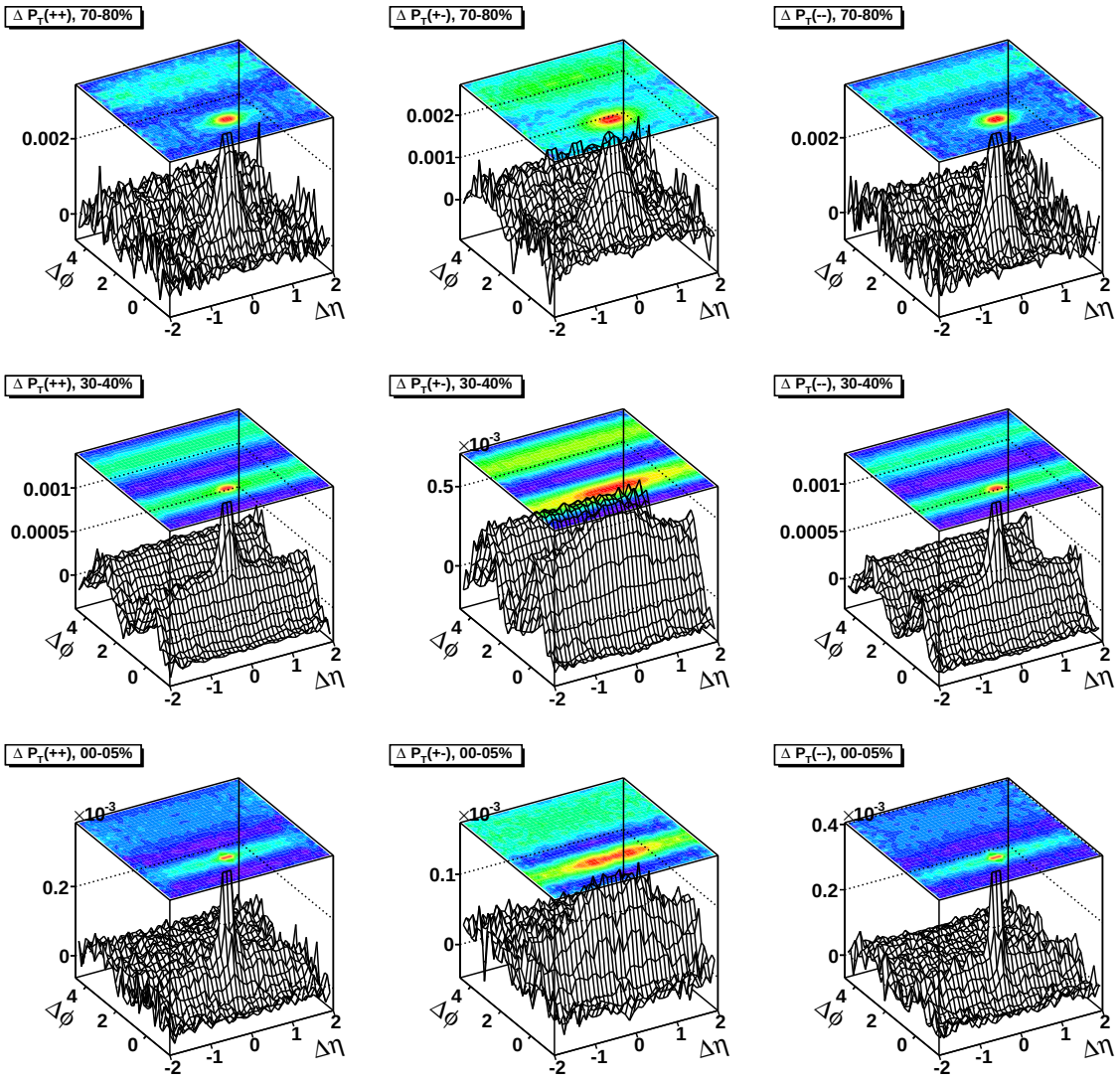

Figure 6.11: Correlation functions $\Delta P_T^{++}(\Delta\eta, \Delta\phi)$ (*left*), $\Delta P_T^{+-}(\Delta\eta, \Delta\phi)$ (center), $\Delta P_T^{--}(\Delta\eta, \Delta\phi)$ (*right*), for charged particles in the ranges $|\eta| < 1.0$, $0.2 < p_T < 2.0$ GeV/c for three representative collision centralities.

possible enhancement of signal due to the HBT effect. When two identical particles are bosons, such as the pions which make up the vast majority of particles created in heavy ion collisions, their correlation signal can be enhanced due to constructive interference if the four-momentum difference **q** between them is sufficiently small, an effect known as HBT after its discoverers Hanbury-Brown and Twiss [33]. Further study is underway to determine if the narrow like-sign peak in ΔP_T may be eliminated by cutting on pairs of particles with very small **q**.

As with R_2 and C, the charge dependent *cd* plot of ΔP_T is consistent with zero almost everywhere except in the neighborhood of the origin. However, the *cd* plot for ΔP_T has a much smaller remnant region than the *cd* plots of R_2 and C, indicating that charge conservation is less of a factor. Also, due to the anomalous narrow peak in the like-sign plot of ΔP_T, the *cd* values at the origin become pointedly negative, exactly the reverse of the situation in the *cd* plots of R_2 and C where the unlike-sign peak due to charge conservation dominates.

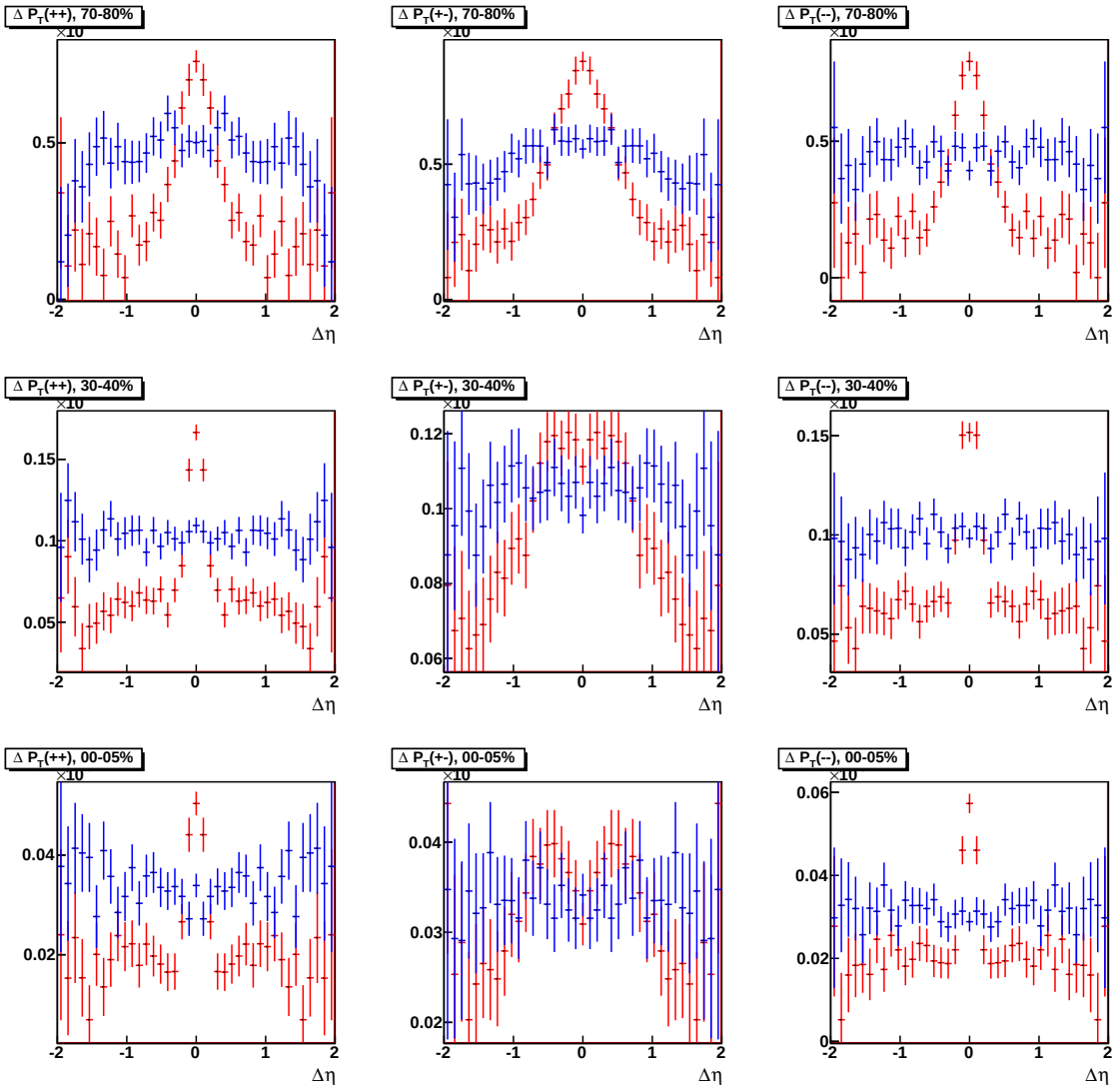

Figure 6.12: Near- (red) and away-side (blue) projections of the correlation functions $\Delta P_T^{++}(\Delta\eta, \Delta\phi)$ (*left*), $\Delta P_T^{+-}(\Delta\eta, \Delta\phi)$ (center), $\Delta P_T^{--}(\Delta\eta, \Delta\phi)$ (*right*), for charged particles in the ranges $|\eta| < 1.0$, $0.2 < p_T < 2.0$ GeV/c for three representative collision centralities.

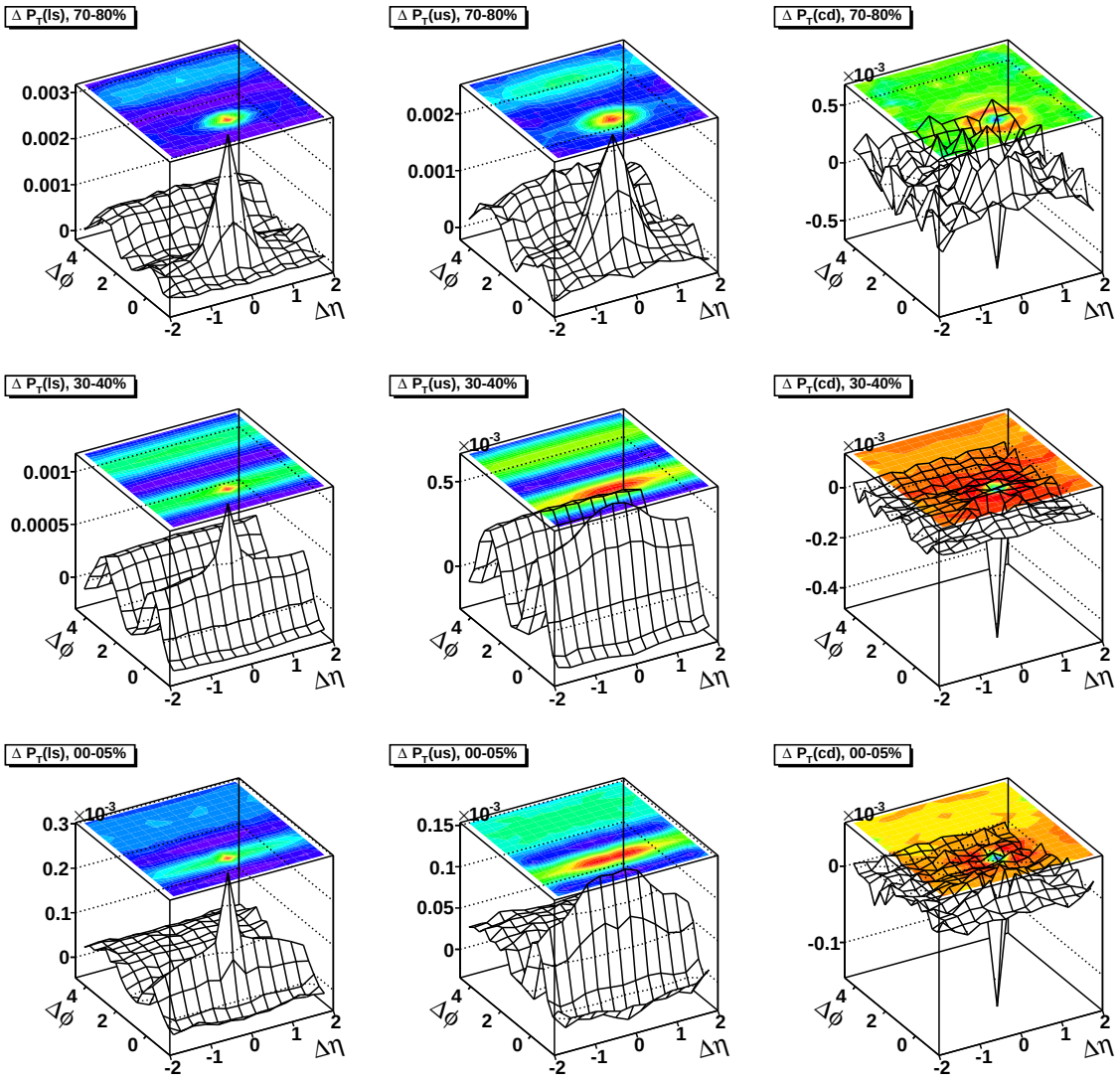

Figure 6.13: Correlation functions $\Delta P_T^{ls}(\Delta\eta, \Delta\phi)$ (*left*), $\Delta P_T^{us}(\Delta\eta, \Delta\phi)$ (center), $\Delta P_T^{cd}(\Delta\eta, \Delta\phi)$ (*right*), for charged particles in the ranges $|\eta| < 1.0$, $0.2 < p_T < 2.0$ GeV/c for three representative collision centralities.

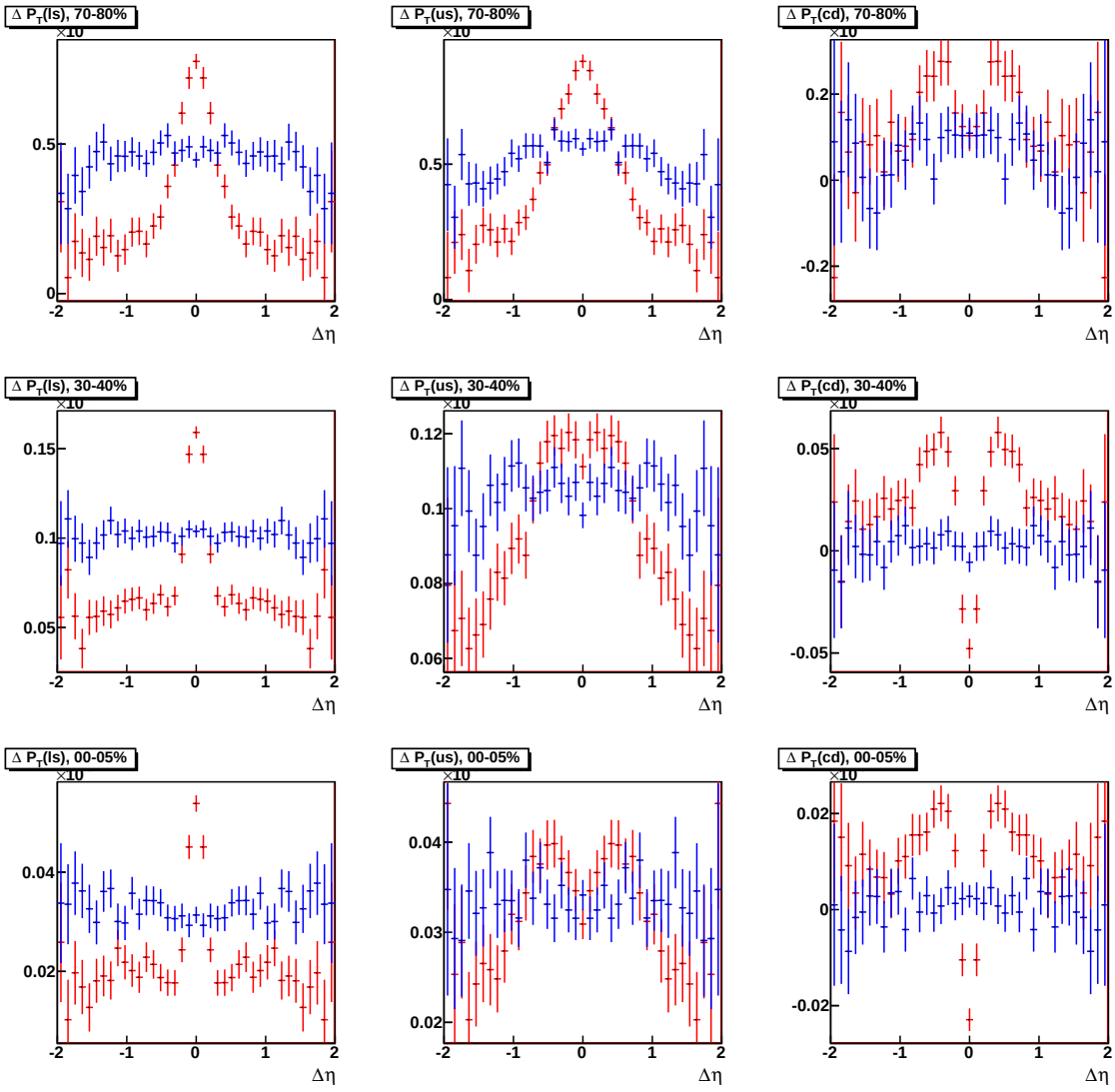

Figure 6.14: Near- (red) and away-side (blue) projections of the correlation functions $\Delta P_T^{ls}(\Delta\eta, \Delta\phi)$ (*left*), $\Delta P_T^{us}(\Delta\eta, \Delta\phi)$ (center), $\Delta P_T^{cd}(\Delta\eta, \Delta\phi)$ (*right*), for charged particles in the ranges $|\eta| < 1.0$, $0.2 < p_T < 2.0$ GeV/c for three representative collision centralities.

6.5 Fourier Decomposition of R_2, C, ΔP_T

Recent research on two-particle correlations has emphasized the role of lumpy initial conditions causing the appearance of higher harmonics in the Fourier decomposition of R_2 [34]. The v_3 amplitude may explain certain features on the away-side of the most central events, so-called "Mach cone" effects. Presented in Figure 6.15 through Figure 6.19 are graphs of the first six Fourier coefficients for the three observables R_2, C, ΔP_T taken from slices in $\Delta\eta$ that are then projected in $\Delta\phi$ and fitted.

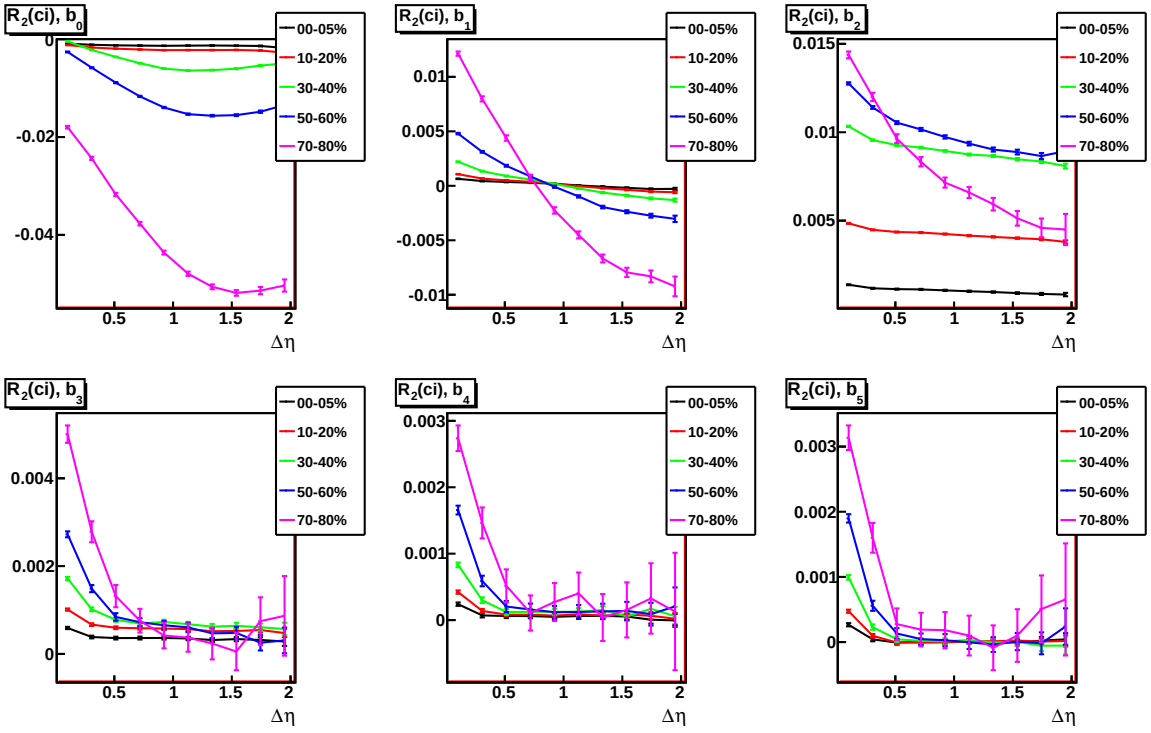

Figure 6.15: Fourier coefficients for $R_2^{ci}(\Delta\phi)$. Slices of R_2 in $\Delta\eta$ are projected in $\Delta\phi$ and then fitted.

The Fourier coefficients to the observables $R_2(NP)$ and $C(NP)$ are also shown immediately following R_2 and C. $R_2(NP)$ and $C(NP)$ are versions of R_2 and C where the cumulants C_2 and $C_2^{p_T}$, respectively, in the numerator have been multiplied by the average number of nucleon participants, $\langle N_{part}\rangle$, for each centrality. Multiplica-

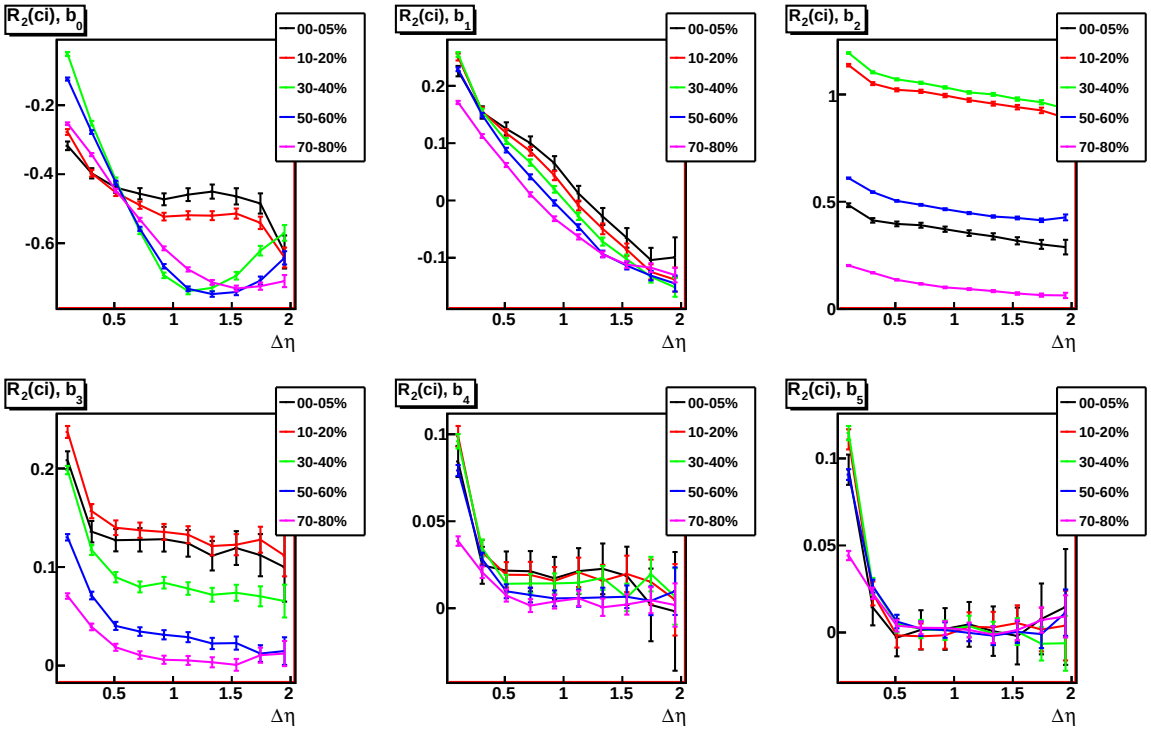

Figure 6.16: Fourier coefficients of $R_2(NP)^{ci}(\Delta\phi)$. R_2 is multiplied by the average number of participants $\langle N_{part}\rangle$ in each centrality bin. Slices of $R_2(NP)^{ci}$ in $\Delta\eta$ are projected in $\Delta\phi$ and then fitted.

tion by $\langle N_{part} \rangle$ removes the effect of dilution of correlations with increasing centrality. The procedure does not apply to ΔP_T since it is normalized by the correlated pair distribution, whereas R_2 and C are normalized using the uncorrelated pair distribution $\rho_1 * \rho_1$. The values of the coefficients and their ordering by centrality are seen to change after multiplication by $\langle N_{part} \rangle$.

Because the Fourier coefficients $\{b_n\}$ have been extracted from a fit to R_2, rather than the particle spectrum $dN/d\phi$, they are not strictly comparable to the flow parameters $\{v_n\}$. However, the behavior of the values of b_2 is similar to those of the elliptic flow parameter v_2 shown in Figure 3.10, with flow greatest at mid-centrality. The comparison with elliptic flow is more clear in the fit to $R_2(NP)$ and $C(NP)$, where the values of b_2 for all slices are uniformly ordered by centrality.

Overall, with the exception of b_0 which is a pedestal, the trend of the coefficients $\{b_n\}$ for the three observables is quite similar as a function of $\Delta\eta$.

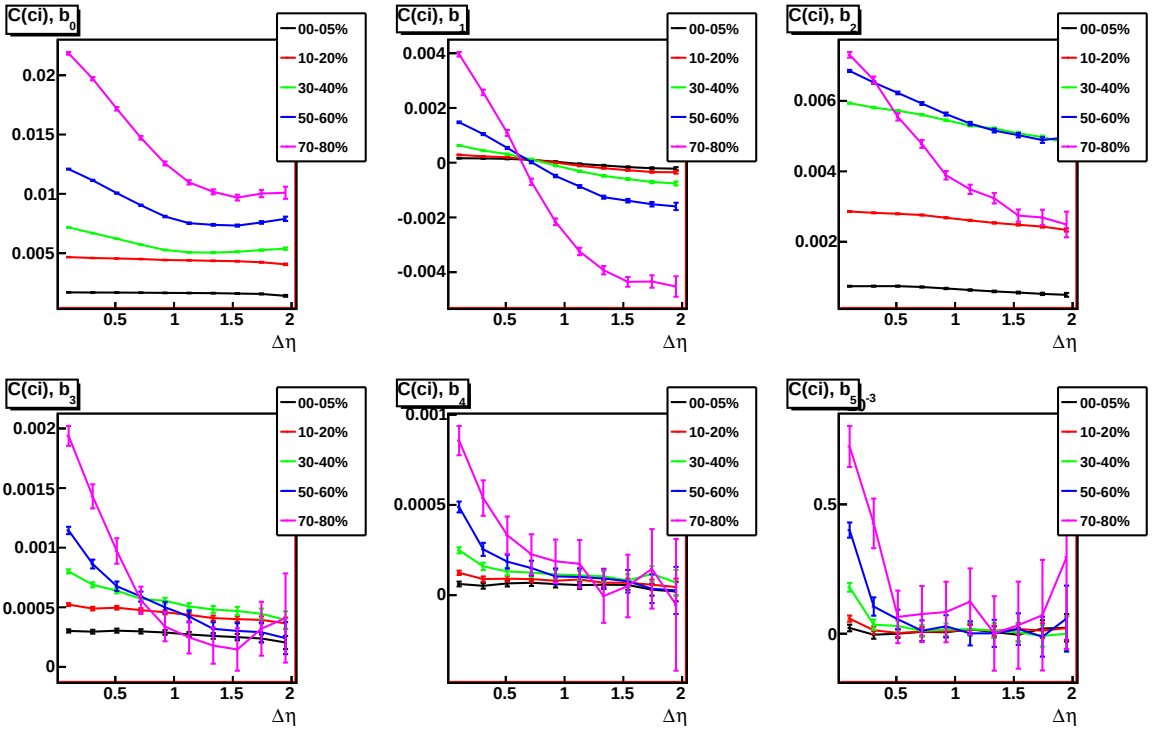

Figure 6.17: Fourier coefficients for $C^{ci}(\Delta\phi)$. Slices of C in $\Delta\eta$ are projected in $\Delta\phi$ and then fitted.

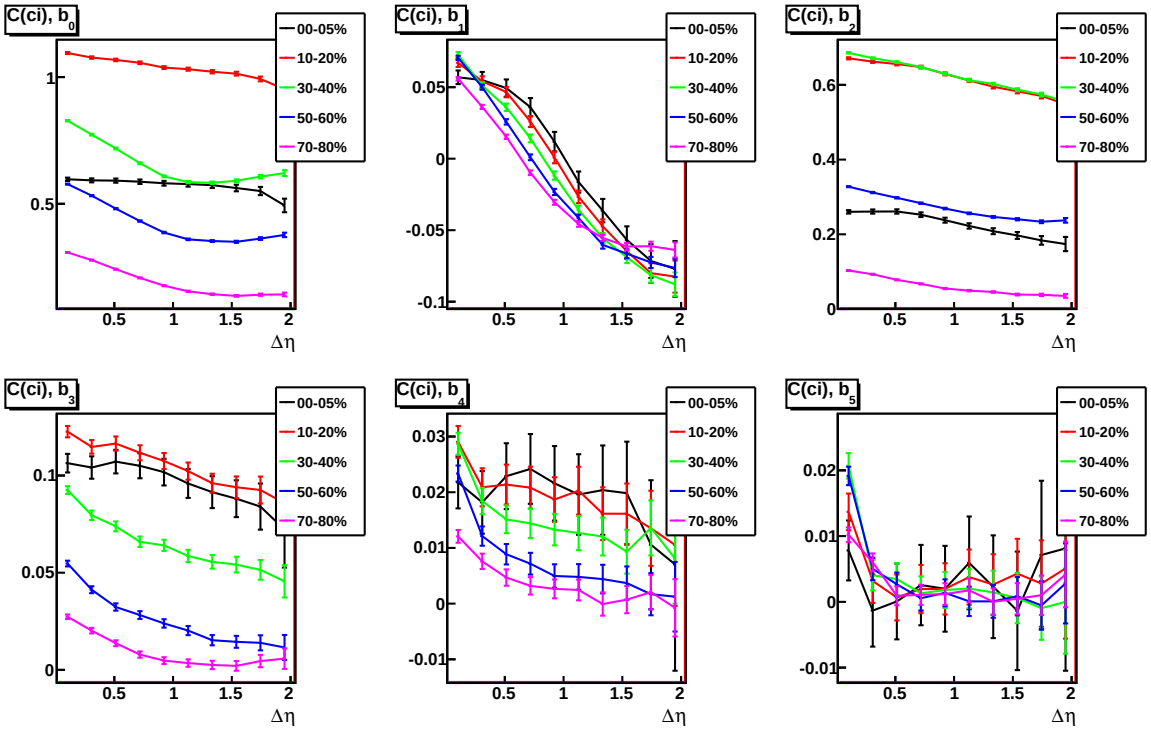

Figure 6.18: Fourier coefficients of $C(NP)^{ci}(\Delta\phi)$. C is multiplied by the average number of participants $\langle N_{part}\rangle$ in each centrality bin. Slices of $C(NP)^{ci}$ in $\Delta\eta$ are projected in $\Delta\phi$ and then fitted.

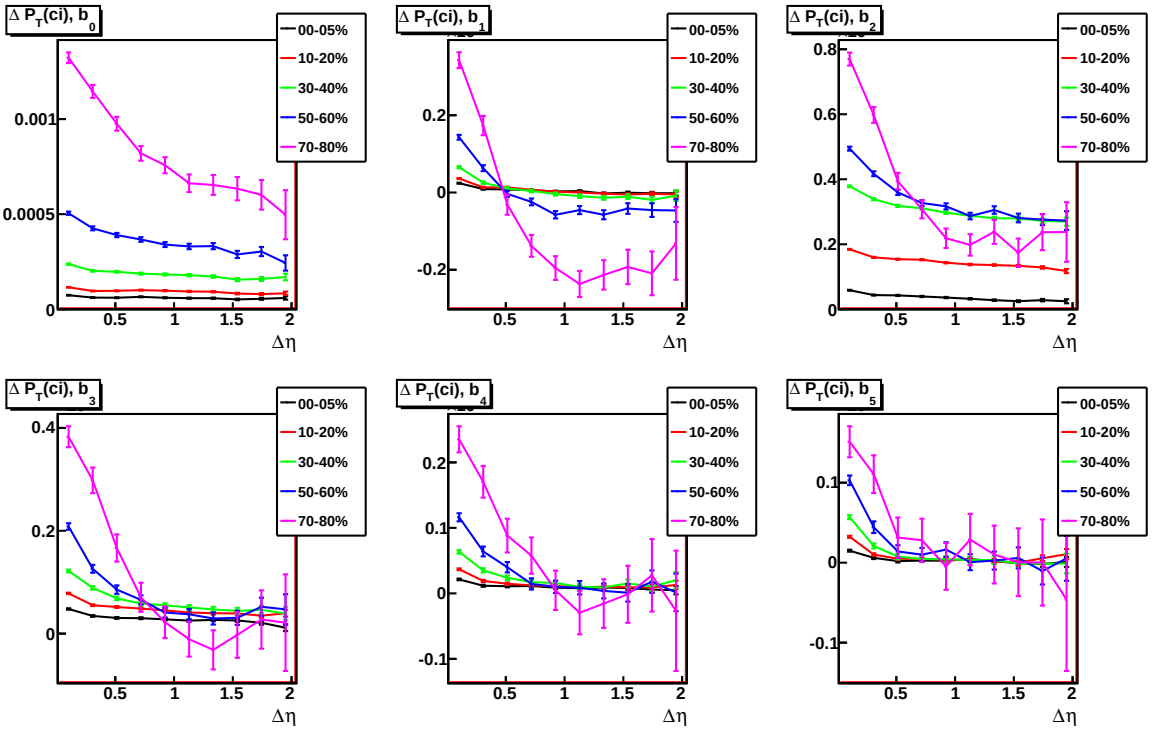

Figure 6.19: Fourier coefficients for $\Delta P_T^{ci}(\Delta\phi)$. Slices of ΔP_T in $\Delta\eta$ are projected in $\Delta\phi$ and then fitted.

Chapter 7

Comparison with Simulated Data

To investigate the features of the R_2 correlation function on real data, two simulated sets of data were produced, and the R_2 correlation function was constructed for each simulated data set. The first set of simulted data was produced using Relativistic Quantum Molecular Dynamics (RQMD) simulation. RQMD incorporates quantum mechanical processes in the production of particles which are then propagated using hydrodynamic transport subroutines [35]. The second set of data was a simple cluster model in which an invariant mass was decayed in its rest frame and then boosted first lontigudinally and then transversely. Simulated data for the cluster model was produced both with and without the additional transverse boost.

For the first set of simulated data, using RQMD, the R_2 correlation function shows all of the expected effects of charge conservation, momentum conservation, cluster production, but no near-side "ridge" of enhanced correlations in rapidity. For the second set of simulated data, using a simple cluster model, the correlation function shows no quantum mechanical effects (no such effects are expected since the particle production model is classical and deterministic), however, it does show a near-side "ridge". The ridge is only present for the variant of the cluster model which contains a transverse boost in addition to the longitudinal boost.

7.1 RQMD Plots

We present here the plots from RQMD simulated data. In Figure 7.1 *et seq.* are shown the R_2 plots for like-sign and unlike-sign particle pairs. The plots shown were obtained from a dataset of 329,601 RQMD simulated Au+Au $\sqrt{s_{NN}}$ = 200 GeV collision events. The R_2 plots compare central collisions with impact parameter $0 < b < 2$ fermi with more peripheral collisions of $4 < b < 6$ fermi. Cuts on particles with $p_T > 2.0$ GeV restricts particle pairs to the domain of bulk multiparticle production. After the p_T cuts, the mean multiplicity of charged and uncharged particles for central and mid-central collisions was, respectively $\langle N^+ \rangle = 1138$, $\langle N^- \rangle = 1106$ and $\langle N^+ \rangle = 730$, $\langle N^- \rangle = 710$. Though neutral particles were created in the simulation, they are omitted from the RQMD plots to facilitate comparison with plots from data.

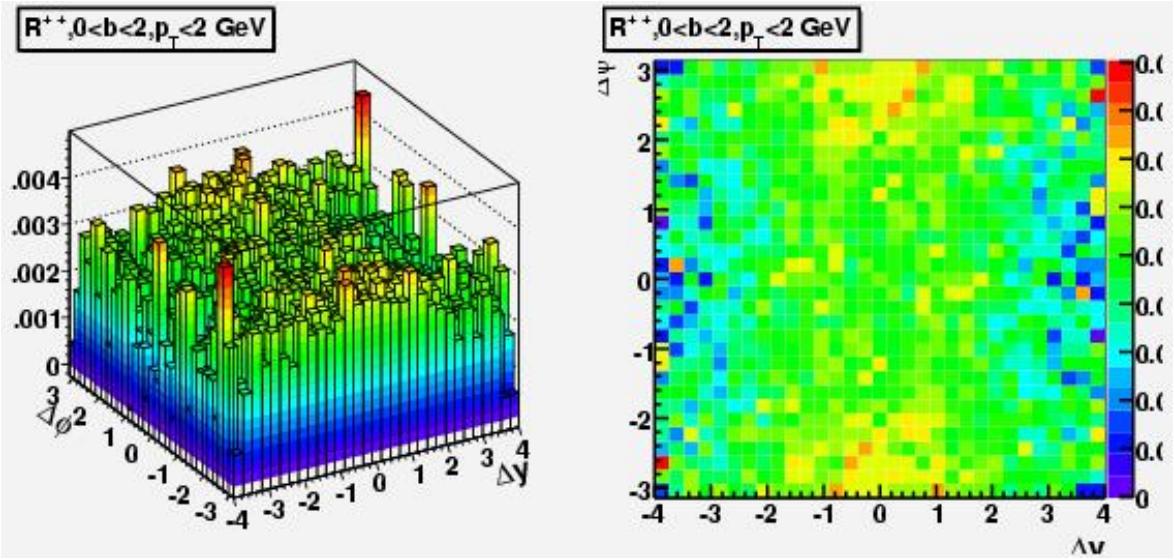

Figure 7.1: R_2^{++} for central ($0 < b < 2$) Au+Au 200 GeV RQMD events.

For all RQMD plots the correlations are rather narrow in $\Delta\eta$ relative to the available phase space. The axis of correlations is predominantly in the $\Delta\phi$ direction. For all plots the away side shows the correlations expected from global conservation of momentum, but they are no broader than on the near side. For the unlike-sign plots, enhanced correlations from charge conservation in back-to-back particle production

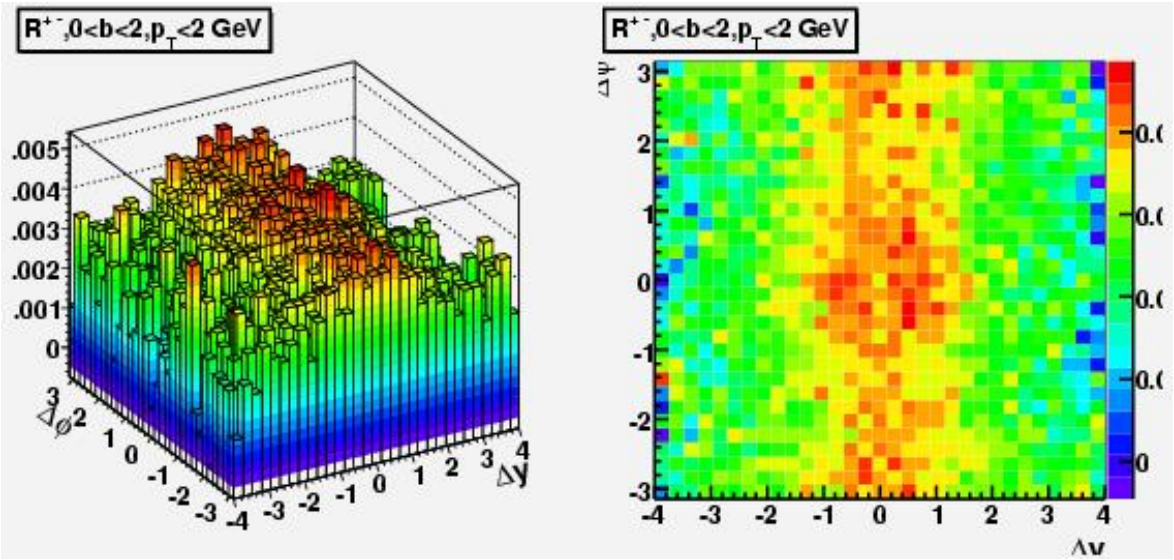

Figure 7.2: R_2^{+-} for central ($0 < b < 2$) Au+Au 200 GeV RQMD events.

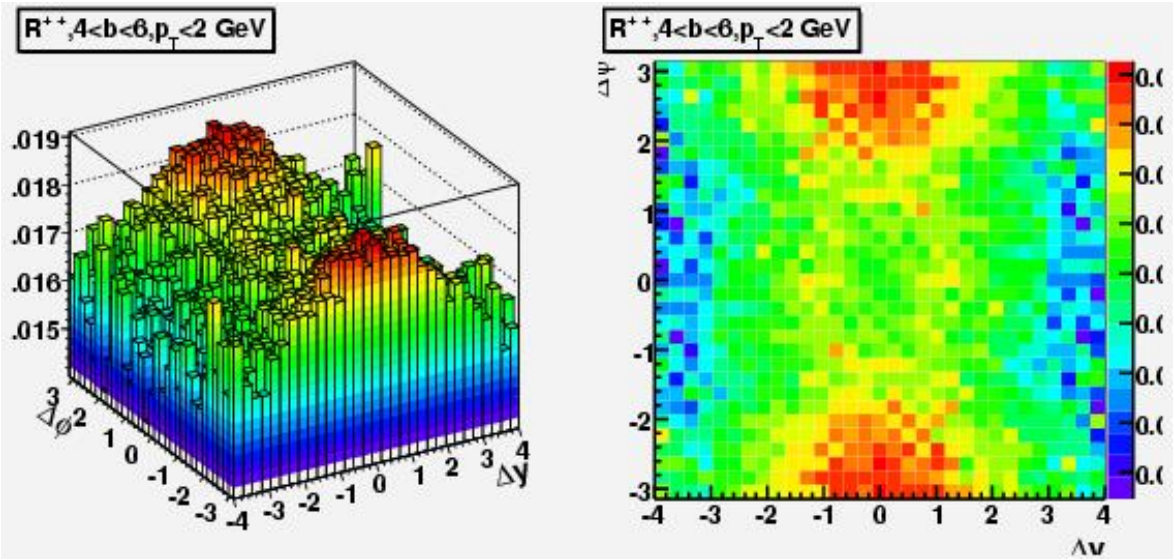

Figure 7.3: R_2^{++} for mid-central ($4 < b < 6$) Au+Au 200 GeV RQMD events.

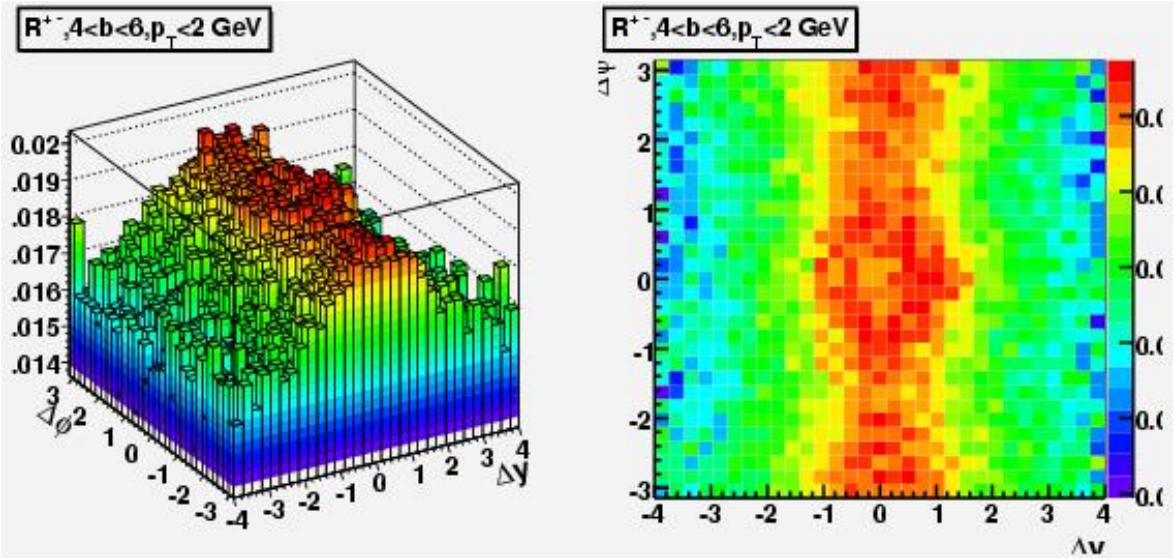

Figure 7.4: R_2^{+-} for mid-central ($4 < b < 6$) Au+Au 200 GeV RQMD events.

are also present on the away side. For both central ($0 < b < 2$) and more peripheral collisions ($4 < b < 6$), the unlike-sign R^{+-} plots show strongly enhanced short-range positive correlations in the neighborhood of $(\Delta y, \Delta\phi) = (0, 0)$ (Figure 7.2 and Figure 7.4). Such correlations are expected due to charge conservation within produced clusters. As expected, the like-sign R_2 plots lack the enhanced correlations in the neighborhood of the origin due to charge conservation seen in the unlike-sign plots. Looking for $\cos(2\Delta\phi)$ modulation as evidence of elliptic flow, none is seen in the RQMD plots.

In short we find that many key features of the R_2 correlation function apparent in plots from Run IV data, such as a narrow peak around $(0, 0)$ in more peripheral events, the formation of the ridge at mid-centrality and the presence of elliptic flow at mid-centrality, are not reproduced by RQMD simulations.

7.2 Cluster Model

We turn now to the simple deterministic cluster model. As an event generator, we consider the simple cluster model as a cartoon or caricature of reality made with

as few brushstrokes as possible, yet each brushstroke in the model adds a crucial element present in the plots of real data. Though the model is quite basic, it succeeds in reproducing key features of hadronic collisions. Throughout, we will show the R_2 correlation function in two plots, using the decomposition $R_2 = R_S + R_L$ described earlier, as it provides insight into the origins of the correlations.

The parameters of the model are as follows: a cluster, that is an invariant mass in the range $2 < m_{\text{eff}} < 4$ GeV with mean $\langle m_{\text{eff}} \rangle = 3$ GeV, decays in its rest frame into a random number of particles between 2 and 5 each with pion mass 140 MeV, with Poisson distribution. The simulated decay into particles is accomplished using the TGenPhaseSpace class of ROOT software. The decay process conserves energy and momentum. The invariant mass is not boosted. In each collision, a single cluster forms and decays. The plots of R_S and R_L for this simulation, labeled $p+p$ (1a), are shown in Figure 7.5.

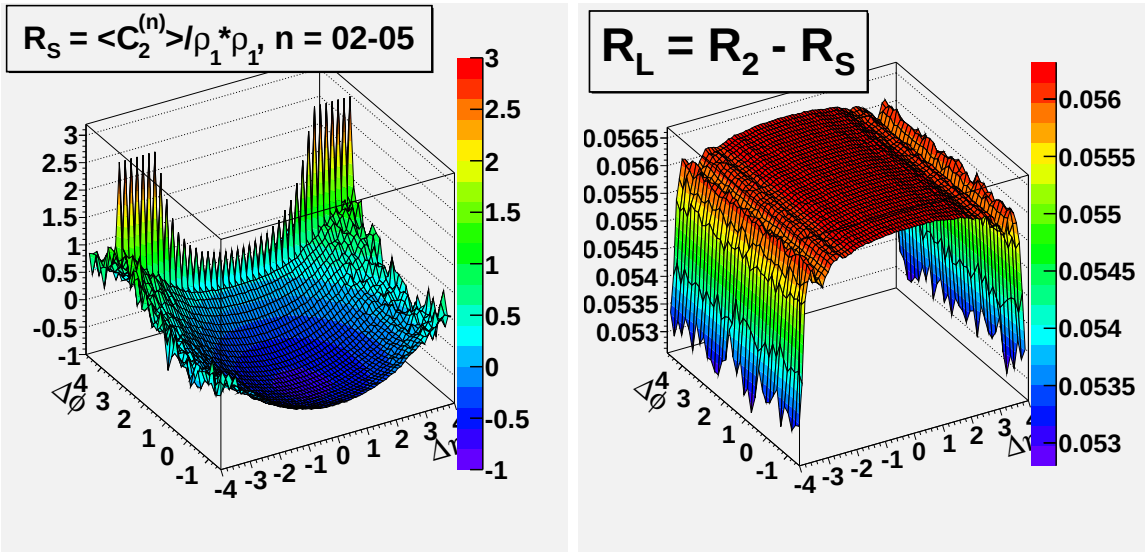

Figure 7.5: R_S, R_L for simulated $p+p$ with no boosts (model 1a).

This is the first, broad stroke, and the portrait is very crude. At $\Delta\phi$ equal to π there is a binning anomaly attributable to the n equals 2 decay mode, which is a back-to-back decay into two collinear particles. For such decays, the $\Delta\eta$ bin cannot

vary in integer increments, but must change by an even number of bins. The reader is invited to make a mental correction at $\Delta\phi = \pi$ so that each bin is filled, but at half the amplitude shown. As TGenPhaseSpace conserves energy and momentum, so they are conserved in this plot as well.

The next brushstroke in our cartoon is to add a longitudinal boost to the invariant mass prior to its decay. The boost in rapidity, sampled from a uniform distribution on the interval $(-3, 3)$, is intended as a proxy for the disparity in the fraction x of longitudinal momentum carried by the colliding partons in a nucleon-nucleon collision. The plots of R_S and R_L for this simulation, labeled $p+p$ (1b) are shown in Figure 7.6.

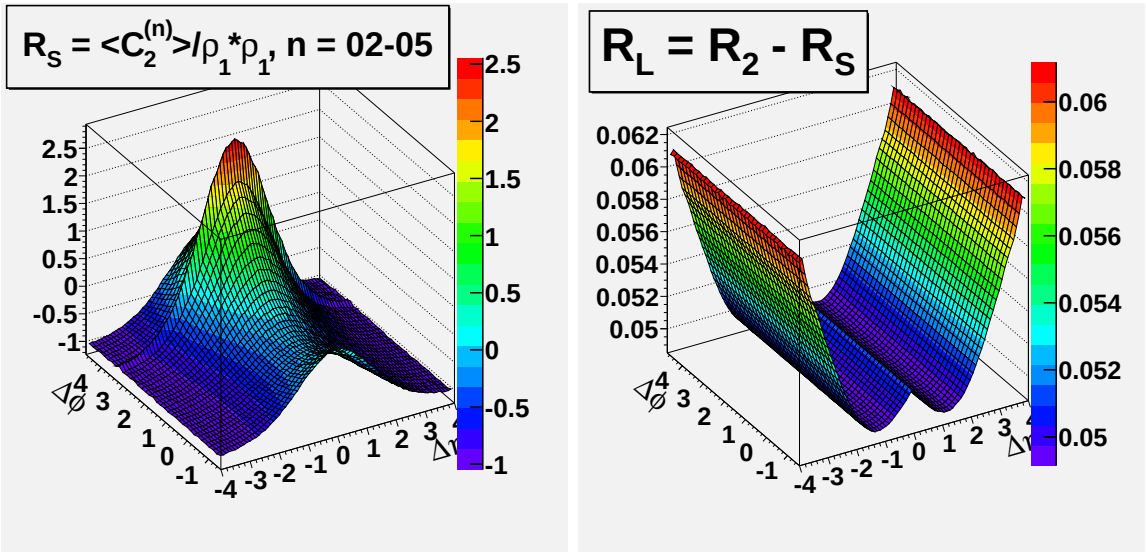

Figure 7.6: R_S, R_L for simulated $p + p$. A single cluster decays per event, with longitudinal boost (model 1b).

The binning anomaly at $\Delta\phi$ equal to π is now resolved, and the R_2 plot has become somewhat more realistic, beginning to resemble an R_2 plot for $p + p$ collisions using real data. We now increase the number of clusters, from a single cluster per event to a Poisson distribution with a mean of six. We observe the effect of the increase in clusters on R_S and R_L respectively in Figure 7.7. This is model $p + p$ (2).

As expected from simple superposition, increasing the number of clusters per event by a factor of six has diluted the intrinsic correlations R_S by the same factor. The

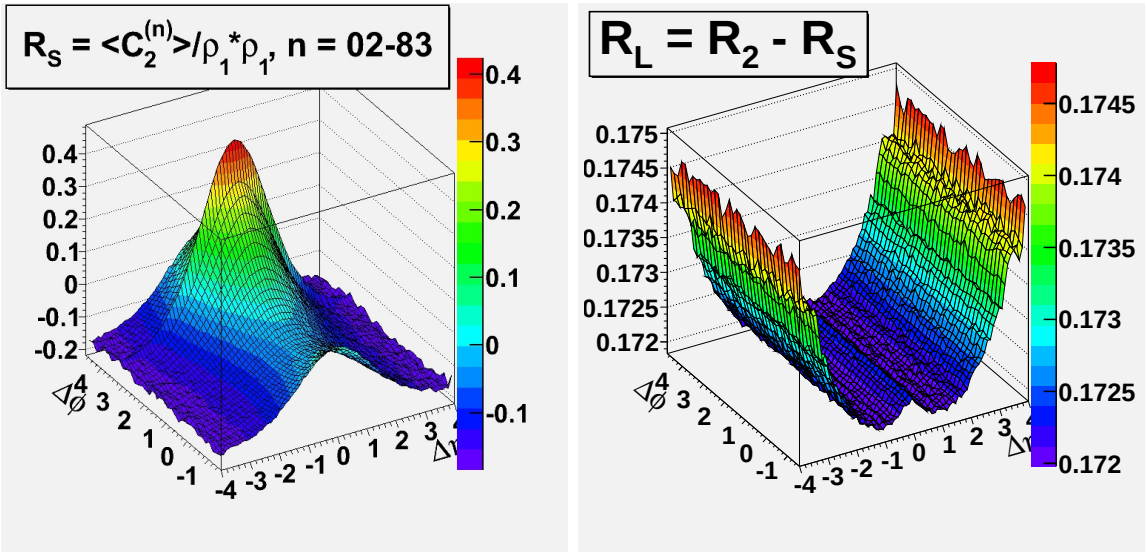

Figure 7.7: R_S, R_L for simulated p+p. Six clusters decay per event, each with distinct longitudinal boost (model 2).

multiplicity correlations R_L have the *same shape* that is seen when we subtract the Au+Au R_2 plots for two different multiplicity centralities $|\eta| < 0.5$ and $|\eta| < 1.3$, as shown in Figure 7.8. (In this example the plots were multiplied by the average number of participants in each centrality bin, $\langle N_{part} \rangle$, prior to subtraction.) We infer that the different defintions of centrality affect R_L, but not R_S, since R_S disappears *for all centrality bins* when the two definitions are subtracted.

We add another brushstroke. An examination of the p_T plot at left in Figure 7.9 shows a sharp, unphysical cutoff. To achieve a more realistic p_T distribution, a small transverse "thermal" motion is applied to each invariant mass, before applying the longitudinal boost.

The p_T distribution now takes on a more realistic exponential shape, as seen in Figure 7.9 at right. This is $p+p$ model (3). A comparison of the R_S plots before and after the addition of thermal motion is shown in Figure 7.10.

Using the simulated data from the "thermal" $p+p$ simulation (model 3), we now construct R_2 according to the same formula used for the PHOBOS R_2 observable in Figure 3.14, which we have labeled $R_2[NP]$. $R_2[NP]$ is a weighted average over

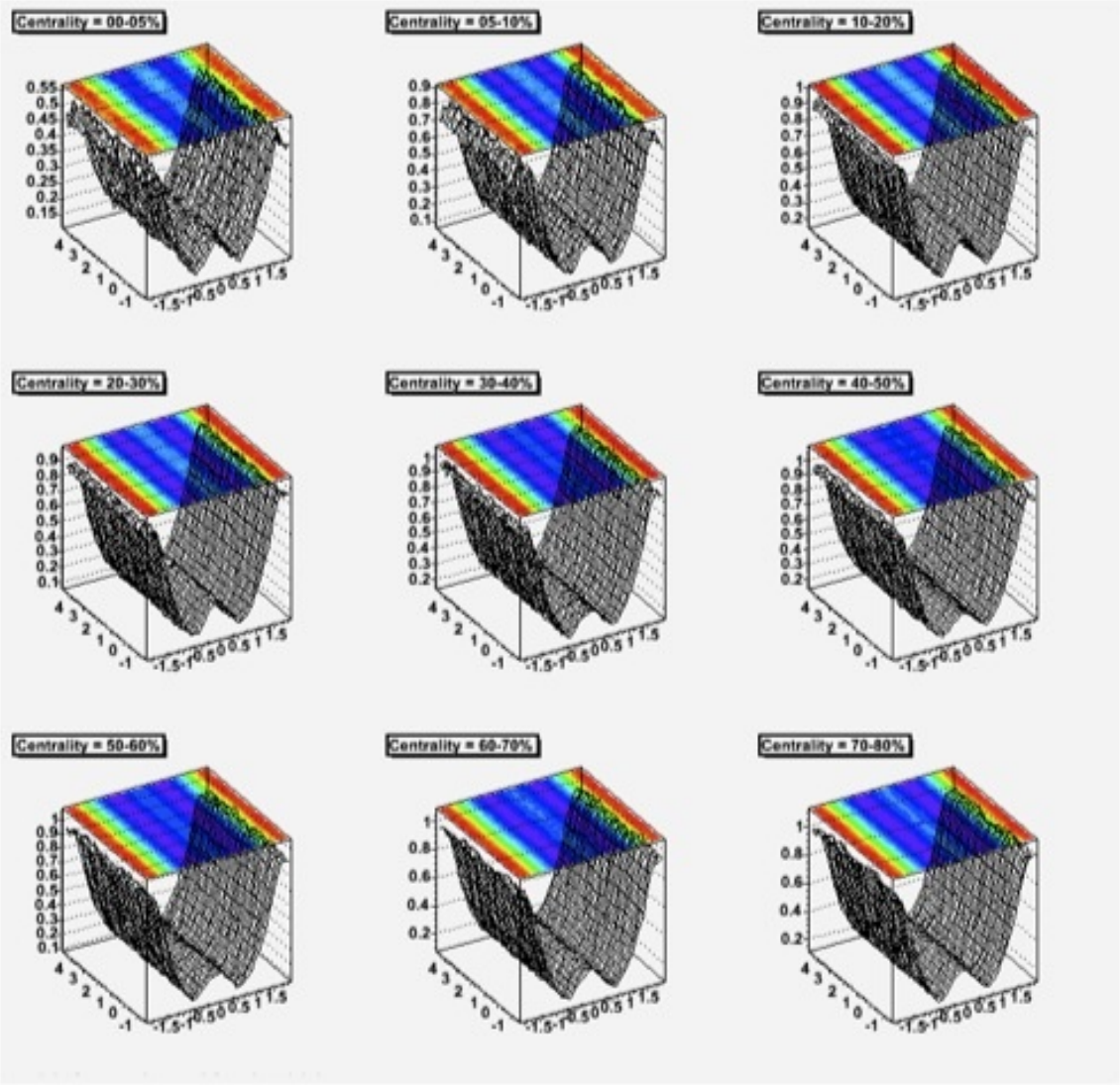

Figure 7.8: Difference plot that results from subtraction of Au+Au $R_2(\Delta\eta, \Delta\phi)$ plots using two different multiplicity centralities, $|\eta| < 0.5$ and $|\eta| < 1.3$. Note similarity to R_L plots in cluster model simulated data.

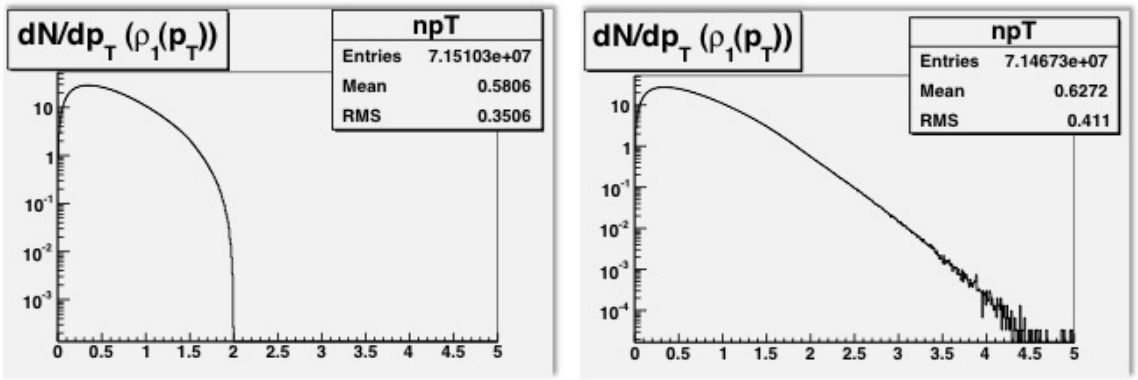

Figure 7.9: Change in p_T distribution after addition of thermal motion to each cluster. Model $p+p$ (2) (*left*), model $p+p$ (3) (*right*). See text for details.

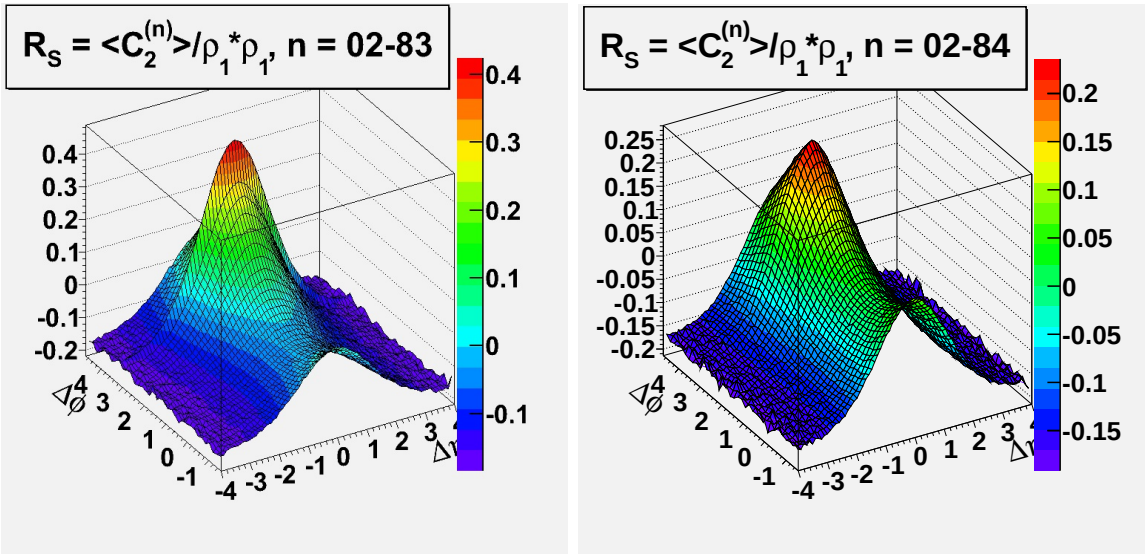

Figure 7.10: R_S for simulated $p+p$. Change in R_S after addition of thermal motion to each cluster. Model $p+p$ (2) (*left*), model $p+p$ (3) (*right*). See text for details.

multiplicity that uses distribution functions normalized to unity. (*Note:* $R_2[NP]$ differs from $R_2(NP)$ in the section on Fourier coefficients). The formula for $R_2[NP]$ is given by:

$$R_2[NP] = \left\langle (n-1)\left(\frac{\rho^{(n)}}{n(n-1)}\frac{\langle n\rangle^2}{\rho_1 * \rho_1} - 1\right)\right\rangle \tag{7.1}$$

As shown in Figure 7.11, the $R_2[NP]$ plot using simulated $p+p$ model (3) reproduces well the key features of the published PHOBOS $p+p$ correlation plot based on real data. This remarkable result has been obtained with only the simplest assumptions, that of cluster production of particles, absence of correlation between clusters, isotropic rest frame decay, and a modest accommodation of quantum physics by the addition of the thermal motion.

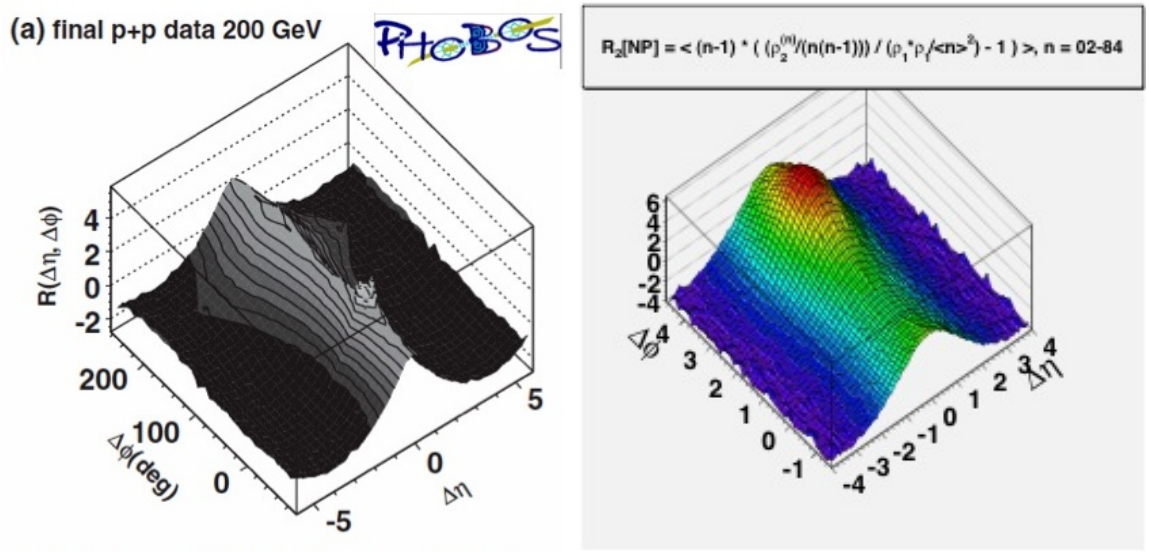

Figure 7.11: Comparison of PHOBOS R_2 for 200 GeV $p+p$ collisions with "thermal" $p+p$ simulation (model 3).

Our last brushstroke adds a transverse boost. To recap: we have an average of six clusters per event, each cluster is given a random transverse thermal motion, followed by a random longitudinal boost in rapidity, then all six clusters are given either an *individual* or a *collective* transverse boost according to a linear distribution. The transverse boost is intended to model radial flow, and the linear distribution supposes

the flow is proportional to the transverse radial distance from a hypothetical collision center. The plots for individual (model 4a) and collective (model 4b) transverse boosts are shown in Figure 7.12.

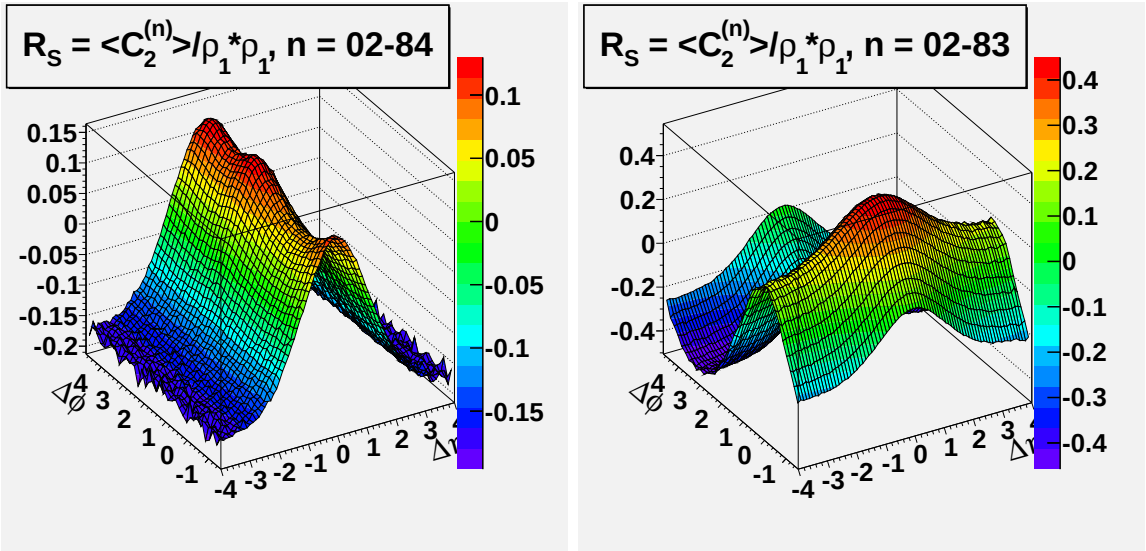

Figure 7.12: R_S plots for *individual* (model 4a) and *collective* (model 4b) transverse boosts.

The effect of giving each individual cluster a transverse boost is to produce an away-side dip at $\Delta\phi \sim \pi$. The effect of giving all clusters an identical transverse boost is to produce a near-side ridge of enhanced correlations in $\Delta\eta$.

One would infer from the dramatic effect of the transverse boost to produce a ridge in our simple model (4b) that the observed difference between the R_2 correlation plots of $p + p$ and heavy ion collisions, or between peripheral and central Au+Au collisions, is likewise due to the addition of radial boost. Our cluster model result is thus consistent with the interpretation of ridge formation as a consequence of the appearance, once a threshold energy density has been achieved, of radial flow due to the creation of a fluid-like state of matter.

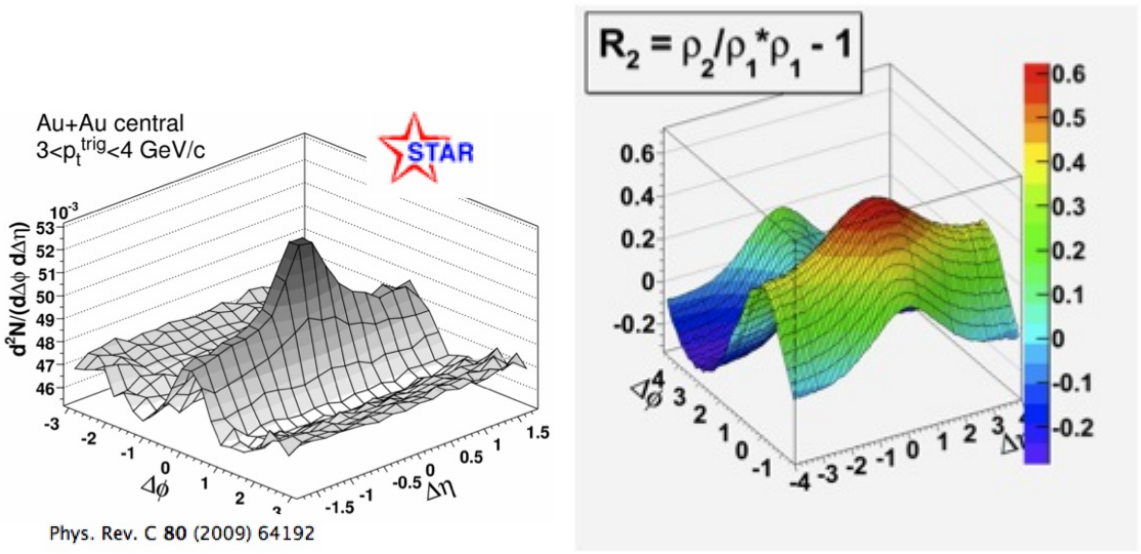

Figure 7.13: Comparison of triggered ridge at STAR with $p + p$ simulation with longitudinal and collective transverse boost (model 4b).

Chapter 8

Summary

We have presented three bulk correlation observables involving number and transverse momentum denoted R_2, C, and ΔP_T as a function of centrality and charge combination. The analysis is based on nearly 14 million STAR Run IV Au+Au collisions at $\sqrt{s_{NN}} = 200$ GeV beam energy. Data corrections were made to remove artifacts due to centrality definition, detector effects, collision z vertex variation, and finite centrality binning.

Plots of the three observables differ quantitatively, with R_2 having greatest amplitude and ΔP_T the least, but all show a ridge in central and mid-central collisions. Modulation by elliptic flow is the dominant effect in mid-central collisions, with pronounced $\cos(2\Delta\phi)$ variation in all three observables.

Like-sign and unlike-sign correlations show similar evolution with centrality, with unlike-sign correlations having additionally a robust near-side peak around the origin that is attributable to charge conservation. However, the effect of charge conservation is seen to be local. Accordingly, charge dependent plots formed from the difference of unlike- and like-sign plots are statistically zero except at the origin, where the robust unlike-sign peak survives.

The three observables exhibit somewhat different behavior about the origin in $(\Delta\eta, \Delta\phi)$ space, where the combined effects of resonance decays, charge conservation, Hanbury-Brown/Twiss quantum interference and uncorrected track merging compli-

cate interpretation. A narrow peak at the origin in the like-sign plot of ΔP_T, not found in R_2 or C, is likely attributable to HBT enhancement.

We have shown that simple kinematic cluster models reproduce well the qualitative features of two-particle correlations in $p + p$ and Au+Au data. Simulated particle production using decay of an invariant mass "cluster" that is longitudinally boosted creates Gaussian correlations in $\Delta\eta$ that are similar to $p + p$ data correlation plots. Adding a radial tranverse boost collectively to several clusters at once produces an extended Gaussian ridge in $\Delta\eta$ that is similar to the "ridge" seen in Au+Au data correlation plots. The comparison with $p + p$ and Au+Au data is remarkable given that there are no QCD effects in the cluster model, only kinematic effects are used.

In the children's story *Pinocchio* we are told that "Lies are of two kinds: there are lies that have short legs, and lies that have a long nose." If the converse statement applies to Truth, then may it be said that we have tried in this work to produce results with long legs, not to shorten any noses.

Chapter 9

Appendices

9.1 Appendix A. Kinematic Variables

Kinematic variables commonly used in laboratory analysis of multiparticle production [7] are *transverse momentum* p_T, *transverse mass* m_T and *rapidity* y. With angle θ taken with respect to the beam axis and c=1 we have:

$$p_T = |p| \sin\theta \tag{9.1}$$

$$m_T \equiv \sqrt{m^2 + p_T^2} \tag{9.2}$$

Transverse mass amounts to a repartition of the energy-momentum relation in terms of more convenient observables:

$$m_T^2 + p_L^2 = m^2 + p_T^2 + p_L^2 = E^2 \tag{9.3}$$

Rapidity is a logarithmic re-scaling of the longitudinal velocity $\beta_L = p_L/E$:

$$y \equiv \tanh^{-1}\left(\frac{p_L}{E}\right) = \frac{1}{2}\log\frac{E+p_L}{E-p_L} = \frac{1}{2}\log\frac{1+\beta_L}{1-\beta_L} \approx \beta_L \ (\beta_L \ll 1) \tag{9.4}$$

Rapidity has a simple transformation property under a Lorentz boost y_β: $y' = y + y_\beta$. Then $dy' = dy$, consequently distributions with respect to rapidity are Lorentz

invariant. Substituting p for E one obtains the *pseudorapidity* η:

$$\eta \equiv \tanh^{-1}(p_L/p) = \tanh^{-1}(\cos\theta) = -\log(\tan(\theta/2)) \tag{9.5}$$

For $m^2 \ll E^2$ pseudorapidity is an excellent approximation to the rapidity, and has the advantage of depending on a simple geometric observable.

The key quantity of interest in the study of inclusive distributions of the form $A + B \longrightarrow C + X$, with projectile A a hadron such as proton, pion or kaon and B a fixed proton target, is the Lorentz invariant differential cross-section. Writing the kinematic dependences explicitly gives:

$$\frac{E_C}{\sigma_{tot}(s_{AB})} \frac{d\sigma(\mathbf{p}_C, s_{AB})}{d^3 p_C} \tag{9.6}$$

The total cross-section σ_{tot} is related to the elastic scattering amplitude $f_{AB \longrightarrow AB}$ via the optical theorem:

$$\sigma_{tot} = 4\pi^2 \mathrm{Im} f_{AB \longrightarrow AB} \mid_{Q^2=0} \tag{9.7}$$

The desired normalized distribution function is then obtained by dividing by the total cross-section:

$$\rho(\mathbf{p}) \equiv \frac{E}{\sigma_{tot}} \frac{d\sigma}{d^3 p} \tag{9.8}$$

In 1969 R.P. Feynman proposed a "scaling hypothesis": with increasing beam energy, production cross-sections should depend only on the produced particle's fraction of the projectile longitudinal momentum, rather than directly on beam energy [36]. One commonly finds in the literature the Feynman scaling variable x_F:

$$x \equiv \frac{p_L^{CM}}{p_{max}^{CM}} \approx \frac{2p_L^{CM}}{\sqrt{s}} \tag{9.9}$$

Depending on the kinematic variables used for the momentum space volume element, the differential cross-section may take many equivalent forms:

$$E\frac{d\sigma}{d^3p} = \frac{E}{\pi}\frac{d^2\sigma}{dp_L dp_T^2} = \frac{1}{\pi}\frac{d^2\sigma}{dy dp_T^2} = \frac{E_{CM}}{\pi p_{CM}}\frac{d^2\sigma}{dx dp_T^2} \tag{9.10}$$

The one- and two-particle rapidity densities may be defined analytically in terms of the differential cross-section:

$$\rho_1(y) = \frac{dN}{dy} = \frac{1}{\sigma}\int \frac{d\sigma}{dp_T^2 dy} dp_T^2 \tag{9.11}$$

$$\rho_2(y_1, y_2) = \frac{d^2N_{pair}}{dy_1 dy_2} = \frac{1}{\sigma}\int \frac{d\sigma}{dp_{T_1}^2 dy_1}\frac{d\sigma}{dp_{T_2}^2 dy_2} dp_{T_1} dp_{T_2}^2 \tag{9.12}$$

Azimuthal densities are defined similarly. Due to detector constraints, the experimentalist works not with the differential cross-section $(E/\sigma)d\sigma/d^3p$ but rather with the charged particle multipicity distribution d^3N/d^3p, with N being the number of charged particles. In practice the most commonly encountered global observable is the charged particle pseudorapidity distribution $dN/d\eta$ acting as a proxy for dN/dy.

9.2 Appendix B. The R_2 bulk correlation function with a hybrid centrality

In this appendix we present the R_2 correlation function using a hybrid centrality based on both the Zero-Degree Calorimeter (ZDC) and the Central Trigger Barrel (CTB) detectors. A histogram of the number of Reverse Full Field events using the ZDC/CTB is shown below.

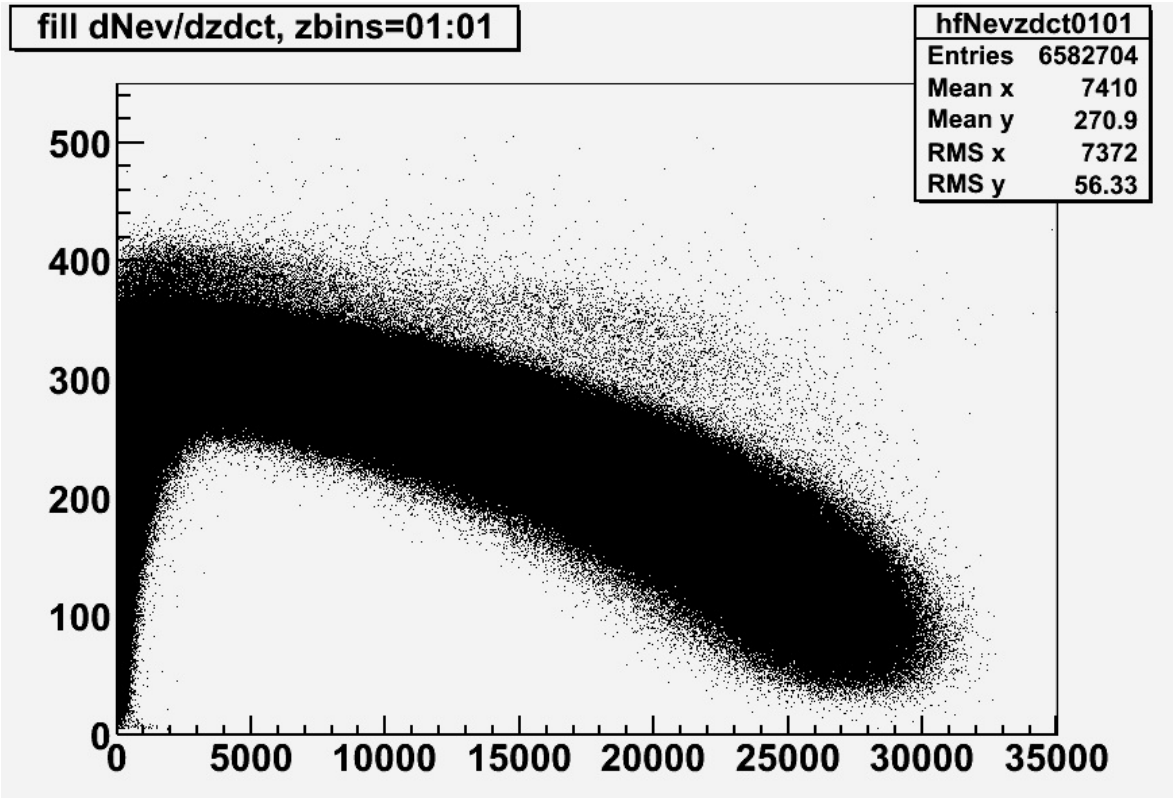

Figure 9.1: $d^2N_{ev}/d(ctb)d(zdc))$, Reverse Full Field

It may be seen that there is not a monotonic correlation between energy deposited in the ZDC and energy recorded by the CTB. Rather, the correlation changes sign from the most peripheral events, where CTB deposition is small and the correlation with ZDC is positive, to the most central events at the right of the plot, where the correlation between CTB and ZDC becomes negative. This degeneracy prevents us from using the ZDC alone as a measure of centrality over a full range of percentiles.

For the most central events where the correlation is weakly negative, we may

integrate out the Central Trigger Barrel data, and the remaining ZDC dependence can then be integrated to form the centrality percentile ranges for 0-5 percent most central, 5-10 percent, 10-20 percent, but no further. (This procedure was followed in the chapter on Data Corrections to create a ZDC centrality limited to the most central events.) However, we cannot extend this procedure beyond the point of the graph where the sign of the correlation changes since, as the slope is zero, there is effectively no correlation between the ZDC and CTB in that region. Alternatively we might use the same procedure but begin at the other end of the plot, calculating percentiles for the most peripheral centralities where the correlation is strongly positive. However, we cannot continue the procedure beyond the mid-central percentiles; the degeneracy of the plot is fundamental, and we cannot extract a one-parameter set of centrality percentiles based on the ZDC alone. However, we can employ a ruse that utilizes the ZDC and CTB together to establish a complete set of centrality percentiles in the following way.

We choose a point on the CTB axis (for convenience we choose the mean value 7410 of the CTB recorded energy) and from that point we extend a ray at a fixed angle to the CTB axis that crosses the band of ZDC/CTB data points. When a radius is drawn in this way, from a midway point on the CTB axis, it crosses the two dimensional band of the histogram nearly orthogonal to the contour path that follows the maxima of the ZDC/CTB distribution. Thus for any fixed angle, the width of the distribution of ZDC/CTB points is minimized because the subtending radius crosses the maximum contour approximately parallel to the gradient, and perpendicular to the level contour of the maximum.

Those points along the radial segment for fixed values of the angle can be taken together to form a single centrality. As we vary the angle from 0 to 180 degrees the entire two-dimensional distribution is scanned from most central to most peripheral. If we take the cosine of the angle and plot the distribution, we obtain the plot of

$dN_{ev}/d(cz)$ shown in Figure 9.2.

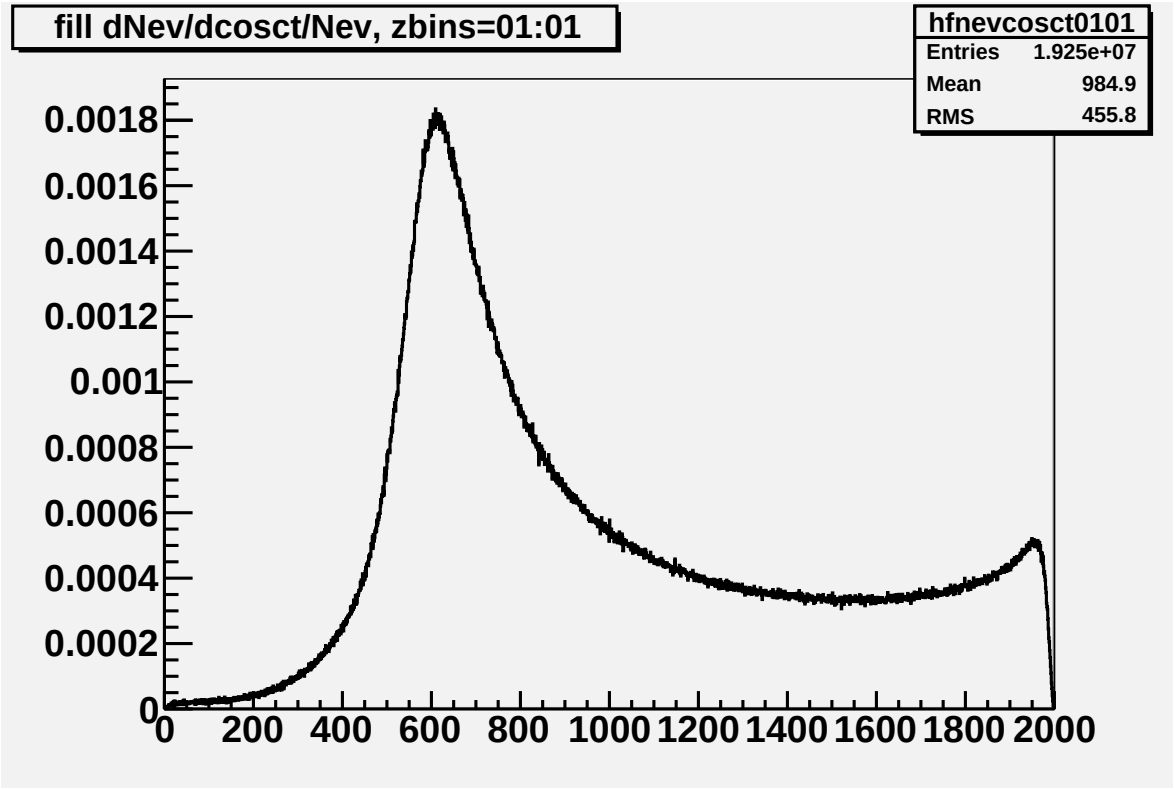

Figure 9.2: $dN_{ev}/d(cz)$, Reverse Full Field

If we now integrate the $dN_{ev}/d(cz)$ plot from most central to peripheral, we define a hybrid centrality based on information from both the ZDC and the CTB that may be used as a centrality definition for the R_2 correlation function. The plots and projections for R_2 sign combinations ls, us, ci, and cd are shown in Figure 9.2 through Figure 9.2. The same data corrections are applied as was done for the $|\eta| < 1.0$ multiplicity centrality definition used for R_2, C and ΔP_T.

The purpose of showing R_2 for this hybrid centrality is to make the point that every centrality definition is a different ordering of the events of the data ensemble. The most central and mid-central events of our hybrid centrality closely resemble those of the $|\eta| < 1.0$ multiplicity centrality used in our analysis. However, upon reaching the peripheral events, something new is seen. No plot published to date of

peripheral collisions for Au+Au $\sqrt{s} = 200$ GeV RHIC collisions more resembles a $p + p$ plot than do the ci plots for 70-80 percent centrality shown in Figure 9.2.

The plots for 80-100 percent centrality are anomalous, resembling a simple same-event pair distribution as seen in ρ_2.

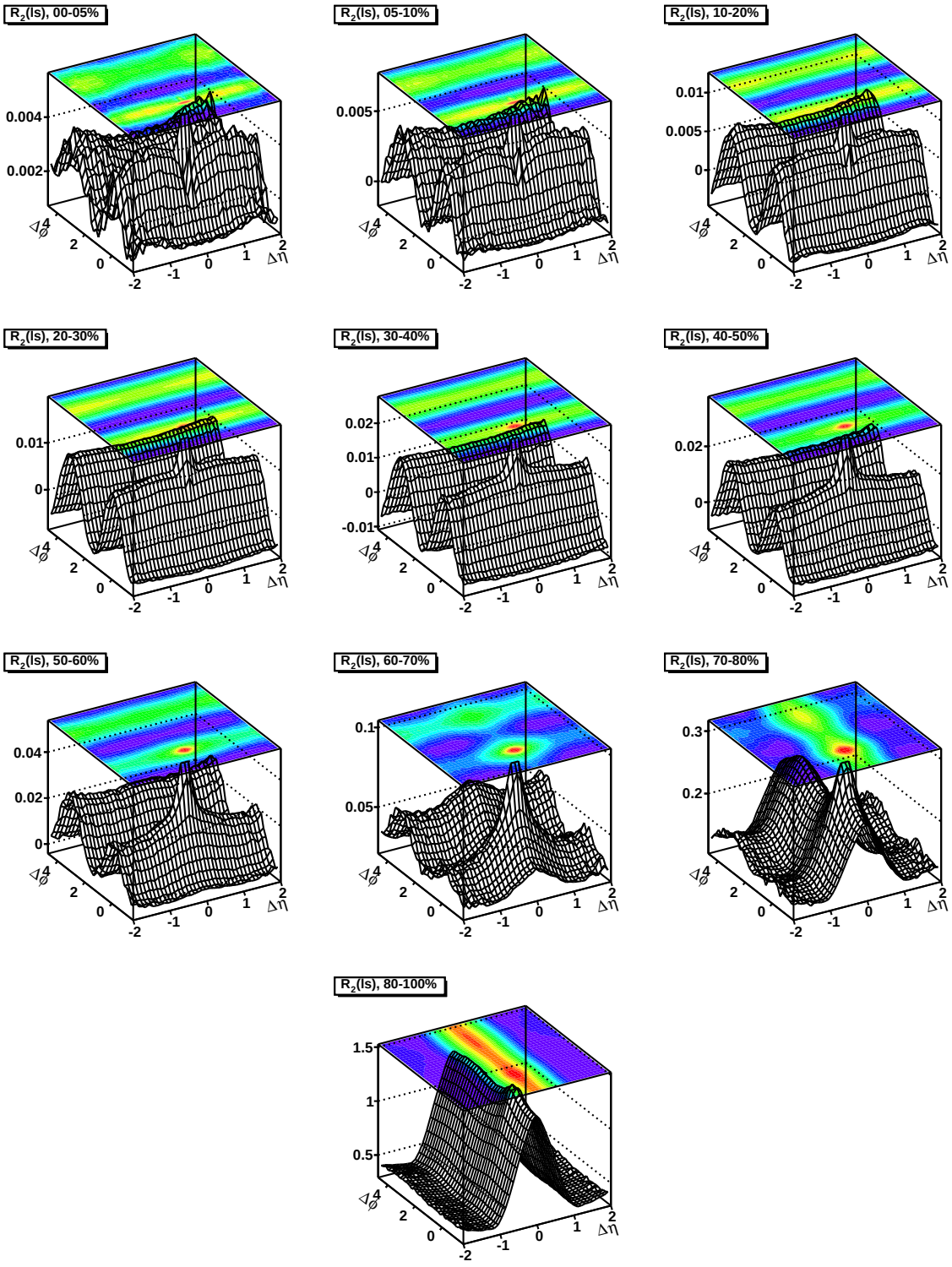

Figure 9.3: $R_2^{ls}(\Delta\eta, \Delta\phi)$

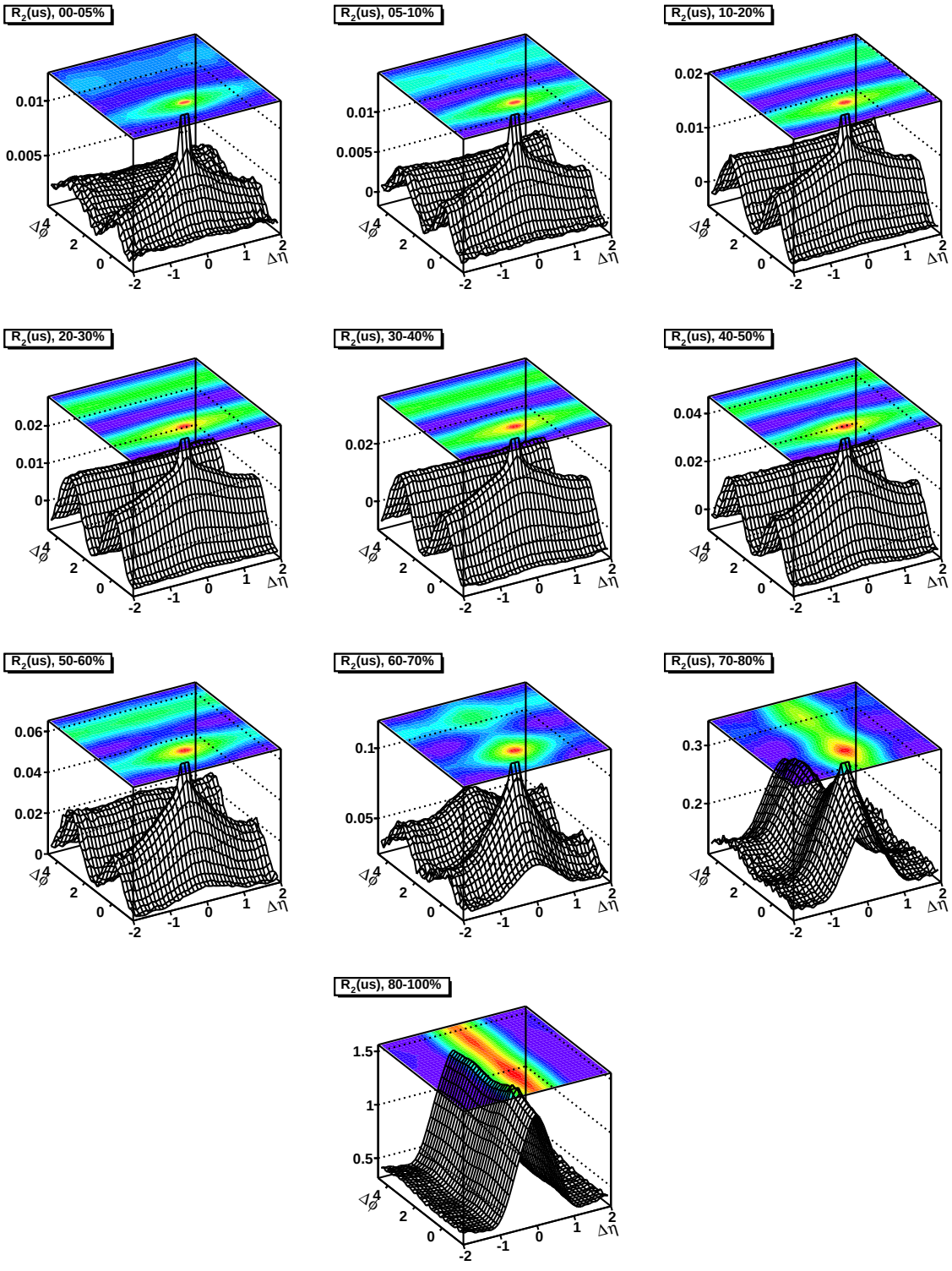

Figure 9.4: $R_2^{us}(\Delta\eta, \Delta\phi)$

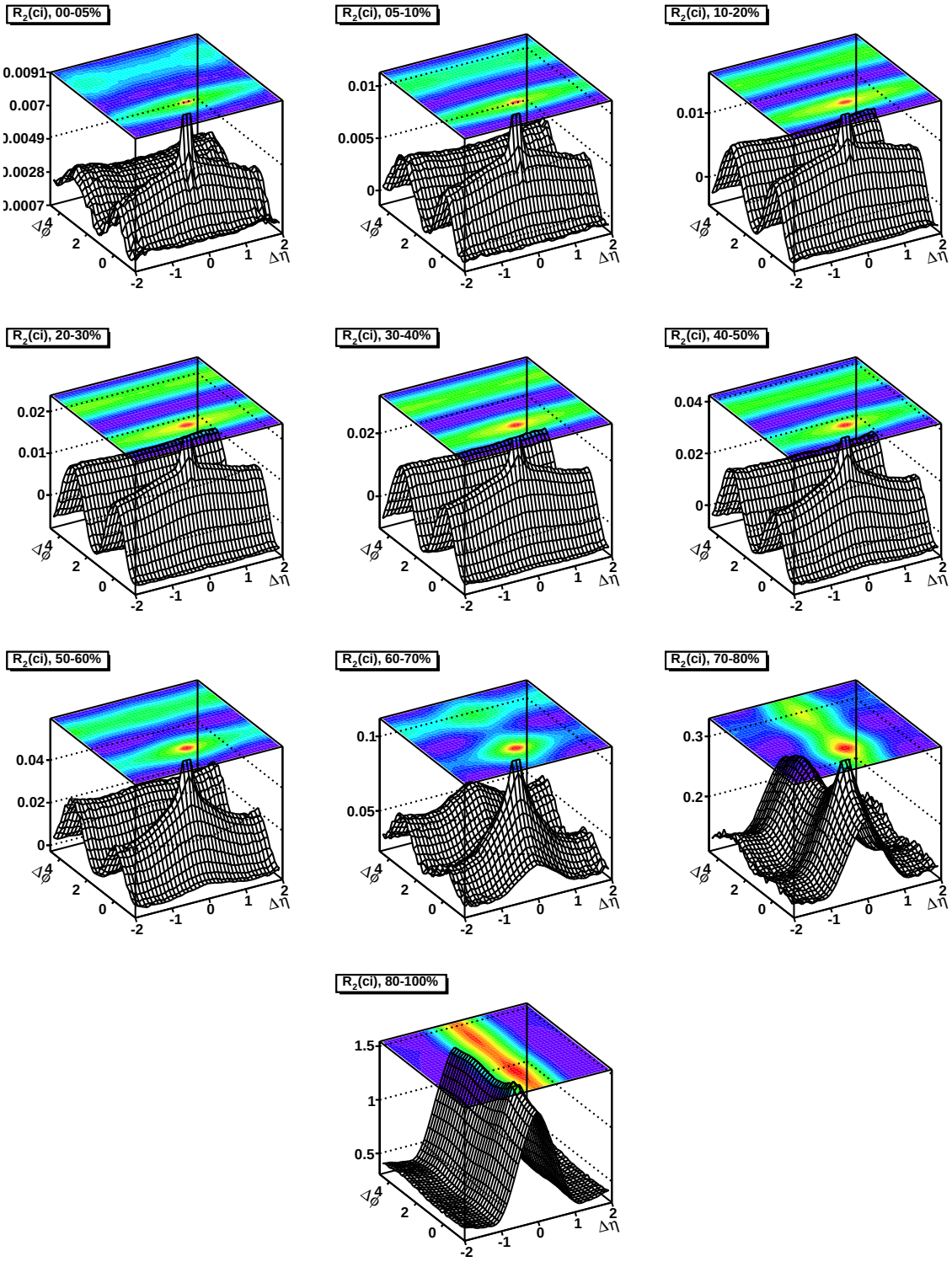

Figure 9.5: $R_2^{ci}(\Delta\eta, \Delta\phi)$

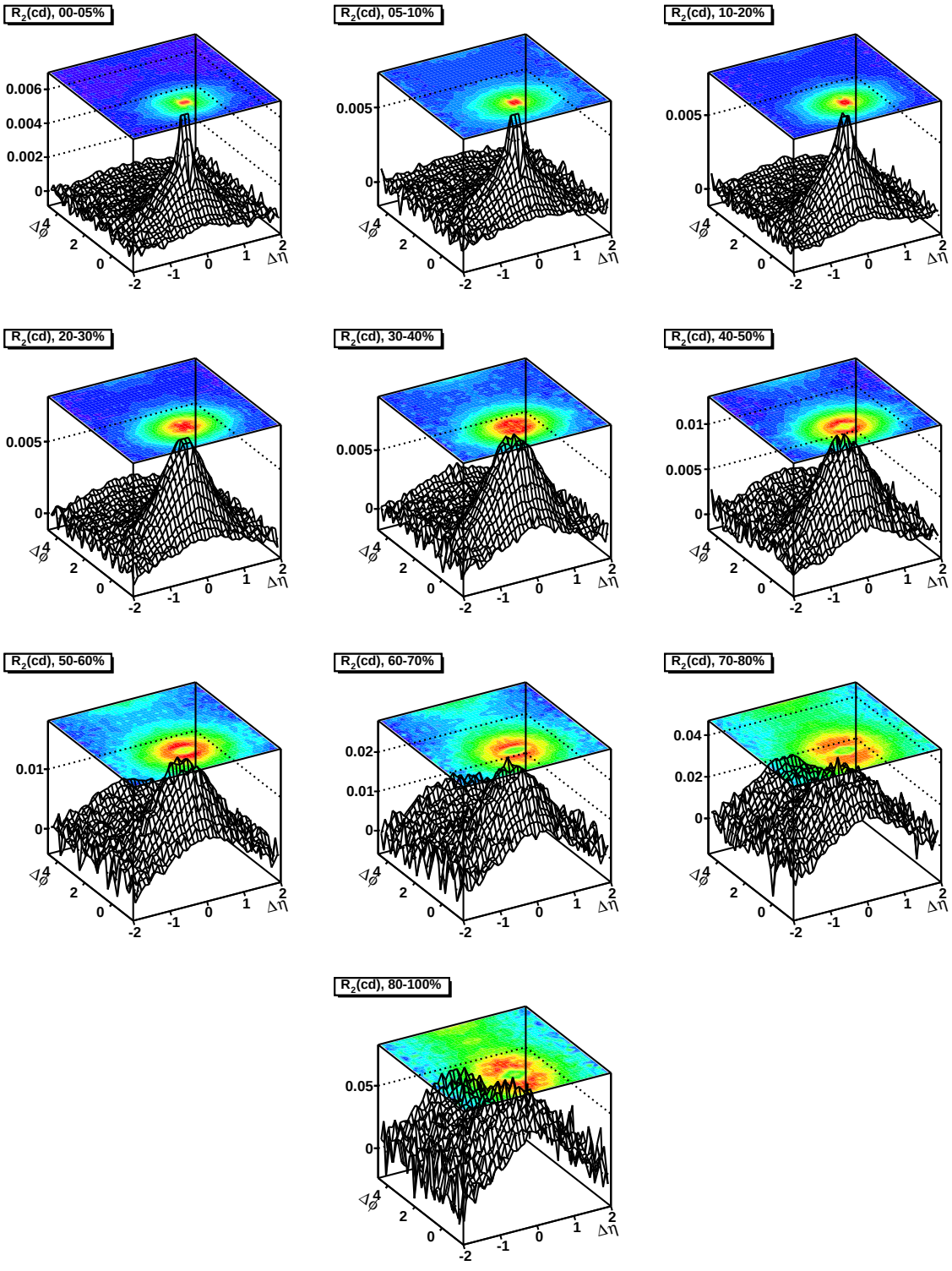

Figure 9.6: $R_2^{cd}(\Delta\eta, \Delta\phi)$

9.3 Appendix C. Comparison of bulk and triggered correlations for R_2, C, ΔP_T

Triggered correlations are obtained by subtracting the bulk correlation function for particles in the range $0.2 < p_{T1}, p_{T2} < 2.0$ GeV/c from the inclusive correlation function which has no upper p_T limit.

Some immediate observations:

- In R_2 and C the amplitude of the triggered correlations is an order of magnitude lower than for bulk, however in ΔP_T the amplitude of correlations is nearly equal.

- For all three observables, the charge-dependent *cd* plot has a narrower peak in triggered than bulk correlations, likely due to greater collimation at high p_T.

- With the exception of amplitude, C changes very little from bulk to triggered correlations.

- The unexpected narrow near-side peak noted in like-sign ΔP_T bulk correlations is not present in the triggered correlation, as a result the charge dependent *cd* plot for triggered correlations is no longer inverted at (0,0), and thus closely resembles the *cd* plots of R_2 and C.

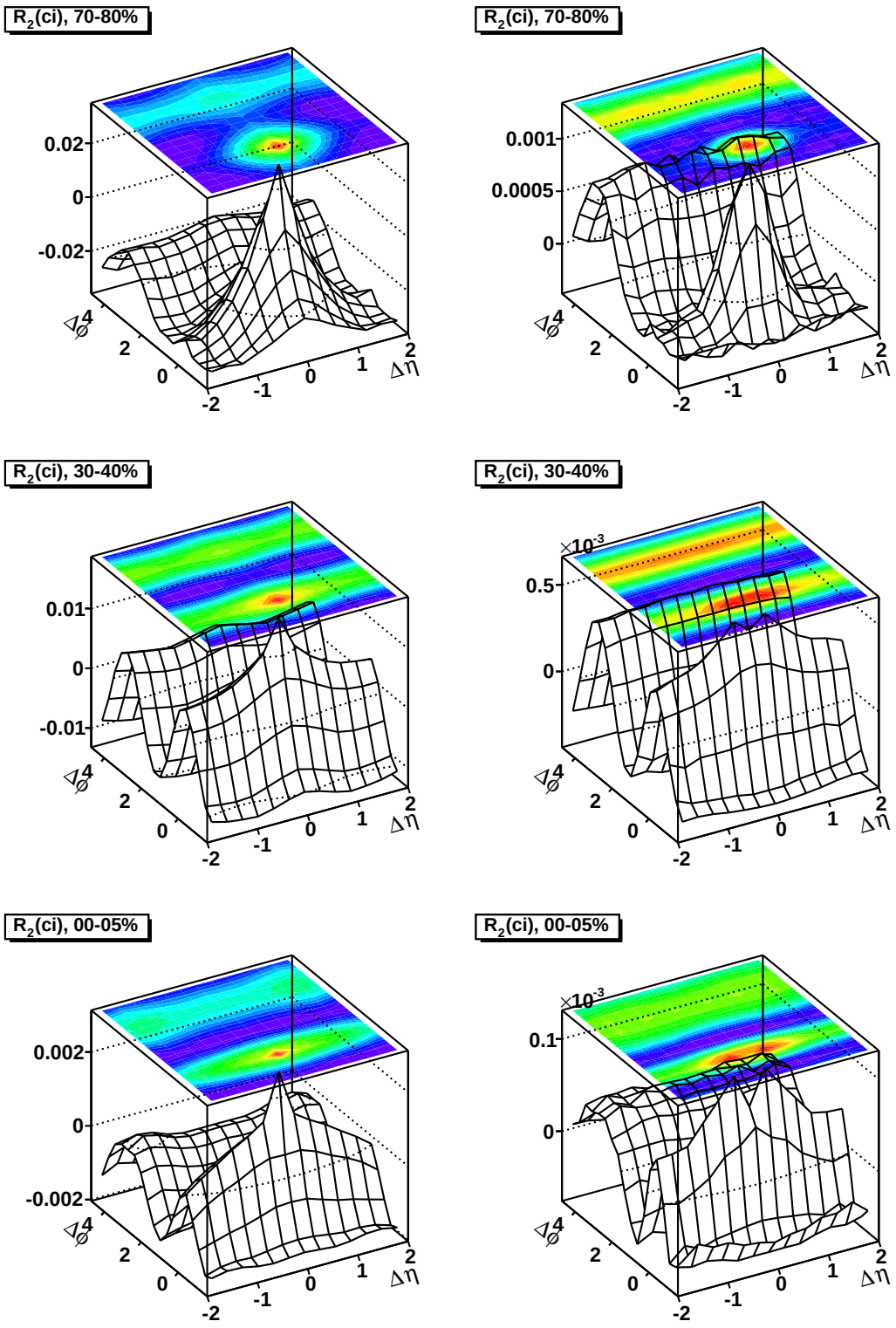

Figure 9.7: Bulk (*left*) and triggered (*right*) correlation functions $R_2^{ci}(\Delta\eta, \Delta\phi)$, for three representative collision centralities.

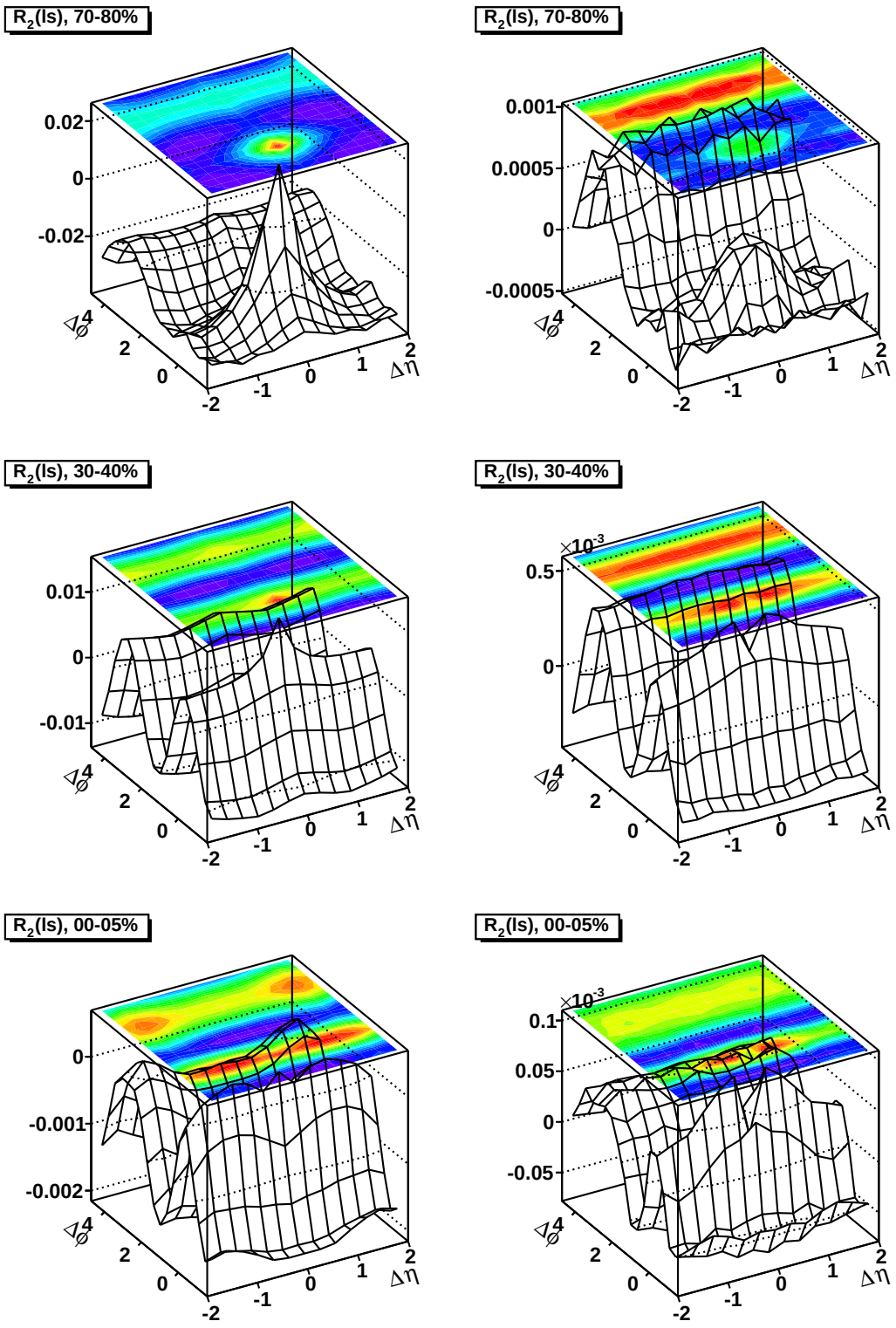

Figure 9.8: Bulk (*left*) and triggered (*right*) correlation functions $R_2^{ls}(\Delta\eta, \Delta\phi)$, for three representative collision centralities.

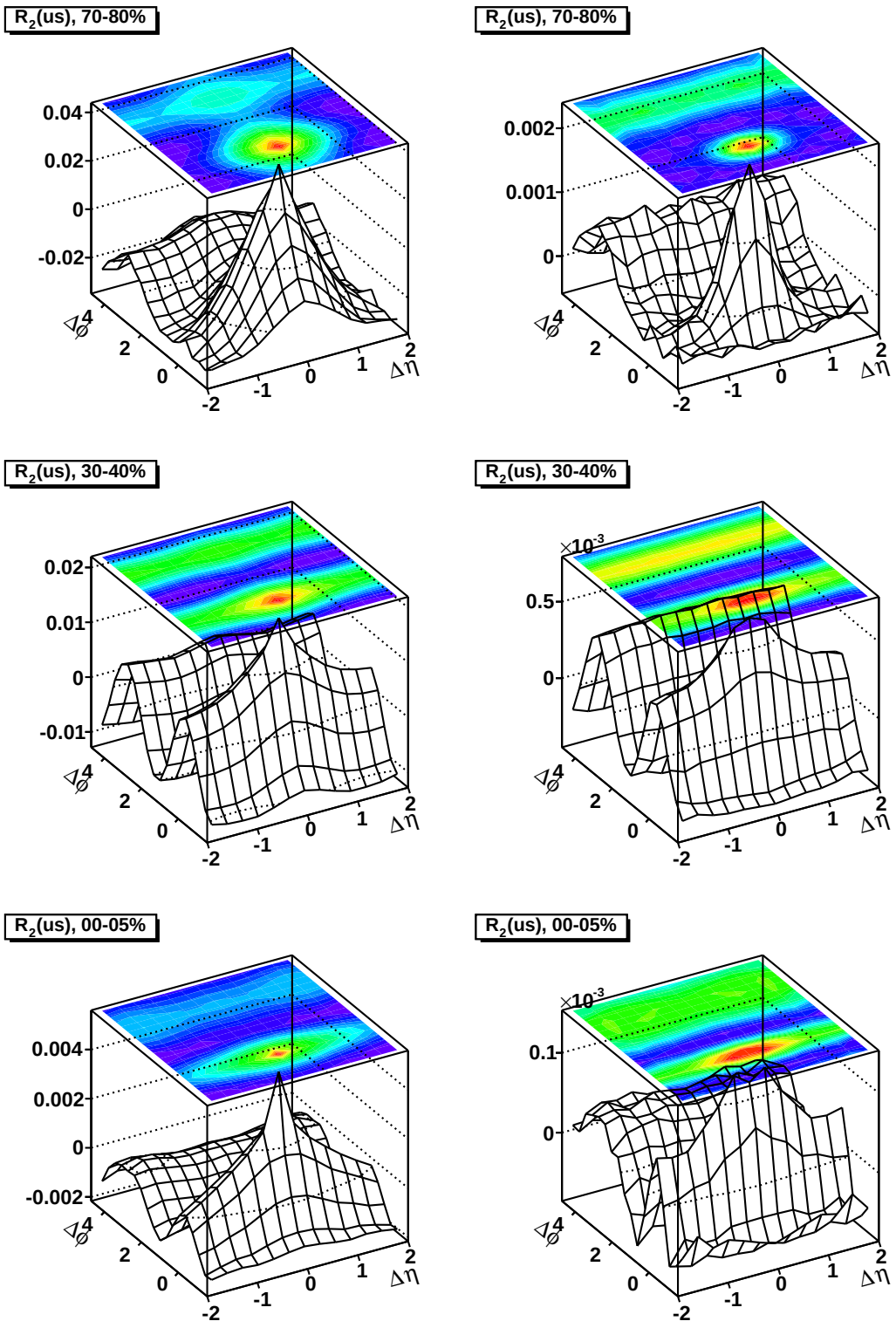

Figure 9.9: Bulk (*left*) and triggered (*right*) correlation functions $R_2^{us}(\Delta\eta, \Delta\phi)$, for three representative collision centralities.

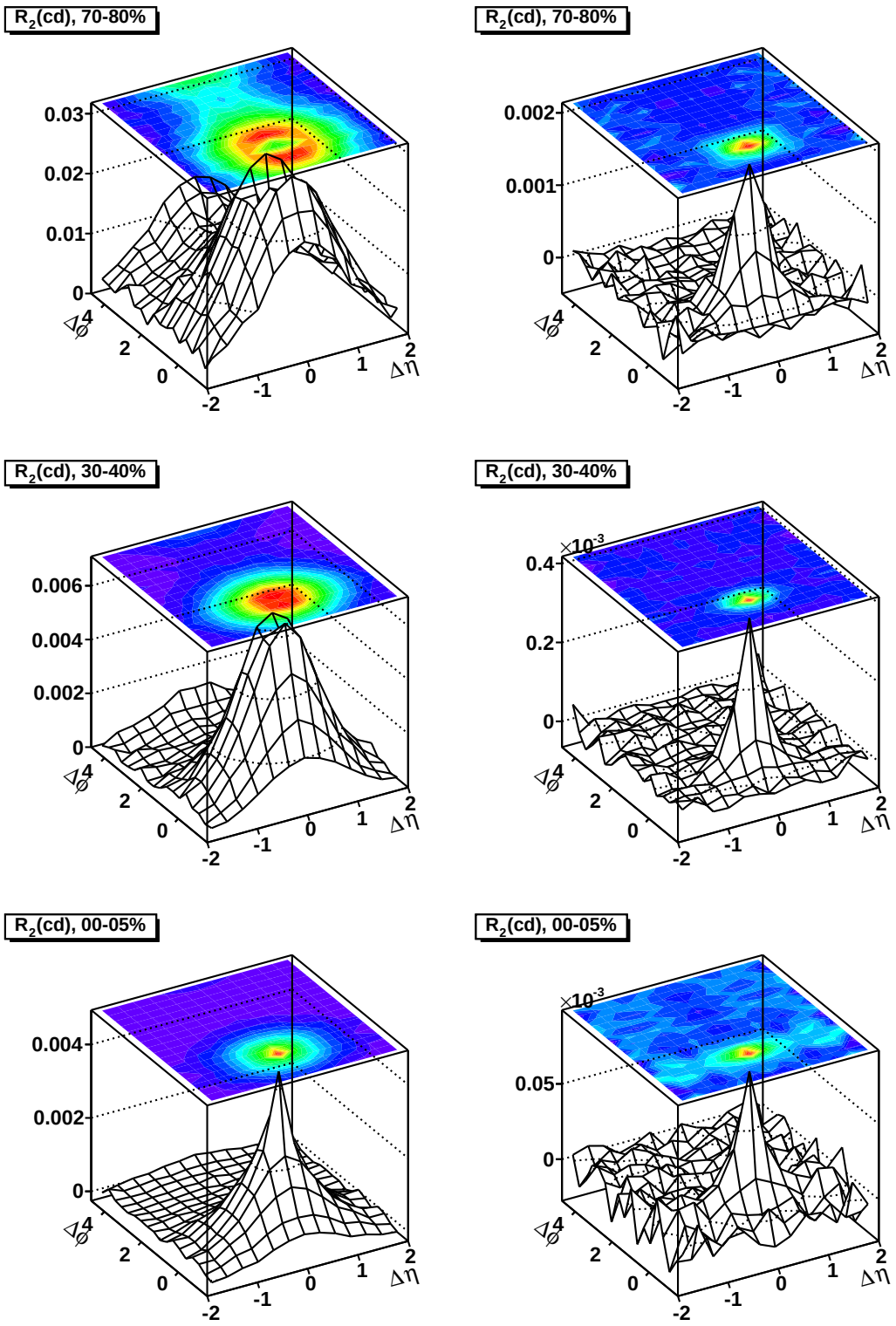

Figure 9.10: Bulk (*left*) and triggered (*right*) correlation functions $R_2^{cd}(\Delta\eta, \Delta\phi)$, for three representative collision centralities.

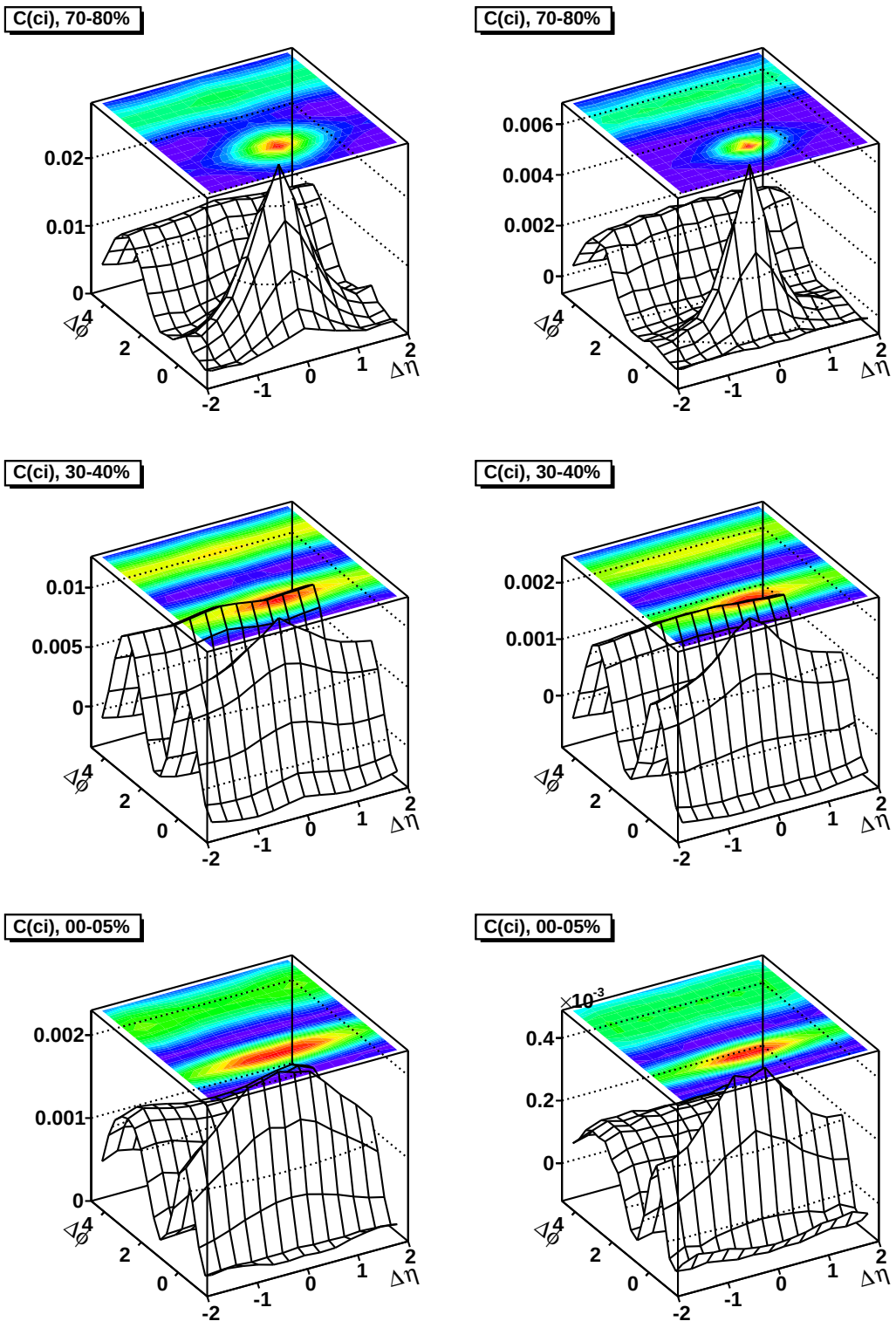

Figure 9.11: Bulk (*left*) and triggered (*right*) correlation functions $C^{ci}(\Delta\eta, \Delta\phi)$, for three representative collision centralities.

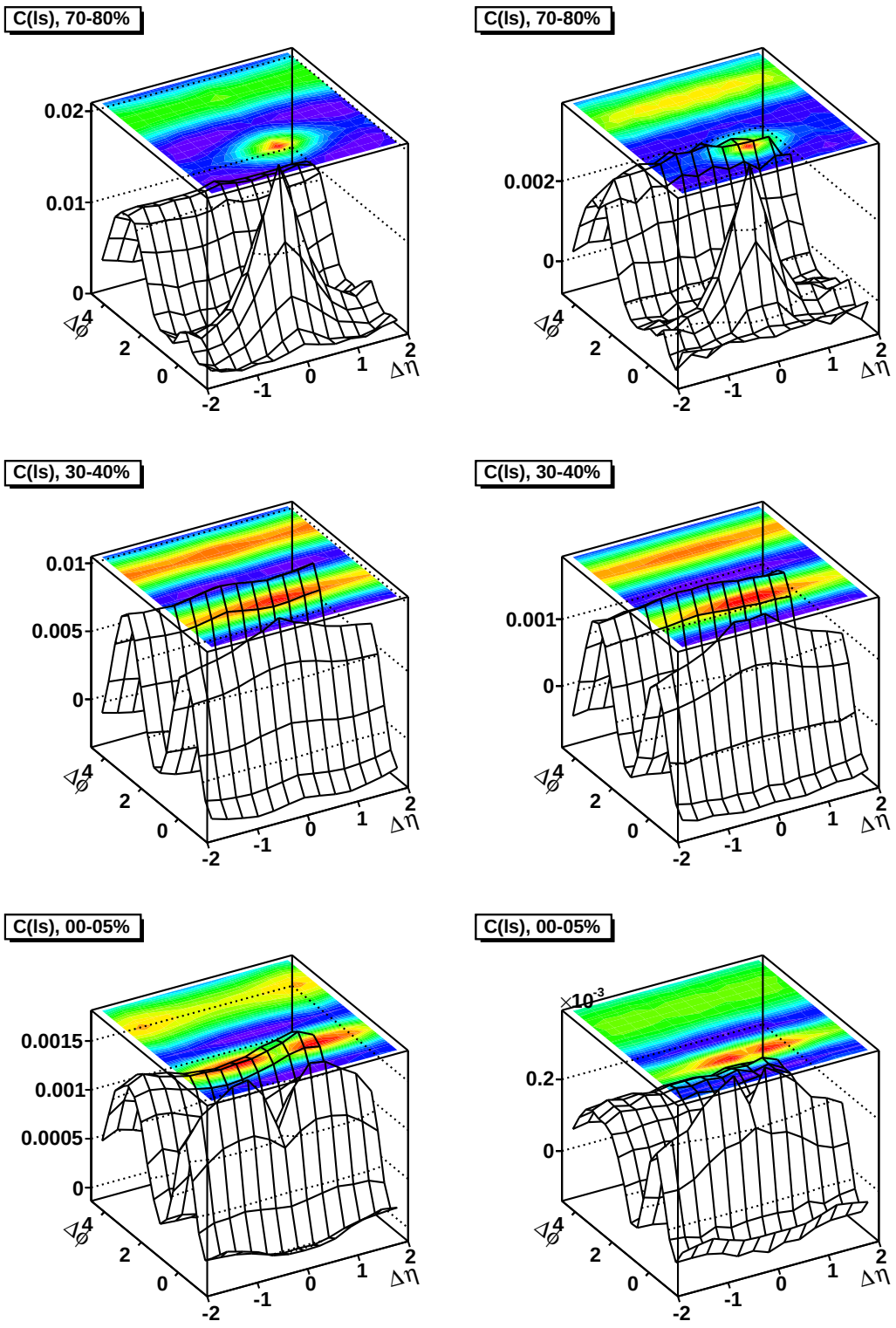

Figure 9.12: Bulk (*left*) and triggered (*right*) correlation functions $C^{ls}(\Delta\eta, \Delta\phi)$, for three representative collision centralities.

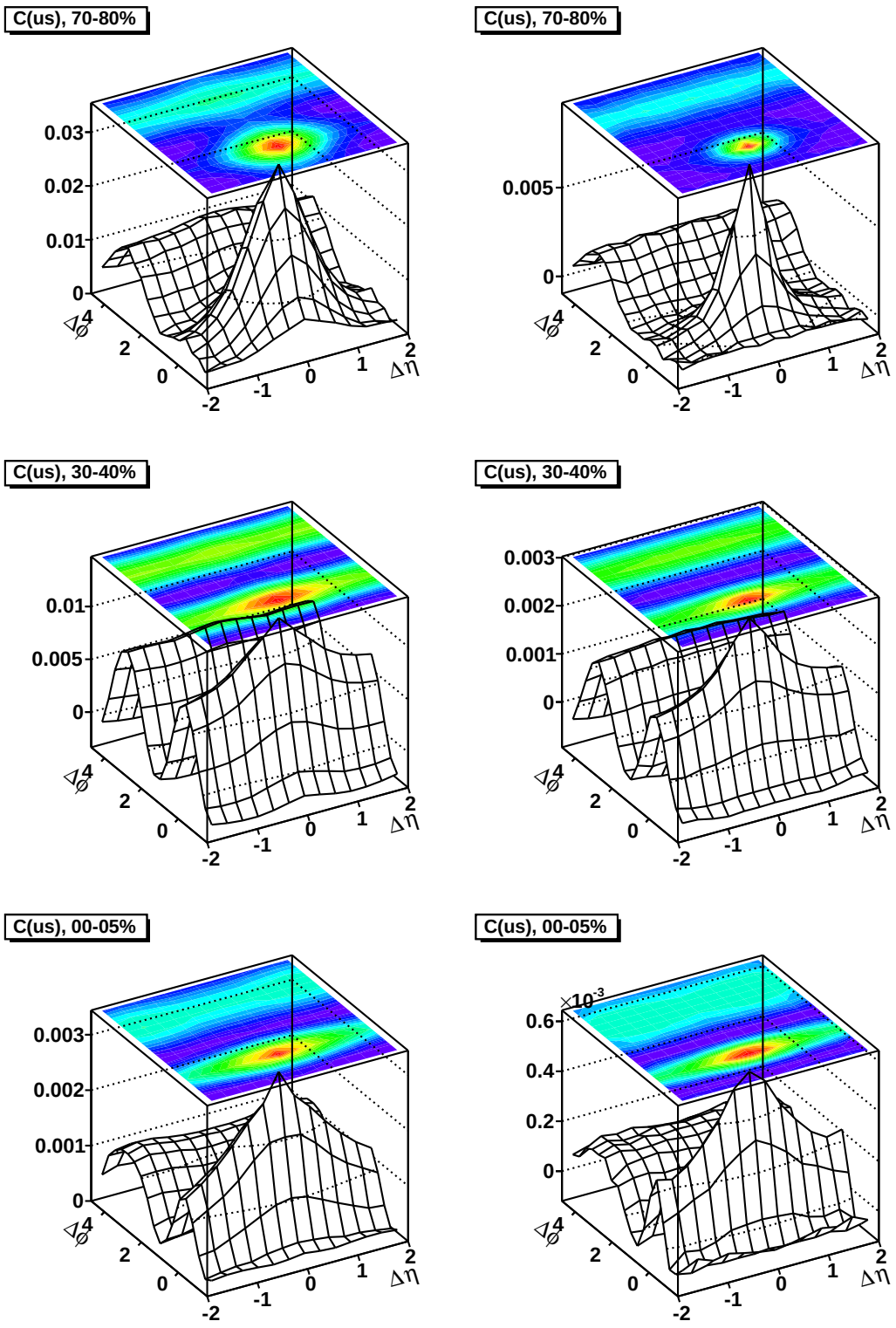

Figure 9.13: Bulk (*left*) and triggered (*right*) correlation functions $C^{us}(\Delta\eta, \Delta\phi)$, for three representative collision centralities.

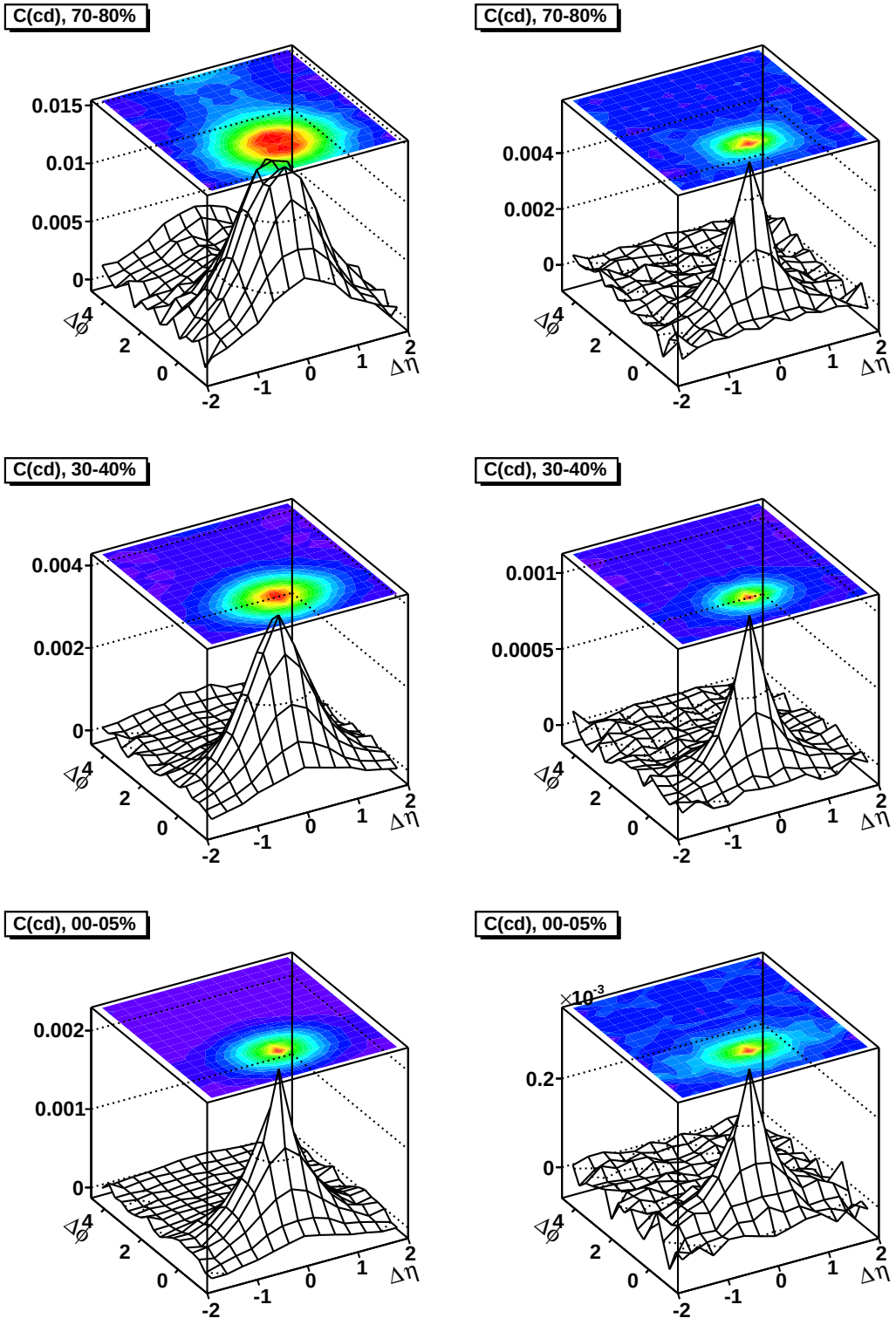

Figure 9.14: Bulk (*left*) and triggered (*right*) correlation functions $C^{cd}(\Delta\eta, \Delta\phi)$, for three representative collision centralities.

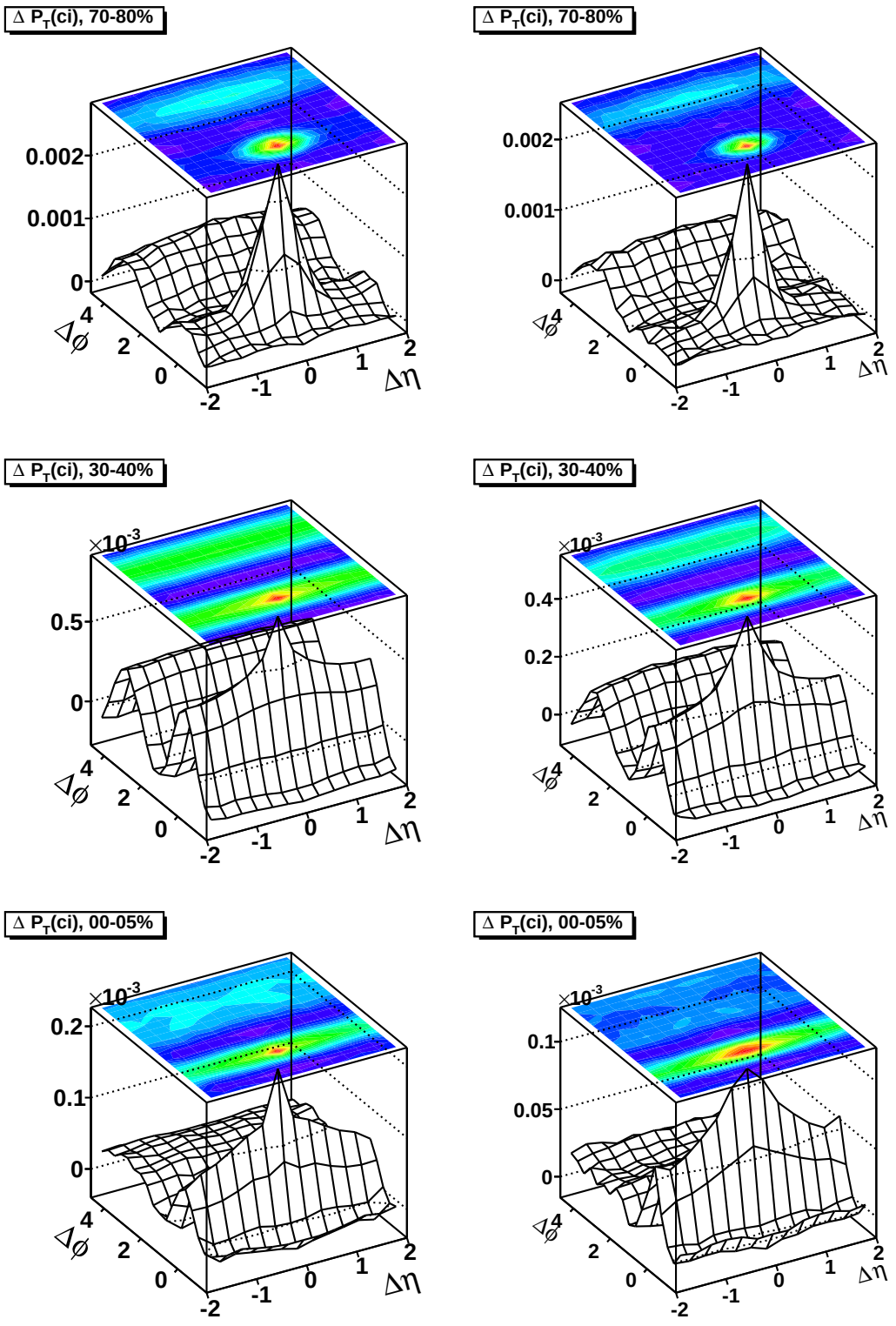

Figure 9.15: Bulk (*left*) and triggered (*right*) correlation functions $\Delta {P_T}^{ci}(\Delta\eta, \Delta\phi)$, for three representative collision centralities.

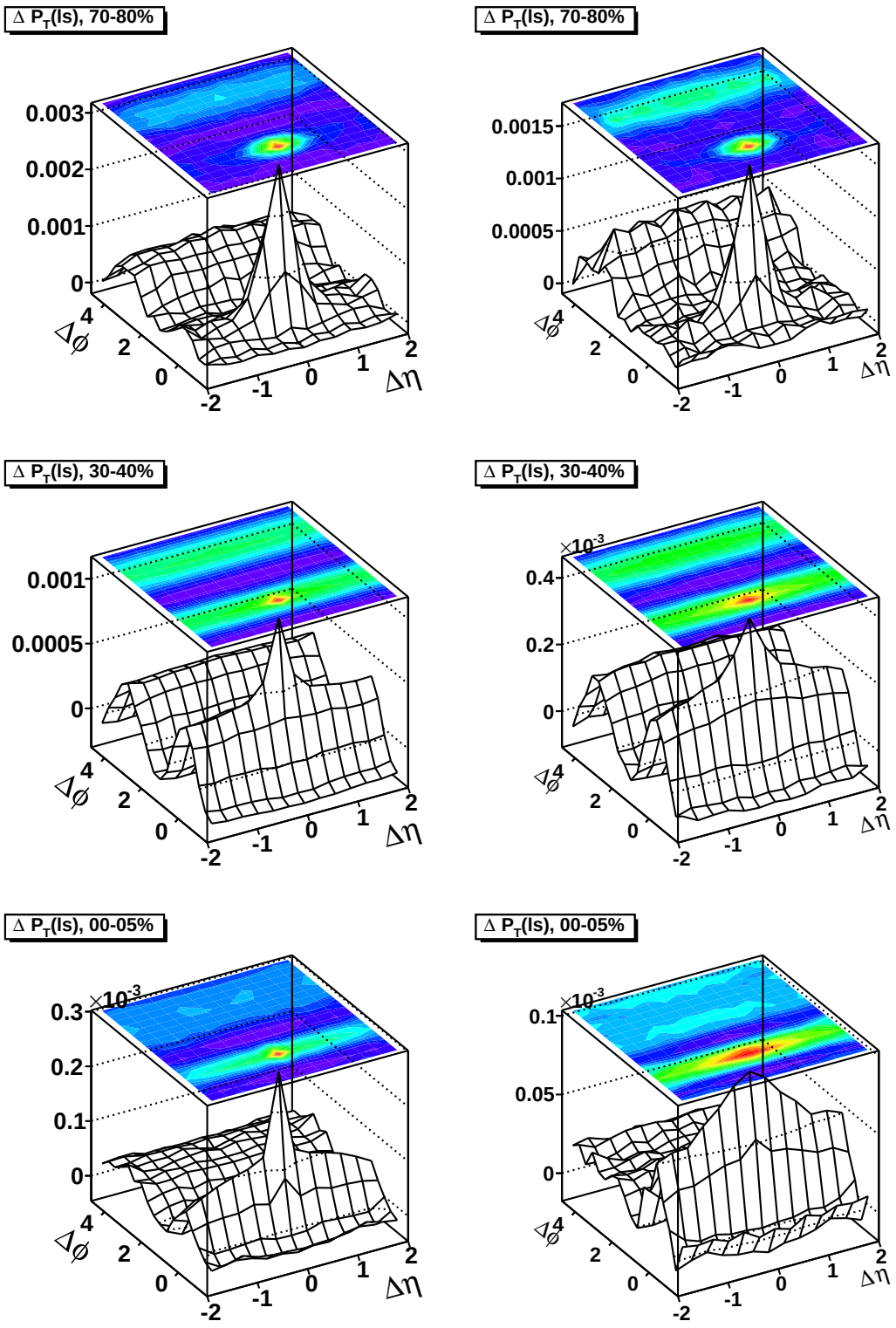

Figure 9.16: Bulk (*left*) and triggered (*right*) correlation functions $\Delta {P_T}^{ls}(\Delta\eta, \Delta\phi)$, for three representative collision centralities.

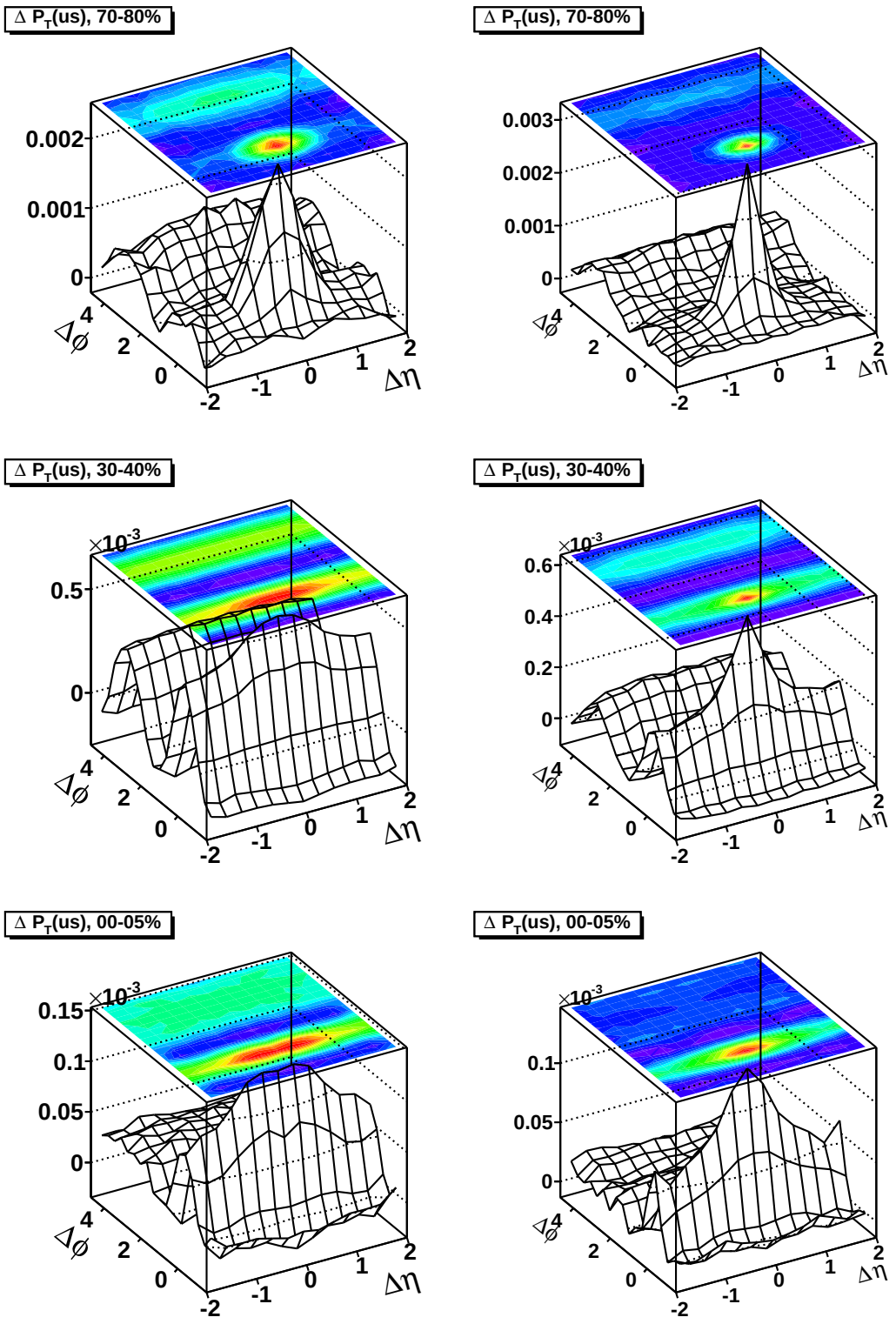

Figure 9.17: Bulk (*left*) and triggered (*right*) correlation functions $\Delta {P_T}^{us}(\Delta\eta, \Delta\phi)$, for three representative collision centralities.

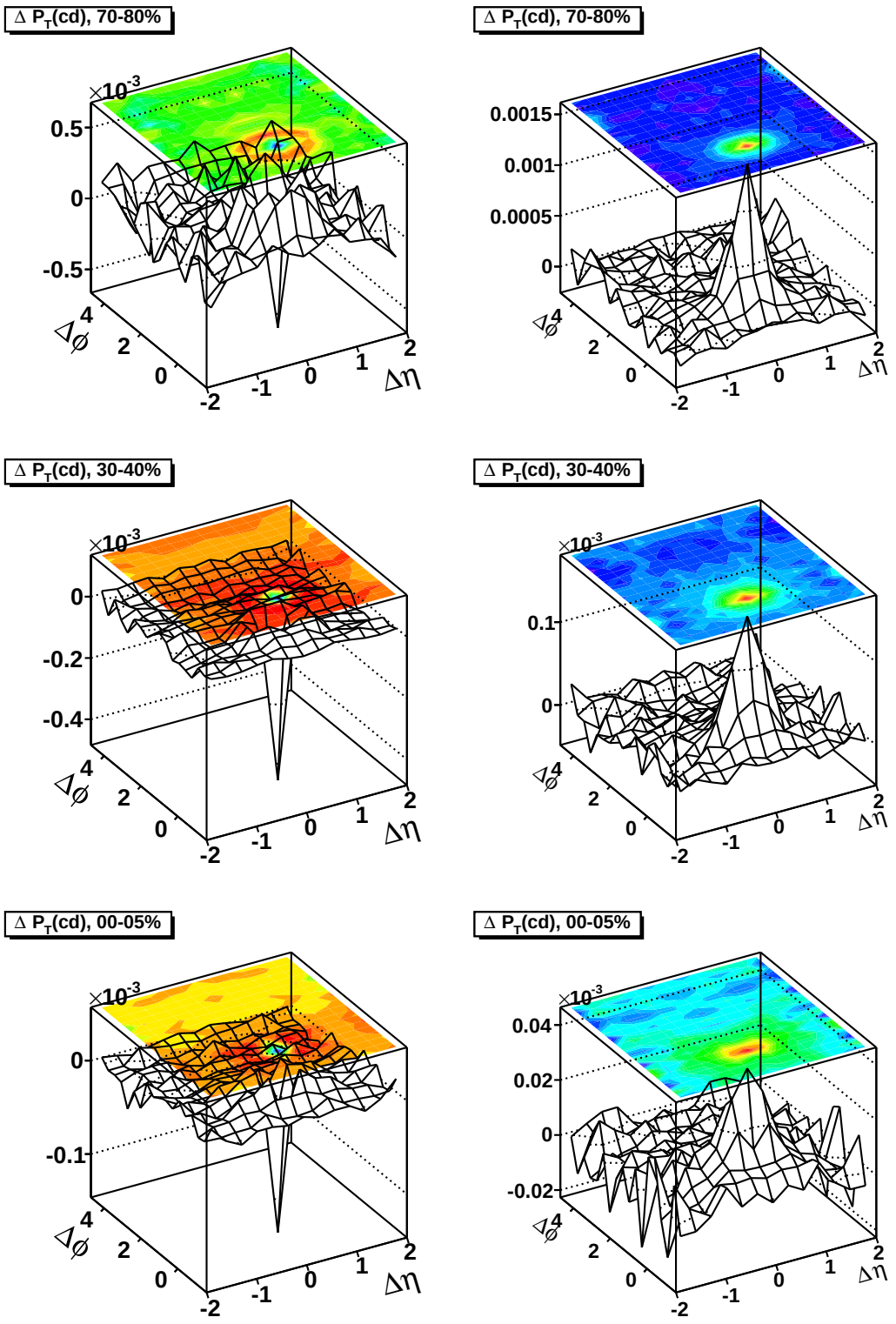

Figure 9.18: Bulk (*left*) and triggered (*right*) correlation functions $\Delta {P_T}^{cd}(\Delta\eta, \Delta\phi)$, for three representative collision centralities.

Chapter 10

Catalog of Distributions, Convolutions and Plots for Au+Au $\sqrt{s_{NN}} = 200$ GeV

10.1 Bulk Correlations, Full Field ++

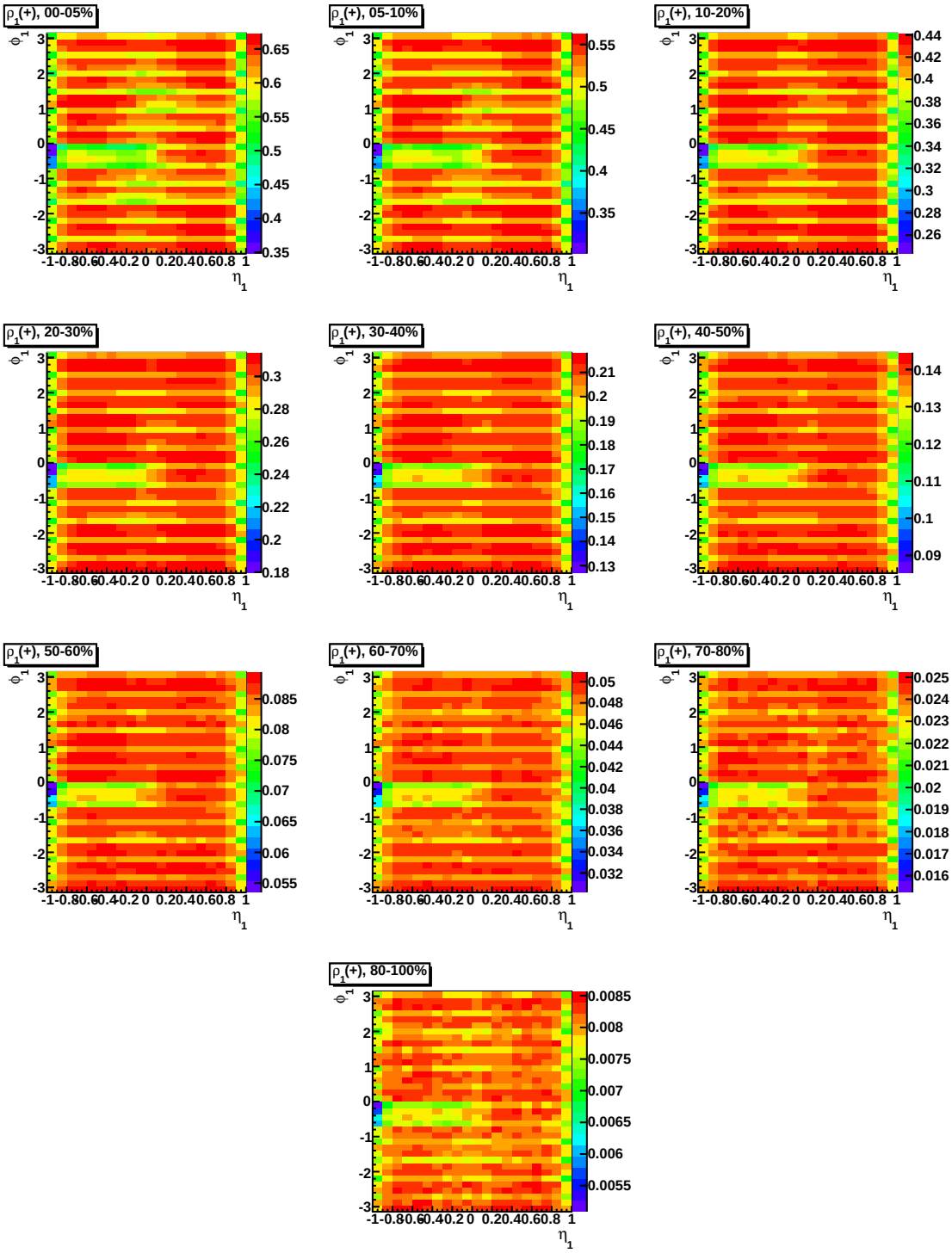

Figure 10.1: $\rho_1^+(\eta, \phi)$

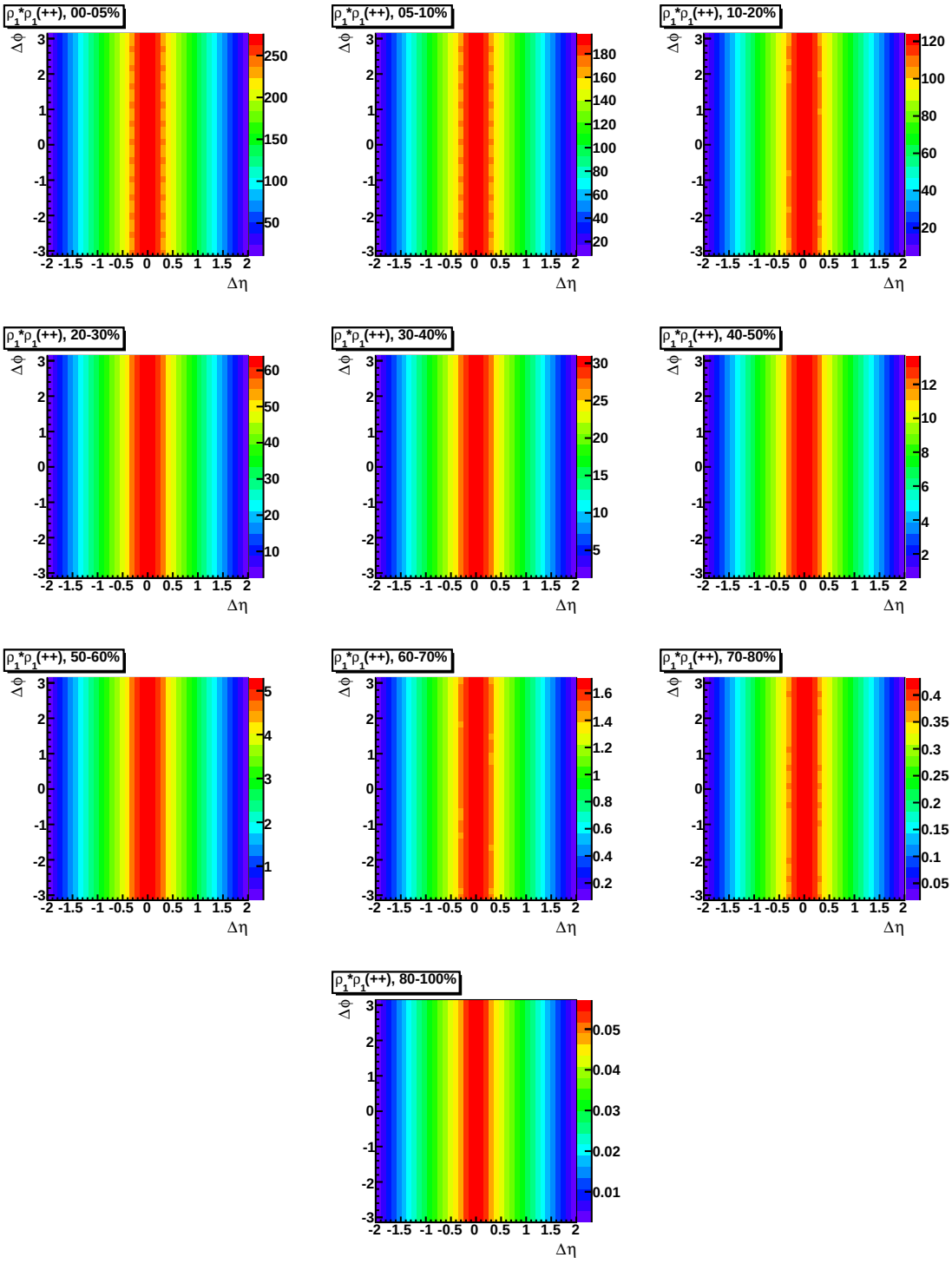

Figure 10.2: $\rho_1^+ * \rho_1^+(\Delta\eta, \Delta\phi)$

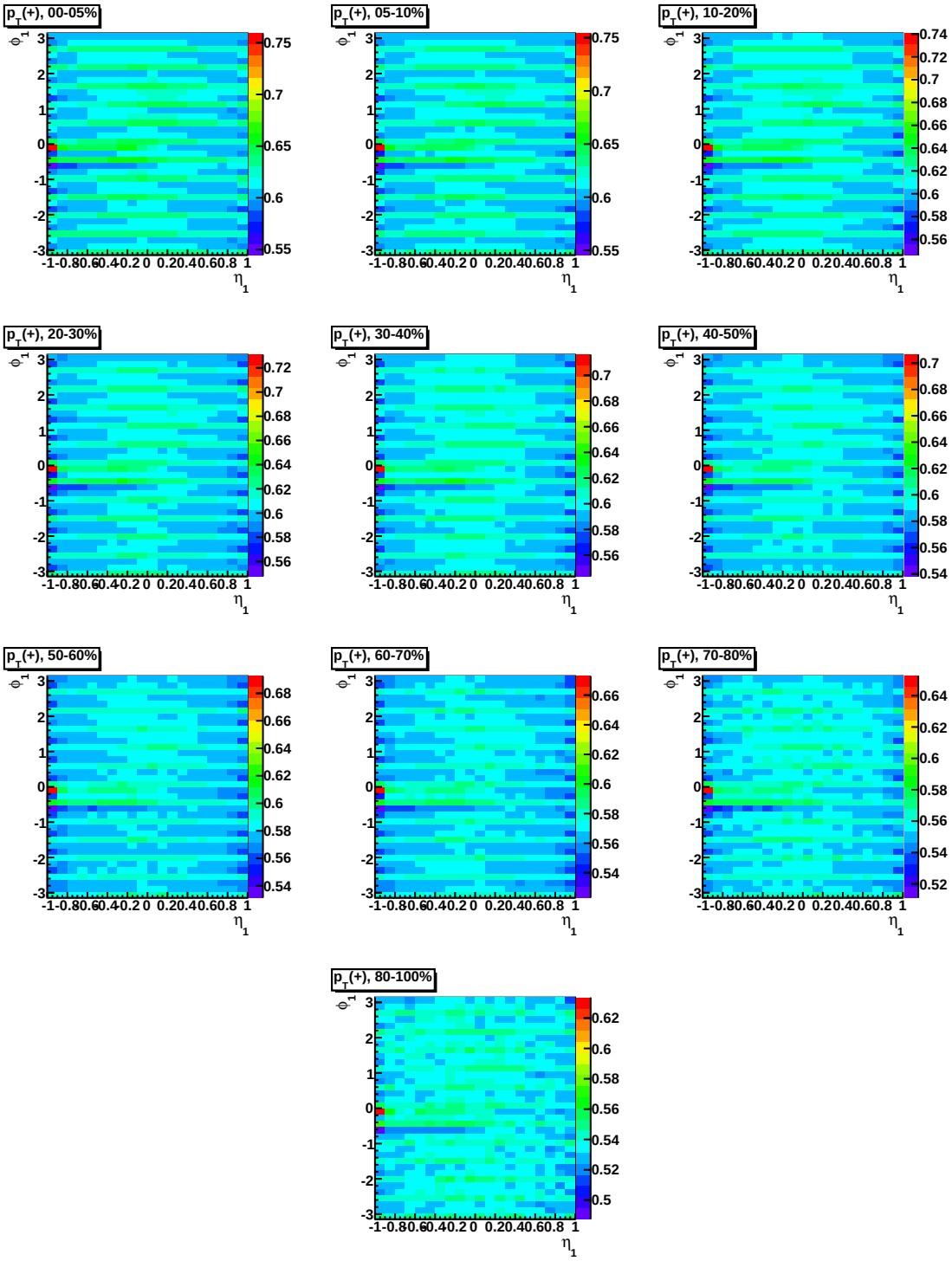

Figure 10.3: $\overline{p}_T^+(\eta, \phi)$

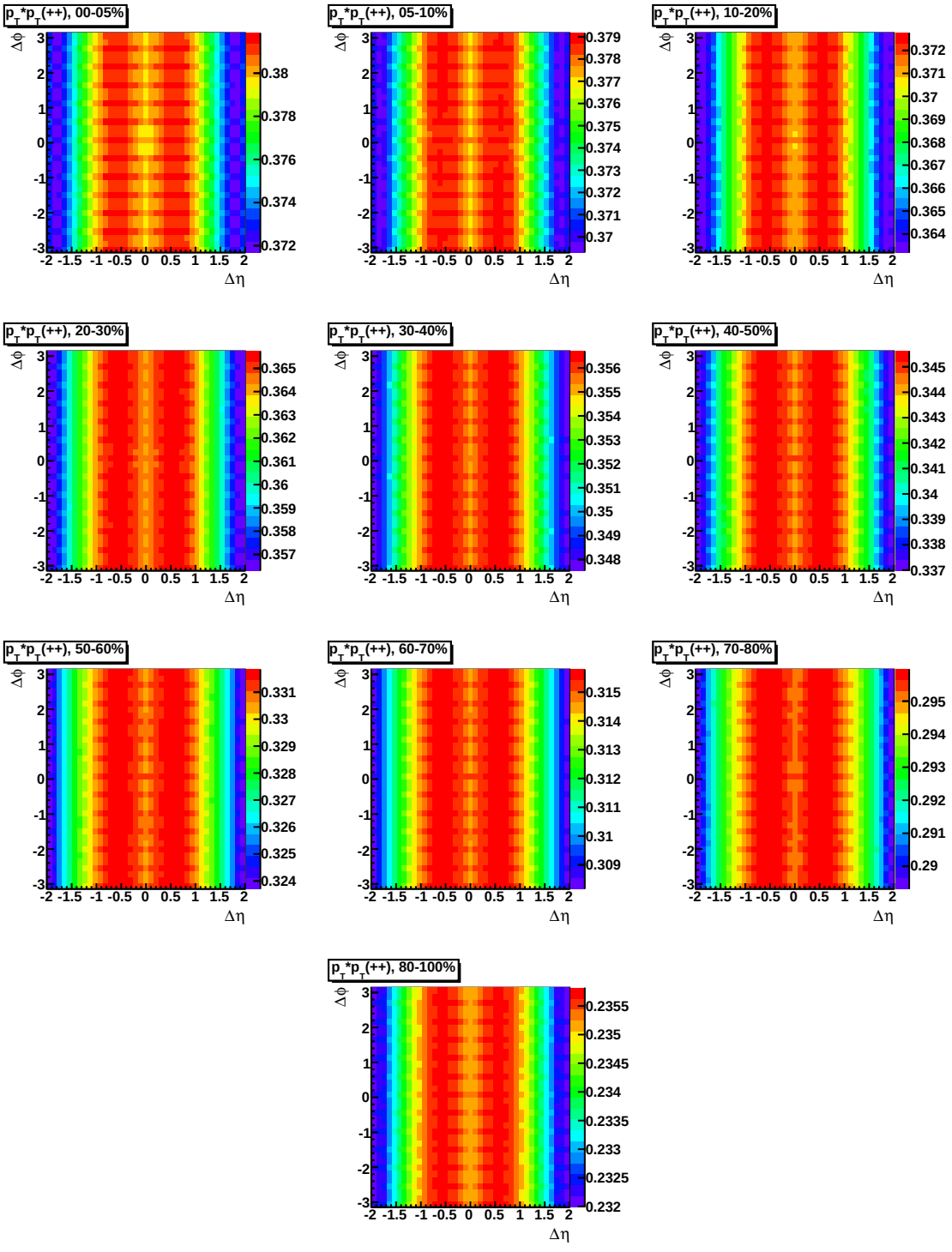

Figure 10.4: $\overline{p}_T^+ * \overline{p}_T^+(\Delta\eta, \Delta\phi)$

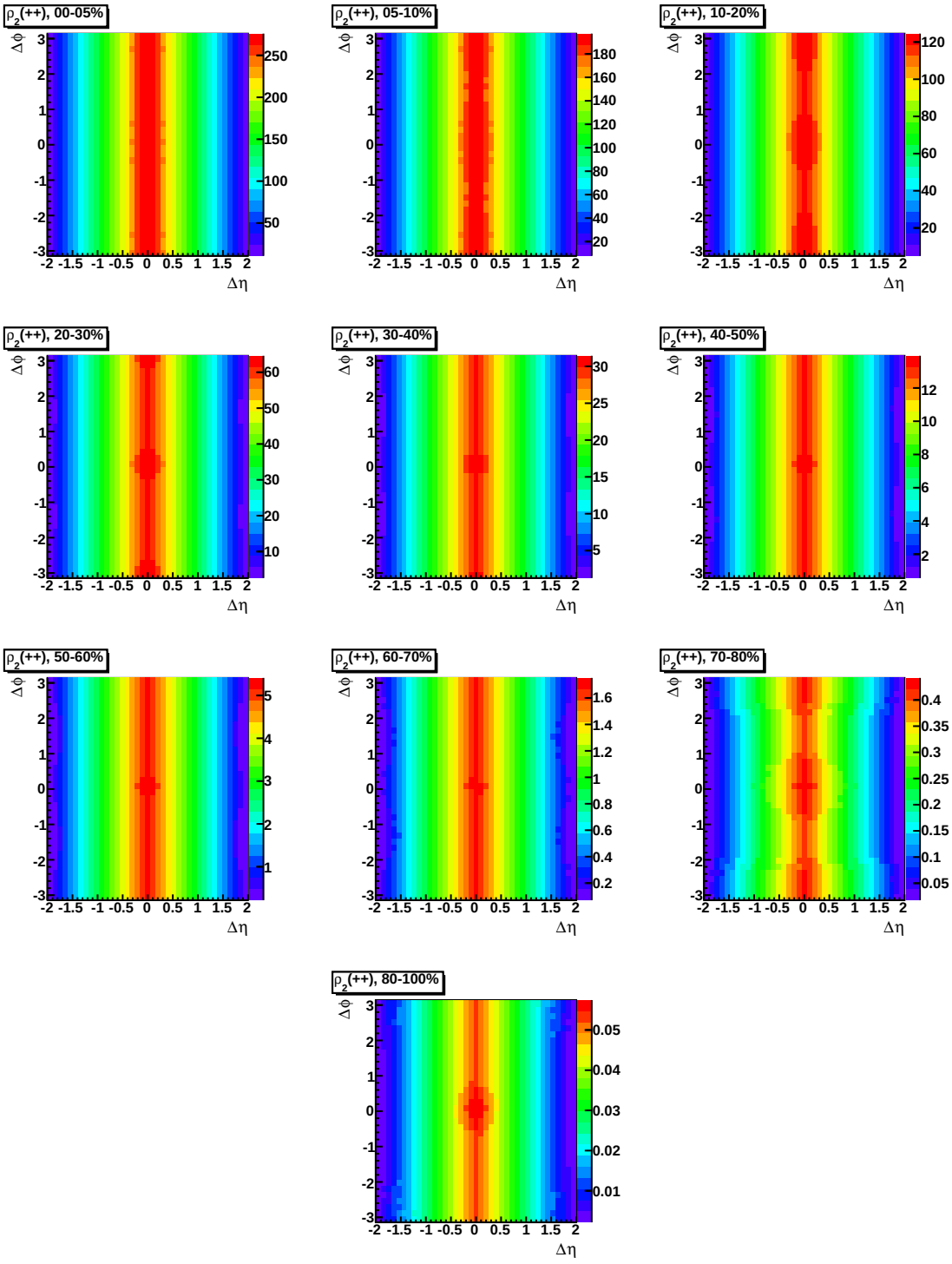

Figure 10.5: $\rho_2^{++}(\Delta\eta, \Delta\phi)$

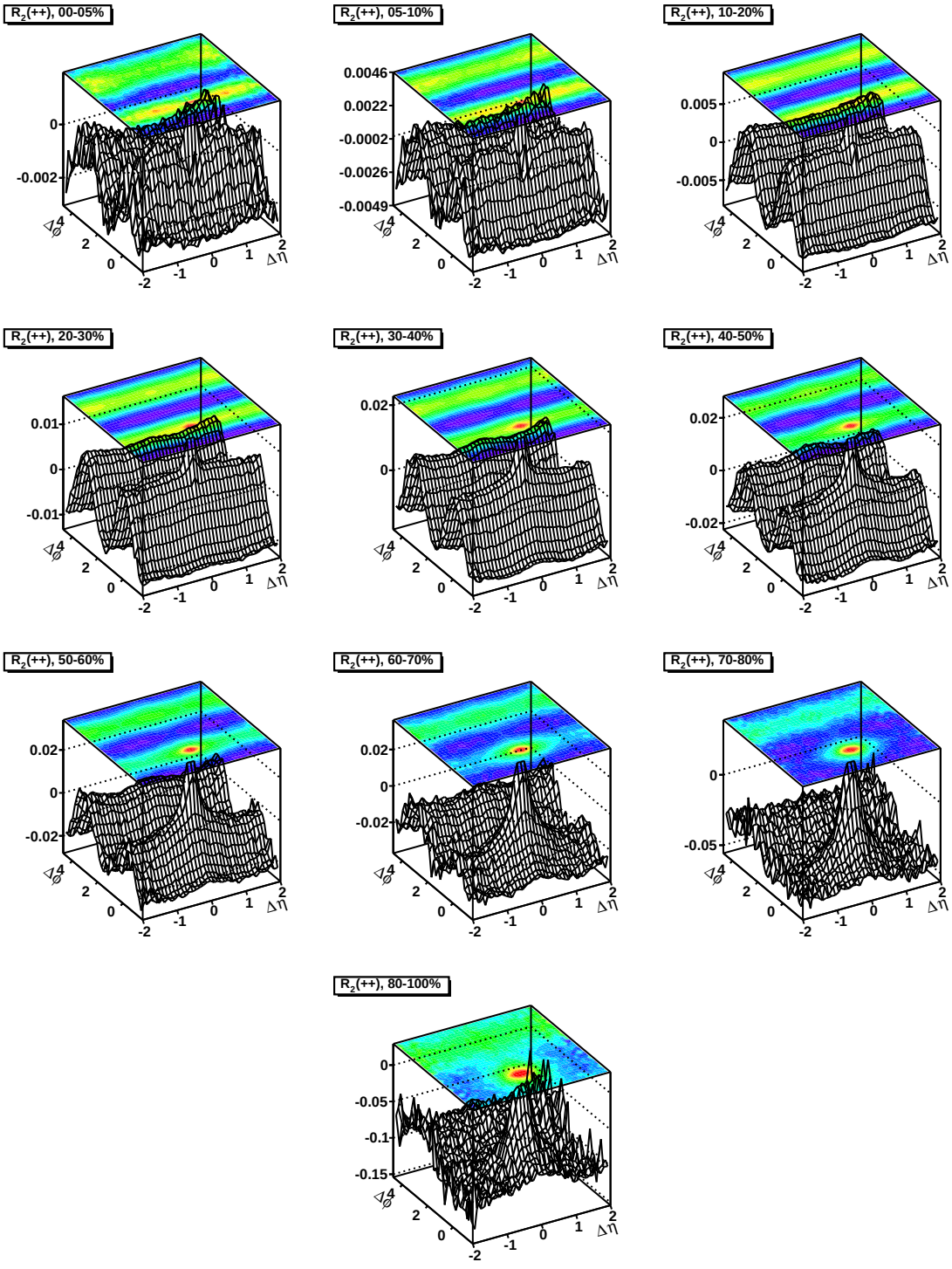

Figure 10.6: $R_2^{++}(\Delta\eta, \Delta\phi) = \rho_2^{++}(\Delta\eta, \Delta\phi)/\rho_1^{+} * \rho_1^{+}(\Delta\eta, \Delta\phi) - 1$

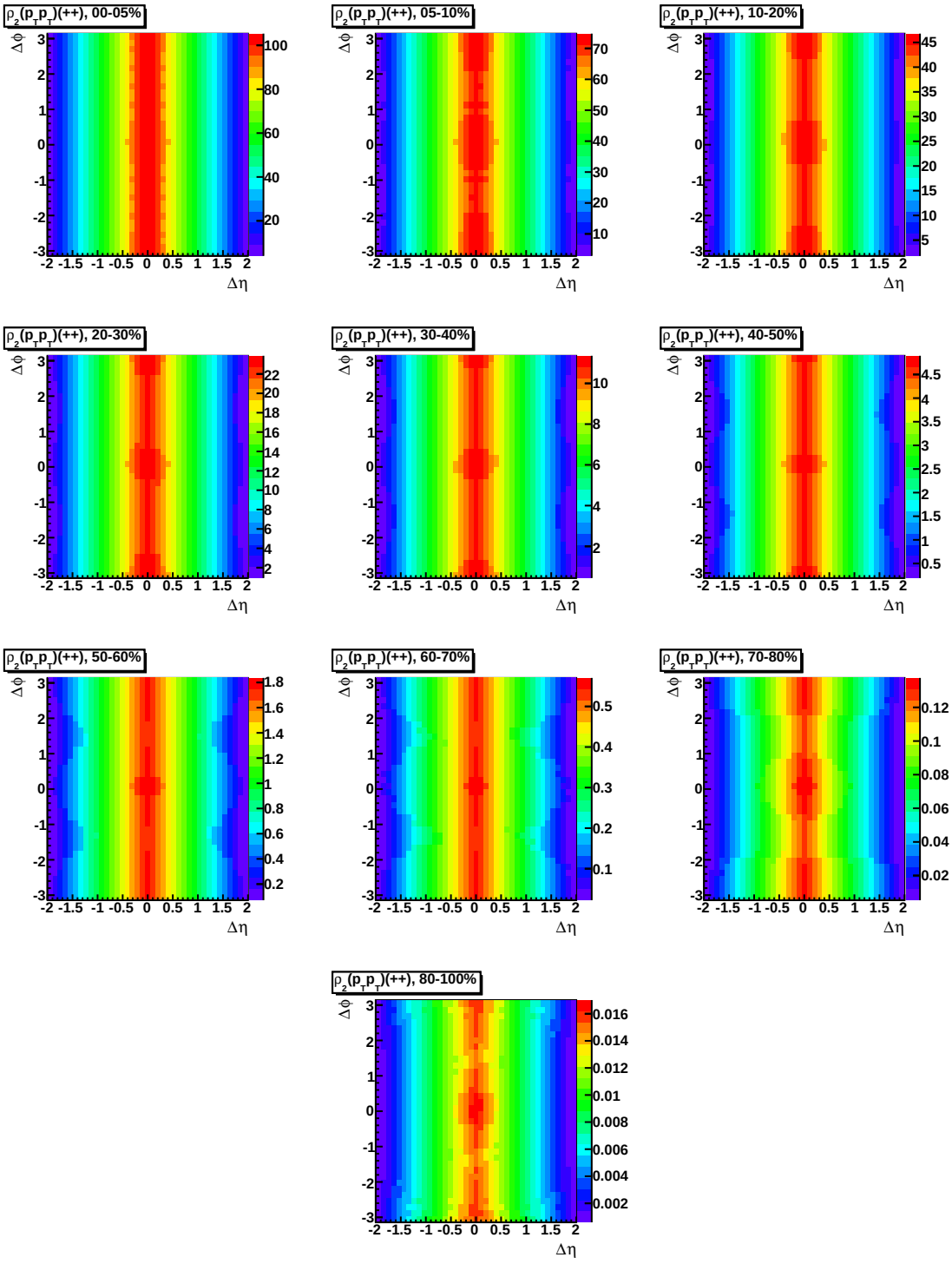

Figure 10.7: $\rho_2^{p_T^+ p_T^+}(\Delta\eta, \Delta\phi)$

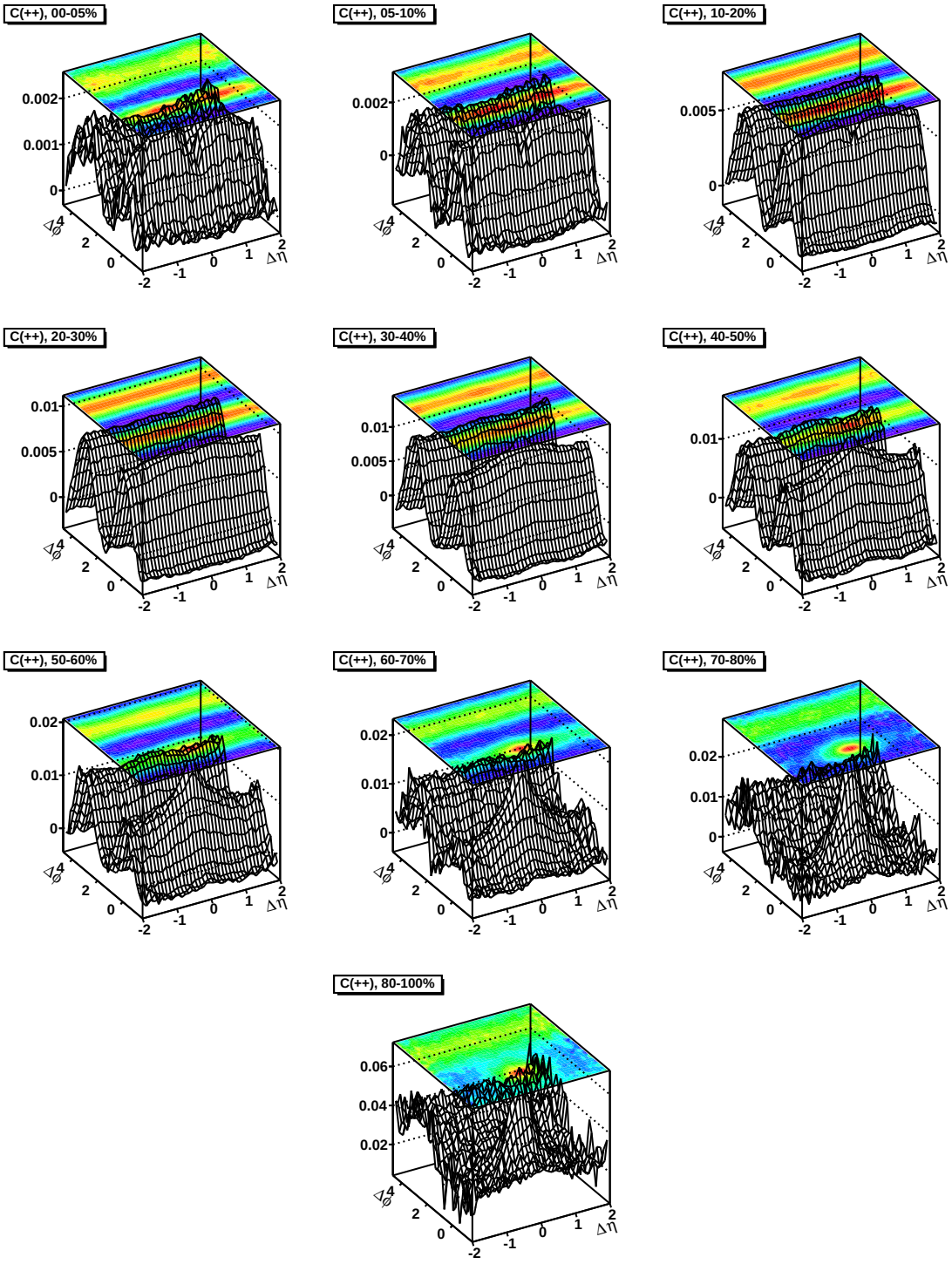

Figure 10.8: $C^{++}(\Delta\eta, \Delta\phi) = \rho_2^{p_T^+ p_T^+}(\Delta\eta, \Delta\phi)/\rho_1^+ * \rho_1^+(\Delta\eta, \Delta\phi) - \overline{p}_T^+ * \overline{p}_T^+(\Delta\eta, \Delta\phi)$

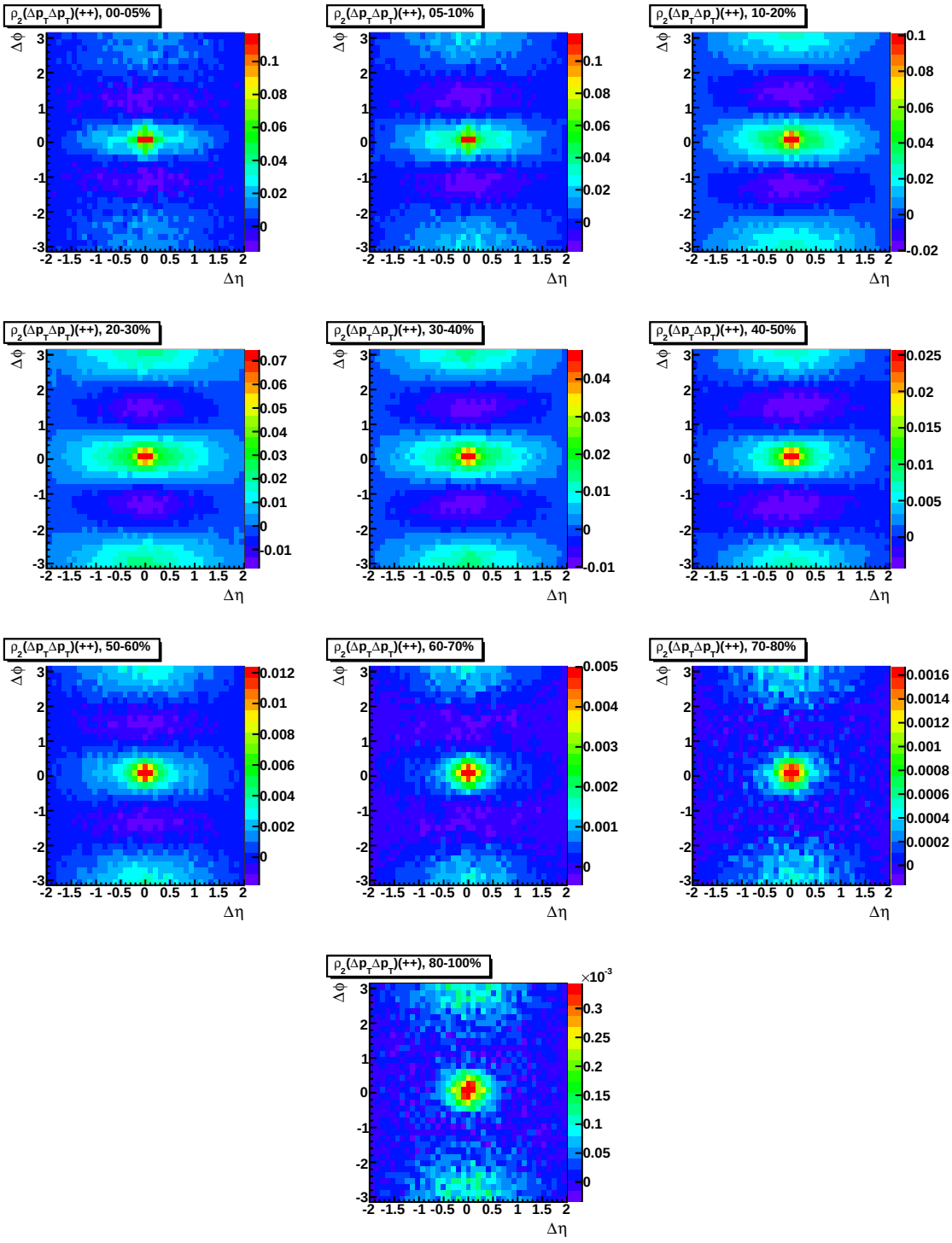

Figure 10.9: $\rho_2^{\Delta p_T^+ \Delta p_T^+}(\Delta\eta, \Delta\phi)$

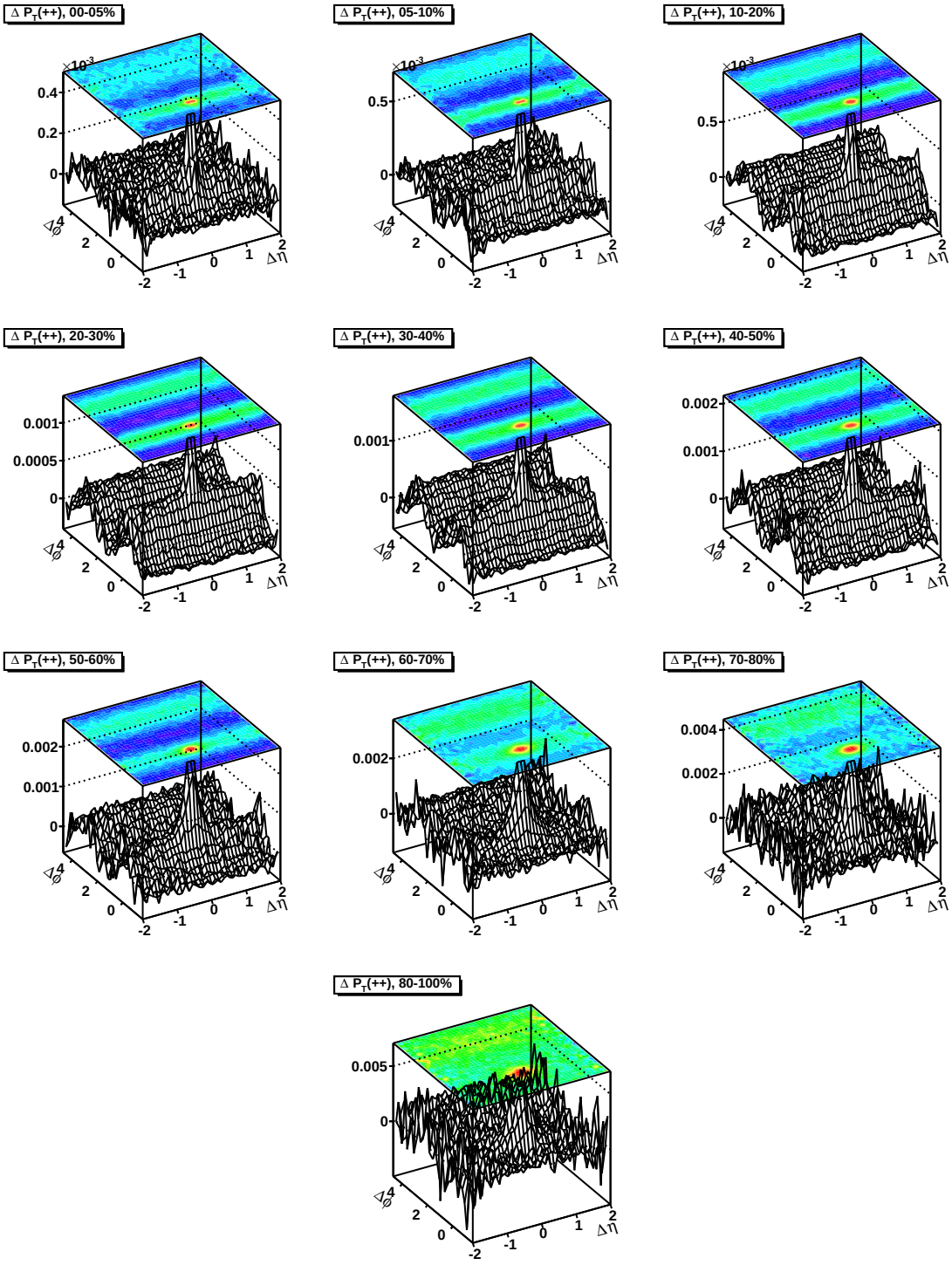

Figure 10.10: $\Delta P_T^{++} = \rho_2^{\Delta p_T^+ \Delta p_T^+}(\Delta\eta, \Delta\phi)/\rho_2^{++}(\Delta\eta, \Delta\phi)$

10.2 Bulk Correlations, Full Field +-

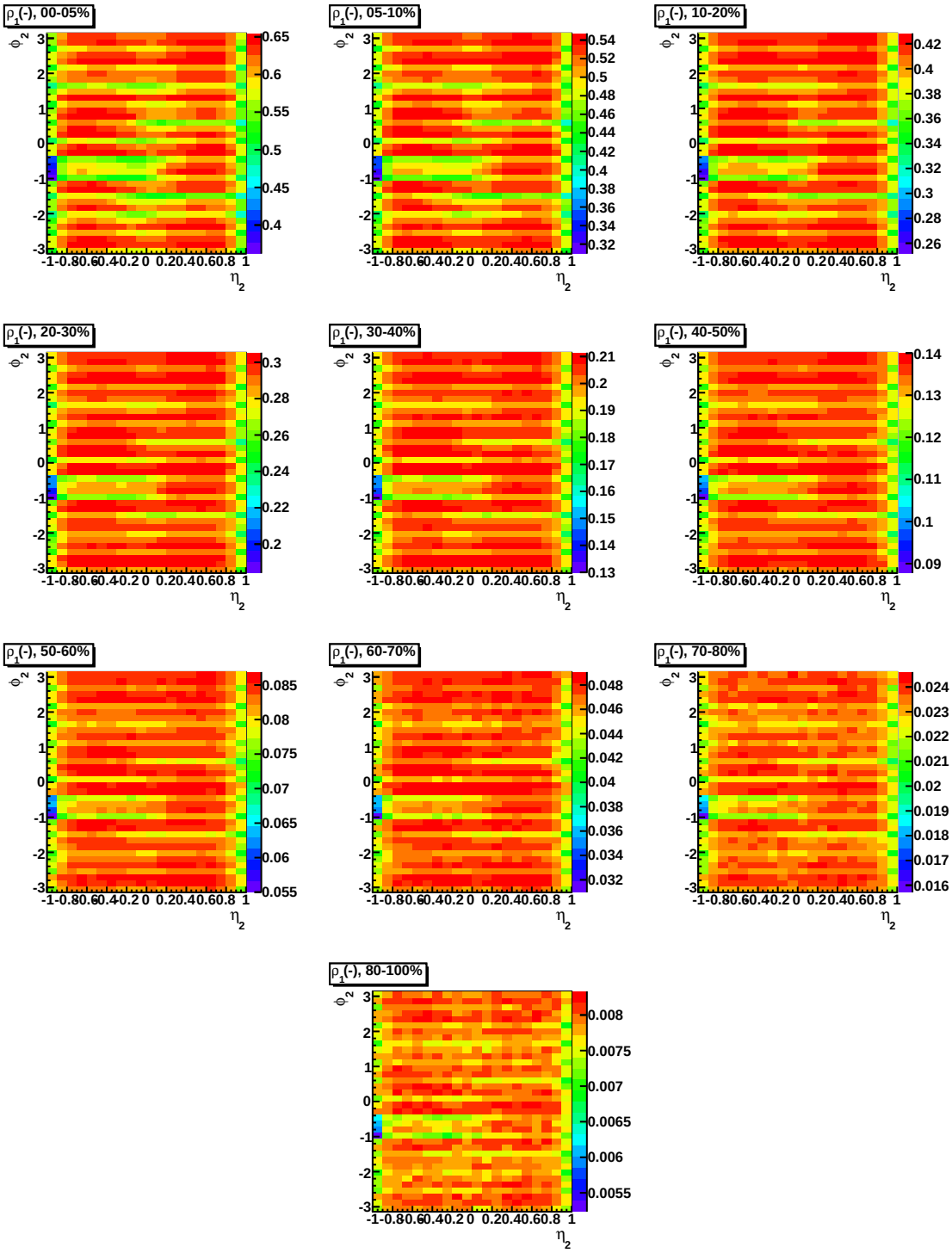

Figure 10.11: $\rho_1^-(\eta, \phi)$

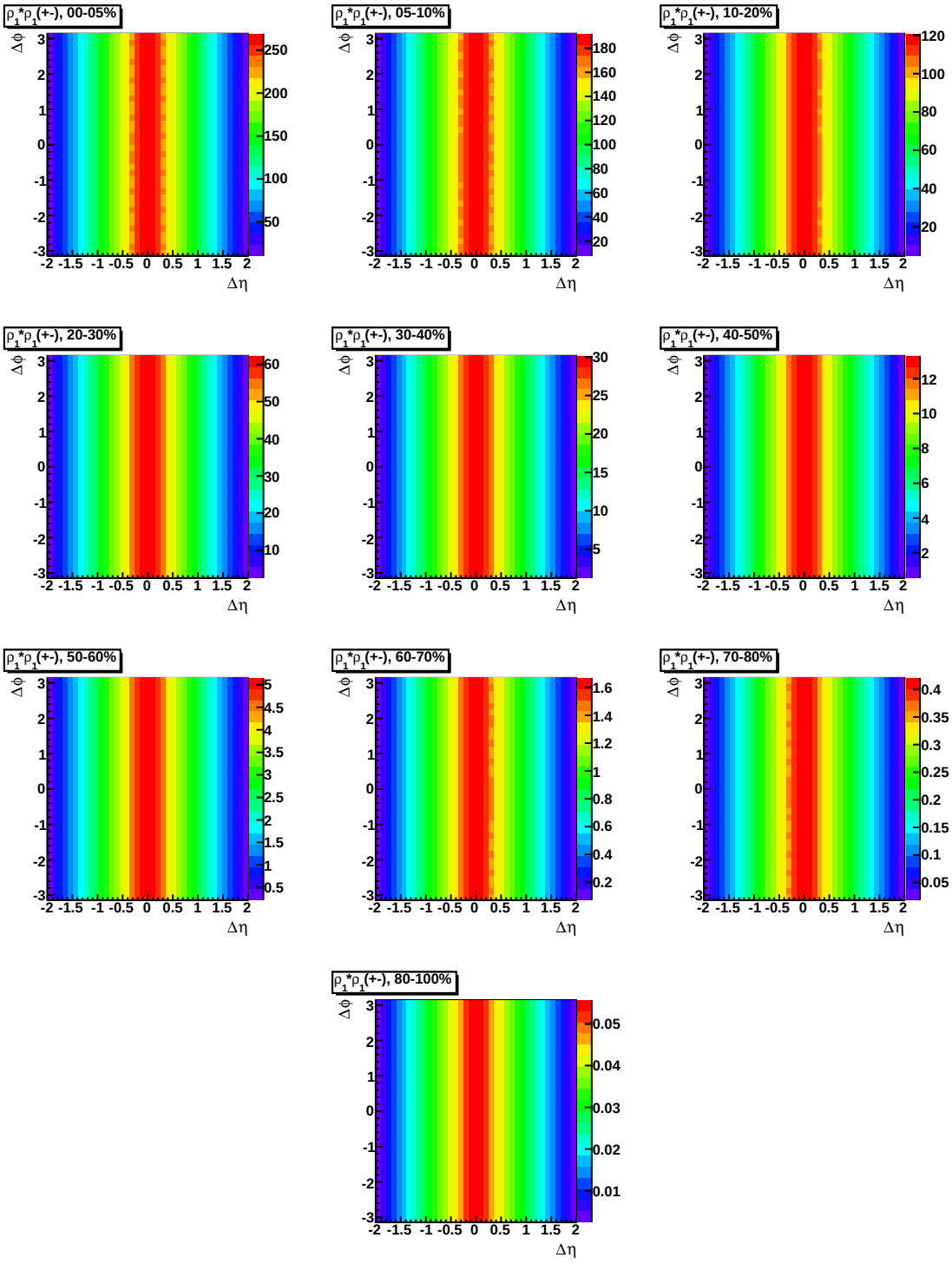

Figure 10.12: $\rho_1^+ * \rho_1^-(\Delta\eta, \Delta\phi)$

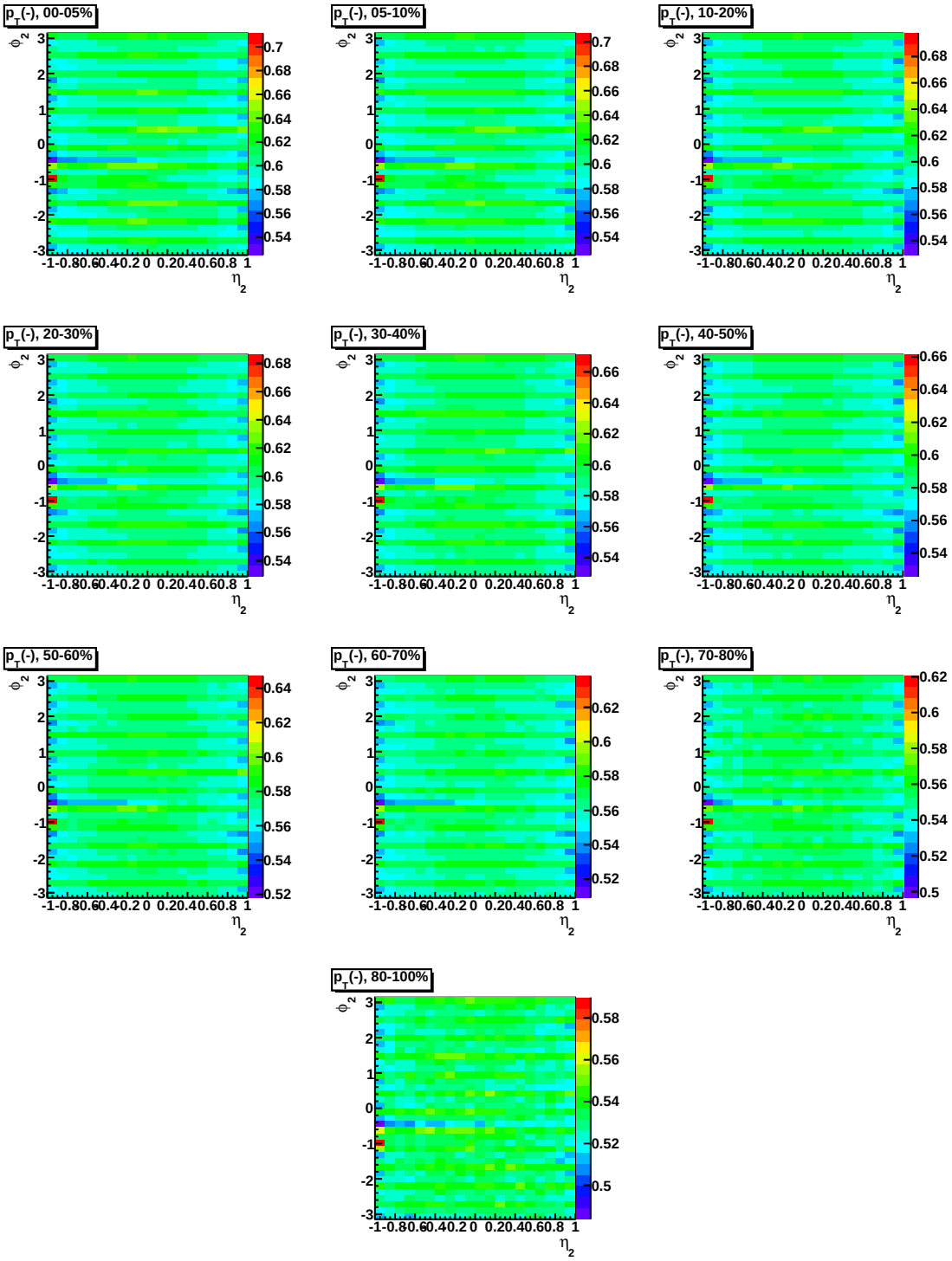

Figure 10.13: $\overline{p_T^-}(\eta, \phi)$

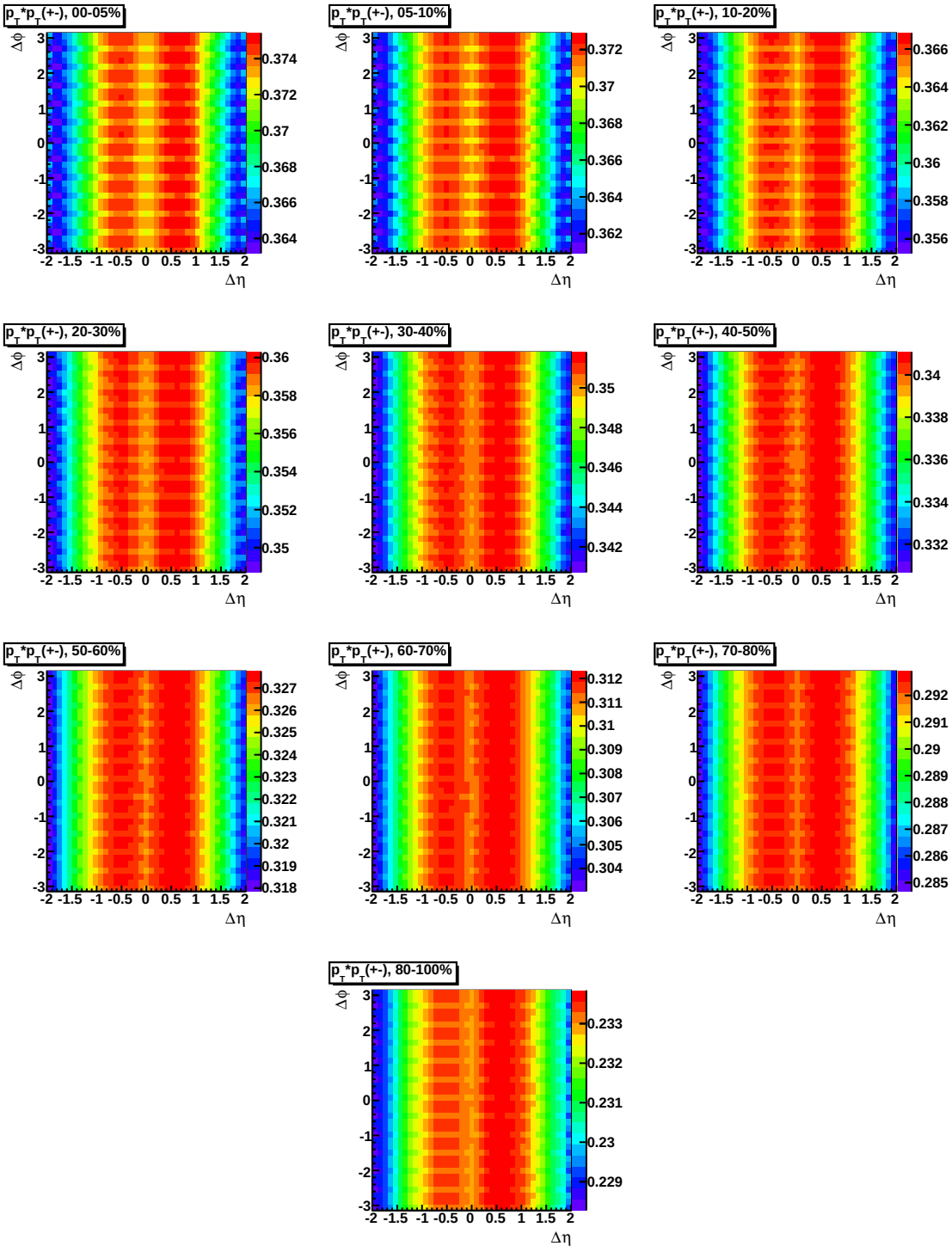

Figure 10.14: $\overline{p}_T^+ * \overline{p}_T^-(\Delta\eta, \Delta\phi)$

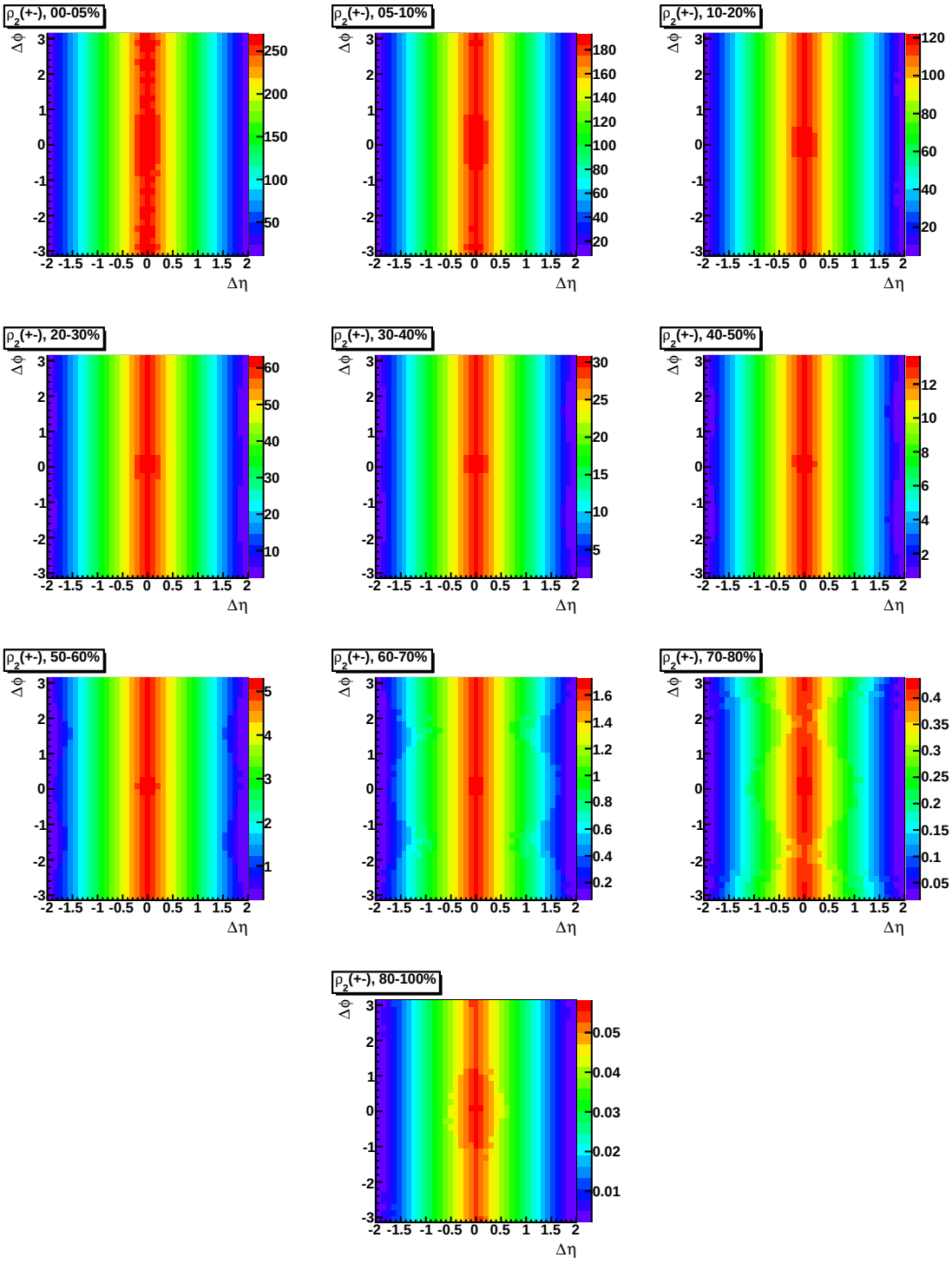

Figure 10.15: $\rho_2^{+-}(\Delta\eta, \Delta\phi)$

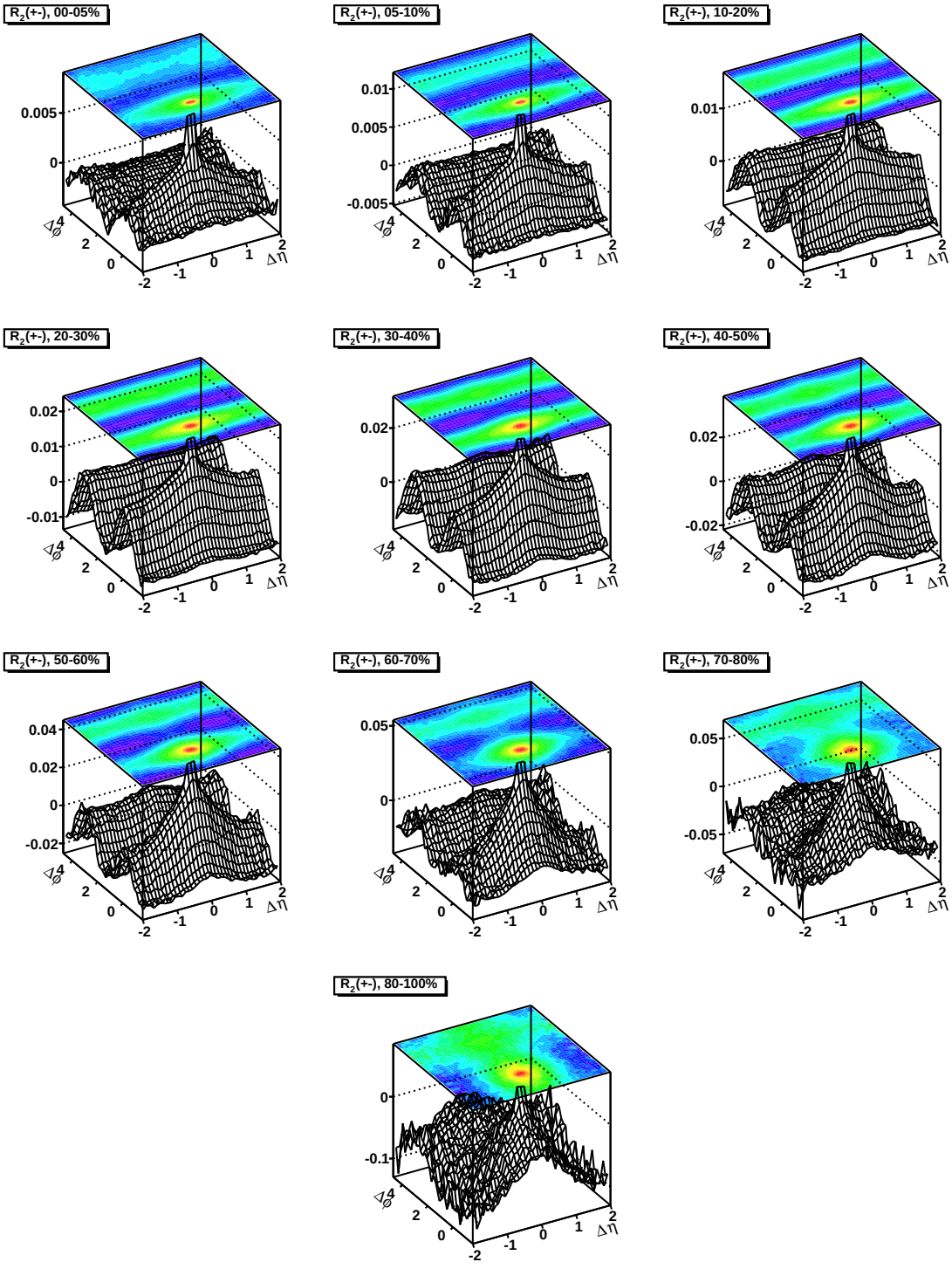

Figure 10.16: $R_2^{+-}(\Delta\eta, \Delta\phi) = \rho_2^{+-}(\Delta\eta, \Delta\phi)/\rho_1^{+} * \rho_1^{-}(\Delta\eta, \Delta\phi) - 1$

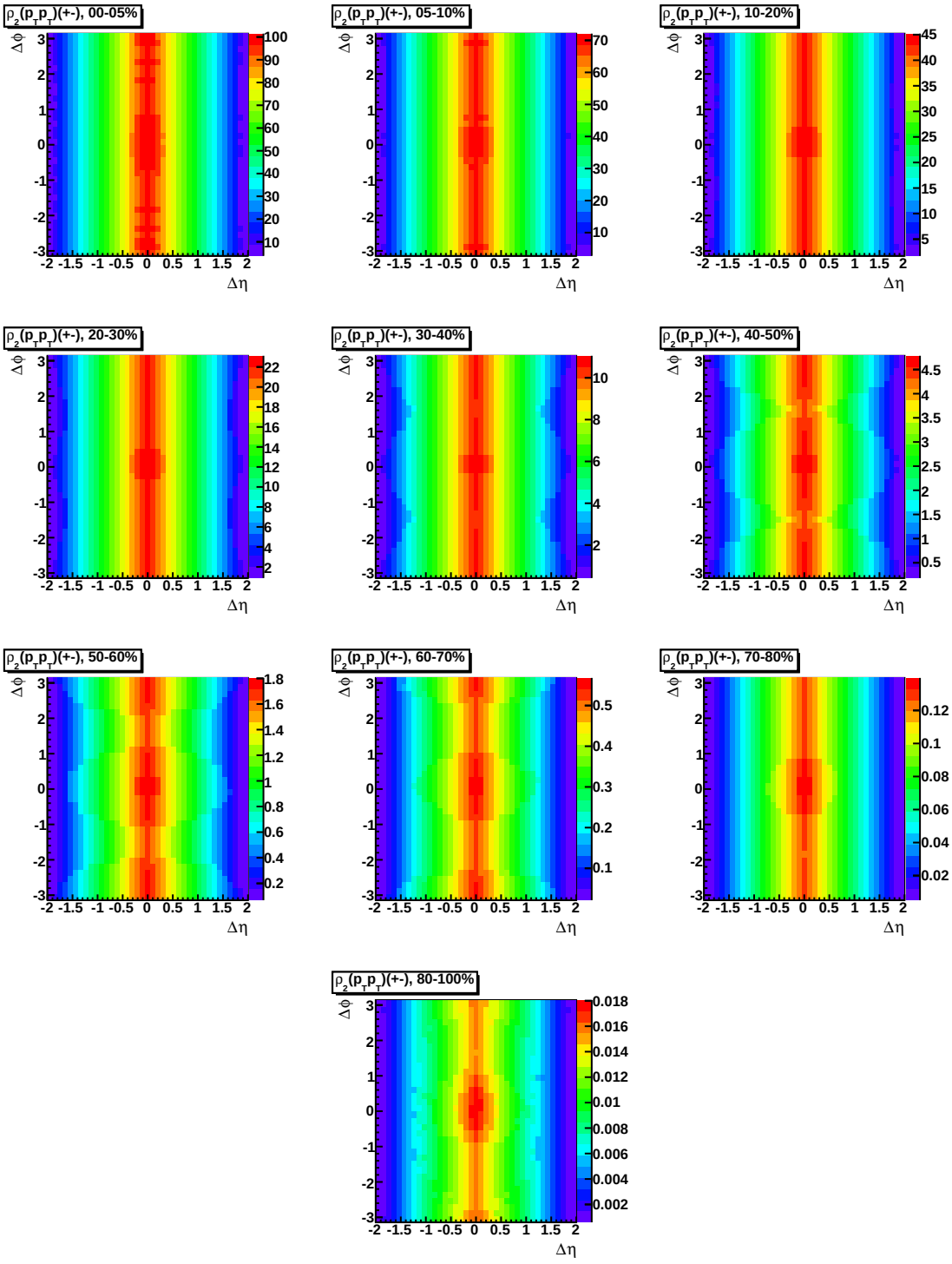

Figure 10.17: $\rho_2^{p_T^+ p_T^-}(\Delta\eta, \Delta\phi)$

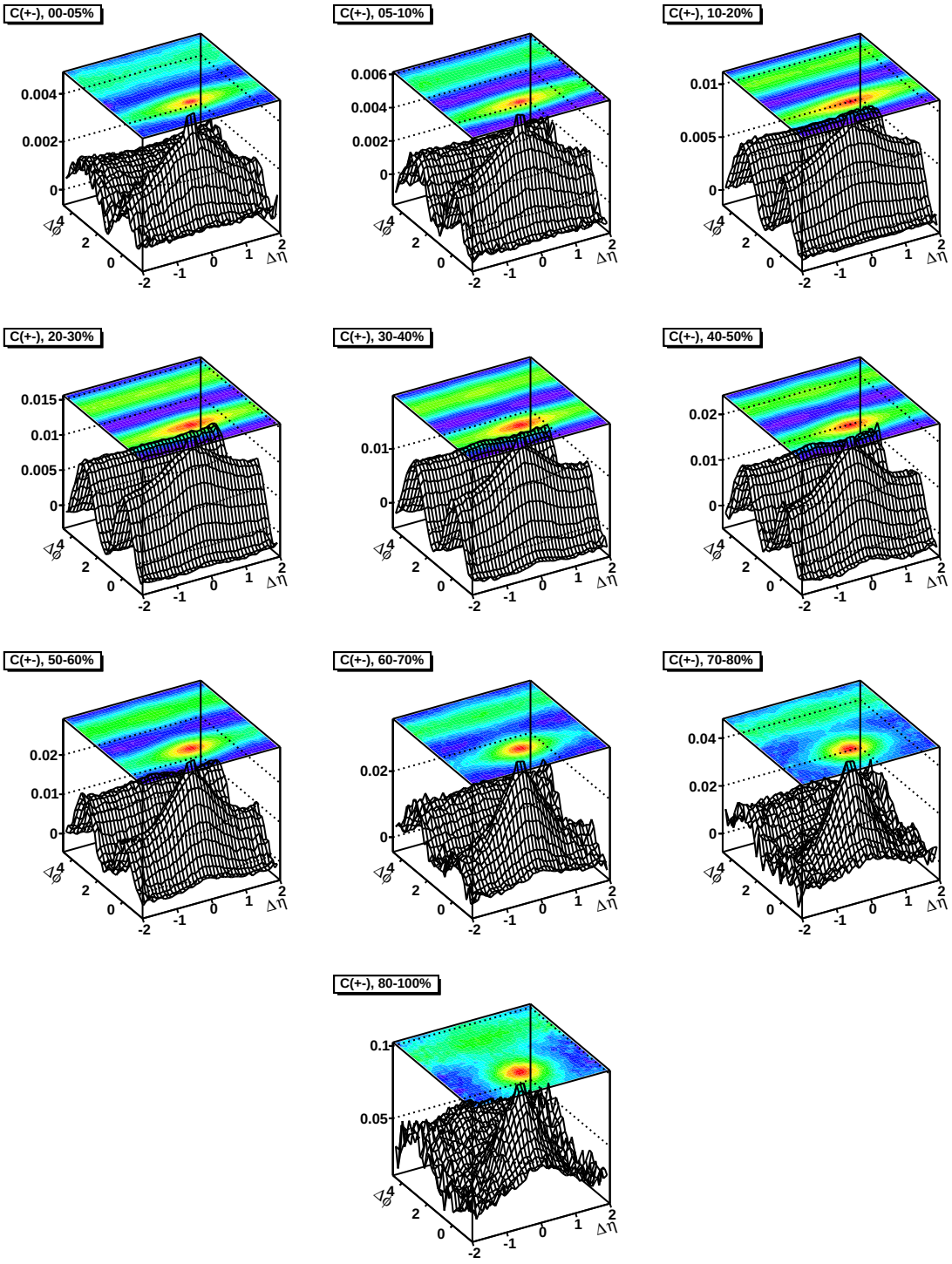

Figure 10.18: $C^{+-}(\Delta\eta, \Delta\phi) = \rho_2^{p_T^+ p_T^-}(\Delta\eta, \Delta\phi)/\rho_1^+ * \rho_1^-(\Delta\eta, \Delta\phi) - \overline{p}_T^+ * \overline{p}_T^-(\Delta\eta, \Delta\phi)$

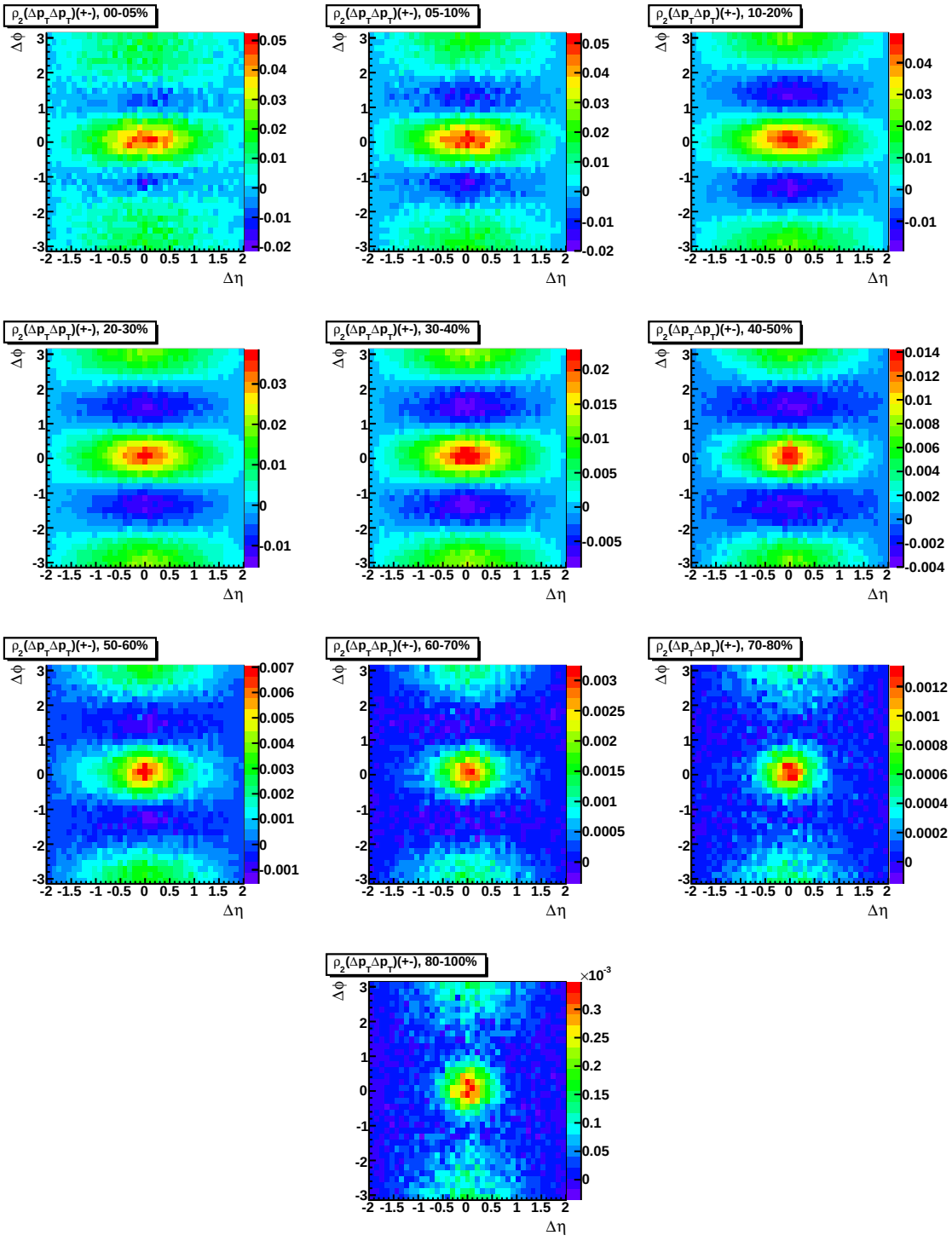

Figure 10.19: $\rho_2^{\Delta p_T^+ \Delta p_T^-}(\Delta\eta, \Delta\phi)$

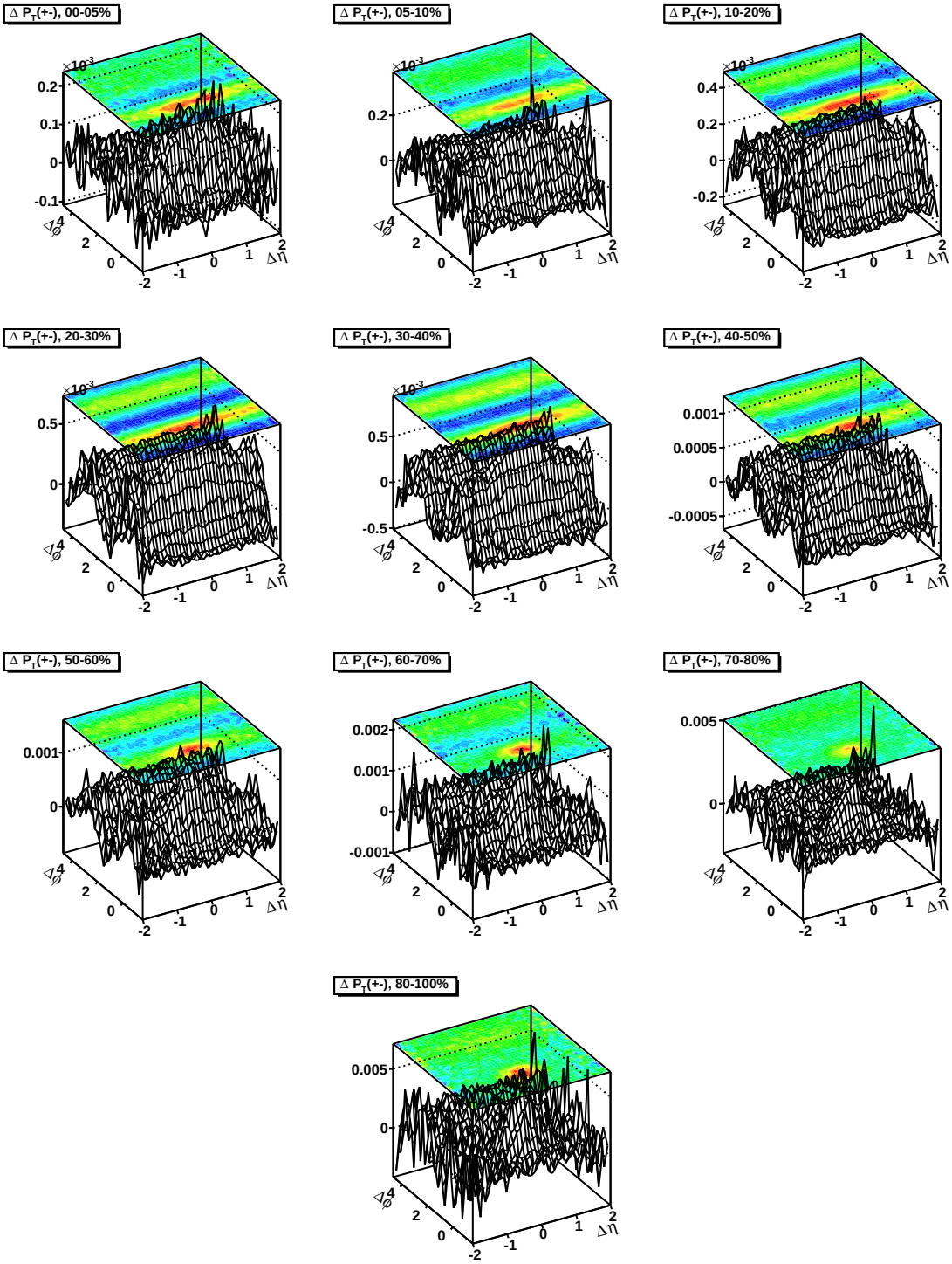

Figure 10.20: $\Delta P_T^{+-} = \rho_2^{\Delta p_T^+ \Delta p_T^-}(\Delta\eta, \Delta\phi)/\rho_2^{+-}(\Delta\eta, \Delta\phi)$

10.3 Bulk Correlations, Both Fields, ls/us/ci/cd

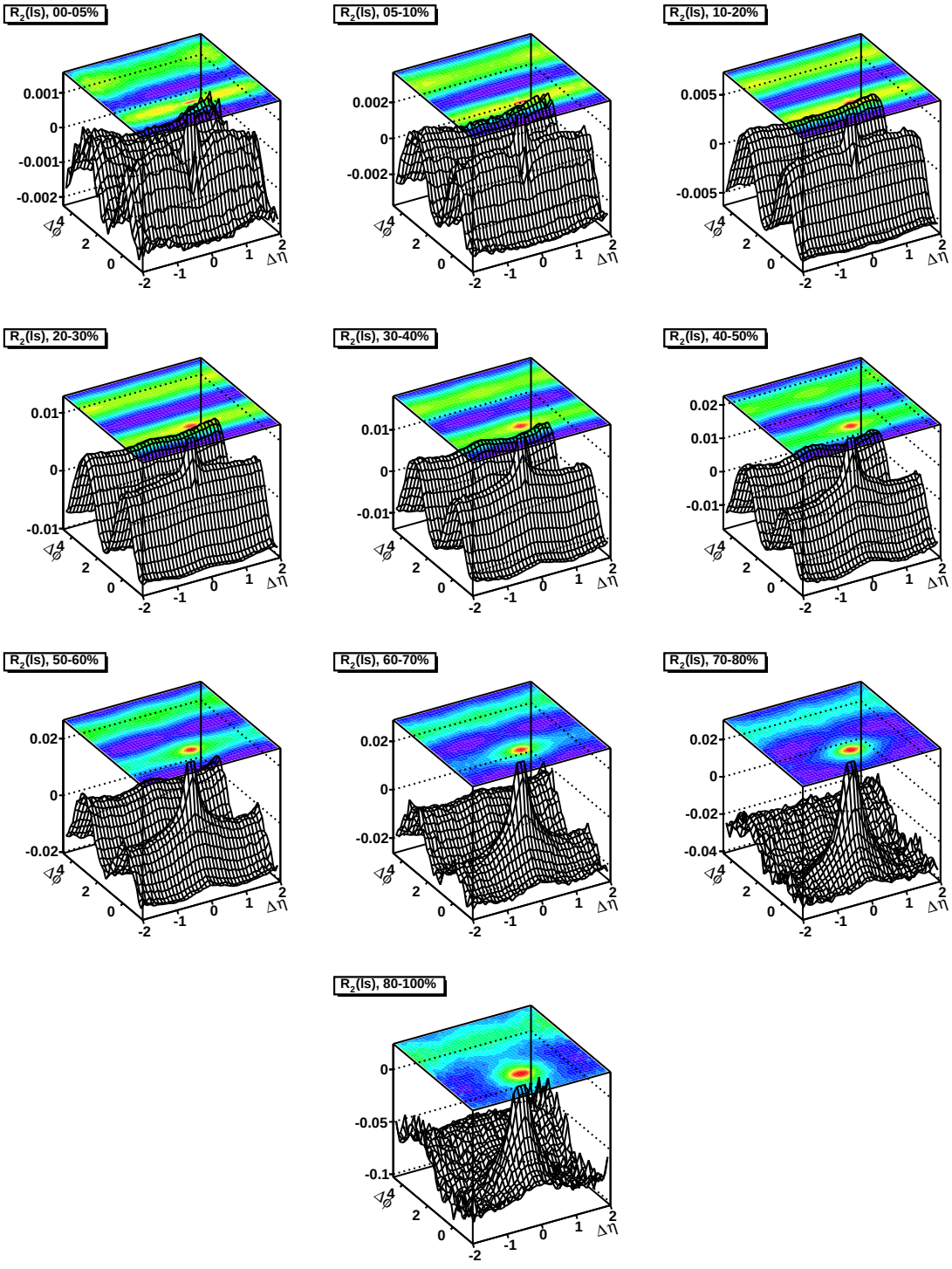

Figure 10.21: $R_2^{ls}(\Delta\eta, \Delta\phi)$

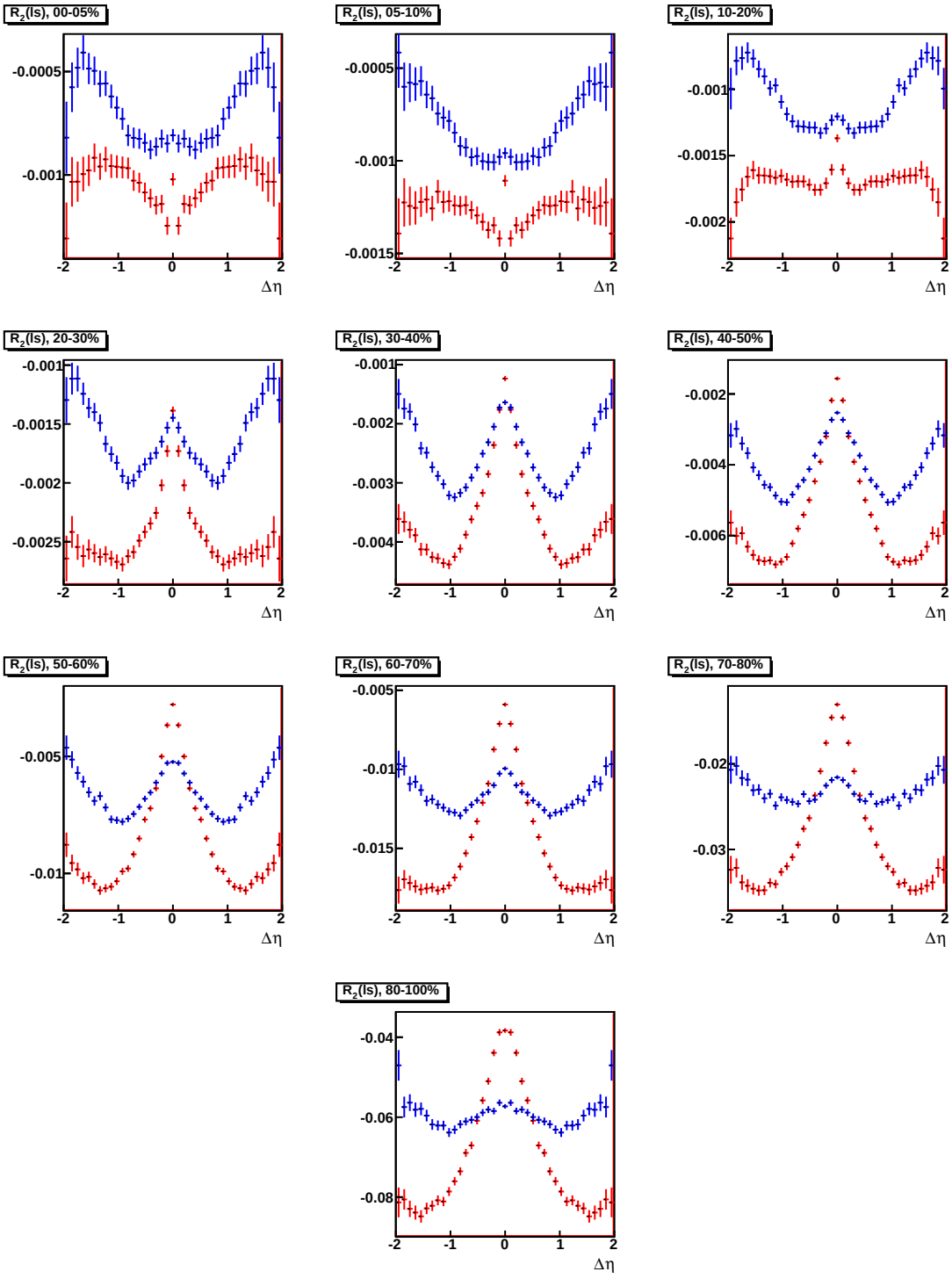

Figure 10.22: $R_2^{ls}(\Delta\eta)$

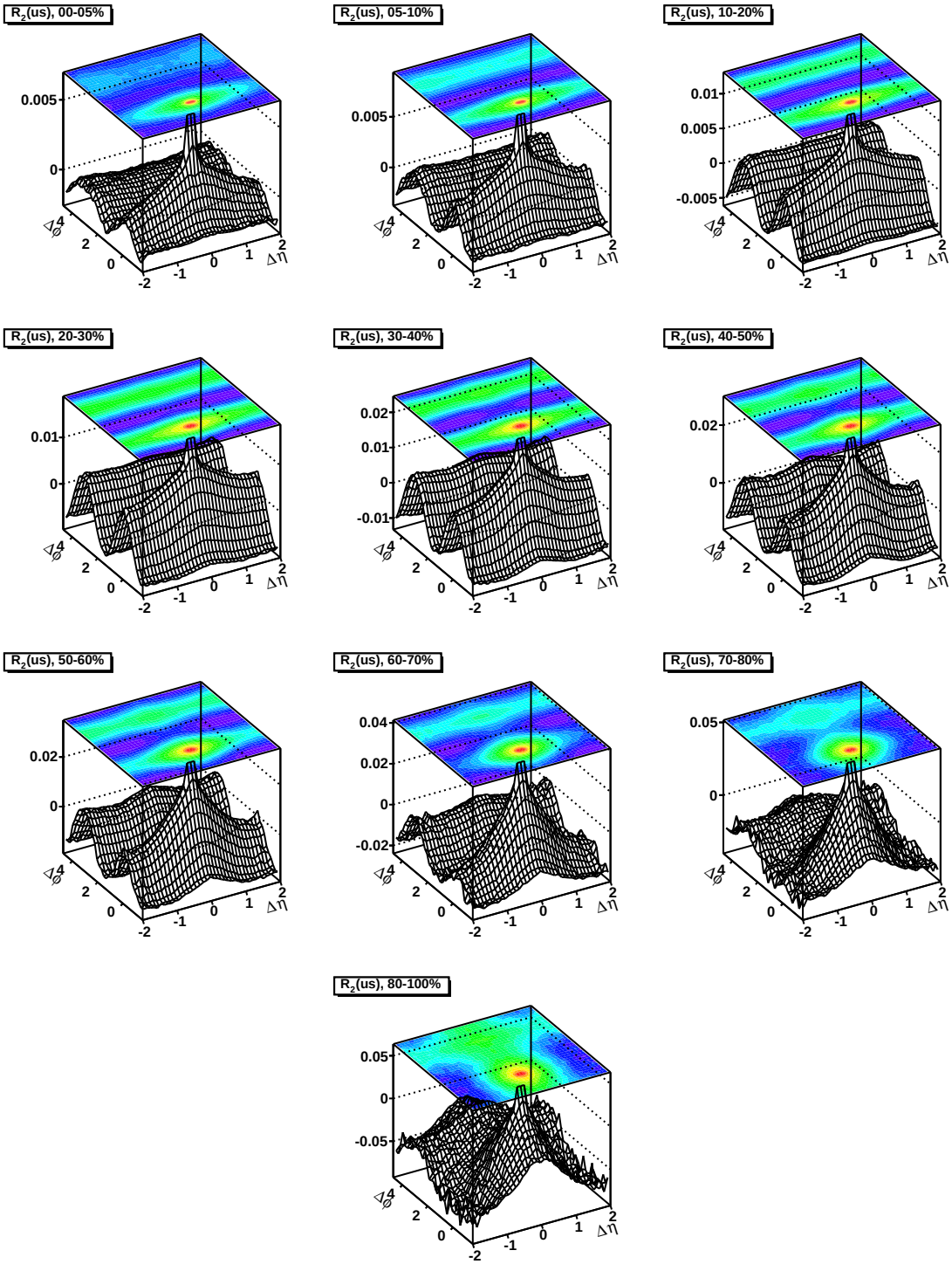

Figure 10.23: $R_2^{us}(\Delta\eta, \Delta\phi)$

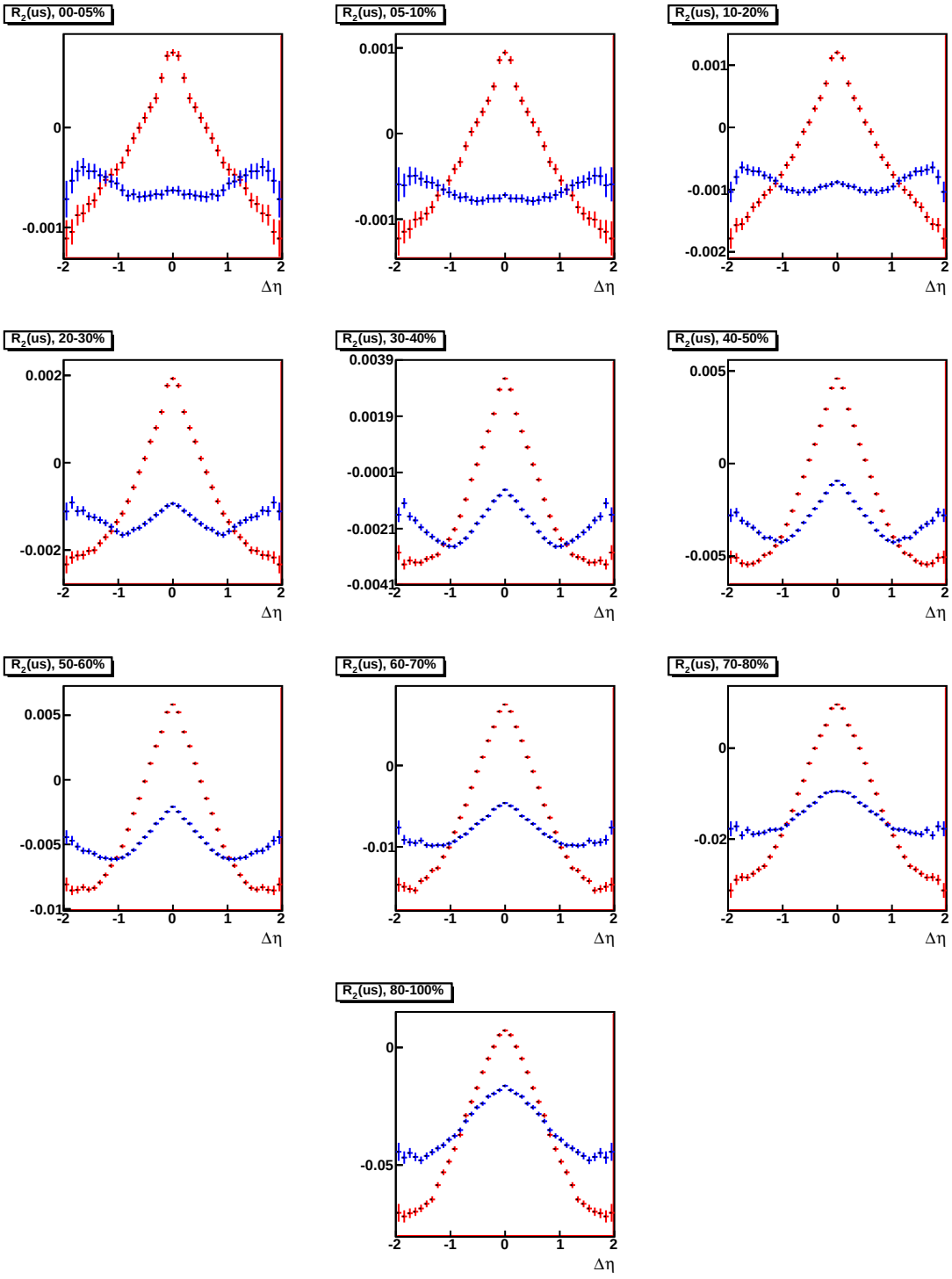

Figure 10.24: $R_2^{us}(\Delta\eta)$

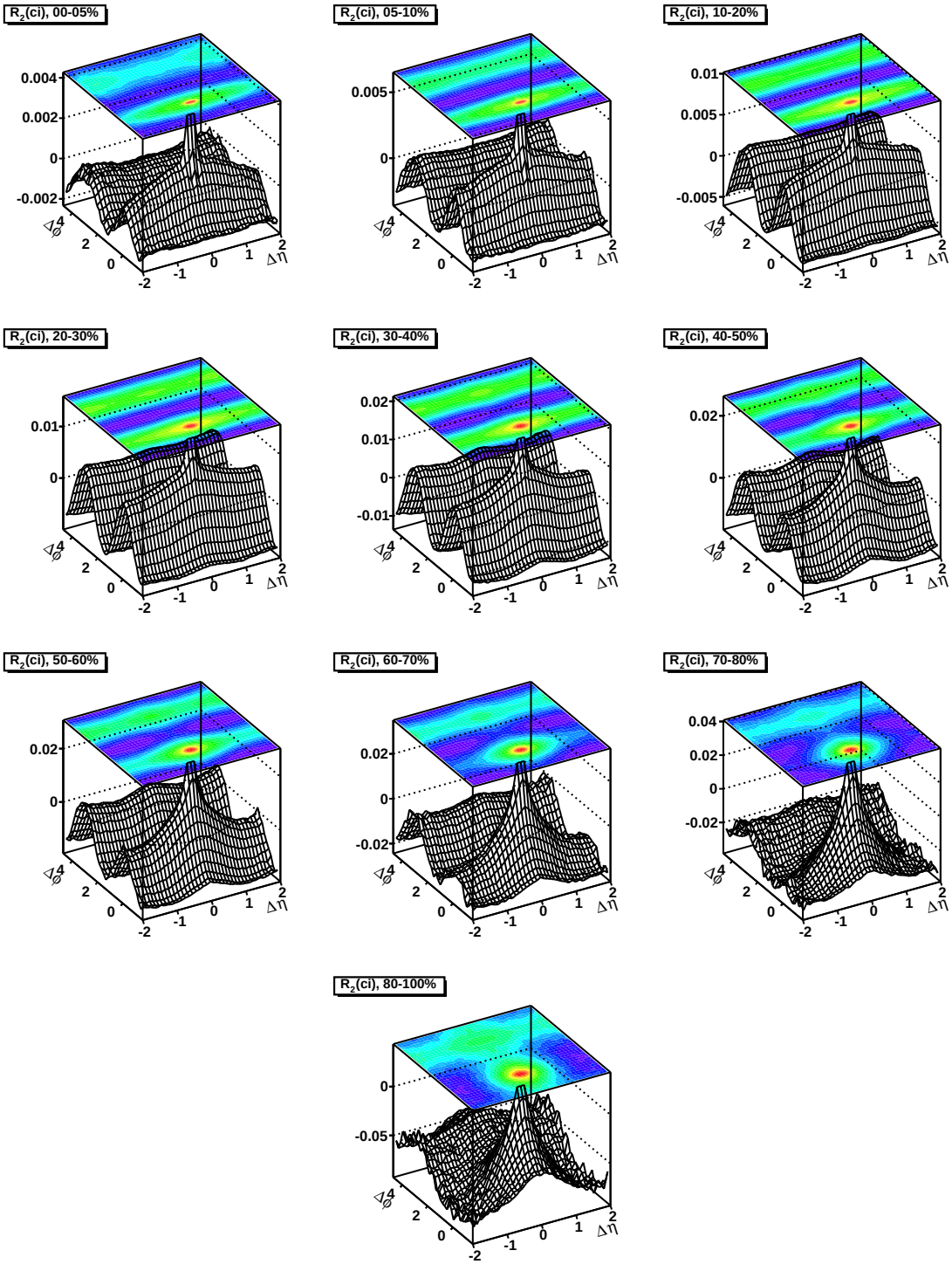

Figure 10.25: $R_2^{ci}(\Delta\eta, \Delta\phi)$

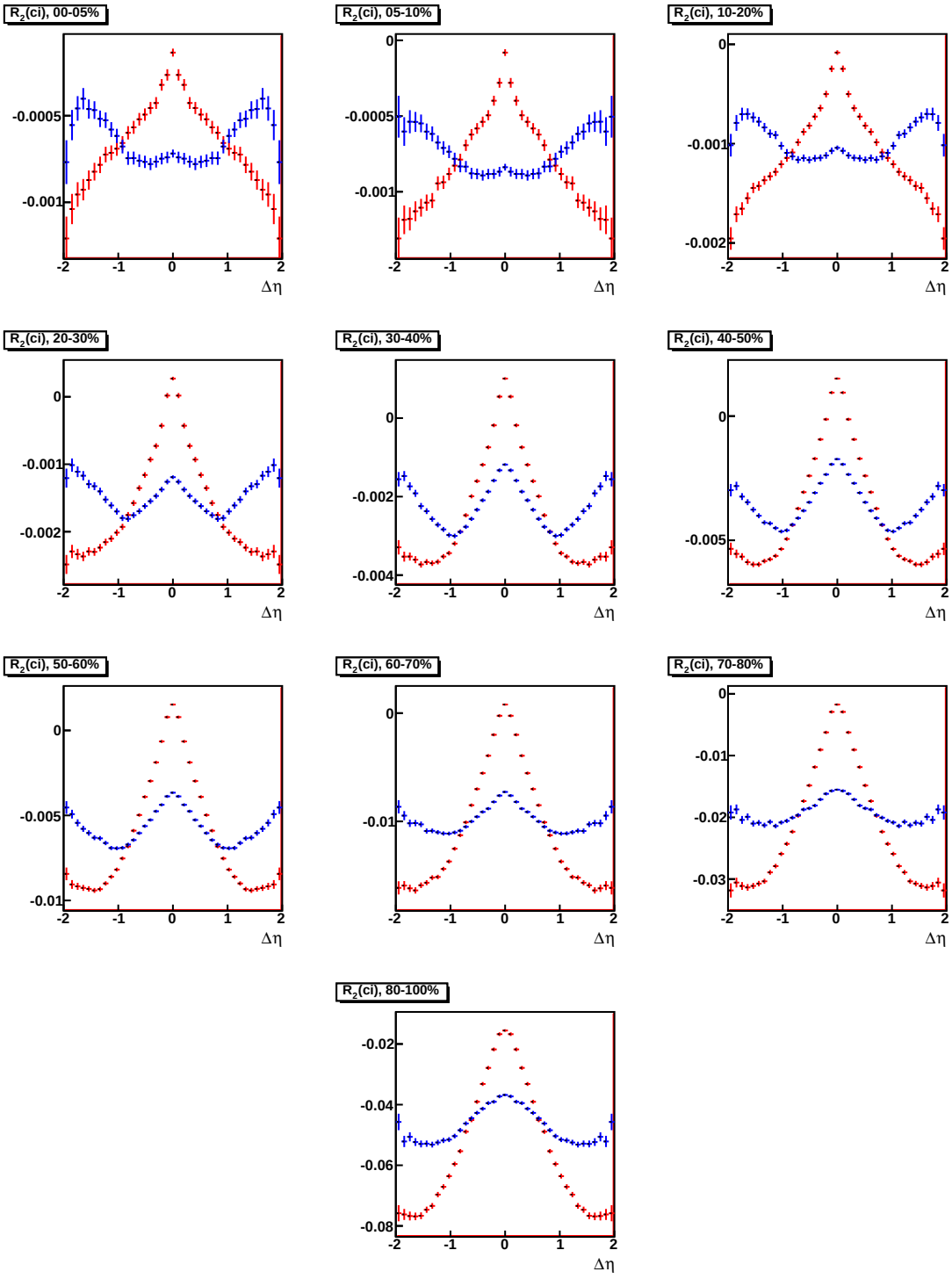

Figure 10.26: $R_2^{ci}(\Delta\eta)$

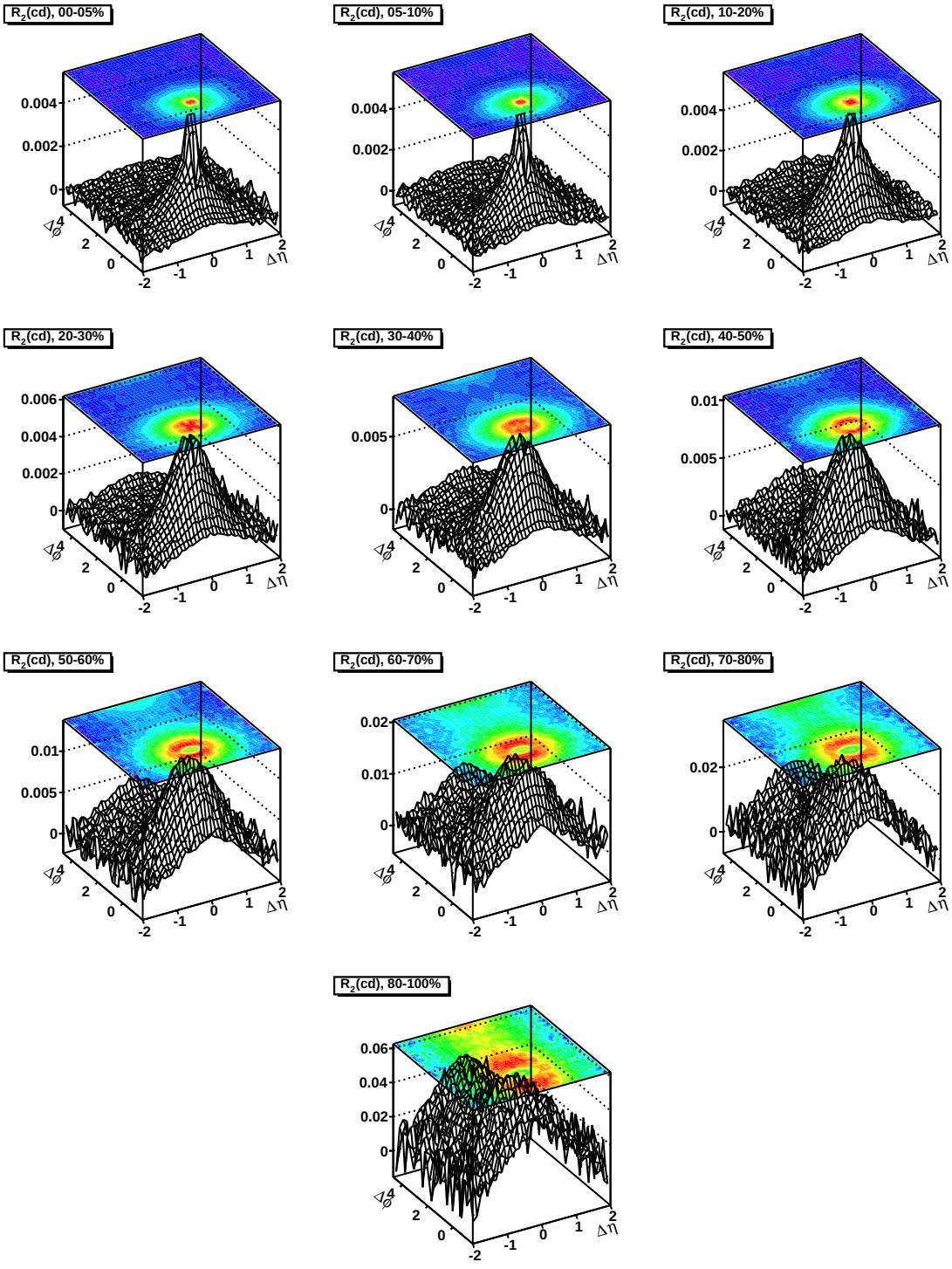

Figure 10.27: $R_2^{cd}(\Delta\eta, \Delta\phi)$

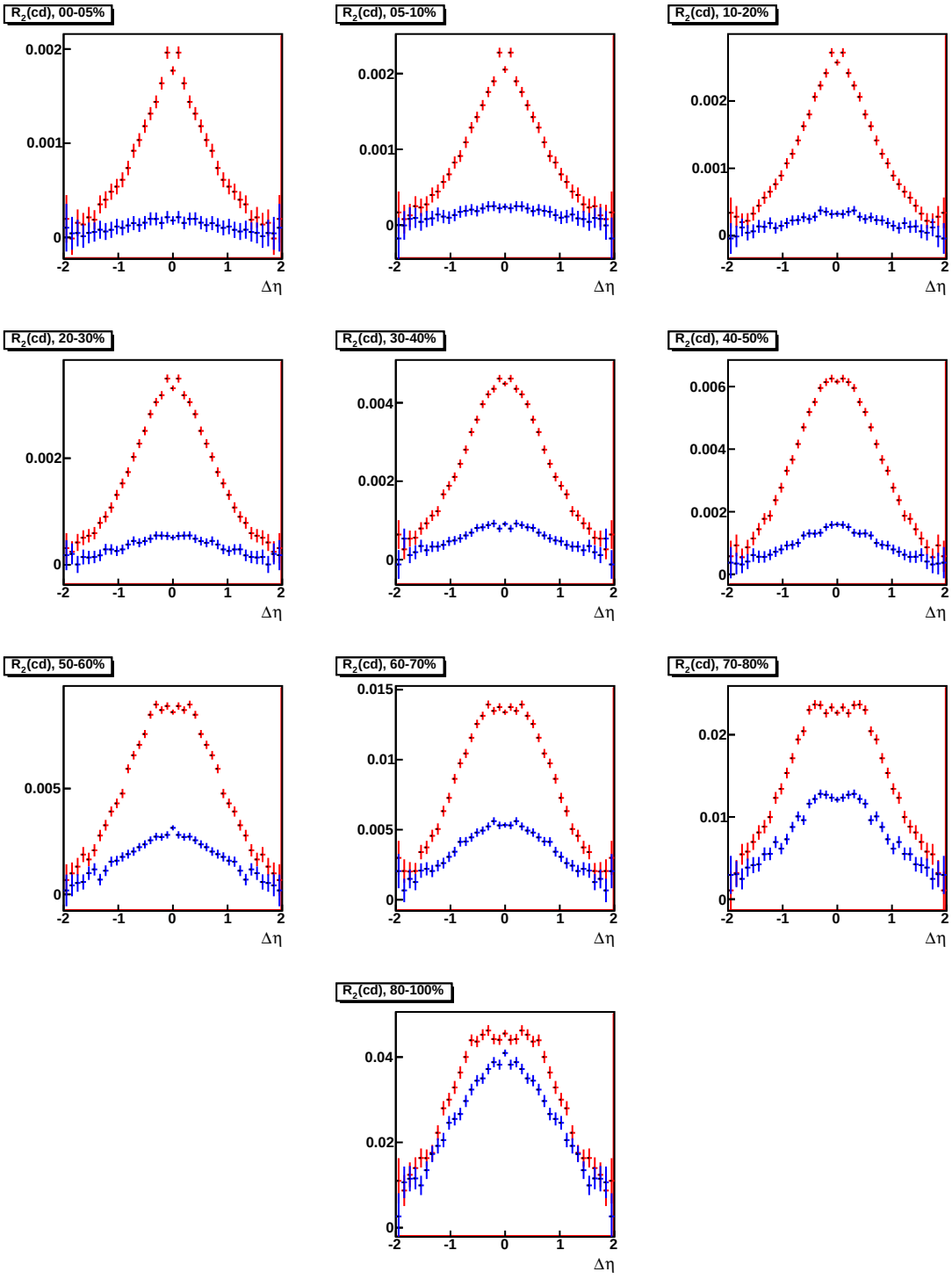

Figure 10.28: $R_2^{cd}(\Delta\eta)$

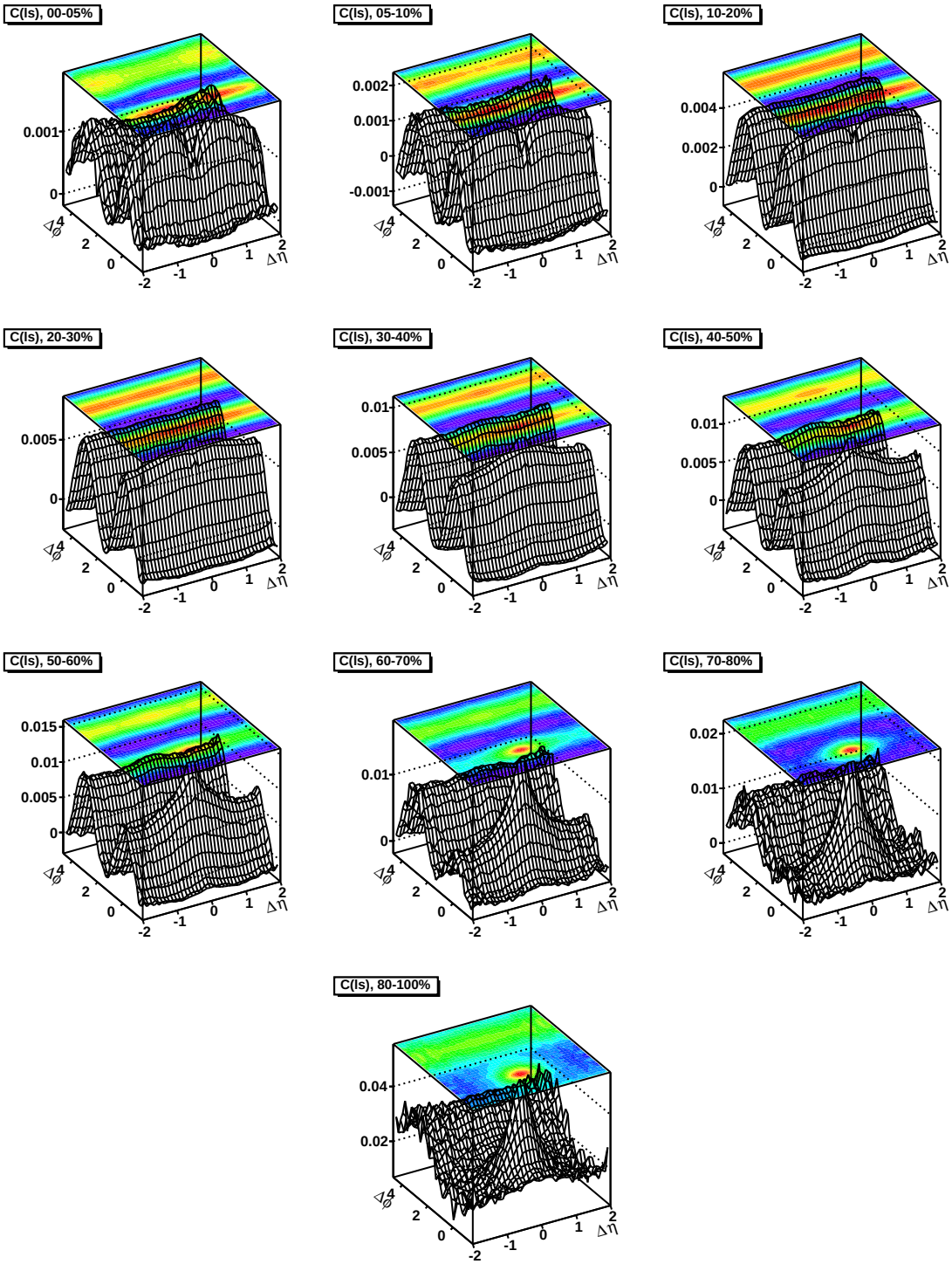

Figure 10.29: $C^{ls}(\Delta\eta, \Delta\phi)$

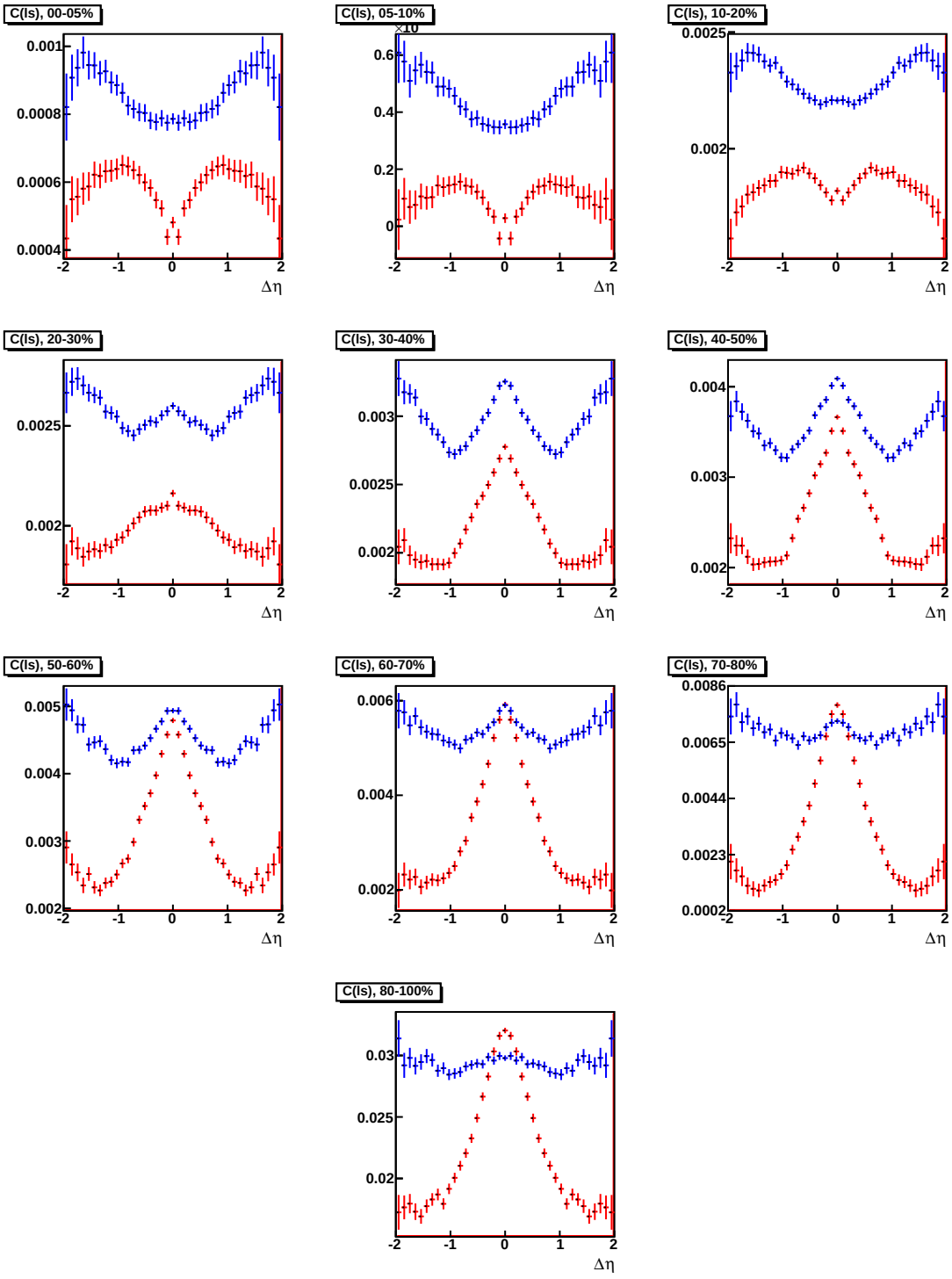

Figure 10.30: $C^{ls}(\Delta\eta)$

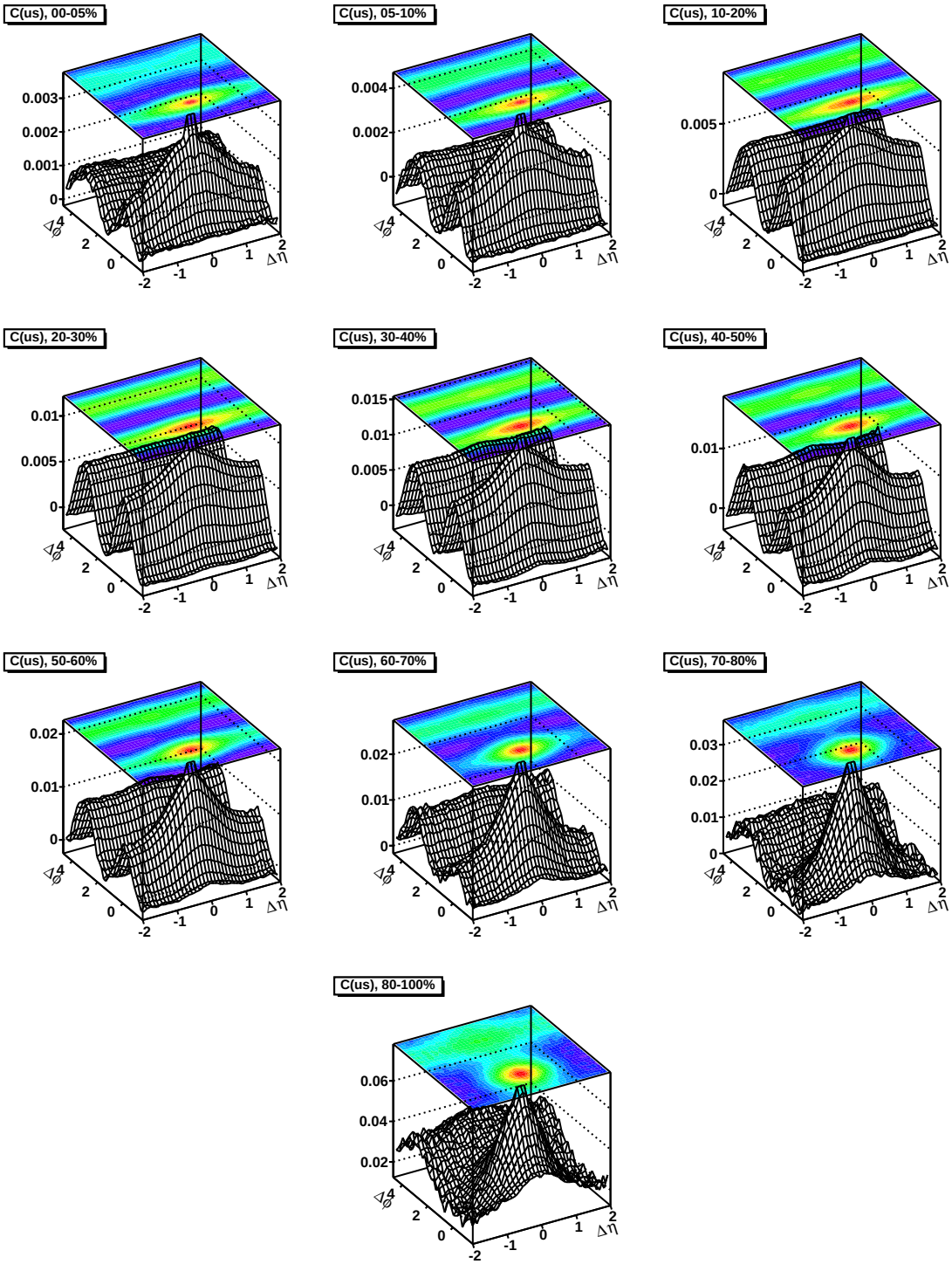

Figure 10.31: $C^{us}(\Delta\eta, \Delta\phi)$

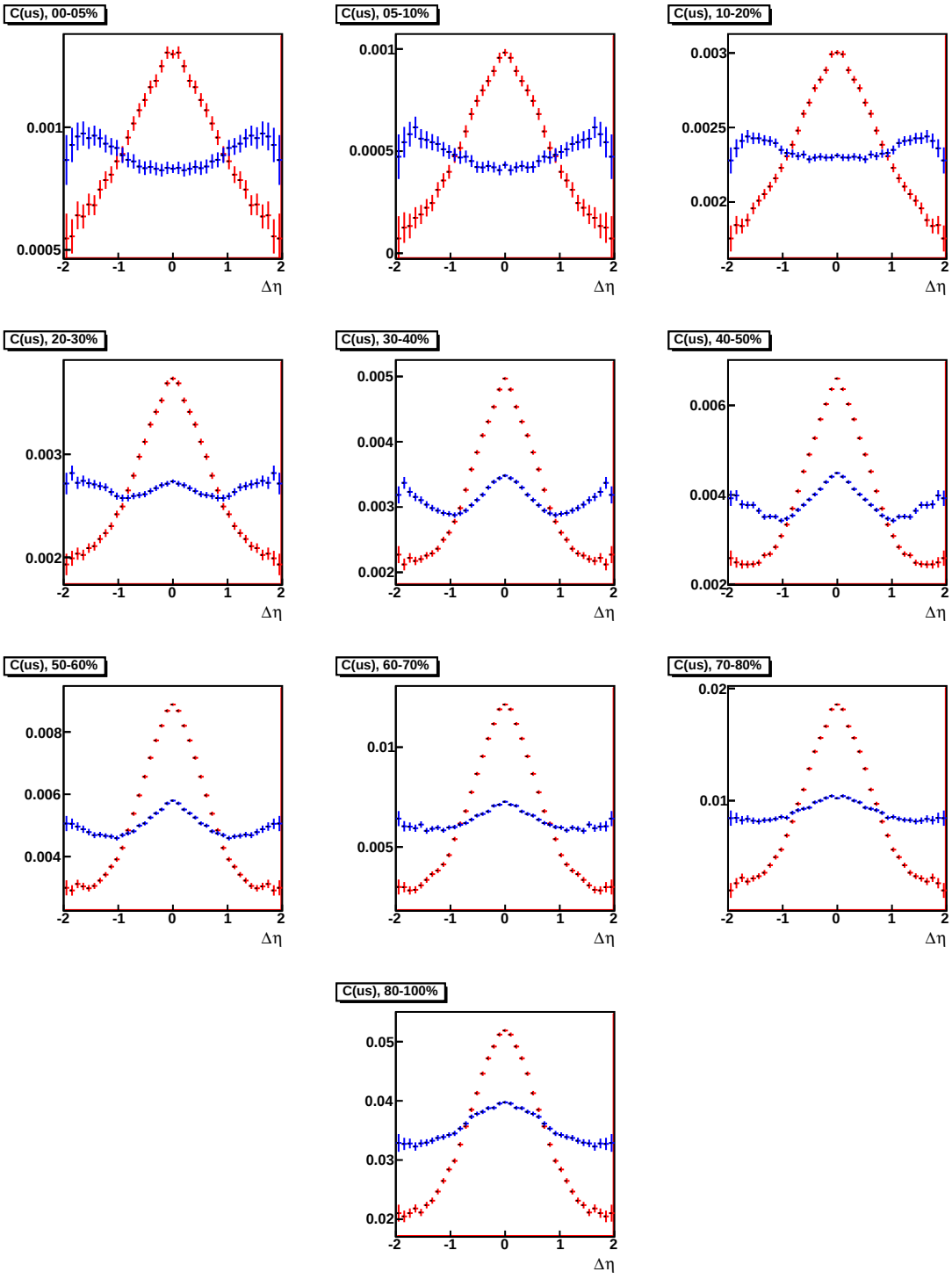

Figure 10.32: $C^{us}(\Delta\eta)$

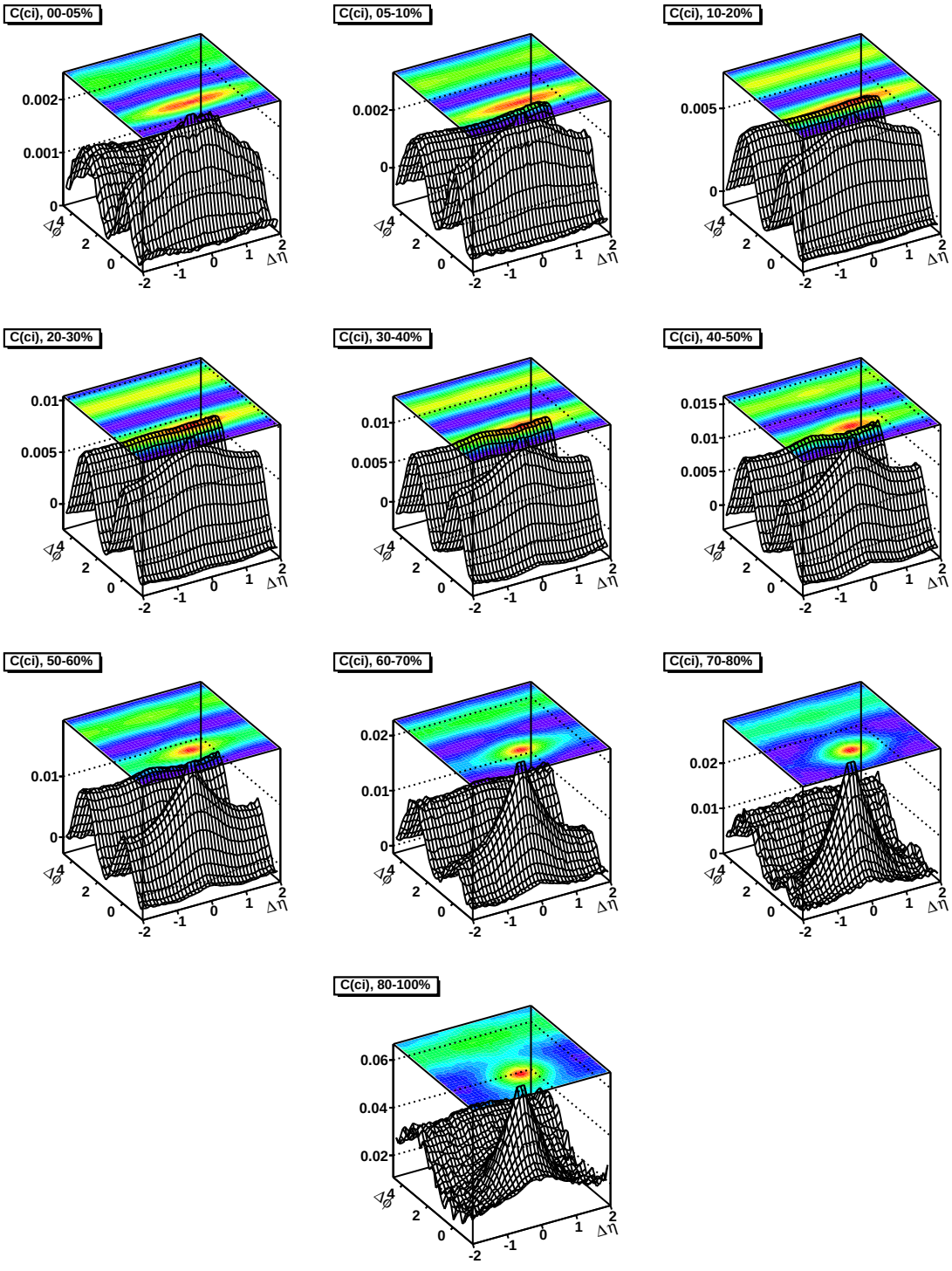

Figure 10.33: $C^{ci}(\Delta\eta, \Delta\phi)$

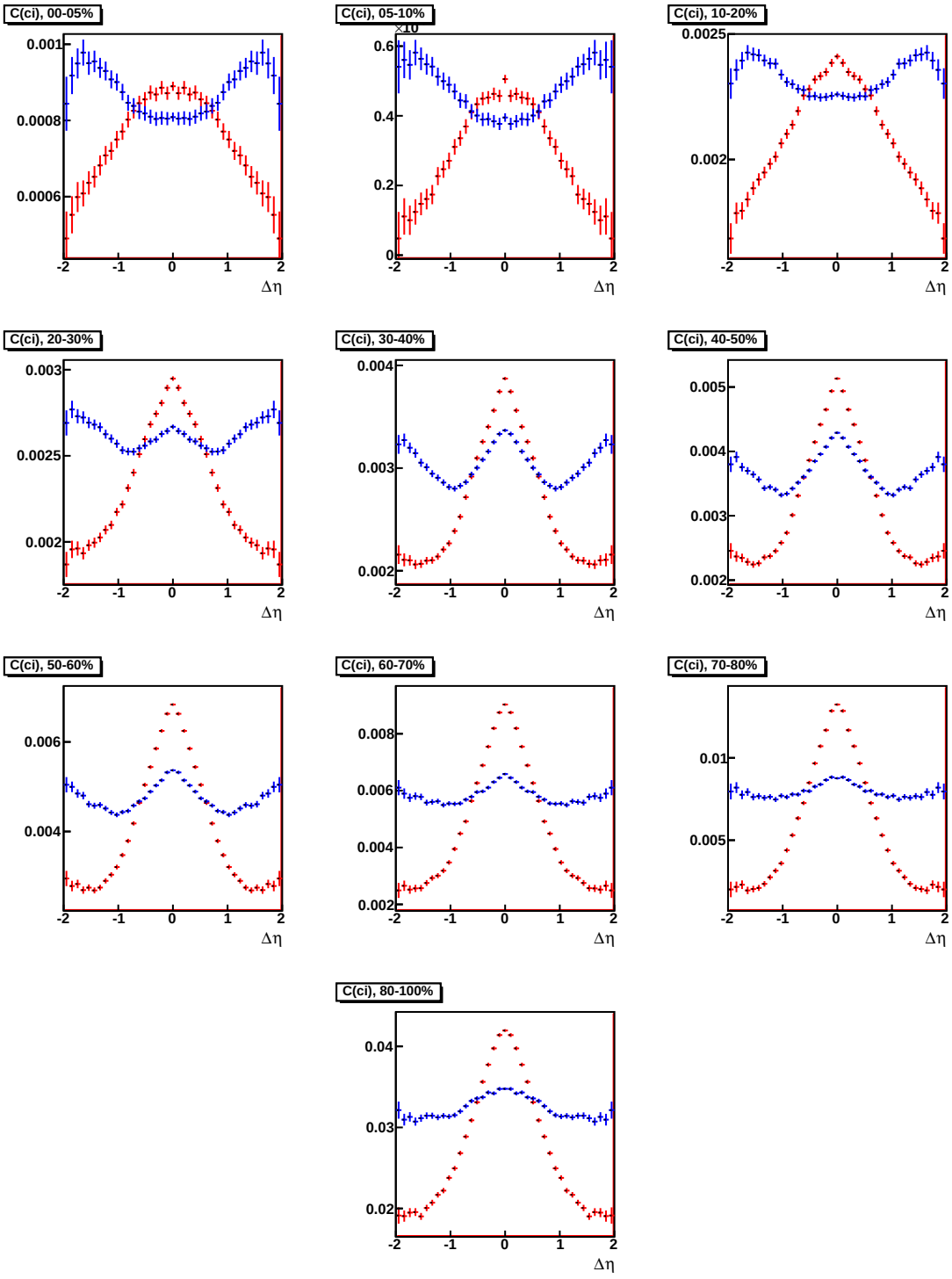

Figure 10.34: $C^{ci}(\Delta\eta)$

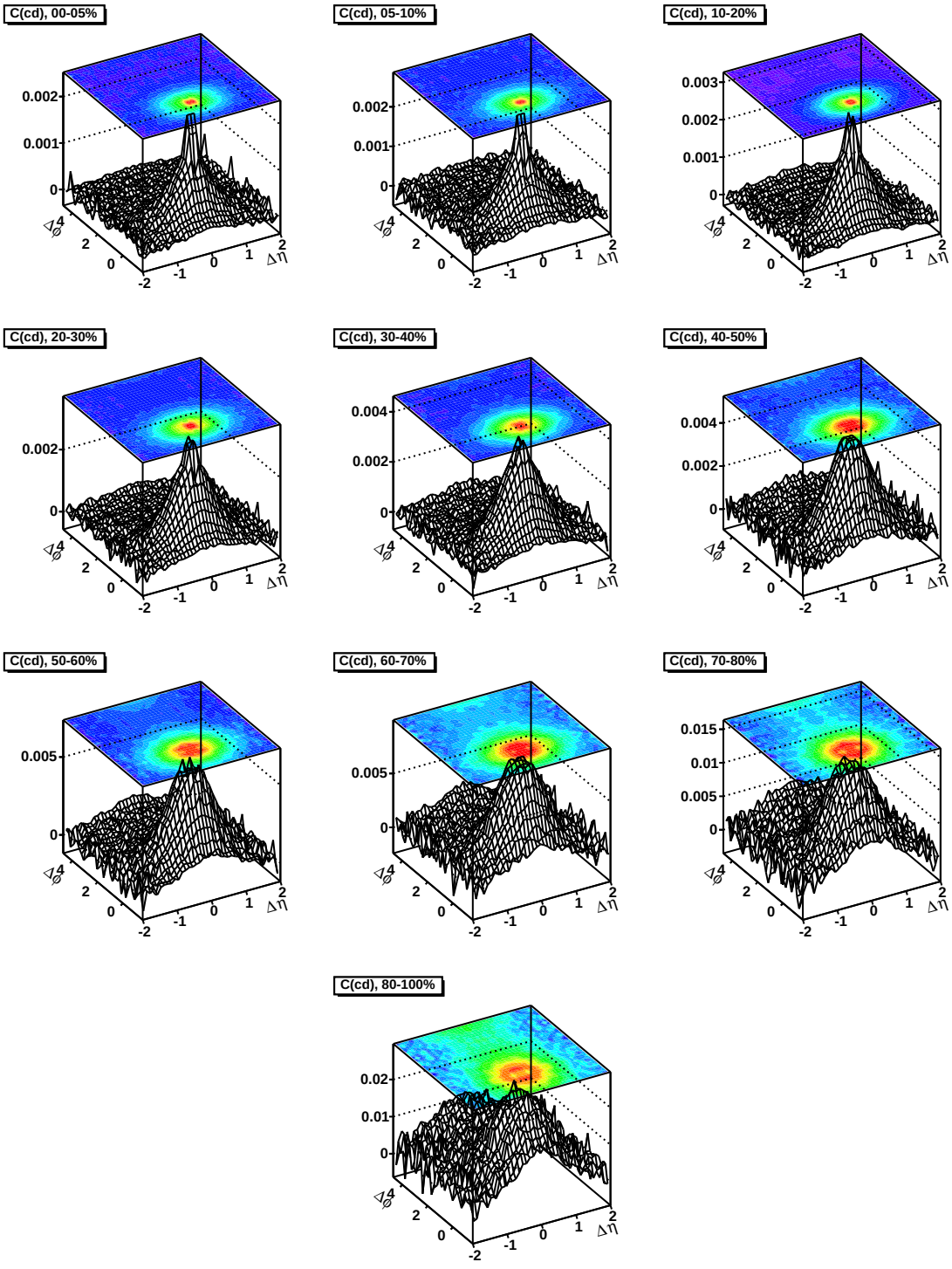

Figure 10.35: $C^{cd}(\Delta\eta, \Delta\phi)$

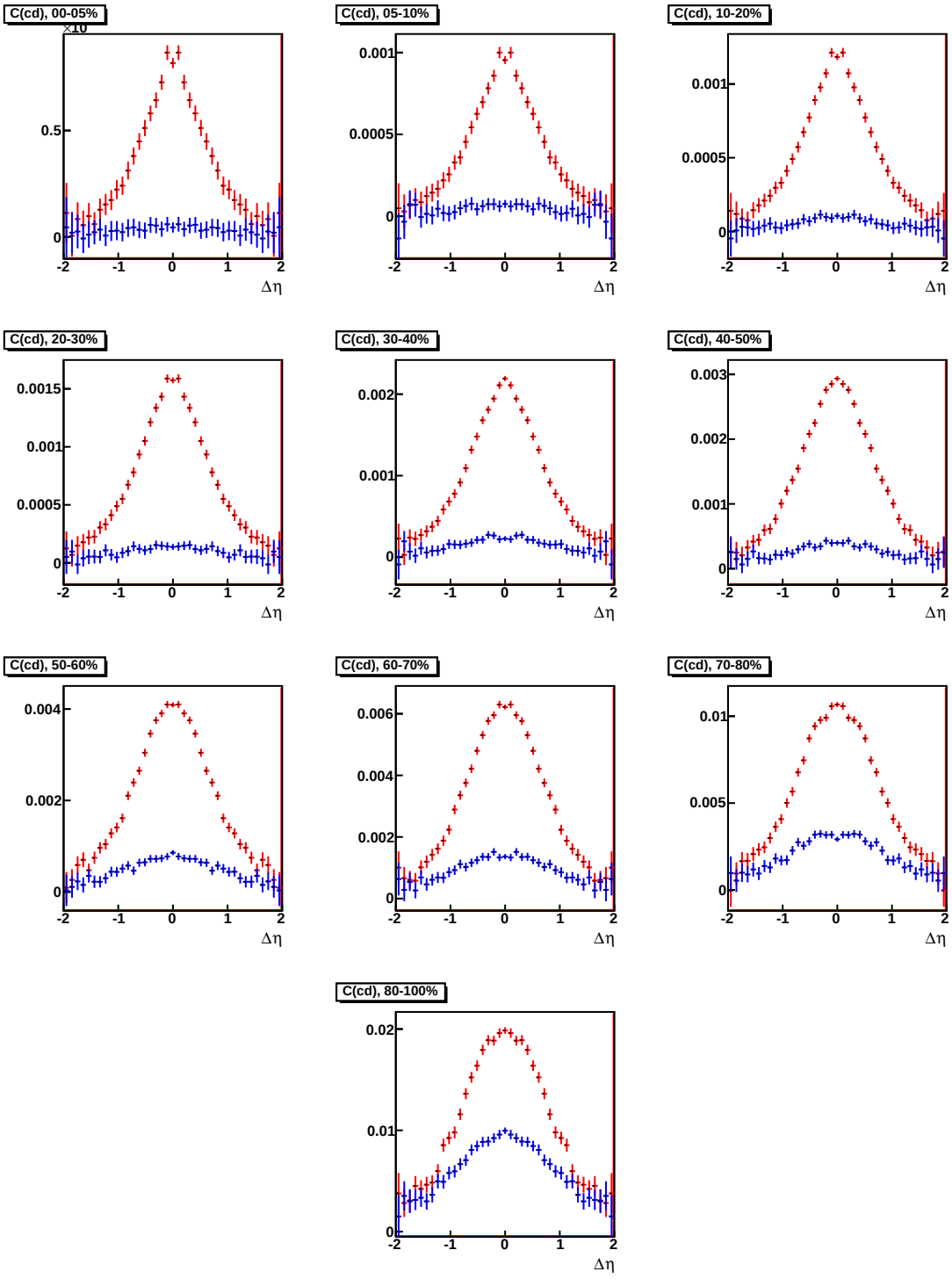

Figure 10.36: $C^{cd}(\Delta\eta)$

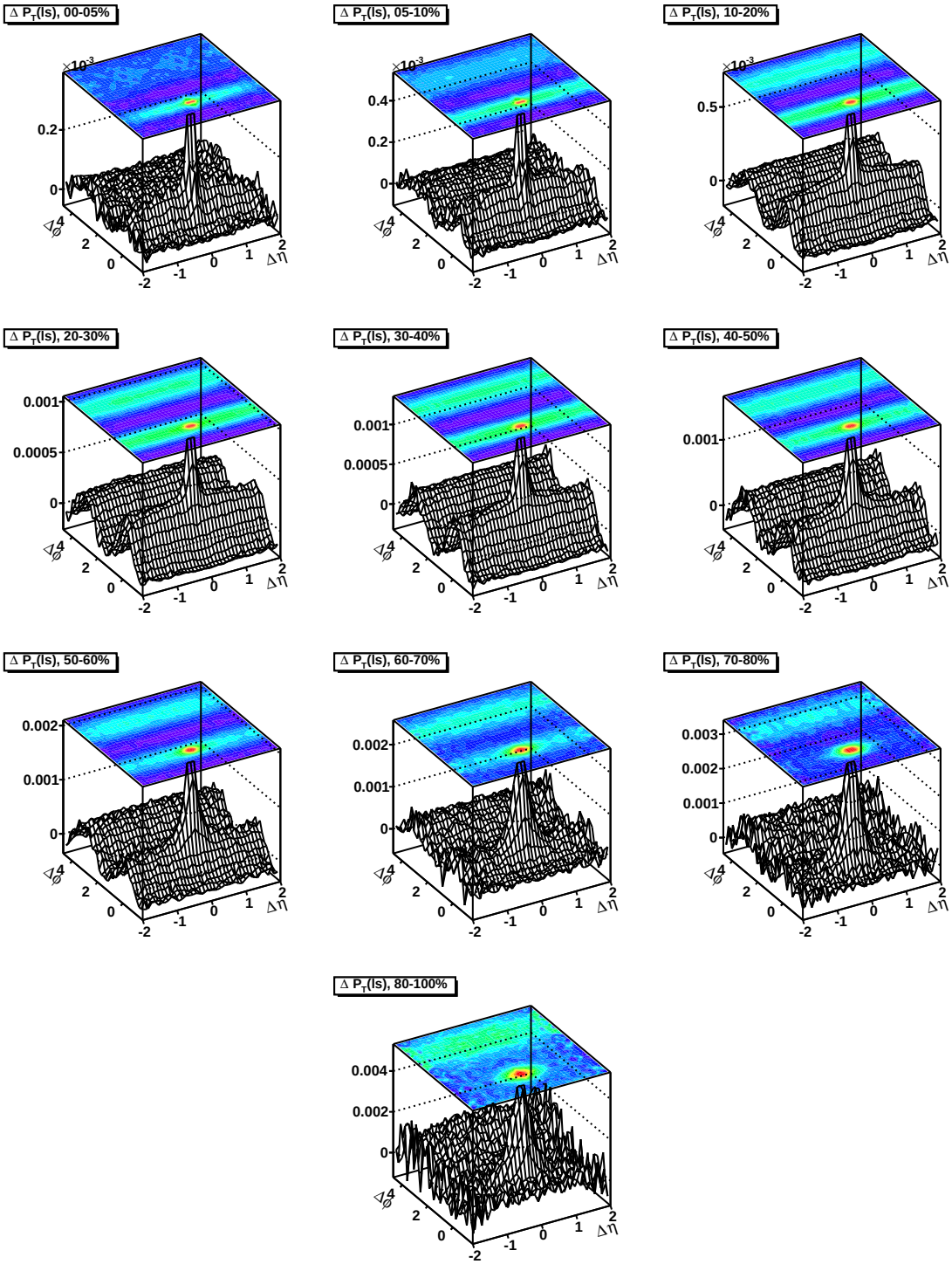

Figure 10.37: $\Delta {P_T}^{ls}(\Delta\eta, \Delta\phi)$

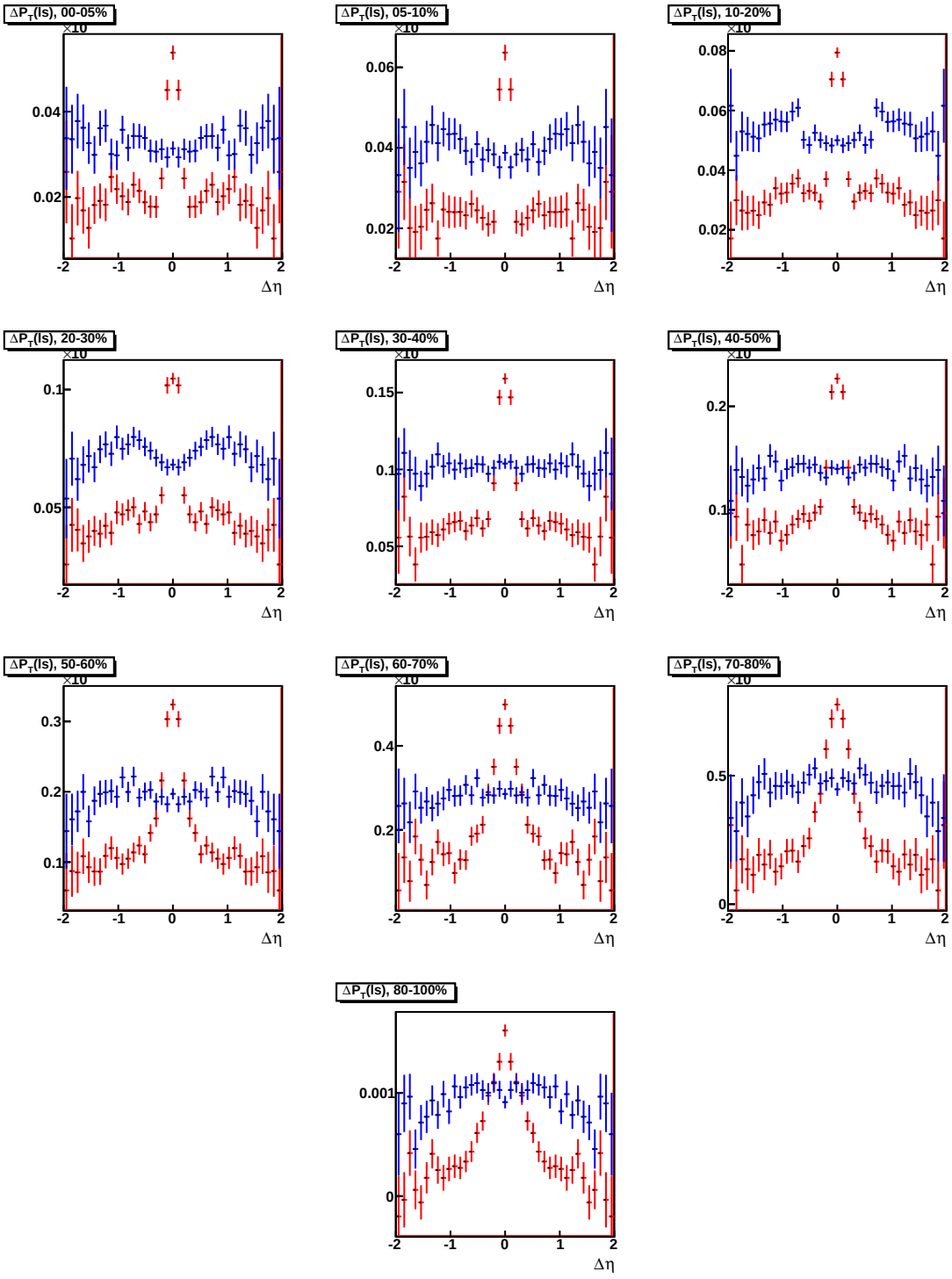

Figure 10.38: $\Delta {P_T}^{ls}(\Delta\eta)$

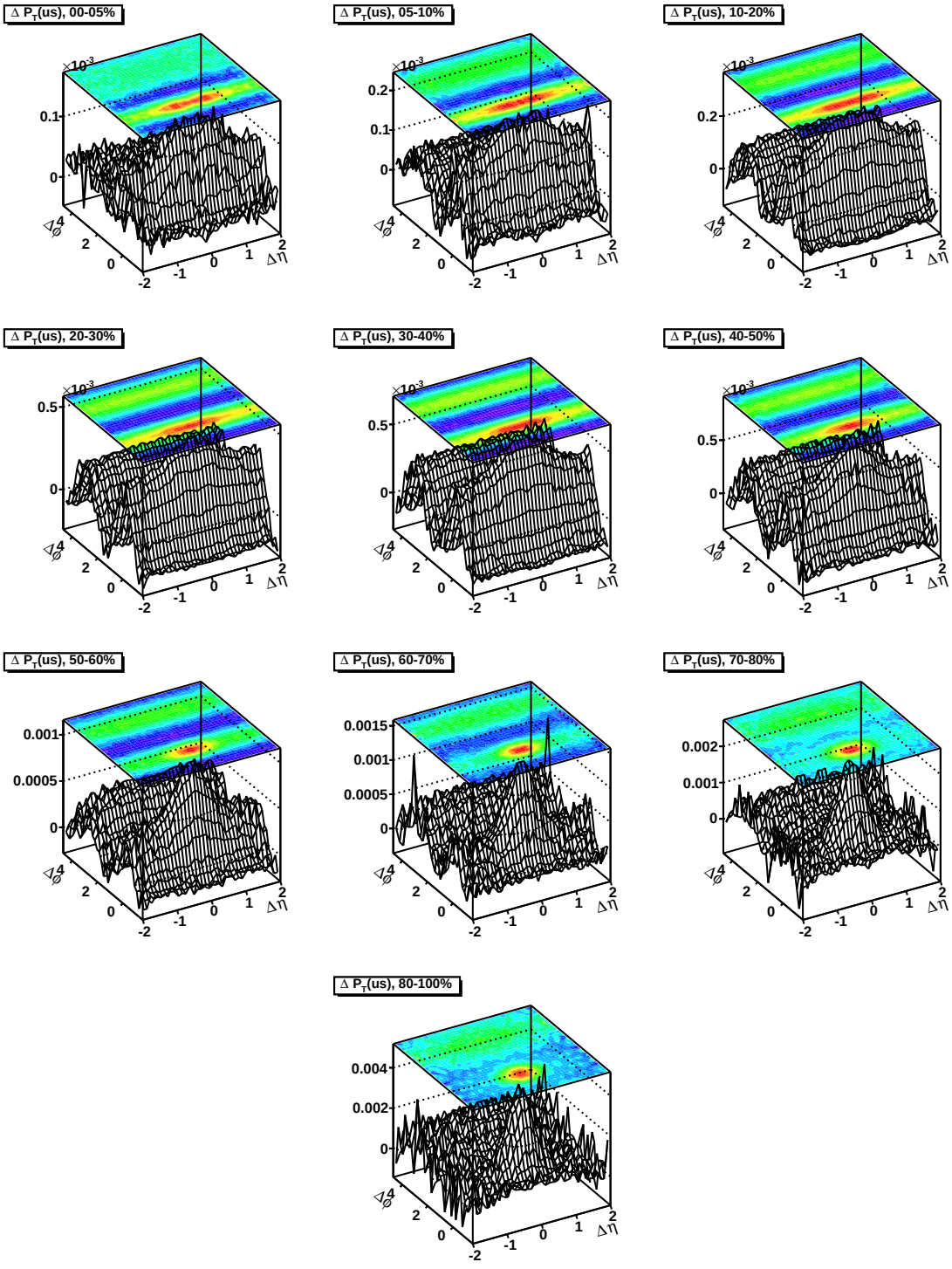

Figure 10.39: $\Delta {P_T}^{us}(\Delta\eta, \Delta\phi)$

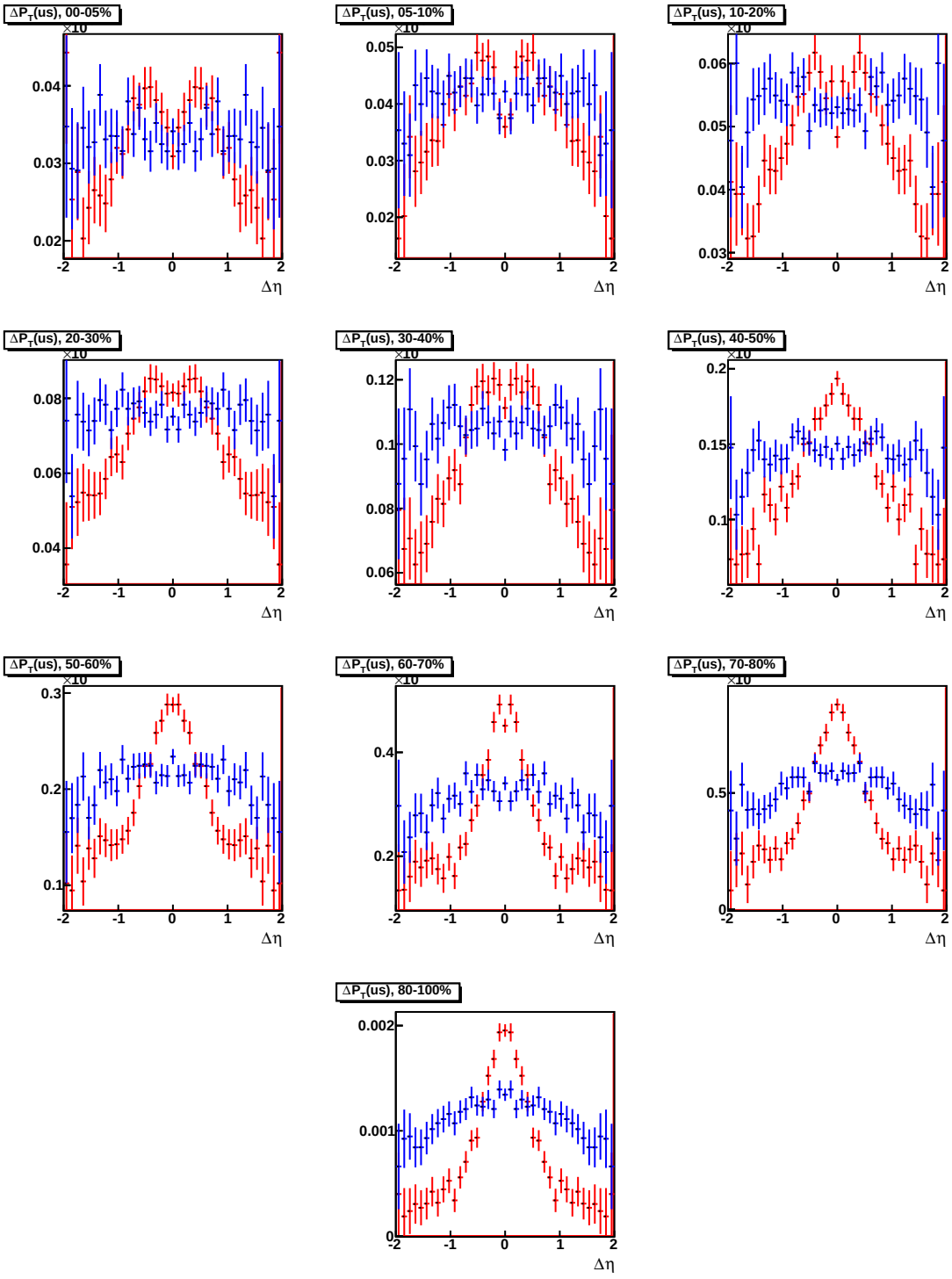

Figure 10.40: $\Delta {P_T}^{us}(\Delta\eta)$

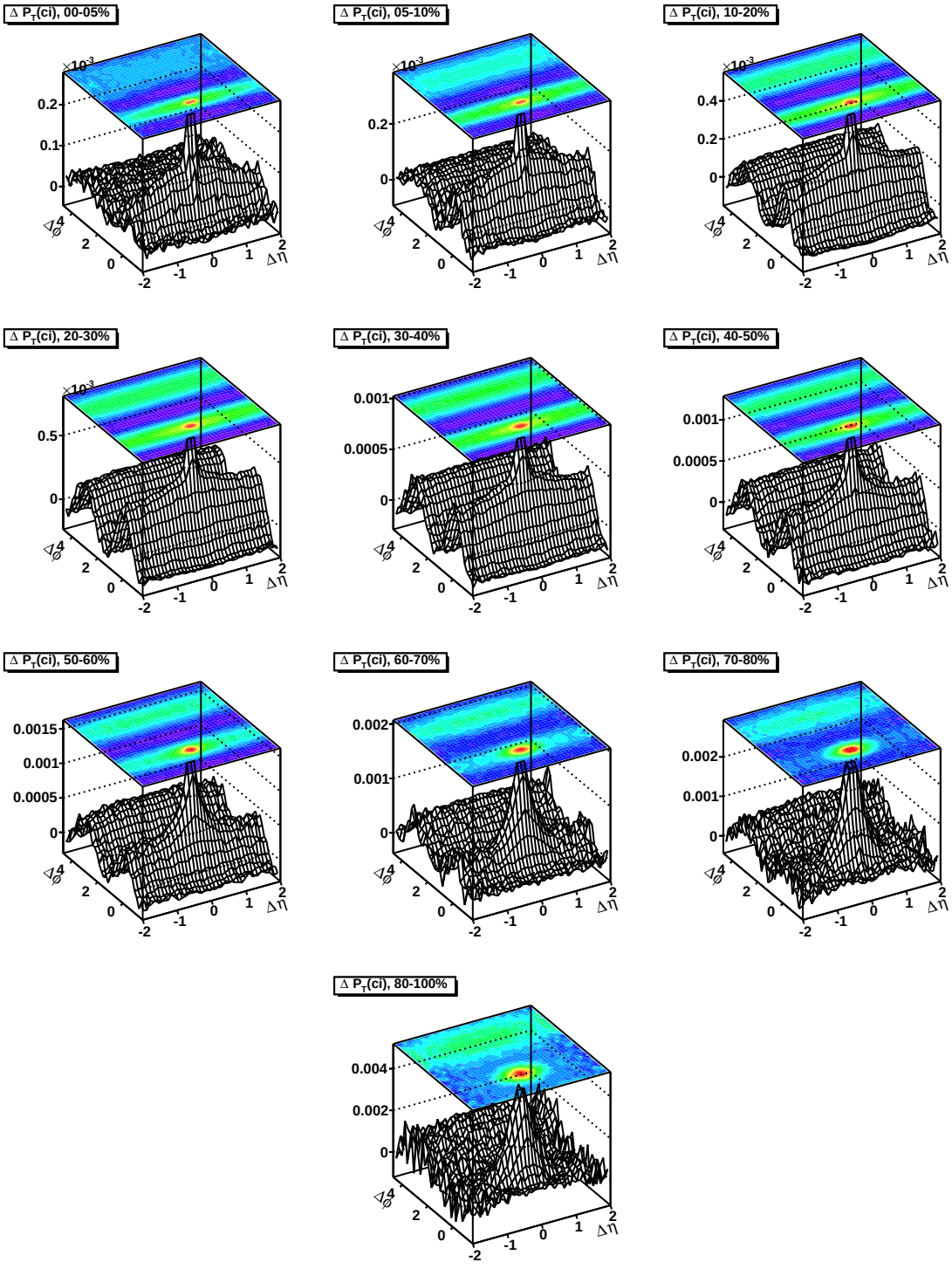

Figure 10.41: $\Delta {P_T}^{ci}(\Delta\eta, \Delta\phi)$

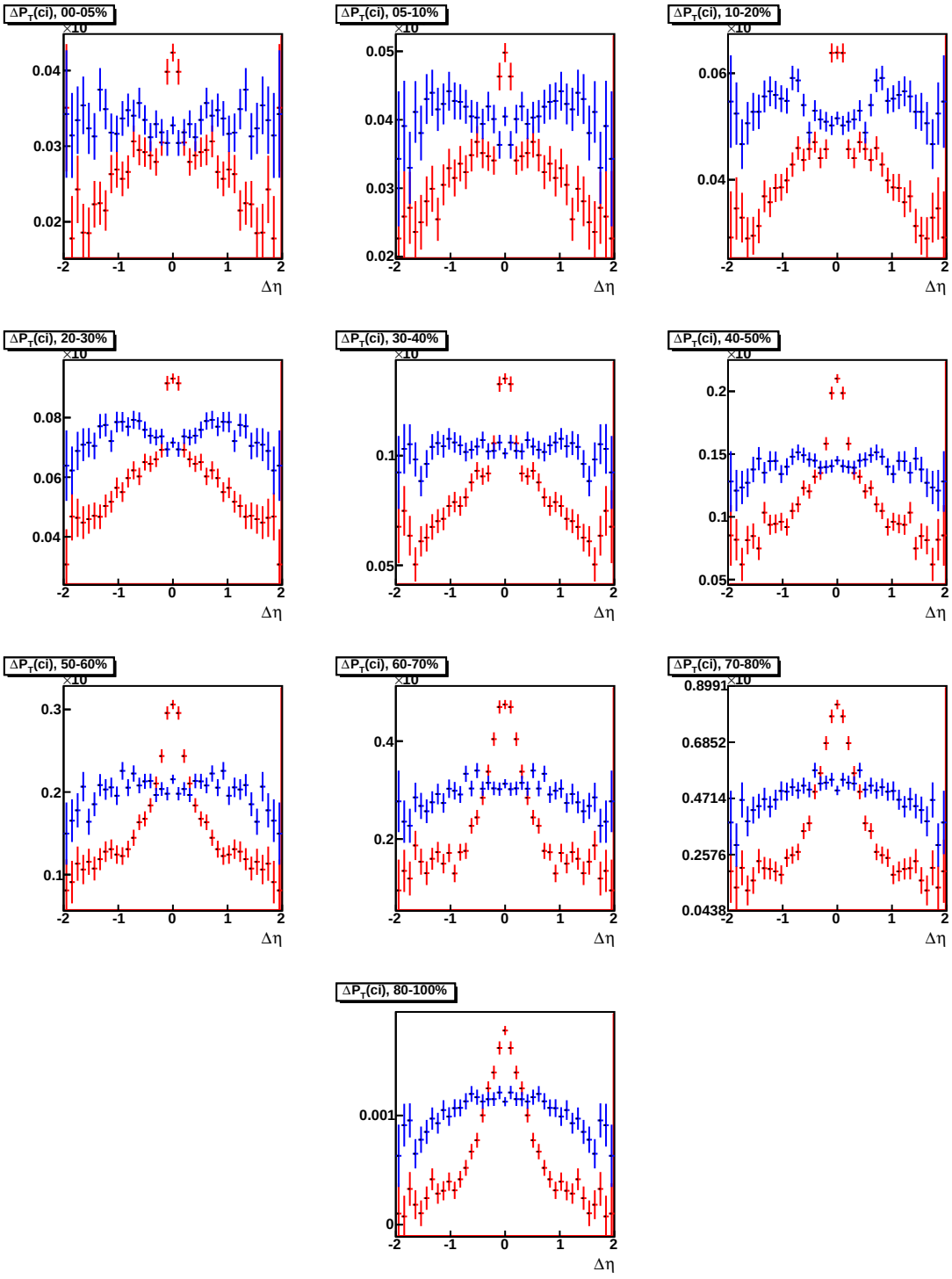

Figure 10.42: $\Delta P_T{}^{ci}(\Delta\eta)$

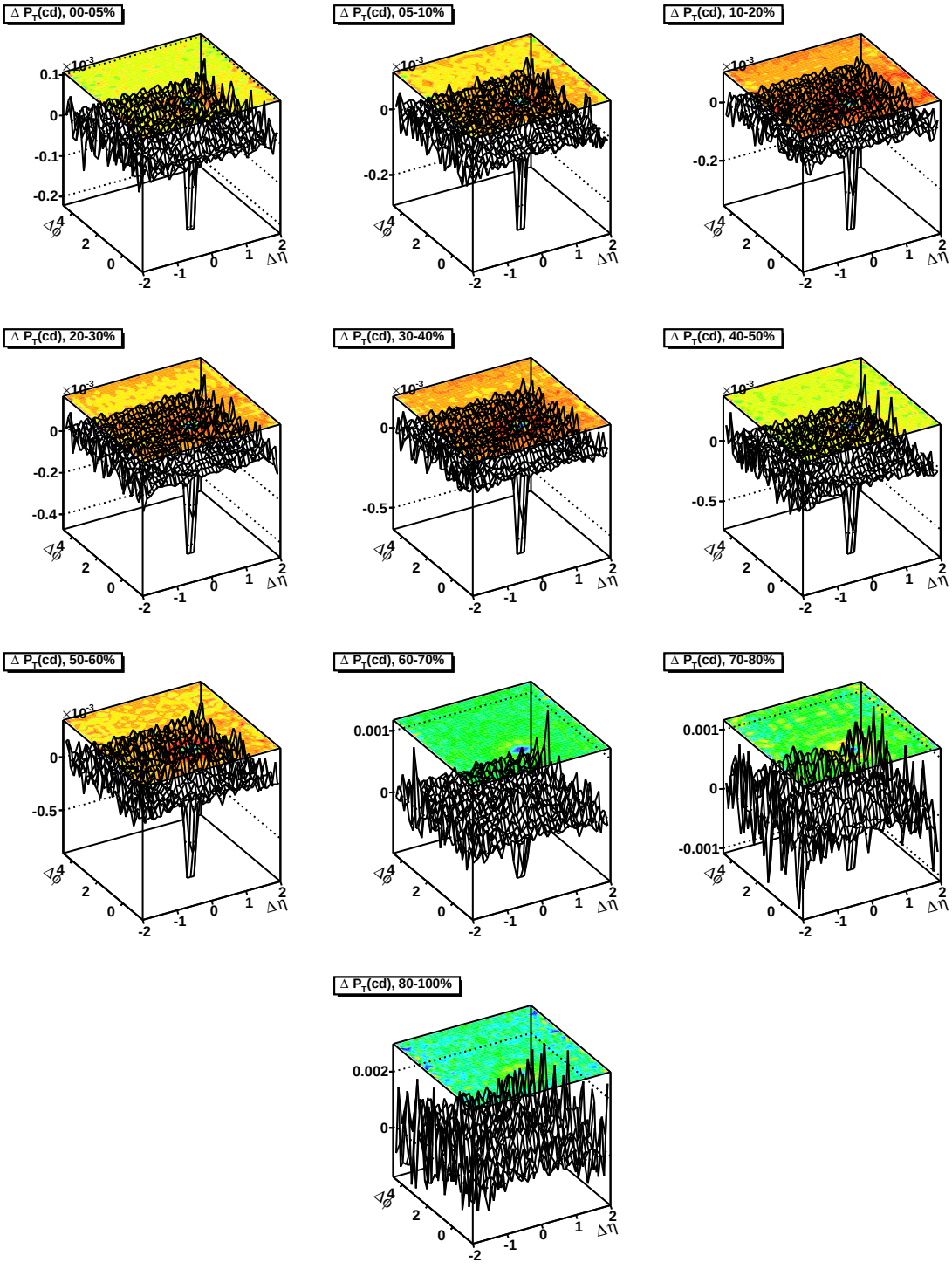

Figure 10.43: $\Delta {P_T}^{cd}(\Delta\eta, \Delta\phi)$

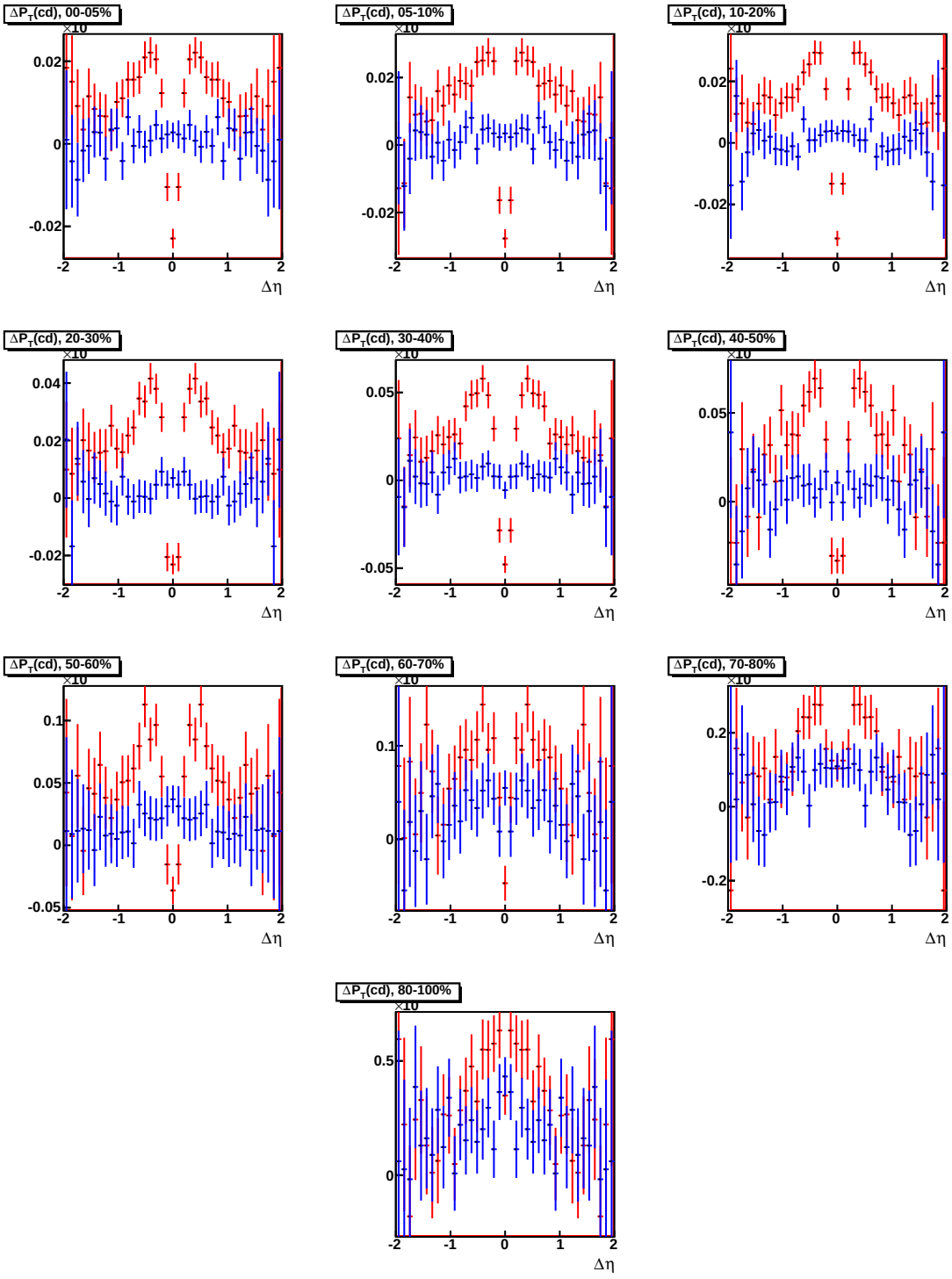

Figure 10.44: $\Delta P_T{}^{cd}(\Delta\eta)$

10.4 Inclusive Correlations, Both Fields, ls/us/ci/cd

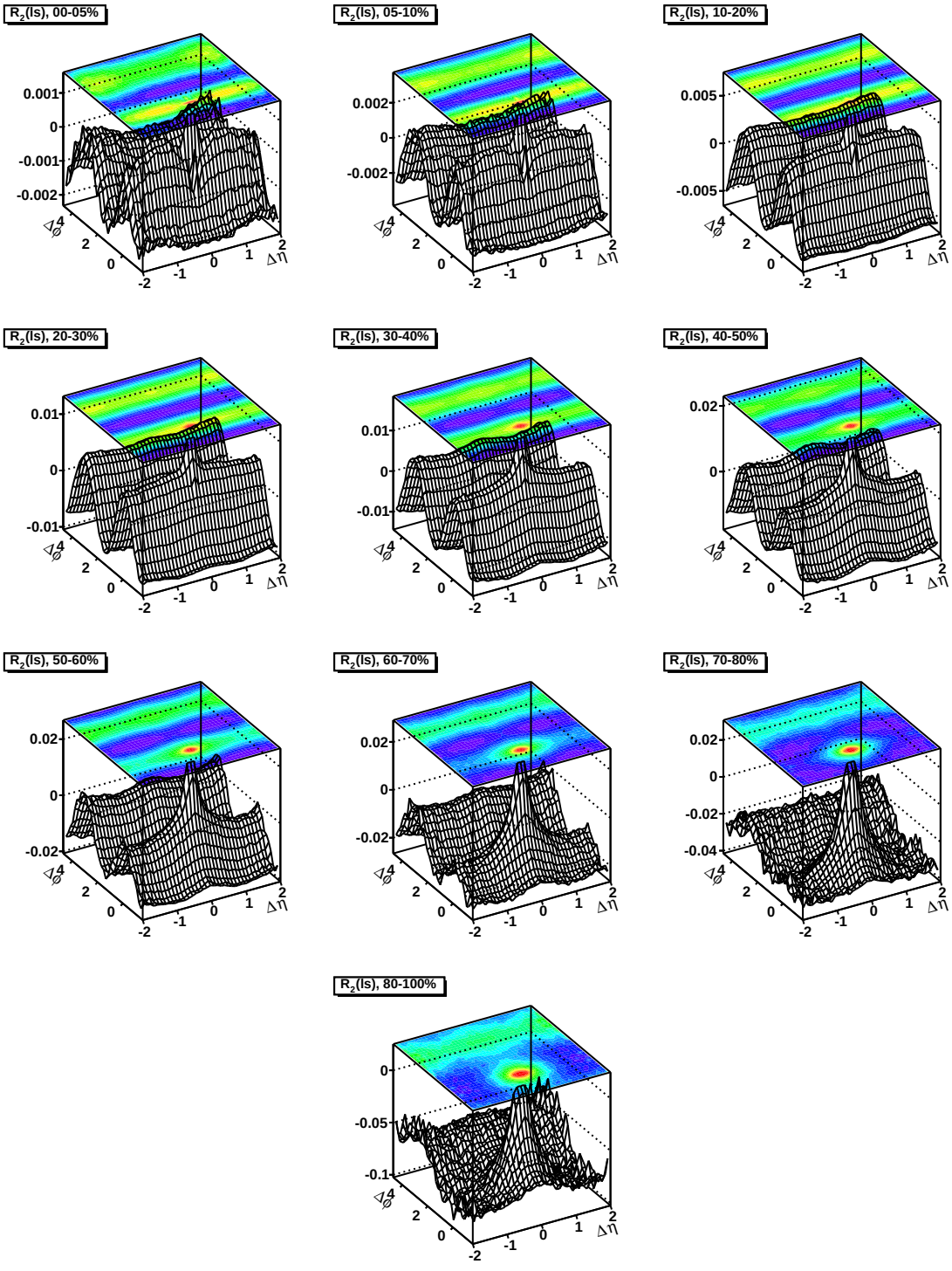

Figure 10.45: $R_2^{ls}(\Delta\eta, \Delta\phi)$

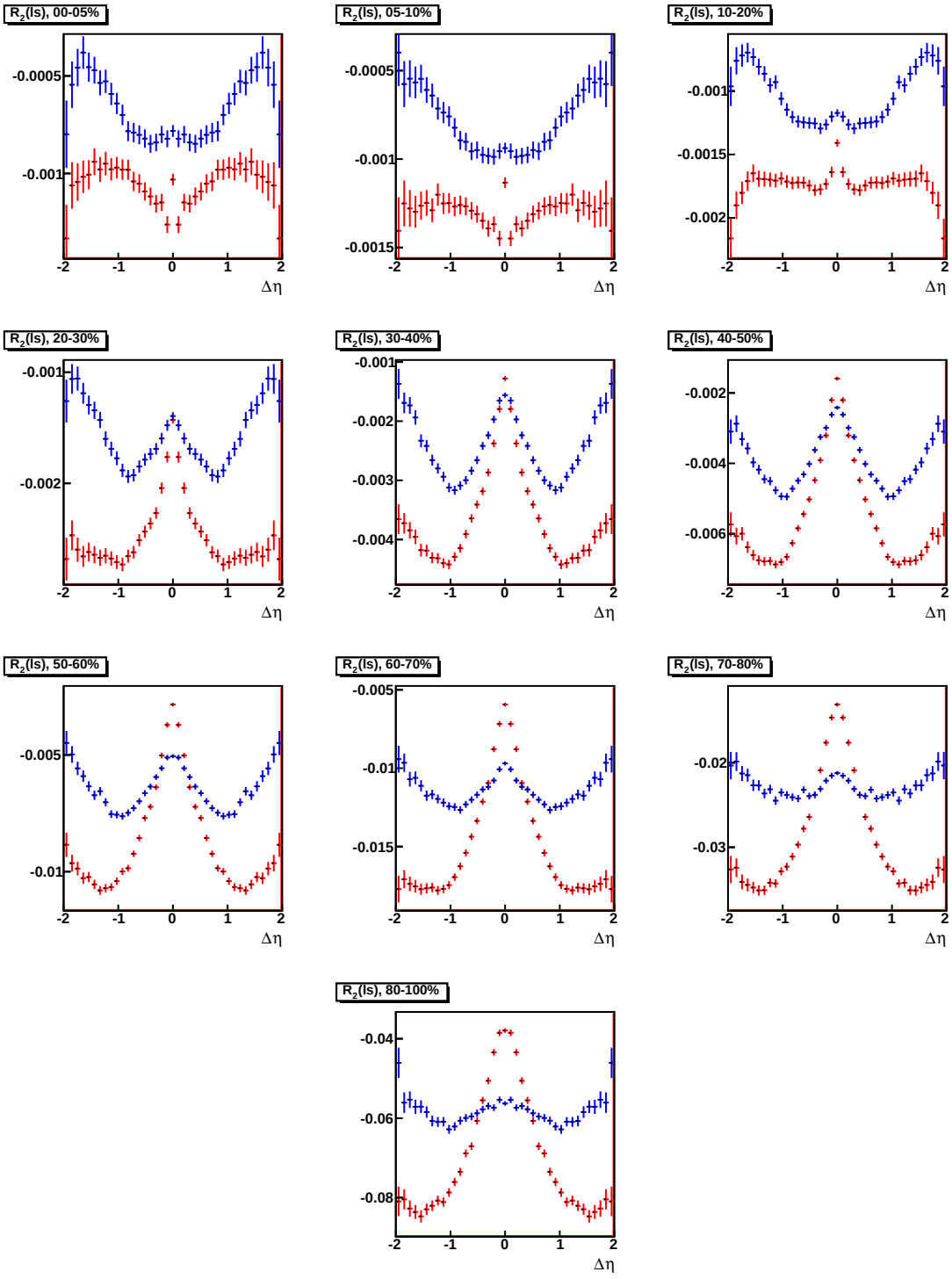

Figure 10.46: $R_2^{ls}(\Delta\eta)$

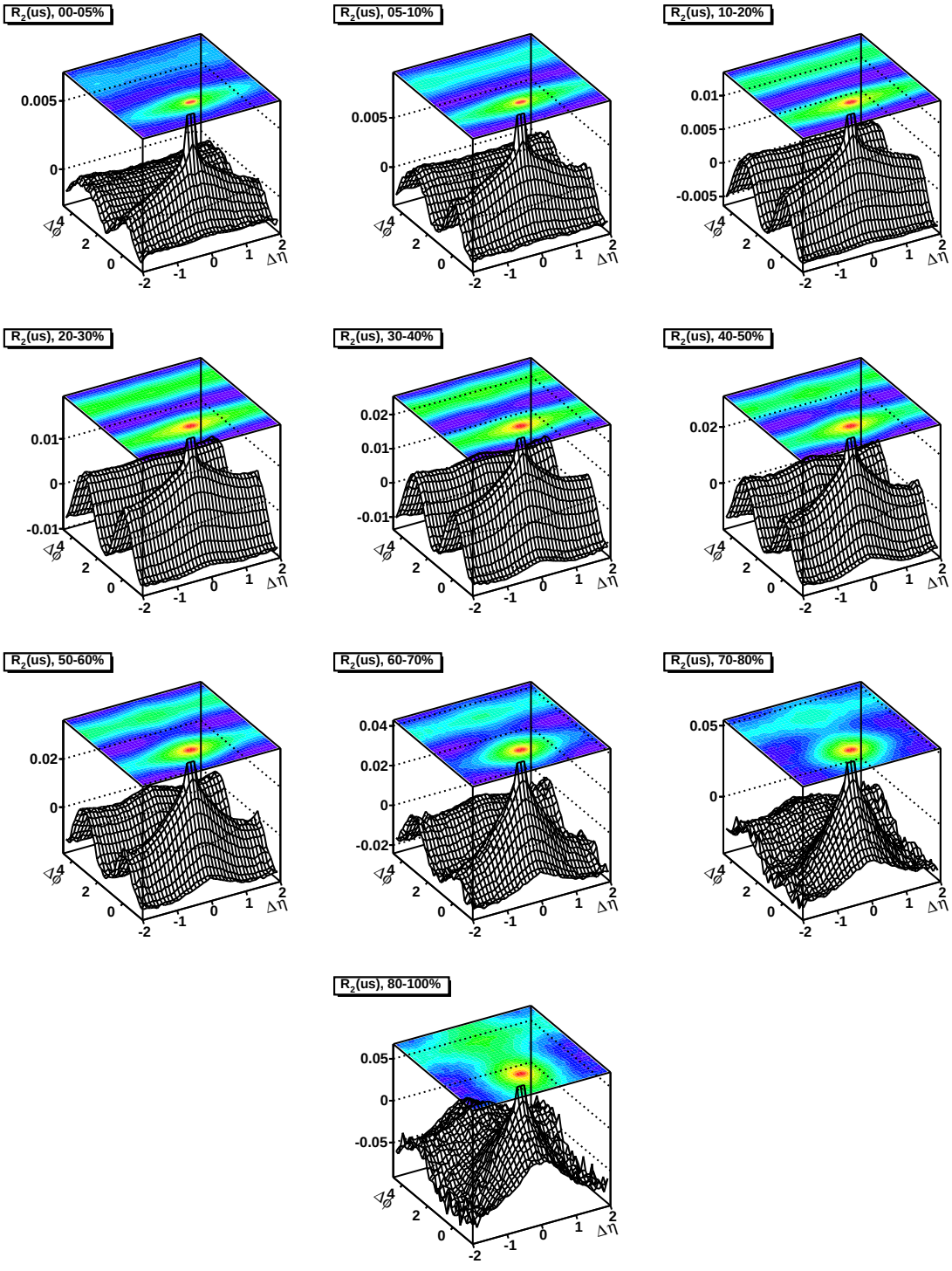

Figure 10.47: $R_2^{us}(\Delta\eta, \Delta\phi)$

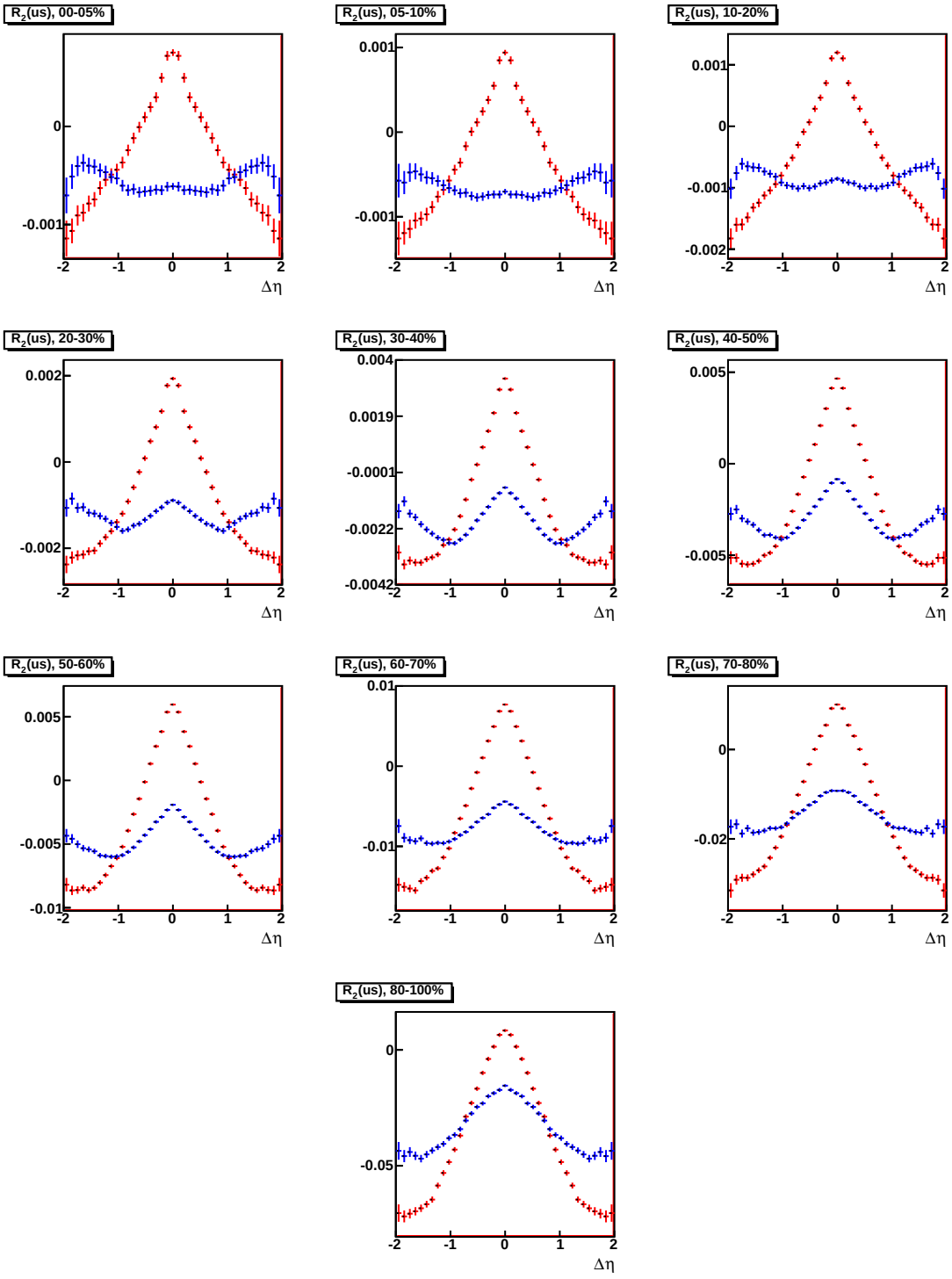

Figure 10.48: $R_2^{us}(\Delta\eta)$

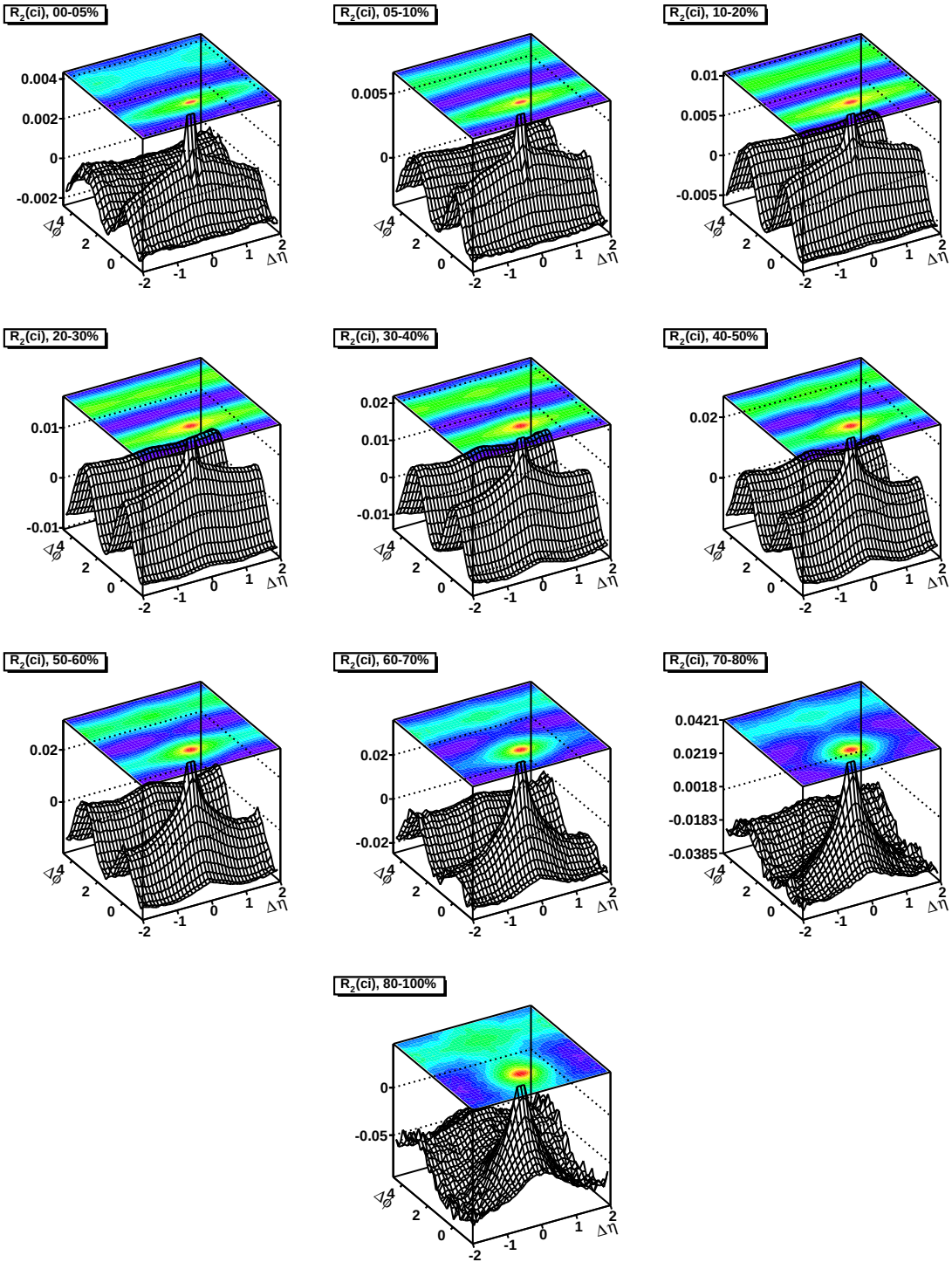

Figure 10.49: $R_2^{ci}(\Delta\eta, \Delta\phi)$

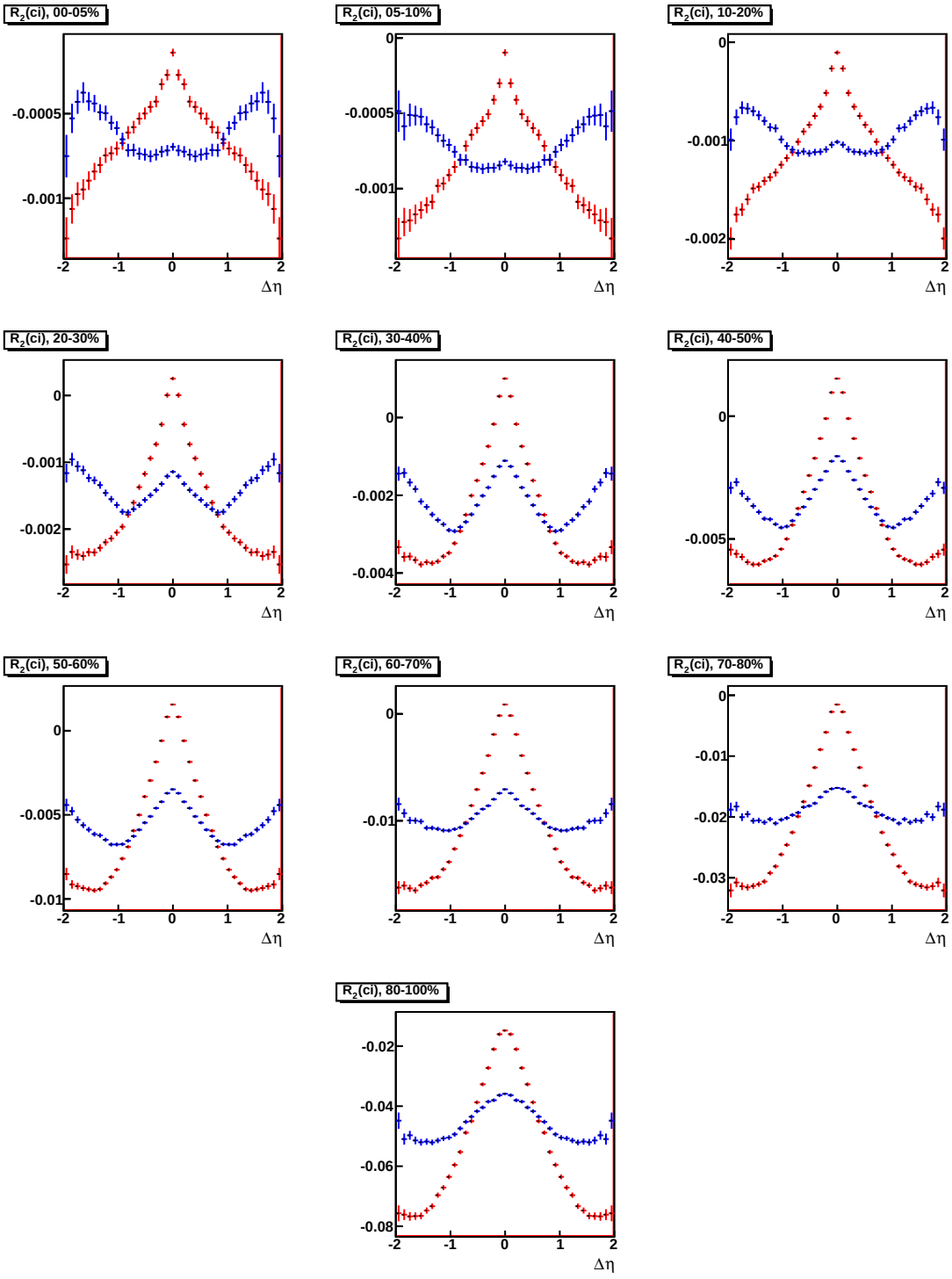

Figure 10.50: $R_2^{ci}(\Delta\eta)$

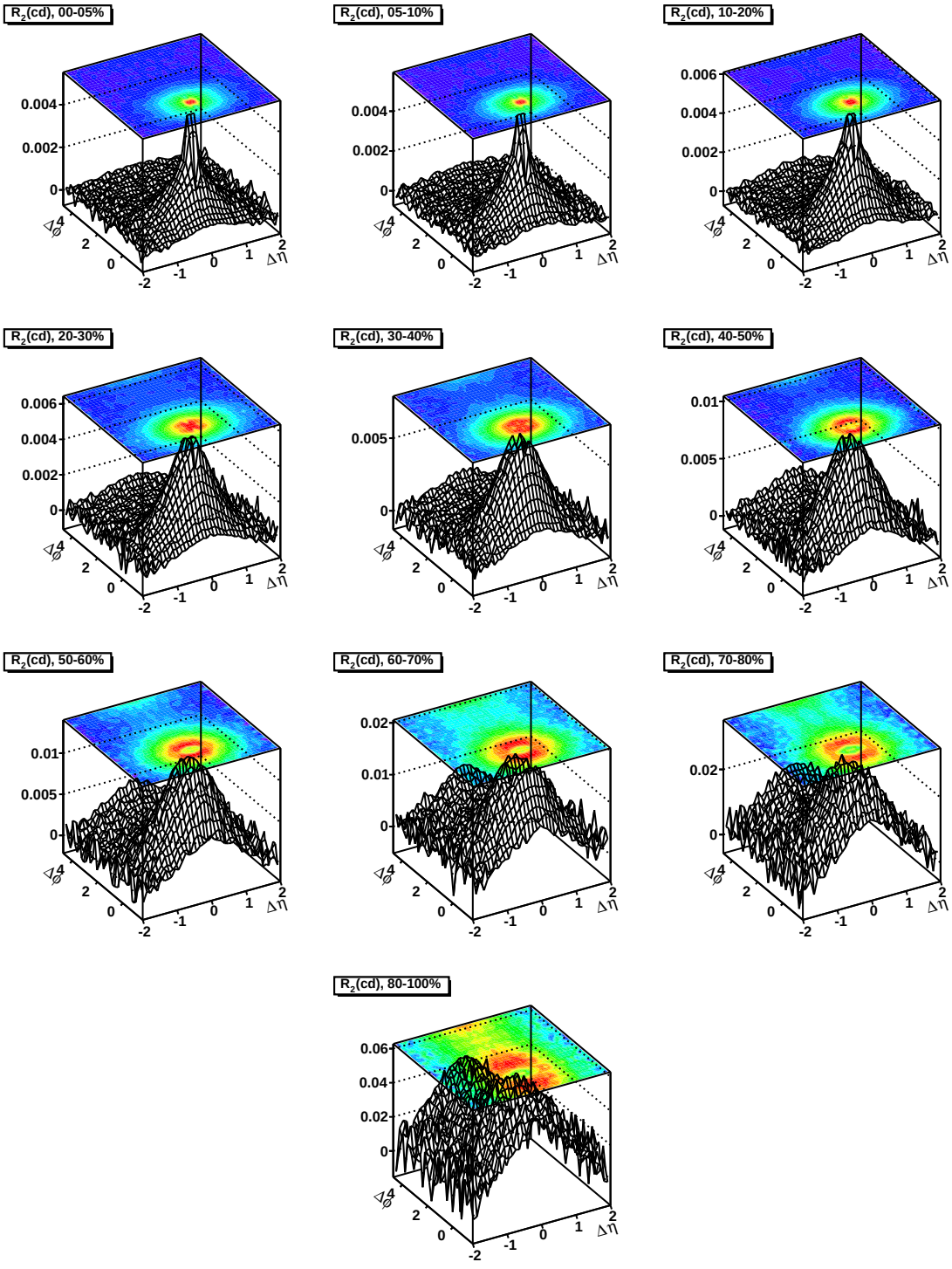

Figure 10.51: $R_2^{cd}(\Delta\eta, \Delta\phi)$

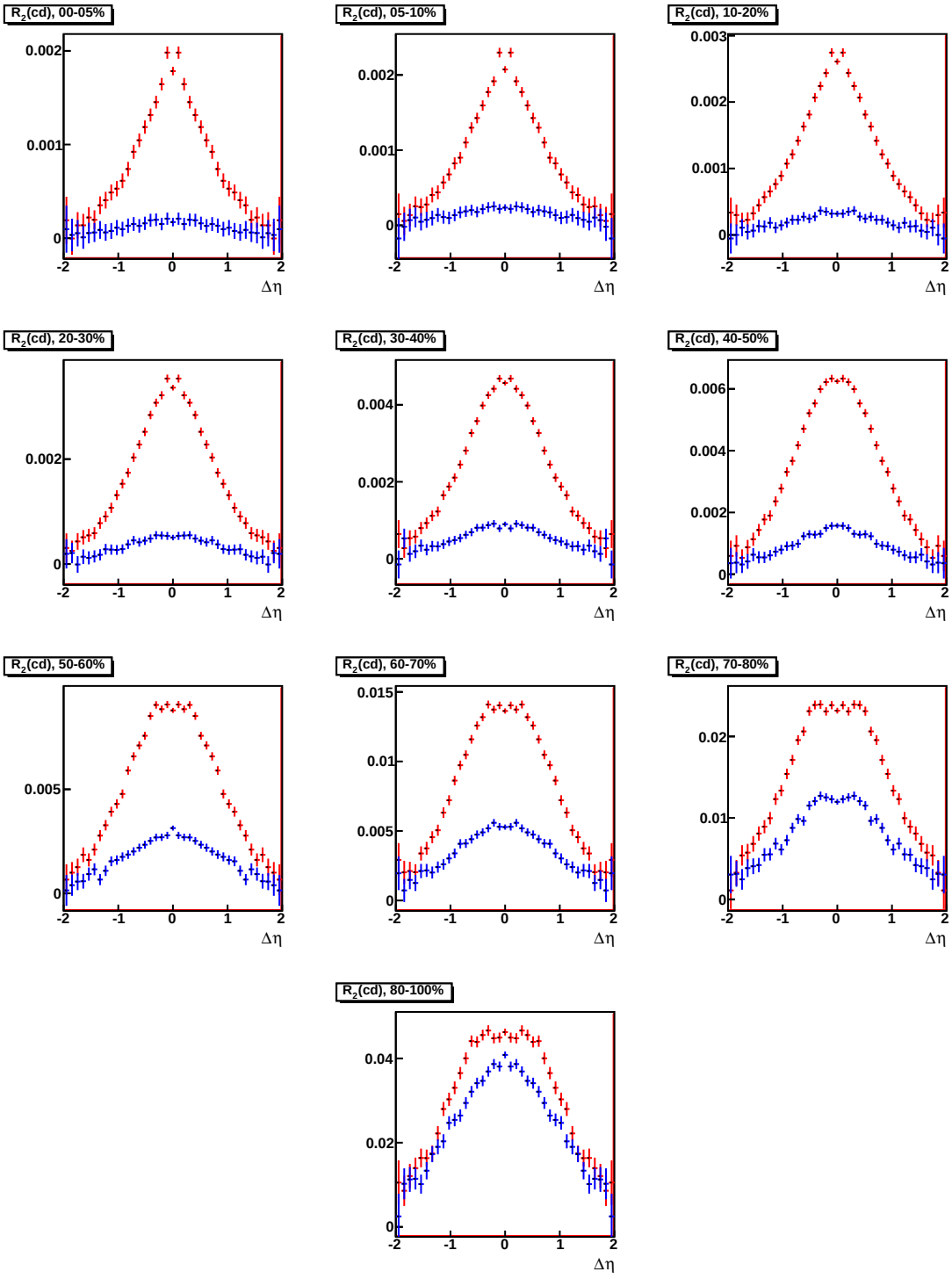

Figure 10.52: $R_2^{cd}(\Delta\eta)$

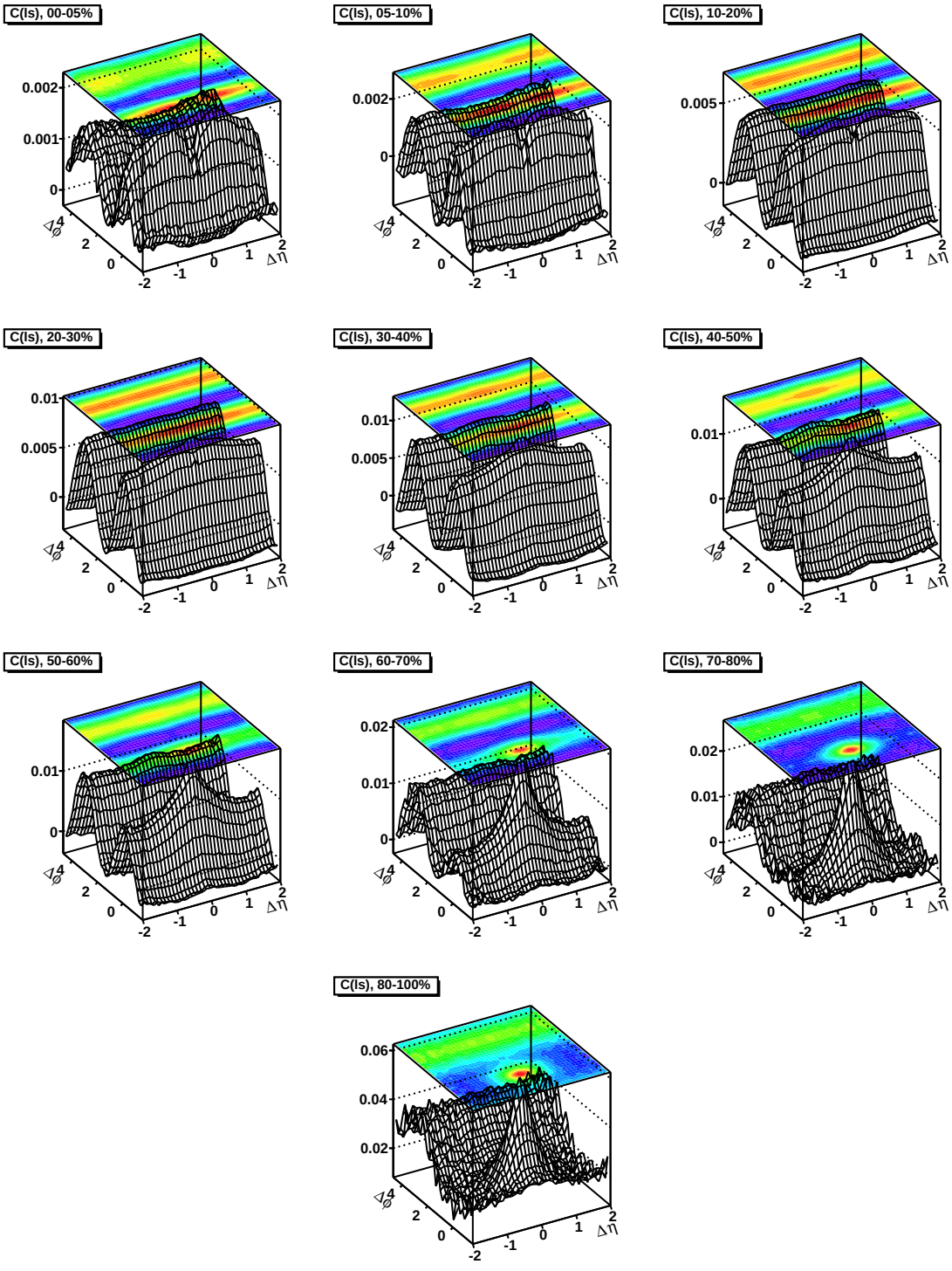

Figure 10.53: $C^{ls}(\Delta\eta, \Delta\phi)$

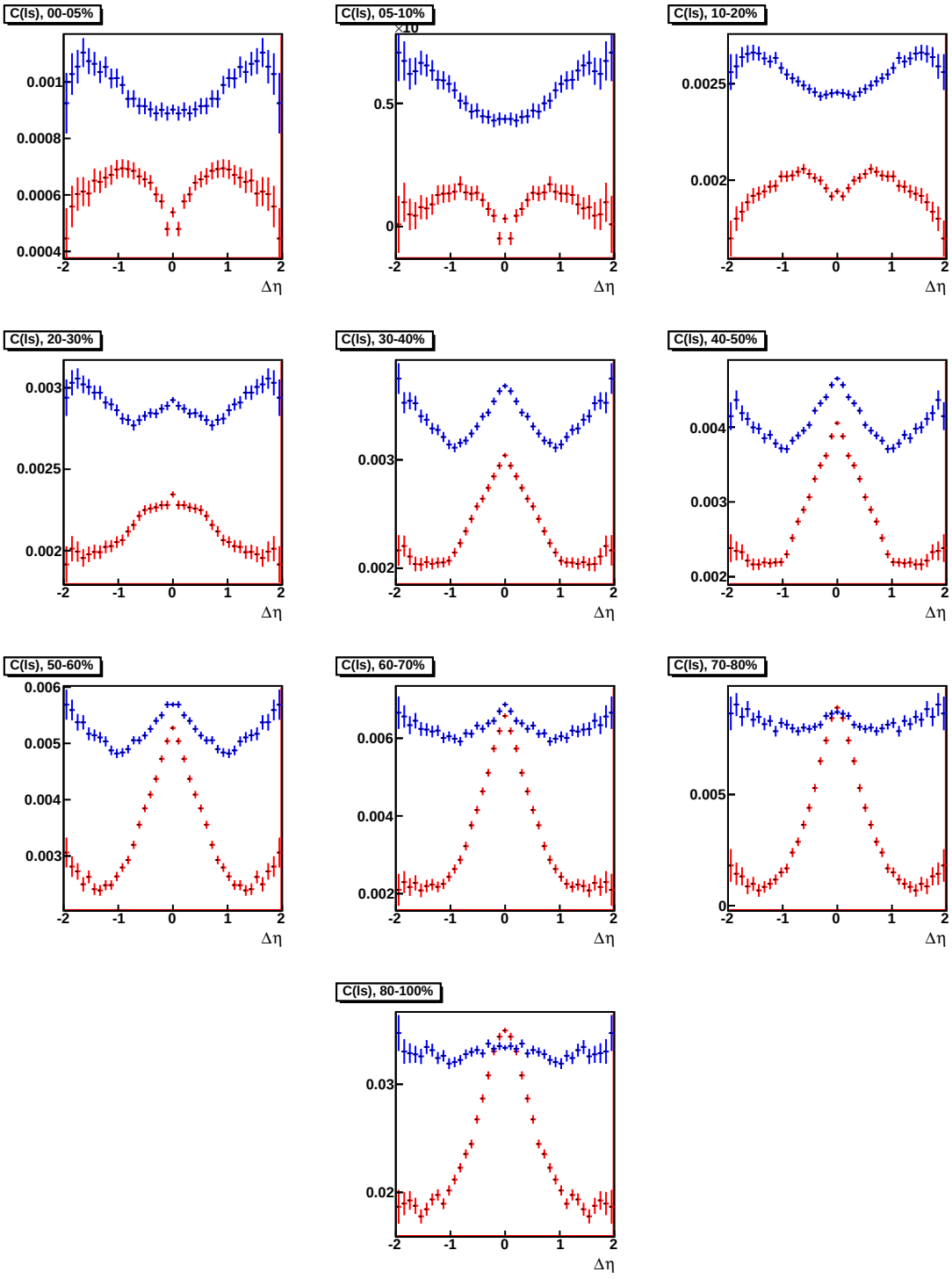

Figure 10.54: $C^{ls}(\Delta\eta)$

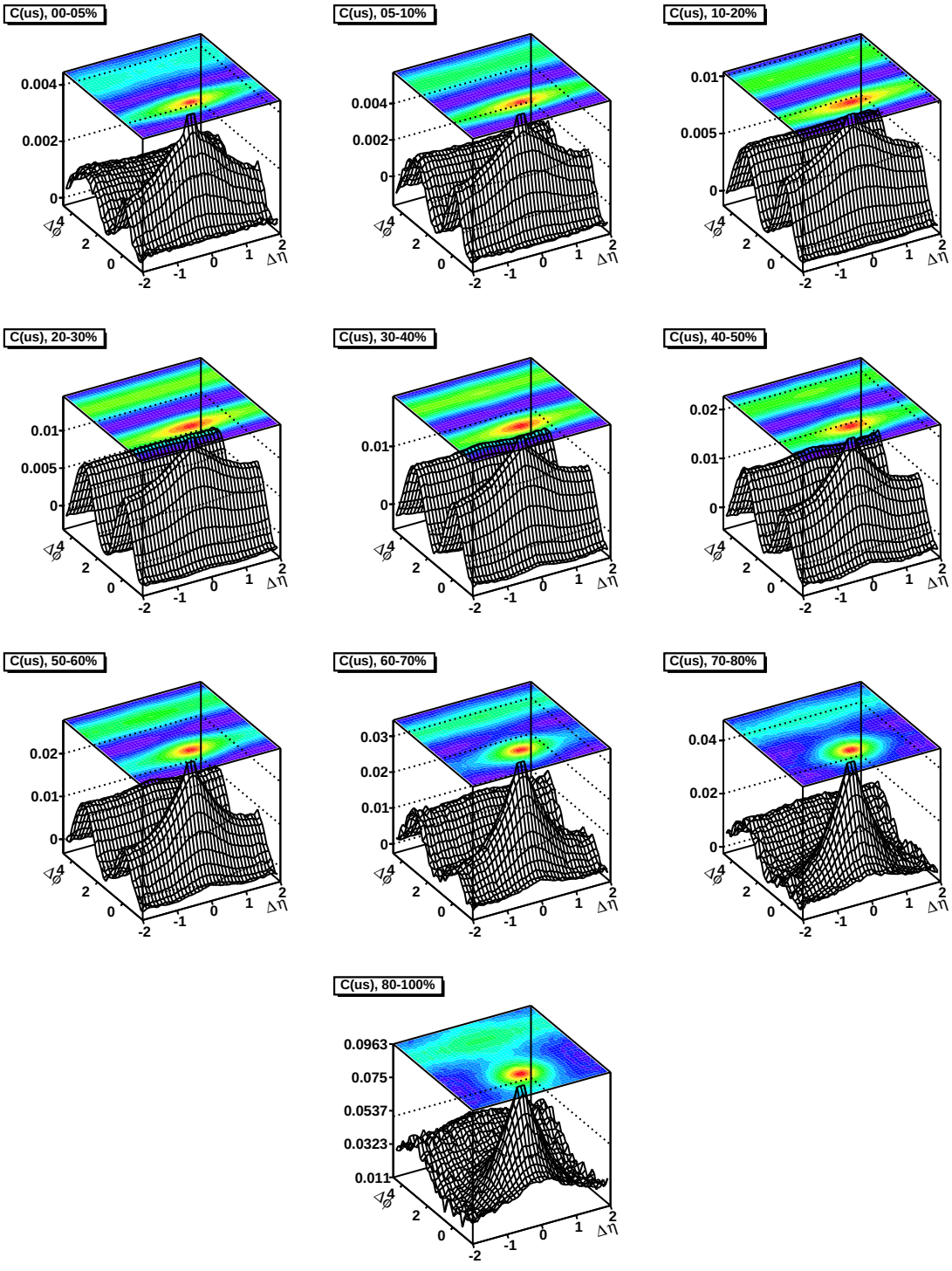

Figure 10.55: $C^{us}(\Delta\eta, \Delta\phi)$

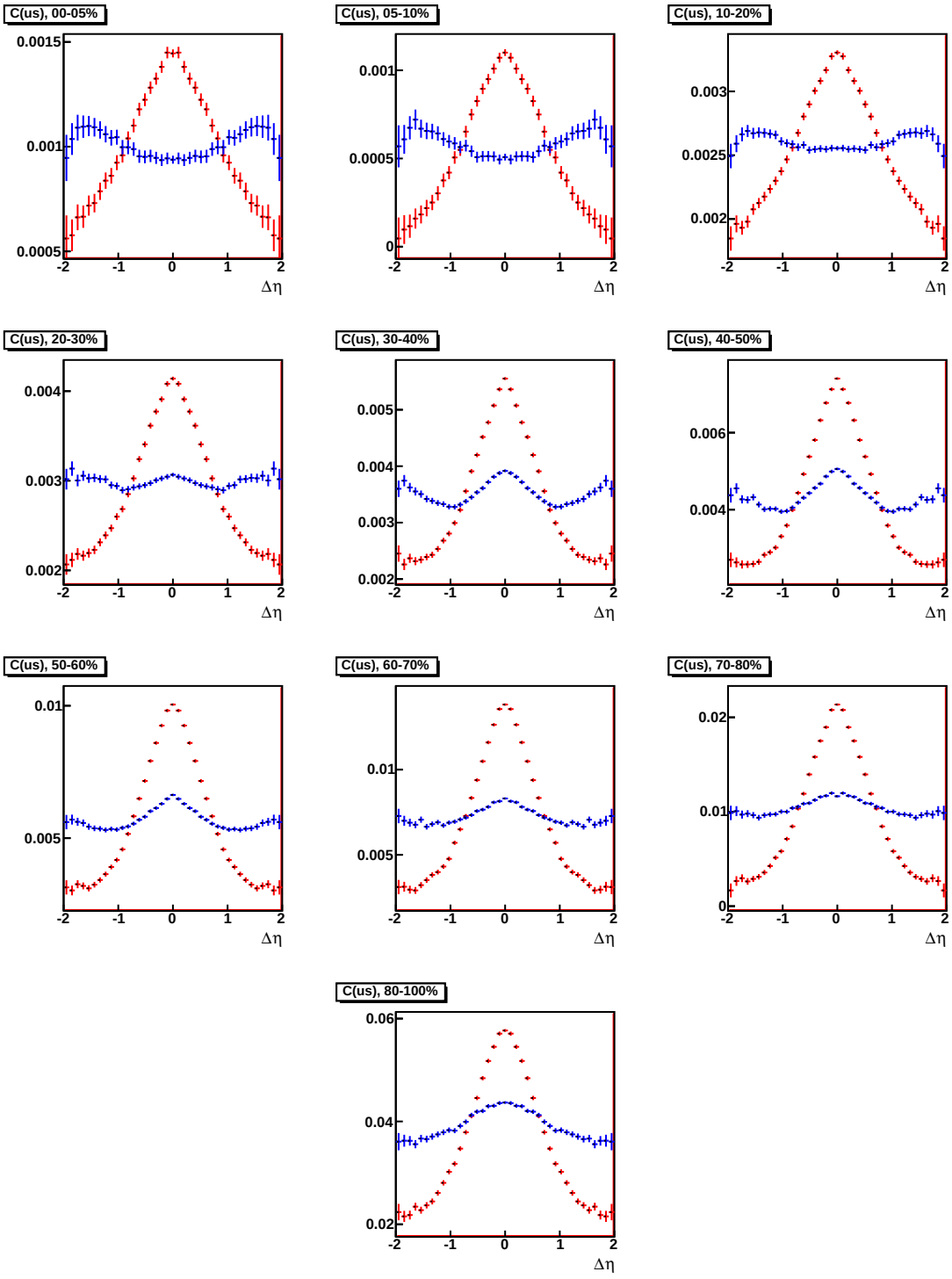

Figure 10.56: $C^{us}(\Delta\eta)$

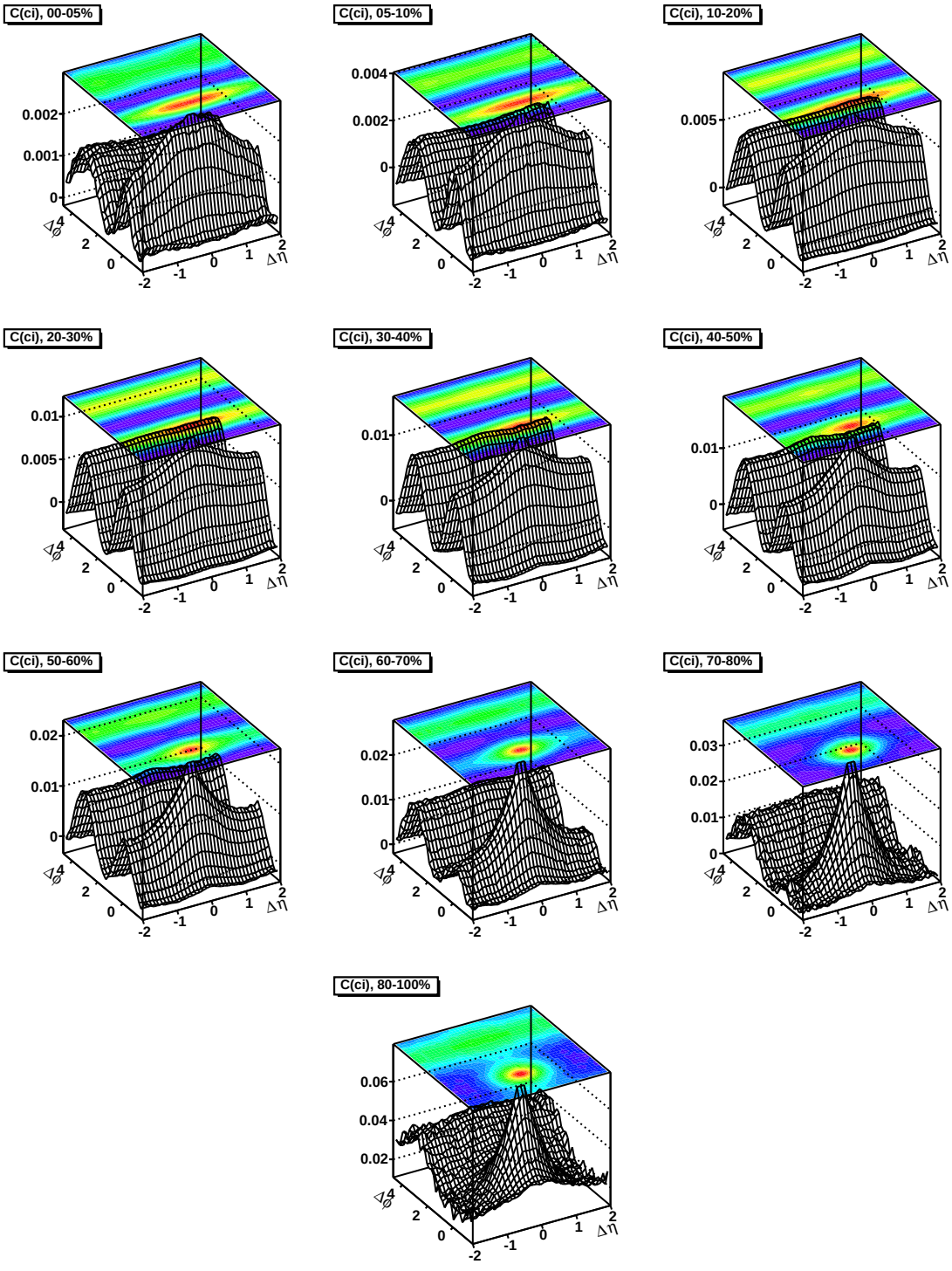

Figure 10.57: $C^{ci}(\Delta\eta, \Delta\phi)$

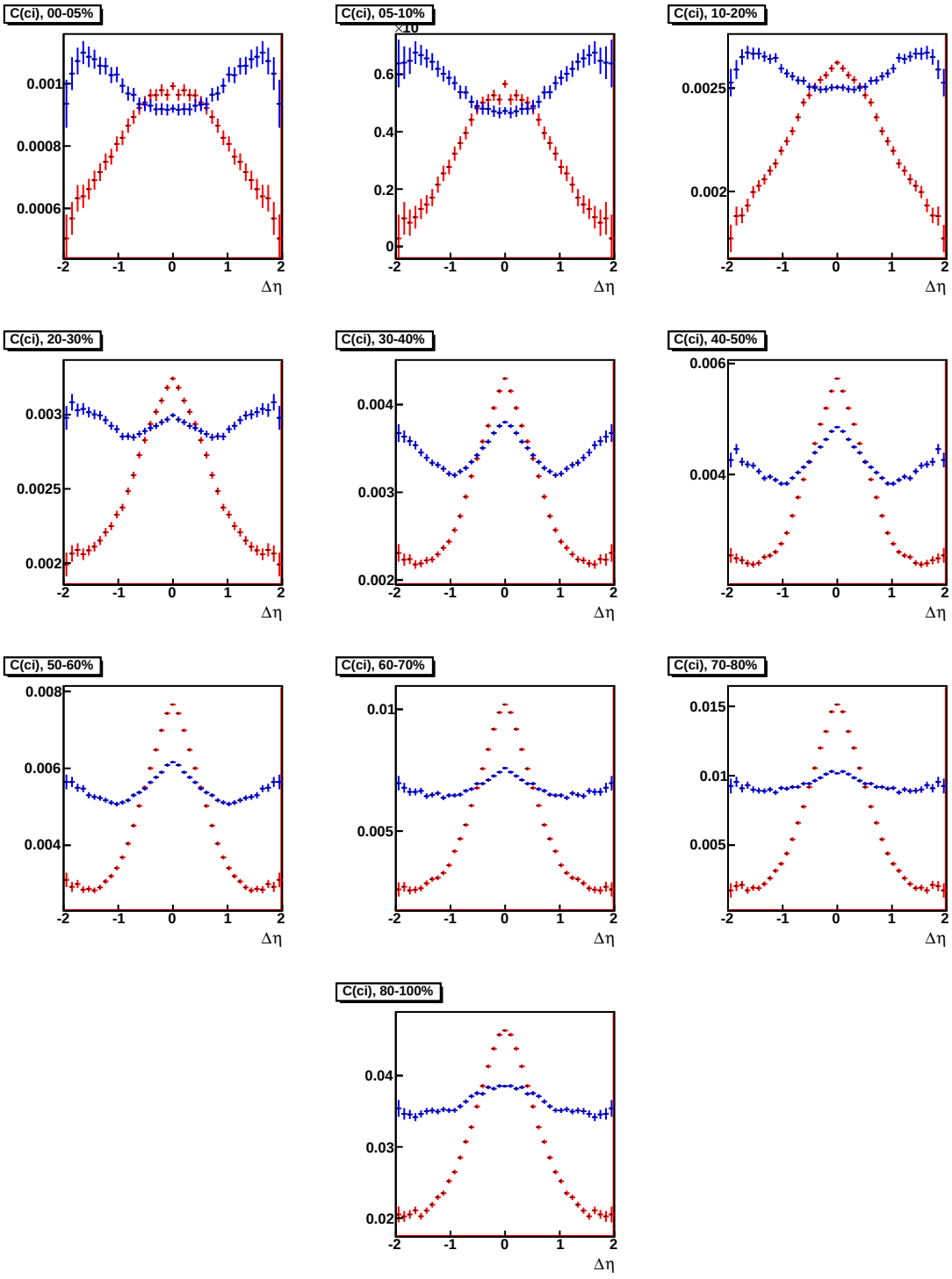

Figure 10.58: $C^{ci}(\Delta\eta)$

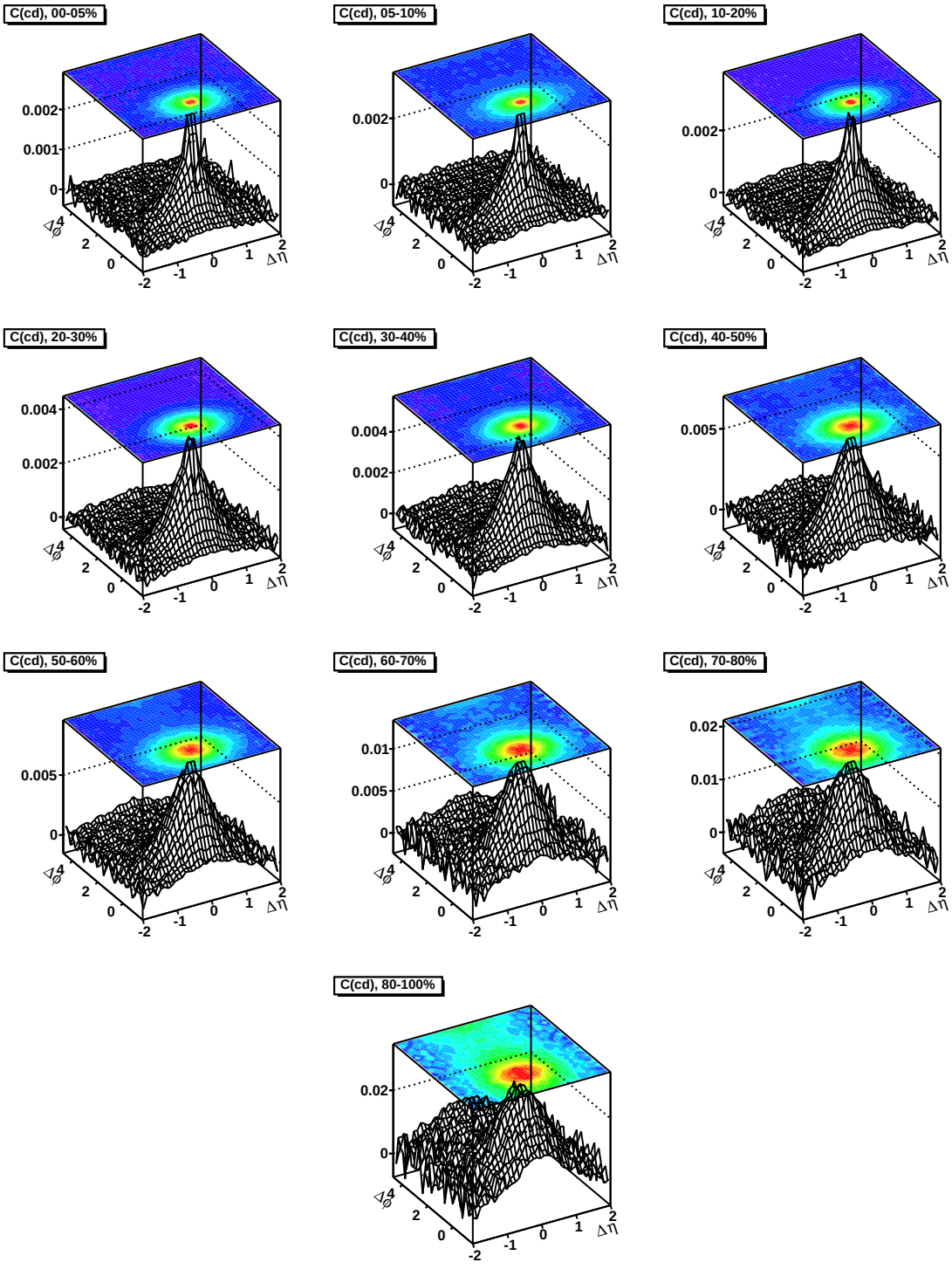

Figure 10.59: $C^{cd}(\Delta\eta, \Delta\phi)$

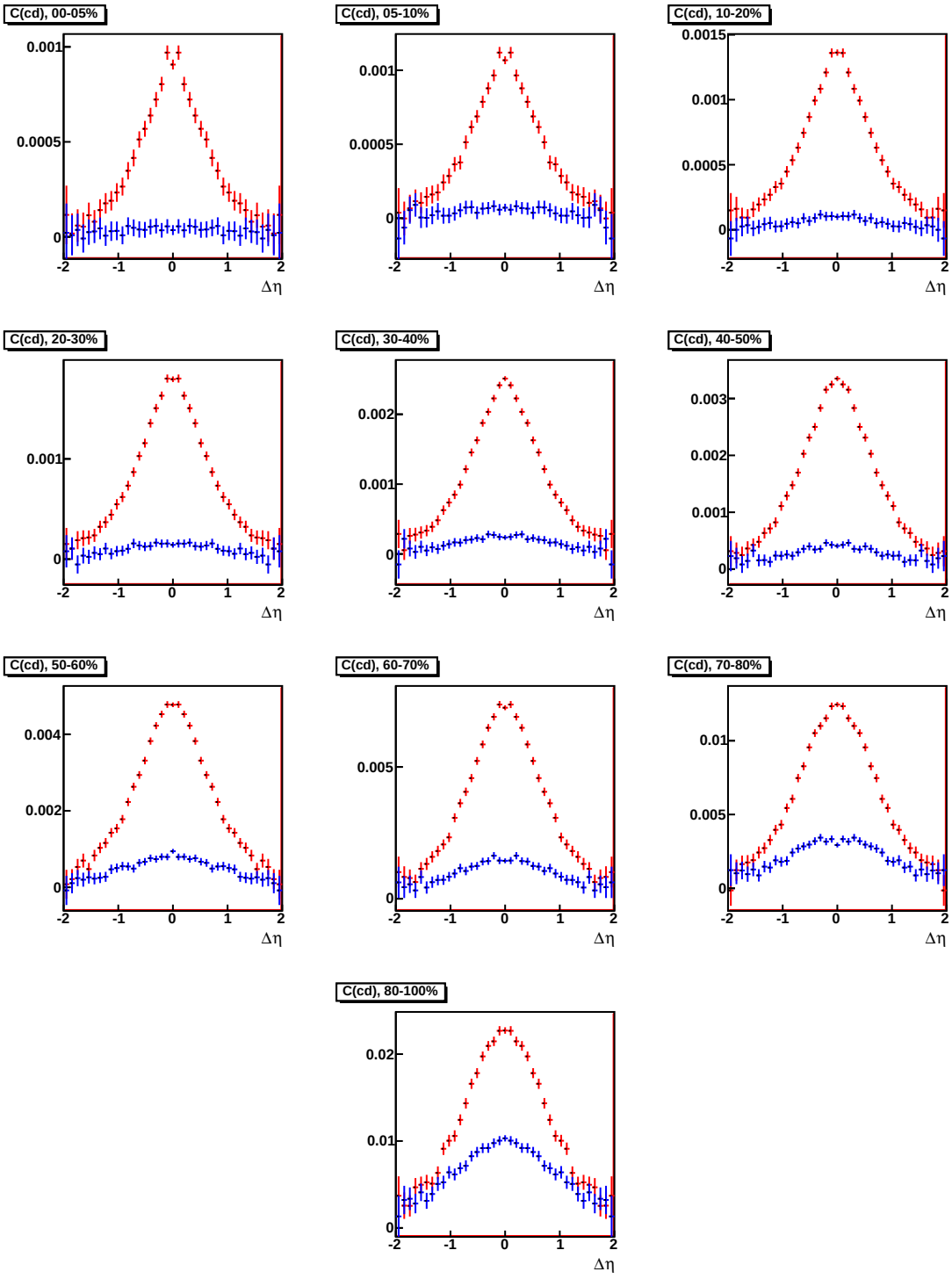

Figure 10.60: $C^{cd}(\Delta\eta)$

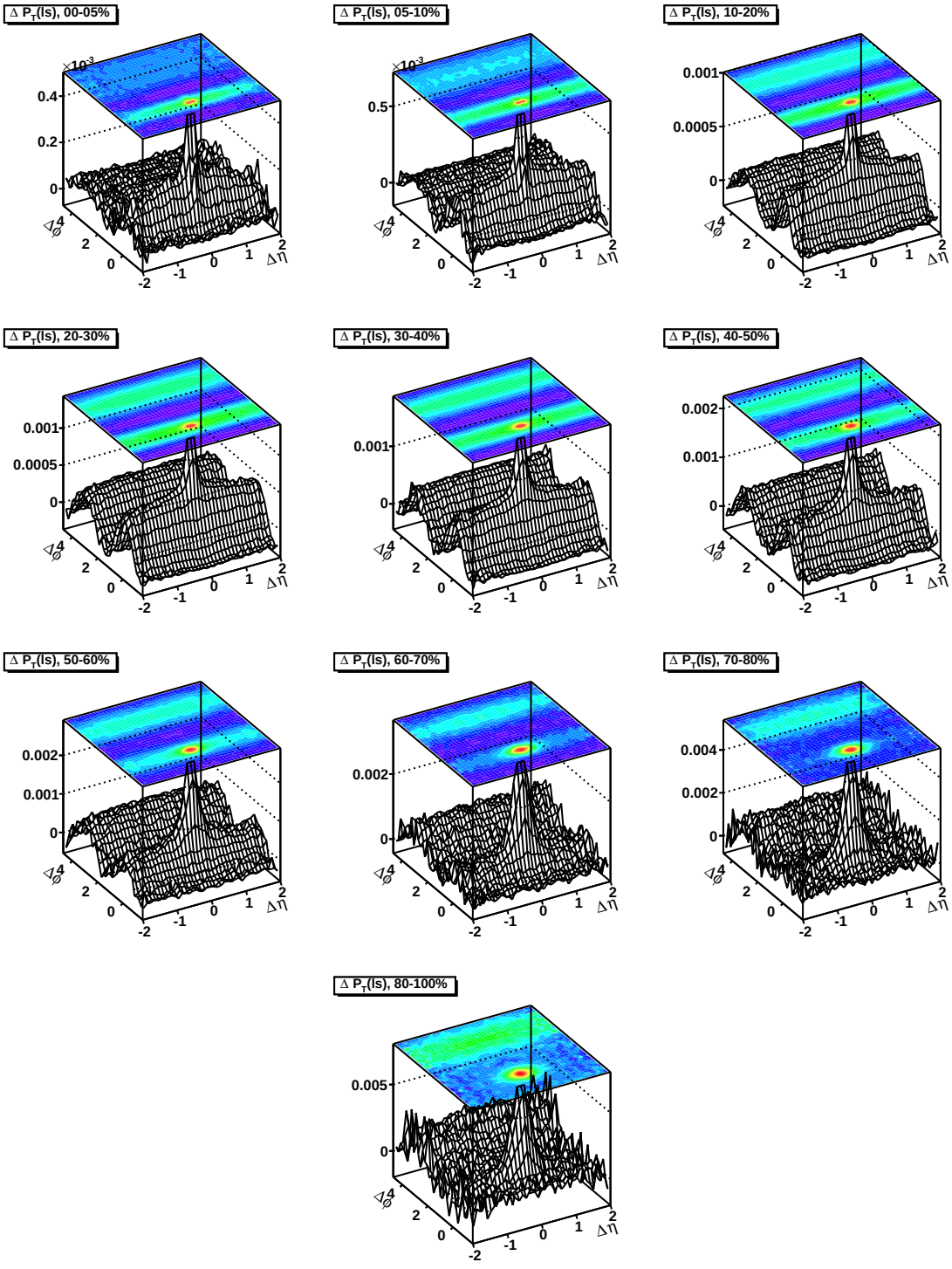

Figure 10.61: $\Delta {P_T}^{ls}(\Delta\eta, \Delta\phi)$

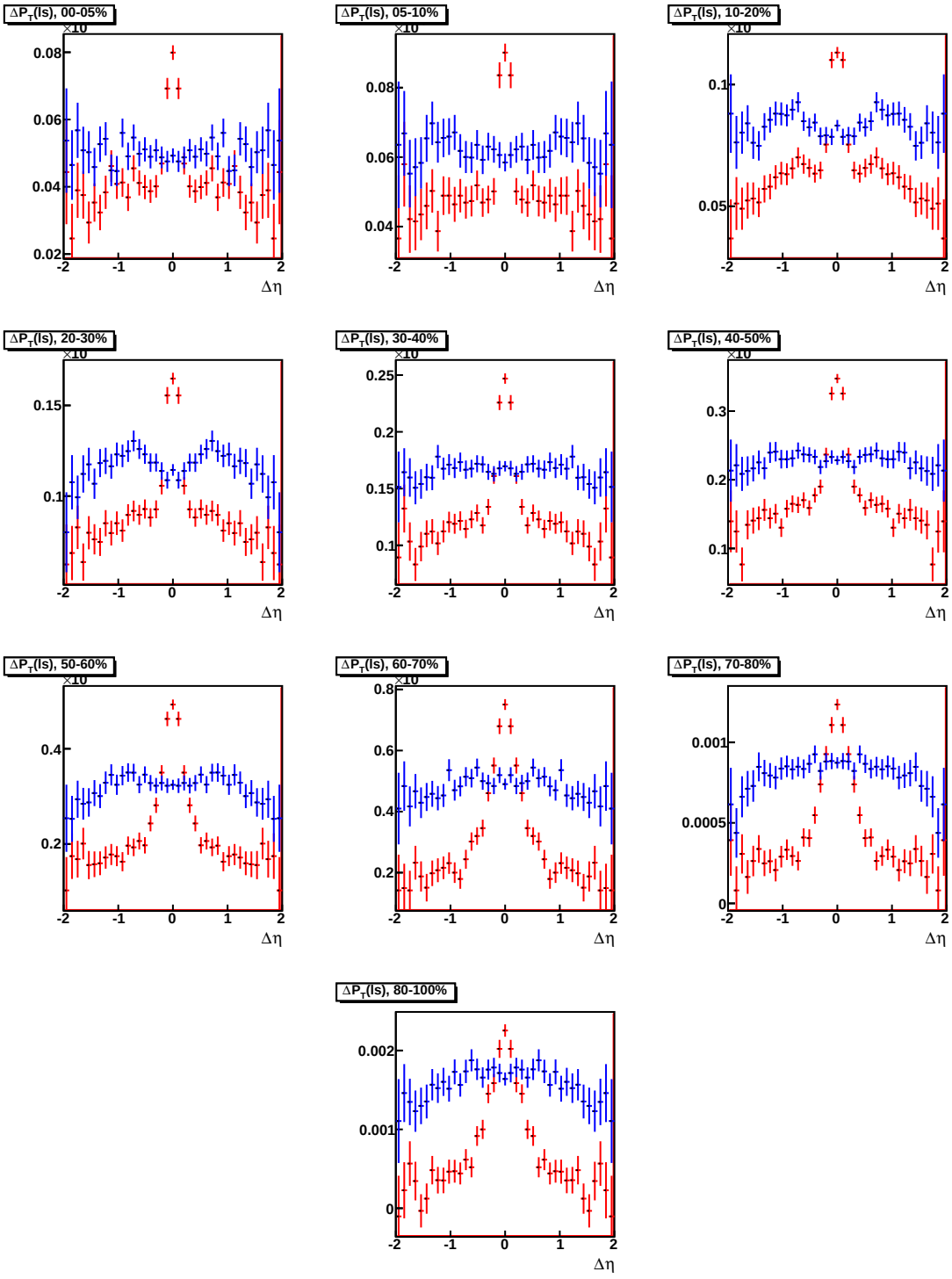

Figure 10.62: $\Delta P_T{}^{ls}(\Delta\eta)$

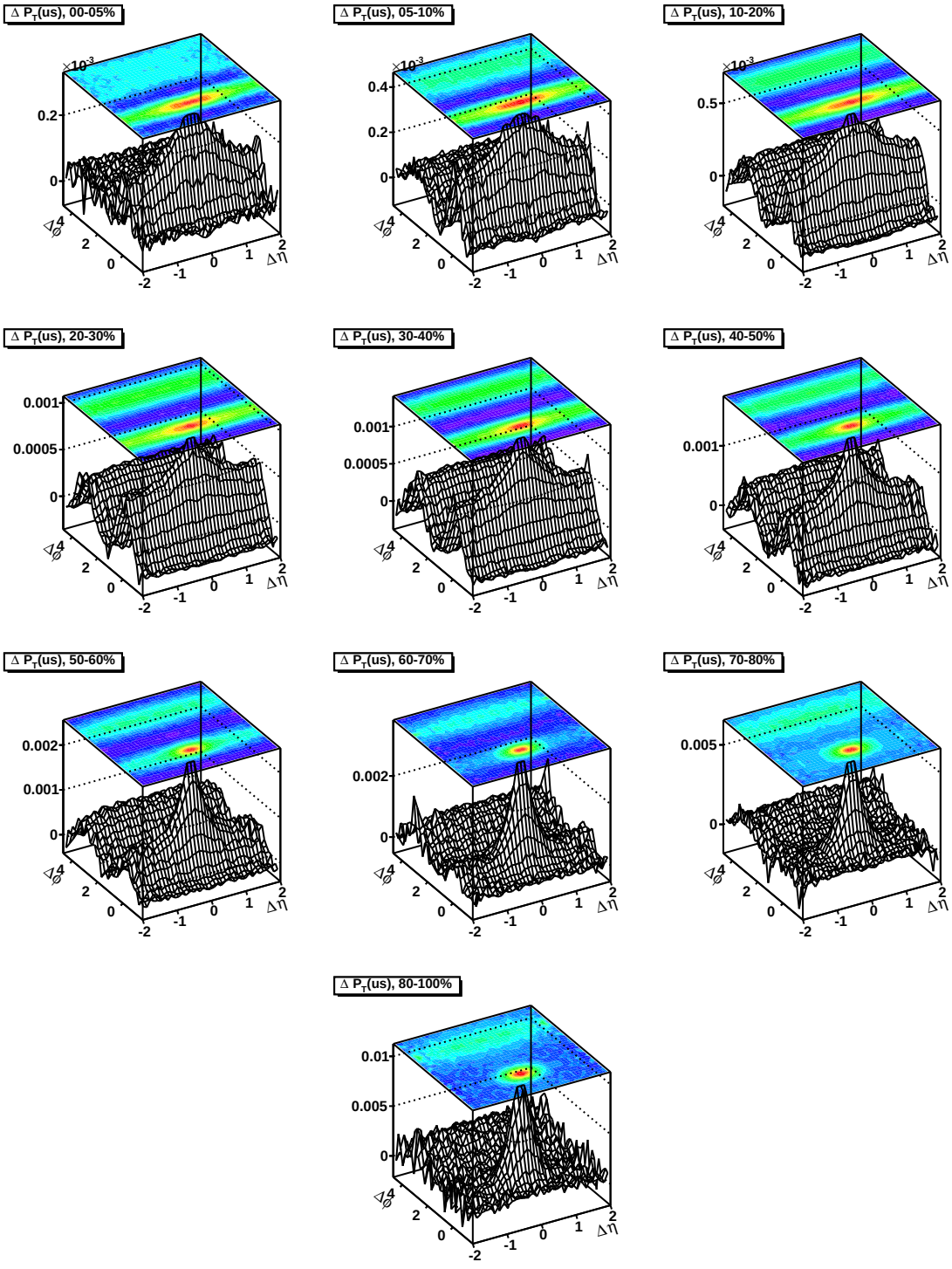

Figure 10.63: $\Delta P_T{}^{us}(\Delta\eta, \Delta\phi)$

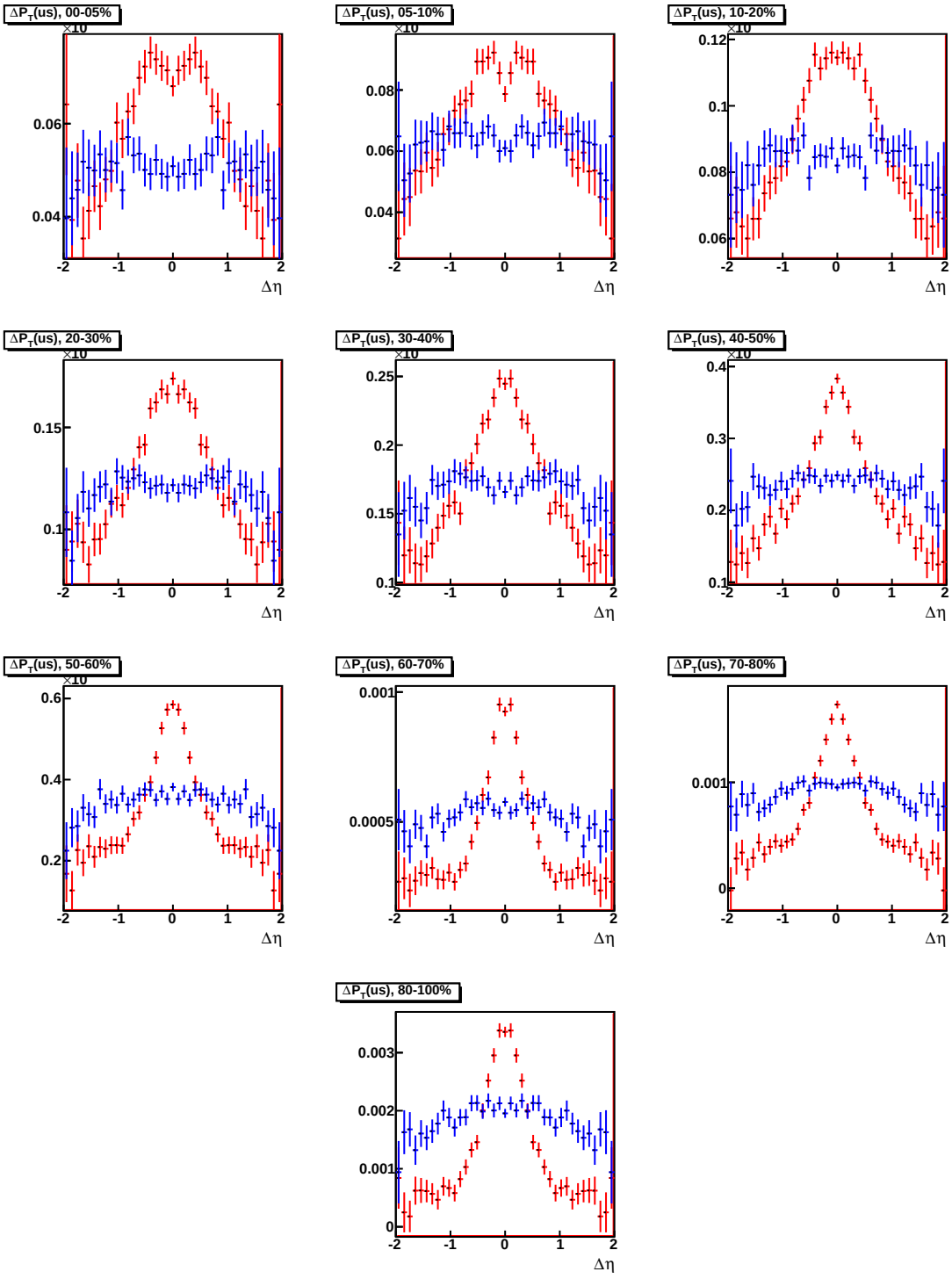

Figure 10.64: $\Delta P_T{}^{us}(\Delta\eta)$

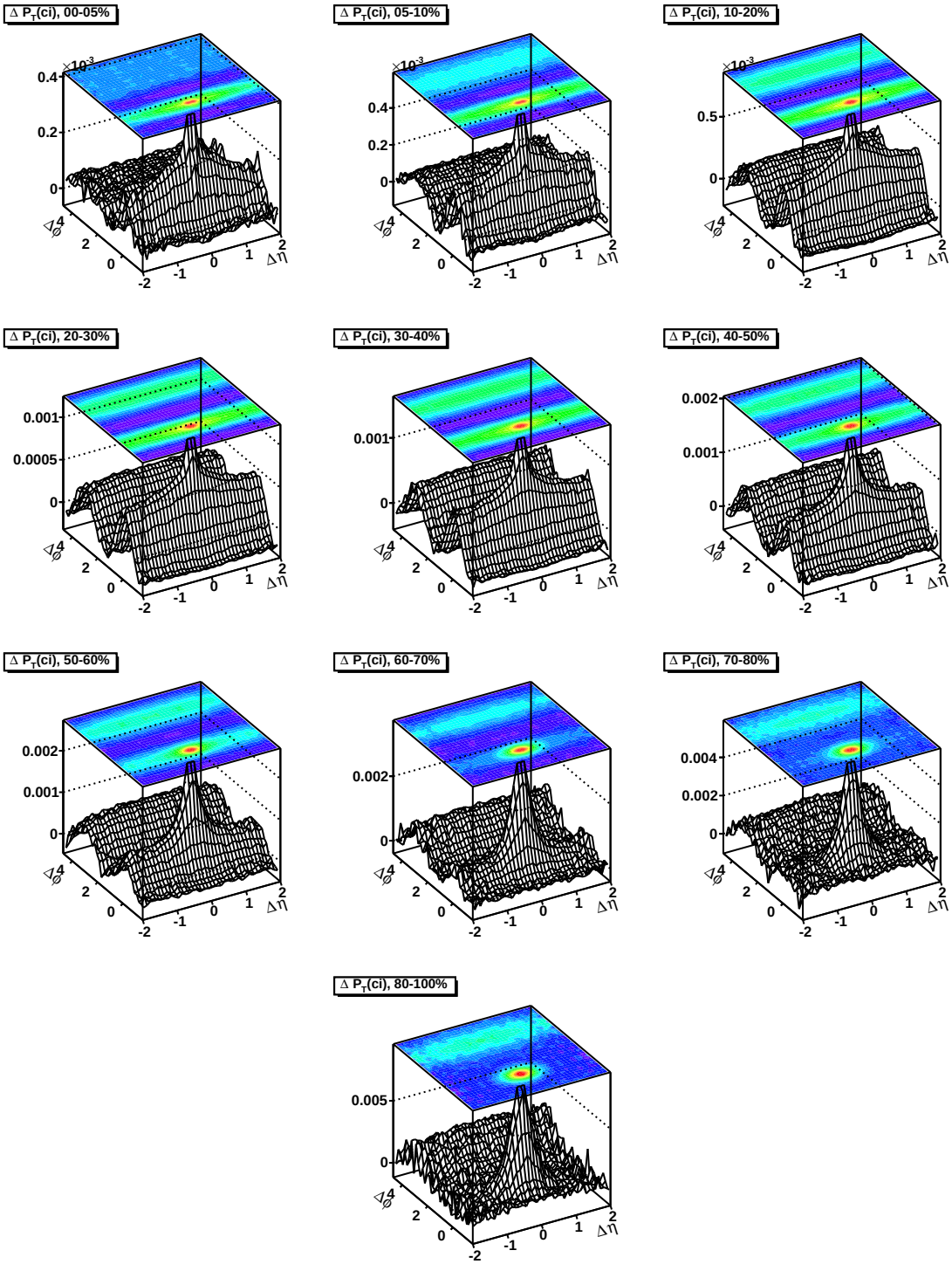

Figure 10.65: $\Delta {P_T}^{ci}(\Delta\eta, \Delta\phi)$

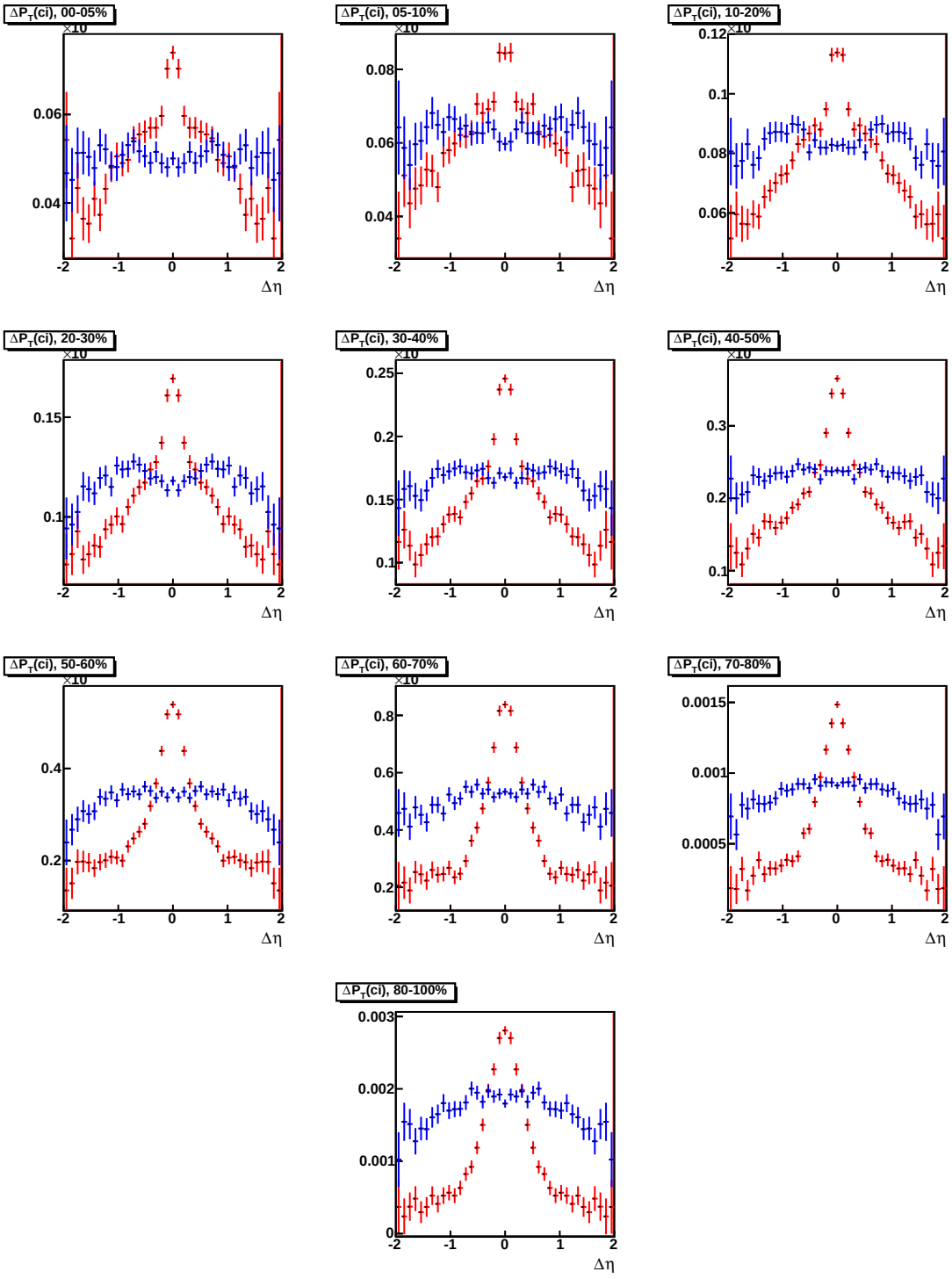

Figure 10.66: $\Delta P_T{}^{ci}(\Delta\eta)$

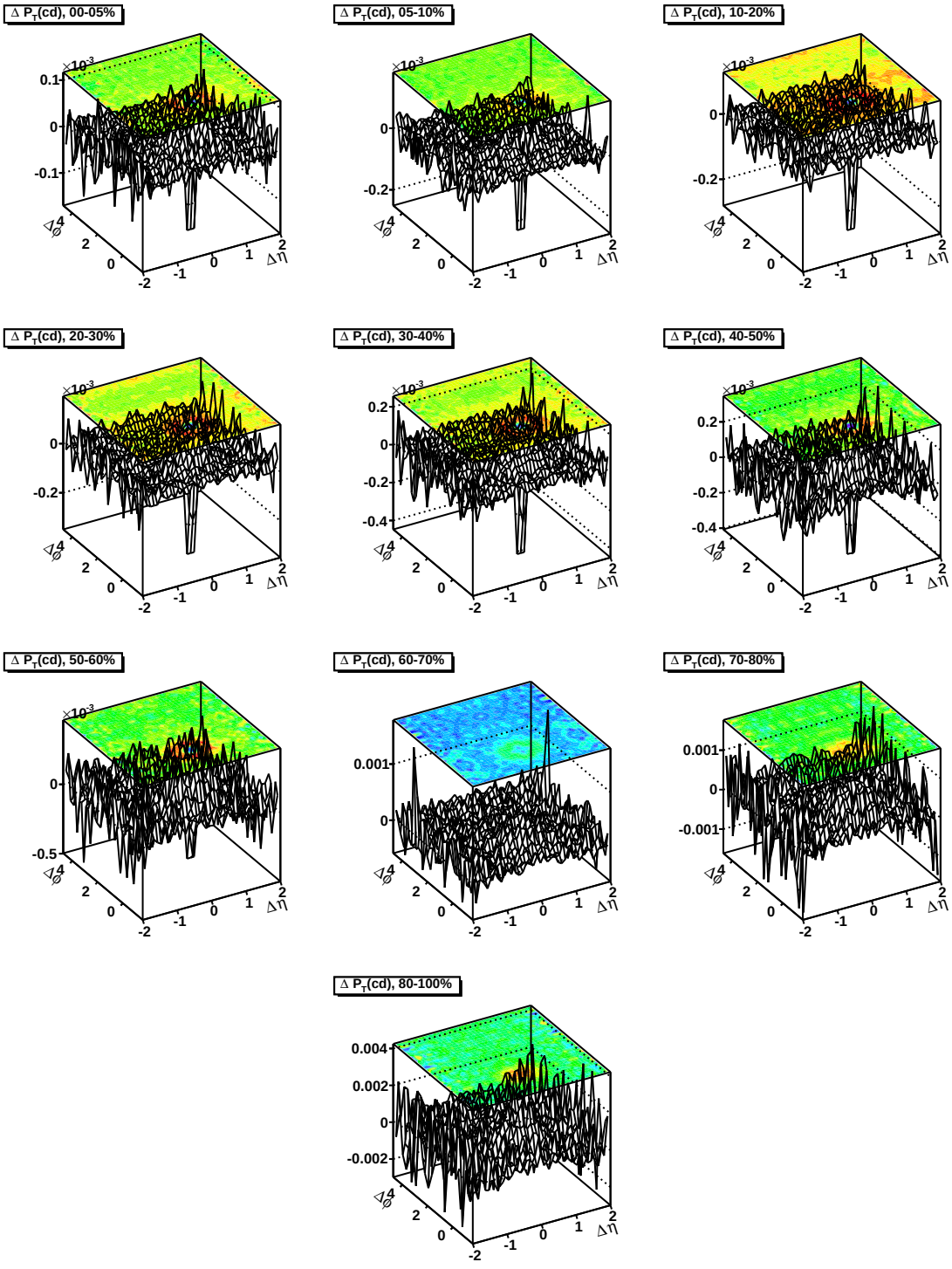

Figure 10.67: $\Delta {P_T}^{cd}(\Delta\eta, \Delta\phi)$

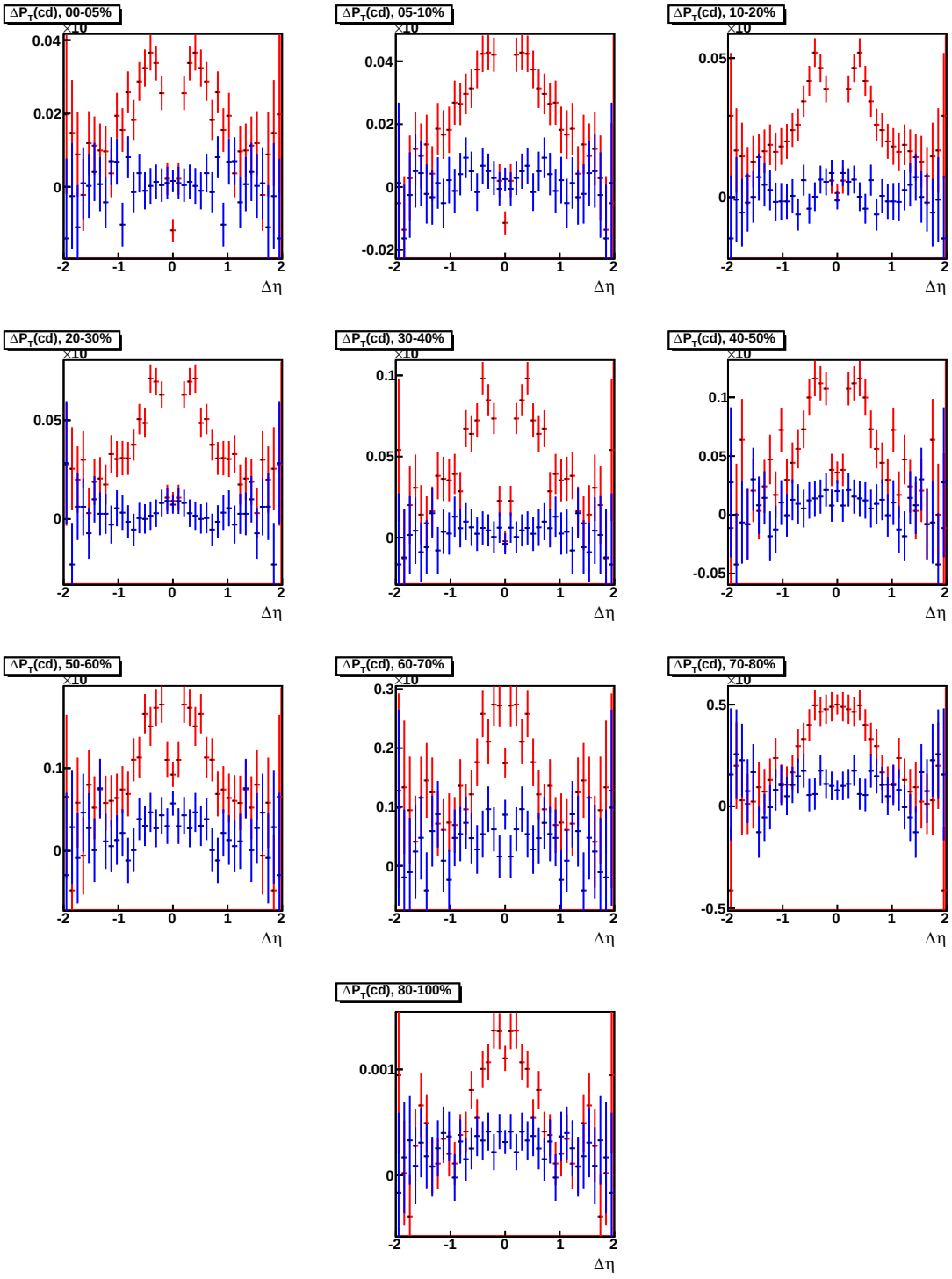

Figure 10.68: $\Delta P_T{}^{cd}(\Delta\eta)$

Chapter 11

Catalog of Distributions, Convolutions and Plots of Cluster Model Simulation

Data generation is based on Foa's review criteria: 1) absence of correlations among clusters, 2) isotropic decay of clusters in their rest frames, and 3) energy independence of decay parameters [6]. Event generation is done using a Root version of GENBOD, CERNLIB w515. Model parameters consist of: distribution of clusters, cluster effective mass, decay particle mass. Clusters receive a longitudinal or radial transverse boost, either randomly by cluster or identically for all clusters created in the event.

Cluster model simulation parameters have been chosen for broad physical plausibility, primarily for illustrative purposes, without attempting to fine-tune the parameters to match the existing data. In all models, an *event* consists of 1 collision which produces *clusters* that decay into 2-5 *particles*. The effective mass of each cluster is from 2-4 GeV with mean 3 GeV. The distribution of clusters may be one single cluster per collision or a Poisson distribution with mean 6. The distribution of particles in a cluster is approximately Poisson with mean 4.

The following simulated $p + p$ datasets were created:

- Model pp1a: A single cluster decays in its rest frame.
- Model pp1b: A single cluster decays in its rest frame, then is boosted longitudinally with rapidity distributed uniformly on (-3,3).
- Model pp2: Same as pp1b, but with cluster distribution Poisson(6) (not shown).

- Model pp3: Same as pp2b, but with transverse momentum added in the rest frame of each individual cluster, distributed normally with variance 1 GeV.

- Model pp4a: Same as pp2b, but with a transverse rapidity boost in the rest frame of each individual cluster, distributed linearly on (0,0.7).

- Model pp4b: Same as pp4a, but the boost is applied collectively to all clusters in a collision, rather than individually.

Model pp1a is highly unphysical and is included primarily as a reference. The unusual "rake"-like formation at $\Delta\phi$ equal to π is due to a binning anomaly of two-particle back-to-back decays when symmetric binning about the value zero is used. Model pp1b, with an added longitudinal rapidity boost of the cluster, immediately produces nearly Gaussian correlations in $R_2(\Delta\eta)$.

With Model pp2 the Poisson(6) cluster distribution generates realistic particle multiplicities, however the transverse momentum spectrum is highly unphysical, terminating abruptly at 2 Gev. As a remedy Model pp3 introduces a thermal-type motion that produces a more physical p_T spectrum that decreases exponentially; Model pp3 is used as a proxy for $p + p$ in this paper.

To build a model for $A + A$ events, we add a radial transverse boost to a $p + p$ collision. Model pp4a applies a random radial transverse boost to each individual cluster in a collision; Model pp4a reproduces the away-side dip seen in most central $A + A$ events characterized by v_3. Model pp4b applies the same radial transverse boost as pp4a identically to all clusters in a collision. For both, the boost is in units of rapidity distributed linearly on (0,0.7). On this interval rapidity is approximately equal to velocity (in natural units), so the rapidity distribution models a physical situation in which the transverse velocity of a cluster is proportional to r, the transverse radial distance of the cluster from the "center" of the event.

The collective radial transverse boost of Model pp4b produces the R_2 correlation

with the feature we seek to model, namely the appearance of a longitudinal ridge extended in $\Delta\eta$ that is amplified about (0,0).

11.1 $p + p$ (1a)

Model pp1a: A single cluster decays in its rest frame.

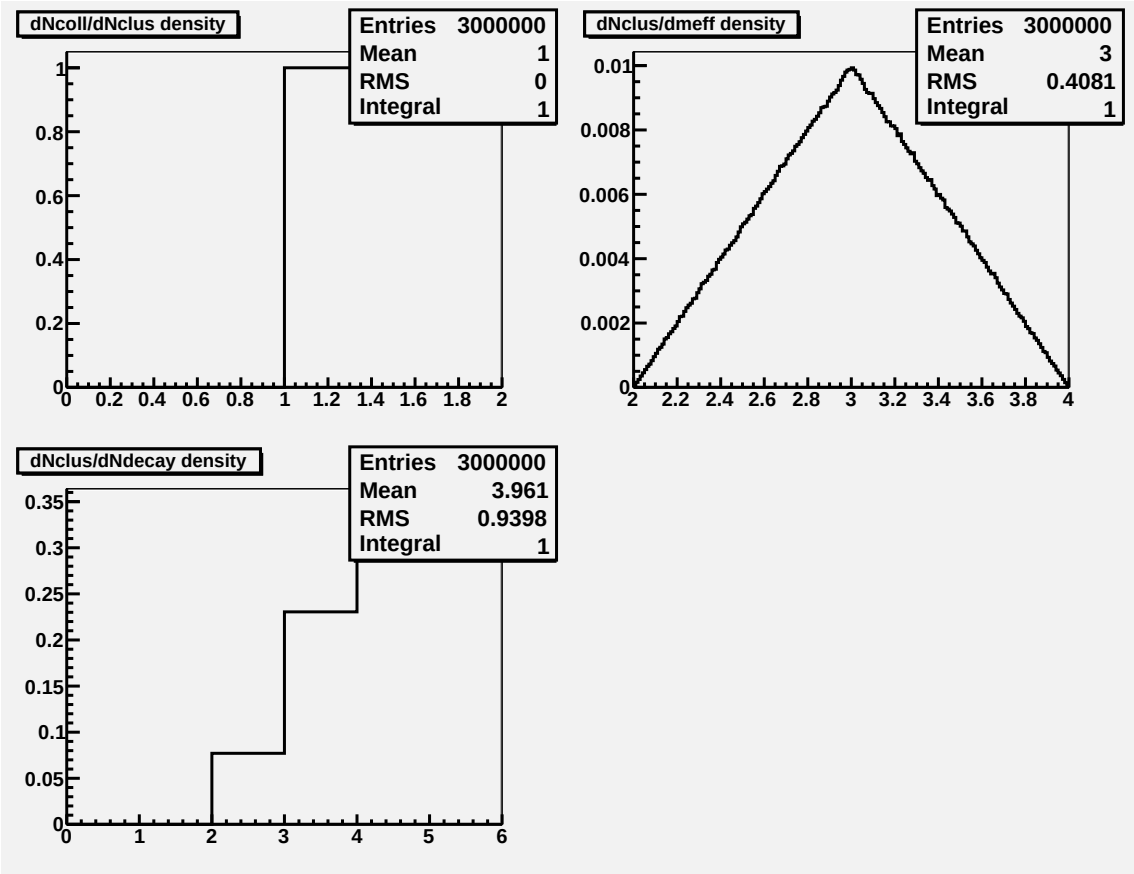

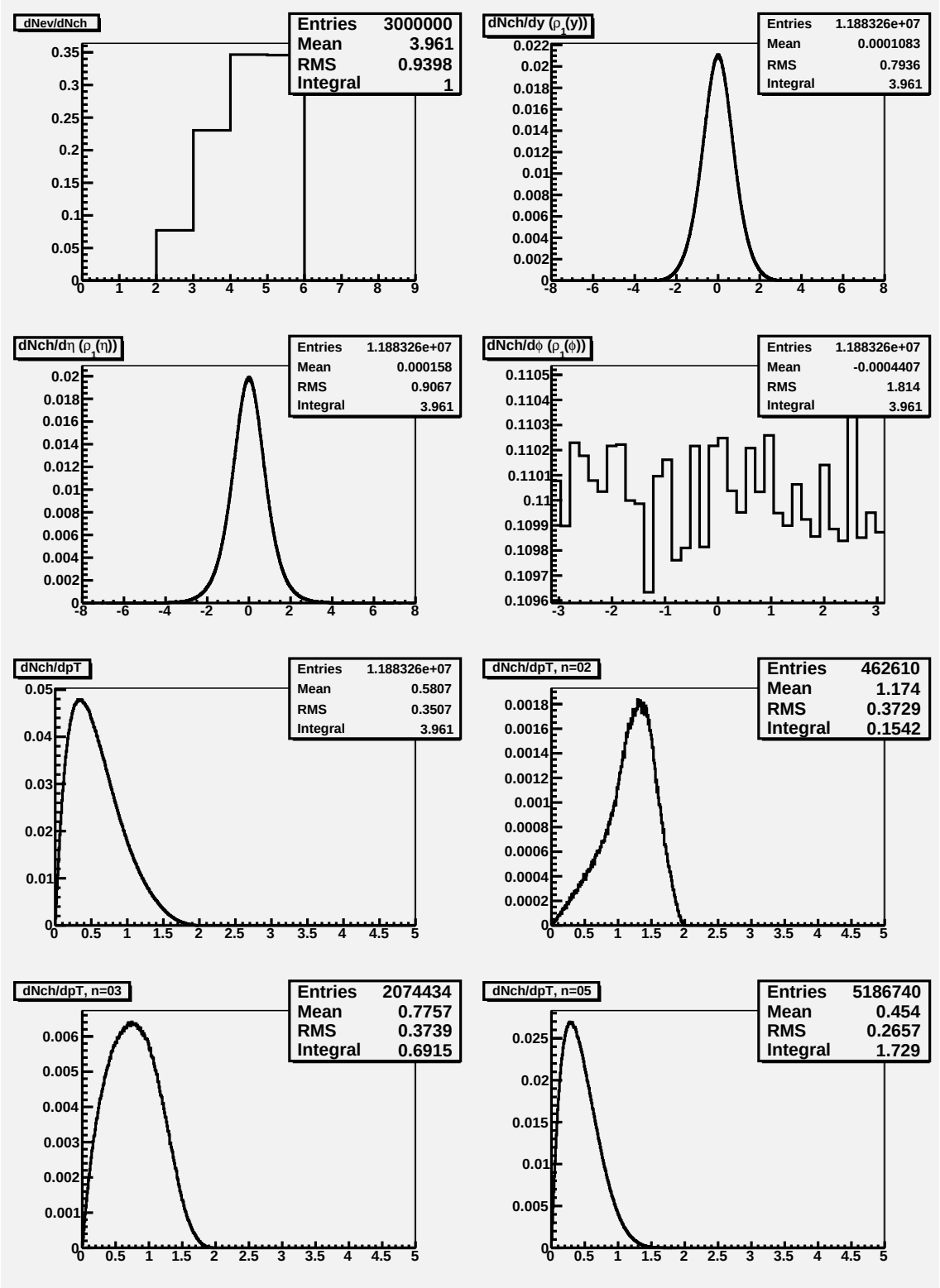
dNev/dNch
Entries 3000000
Mean 3.961
RMS 0.9398
Integral 1
dNch/dy (ρ1(y))
Entries 1.188326e+07
Mean 0.0001083
RMS 0.7936
Integral 3.961
dNch/dη (ρ1(η))
Entries 1.188326e+07
Mean 0.000158
RMS 0.9067
Integral 3.961
dNch/dφ (ρ1(φ))
Entries 1.188326e+07
Mean -0.0004407
RMS 1.814
Integral 3.961
dNch/dpT
Entries 1.188326e+07
Mean 0.5807
RMS 0.3507
Integral 3.961
dNch/dpT, n=02
Entries 462610
Mean 1.174
RMS 0.3729
Integral 0.1542
dNch/dpT, n=03
Entries 2074434
Mean 0.7757
RMS 0.3739
Integral 0.6915
dNch/dpT, n=05
Entries 5186740
Mean 0.454
RMS 0.2657
Integral 1.729

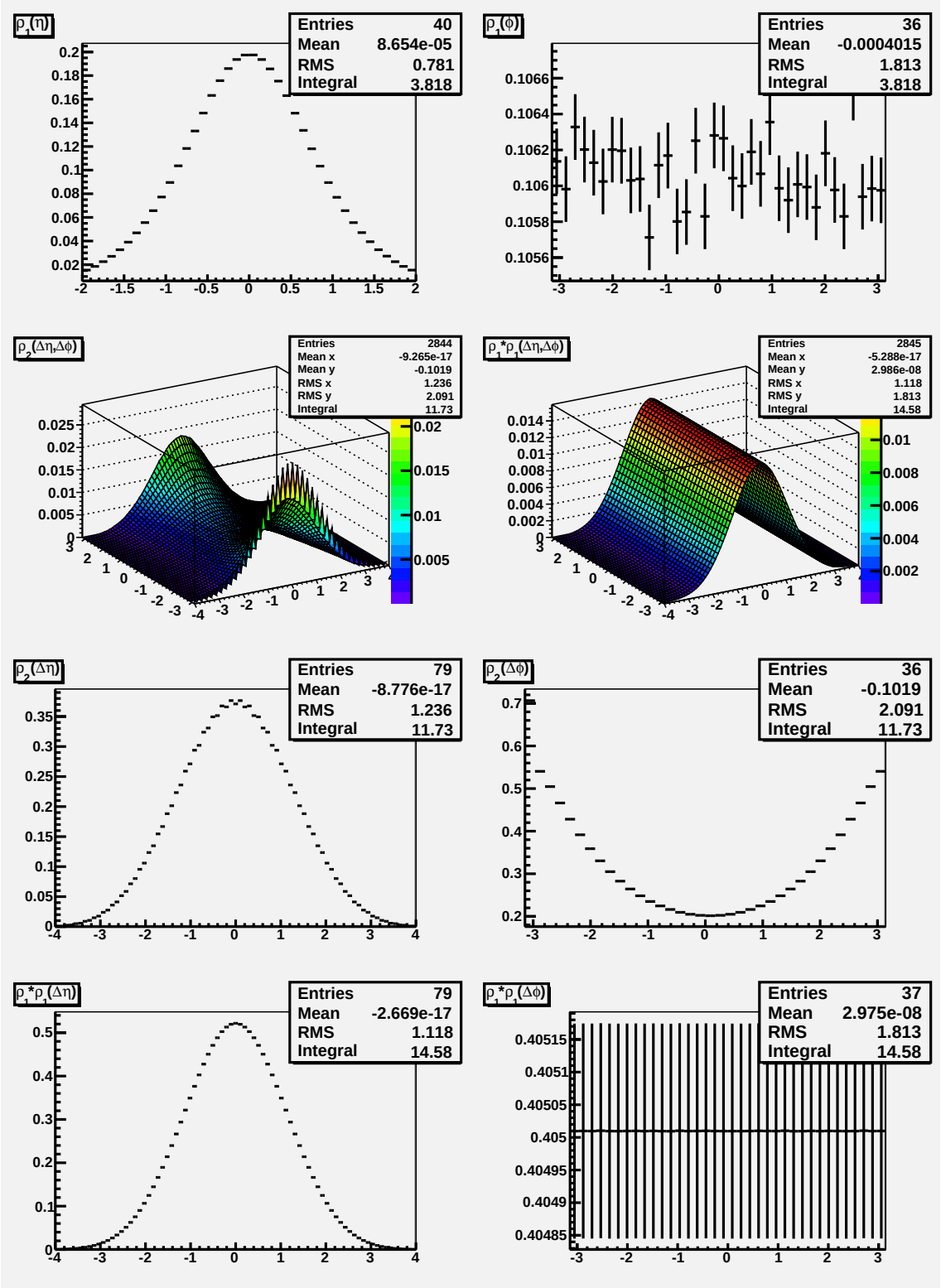
ρ1(η)
Entries 40
Mean 8.654e-05
RMS 0.781
Integral 3.818
ρ1(φ)
Entries 36
Mean -0.0004015
RMS 1.813
Integral 3.818
ρ2(Δη,Δφ)
Entries 2844
Mean x -9.265e-17
Mean y -0.1019
RMS x 1.236
RMS y 2.091
Integral 11.73
ρ1*ρ1(Δη,Δφ)
Entries 2845
Mean x -5.288e-17
Mean y 2.986e-08
RMS x 1.118
RMS y 1.813
Integral 14.58
ρ2(Δη)
Entries 79
Mean -8.776e-17
RMS 1.236
Integral 11.73
ρ2(Δφ)
Entries 36
Mean -0.1019
RMS 2.091
Integral 11.73
ρ1*ρ1(Δη)
Entries 79
Mean -2.669e-17
RMS 1.118
Integral 14.58
ρ1*ρ1(Δφ)
Entries 37
Mean 2.975e-08
RMS 1.813
Integral 14.58

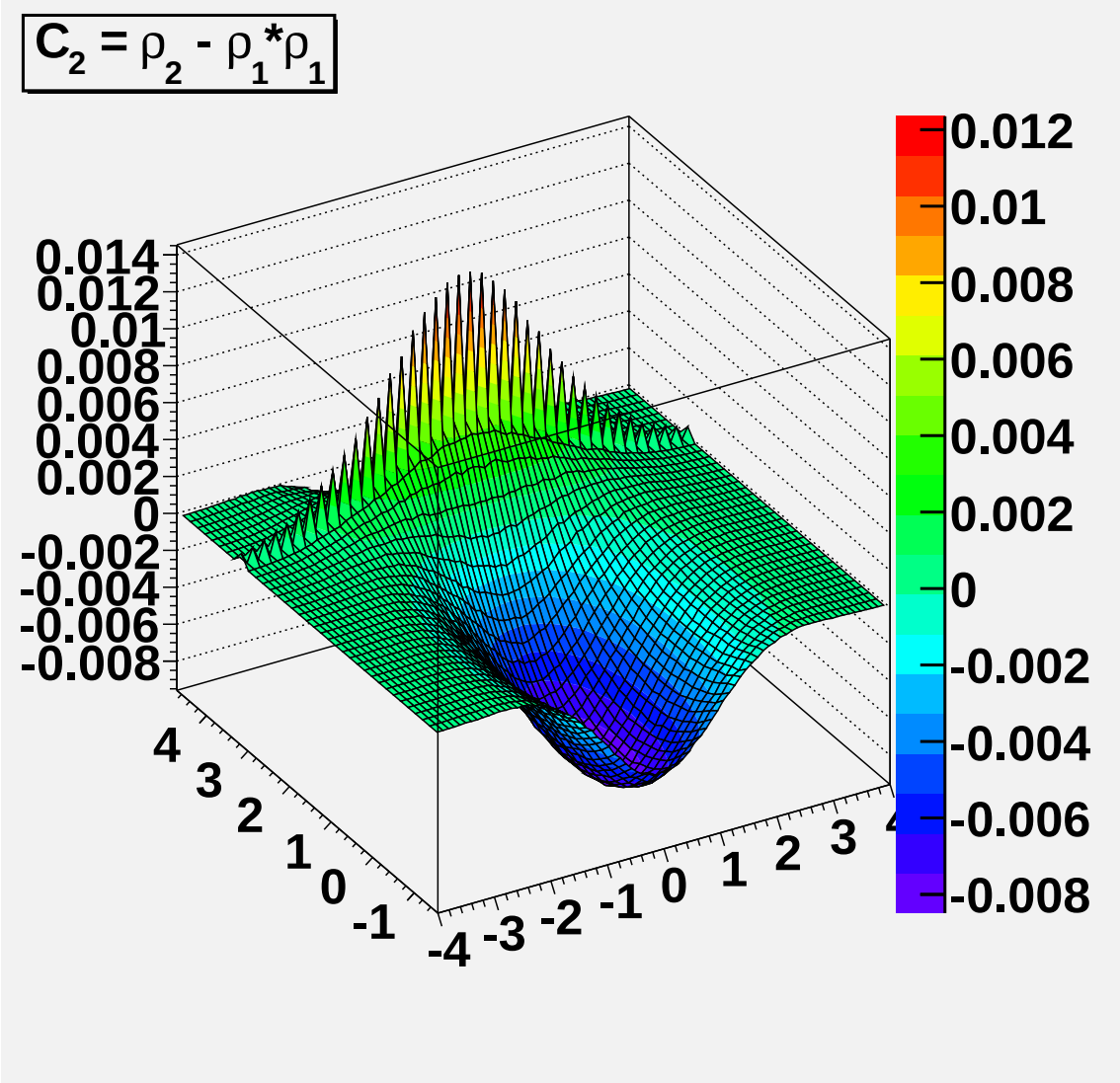

Figure 11.1: $C_2(\Delta\eta, \Delta\phi)$

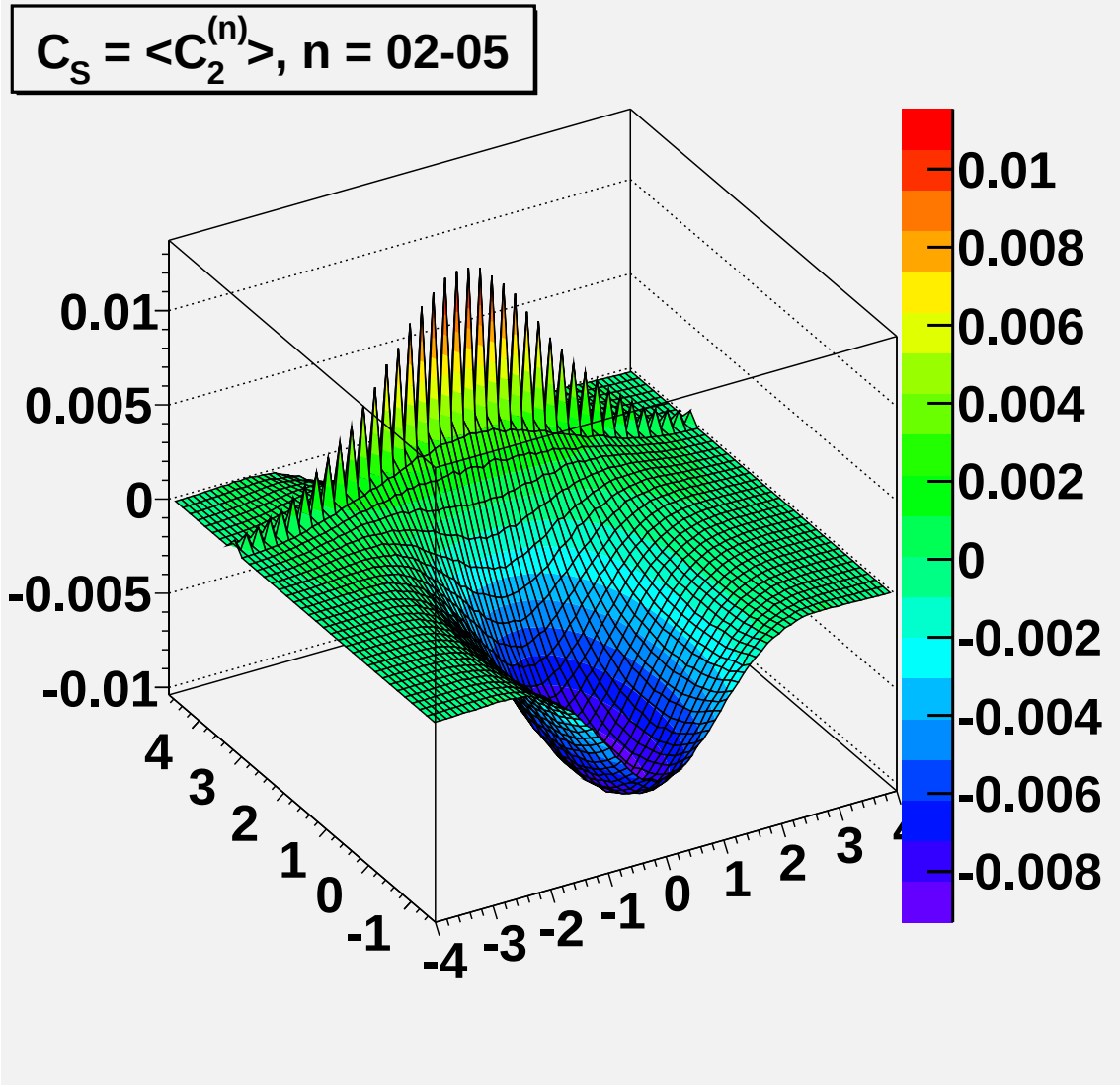

Figure 11.2: $C_S = \langle C_2^{(n)}(\Delta\eta, \Delta\phi)\rangle$

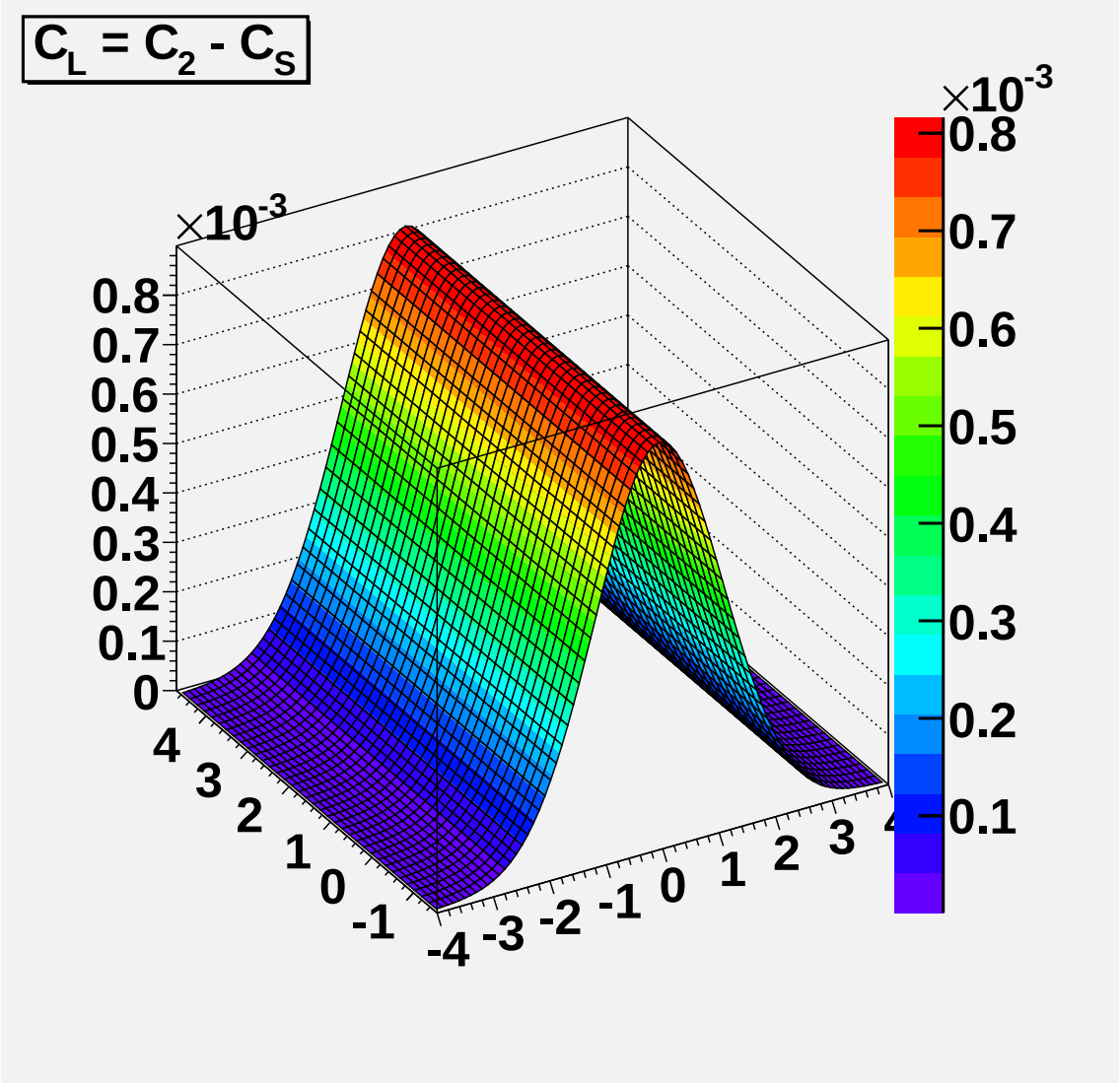

Figure 11.3: $C_L = C_2(\Delta\eta, \Delta\phi) - \langle C_2^{(n)}(\Delta\eta, \Delta\phi)\rangle$

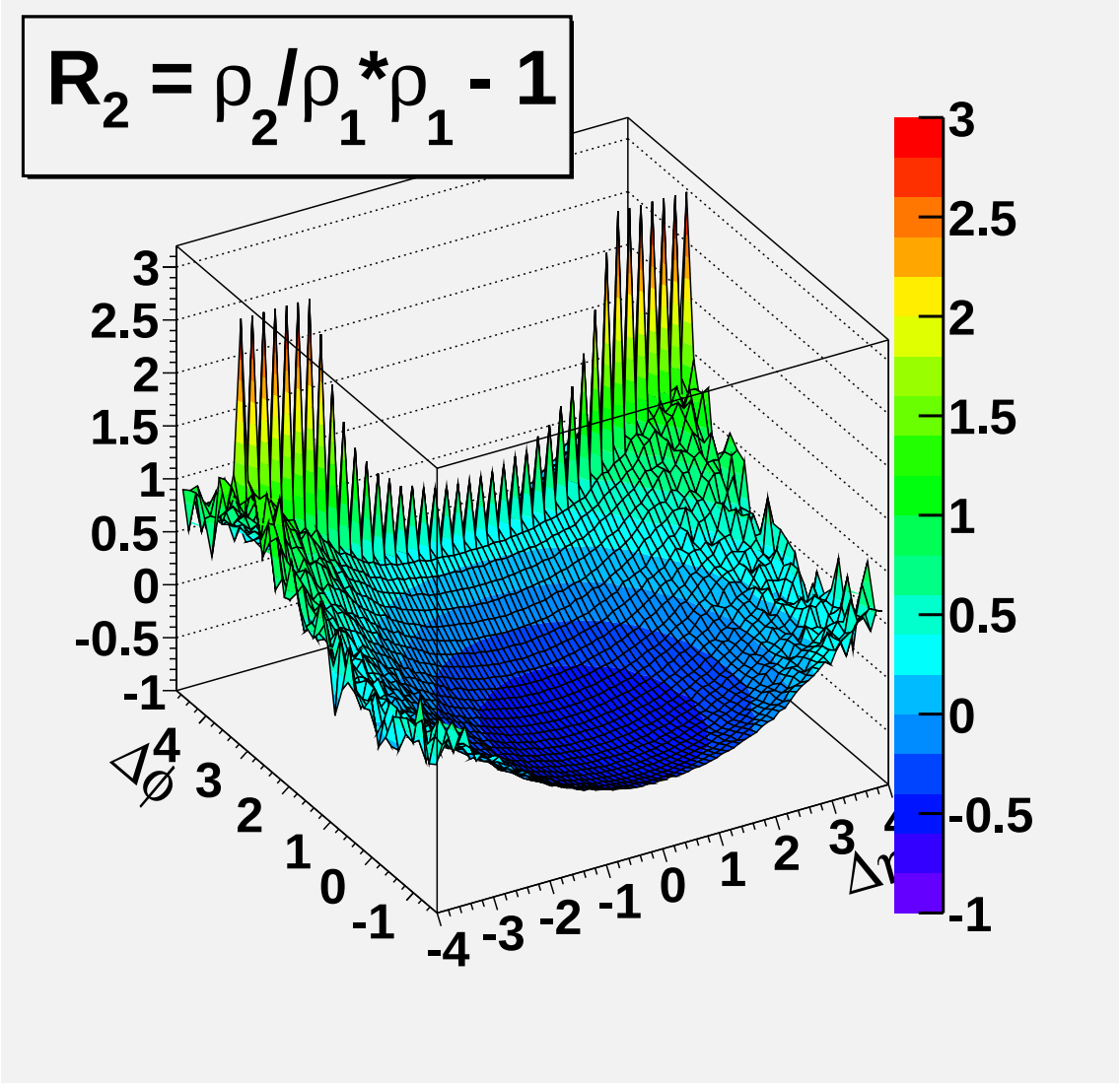

Figure 11.4: $R_2(\Delta\eta, \Delta\phi)$

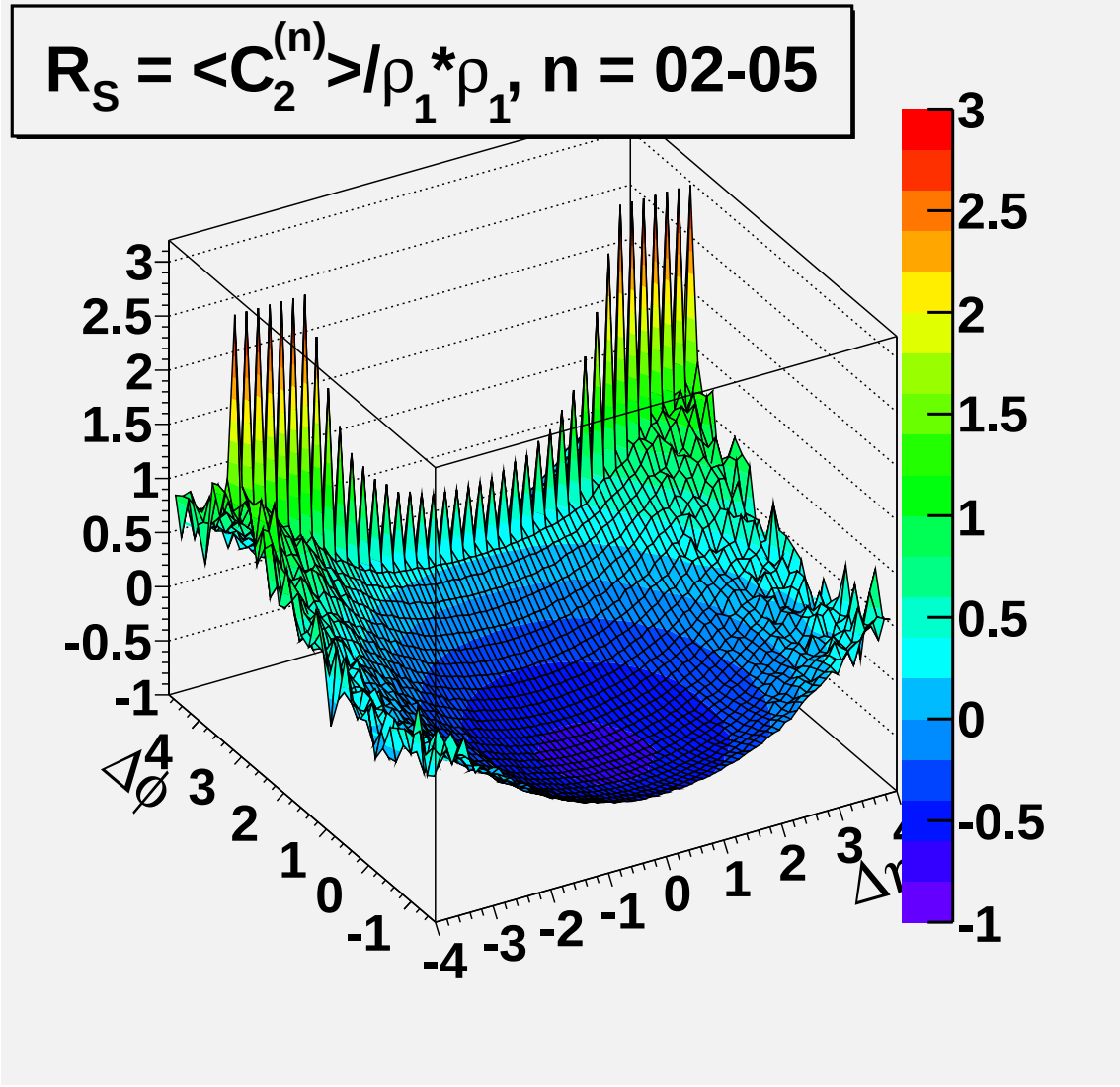

Figure 11.5: $R_S = \langle C_2^{(n)}(\Delta\eta, \Delta\phi)\rangle / \rho_1 * \rho_1(\Delta\eta, \Delta\phi)$

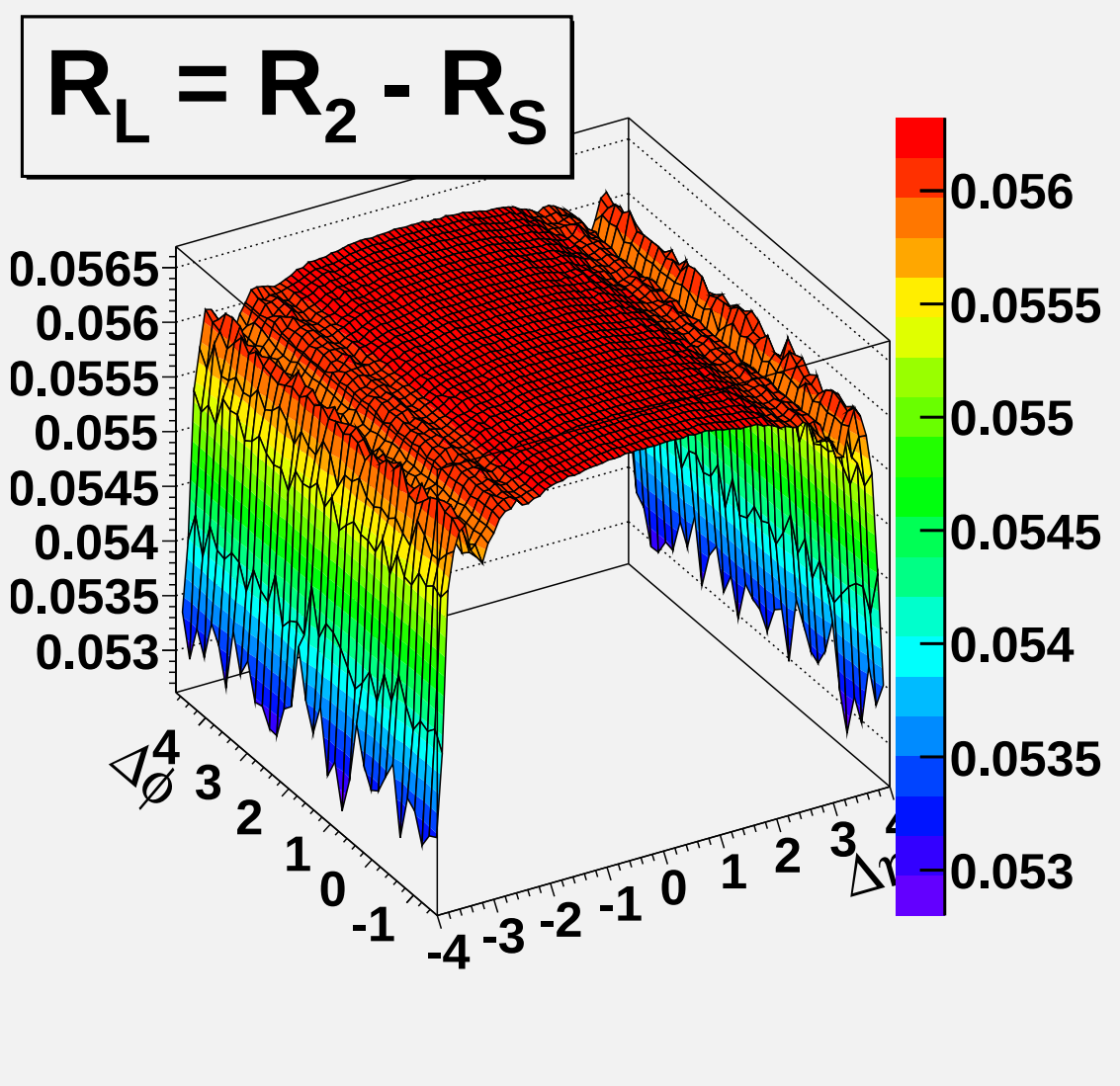

Figure 11.6: $R_L = R_2(\Delta\eta, \Delta\phi) - \langle C_2^{(n)}(\Delta\eta, \Delta\phi)\rangle / \rho_1 * \rho_1(\Delta\eta, \Delta\phi)$

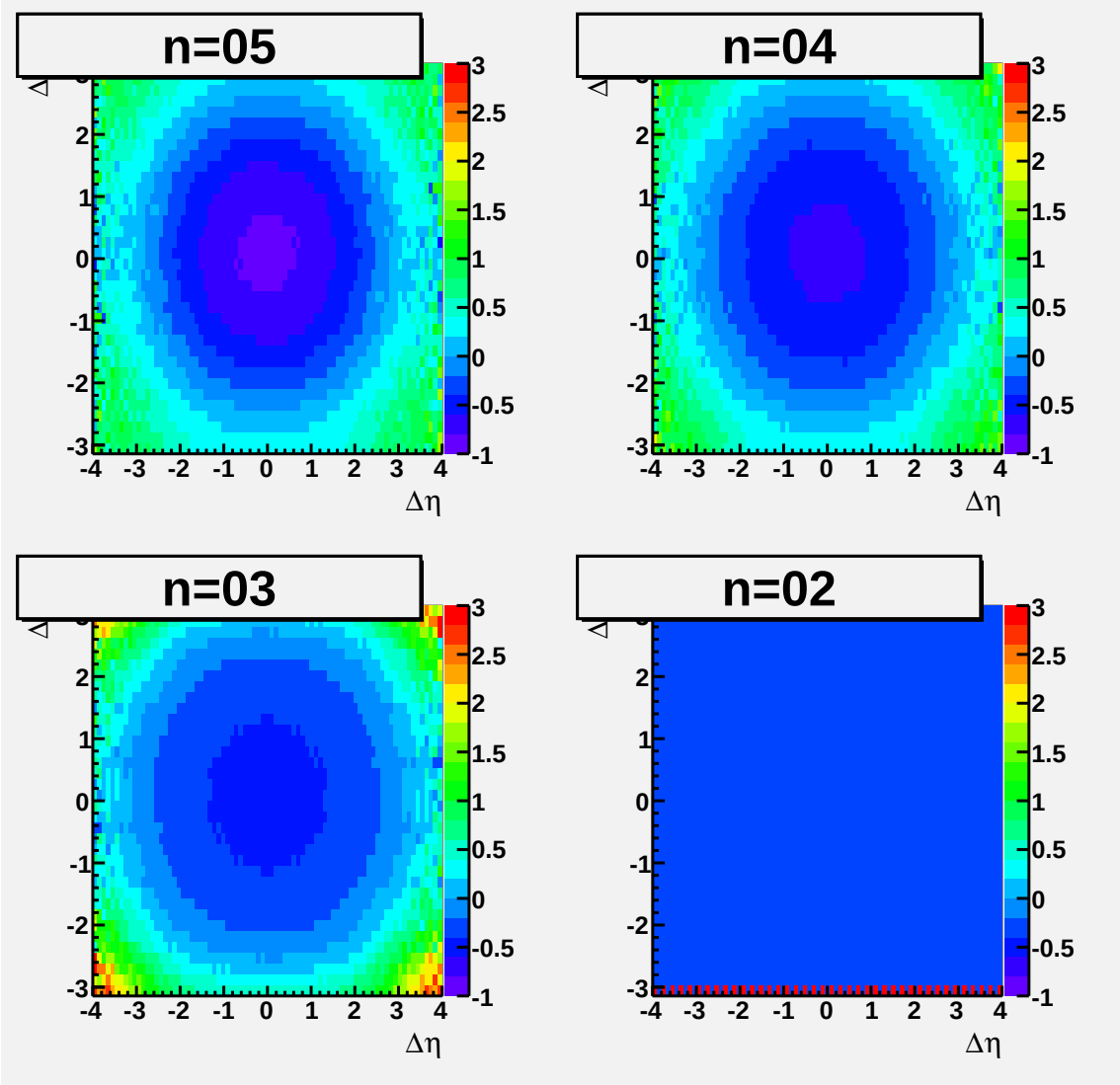

Figure 11.7: $R_2^{(n)} = C_2^{(n)}(\Delta\eta, \Delta\phi)/\rho_1 * \rho_1(\Delta\eta, \Delta\phi)$

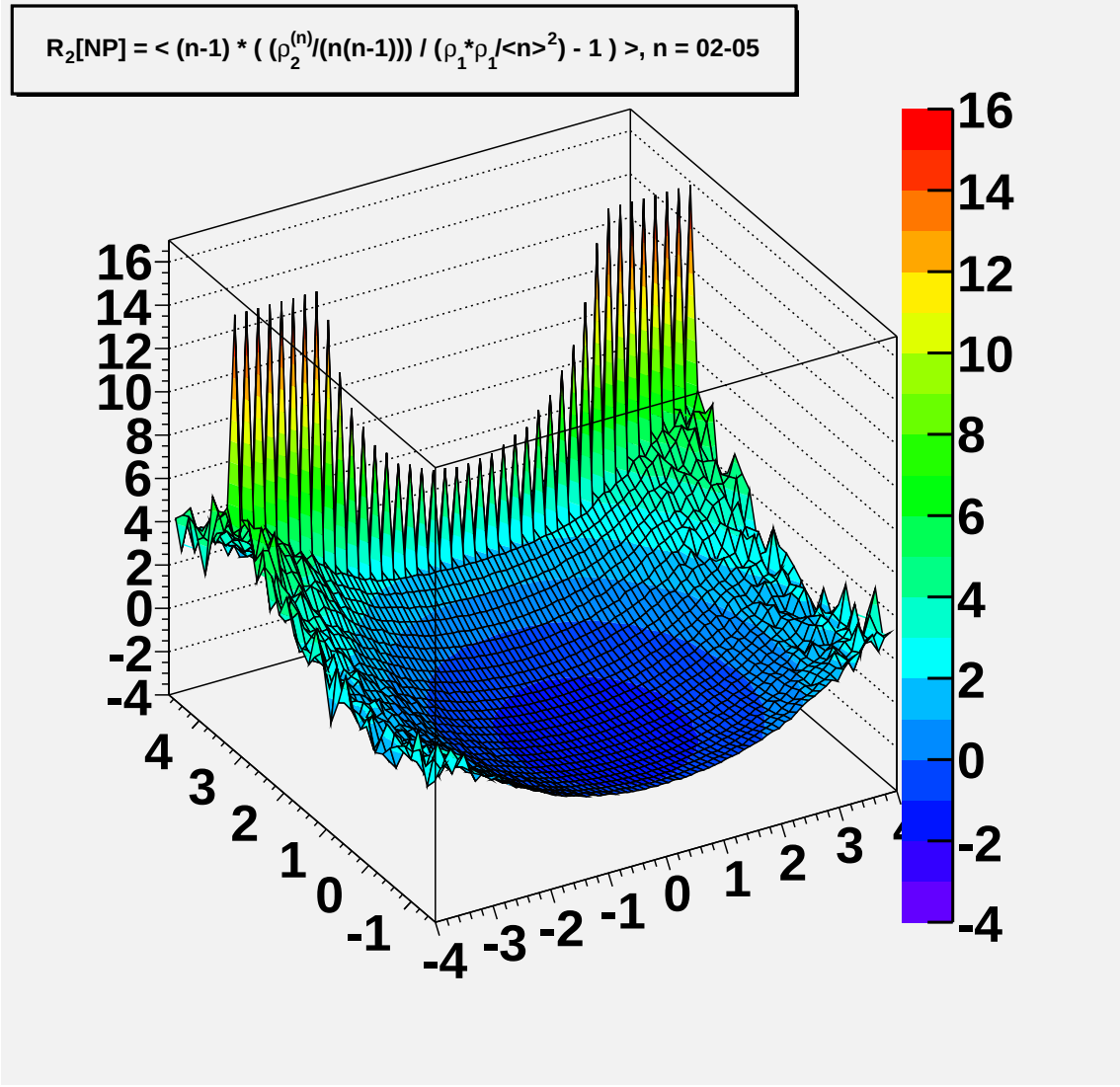

Figure 11.8: $\langle R_2^{(n)}[NP](\Delta\eta, \Delta\phi)\rangle$

11.2 $p + p$ (1b)

Model pp1b: A single cluster decays in its rest frame, then is boosted longitudinally with rapidity distributed uniformly on (-3,3).

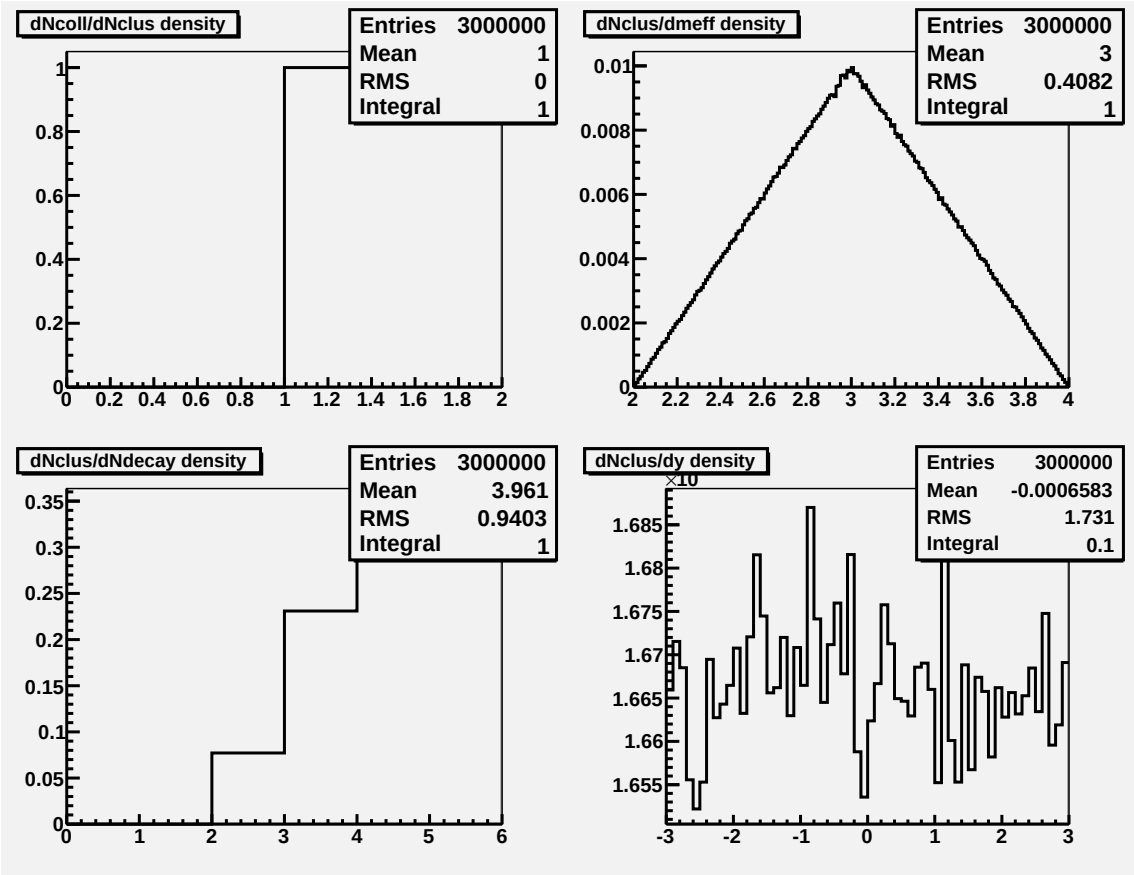

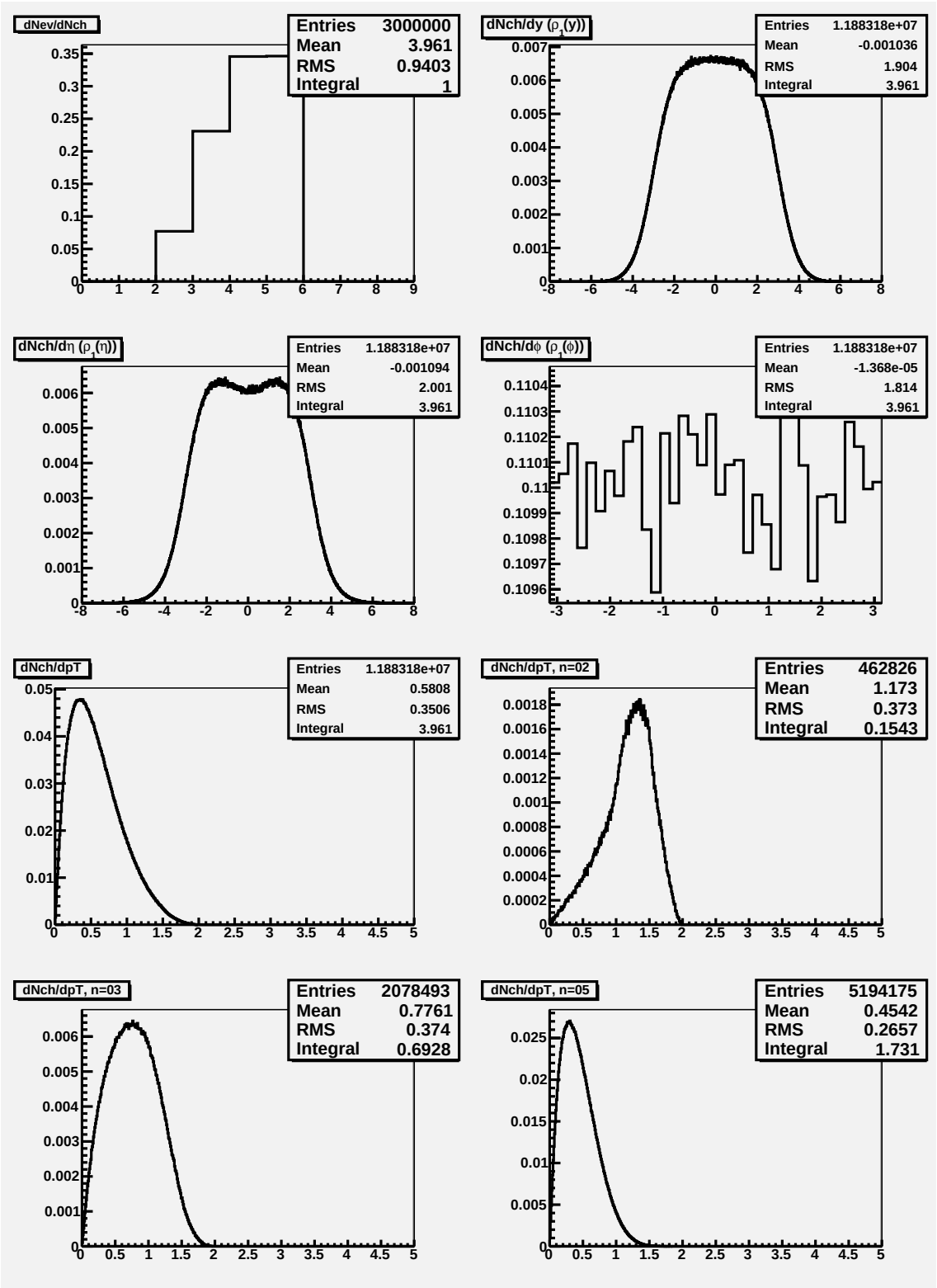
dNev/dNch
Entries 3000000
Mean 3.961
RMS 0.9403
Integral 1
dNch/dy (ρ1(y))
Entries 1.188318e+07
Mean -0.001036
RMS 1.904
Integral 3.961
dNch/dη (ρ1(η))
Entries 1.188318e+07
Mean -0.001094
RMS 2.001
Integral 3.961
dNch/dφ (ρ1(φ))
Entries 1.188318e+07
Mean -1.368e-05
RMS 1.814
Integral 3.961
dNch/dpT
Entries 1.188318e+07
Mean 0.5808
RMS 0.3506
Integral 3.961
dNch/dpT, n=02
Entries 462826
Mean 1.173
RMS 0.373
Integral 0.1543
dNch/dpT, n=03
Entries 2078493
Mean 0.7761
RMS 0.374
Integral 0.6928
dNch/dpT, n=05
Entries 5194175
Mean 0.4542
RMS 0.2657
Integral 1.731

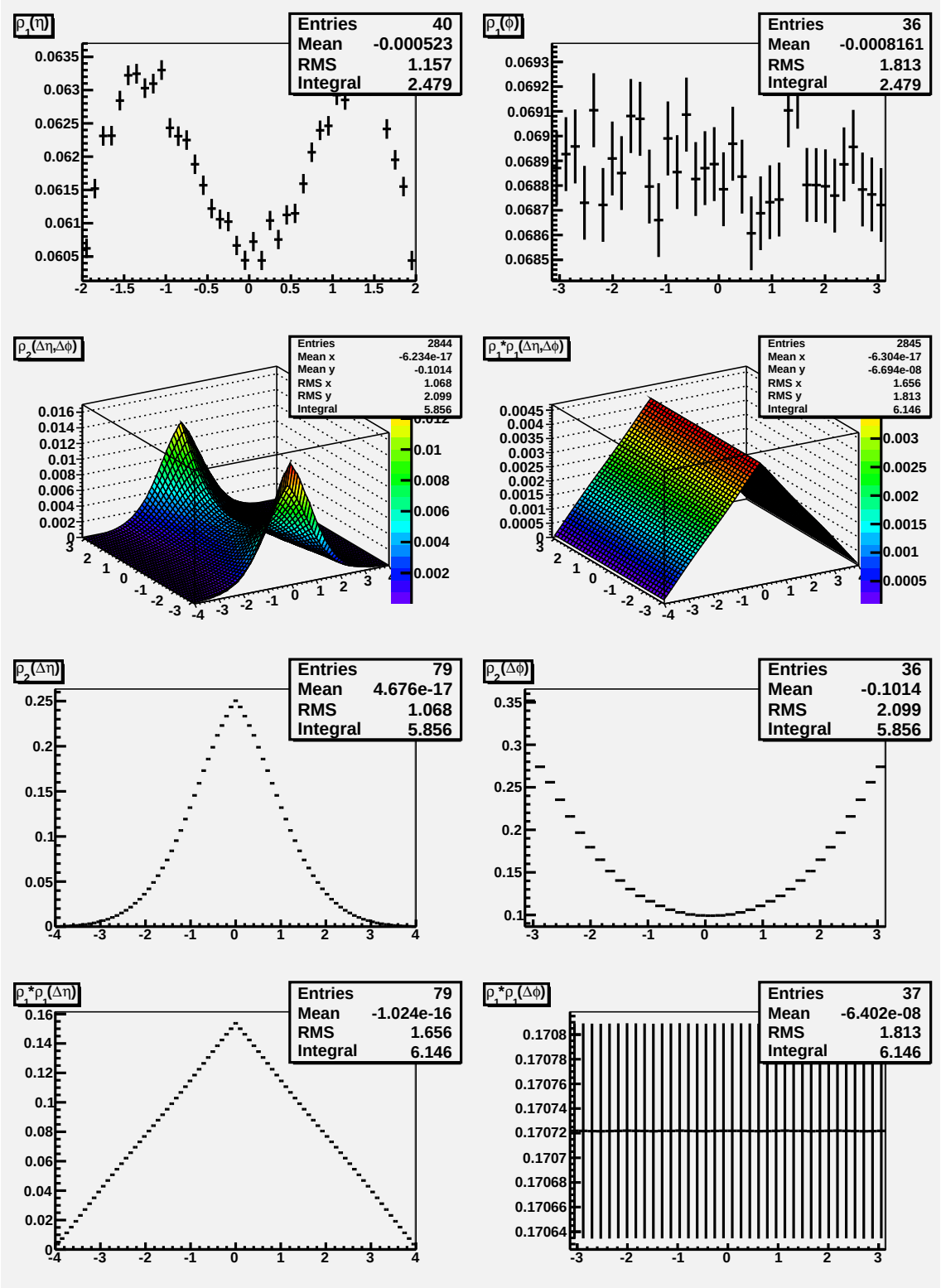
ρ1(η)
Entries 40
Mean -0.000523
RMS 1.157
Integral 2.479
ρ1(φ)
Entries 36
Mean -0.0008161
RMS 1.813
Integral 2.479
ρ2(Δη,Δφ)
Entries 2844
Mean x -6.234e-17
Mean y -0.1014
RMS x 1.068
RMS y 2.099
Integral 5.856
ρ1*ρ1(Δη,Δφ)
Entries 2845
Mean x -6.304e-17
Mean y -6.694e-08
RMS x 1.656
RMS y 1.813
Integral 6.146
ρ2(Δη)
Entries 79
Mean 4.676e-17
RMS 1.068
Integral 5.856
ρ2(Δφ)
Entries 36
Mean -0.1014
RMS 2.099
Integral 5.856
ρ1*ρ1(Δη)
Entries 79
Mean -1.024e-16
RMS 1.656
Integral 6.146
ρ1*ρ1(Δφ)
Entries 37
Mean -6.402e-08
RMS 1.813
Integral 6.146

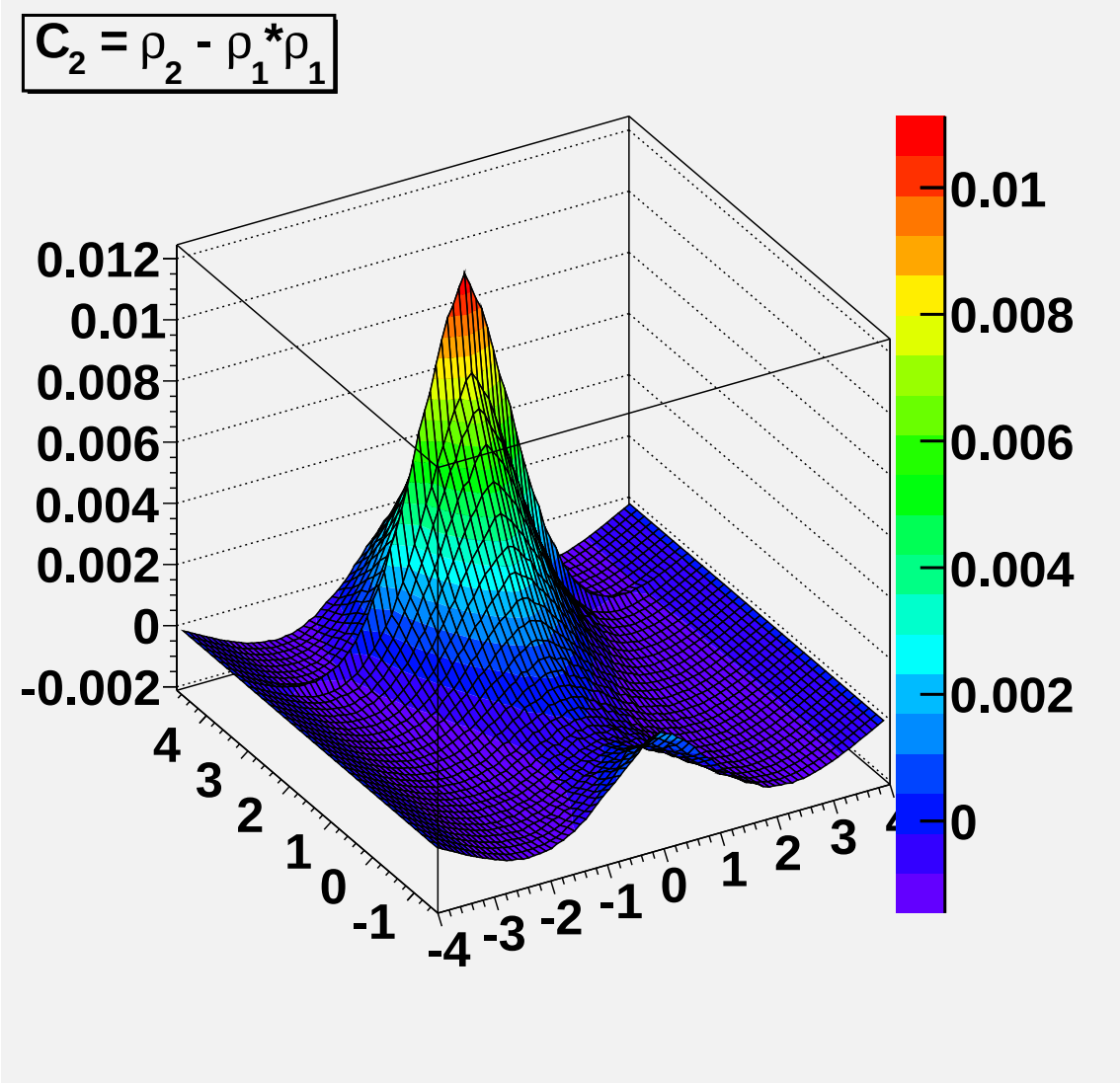

Figure 11.9: $C_2(\Delta\eta, \Delta\phi)$

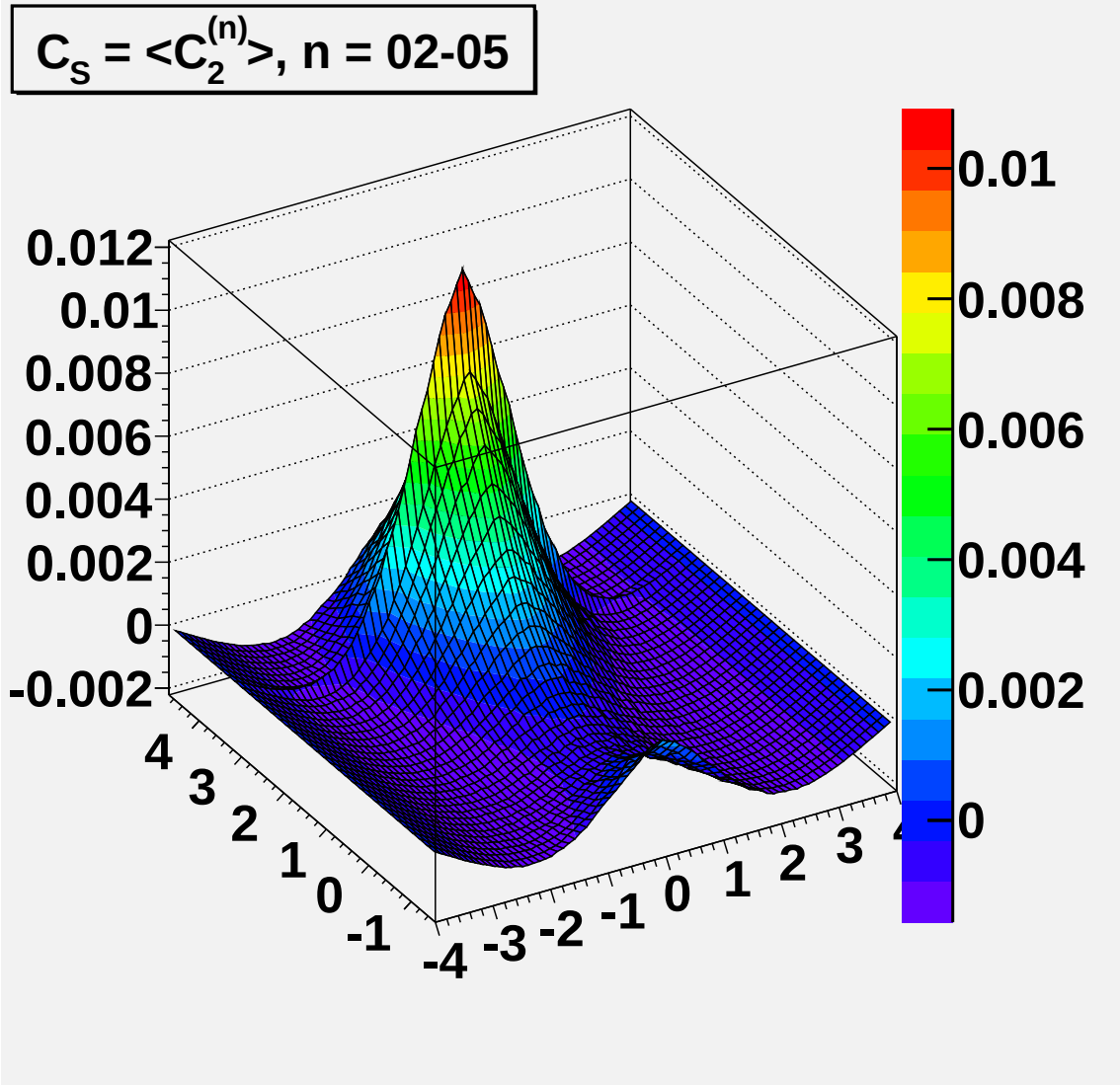

Figure 11.10: $C_S = \langle C_2^{(n)}(\Delta\eta, \Delta\phi)\rangle$

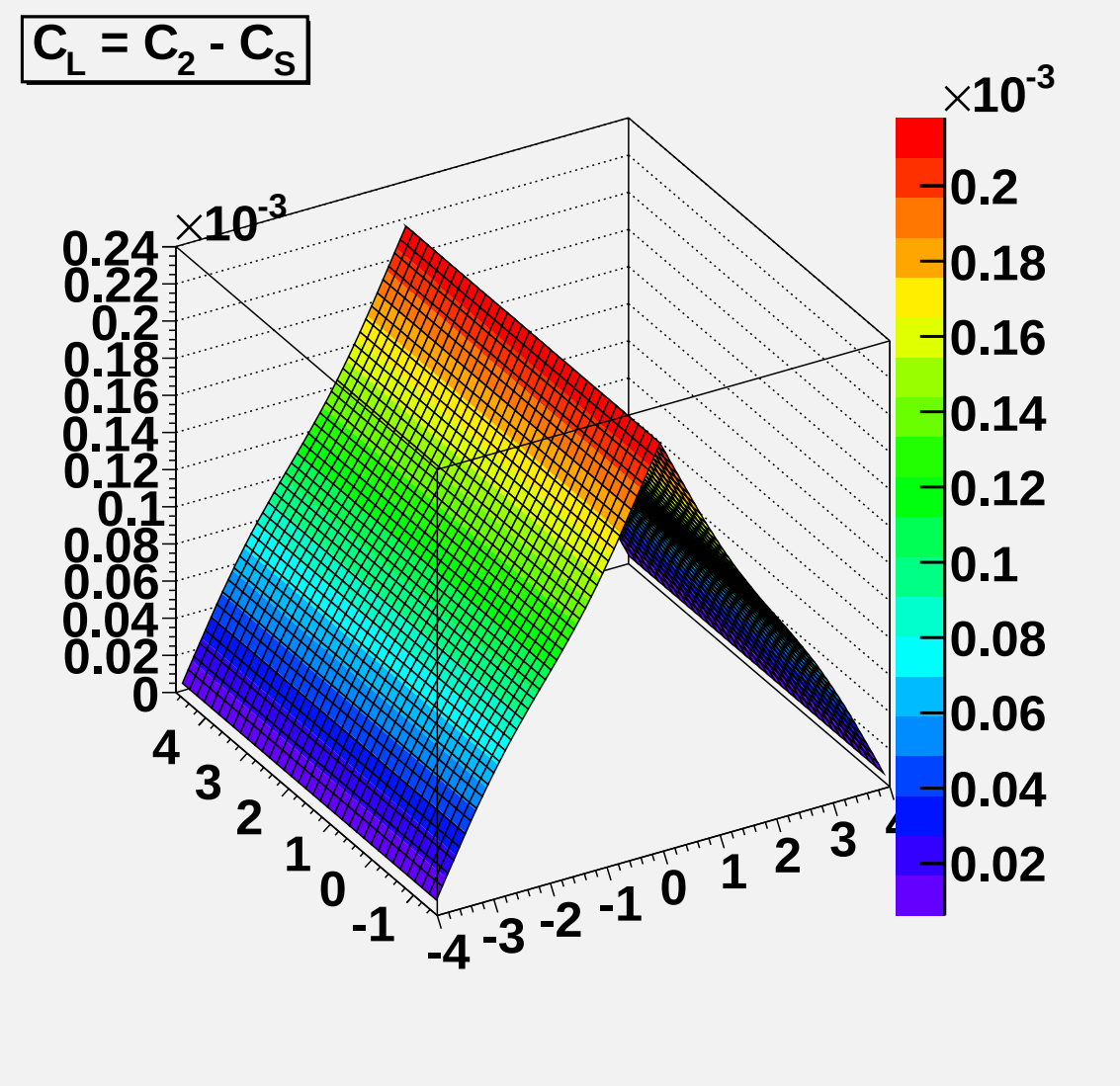

Figure 11.11: $C_L = C_2(\Delta\eta, \Delta\phi) - \langle C_2^{(n)}(\Delta\eta, \Delta\phi)\rangle$

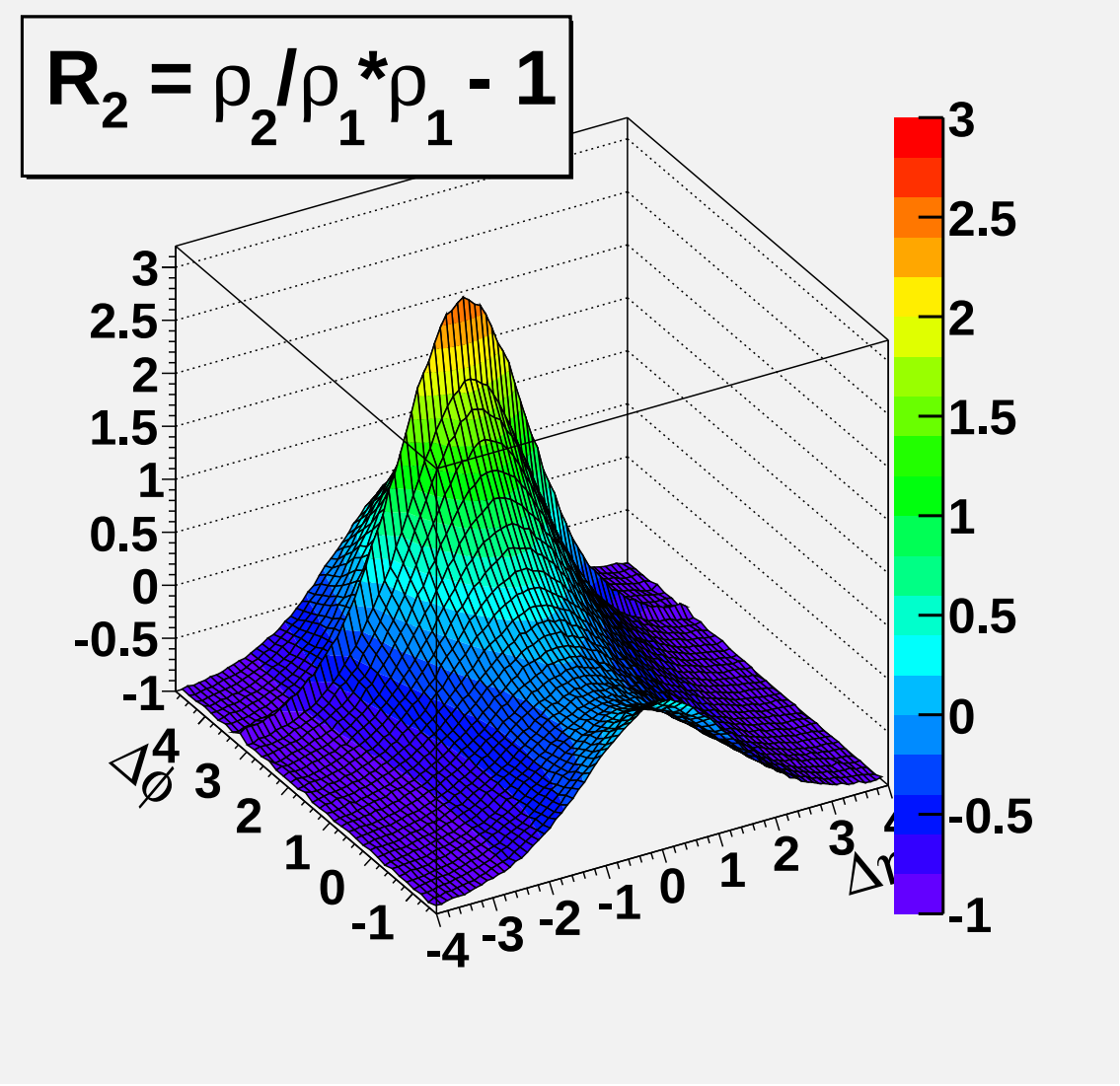

Figure 11.12: $R_2(\Delta\eta, \Delta\phi)$

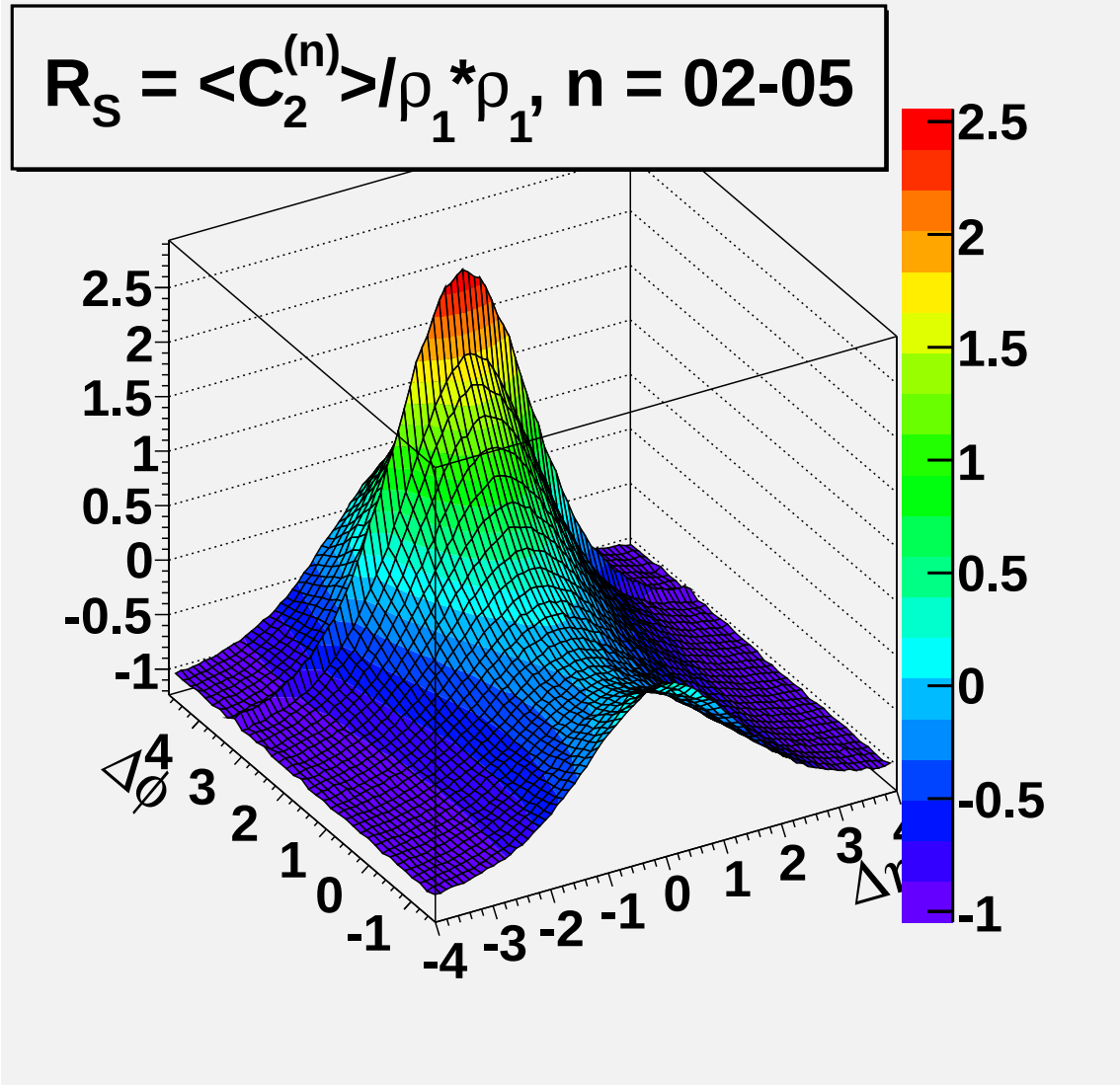

Figure 11.13: $R_S = \langle C_2^{(n)}(\Delta\eta, \Delta\phi)\rangle / \rho_1 * \rho_1(\Delta\eta, \Delta\phi)$

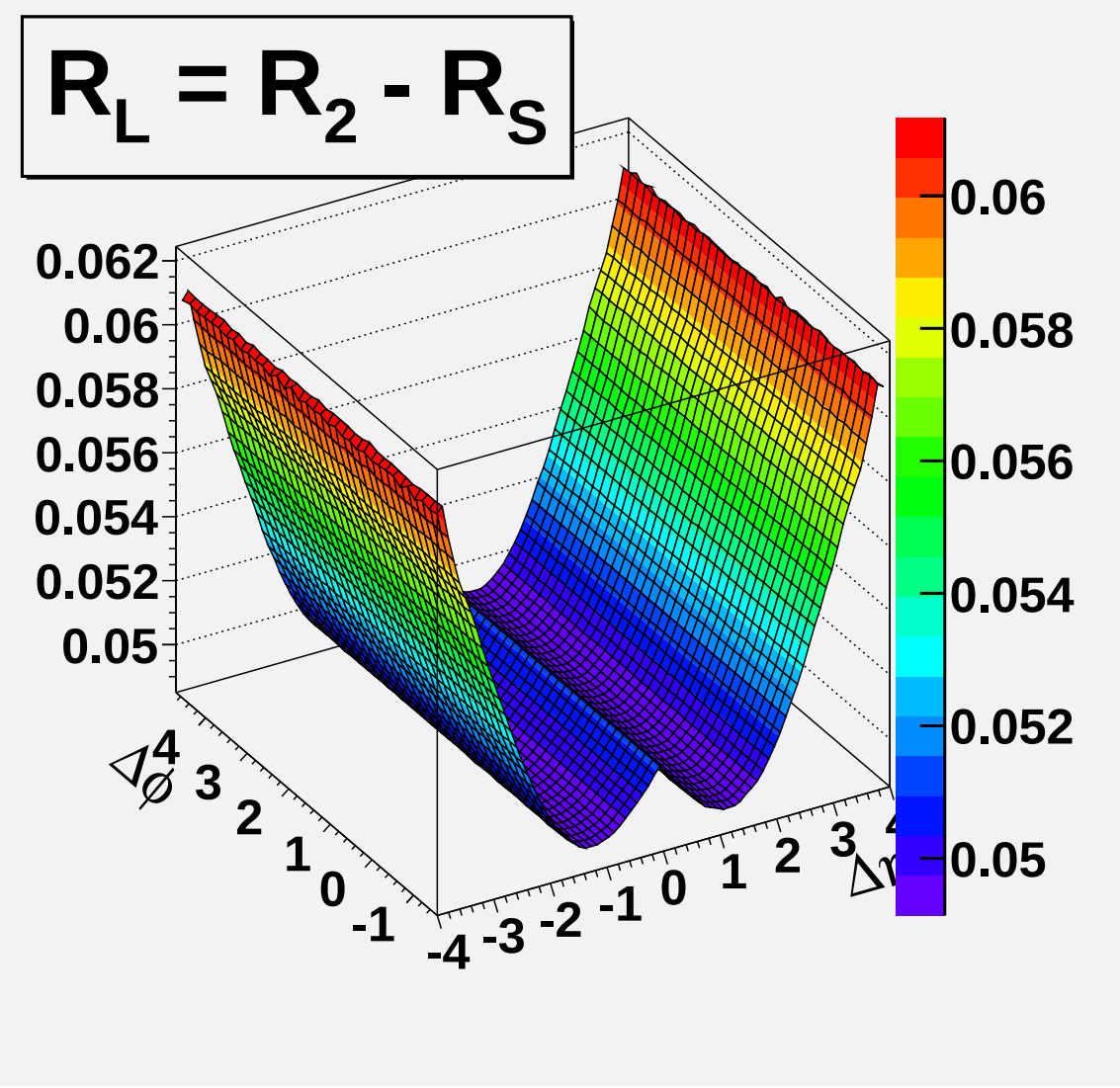

Figure 11.14: $R_L = R_2(\Delta\eta, \Delta\phi) - \langle C_2^{(n)}(\Delta\eta, \Delta\phi)\rangle / \rho_1 * \rho_1(\Delta\eta, \Delta\phi)$

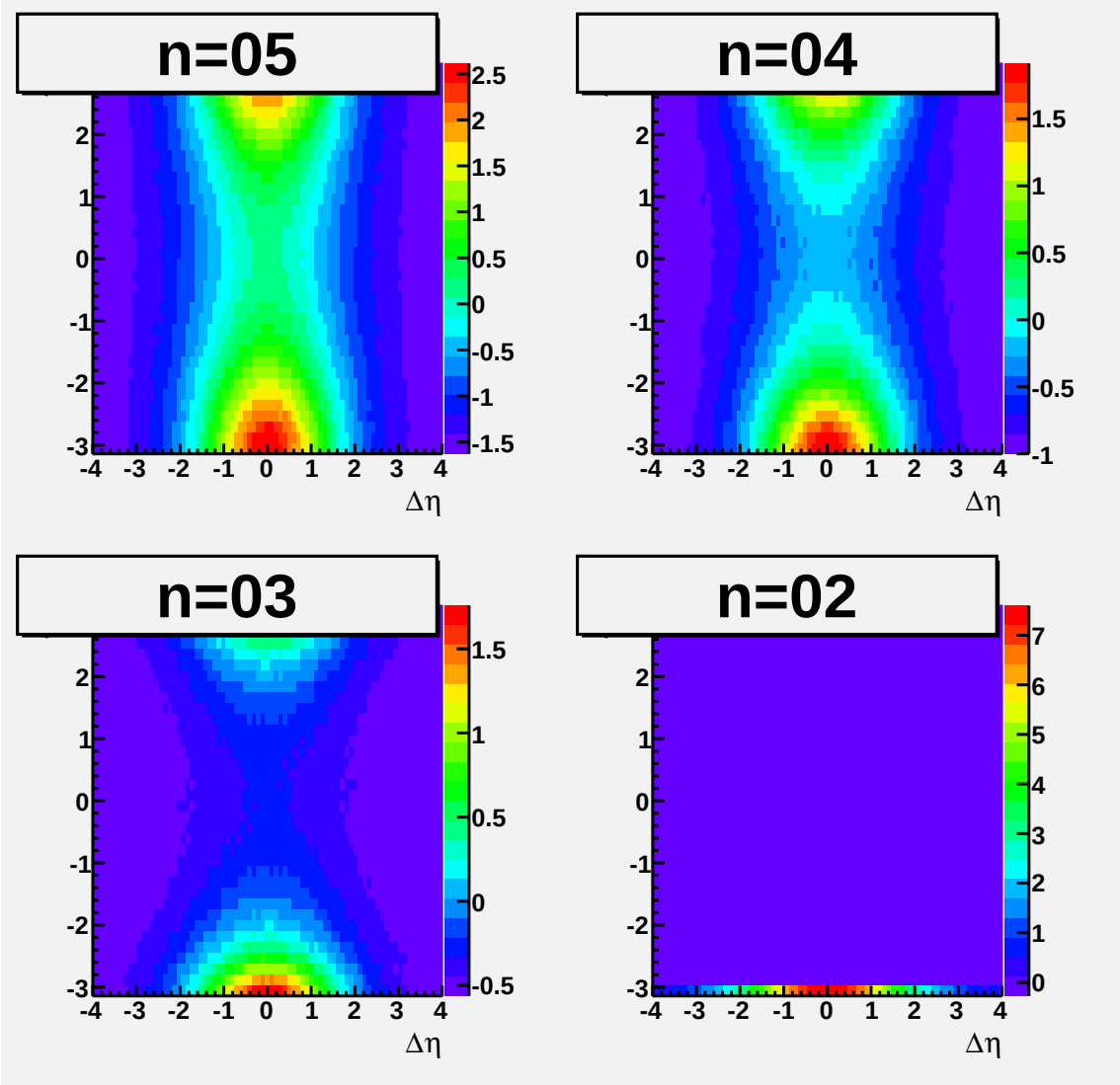

Figure 11.15: $R_2^{(n)} = C_2^{(n)}(\Delta\eta, \Delta\phi)/\rho_1 * \rho_1(\Delta\eta, \Delta\phi)$

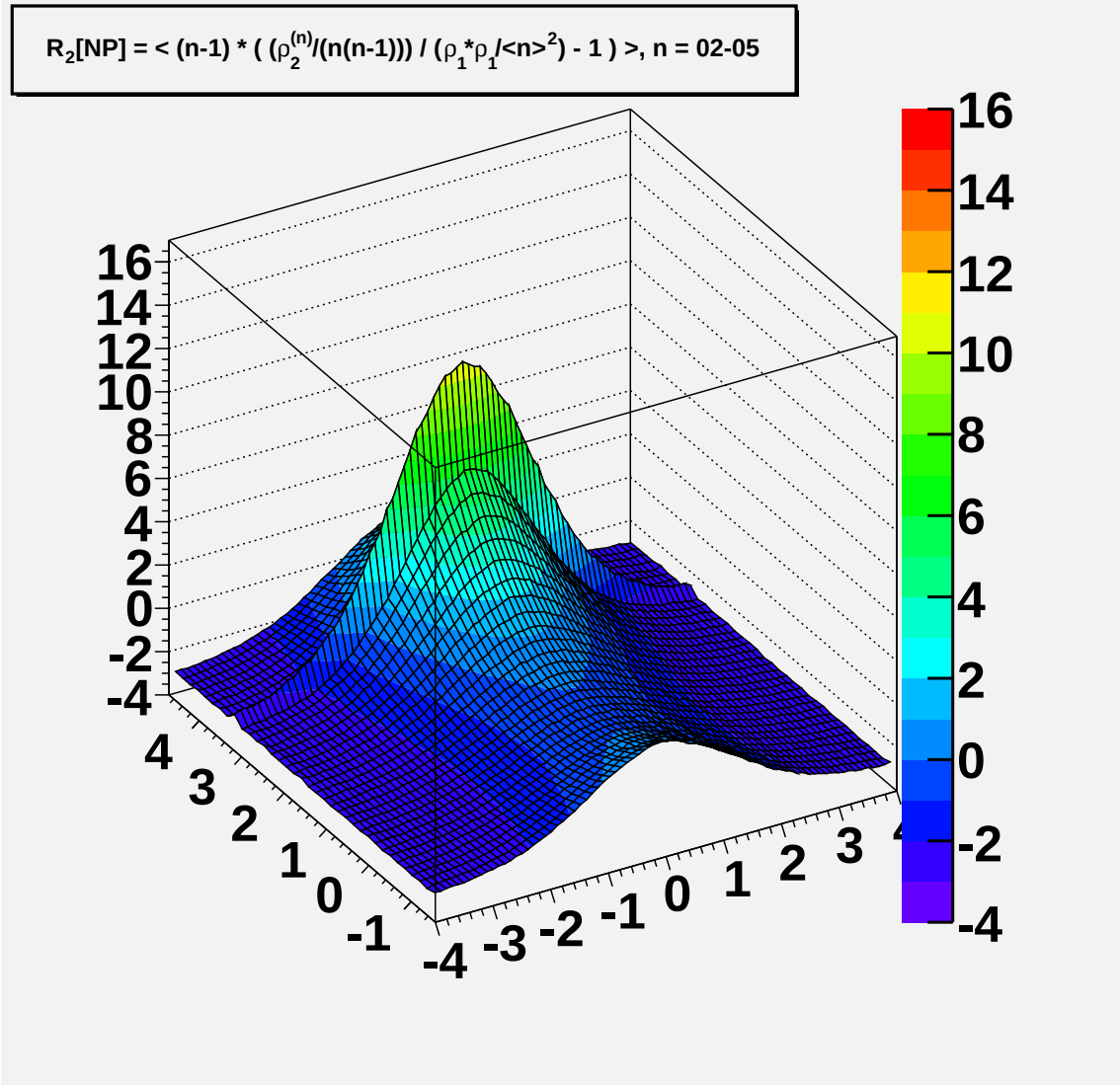

Figure 11.16: $\langle R_2^{(n)}[NP](\Delta\eta, \Delta\phi)\rangle$

11.3 $p + p$ (3)

Model pp3: Same as pp2b, but with transverse momentum added in the rest frame of each individual cluster, distributed normally with variance 1 GeV.

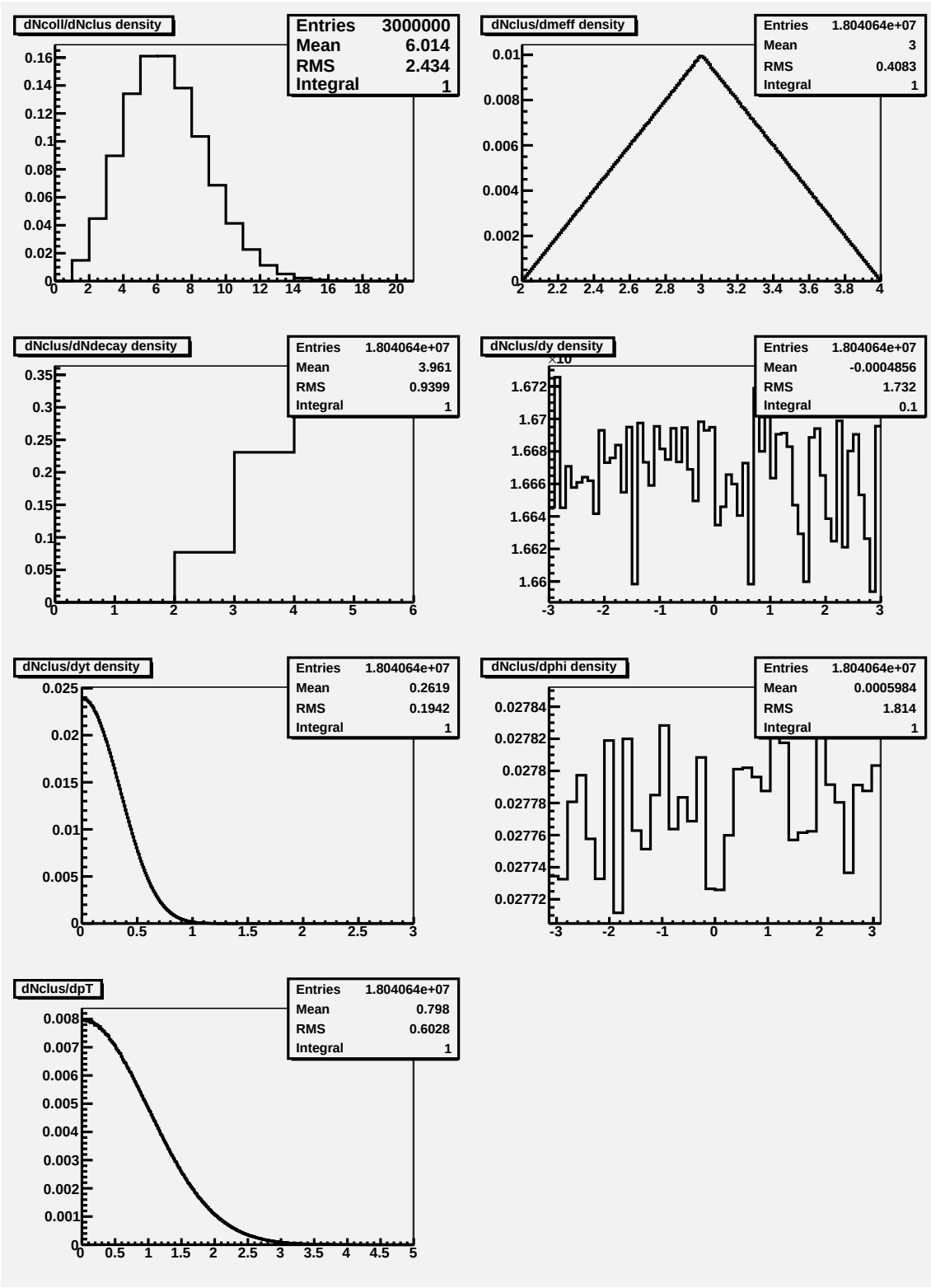
dNcoll/dNclus density
Entries 3000000
Mean 6.014
RMS 2.434
Integral 1
dNclus/dmeff density
Entries 1.804064e+07
Mean 3
RMS 0.4083
Integral 1
dNclus/dNdecay density
Entries 1.804064e+07
Mean 3.961
RMS 0.9399
Integral 1
dNclus/dy density
Entries 1.804064e+07
Mean -0.0004856
RMS 1.732
Integral 0.1
dNclus/dyt density
Entries 1.804064e+07
Mean 0.2619
RMS 0.1942
Integral 1
dNclus/dphi density
Entries 1.804064e+07
Mean 0.0005984
RMS 1.814
Integral 1
dNclus/dpT
Entries 1.804064e+07
Mean 0.798
RMS 0.6028
Integral 1

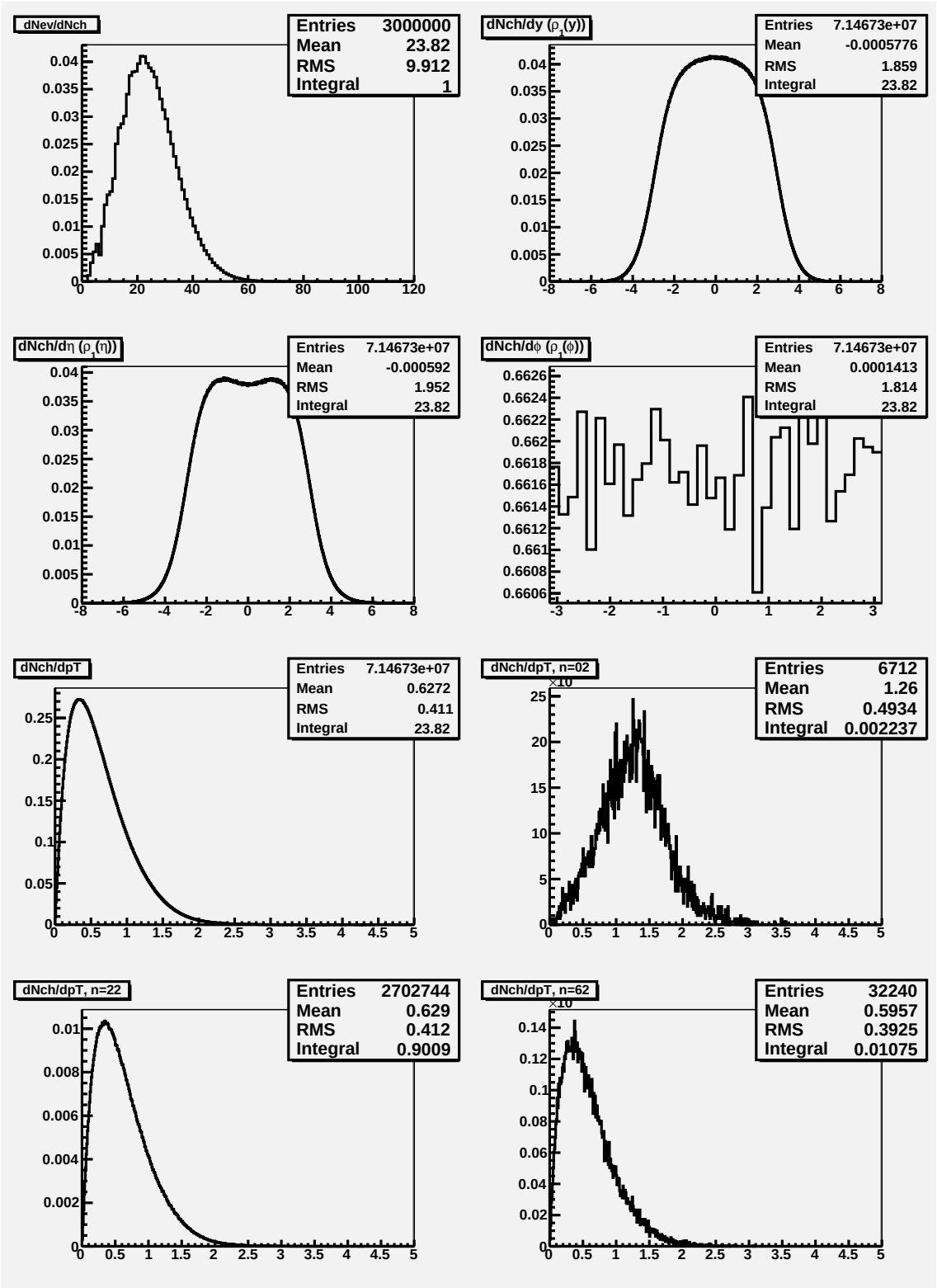
dNev/dNch
Entries 3000000
Mean 23.82
RMS 9.912
Integral 1
dNch/dy (ρ1(y))
Entries 7.14673e+07
Mean -0.0005776
RMS 1.859
Integral 23.82
dNch/dη (ρ1(η))
Entries 7.14673e+07
Mean -0.000592
RMS 1.952
Integral 23.82
dNch/dφ (ρ1(φ))
Entries 7.14673e+07
Mean 0.0001413
RMS 1.814
Integral 23.82
dNch/dpT
Entries 7.14673e+07
Mean 0.6272
RMS 0.411
Integral 23.82
dNch/dpT, n=02
Entries 6712
Mean 1.26
RMS 0.4934
Integral 0.002237
dNch/dpT, n=22
Entries 2702744
Mean 0.629
RMS 0.412
Integral 0.9009
dNch/dpT, n=62
Entries 32240
Mean 0.5957
RMS 0.3925
Integral 0.01075

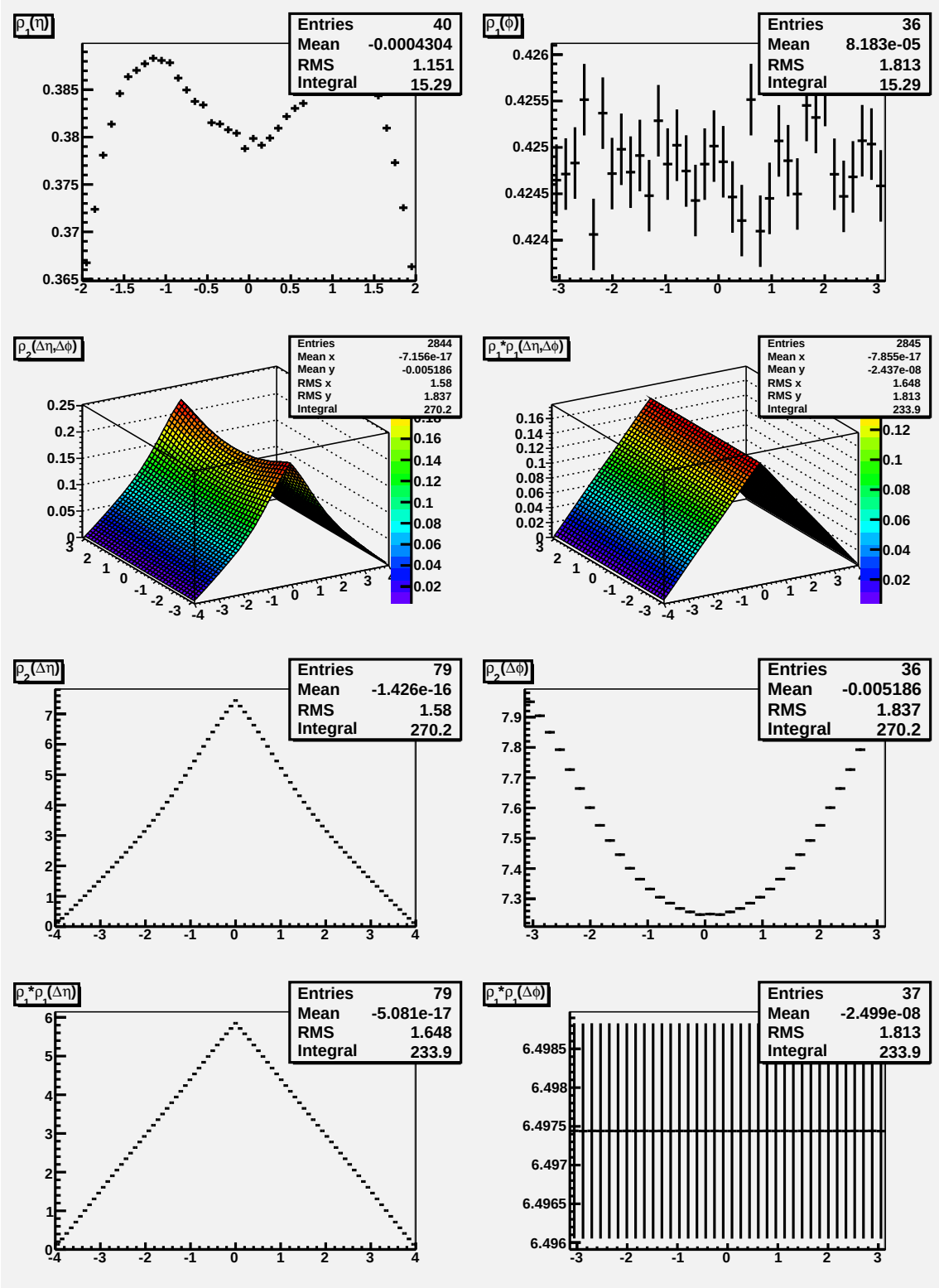
ρ1(η)
Entries 40
Mean -0.0004304
RMS 1.151
Integral 15.29
ρ1(φ)
Entries 36
Mean 8.183e-05
RMS 1.813
Integral 15.29
ρ2(Δη,Δφ)
Entries 2844
Mean x -7.156e-17
Mean y -0.005186
RMS x 1.58
RMS y 1.837
Integral 270.2
ρ1*ρ1(Δη,Δφ)
Entries 2845
Mean x -7.855e-17
Mean y -2.437e-08
RMS x 1.648
RMS y 1.813
Integral 233.9
ρ2(Δη)
Entries 79
Mean -1.426e-16
RMS 1.58
Integral 270.2
ρ2(Δφ)
Entries 36
Mean -0.005186
RMS 1.837
Integral 270.2
ρ1*ρ1(Δη)
Entries 79
Mean -5.081e-17
RMS 1.648
Integral 233.9
ρ1*ρ1(Δφ)
Entries 37
Mean -2.499e-08
RMS 1.813
Integral 233.9

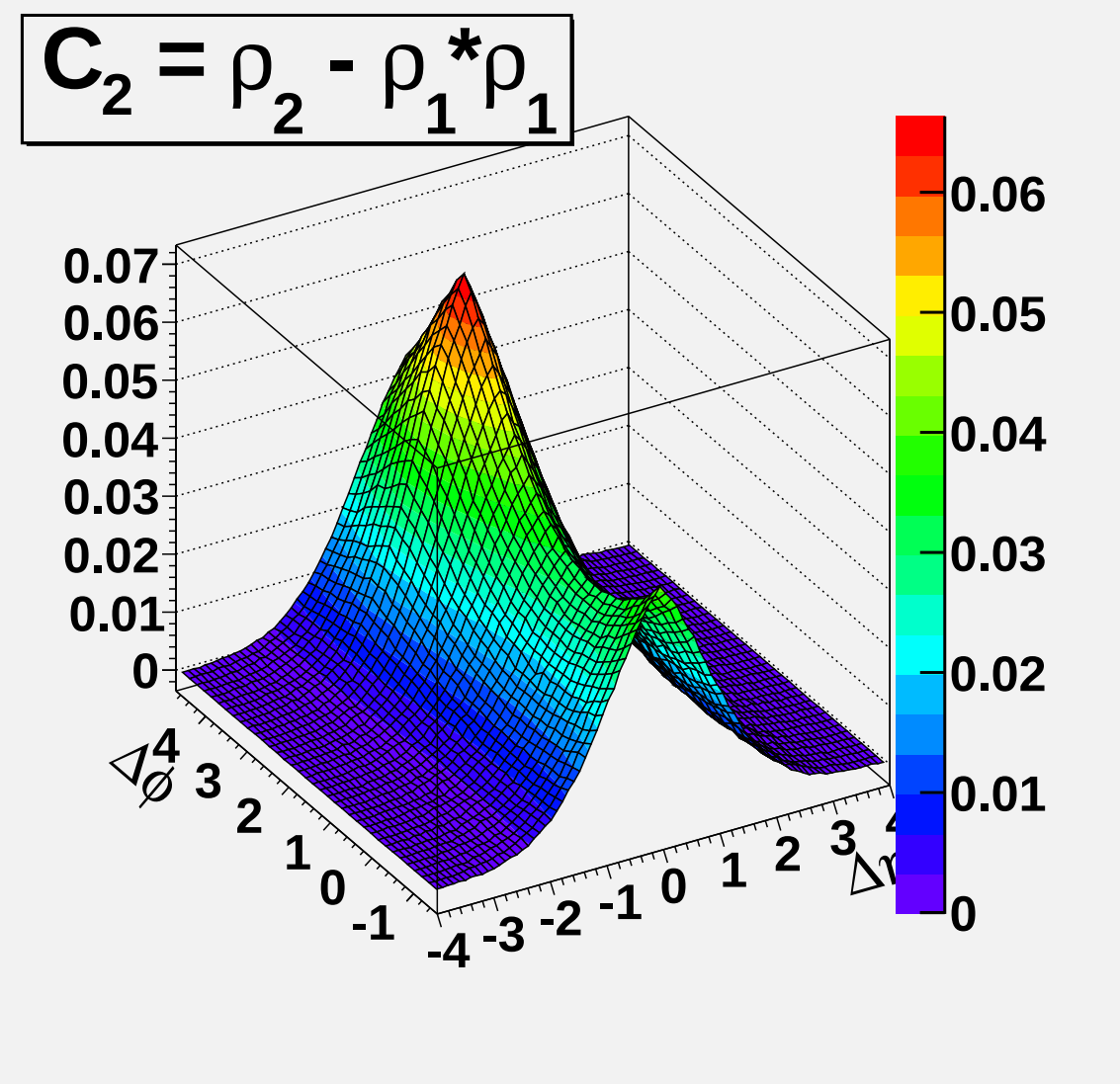

Figure 11.17: $C_2(\Delta\eta, \Delta\phi)$

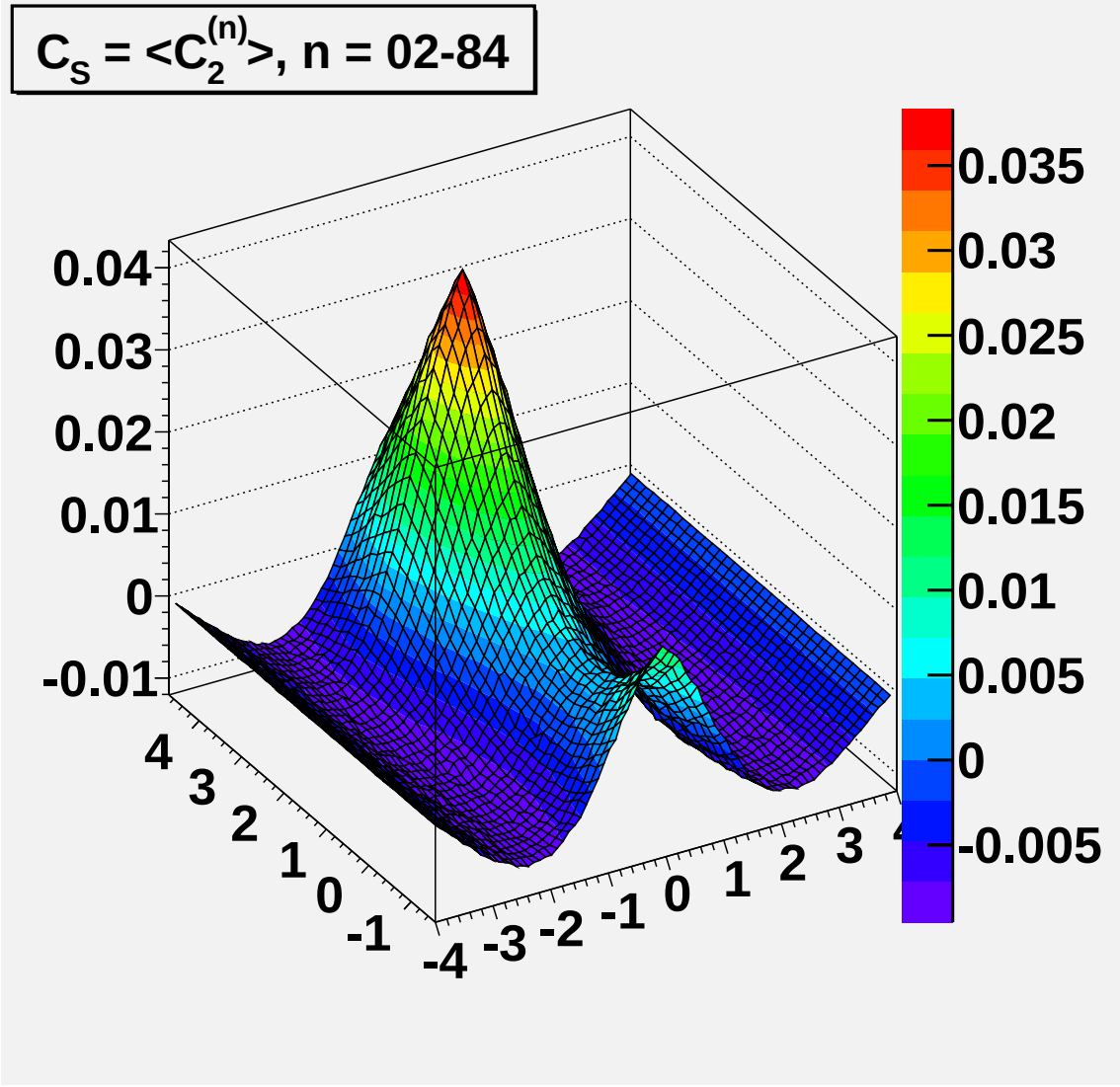

Figure 11.18: $C_S = \langle C_2^{(n)}(\Delta\eta, \Delta\phi)\rangle$

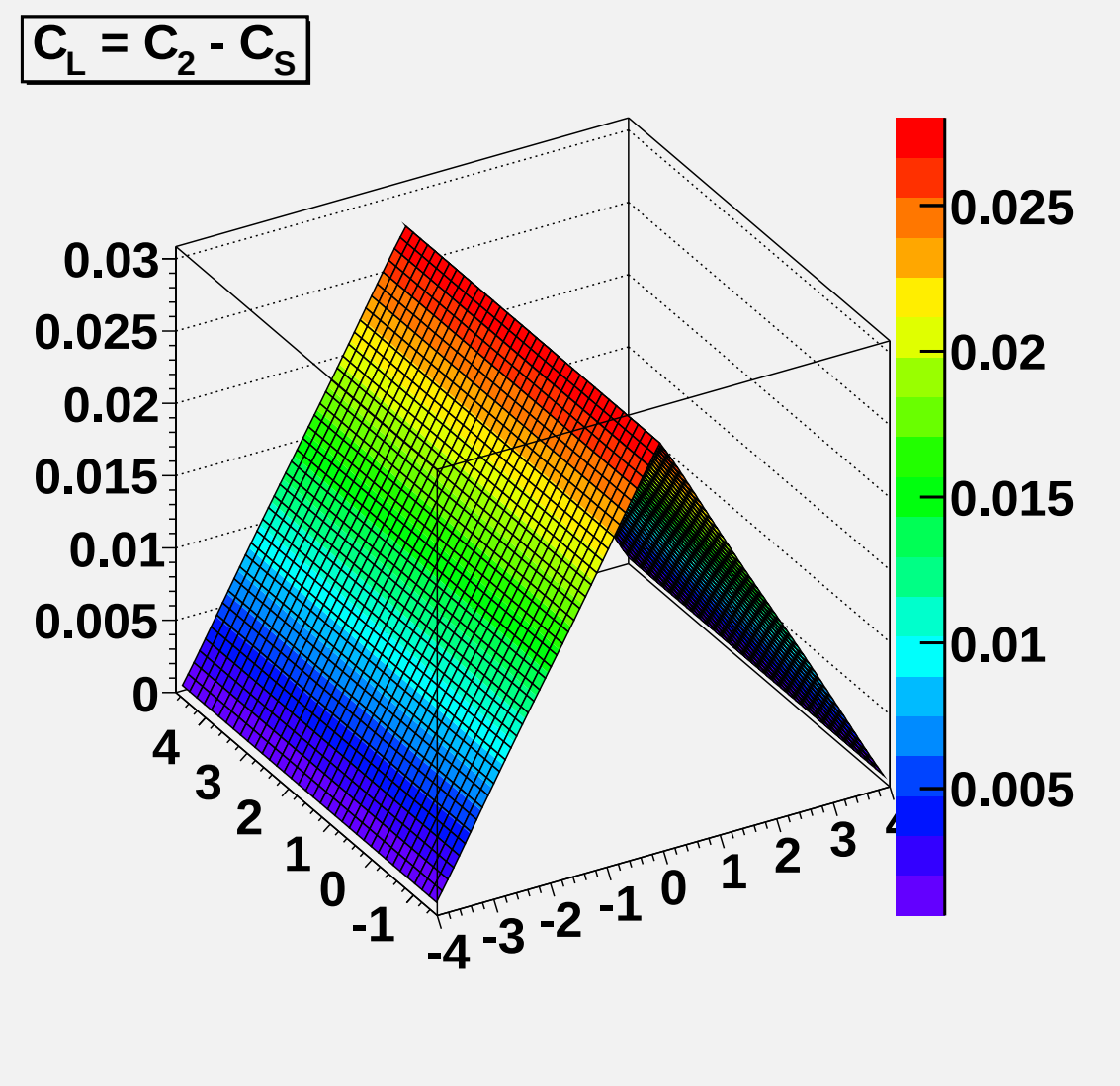

Figure 11.19: $C_L = C_2(\Delta\eta, \Delta\phi) - \langle C_2^{(n)}(\Delta\eta, \Delta\phi)\rangle$

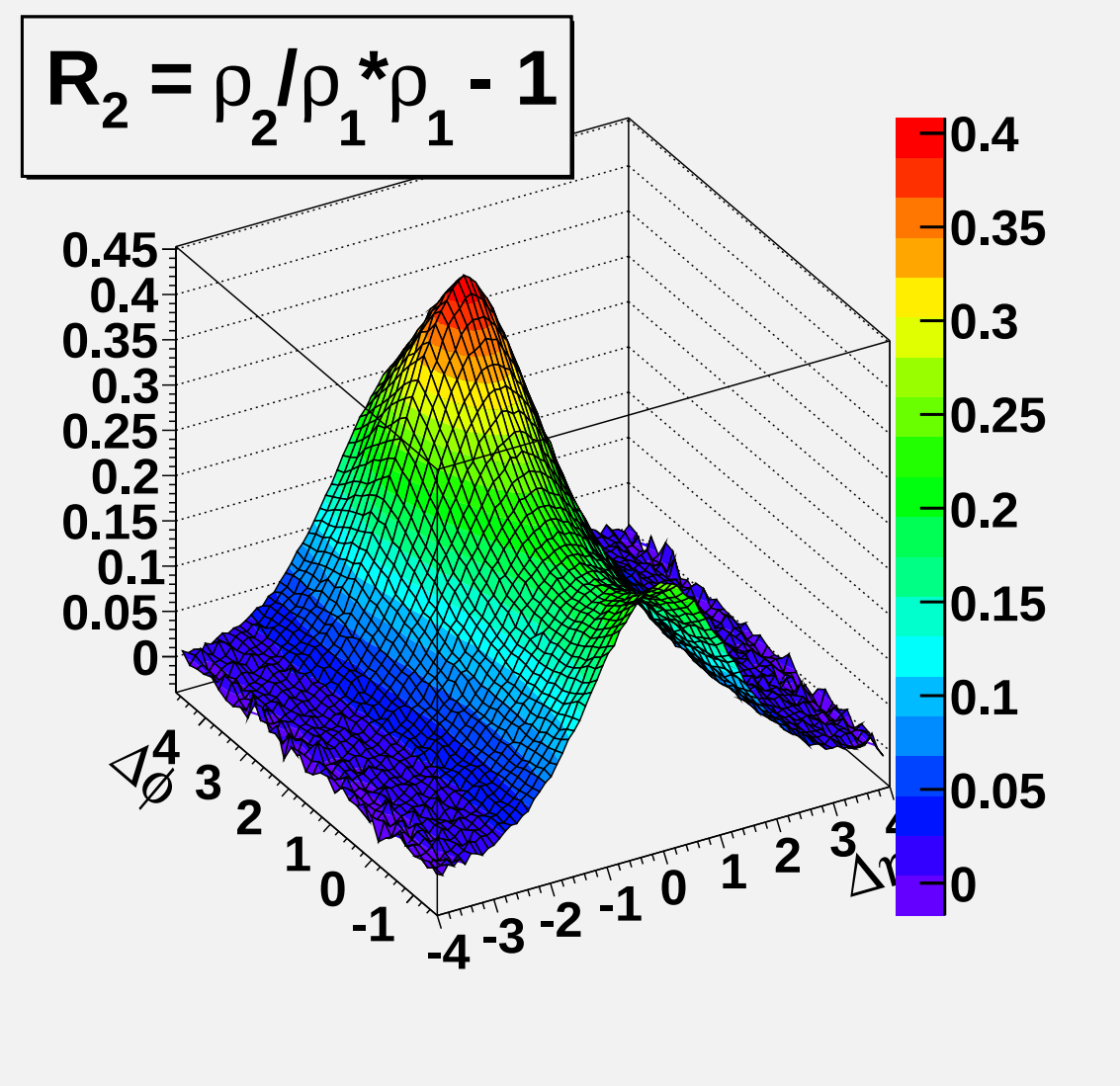

Figure 11.20: $R_2(\Delta\eta, \Delta\phi)$

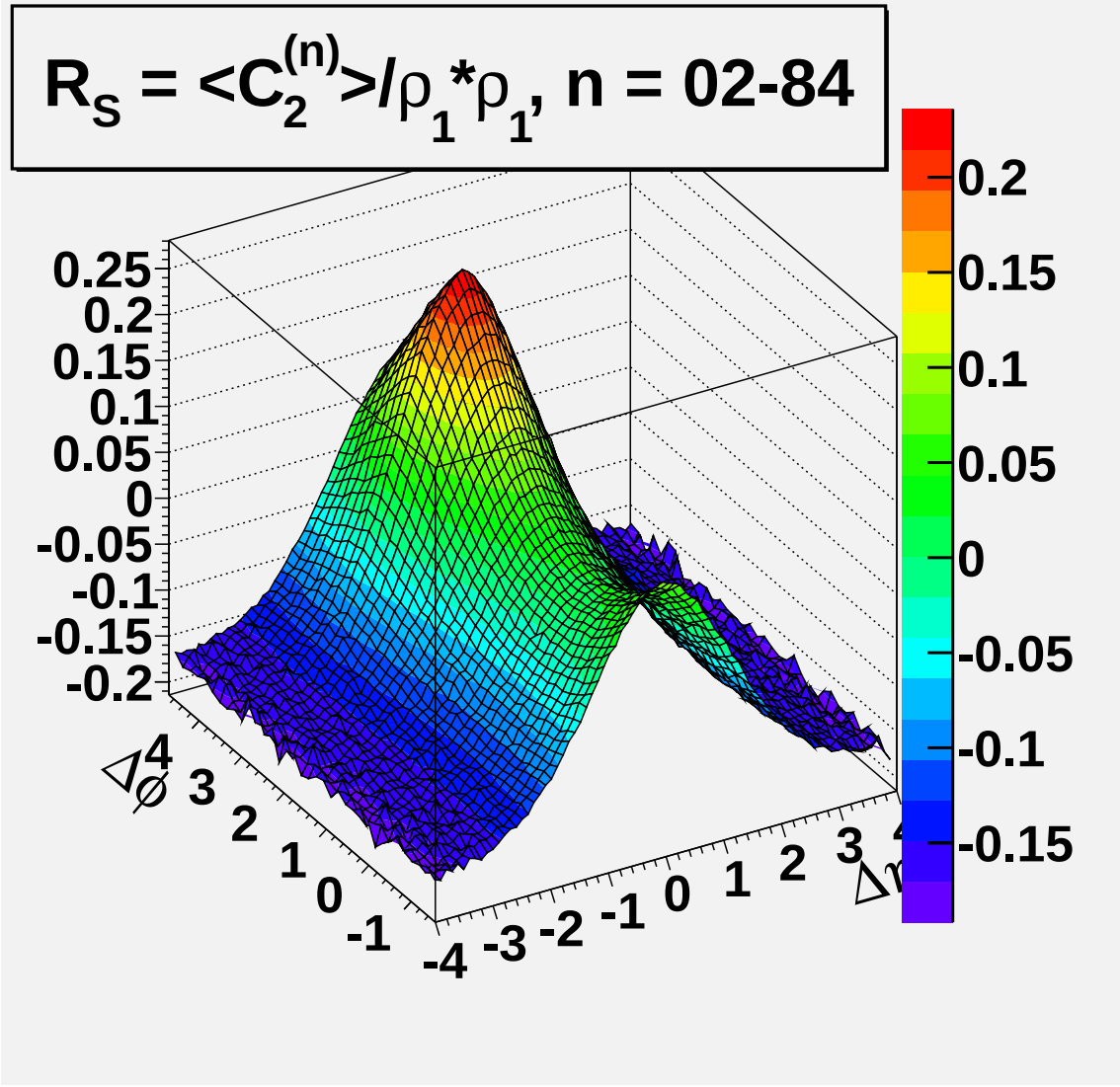

Figure 11.21: $R_S = \langle C_2^{(n)}(\Delta\eta, \Delta\phi)\rangle / \rho_1 * \rho_1(\Delta\eta, \Delta\phi)$

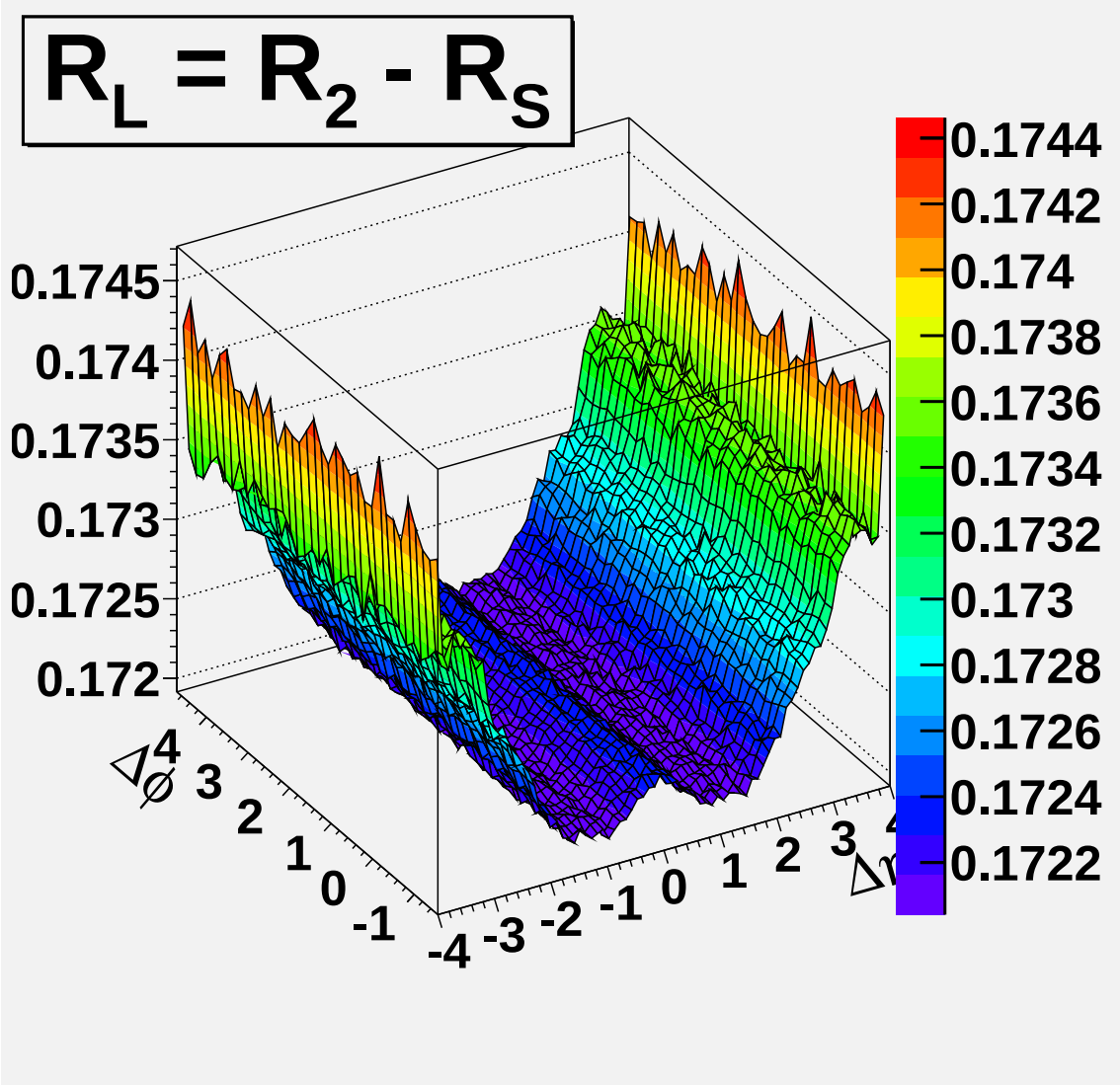

Figure 11.22: $R_L = R_2(\Delta\eta, \Delta\phi) - \langle C_2^{(n)}(\Delta\eta, \Delta\phi)\rangle / \rho_1 * \rho_1(\Delta\eta, \Delta\phi)$

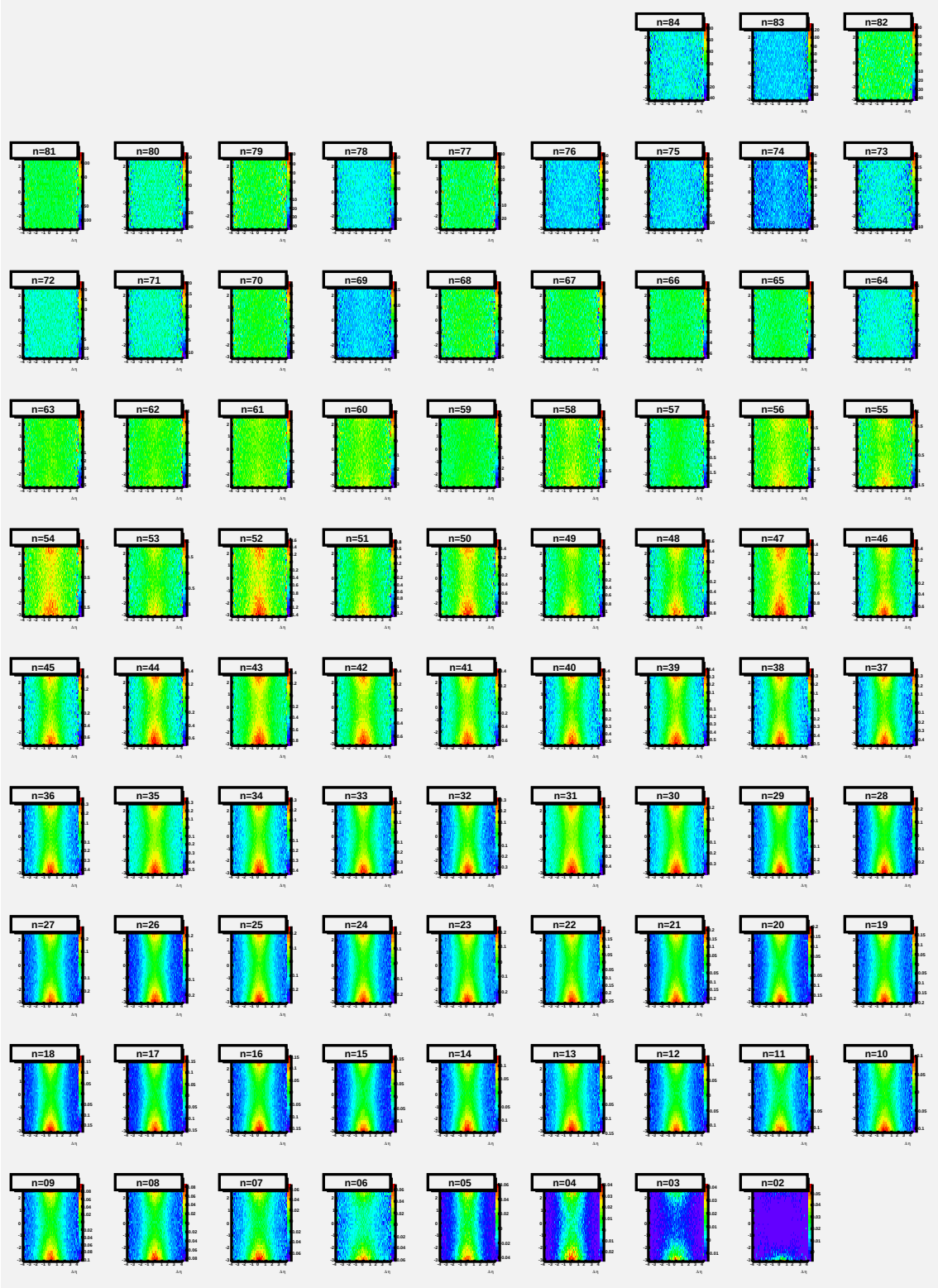

Figure 11.23: $R_2^{(n)} = C_2^{(n)}(\Delta\eta, \Delta\phi)/\rho_1 * \rho_1(\Delta\eta, \Delta\phi)$

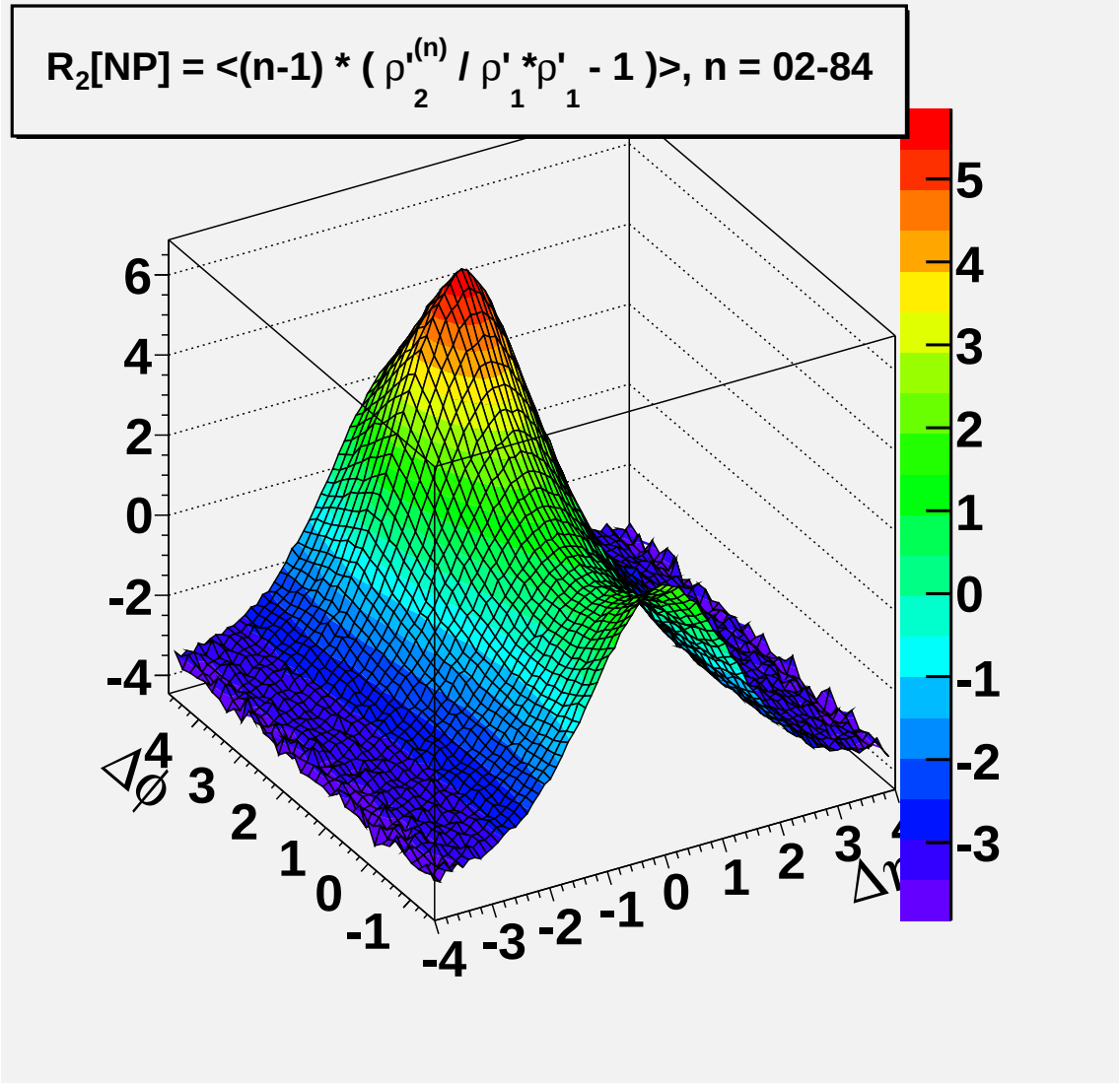

Figure 11.24: $\langle R_2^{(n)}[NP](\Delta\eta, \Delta\phi)\rangle$

11.4 $p + p$ (4a)

Model pp4a: Same as pp2b, but with a transverse rapidity boost in the rest frame of each individual cluster, distributed linearly on (0,0.7).

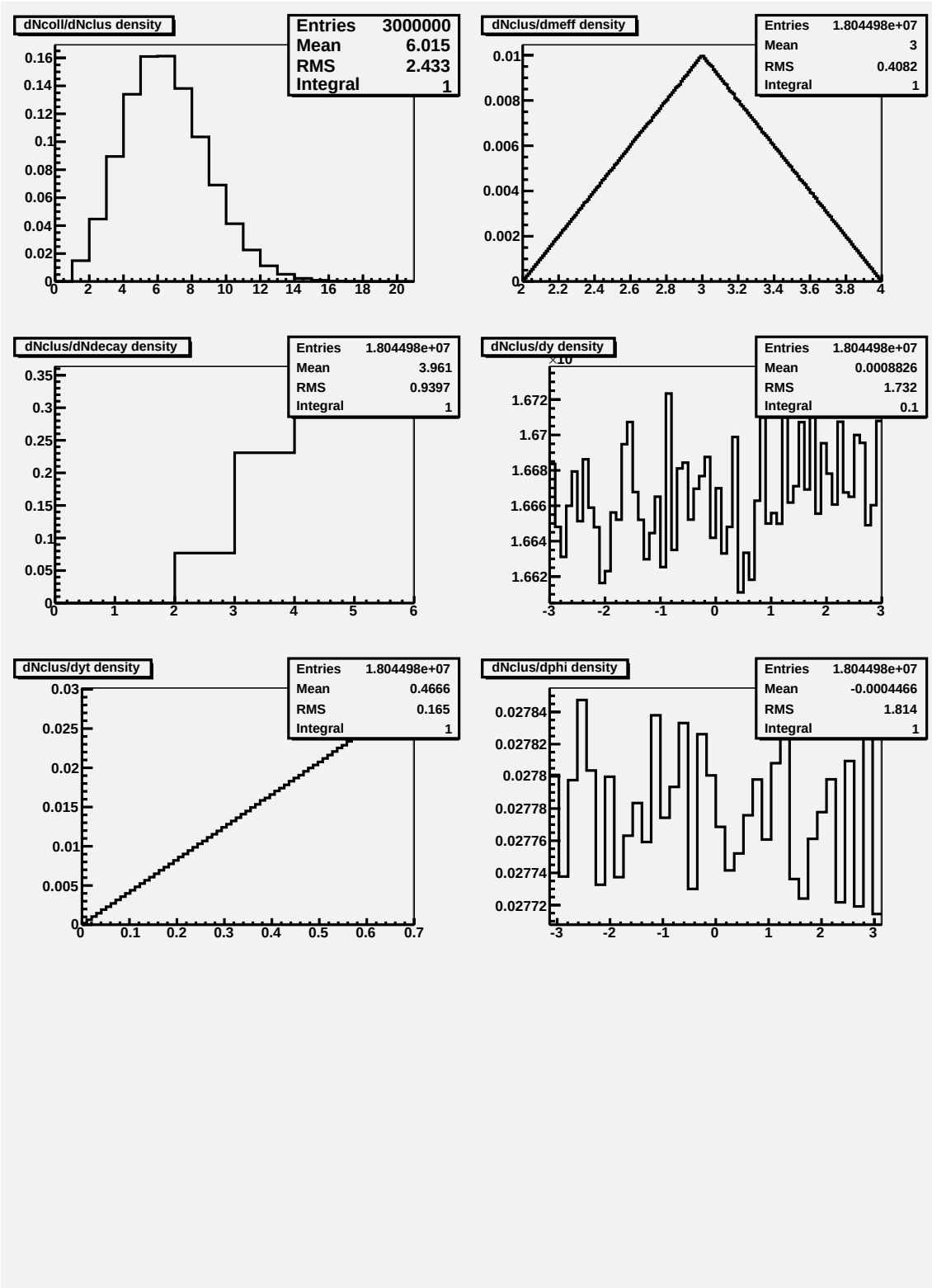
dNcoll/dNclus density
Entries 3000000
Mean 6.015
RMS 2.433
Integral 1
dNclus/dmeff density
Entries 1.804498e+07
Mean 3
RMS 0.4082
Integral 1
dNclus/dNdecay density
Entries 1.804498e+07
Mean 3.961
RMS 0.9397
Integral 1
dNclus/dy density
Entries 1.804498e+07
Mean 0.0008826
RMS 1.732
Integral 0.1
dNclus/dyt density
Entries 1.804498e+07
Mean 0.4666
RMS 0.165
Integral 1
dNclus/dphi density
Entries 1.804498e+07
Mean -0.0004466
RMS 1.814
Integral 1

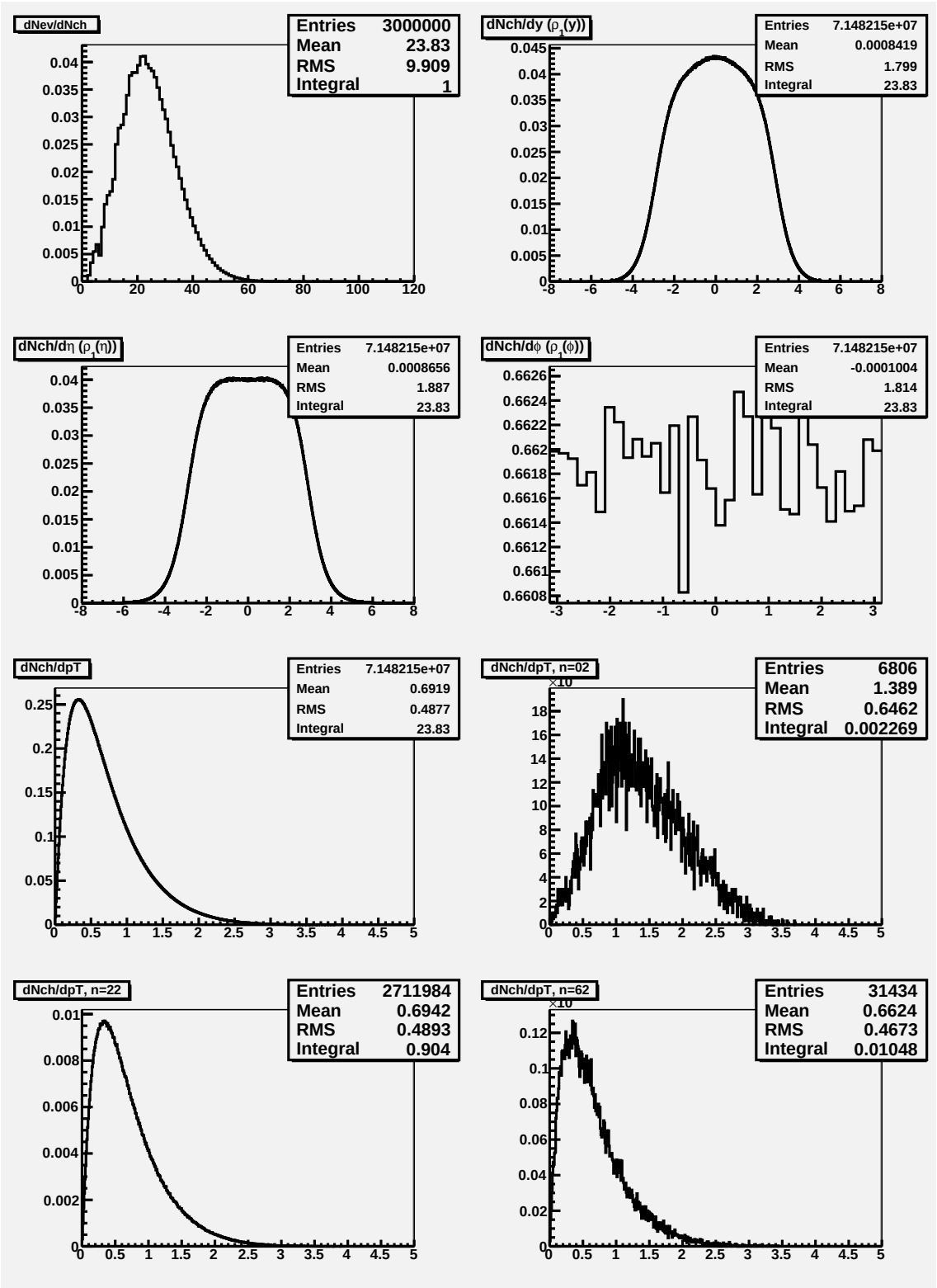
dNev/dNch
Entries 3000000
Mean 23.83
RMS 9.909
Integral 1
dNch/dy (ρ1(y))
Entries 7.148215e+07
Mean 0.0008419
RMS 1.799
Integral 23.83
dNch/dη (ρ1(η))
Entries 7.148215e+07
Mean 0.0008656
RMS 1.887
Integral 23.83
dNch/dφ (ρ1(φ))
Entries 7.148215e+07
Mean -0.0001004
RMS 1.814
Integral 23.83
dNch/dpT
Entries 7.148215e+07
Mean 0.6919
RMS 0.4877
Integral 23.83
dNch/dpT, n=02
Entries 6806
Mean 1.389
RMS 0.6462
Integral 0.002269
dNch/dpT, n=22
Entries 2711984
Mean 0.6942
RMS 0.4893
Integral 0.904
dNch/dpT, n=62
Entries 31434
Mean 0.6624
RMS 0.4673
Integral 0.01048

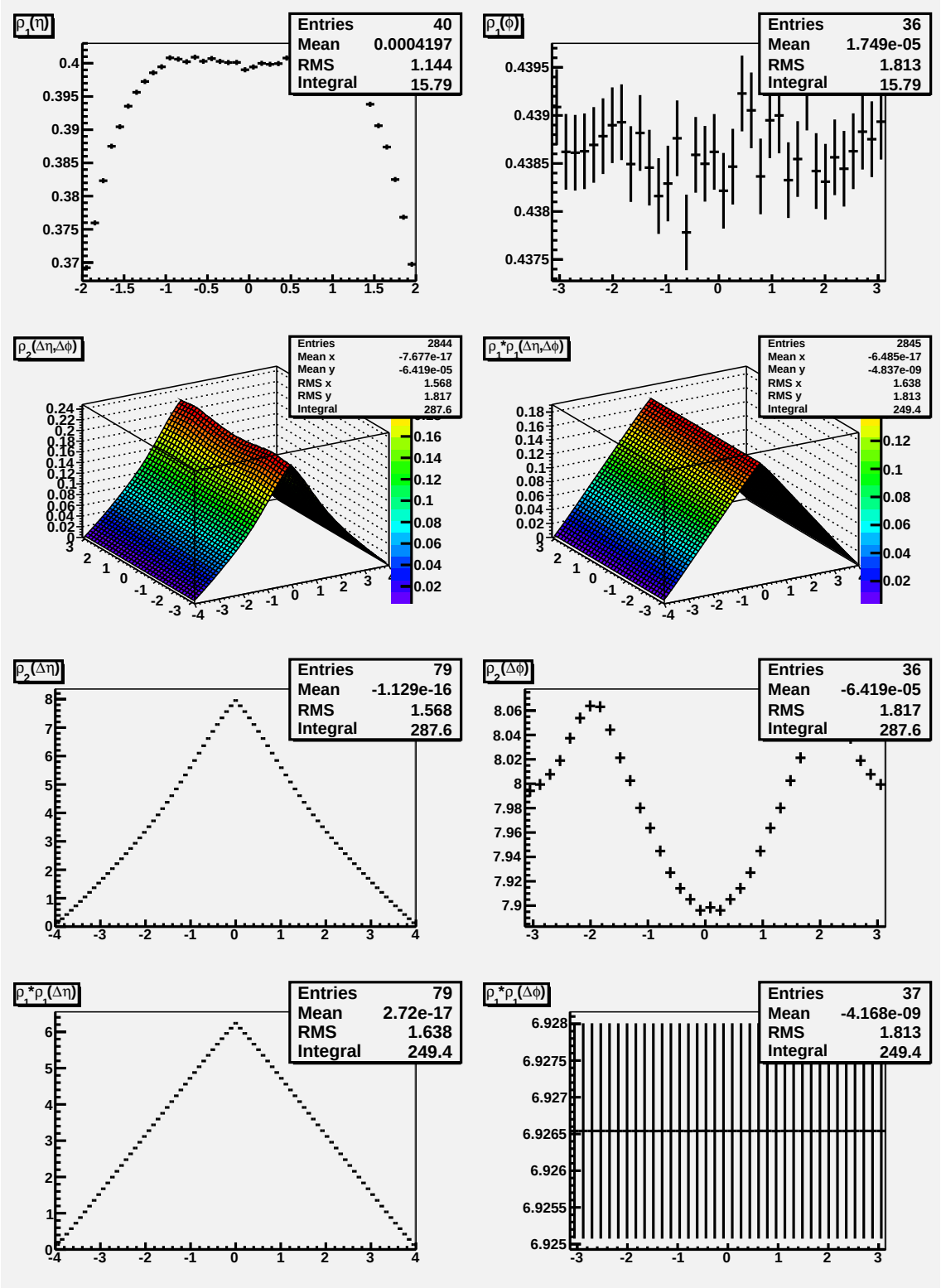
ρ1(η)
Entries 40
Mean 0.0004197
RMS 1.144
Integral 15.79
ρ1(φ)
Entries 36
Mean 1.749e-05
RMS 1.813
Integral 15.79
ρ2(Δη,Δφ)
Entries 2844
Mean x -7.677e-17
Mean y -6.419e-05
RMS x 1.568
RMS y 1.817
Integral 287.6
ρ1*ρ1(Δη,Δφ)
Entries 2845
Mean x -6.485e-17
Mean y -4.837e-09
RMS x 1.638
RMS y 1.813
Integral 249.4
ρ2(Δη)
Entries 79
Mean -1.129e-16
RMS 1.568
Integral 287.6
ρ2(Δφ)
Entries 36
Mean -6.419e-05
RMS 1.817
Integral 287.6
ρ1*ρ1(Δη)
Entries 79
Mean 2.72e-17
RMS 1.638
Integral 249.4
ρ1*ρ1(Δφ)
Entries 37
Mean -4.168e-09
RMS 1.813
Integral 249.4

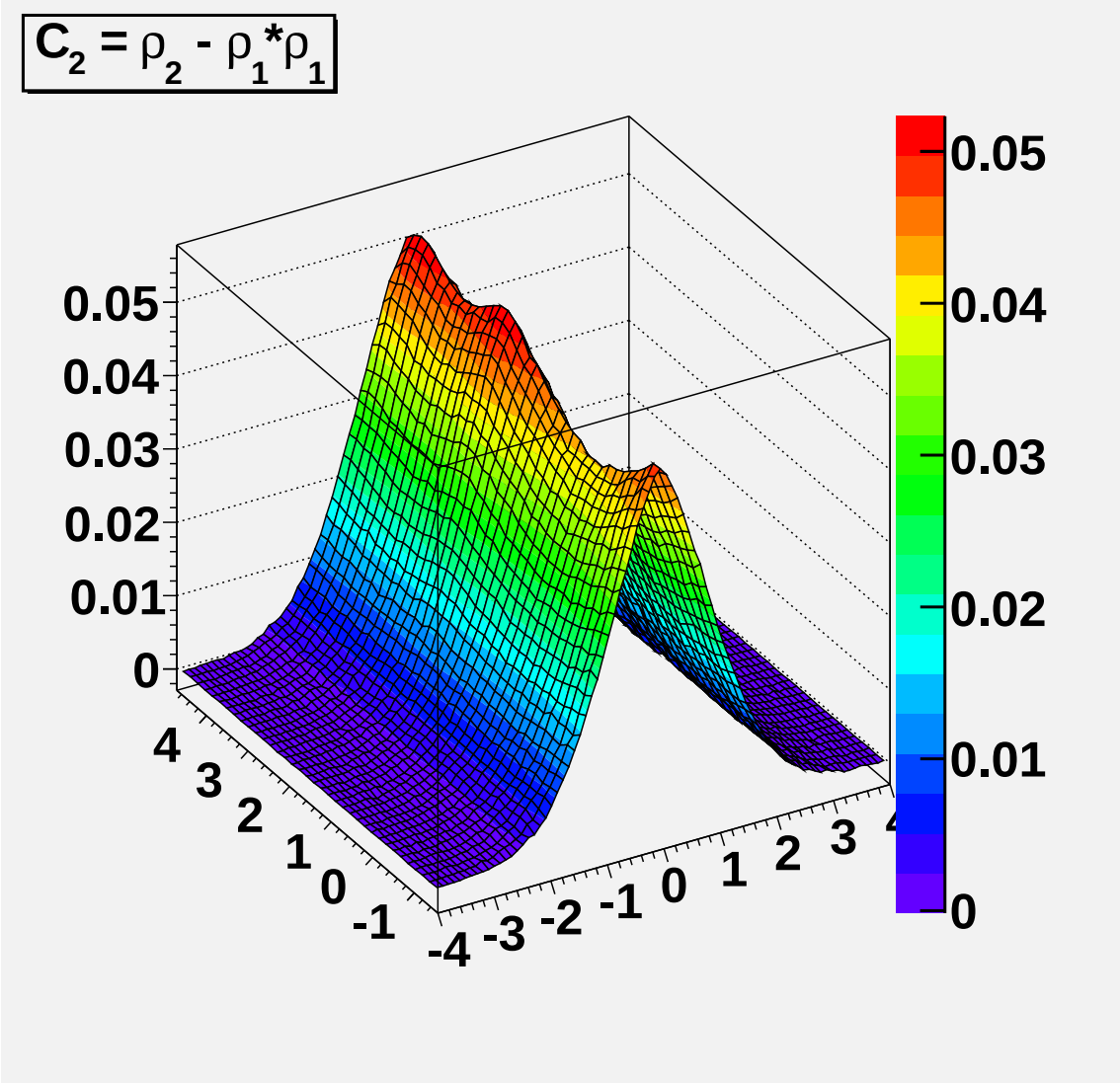

Figure 11.25: $C_2(\Delta\eta, \Delta\phi)$

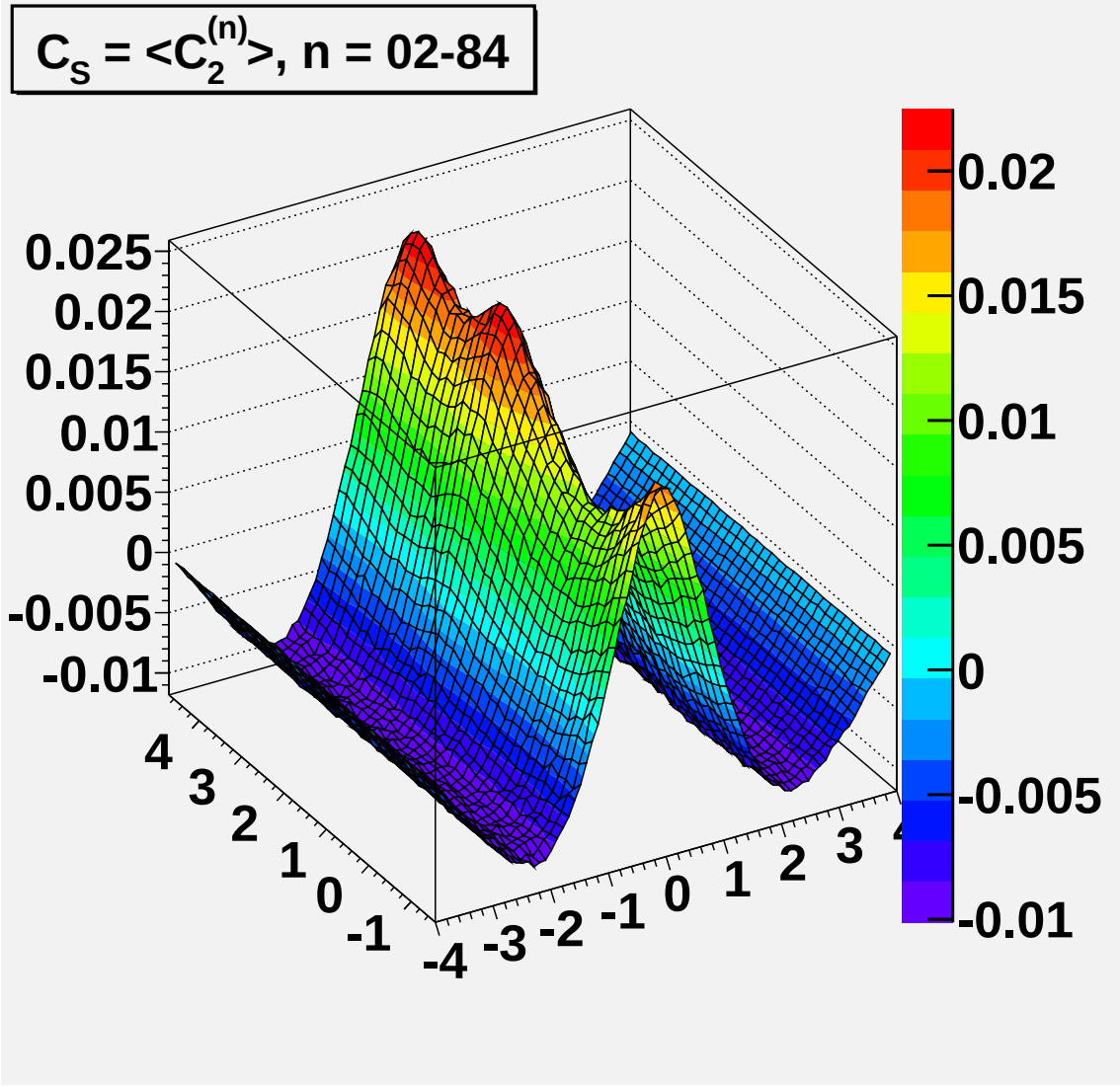

Figure 11.26: $C_S = \langle C_2^{(n)}(\Delta\eta, \Delta\phi)\rangle$

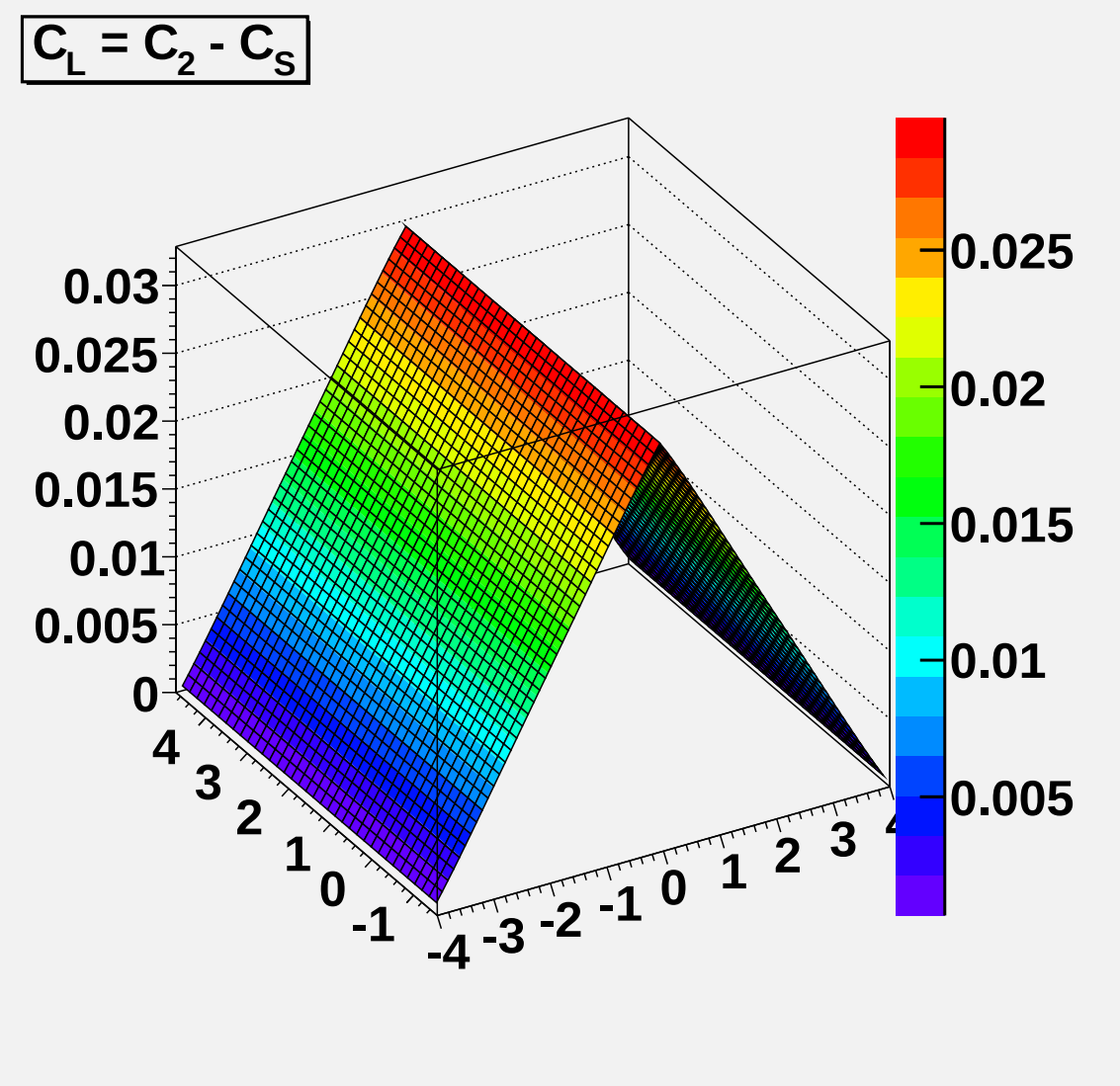

Figure 11.27: $C_L = C_2(\Delta\eta, \Delta\phi) - \langle C_2^{(n)}(\Delta\eta, \Delta\phi)\rangle$

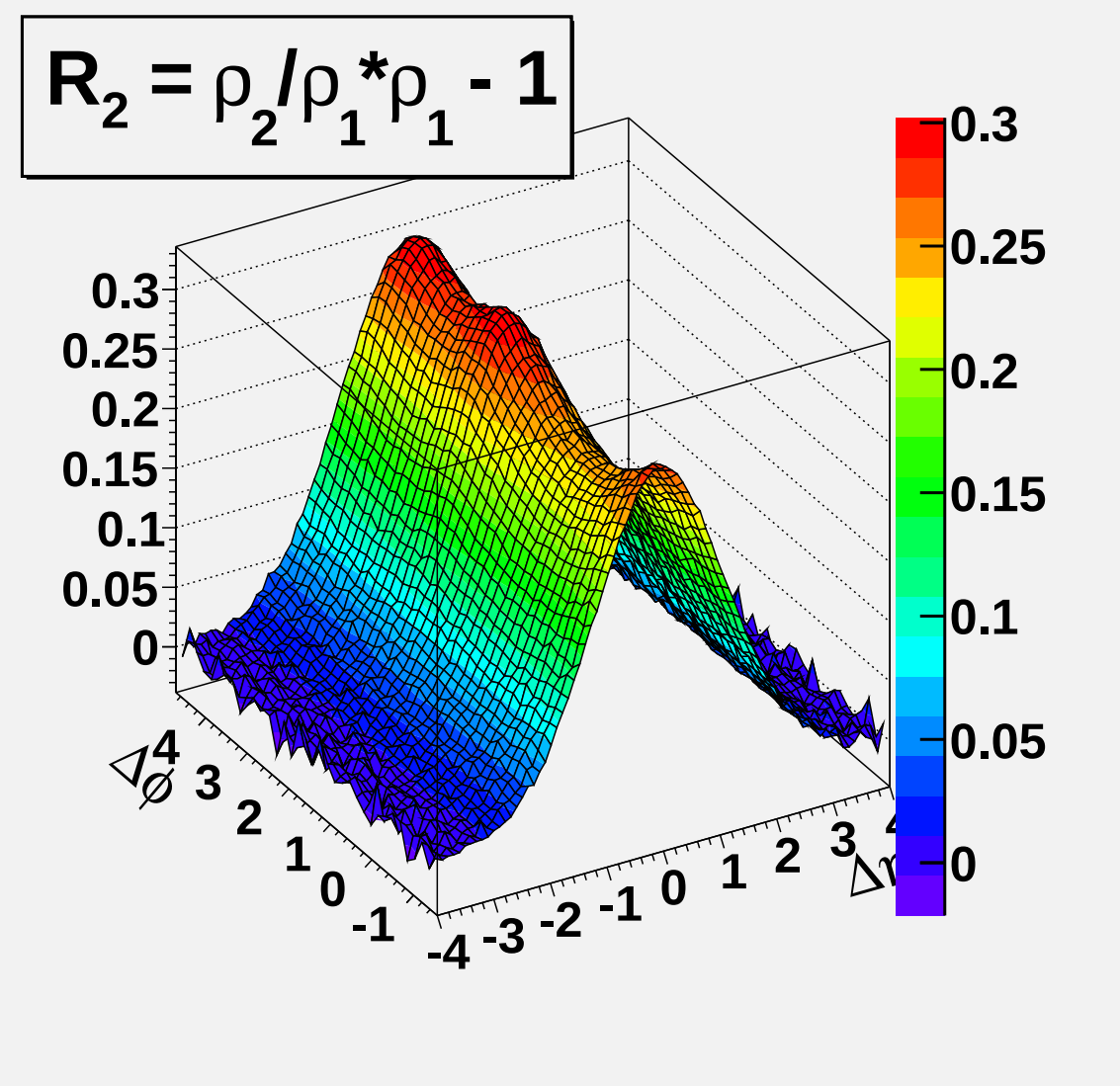

Figure 11.28: $R_2(\Delta\eta, \Delta\phi)$

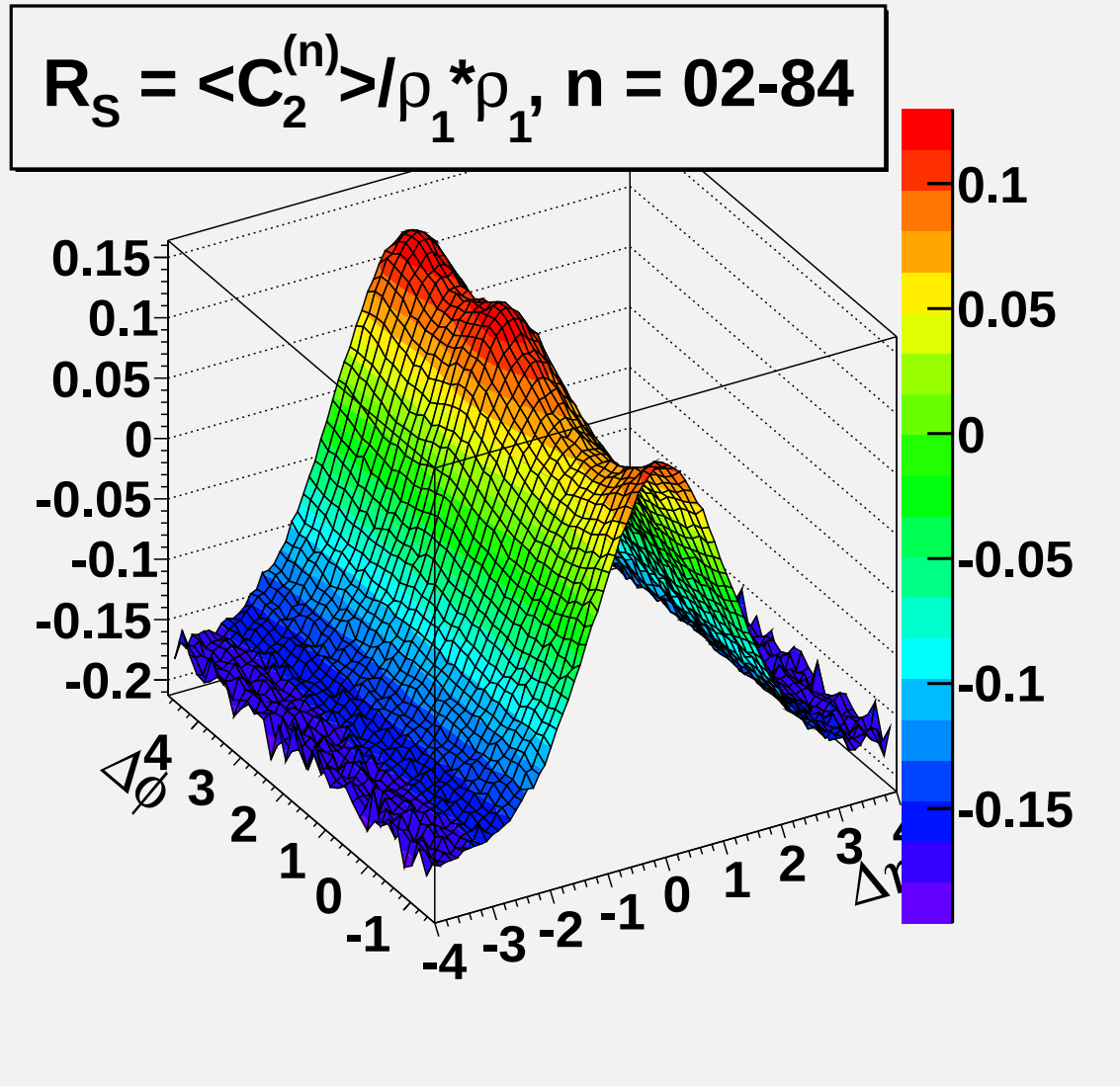

Figure 11.29: $R_S = \langle C_2^{(n)}(\Delta\eta, \Delta\phi)\rangle / \rho_1 * \rho_1(\Delta\eta, \Delta\phi)$

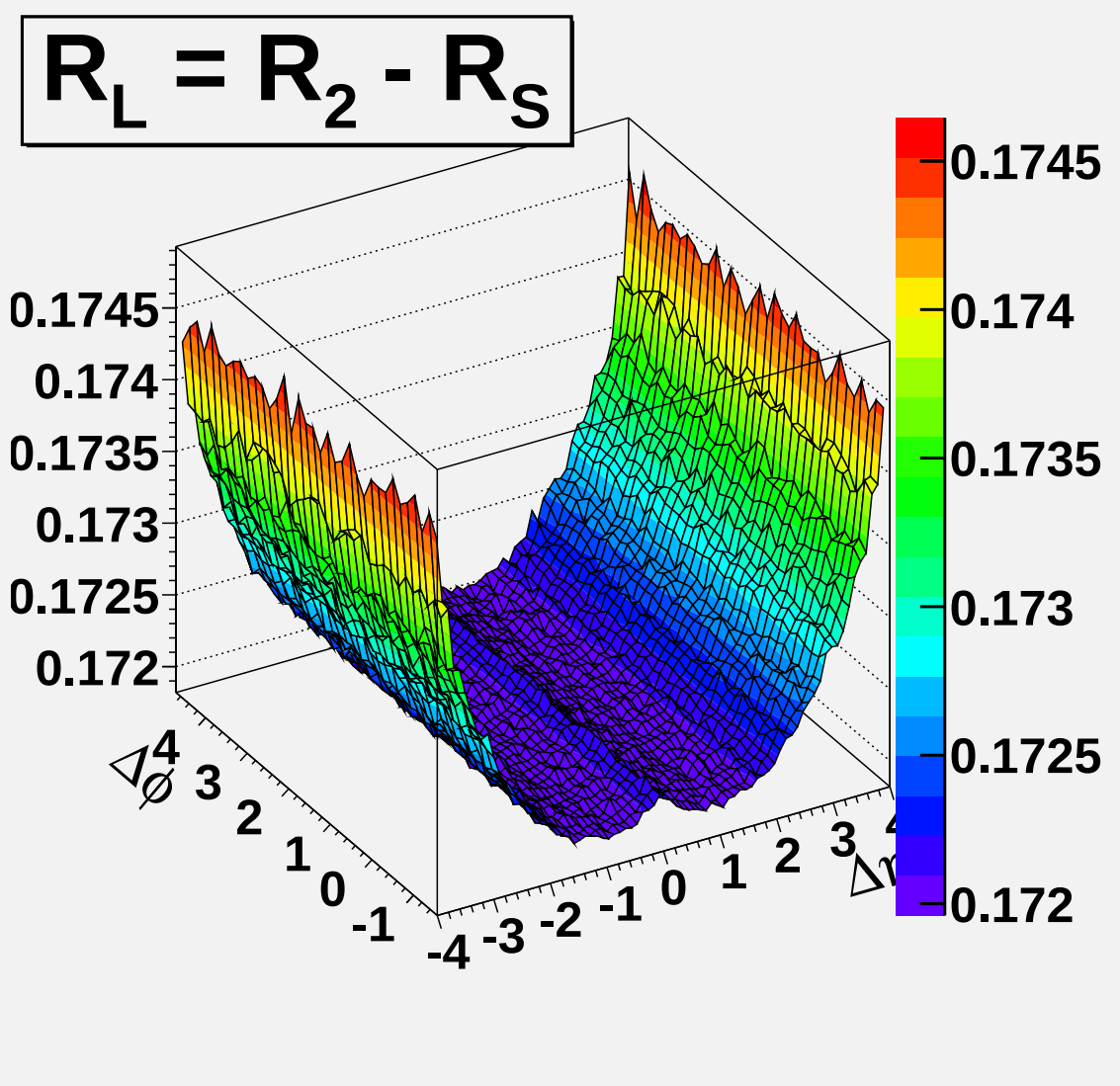

Figure 11.30: $R_L = R_2(\Delta\eta, \Delta\phi) - \langle C_2^{(n)}(\Delta\eta, \Delta\phi)\rangle / \rho_1 * \rho_1(\Delta\eta, \Delta\phi)$

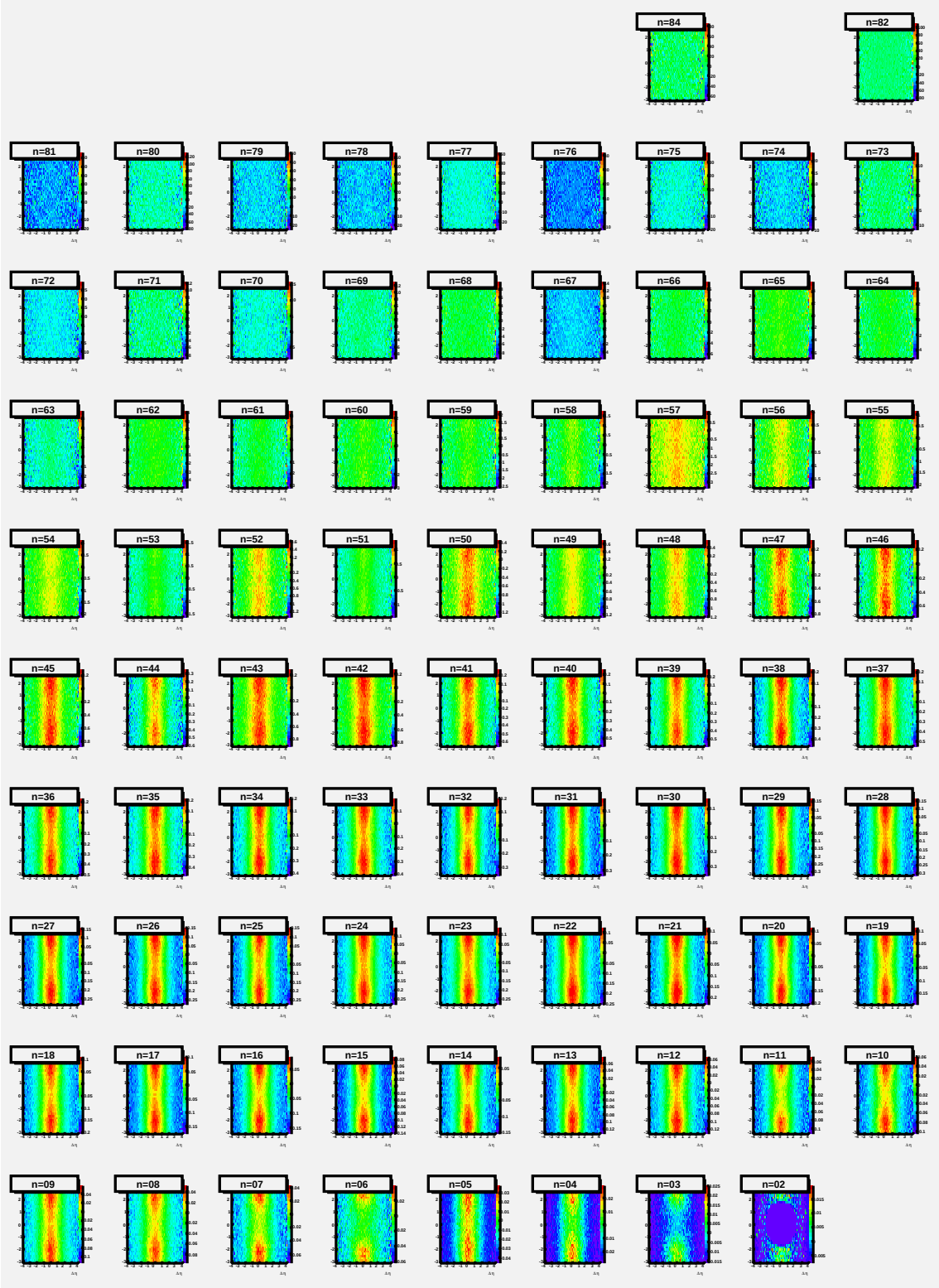

Figure 11.31: $R_2^{(n)} = C_2^{(n)}(\Delta\eta, \Delta\phi)/\rho_1 * \rho_1(\Delta\eta, \Delta\phi)$

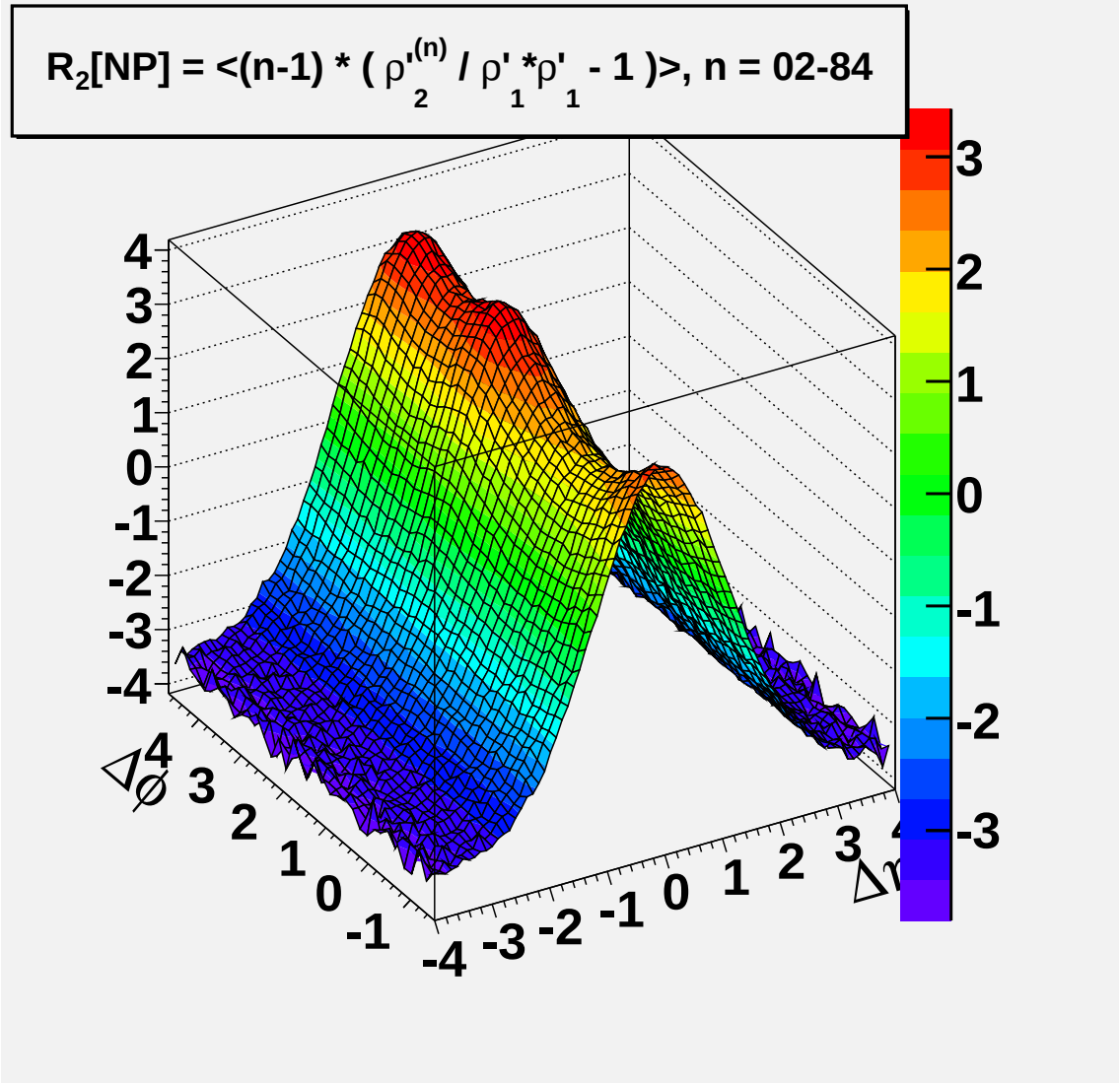

Figure 11.32: $\langle R_2^{(n)}[NP](\Delta\eta, \Delta\phi)\rangle$

11.5 $p + p$ (4b)

Same as pp4a, but the boost is applied collectively to all clusters in a collision, rather than individually.

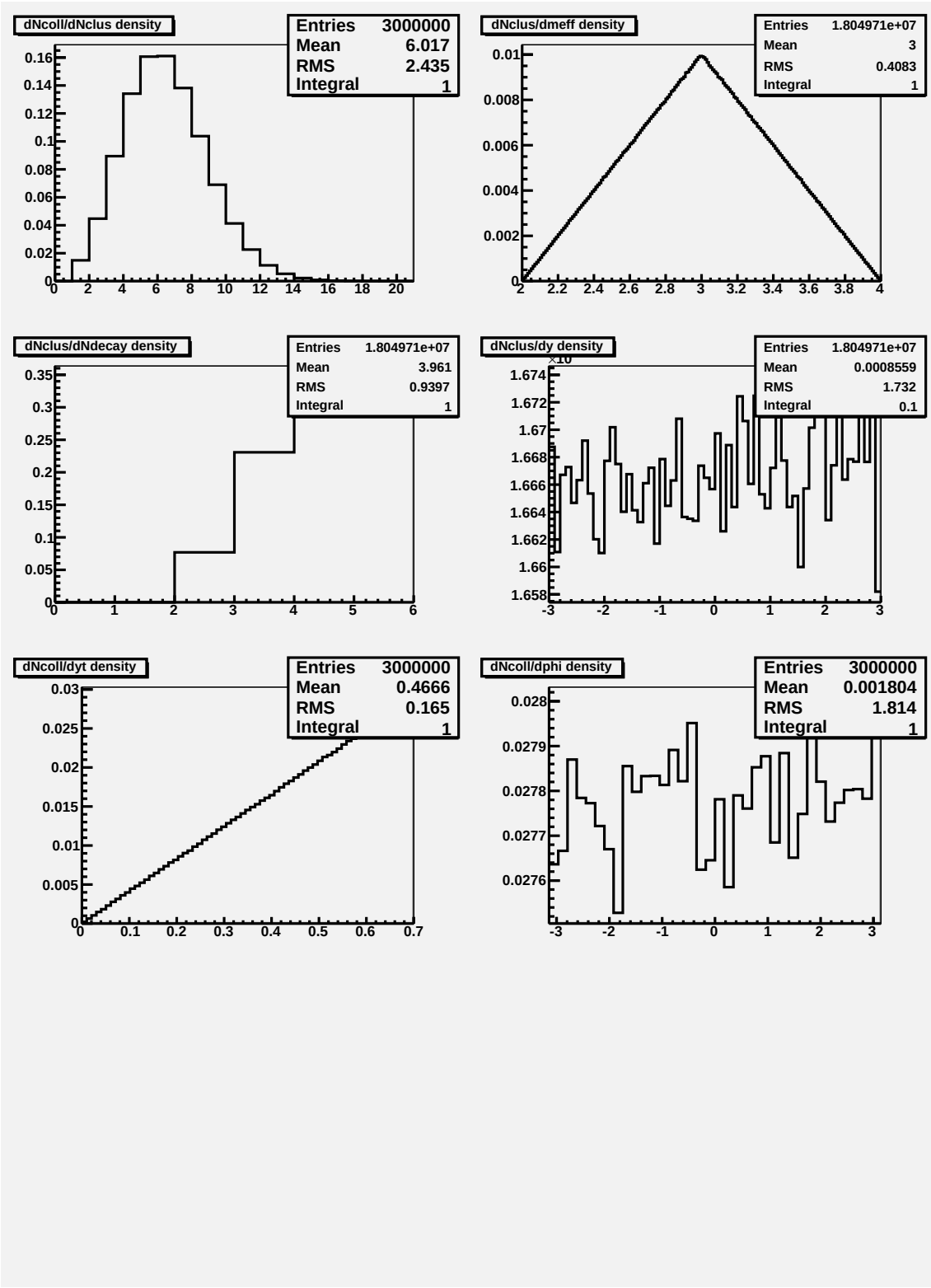
dNcoll/dNclus density
Entries 3000000
Mean 6.017
RMS 2.435
Integral 1
dNclus/dmeff density
Entries 1.804971e+07
Mean 3
RMS 0.4083
Integral 1
dNclus/dNdecay density
Entries 1.804971e+07
Mean 3.961
RMS 0.9397
Integral 1
dNclus/dy density
Entries 1.804971e+07
Mean 0.0008559
RMS 1.732
Integral 0.1
dNcoll/dyt density
Entries 3000000
Mean 0.4666
RMS 0.165
Integral 1
dNcoll/dphi density
Entries 3000000
Mean 0.001804
RMS 1.814
Integral 1

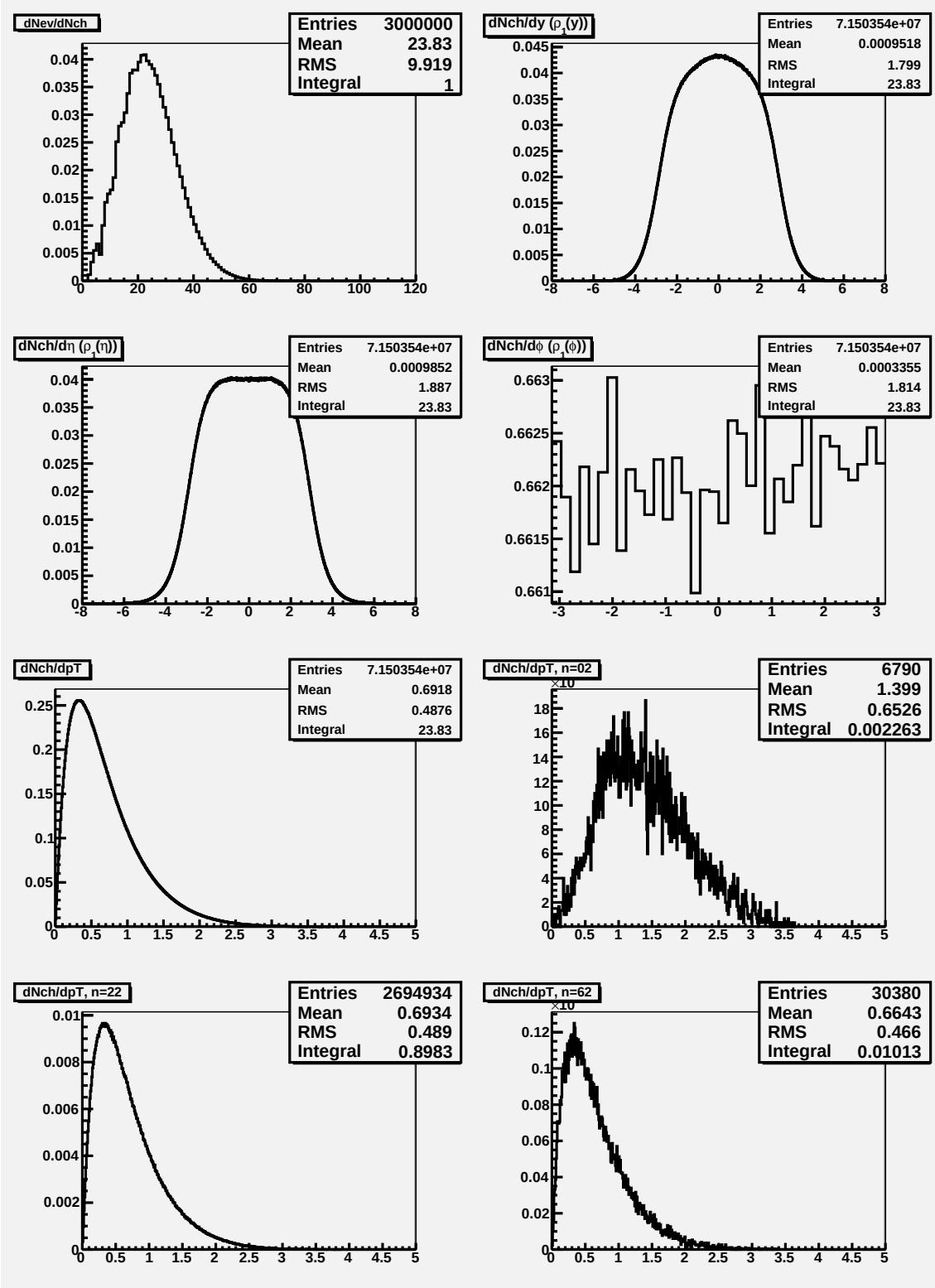
dNev/dNch
Entries 3000000
Mean 23.83
RMS 9.919
Integral 1
dNch/dy (ρ1(y))
Entries 7.150354e+07
Mean 0.0009518
RMS 1.799
Integral 23.83
dNch/dη (ρ1(η))
Entries 7.150354e+07
Mean 0.0009852
RMS 1.887
Integral 23.83
dNch/dφ (ρ1(φ))
Entries 7.150354e+07
Mean 0.0003355
RMS 1.814
Integral 23.83
dNch/dpT
Entries 7.150354e+07
Mean 0.6918
RMS 0.4876
Integral 23.83
dNch/dpT, n=02
Entries 6790
Mean 1.399
RMS 0.6526
Integral 0.002263
dNch/dpT, n=22
Entries 2694934
Mean 0.6934
RMS 0.489
Integral 0.8983
dNch/dpT, n=62
Entries 30380
Mean 0.6643
RMS 0.466
Integral 0.01013

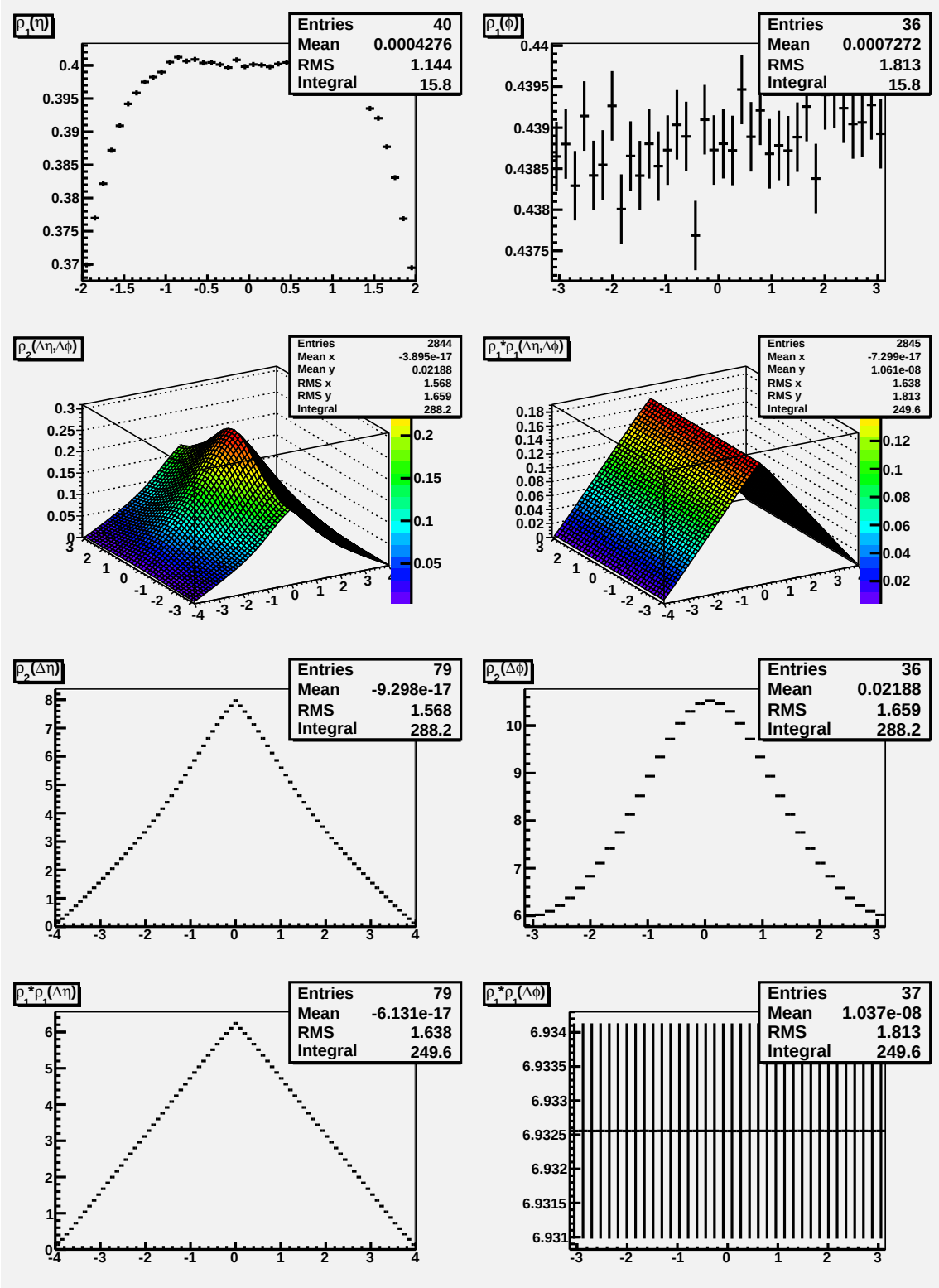
ρ1(η)
Entries 40
Mean 0.0004276
RMS 1.144
Integral 15.8
ρ1(φ)
Entries 36
Mean 0.0007272
RMS 1.813
Integral 15.8
ρ2(Δη,Δφ)
Entries 2844
Mean x -3.895e-17
Mean y 0.02188
RMS x 1.568
RMS y 1.659
Integral 288.2
ρ1*ρ1(Δη,Δφ)
Entries 2845
Mean x -7.299e-17
Mean y 1.061e-08
RMS x 1.638
RMS y 1.813
Integral 249.6
ρ2(Δη)
Entries 79
Mean -9.298e-17
RMS 1.568
Integral 288.2
ρ2(Δφ)
Entries 36
Mean 0.02188
RMS 1.659
Integral 288.2
ρ1*ρ1(Δη)
Entries 79
Mean -6.131e-17
RMS 1.638
Integral 249.6
ρ1*ρ1(Δφ)
Entries 37
Mean 1.037e-08
RMS 1.813
Integral 249.6

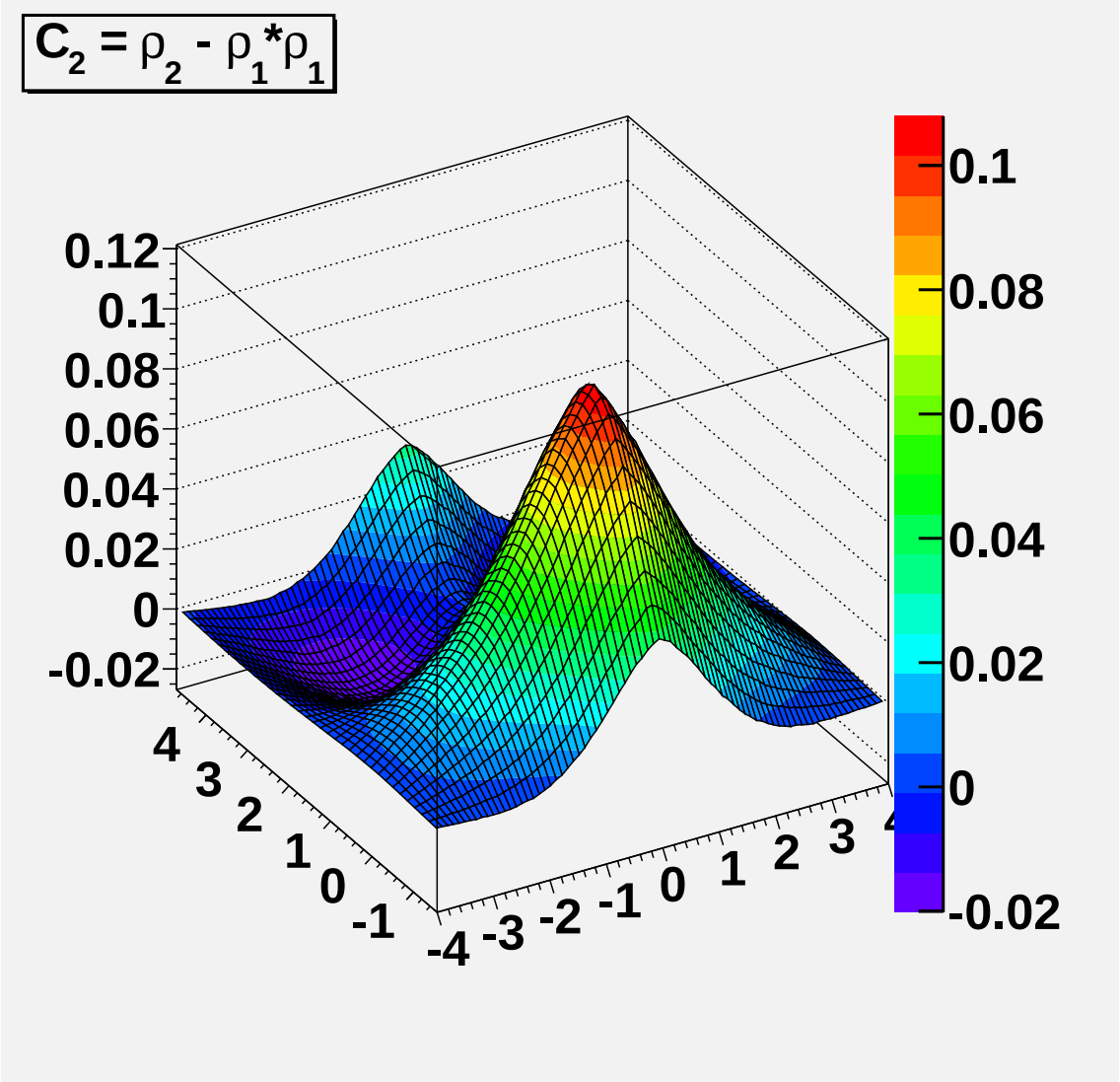

Figure 11.33: $C_2(\Delta\eta, \Delta\phi)$

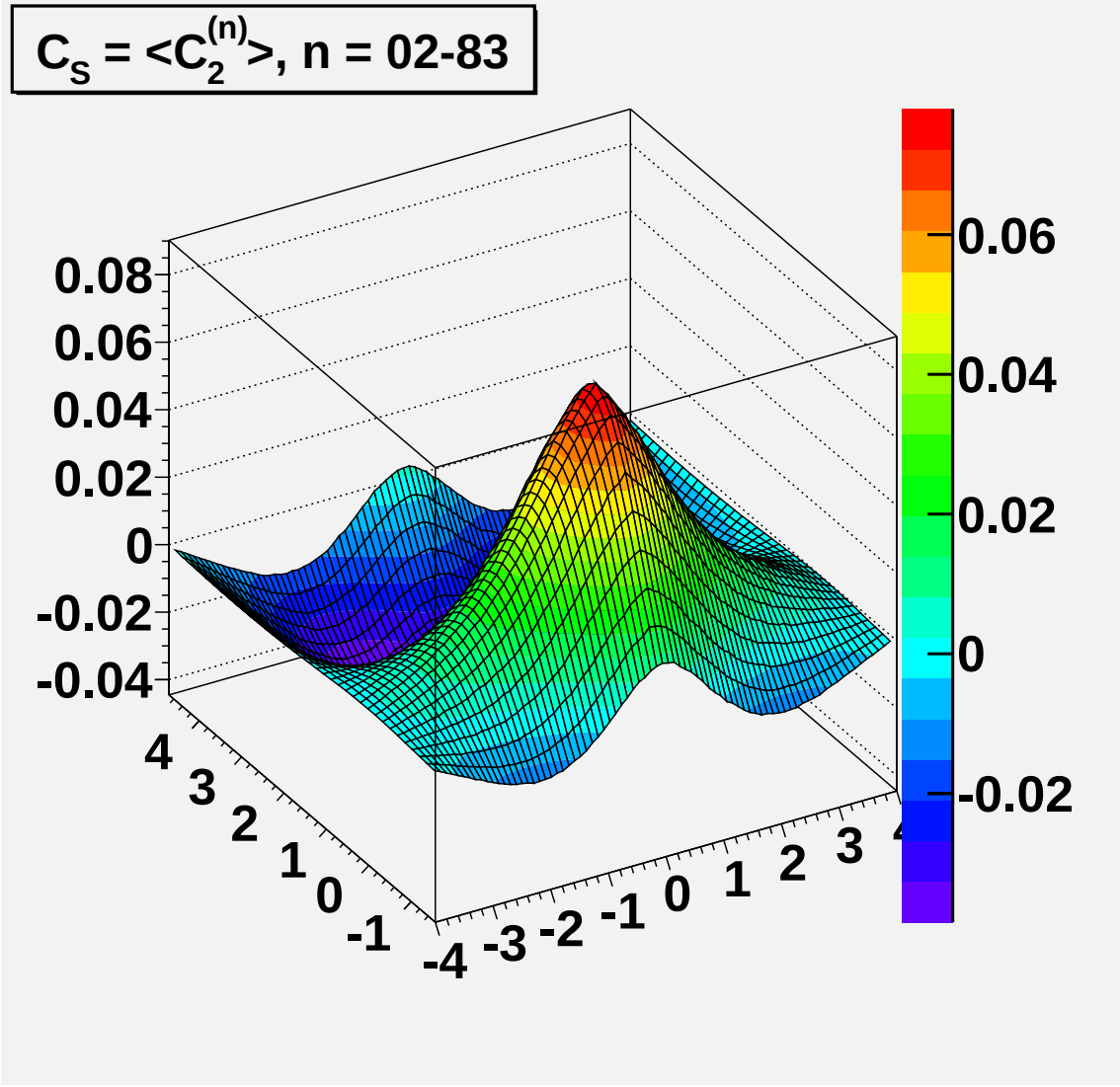

Figure 11.34: $C_S = \langle C_2^{(n)}(\Delta\eta, \Delta\phi)\rangle$

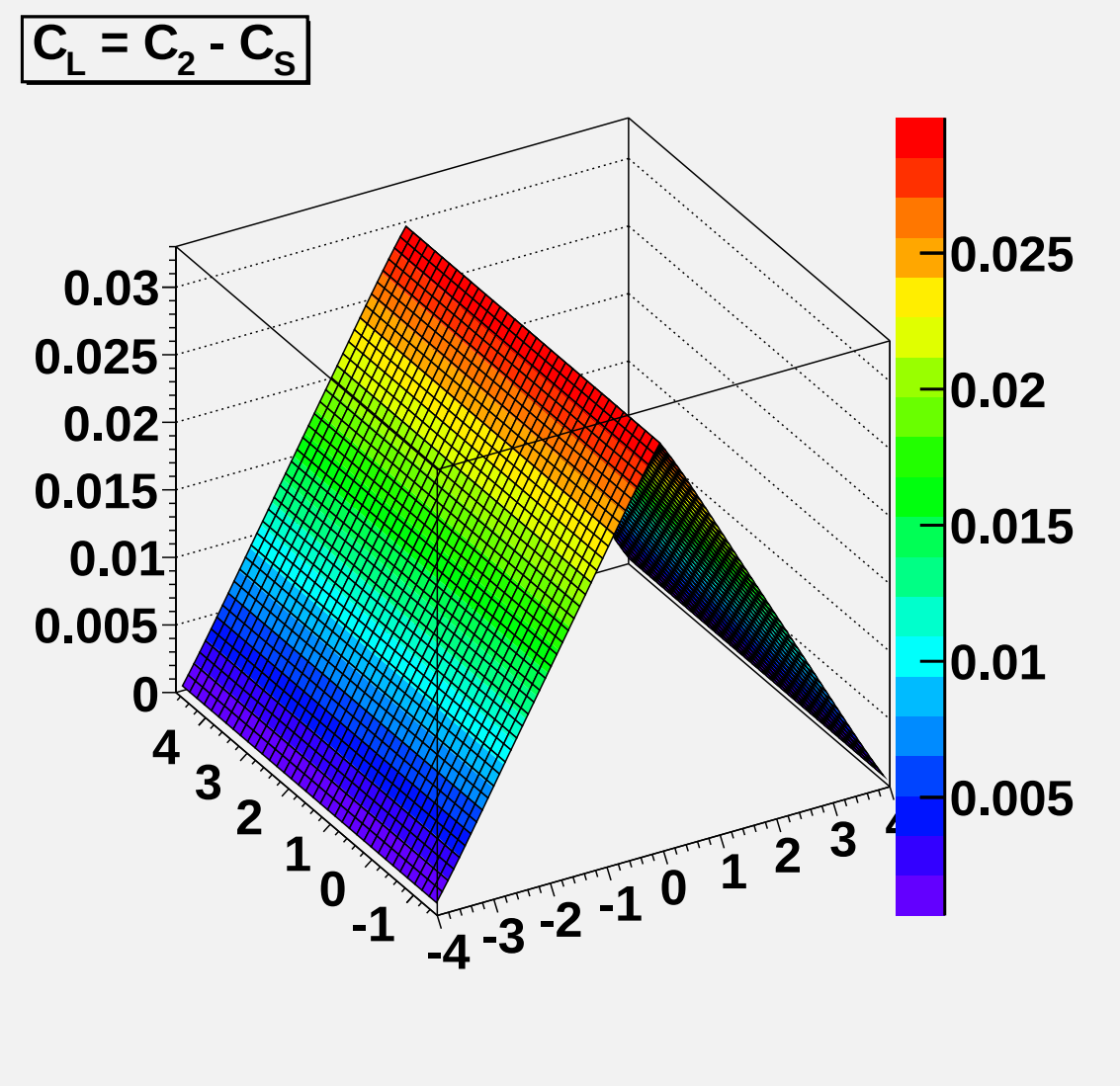

Figure 11.35: $C_L = C_2(\Delta\eta, \Delta\phi) - \langle C_2^{(n)}(\Delta\eta, \Delta\phi)\rangle$

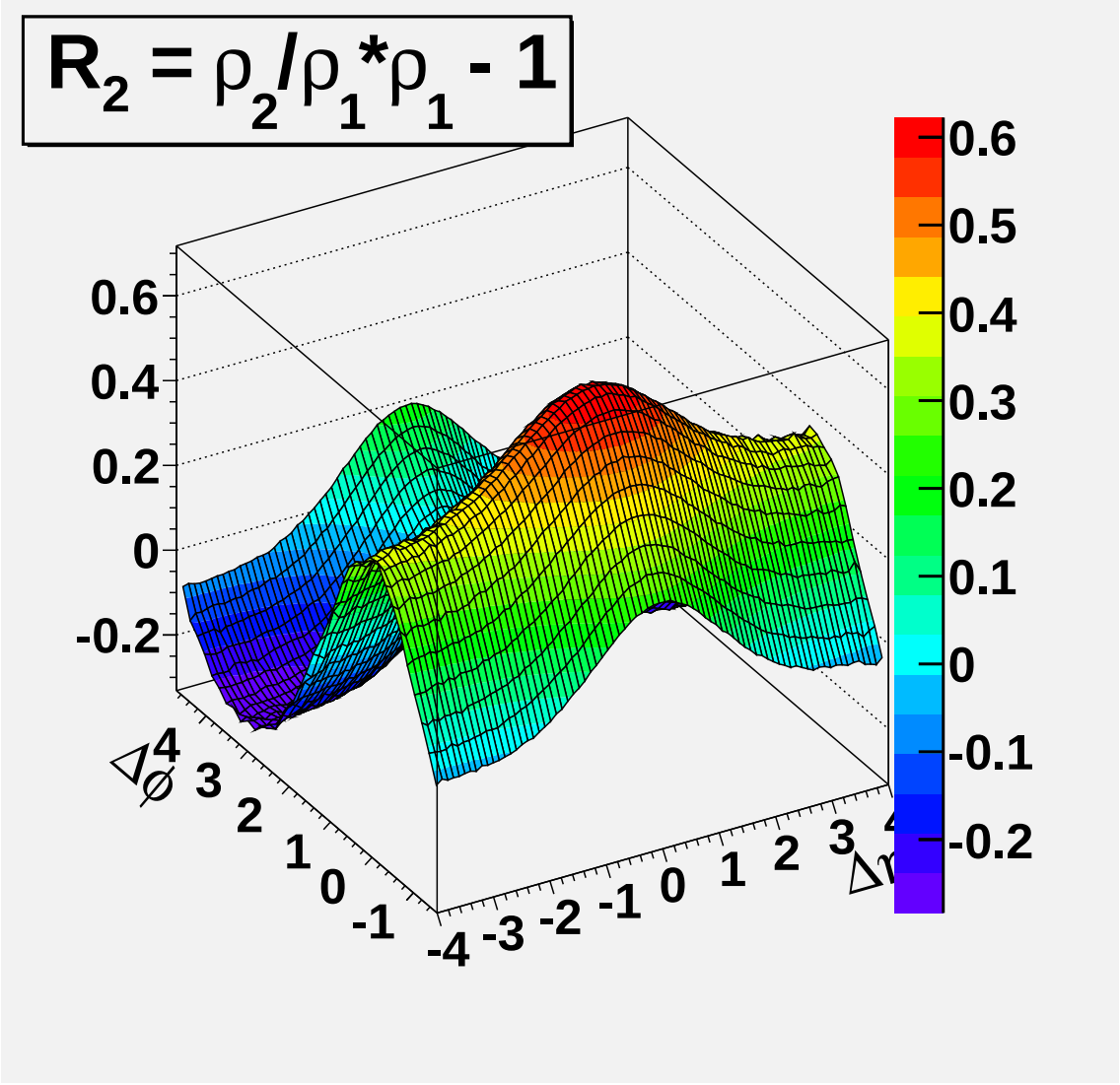

Figure 11.36: $R_2(\Delta\eta, \Delta\phi)$

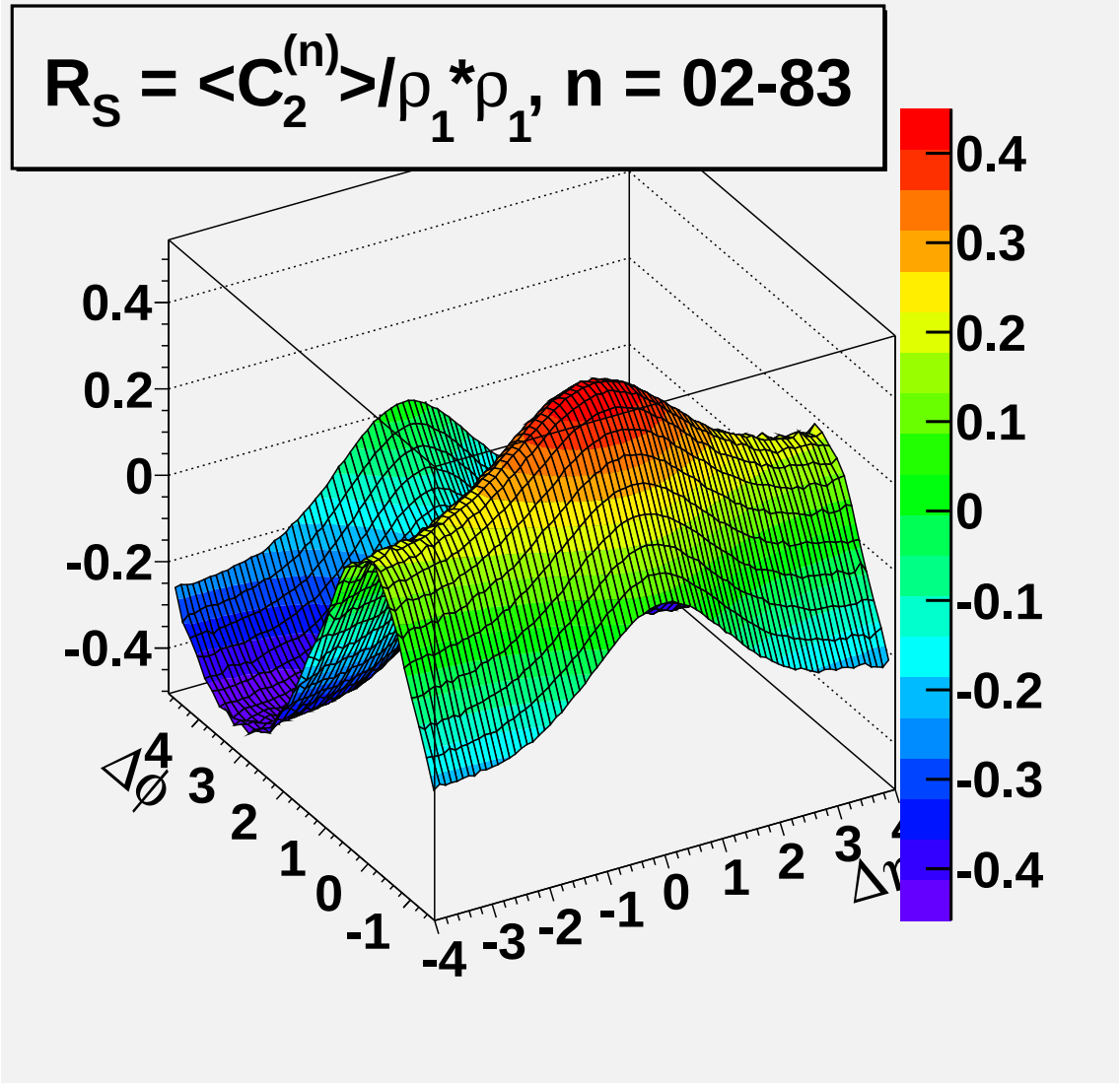

Figure 11.37: $R_S = \langle C_2^{(n)}(\Delta\eta, \Delta\phi)\rangle / \rho_1 * \rho_1(\Delta\eta, \Delta\phi)$

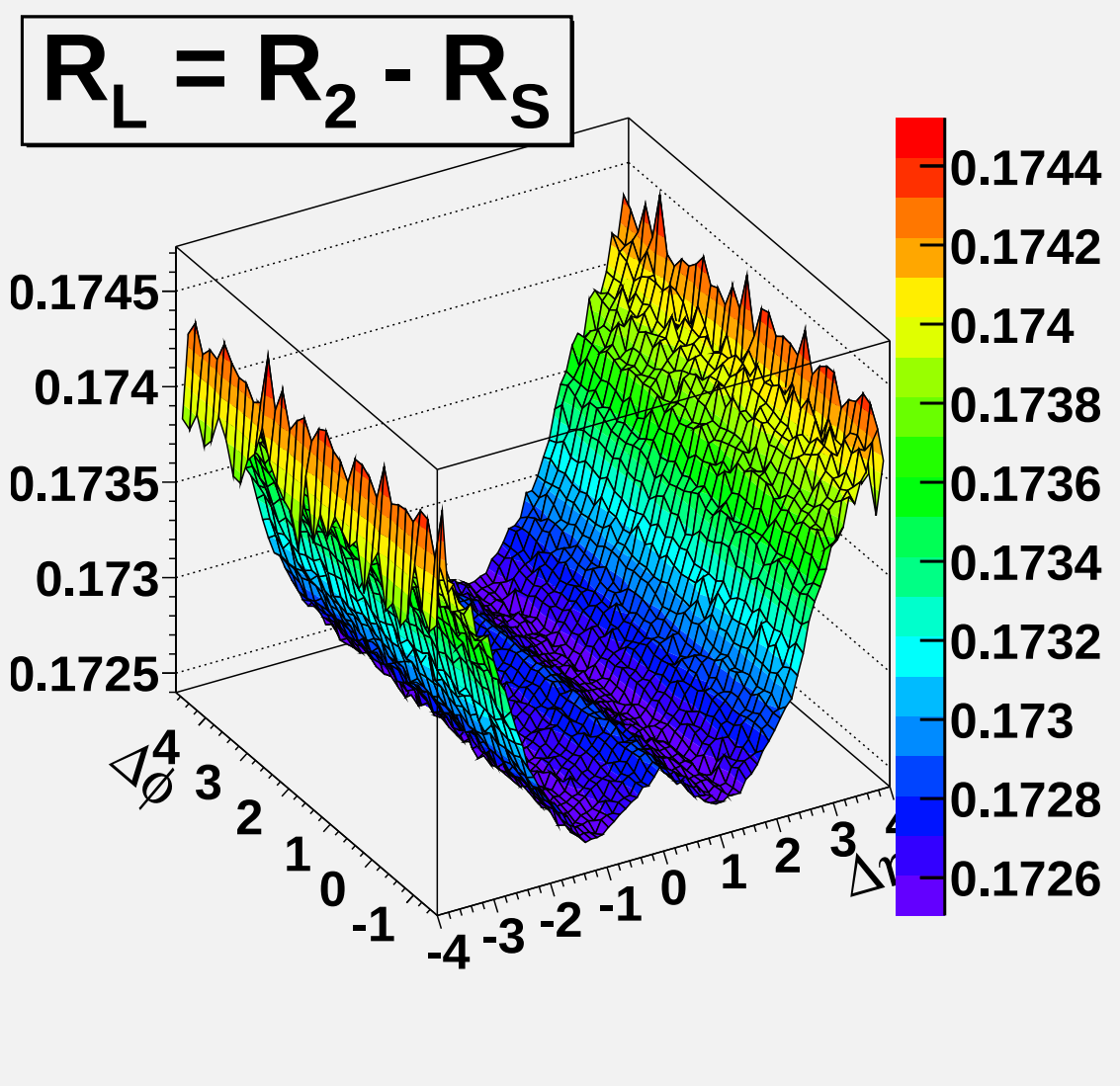

Figure 11.38: $R_L = R_2(\Delta\eta, \Delta\phi) - \langle C_2^{(n)}(\Delta\eta, \Delta\phi)\rangle / \rho_1 * \rho_1(\Delta\eta, \Delta\phi)$

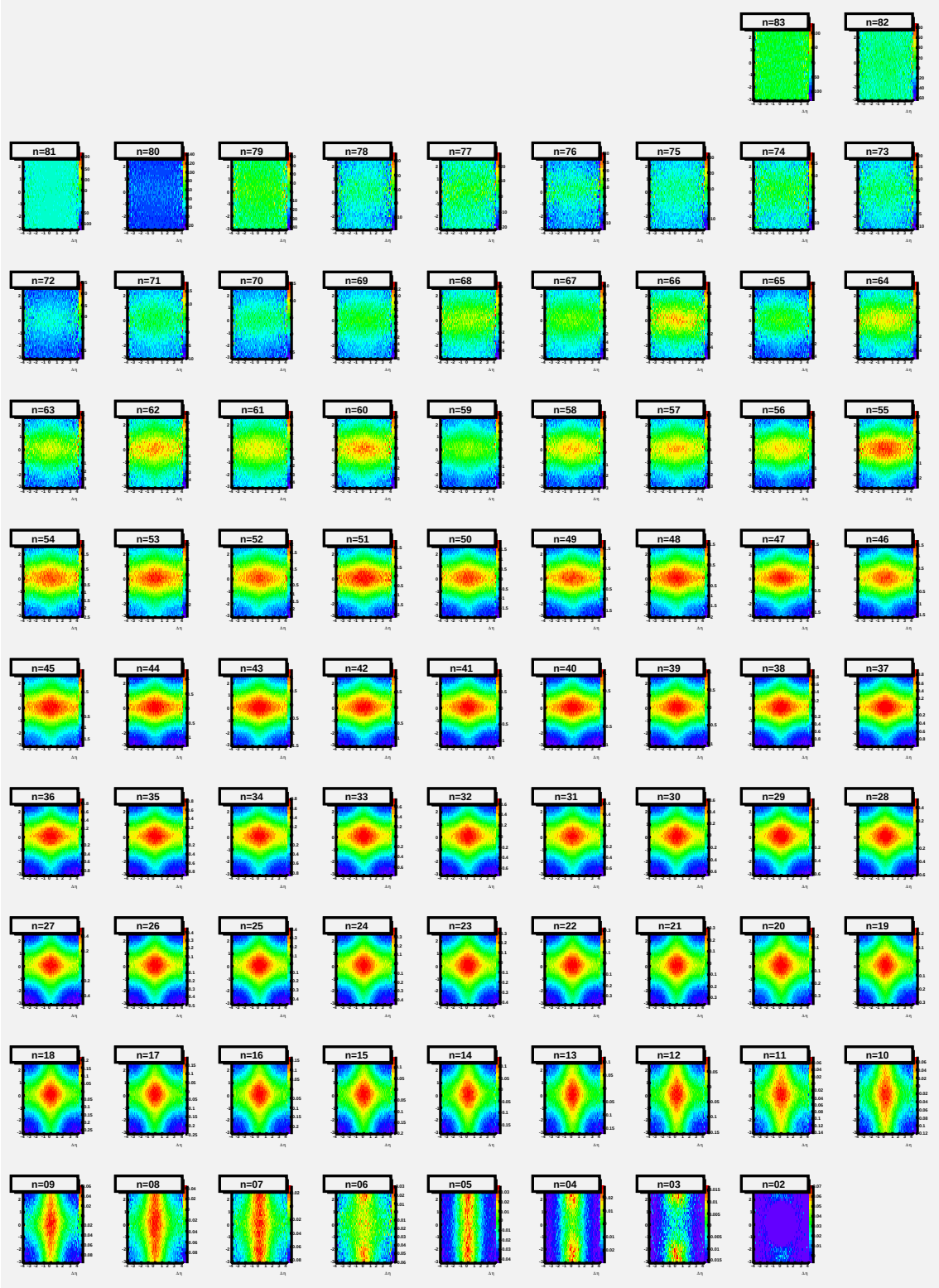

Figure 11.39: $R_2^{(n)} = C_2^{(n)}(\Delta\eta, \Delta\phi)/\rho_1 * \rho_1(\Delta\eta, \Delta\phi)$

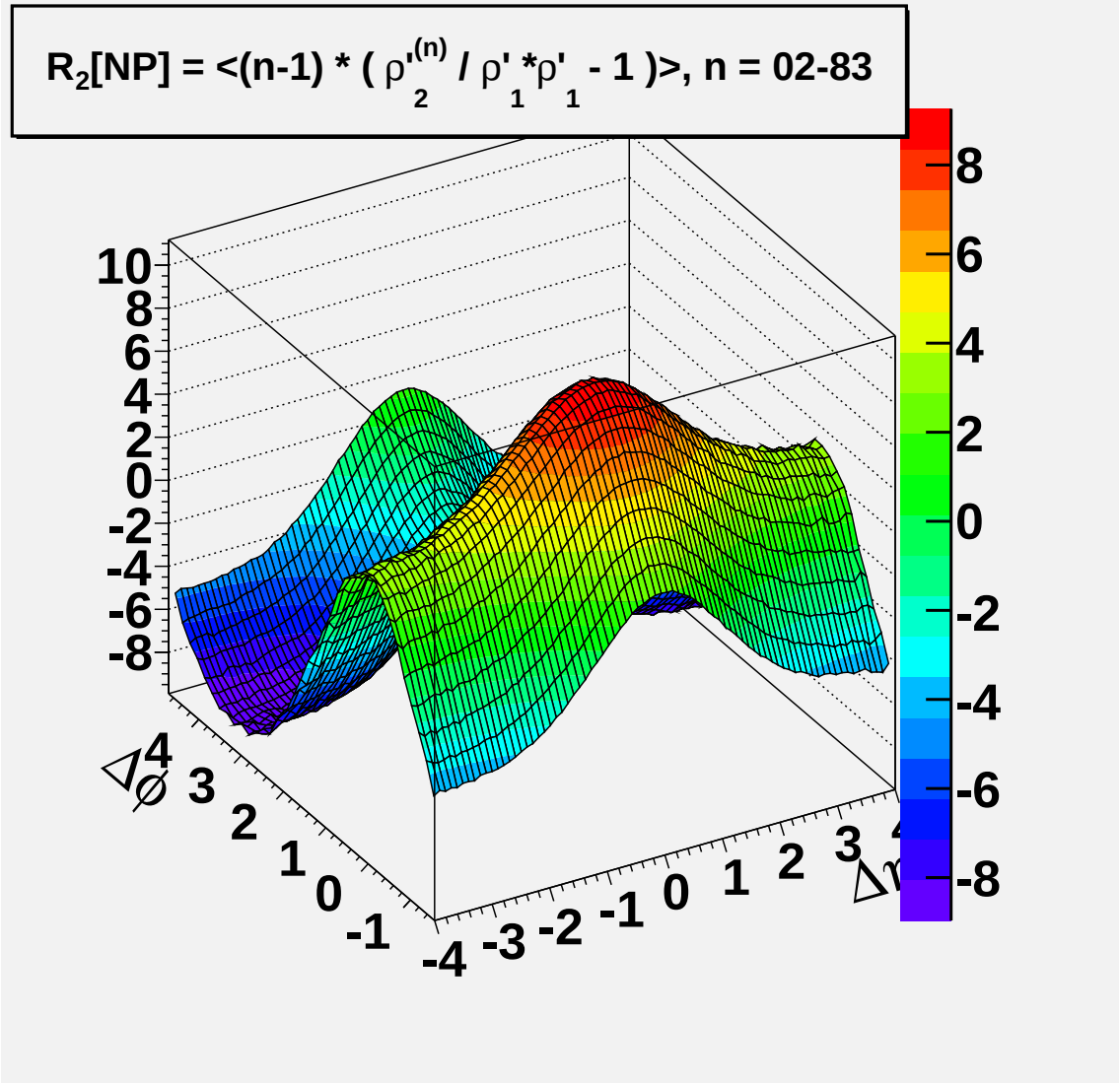

Figure 11.40: $\langle R_2^{(n)}[NP](\Delta\eta, \Delta\phi)\rangle$

BIBLIOGRAPHY

[1] K. Huang, *Quarks, Leptons and Gauge Fields*. World Scientific, 1992.

[2] F. Halzen and A. Martin, *Quarks and Leptons*. Wiley, 1984.

[3] O. Greenberg, "Spin and Unitary-Spin Independence in a Paraquark Model of Baryons and Mesons," *Phys. Rev. Lett.* **13** (1964) 598602.

[4] J. Bernstein, *The Tenth Dimension*. McGraw-Hill, 1989.

[5] B. Muller and J. Nagle, "Results from the Relativistic Heavy Ion Collider," *Annu. Rev. Nucl. Sci.* **56** (2006) 93–135.

[6] L. Foà, "Inclusive Study of High-Energy Multiparticle Production and Two-Body Correlations," *Phys. Lett.* **C22** (1975) 1–56.

[7] H. Bøggild and T. Ferbel, "Inclusive Reactions," *Annu. Rev. Nucl. Sci.* **24** (1974) 451–514.

[8] T. Lee, "Abnormal nuclear states and vacuum excitation," *Phys. Rev. Lett.* **47** (1975) 267–275.

[9] E. Kolb and M. Turner, *The Early Universe*. Addison-Wesley, 1990.

[10] F. Karsch, "Lattice Results on QCD Thermodynamics," *Nucl. Phys.* **A698** (2002) 199.

[11] S. Katz, "Equation of State from Lattice QCD," *Nucl. Phys.* **A774** (2006) 159–168.

[12] K. Adcox *et al.*, (PHENIX collaboration), "Suppression of Hadrons with Large Transverse Momentum in Central Au+Au Collisions at $\sqrt{s_{NN}}$=130 GeV," *Phys. Rev. Lett.* **88** (2002) 022301.

[13] C. Adler *et al.*, (STAR collaboration), "Measurement of Inclusive Antiprotons from Au+Au Collisions at $\sqrt{s_{NN}}$=130 GeV," *Phys. Rev. Lett.* **87** (2001) 262302.

[14] I. Arsene *et al.*, (BRAHMS collaboration), "Quark Gluon Plasma an Color Glass Condensate at RHIC? The perspective from the BRAHMS experiment," *Nucl. Phys.* **A757** (2005) 1–27.

[15] B. B. Back *et al.*, (PHOBOS collaboration), "The PHOBOS perspective on discoveries at RHIC," *Nucl. Phys.* **A757** (2005) 28–101.

[16] J. Adams *et al.*, (STAR collaboration), "Experimental and theoretical challenges in the search for the quark gluon plasma: The STAR collaboration's critical assessment of the evidence from RHIC collisions," *Nucl. Phys.* **A757** (2005) 102–183.

[17] K. Adcox *et al.*, (PHENIX collaboration), "Formation of dense partonic matter in relativistic nucleus nucleus collisions at RHIC: Experimental evaluation by the PHENIX collaboration," *Nucl. Phys.* **A757** (2005) 184–283.

[18] J. Adams *et al.*, (STAR collaboration), "Evidence from d+Au measurements for final-state suppression of high-p_T hadrons in Au+Au collisions at RHIC," *Phys. Rev. Lett.* **91** (2003) 072304.

[19] N. Armesto *et al.*, "Measuring the Collective Flow with Jets," *Phys. Rev. Lett.* **93** (2004) 242301.

[20] A. Majumder, B. Muller, and S. A. Bass, "Longitudinal Broadening of Quenched Jets in Turbulent Color Fields," *Phys. Rev. Lett.* **99** (2007) 042301, arXiv:hep-ph/0611135.

[21] P. Romatschke, "Momentum broadening in an anisotropic plasma," *Phys. Rev.* **C75** (2007) 014901, arXiv:hep-ph/0607327.

[22] S. Voloshin, "Two particle rapidity, transverse momentum, and azimuthal correlations in relativistic nuclear collisions and transverse radial expansion," *Nucl. Phys.* **A749** (2005) 287.

[23] C. B. Chiu and R. C. Hwa, "Dependence of Ridge Formation on Trigger Azimuth: Correlated Emission Model," *Phys. Rev.* **C79** (2009) 034901, arXiv:0809.3018 [nucl-th].

[24] G. Moschelli, *Two-Particle Correlations and the Ridge in Relativistic Heavy Ion Collisions*. PhD thesis, 2009.

[25] S. Voloshin, "Transverse radial expansion in nuclear collisions and two particle correlations," *Phys. Lett.* **B632** (2006) 490–494.

[26] P. Jacobs and X.-N. Wang, "Matter *in extremis*: ultrarelativistic nuclear collisions at RHIC," *Prog. Part. Nucl. Phys.* **54** (2005) 443.

[27] M. Anderson *et al.*, "The STAR time projection chamber: a unique tool for studying high multiplicity events at RHIC," *Nucl. Instr. Meth.* **A499** (2003) 659–678.

[28] K. Ackermann *et al.*, (STAR collaboration), "STAR Detector Overview," *Nucl. Instr. Meth.* **A499** (2003) 624–632.

[29] C. Adler *et al.*, "The RHIC Zero Degree Calorimeter," *Nucl. Instr. Meth.* **A470** (2001) 488.

[30] P. Carruthers, "Structure of Correlation Functions," *Phys. Rev.* **A43** (1991) 2632–2639.

[31] S. Gavin and M. Abdel-Aziz, "Measuring Shear Viscosity Using Transverse Momentum Correlations in Relativistic Nuclear Collisions," *Phys. Rev. Lett.* **97** (2006) 162302.

[32] M. Miller *et al.*, "Glauber Modeling in High-Energy Nuclear Collisions," *Annu. Rev. Nucl. Part. Sci.* **57** (2007) 205–43.

[33] R. Hanbury Brown and R. Twiss, "A Test of a New Type of Stellar Interferometer on Sirius," *Nature* **178** (1956) 1046.

[34] B. Alver and G. Roland, "Collision geometry fluctuations and triangular flow in heavy-ion collisions," *Phys. Rev.* **C81** (2010) 054905.

[35] H. Sorge, "Flavor Production in Pb(160AGeV) on Pb Collisions: Effect on Color Ropes and Hadronic Rescattering," *Phys. Rev.* **C52** (1995) 3291.

[36] R. Feynman, "Hypothesis of Limiting Fragmentation in High-Energy Collisions," *Phys. Rev. Lett.* **23** (1969) 1415.

ABSTRACT

CENTRALITY DEPENDENCE OF TWO-PARTICLE NUMBER AND TRANSVERSE MOMENTUM CORRELATIONS IN $\sqrt{s_{NN}} = 200$ GeV Au+Au COLLISIONS AT RHIC

by

LAURENCE TARINI

August 2011

Adviser: Dr. Sergei Voloshin

Major: Nuclear Physics

Degree: Doctor of Philosophy

We present plots of the pattern of particle formation in $\sqrt{s_{NN}} = 200$ GeV Au+Au heavy ion collisions at the Relativistic Heavy Ion Collider (RHIC) using three different two-particle correlation measurements of number and transverse momentum as a function of relative azimuth, pseudorapidity and centrality. All three observables show the onset with increasing centrality of a near-side "ridge" of enhanced correlations in pseudorapidity . The plots of real data are compared to plots of simulations using RQMD data and data from a simple "cluster" model. RQMD (relativistic quantum molecular dynamics) program uses a transport theoretical model of hadron collisions. The "cluster" dataset is a simplistic cartoon of a decay event involving an invariant mass that receives a longitudinal and then transverse Lorentz boost. The effect of radial flow on clusters is shown with a radial boost applied both collectively and to individual clusters. We find that the kinematic effect of radial flow in simulated cluster data produces a near-side "ridge" similar to that seen in the data.

AUTOBIOGRAPHICAL STATEMENT

Laurence Henry Tarini	born Detroit, MI, USA
father, Anteo John Tarini	born Pesaro, PU, Italia
mother, Grace Mullison Tarini	born Brush, CO, USA
1982 – 1984	B.A. Mathematics Columbia University New York NY
1984 – 1987	M.A. Mathematics University of California Berkeley CA
2005 – 2011	Ph.D. Physics Wayne State University Detroit MI